

STABLE ISOTOPE SYSTEMATICS OF CALCITE

by

ELLEN K. OLSEN

A DISSERTATION

Presented to the Department of Earth Sciences
and the Division of Graduate Studies of the University of Oregon
in partial fulfillment of the requirements
for the degree of
Doctor of Philosophy

June 2023

DISSERTATION APPROVAL PAGE

Student: Ellen K. Olsen

Title: Stable Isotope Systematics of Calcite

This dissertation has been accepted and approved in partial fulfillment of the requirements for the Doctor of Philosophy degree in the Department of Earth Sciences by:

James M. Watkins	Chairperson/Advisor
Mark H. Reed	Core Member
Paul J. Wallace	Core Member
Daniel G. Gavin	Institutional Representative

and

Krista Chronister	Vice Provost for Graduate Studies
-------------------	-----------------------------------

Original approval signatures are on file with the University of Oregon Division of Graduate Studies.

Degree awarded June 2023

© 2023 Ellen K. Olsen

DISSERTATION ABSTRACT

Ellen K. Olsen

Doctor of Philosophy

Department of Earth Sciences

June 2023

Title: Stable Isotope Systematics of Calcite

The oxygen isotopic composition of calcite is widely used in paleoclimate studies to infer the temperatures of carbonate formation across a wide range of geologic environments including hydrothermal veins, caves, lakes, surface oceans, and in marine sediments.

Carbonate-based temperature reconstructions depend on empirical $\delta^{18}\text{O}$ - T relationships that are affected by factors such as carbonate growth rate, solution composition, pH, and source(s) of dissolved inorganic carbon (DIC). We carried out calcite growth experiments over a range of pH (7.5-12.8), temperature ($T = 10$ - 25°C), ionic strength ($I = 0.1$ - 1.6 ; $[\text{NaCl}] = 0$ - 1.4 M) and concentration of the enzyme carbonic anhydrase ($[\text{CA}] = 0$ - 3 μM).

The enzyme CA promotes isotopic equilibration of the DIC pool, which in turn, has a strong influence on the isotopic composition of the mineral. We divide the experimental results into two categories: (1) calcite grown from an equilibrated DIC pool, and (2) calcite grown from a non-equilibrated DIC pool. Results from (1) are used to determine the kinetic isotope effects (KIEs) attending the crystal growth reaction as a function of pH and ionic strength. No evidence of an ionic strength effect on oxygen isotope partitioning between calcite and DIC was found for NaCl concentrations up to 0.35 M, but in higher ionic strength solutions, NaCl was found to inhibit the efficacy of CA and prevent complete isotopic equilibration of the DIC pool, resulting in lower and more variable oxygen isotope fractionations. The oxygen isotope partitioning between calcite and water was found to systematically decrease with increasing pH. Results from (2) are used to determine the KIEs attending the CO_2 hydration and hydroxylation reactions as a function of T , pH, ionic strength and $[\text{CA}]$. This study is the first to separately quantify

the kinetic fractionation factors (KFFs) for CO_2 and OH^- separately during CO_2 hydroxylation. The experimental results have been used to develop a generalizable model of oxygen isotope effects in the CaCO_3 -DIC- H_2O system. The model can be used to predict the $\delta^{18}\text{O}$ of calcites grown from variably-equilibrated DIC pools and can explain why different experimental setups have yielded different $\delta^{18}\text{O}$ - T relationships for inorganic calcite.

This dissertation includes previously published and unpublished co-authored material.

CURRICULUM VITAE

NAME OF AUTHOR: Ellen K. Olsen

GRADUATE AND UNDERGRADUATE SCHOOLS ATTENDED:

University of Oregon, Eugene

Western Washington University, Bellingham, WA

DEGREES AWARDED:

Doctor of Philosophy, Earth Sciences, 2023, University of Oregon

Bachelor of Science, Geology, Thesis Option, 2015, Western Washington
University

AREAS OF SPECIAL INTEREST:

Isotope Geochemistry

Experimental Petrology

Paleoclimate

PROFESSIONAL EXPERIENCE:

Graduate Employee, University of Oregon, 2016-2022

Research Assistant, Western Washington University, 2016

GRANTS, AWARDS, AND HONORS:

Earth Sciences Research Recognition Award, University of Oregon, 2022

Geological Society of America Graduate Student Research Grant, 2021-2022

Central Oregon Geoscience Society Student Research Grant, 2021-2022

UO General University Scholarship, University of Oregon, 2021-2022

Marthe E. Smith Memorial Scholarship, University of Oregon, 2021-2022

Earth Sciences Good Citizen Award, 2021
Harvey E Lee Grad Scholarship, University of Oregon, 2020-2021
ArtSci Oregon Research as Art Exhibition winner, University of Oregon, 2020
Baldwin Scholarship, University of Oregon, 2018-2019
Marthe E. Smith Memorial Scholarship, University of Oregon, 2017-2018
Elma Hendricks Scholarship, University of Oregon, 2017-2018
Johnston Scholarship, University of Oregon, 2016-2017
Department of Geology Outstanding Graduate Award, Western Washington
University, 2014-2015
Geology Department Advance for Research, Western Washington University,
2013-2014
Research and Sponsored Programs Undergraduate Student Grant, Western
Washington University, 2013-2014
Skagit Rock and Gem Club Scholarship, 2013-2014
James L. Talbot Scholarship, Western Washington University, 2012-2013
President's Scholarship, Western Washington University 2011-2013

PUBLICATIONS:

- Olsen, E.K.**, Watkins, J.M., and Devriendt, L.S. (2022). Oxygen isotopes of calcite precipitated at high ionic strength: CaCO₃-DIC fractionation and carbonic anhydrase inhibition. *Geochimica et Cosmochimica Acta* 325, 170-186.
- Devriendt, L.S., Mezger, E.M., **Olsen, E.K.**, Watkins, J.M., Kaczmarek, K., Nehrke, G., de Nooijer, L.J., and Reichart, G.-J. (2021). Sodium incorporation into inorganic CaCO₃ and implications for biogenic carbonates. *Geochimica et Cosmochimica Acta* 314, 294-312.

ACKNOWLEDGMENTS

I am incredibly grateful to my adviser, James Watkins, for his support, patience, and mentorship that have helped me become a better scientist. Thank you, Jim, for always providing encouragement and quality pep talks when I needed them. Thank you to Mark Reed for insightful aqueous geochemistry conversations and for providing a bounty of neat rocks to look at. I would also like to sincerely thank Paul Wallace and Daniel Gavin for their insights and feedback. Thank you to Marla Trox, Dave Stemple, and Sandy Thoms, as well the UO Earth Sciences department, for their support in getting to the finish line. Thank you to Andrew Ross and Jennifer McKay at the OSU CEOAS Stable Isotope Laboratory, and James Palandri at the UO Stable Isotope Laboratory for isotope analyses and helpful technical conversations over the years. Special thanks to Edward Vinis for help with modifying the experimental design and conducting early experiments of Chapter V. I am so grateful for the intellectual discussions, collaboration, support, and camaraderie of my lab mates over the years, with particular thanks to Marisa Acosta, Molly Pickerel, Laurent Devriendt, and Edward Vinis. I cannot thank my friends enough for their insightful geologic conversations, as well as endless support, without which this would not have been possible. Special thanks to those from my original cohort, including Anne Fulton, Michelle Muth, and Michael Hudak, as well those met along the journey, with particular recognition for Ryan Seward, Kellum Tate-Jones, Annika Dechert, Christina Cauley, and Kate Scholz. Thank you to my mom, my dad, my sister, and my aunts, for all of their support and encouragement. And finally, a very special thanks to my cat, Crumpet. This research was supported by NSF grant no. EAR1749183 awarded to J.M. Watkins.

For Crumpet

TABLE OF CONTENTS

Chapter	Page
I. INTRODUCTION.....	19
II. CaCO ₃ -DIC-H ₂ O SYSTEM BACKGROUND.....	22
1. Carbonates in Seawater	22
1.1 Seawater Composition and pH.....	23
2. Isotopic Fractionation.....	24
2.1 Equilibrium vs. Kinetic Fractionation.....	24
2.2 Isotope and Fractionation Factor Notation.....	25
2.3 $\delta^{13}\text{C}$ and $\delta^{18}\text{O}$ of Common Geologic Reservoirs.....	26
3. Dissolved Inorganic Carbon Speciation.....	26
4. CaCO ₃ -DIC-H ₂ O Chemical Reactions and Isotopic Fractionations	30
4.1 CO ₂ Dissolution.....	31
4.2 CO ₂ (De)hydration and (De)hydroxylation.....	31
4.3 HCO ₃ ⁻ (De)protonation	34
4.4 CaCO ₃ Precipitation/Dissolution	36
4.5 H ₂ O Dissociation	37
5. Isotopic Composition of Calcite	38
5.1 Oxygen Isotopes: $\delta^{18}\text{O-T}$	38
5.2 Clumped isotopes: $\Delta_{47}\text{-T}$	40
6. Paleoenvironment Applications.....	40

Chapter	Page
6.1 Trace Elements	42
7. Bridge	44
III. OXYGEN ISOTOPES OF CALCITE PRECIPITATED AT HIGH IONIC STRENGTH: CaCO ₃ -DIC FRACTIONATION AND CARBONIC ANHYDRASE INHIBITION	45
1. Introduction	45
2. Methods	46
2.1 Calcite Growth Experiments	46
2.2 $\delta^{18}\text{O}$, $\delta^{13}\text{C}$, and [DIC] Measurements	50
3. Results	51
3.1 Oxygen Isotope Fractionation	51
4. Model for Calcite Growth from a DIC Pool with Variable Level of Isotopic Equilibration.....	53
4.1 Chemical Reactions	55
4.2 CaCO ₃ Flux.....	56
4.3 CO ₂ Flux.....	58
5. Model Results	59
6. Discussion	61
6.1 The Effect of Ionic Strength on the Oxygen Isotope Fractionation Between Calcite and the EIC.....	61
6.2 The Origin of $\delta^{18}\text{O}_{\text{calcite}}$ Variability at High Ionic Strength.....	61
6.2.1 Effect of Dissolved Ions on $\delta^{18}\text{O}_{\text{w}}$	61

Chapter	Page
6.2.2 Effect of Ion Pairing on Oxygen Isotope Fractionation Between DIC Species and H ₂ O.....	61
6.2.3 Effect of DIC Speciation on $\delta^{18}\text{O}_{\text{calcite}}$	62
6.2.4 Effect of NaCl on the Kinetics of Catalyzed CO ₂ (De)hydration	62
7. Implications.....	64
7.1 Towards a General Model for Kinetic Oxygen Isotope Effects.....	64
7.2 Application to Marine Calcifiers	66
8. Summary.....	66
9. Bridge	67
 IV. EFFECT OF pH ON THE ISOTOPIC COMPOSITION OF CALCITE GROWN FROM CO ₂ -FED SOLUTIONS: EXPERIMENTS AND MODELING.....	 68
1. Introduction	68
2. Methods	69
3. Experimental Results	70
3.1 Carbon Isotopic Fractionation	75
3.2 Oxygen Isotopic Fractionation	77
4. Updating the Ion-by-Ion Model	78
5. Summary.....	84
6. Bridge	84

Chapter	Page
V. EXTREME ISOTOPIC FRACTIONATIONS IN CaCO_3 FROM A HYPERALKALINE SPRING ANALOG: QUANTIFYING KINETIC FRACTIONATIONS ATTENDING CO_2 HYDROXYLATION	86
1. Introduction	86
1.1 CO_2 Captured as CaCO_3	87
1.2 OH- H_2O Fractionation	89
1.3 Motivation.....	89
2. Methods	90
3. Results and Discussion.....	95
3.1 Experiment Results.....	95
3.1.1 CaCO_3 Precipitates.....	95
3.1.2 Impacting of Varying Experimental Parameters	96
3.2 Isotopic Results	99
3.2.1 CO_2 , DIC, and CaCO_3	99
3.2.2 Outliers.....	102
3.2.3 CaCO_3 Precipitated via CO_2 Hydroxylation.....	104
4. Box Model Approach	107
4.1 Model Assumptions.....	108
4.2 Concentrations	109
4.3 Isotopes	109
4.4 Comparison to Previous Work.....	111
5. CO_2 Hydroxylation KFFs	114
5.1 Complications and Possible Causes of Variability.....	114

Chapter	Page
6. Summary	116
VI. SUMMARY	118
APPENDICES	120
A. APPENDIX A	120
B. APPENDIX B	130
C. APPENDIX C	194
D. APPENDIX D	199
E. APPENDIX E	230
REFERENCES CITED	271

LIST OF FIGURES

Figure	Page
Chapter II	
1. DIC speciation in seawater solutions and in NaCl solutions.....	29
2. Schematic depiction of reactions of the CaCO ₃ -DIC-H ₂ O system.....	30
3. Carbon and oxygen isotopic fractionation for DIC species over solution pH.....	32
4. Compilation of δ ¹⁸ O vs. temperature calibrations for CaCO ₃	39
5. Compilation of Δ ₄₇ vs. temperature calibrations for CaCO ₃	41
Chapter III	
1. Behavior of the calcite growth experiments.....	48
2. Variations in total alkalinity, dissolved inorganic carbon, and calcite saturation state during each calcite growth experiment	49
3. Calcite-water oxygen isotope fractionation expressed as 1000lnα _{c/w}	54
4. Effect of solution saturation on calcite growth rate.....	58
5. Model for the time-dependent behavior in experiments at T = 25°C, pH = 8.3 and [NaCl] = 0 M	60
6. The pH-stat assays of Nielsen and Frieden (1972) suggest an exponential dependence of CO ₂ (de)hydration reaction velocity on [NaCl].....	63
7. Data-model comparison for the calcite-water oxygen isotope fractionation (1000lnα _{c/w}) in solutions with different NaCl concentrations (0-1.4 M)	65
Chapter IV	
1. Experiment headspace CO ₂ concentration, total alkalinity (TA), NaOH added, DIC δ ¹³ C, DIC concentration, and calculated degree of supersaturation (Ω).....	71

Figure	Page
2. Over the pH range 7.5-9.3, Ω increases, growth rate decreases, and ion activity ratio decreases.....	74
3. Calcite-DIC carbon isotope fractionation expressed as $1000\ln\alpha_{c-DIC}$	76
4. Oxygen isotope fractionation between calcite and experimental solution expressed as $1000\ln\alpha_{c-w}$	79
5. Updated ion-by-ion model of calcite growth at 25°C in CaCl ₂ solutions.....	82
 Chapter V	
1. Experimental apparatus.....	92
2. Experimental headspace CO ₂ concentration and solution pH over the course of each experiment	94
3. SEM images of CaCO ₃ precipitates	97
4. Isotopic compositions of precipitated carbonates and gas sources	100
5. The $\delta^{13}C$ of CaCO ₃ and DIC.....	103
6. Carbon and bulk oxygen kinetic isotope fractionations (KIFs) for all experiments of this study.....	106
7. Schematic denoting the carbon reservoirs in our box model, and the fluxes and fractionations between them.....	108
8. Model outputs showing how the KIEs change with increasing F_f relative to a fixed hydroxylation flux F_H	111
9. Box model results of $\epsilon^{18}_{EIC/CO_2+H_2O}/\epsilon^{13}_{EIC/CO_2}$ slopes using different KFF values for ¹⁸ O on CO ₂ , and correspondingly on OH ⁻ , during CO ₂ hydroxylation with increasing degrees of CO ₂ (aq) distillation.....	112
10. Results from Clark et al. (1992) showing isotopic distillation of headspace CO ₂ during hydroxylation	113
11. Carbon and bulk oxygen KFFs over temperature from our open-air experiments and from past studies.....	115

LIST OF TABLES

Table	Page
Chapter II	
1. $\delta^{18}\text{O}$ and $\delta^{13}\text{C}$ of Common Geologic Reservoirs	27
2. Equilibrium Oxygen and Carbon Fractionation Factors.....	33
3. Kinetic Oxygen and Carbon Fractionation Factors	35
Chapter III	
1. Experimental parameters and isotopic data for all experiments of this study	52
2. Compilation of equilibrium fractionation factors (EFFs; T in Kelvin)	53
3. Constants and parameters used in the model	57
Chapter IV	
1. Experimental parameters	72
2. Isotopic data	77
3. Model input parameters	81
4. Model parameters calculated from input parameters.....	81
5. Oxygen and carbon fractionation factors used to generate the ion-by-ion model curves.....	83
Chapter V	
1. Experimental parameters, solution composition and pH for all experiments	91
2. Direct experimental solution measurements.....	93
3. Isotopic data for all experiments.....	101

Table	Page
4. Carbon and bulk oxygen kinetic isotope fractionations	107
5. Model parameters	108
6. Model curves varying KFFs for CO ₂ hydroxylation	112
7. Literature compilation of KFFs during CO ₂ hydroxylation.....	114

CHAPTER I

INTRODUCTION

Calcite grows in a wide variety of geologic settings and conditions including caves, lakes, surface oceans, marine sediments, and hydrothermal veins. It has been a feature of ocean sediments since the Archean, as the oceans have been inferred to be supersaturated with respect to calcite for most of the earth's history. It takes up trace element impurities into its structure, which can serve as a sink for metal contaminants in the environment. Trace impurities, as well as isotopic ratios of major and minor constituents, can also serve as paleoclimate archives, which are valuable in part because calcite is such a common mineral. Shifts in the oxygen and carbon isotopic compositions of seafloor carbonate sediments have been correlated to global climate signals (e.g. sea surface temperature, glaciations) and global biotic events (e.g. level of productivity, species diversifications). A more recent avenue of interest in carbonate minerals has been their CO₂ sequestration potential for carbon capture and storage, which could be engineered at a scale so that significant amounts of CO₂ may be removed from the atmosphere.

While many paleoproxies based on trace element and/or isotopic composition of carbonate minerals have been studied, the $\delta^{18}\text{O}$ -T relationship of carbonate formation and thereby the temperature of the aqueous solution from which it grew (e.g. seawater) has been studied the most extensively. When calcite grows slowly enough for isotopic equilibrium to be maintained between the mineral and the solution, the oxygen isotope partitioning between the phases is a function of solution temperature. However, isotopic equilibrium is not maintained in the majority of cases for either natural or synthetic calcite, and therefore factors such as mineral growth rate, solution composition, pH, and dissolved inorganic carbon (DIC) source(s) may have an effect on the oxygen isotope fractionation between calcite and solution. As an additional complexity, the majority of calcic seafloor sediments are biogenic, meaning calcifying organisms mediated the precipitation of CaCO₃ which imparts "vital effects" on the isotopic and trace element composition of the mineral that are poorly understood. These vital effects may involve a combination of enzymatic and metabolic processes that act to regulate the pH of the calcifying fluid, increase the degree of supersaturation, and exclude growth inhibitors.

This work aims to better understand how the stable isotope composition of calcite is affected by inorganic and biogenic processes by carrying out well-controlled calcite growth experiments over a range of pH, temperature, ionic strength, and concentration of the enzyme carbonic anhydrase (CA). The enzyme CA catalyzes CO₂ (de)hydration reactions, which acts to promote isotopic equilibration of the dissolved inorganic carbon (DIC) pool since those reactions are some of the

slowest in the DIC-H₂O system. When calcite grows from an equilibrated DIC pool, any kinetic isotope effects (KIEs) recorded in the calcite may be attributed to processes occurring at the mineral-solution interface as the mineral grows.

In Chapter II, I provide a background of the CaCO₃-DIC-H₂O system. I introduce the concepts of isotopic fractionation, both equilibrium and kinetic, and provide equations and notation relevant to understanding the isotopic data presented in the later chapters. I discuss the DIC system reactions and corresponding isotopic fractionations, as well as how various factors affect the isotopic composition of inorganic and biogenic calcite. I close the chapter with brief descriptions of a range of trace element and/or isotopic-based paleoproxies and their application to paleoenvironment interpretations. This chapter sets the foundation of concepts that are explored more in-depth in the following chapters.

The first two suites of experiments (Chapters III and IV) were carried out under near-isotopic-equilibrium growth conditions, systematically varying the solution ionic strength and pH across a range that mimics that of natural calcite precipitation environments (e.g. seawater, estuaries, freshwater lakes, alkaline lakes). The results from these chapters give insight into the fairly small magnitude nonequilibrium isotope effects typical of natural and experimental calcite that may be viewed as deviations from the empirical $\delta^{18}\text{O}$ - T equilibrium. In the third suite of experiments (Chapter V), carbonate minerals grew under uncommon, far-from-isotopic-equilibrium conditions and recorded large kinetic isotope effects (KIEs). While equilibrium-based paleoproxies aren't applicable, these carbonates may still record useful paleoenvironmental information.

In Chapter III, calcite growth experiments were performed over a range of ionic strength ($I = 0.1$ - 1.6 ; $[\text{NaCl}] = 0$ - 1.4 M) at 25°C and pH 8.3 in order to examine the effect of solution composition and background electrolytes on oxygen isotope partitioning between calcite and water. No evidence of an ionic strength effect on oxygen isotope partitioning between calcite and DIC was found for NaCl concentrations up to 0.35 M. In higher ionic strength solutions, however, NaCl was found to inhibit the efficacy of carbonic anhydrase (bCA) and prevent complete isotopic equilibration of the DIC pool, resulting in lower and more variable oxygen isotope fractionations between calcite and water. We then modeled the experimental results with an isotopic box model, and quantified the salt inhibition of bCA, which has implications for kinetic isotope effects in biogenic calcite since biocalcifiers use carbonic anhydrase in their calcifying fluid.

In Chapter IV, calcite growth experiments were carried out over pH 7.5-9.3 at 25°C and low ionic strength to investigate the effect of pH on isotope partitioning between calcite and water. The oxygen isotopic composition of calcite decreased with increasing pH. We updated the ion-by-ion model to reflect these new experimental constraints, which is a generalizable model for calcite growth that can be applied to a wide range of natural and experimental calcites.

In Chapter V, we carry out experiments that mimic the travertine precipitation that occurs upon contact with atmospheric CO₂ at hyperalkaline springs upwelling through peridotites. In these experiments, high pH, DIC-free, CaCl₂ solutions rapidly precipitate carbonate minerals upon contact with gaseous CO₂, with the large kinetic isotopic fractionations for both carbon and oxygen

likely reflecting unidirectional CO₂ hydroxylation. We successfully reproduced the isotopic fractionations observed in both natural and laboratory settings, and are the first experimental study to separately quantify the kinetic fractionation factors (KFFs) of oxygen on CO₂ and OH⁻ during CO₂ hydroxylation.

Chapter III is co-authored with James M. Watkins and Laurent S. Devriendt, and is published in *Geochimica et Cosmochimica Acta*. Chapters IV and V are also co-authored with James M. Watkins and Laurent S. Devriendt, and are in preparation for submission to *Geochemistry, Geophysics, Geosystems*.

CHAPTER II

CACO₃-DIC-H₂O SYSTEM BACKGROUND

1 Carbonates in seawater

Calcium carbonate minerals have been a mainstay of oceanic sediments since the Archean, long before the rise of biocalcifiers that dominate calcic sediments in the modern ocean (Grotzinger and Kasting, 1993; Zeebe and Wolf-Gladrow, 2001). The main CaCO₃ polymorphs are calcite and aragonite, characterized by rhombohedral and orthorhombic crystal structures, respectively, which leads to differences between the minerals including solubility, crystal habit, trace element uptake, and isotopic composition (Zeebe and Wolf-Gladrow, 2001).

The Mg/Ca ratio of the host solution generally determines which inorganic CaCO₃ polymorph will precipitate, with low-Mg calcite at Mg/Ca < 2, both high-Mg calcite and aragonite for the range 2 < Mg/Ca < 5.3, and aragonite at Mg/Ca > 5.3 (Hardie, 1996). Mg increases the surface energy of calcite, thereby promoting precipitation of aragonite instead (Sun et al., 2015). CaCO₃ polymorph formation is also influenced by temperature, with lower temperatures favoring calcite (Folk, 1994; Morse et al., 1997). Experiments by Morse et al. (1997) found that calcite precipitated at < 6°C in modern seawater (Mg/Ca = 5). Globally, aragonite and high-Mg calcite are found in warm ocean waters, while low-Mg calcite is typical at higher latitudes or in deep bottom waters (Morse et al., 1997). Mg-calcites grown in cool seawater and seawater with low carbonate ion concentration ([CO₃²⁻]) contain less Mg than calcite grown in warmer seawater (Major and Wilber, 1991).

While the Mg/Ca, and to a lesser extent water temperature, dictate inorganic CaCO₃ polymorph precipitation, biocalcifiers are not restricted as such. In the modern ocean, corals generally build their skeletons out of aragonite, while foraminifera and coccolithophores typically precipitate calcite tests and shells. Calcifying organisms impart “vital effects” on the isotopic and trace element composition of the mineral that are not yet fully understood, and are likely species-dependent. These vital effects are inferred to be due to a combination of different processes, including enzymatic activity and metabolic processes involved in the regulation of the calcifying fluid composition (McConnaughey, 1989; Chen et al., 2018). Biocalcifiers do not typically create their skeletons directly from seawater, but from a calcifying fluid modified from seawater composition via preferential pumping of Ca²⁺ in and H⁺ out of the calcifying space, creating an environment of higher pH and increased degree of supersaturation with respect to CaCO₃ (Chen et al., 2018).

Zachos et al. (2001) presents carbon and oxygen isotopic data of foraminiferal carbonate sediments from the seafloor that spanned the last 65 million years, correlating shifts in the isotopic compositions to global climate signals for oxygen and global biotic events for carbon. Since the vast majority of calcic seafloor sediments are biogenic (Zeebe and Wolf-Gladrow, 2001), understanding biocalcification processes is of high priority since those biogenic sediments serve as an important paleoclimate archive.

1.1 Seawater composition and pH

The geochemical composition and pH of seawater have varied over geologic time. Shifts in seawater composition can be inferred from variable evaporite mineralogy, with aragonite and MgSO_4 salts appearing together (Precambrian, Permian, modern), and K, Mg, Ca-bearing salts appearing with calcite (Cambrian, Silurian, Cretaceous) (Hardie, 1996; Lowenstein et al., 2001). The modern ocean is an “aragonite sea” characterized by high $[\text{Na}^+]$, high Mg/Ca, and low $\text{Ca}^{2+}/\text{SO}_4^{2-}$ (Hardie, 1996; Lowenstein et al., 2001). The major ions in seawater (Na^+ , Cl^- , Mg^{2+} , SO_4^{2-} , Ca^{2+} , K^+) have been consistent over geologic time but their relative proportions, and therefore overall seawater composition, have varied (Lowenstein et al., 2001; Turchyn and DePaolo, 2019). The relative ion proportions in seawater plays an important role in CaCO_3 polymorph control, trace element partitioning into CaCO_3 , evaporite mineralogy and precipitation sequence, and more (Ichikuni, 1973; Folk, 1994; Lowenstein et al., 2001; Coggon et al., 2010).

It is challenging to reconstruct paleo-ocean salinity and overall geochemical composition. One technique is based on fluid inclusions trapped in halite, which only precipitates after $\sim 90\%$ of seawater has evaporated, so ancient ocean composition is back-calculated with many limitations since some of the major ions will have been depleted prior to onset of halite precipitation (McCaffrey et al., 1987; Lowenstein et al., 2001; Brennan et al., 2004). Other techniques to reconstruct ancient ocean salinity and composition involve box models or calculations of fluxes of ions into the oceans (e.g. river water input, terrestrial silicate weathering processes, hydrothermal brines from mid-ocean ridges) and fluxes of ions out (e.g. precipitation of stable minerals, evaporation), which generally correlate significant shifts in seawater composition to global tectonics and climate (Hardie, 1998; Turchyn and DePaolo, 2019).

While the pH of modern ocean surface waters typically falls within a narrow range of 8.1-8.3, the pH of the oceans varies with depth (pH 7.8-8.1), and has also varied over geologic time (Grotzinger and Kasting, 1993; Beck et al., 2005; Halevy and Bachan, 2017). The pH of the ocean continues to change as a result of human activities, with projections under the “business-as-usual” scenario predicting the average surface ocean pH to decrease to 7.73 by the end of the 21st century (Jiang et al., 2019). The $\delta^{18}\text{O}$ of foraminiferal calcite has been observed to vary with seawater carbonate ion concentration, recording isotopically lower values with increasing $[\text{CO}_3^{2-}]$ or pH (Zeebe, 1999). Increasing ocean pH by 0.2-0.3 would correspondingly result in a decrease of $\delta^{18}\text{O}$ of calcite by $\sim 0.22\text{-}0.33\text{‰}$, which would typically be interpreted as an increase in ocean temperature (see section 5.1; Zeebe, 1999). An independent measure of seawater pH may help constrain the $\delta^{18}\text{O}$ kinetic

isotope effects that are due to pH and not temperature. The $\delta^{11}\text{B}$ of marine biocalcifiers is a promising paleo-pH proxy that does not seem to be significantly affected by diagenetic processes (Zeebe and Wolf-Gladrow, 2001; Edgar et al., 2015; Mavromatis et al., 2015; Uchikawa et al., 2015).

2 Isotopic fractionation

Before going into further depth on the $\text{CaCO}_3\text{-DIC-H}_2\text{O}$ system and its reactions, I will take a step back to introduce some key concepts of isotope geochemistry, including the principles of isotopic fractionation and relevant notation.

2.1 Equilibrium vs. kinetic fractionation

Isotopes are atoms of the same element that contain different amounts of neutrons, thus resulting in different atomic masses. Isotopic fractionation is the enrichment of one isotope relative to the other isotopes of that element among coexisting phases, which may occur through various physical, chemical, and biological processes. The majority of isotopic fractionations are due to the difference in mass of the isotopes. The percent of mass difference determines the extent of fractionation, with elements with large relative mass differences exhibiting greater fractionation. This partitioning of isotopes may be described as either equilibrium or kinetic isotopic fractionation.

Equilibrium isotopic fractionation occurs when reversible reactions have equal forward and backward reaction rates. The equilibrium fractionation is the distribution of isotopes that minimizes the overall Gibbs free energy of the system. Heavier isotopes are preferentially fractionated into phases in which they are most strongly or stably bound, due to vibrational energies that correlate negatively with atomic mass. Equilibrium fractionation is usually temperature-dependent. Due to commonly strong relationships between isotopic signature and temperature for equilibrium isotopic fractionation, many “isotope thermometers” have been developed for a wide range of geologic environments and conditions.

Kinetic isotopic fractionation occurs during unidirectional reactions, during reversible reactions that have not yet reached equilibrium, during diffusion, or during differential bond-breaking. It may be a result of reservoir distillation including Rayleigh processes, or during physical processes including freezing or evaporation. Biological processes resulting in isotopic fractionation are lumped together as “vital effects”, which are poorly understood but may relate to enzymatic activity, metabolism, or other processes. Heavier isotopes move more slowly, and therefore react more slowly, than lighter isotopes. More energy is required to break bonds involving heavy isotopes due to their greater mass, which is another reason that reaction rates involving heavy isotopes proceed more slowly than for reactions with light isotopes. Kinetic isotopic fractionation is common with chemical reactions that have not yet reached equilibrium and for which the reaction rates for the heavy and light isotopes are different.

Different environmental factors (e.g. temperature) or the types of phases involved (e.g. solids, liquids, gases, solid-liquid, etc.) promotes or inhibits isotopic equilibration of the system. Generally,

kinetic effects are less common at higher temperatures because isotopic exchange is more rapid at elevated temperatures, so equilibrium isotope partitioning is more readily established. Additionally, isotopes exchange more quickly in gases than in liquids, and in liquids than in solids. Exchange in solid phases at low temperatures is very slow and depends primarily on the diffusion coefficients and the molecular structure of the solid. The diffusion rate of oxygen in calcite at low to moderate temperatures is so slow that oxygen isotope ratios in calcite tend to be preserved even in shells millions of years old.

A kinetic fractionation factor (KFF) describes the partitioning of isotopes that would occur during an instantaneous, unidirectional reaction of one reactant to one product, and therefore represents the kinetic limit or fully expressed kinetic isotope effect for that reaction. At isotopic equilibrium, the forward and backward reaction rates are equal, so the resulting equilibrium fractionation factor (EFF) is the intermediate value between opposing KFFs for the forward and backward reactions. The EFF may be calculated as the ratio between the forward KFF and backward KFF $\alpha^{k+1}/\alpha^{k-1} = \alpha^{eq}$. The isotopic signature of many natural and experimental calcites falls somewhere between the EFF and KFF because it is uncommon to have purely unidirectional reactions (KFF), and for low temperature carbonate precipitation, isotopic equilibrium is often not achieved (EFF) either.

2.2 Isotope and fractionation factor notation

We report isotope ratios using standard δ -notation using the equation:

$$\delta = \left(\frac{R_{\text{sample}}}{R_{\text{standard}}} - 1 \right) \cdot 1000 \quad (1)$$

where R is the isotope ratio of the heavy, rarer isotope over the lighter, more common isotope (e.g. $^{18}\text{O}/^{16}\text{O}$, $^{13}\text{C}/^{12}\text{C}$, $^{44}\text{Ca}/^{40}\text{Ca}$). Carbon isotope compositions are reported relative to the Vienna Pee Dee Belemnite (VPDB) standard, while oxygen isotope compositions are typically reported relative to Vienna Standard Mean Ocean Water (VSMOW) standard. Isotopic data may be converted between the two scales by the following relationship from Coplen et al. (1983):

$$\delta^{18}\text{O}_{\text{VPDB}} = (\delta^{18}\text{O}_{\text{VSMOW}} - 30.91)/1.03091. \quad (2)$$

The atmospheric geoscience community monitors the isotopic composition of atmospheric CO_2 , reporting values using the VPDB- CO_2 scale. For carbon, there is no offset between the VPDB- CO_2 and VPDB scales, but for oxygen there is an approximately 10‰ offset that requires conversion between the two scales using the equation (Swart et al., 1991; Srivastava and Verkouteren, 2018):

$$\delta^{18}\text{O}_{\text{VPDB-CO}_2} = (\delta^{18}\text{O}_{\text{VPDB}} - 10.25)/1.01025. \quad (3)$$

The extent of isotope partitioning between two co-existing phases A and B is described by the isotope fractionation factor α , and is typically expressed as:

$$\alpha_{A/B} = \frac{(^{18}\text{O}/^{16}\text{O})_A}{(^{18}\text{O}/^{16}\text{O})_B} = \frac{\delta^{18}\text{O}_A + 1000}{\delta^{18}\text{O}_B + 1000}. \quad (4)$$

Positive $\alpha_{A/B}$ values indicate that phase A is isotopically heavier than phase B (i.e. relatively enriched in the heavy isotope), with negative $\alpha_{A/B}$ values indicating the opposite. We often choose to report fractionations as $1000\ln\alpha$ values so fractionation values are given in permil (‰) rather than in smaller and less intuitive decimal values (e.g. $\alpha_{\text{calcite/water}} = 1.030197$ is equivalent to $1000\ln\alpha_{\text{calcite/water}} = 29.75\text{‰}$). Equilibrium isotope fractionations are typically expressed in terms of $1000\ln\alpha$, while kinetic fractionations are often expressed as epsilon values (‰):

$$\epsilon_{A/B} = [\alpha_{A/B} - 1] \cdot 1000. \quad (5)$$

2.3 $\delta^{13}\text{C}$ and $\delta^{18}\text{O}$ of common geologic reservoirs

The commonly used standard for carbon isotopic data, Vienna Pee Dee Belemnite (VPDB), normalizes carbon isotope data against the carbon isotopic composition of a Cretaceous marine belemnite fossil that was remarkably enriched in ^{13}C . By convention, the $\delta^{13}\text{C}$ of this belemnite is now considered 0‰ VPDB, resulting in samples commonly having negative $\delta^{13}\text{C}$ compositions when reported relative to this standard. Vienna Standard Mean Ocean Water (VSMOW) is the typical standard for oxygen isotopes, and is based on a mixture of distilled (i.e. pure, salt-free) seawater samples from around the globe. By convention, typical seawater is considered 0‰ VSMOW.

The typical range in $\delta^{13}\text{C}$ and $\delta^{18}\text{O}$ of many common geologic reservoirs are listed in Table 1. The $\delta^{18}\text{O}$ of marine carbonates is typically around 30‰ isotopically heavier than the ~ 0 ‰ ocean water, while the offset between the $\delta^{13}\text{C}$ of shallow foraminifera biocalcifiers (-2 to 2‰) and shallow oceanic DIC (0 to 2.4‰) is considerably smaller (Zeebe and Wolf-Gladrow, 2001; Mackensen and Schmiedl, 2019). DIC in the surface ocean is typically enriched in ^{13}C relative to the deep ocean due to the preferential uptake of ^{12}C by organisms living in the photic zone (Zeebe and Wolf-Gladrow, 2001). Though there is both regional and seasonal variability in the isotopic composition of atmospheric CO_2 , it broadly has shifted to isotopically lighter $\delta^{13}\text{C} \approx -9.5$ to -7.0‰ from the pre-industrial value of -6.3‰ , while the $\delta^{18}\text{O}$ of $\sim 41\text{‰}$ is approximately in isotopic equilibrium with ocean water (Troler et al., 1996; Zeebe and Wolf-Gladrow, 2001; NOAA Global Monitoring Laboratory).

3 Dissolved inorganic carbon speciation

Inorganic carbon in solution occurs as $\text{CO}_2(\text{aq})$, H_2CO_3 , HCO_3^- , and CO_3^{2-} , which collectively constitute the dissolved inorganic carbon (DIC) pool. The relative proportions of the DIC species are primarily a function of solution pH (Fig. 1). To a lesser extent, DIC speciation is also depen-

Table 1: $\delta^{18}\text{O}$ and $\delta^{13}\text{C}$ of common geologic reservoirs

Reservoir	Value	Reference
Oxygen	$\delta^{18}\text{O}$ ‰ (VSMOW)	
atmospheric CO_2	39.4 to 42.6	Trolier et al., 1996; Zeebe and Wolf-Gladrow, 2001; NOAA Global Monitoring Laboratory
glacial ice	-20 to -55	Zeebe and Wolf-Gladrow, 2001
marine carbonates	27 to 32	Zeebe and Wolf-Gladrow, 2001
meteoric water - Eugene, OR	-12 to -11	My experimental solutions
meteoric water - global	-30 to 0	Bowen and Wilkinson, 2002
ocean water	0	Zeebe and Wolf-Gladrow, 2001
organic matter	15 to 35	Zeebe and Wolf-Gladrow, 2001
Carbon	$\delta^{13}\text{C}$ ‰ (VPDB)	
anthropogenic CO_2	-28 to -26	Mackensen and Schmiedl, 2019
atmospheric CO_2	-9.5 to -7.0	Trolier et al., 1996; Zeebe and Wolf-Gladrow, 2001; NOAA Global Monitoring Laboratory
C3 plants	-21 to -32	O'Leary, 1988; Zeebe and Wolf-Gladrow, 2001
C4 plants	-10 to -16	O'Leary, 1988; Zeebe and Wolf-Gladrow, 2001
foraminifera - planktic (shallow)	-2 to 2	Zeebe and Wolf-Gladrow, 2001; Mackensen and Schmiedl, 2019
foraminifera - benthic (deep)	-4 to 1	Mackensen and Schmiedl, 2019
marine organic matter	-19 to -31	Zeebe and Wolf-Gladrow, 2001; Mackensen and Schmiedl, 2019
oceanic DIC (shallow)	0 to 2.4	Zeebe and Wolf-Gladrow, 2001; Mackensen and Schmiedl, 2019
oceanic DIC (deep)	-0.8 to 1.3	Zeebe and Wolf-Gladrow, 2001; Mackensen and Schmiedl, 2019
volcanic CO_2	-5	Mackensen and Schmiedl, 2019

dent on temperature, pressure, solution salinity and composition (Zeebe and Wolf-Gladrow, 2001; Millero et al., 2006; Millero et al., 2007). The DIC species, or ion pairs including DIC species, are the only reservoirs of inorganic carbon in solution. Isotopic equilibration of aqueous carbon only requires equilibrium to be reached among the DIC species, and as a result carbon isotope equilibration timescales are relatively rapid (< 30 seconds regardless of solution pH) (Zeebe et al., 1999; Zeebe and Wolf-Gladrow, 2001). In contrast, oxygen isotope equilibration requires equilibrium to be achieved between the DIC species and water (H_2O , OH^-) (Zeebe and Wolf-Gladrow, 2001; Uchikawa and Zeebe, 2012). While OH^- - H_2O equilibration is rapid, the only reactions through which DIC exchanges with water (CO_2 hydration and hydroxylation, see section 4.2) proceed rather slowly. Therefore, the timescale for establishing oxygen isotope equilibrium among the DIC species and water is much longer than that required to establish carbon isotope equilibrium between the DIC species, ranging from ~ 10 minutes to equilibrate oxygen isotopes among DIC- H_2O in solutions of $\text{pH} < 5.5$, to ~ 1 -16 hours over the pH range 7.5 to 9.3 (Zeebe and Wolf-Gladrow, 2001; Uchikawa and Zeebe, 2012).

The equilibrium constant (K) for the dissociation of a weak acid (HA) may be calculated as follows:

$$K_a = \frac{a_{\text{H}^+} \cdot a_{\text{A}^-}}{a_{\text{HA}}}, \quad (6)$$

where the activities (a) of each species are a product of the activity coefficient (γ) and the ion concentration:

$$K_a = \frac{\gamma_{\text{H}^+}[\text{H}^+] \cdot \gamma_{\text{A}^-}[\text{A}^-]}{\gamma_{\text{HA}}[\text{HA}]}. \quad (7)$$

The activity coefficients (γ) are folded into the expression when equilibrium constants are determined experimentally (i.e. as functions of T, P, solution composition and concentration, etc.), and are thus presented as K^* values. When modeling the CaCO_3 -DIC- H_2O system, it is important to select $\text{p}K$ values and other constants that are appropriate to the specifics of your system. Just as $\text{pH} = -\log_{10}([\text{H}^+])$, $\text{p}K = -\log_{10}(K)$, where K values are equilibrium constants. K_1 and K_2 are equilibrium constants for the first and second dissociations of carbonic acid, calculated by:

$$K_1^* = \frac{[\text{HCO}_3^-][\text{H}^+]}{[\text{CO}_2]} \quad (8)$$

and

$$K_2^* = \frac{[\text{CO}_3^{2-}][\text{H}^+]}{[\text{HCO}_3^-]}. \quad (9)$$

Another important aqueous geochemistry quantity is the total alkalinity (TA), which may be described as the slight charge imbalance between positive and negative “conservative ions” in solution (i.e. Na^+ , Ca^{2+} , Cl^-), whose concentrations are unaffected by changes in pH, pressure, and temperature (unlike HCO_3^- , CO_3^{2-} , etc.) (Zeebe and Wolf-Gladrow, 2001). In natural waters, a variety of nonconservative ions may be present (e.g. $\text{B}(\text{OH})_4^-$, PO_4^{3-}), but in the simple $\text{CaCl}_2 \pm \text{NaCl} \pm \text{NH}_4\text{Cl}$ solutions of this dissertation, the total alkalinity may be approximated by the carbonate

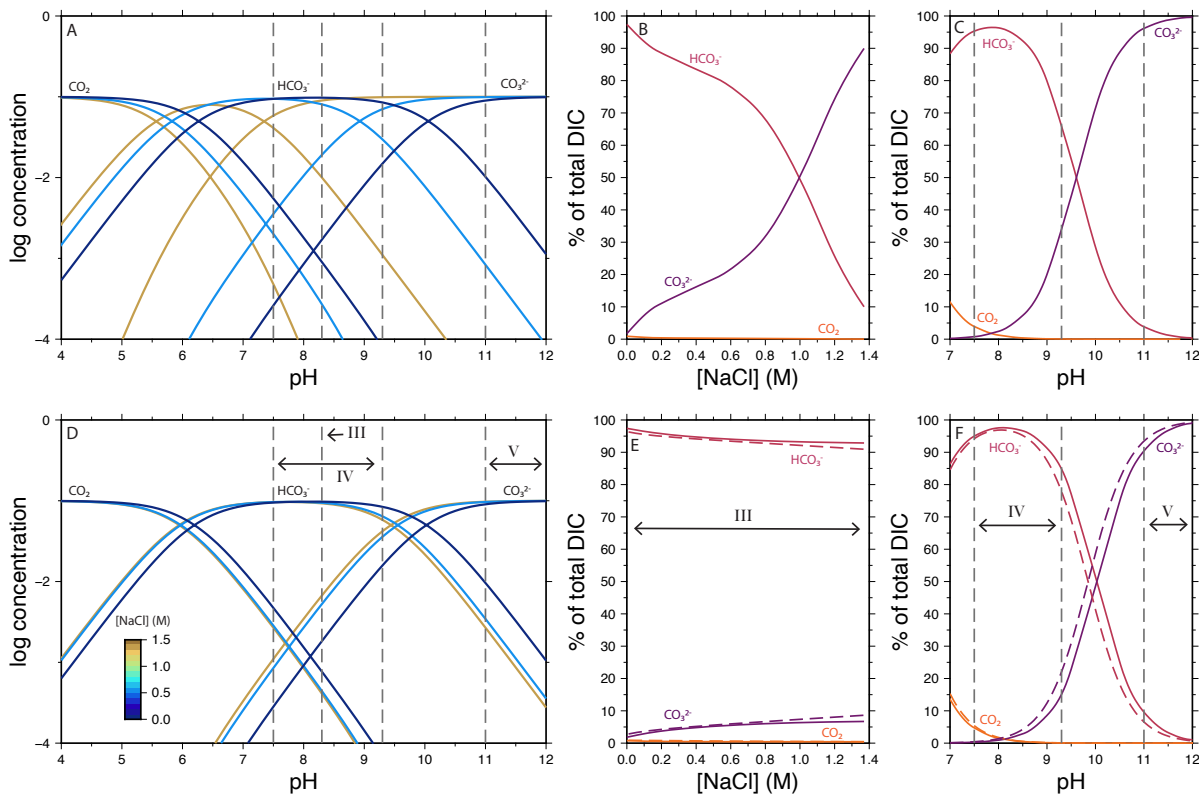


Figure 1: (A-C) DIC speciation in seawater solutions using pK values from Millero et al. (2006), and (D-F) in NaCl solutions using pK values from Millero et al. (2007). The bjerrum plots (A, D) depict speciation for fresh (dark blue), saline (light blue), and supersaline (yellow) waters. On panels E-F, DIC speciation calculated using the R-package of PHREEQC with the Pitzer database (Charlton and Parkhurst, 2011; De Lucia and Kühn, 2013) is demonstrated to provide similar DIC speciation as Millero et al. (2007). Vertical dashed lines depict the ranges in pH covered by calcite growth experiments in this dissertation. Chapter III performs experiments at pH 8.3 and a range of 0-1.4 M [NaCl]. Chapter IV experiments range from pH 7.5-9.3 at low ionic strength. Experiments in Chapter V have initial pH values from 11.0-12.8.

alkalinity ($= [\text{HCO}_3^-] + 2[\text{CO}_3^{2-}]$) (Zeebe and Wolf-Gladrow, 2001).

There are six key quantities that describe the DIC system: $[\text{CO}_2]$, $[\text{HCO}_3^-]$, $[\text{CO}_3^{2-}]$, $[\text{H}^+]$, [DIC], and TA. Because of the relationships among them, if any two are specified, the other four quantities are accordingly fixed and may be calculated (Zeebe and Wolf-Gladrow, 2001). In the experiments of this dissertation, we measure solution pH continuously with a probe, periodically titrate the solution to obtain total alkalinity, and also periodically take solution samples that are later analyzed for [DIC], thereby obtaining quantities for $[\text{H}^+]$, TA, and DIC, and enabling us to calculate $[\text{CO}_2]$, $[\text{HCO}_3^-]$, and $[\text{CO}_3^{2-}]$.

Due to the effects of solution salinity and composition, the equilibrium DIC speciation at a given pH is very different for typical seawater than in simple NaCl solutions. Millero et al (2006) determined robust pK_1 (where $[\text{CO}_2]=[\text{HCO}_3^-]$) and pK_2 (where $[\text{HCO}_3^-]=[\text{CO}_3^{2-}]$) values in natural

seawater by systematically varying temperature and salinity, while Millero et al (2007) quantified pK values in NaCl solutions of variable ionic strength. DIC speciation shifts as a function of salinity in both seawater and NaCl solutions (Fig. 1A, D). Increasing salinity shifts both pK_1 and pK_2 to lower pH, though shifts for pK_1 are much more modest compared to shifts for pK_2 . Therefore, the proportion of CO_2 is much less affected than the proportion of CO_3^{2-} for solutions of intermediate pH. Conversely, decreases in temperature shift pK values to higher pH (Zeebe and Wolf-Gladrow, 2001; Bajnai and Herwartz, 2021).

The experiments addressed in this dissertation were performed in simple solutions containing $\text{CaCl}_2 \pm \text{NaCl} \pm \text{NH}_4\text{Cl}$, which may be adequately described by the pK values determined by Millero et al. (2007) in simple NaCl solutions. We juxtapose this DIC speciation with the distribution of DIC species in seawater (Millero et al., 2006) across the same range in pH and $[\text{NaCl}]$ (Fig. 1). Experiments in Chapters III and IV were conducted in 25°C solutions of 30 mM CaCl_2 and 5 mM NH_4Cl , at pH 8.3 across a range in solution $[\text{NaCl}] = 0\text{-}1.4$ M (Ch. III) or over a range of pH (7.5-9.3) at low ionic strength and minimal $[\text{NaCl}]$ (Ch. IV). Experiments in Chapter V were conducted in 10-25°C solutions of 10-30 mM CaCl_2 at high pH 11.0-12.8.

4 CaCO_3 -DIC- H_2O chemical reactions and isotopic fractionations

This section goes into more detail regarding reactions between species of the CaCO_3 -DIC- H_2O system, as shown in Fig. 2, as well as the equilibrium isotopic fractionations between species (EFFs: Table 2; Figure 3) and isotopic fractionations attending unidirectional reactions (KFFs: Table 3).

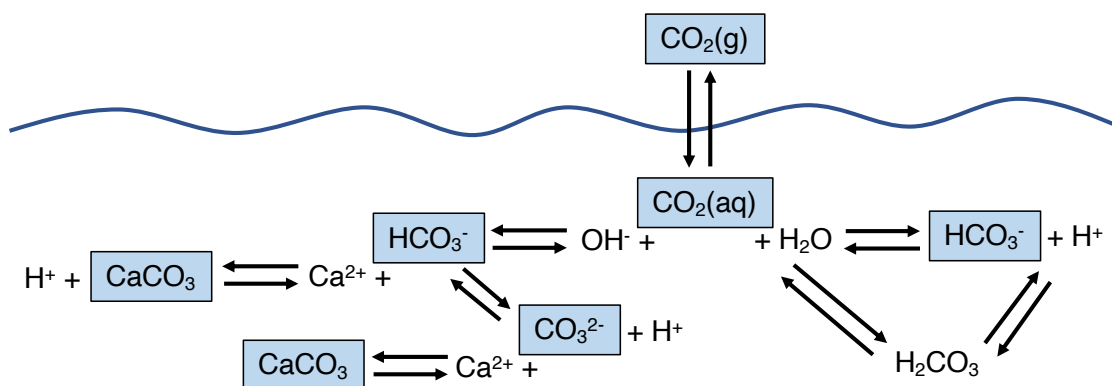


Figure 2: Schematic depiction of reactions of the CaCO_3 -DIC- H_2O system. When CO_2 gas dissolves into solution, the resulting aqueous CO_2 may react with H_2O or OH^- . DIC speciation depends primarily on solution pH, but is affected to a lesser degree by other factors including temperature, pressure, and solution composition.

4.1 CO₂ dissolution

As CO₂ gas diffuses from the atmosphere into the oceans, lakes, or other bodies of water, it dissolves into solution and exchanges isotopes with dissolved inorganic carbon (DIC) by the reaction:

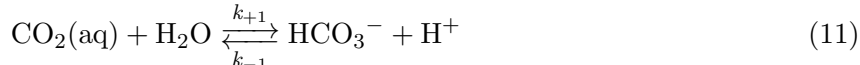


during which the isotopes are fractionated according to mass-dependent processes. During equilibrium isotopic fractionation, the heavier isotopes tend to be enriched in the phase in which they are more strongly bound, and in this case carbon and oxygen have opposite fractionation effects where ¹³C prefers CO₂(g) and ¹⁸O prefers CO₂(aq). At 25°C, the resulting CO₂(aq) is depleted in ¹³C by ~1.1-1.4‰ (Vogel et al., 1970; Zhang et al., 1995; Yumol et al., 2020), and enriched in ¹⁸O by ~0.3‰ (Beck et al., 2005; Barkan and Luz, 2012).

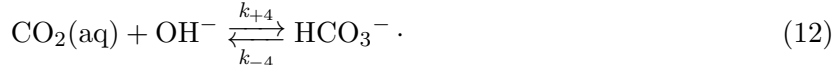
Owing to rapid equilibration between aqueous and gaseous CO₂, the kinetic fractionation factors (KFFs) have not been fully explored, with no studies to my knowledge reporting KFFs for CO₂ degassing. One study quantified the carbon isotope KFF during CO₂ dissolution and found the aqueous CO₂ to be further depleted by ~1‰ from the equilibrium fractionation for a total carbon depletion of ~2.1‰ (Zhang et al., 1995). Vogel et al. (1970) quantified the oxygen isotope KFF during CO₂ dissolution and found CO₂(aq) was enriched in ¹⁸O by 0.8‰, with limitations that this value was applicable ~ 0°C.

4.2 CO₂ (de)hydration and (de)hydroxylation

Upon dissolving into solution, the aqueous CO₂ undergoes hydration:



and/or hydroxylation:



The relative production of HCO₃⁻ from hydration vs. hydroxylation depends primarily on solution pH. At low pH, hydration dominates, while the opposite is true at high pH. At 25°C, the hydration and hydroxylation fluxes are equal at approximately pH 8.5 (Sade and Halevy, 2017, Figure 1). For the pH range of typical ocean water (surface pH 8.1-8.3, deep ocean pH 7.7-7.9) and many lakes or rivers (average pH 6-8), both hydration and hydroxylation appreciably contribute to HCO₃⁻ production. The contribution from CO₂ hydration may be considered negligible in low ionic strength solutions at 25°C at or above pH 10.5 (Devriendt et al., 2017; Bajnai and Herwartz, 2021).

CO₂ hydration and hydroxylation are the only pathways for DIC to exchange isotopes with H₂O, and are also the slowest DIC exchange reactions (Zeebe and Wolf-Gladrow, 2001; Sade and Halevy, 2017, Figure 1). Over the pH range 7-10, both hydration and hydroxylation reactions are several orders of magnitude slower than H₂O-OH⁻ and HCO₃⁻-CO₃²⁻ exchange (Sade and Halevy, Figure

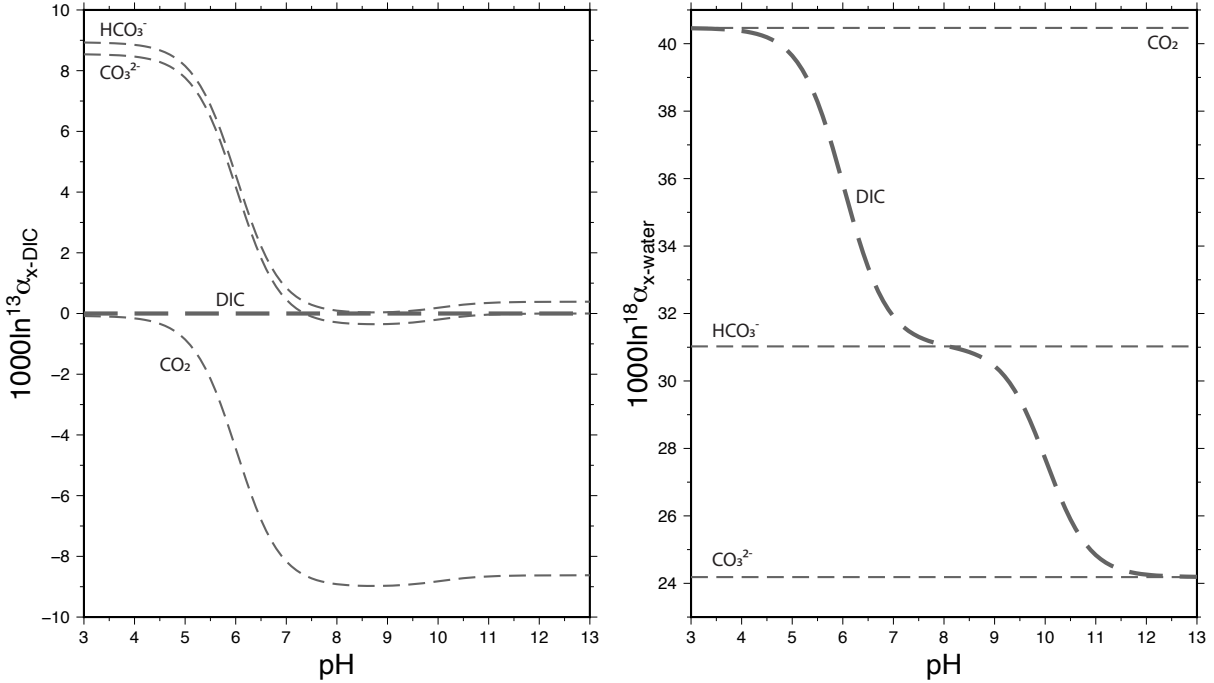


Figure 3: Carbon (left) and oxygen (right) isotopic fractionation for the DIC species over solution pH 3-13. Isotopic fractionation is expressed as $1000 \ln \alpha_{x-DIC}$ for carbon isotopes, and as $1000 \ln \alpha_{x-water}$ for oxygen isotopes. The $\delta^{13}C$ and $\delta^{18}O$ of DIC over the pH range was calculated using the Zeebe (2007) expression, Millero et al. (2007) pK values, and equilibrium fractionation factors from Mook (1986) and Zhang et al. (1995) for carbon, and Beck et al. (2005) for oxygen.

1). Kinetic isotope effects (KIEs) attending these rate-limiting reactions are therefore more likely to be recorded in the EIC (Equilibrated Inorganic Carbon = $HCO_3^- + CO_3^{2-}$) and precipitated carbonate minerals than KIEs attending the other, more rapid DIC- H_2O system reactions (Sade and Halevy, 2017).

Isotopic equilibration of the DIC can be sped up by the addition of carbonic anhydrase (CA), an enzyme that catalyzes CO_2 hydration and dehydration reactions, but does not affect equilibrium DIC speciation (Kupriyanova and Pronina, 2011). Uchikawa and Zeebe (2012) found that oxygen isotopes of DIC species equilibrated twice as quickly with the addition of $3.7 \cdot 10^{-9}$ M CA. Utilizing CA to speed up CO_2 - HCO_3^- interconversion should promote rapid DIC equilibration and minimize or eliminate KIEs in calcite stemming from DIC- H_2O disequilibrium, thereby allowing kinetic effects occurring at the mineral surface (calcite-DIC disequilibrium) to be isolated. However, the addition of carbonic anhydrase does not promote DIC equilibration at high pH (>10) where CO_2 hydroxylation dominates over hydration, because CA does not catalyze (de)hydroxylation reactions.

While most researchers treat the DIC system as consisting of three species, $CO_2(aq) + HCO_3^- + CO_3^{2-}$, there is technically a fourth species: H_2CO_3 . Often, the carbonic acid species is ignored, or rather, lumped in with $CO_2(aq)$ due to its much lower concentration than $CO_2(aq)$ and the fact that H_2CO_3 is not chemically separable from $CO_2(aq)$ (Zeebe and Wolf-Gladrow, 2001). Depending on

Table 2: Equilibrium oxygen and carbon fractionation factors

Fractionation factor	Equation	α (25°C)	Notes
Oxygen			
$\alpha_{\text{CO}_2(\text{g})-\text{w}}^{\text{eq}}$	$\frac{17.611}{T_K} + 0.9821$	1.0412	Zeebe (2007)
$\alpha_{\text{CO}_2(\text{aq})-\text{w}}^{\text{eq}}$	$\exp(\frac{2520}{T_K^2} + 0.01212)$	1.0413	Beck et al. (2005)
$\alpha_{\text{HCO}_3-\text{w}}^{\text{eq}}$	$\exp(\frac{2590}{T_K^2} + 0.00189)$	1.0315	Beck et al. (2005)
$\alpha_{\text{CO}_3-\text{w}}^{\text{eq}}$	$\exp(\frac{2390}{T_K^2} - 0.00270)$	1.0245	Beck et al. (2005)
$\alpha_{\text{c}-\text{w}}^{\text{eq}}$	$\exp((\frac{17747}{T_K} - 29.777)/1000)$	1.0302	Coplen (2007); Watkins et al. (2013)
$\alpha_{\text{c}-\text{HCO}_3}^{\text{eq}}$	$\alpha_{\text{c}-\text{w}}^{\text{eq}}/\alpha_{\text{HCO}_3-\text{w}}^{\text{eq}}$	0.9987	Beck et al. (2005); Copen (2007); Watkins et al. (2013)
$\alpha_{\text{c}-\text{CO}_3}^{\text{eq}}$	$\alpha_{\text{c}-\text{w}}^{\text{eq}}/\alpha_{\text{CO}_3-\text{w}}^{\text{eq}}$	1.0056	Beck et al. (2005); Copen (2007); Watkins et al. (2013)
Carbon			
$\alpha_{\text{CO}_2(\text{g})-\text{HCO}_3}^{\text{eq}}$	$1/((-0.1141 \cdot T_C + 10.78)/1000 + 1)$	0.9921	Zhang et al. (1995)
$\alpha_{\text{CO}_2(\text{aq})-\text{CO}_2(\text{g})}^{\text{eq}}$	$(0.0049 \cdot T_C - 1.31)/1000 + 1$	0.9988	Zhang et al. (1995)
$\alpha_{\text{CO}_3-\text{HCO}_3}^{\text{eq}}$	$(\frac{-867}{T_K} + 2.52)/1000 + 1$	0.9996	Mook (1986)
$\alpha_{\text{CO}_2(\text{aq})-\text{HCO}_3}^{\text{eq}}$	$(\frac{-9866}{T_K} + 24.12)/1000 + 1$	0.9910	Mook (1986)
$\alpha_{\text{CO}_2(\text{g})-\text{c}}^{\text{eq}}$	$\exp((-2.4612 + \frac{7666.3}{T_K} - \frac{2988000}{T_K^2})/1000)$	0.9897	Bottinga (1968)
$\alpha_{\text{c}-\text{HCO}_3}^{\text{eq}}$	$1/(\alpha_{\text{CO}_2(\text{g})-\text{c}}^{\text{eq}}/\alpha_{\text{CO}_2(\text{g})-\text{HCO}_3}^{\text{eq}})$	1.0025	Bottinga (1968); Zhang et al. (1995)
$\alpha_{\text{c}-\text{CO}_3}^{\text{eq}}$	$\alpha_{\text{c}-\text{HCO}_3}^{\text{eq}}/\alpha_{\text{CO}_3-\text{HCO}_3}^{\text{eq}}$	1.0029	Bottinga (1968); Mook (1986); Zhang et al. (1995)

the reaction mechanism and pathway, $\text{CO}_2(\text{aq})$ may follow Eq. 11, or may first convert to H_2CO_3 via the reaction:



before converting to HCO_3^- by:



but the dissociation of H_2CO_3 is many orders of magnitude faster than the hydration and hydroxylation reactions, so its effect on DIC speciation is limited (Zeebe and Wolf-Gladrow, 2001; Sade and Halevy, 2017).

Isotopic fractionations attending reactions that involve multiple species with the same element, such as oxygen during CO_2 (de)hydration and (de)hydroxylation reactions (Eq. 11, 12), are complicated to quantify because there are different fractionations attending the different species. The KFF for carbon during CO_2 hydration would be represented by $\epsilon_{\text{HCO}_3^-/\text{CO}_2(\text{aq})}^{13}$, while for oxygen

two separate KFFs are needed: $\epsilon_{\text{HCO}_3^-/\text{CO}_2(\text{aq})}^{18}$ and $\epsilon_{\text{HCO}_3^-/\text{H}_2\text{O}}^{18}$. However, it is not always possible to separate the KFFs attending the different species, so often a “bulk oxygen” KFF is reported instead, which involves a weighted sum based on how many oxygen atoms each species contributes (see Eq. 11, 12; Dietzel et al., 1992; Christensen et al., 2021).

Equilibrium HCO_3^- is $\sim 9\%$ heavier in carbon and $\sim 9.5\%$ lighter in oxygen than aqueous $\text{CO}_2(\text{aq})$ (Fig. 3, Table 2). The KFFs attending CO_2 (de)hydration have been studied both experimentally (Clark and Lauriol, 1992; Yumol et al., 2020) and theoretically (Guo, 2009; Zeebe, 2014; Guo and Zhou, 2019; Guo, 2020), with no clear consensus. The CO_2 hydration carbon and bulk oxygen KFFs have been estimated between -17.6 to -33% and -13 to -18.8 , respectively (Clark et al., 1992; Zeebe, 2014; Yumol et al., 2020). CO_2 dehydration KFF estimates are larger for carbon (-30 to -32% , Clark and Lauriol, 1992; Guo, 2009; Guo, 2020) and smaller for oxygen (Clark and Lauriol, 1992; Guo and Zhou, 2019) than that of CO_2 hydration, which is in agreement with the opposite behavior observed in equilibrium isotopic partitioning between HCO_3^- and $\text{CO}_2(\text{aq})$ (Fig. 3). Notably, Guo and Zhou (2019) calculated separate KFFs attending CO_2 dehydration for oxygen between $\text{H}_2\text{O}-\text{HCO}_3^-$ and $\text{CO}_2-\text{HCO}_3^-$, with a weighted sum that is in approximate agreement with an earlier experimental study (Clark and Lauriol, 1992).

Unidirectional CO_2 hydroxylation is favored under conditions of high pH and when precipitation of carbonate minerals follows, thus hindering back-reaction by removing the DIC from solution. As with (de)hydration reactions, bulk oxygen KFFs are typically reported as previous studies have been unable to tease apart the oxygen KFFs for $\text{HCO}_3^- - \text{CO}_2$ and $\text{HCO}_3^- - \text{OH}^-$ separately (Zeebe, 2020). Previous studies have examined travertines from natural hyperalkaline springs as well as undertaken laboratory experiments in an effort to quantify the KFFs for CO_2 hydroxylation (Clark et al., 1992; Böttcher et al., 2018; Christensen et al., 2021), though these efforts are complicated by the uncertainty in the equilibrium oxygen isotope fractionation between OH^- and H_2O (see section 4.5; Green and Taube, 1963; Böttcher et al., 2018; Zeebe, 2020; Bajnai and Herwartz, 2021). Many studies agree the carbon KFF is quite large, approximately -17% with little to no temperature dependence, while the bulk oxygen KFF appears to have a stronger temperature-dependence, and an approximate value at 25°C of -7.3% when expressed relative to the weighted sum of $\text{CO}_2 + \text{OH}^-$ (Zeebe; 2020; Christensen et al., 2021, 2022). Theoretical models of CO_2 dehydroxylation suggest a carbon KFF of -22.5% and a bulk oxygen KFF of -16.7% , which is in agreement with a later calculation of separate oxygen KFFs (Guo, 2009; Guo and Zhou, 2019; Guo, 2020).

4.3 HCO_3^- (de)protonation

Bicarbonate deprotonates to carbonate by the reaction:



$\text{HCO}_3^- - \text{CO}_3^{2-}$ exchange is many orders of magnitude faster than hydration hydroxylation over the pH range carbonates precipitate (Eigen, 1964; Pinsent et al., 1956; Zeebe and Wolf-Gladrow, 2001;

Table 3: Kinetic oxygen and carbon fractionation factors

Reaction	Carbon		Oxygen	
	ϵ (‰)	Reference/Note	ϵ (‰)	Reference/Note
$\text{CO}_2(\text{g}) \rightarrow \text{CO}_2(\text{aq})$	-2.1	Zhang et al. (1995)	+0.8	Vogel et al. (1970), 0°C
$\text{CO}_2(\text{aq}) \rightarrow \text{CO}_2(\text{g})$?		?	
$\text{CO}_2(\text{aq}) + \text{H}_2\text{O} \rightarrow \text{HCO}_3^- + \text{H}^+$	-23 to -33	Zeebe (2014)	-13 to -15	Zeebe (2014)
	-17.6	Yumol et al. (2020)	-18.8	Yumol et al. (2020), from $\text{CO}_2(\text{g})$
	-19.7	calculated after Clark and Lauriol (1992), 0°C; Zhang et al. (1995); Yu- mol et al. (2020)		
$\text{HCO}_3^- + \text{H}^+ \rightarrow \text{CO}_2(\text{aq}) + \text{H}_2\text{O}$	-32	Clark and Lauriol (1992); 0°C	-5.5	Clark and Lauriol (1992), 0°C
	-30.0	Guo (2009); Guo (2020)	-4.5	calculated from Guo and Zhou (2019)
			-22.9; +4.7	$\text{H}_2\text{O}-\text{HCO}_3^-$; CO_2- HCO_3^- , Guo and Zhou (2019)
$\text{CO}_2(\text{aq}) + \text{OH}^- \rightarrow \text{HCO}_3^-$	-17.1	Christensen et al. (2021)	-7.3	Christensen et al. (2021, 2022)
$\text{HCO}_3^- \rightarrow \text{CO}_2(\text{aq}) + \text{OH}^-$	-22.5	Guo (2009); Guo (2020)	-16.7	Guo (2009)
			-75.2; +12.6	$\text{OH}^- - \text{HCO}_3^-$; CO_2- HCO_3^- , Guo and Zhou (2019) (in agreement with Guo, 2009)
$\text{HCO}_3^- \rightarrow \text{CO}_3^{2-} + \text{H}^+$?		-5	Devriendt et al. (2017); calculated after Kim et al. (2006)
$\text{CO}_3^{2-} + \text{H}^+ \rightarrow \text{HCO}_3^-$?		?	
$\text{Ca}^{2+} + \text{HCO}_3^- \rightarrow \text{CaCO}_3 + \text{H}^+$	0	Watkins and Hunt (2015)	-4	Watkins et al. (2014)
$\text{CaCO}_3 + \text{H}^+ \rightarrow \text{Ca}^{2+} + \text{HCO}_3^-$	+2.5	Bottinga (1968); Mook (1986); Zhang et al. (1995); Watkins and Hunt (2015)	-1.8	Coplen (2007); Wang et al. (2013); Watkins et al. (2014)
$\text{Ca}^{2+} + \text{CO}_3^{2-} \rightarrow \text{CaCO}_3$	0	Watkins and Hunt (2015)	-2	Watkins et al. (2014)
			-0.5	Devriendt et al. (2017); calculated after Kim et al. (2006)
$\text{CaCO}_3 \rightarrow \text{Ca}^{2+} + \text{CO}_3^{2-}$	+2.1	Bottinga (1968); Zhang et al. (1995); Watkins and Hunt (2015)	-5.3	Coplen (2007); Wang et al. (2013); Watkins et al. (2014)

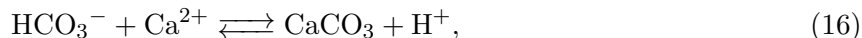
Sade and Halevy, 2017) so that instantaneous isotopic equilibration of HCO_3^- - CO_3^{2-} is typically assumed (Zeebe and Wolf-Gladrow, 2001; Devriendt et al., 2017; Christensen et al., 2021). Equilibrium CO_3^{2-} is -0.4‰ and -6.8‰ isotopically lighter than HCO_3^- for carbon and oxygen, respectively (Mook, 1986; Beck et al., 2005; Christensen et al., 2021).

Due to the rapid equilibration of HCO_3^- - CO_3^{2-} , the KFFs attending the forward and backward reactions of this exchange have not been fully explored. Kim et al. (2006) found their carbonates grown from the quantitative DIC pool recorded isotopically heavier oxygen isotope compositions than carbonates grown from a fraction of the DIC pool (3-91%), and attributed this to preferential deprotonation of isotopically light HCO_3^- . Devriendt et al. (2017) calculated an oxygen KFF of $\epsilon_{\text{CO}_3^{2-}/\text{HCO}_3^-}^{18} = -5\%$ based on the Kim et al. (2006) study.

4.4 CaCO_3 precipitation/dissolution

Isotopic equilibrium is only achieved in rare cases of natural low-temperature calcite growth because commonly, mineral precipitation reactions outpace both the reverse dissolution reactions and isotopic equilibration of DIC species with the much larger H_2O oxygen reservoir.

CaCO_3 mineral precipitation proceeds via both HCO_3^- and CO_3^{2-} pathways. Still, some models assume only CO_3^{2-} contributes to calcite growth (e.g. Devriendt et al., 2017), though there is increasing evidence that both HCO_3^- and CO_3^{2-} participate. Despite HCO_3^- being the dominant DIC species over the range of pH, temperature, and solution composition conditions in which the majority of natural carbonates precipitate (Millero et al., 2006; Millero et al., 2007), CO_3^{2-} is still the main DIC contributor to the mineral lattice even when CO_3^{2-} constitutes <0.5% of total DIC pool (Devriendt et al., 2017; Sade et al., 2020). The direct participation of bicarbonate in carbonate mineral growth proceeds by:



while the carbonate ion pathway follows:



Previous studies of calcite growth kinetics suggest that the rate-limiting process during growth is the dehydration of its constituent ions, which must shed their hydration spheres in order to attach at the mineral surface (Andersson et al., 2016; Zuddas and Mucci, 1998). Calcium ions have higher charge density than carbonate ions, and are therefore more strongly hydrated and take longer to shed their hydration sphere (Helgeson and Kirkham, 1976). The dehydration rate of Ca^{2+} has been estimated at 1-2 orders of magnitude slower than that of anions such as CO_3^{2-} (Larsen et al., 2010). However, in our experimental solutions, as well as seawater and many natural waters, the concentration of Ca^{2+} is three or more orders of magnitude higher than CO_3^{2-} , which suggests the dehydration of (bi)carbonate may be rate-limiting instead (Larsen et al., 2010).

Equilibrium calcite records an oxygen isotope composition 5.5‰ heavier than CO_3^{2-} , but 1.3‰ lighter than HCO_3^- (Beck et al., 2005; Coplen, 2007; Watkins et al., 2013). Kinetic fractionations for CaCO_3 precipitation were fit to the ion-by-ion model results of Watkins et al. (2014) and found to be $\epsilon_{\text{CaCO}_3/\text{CO}_3^{2-}}^{18} = -2\text{‰}$ and $\epsilon_{\text{CaCO}_3/\text{HCO}_3^-}^{18} = -4\text{‰}$. Using these KFFs paired with the Coplen (2007) calcite-water equilibrium fractionation and the Wang et al. (2013) equilibrium fractionations for HCO_3^- -water and CO_3^{2-} -water, the kinetic fractionations for CaCO_3 dissolution were calculated as $\epsilon_{\text{CO}_3^{2-}/\text{CaCO}_3}^{18} = -5.3\text{‰}$ and $\epsilon_{\text{HCO}_3^-/\text{CaCO}_3}^{18} = -1.8\text{‰}$.

4.5 H_2O dissociation

Another reaction within the CaCO_3 -DIC- H_2O system is the dissociation of water:



The timescale of the dissociation of water is short, comparable to the rate of HCO_3^- - CO_3^{2-} exchange (Zeebe and Wolf-Gladrow, 2001), and is therefore regarded as having attained isotopic equilibrium when dealing with the DIC- H_2O system and the much slower equilibration of CO_2 - HCO_3^- . Although dissociation of water is commonly written as Eq. (18), most hydrogen is hydrated in complexes such as H_3O^+ , H_5O_2^+ , etc., though for simplicity we write it in its most reduced form as seen here. Most hydrogen ion does not actually exist as “free hydrogen” in aqueous solutions, though it can be convenient to treat it as such when writing expressions.

The equilibrium oxygen isotopic fractionation between hydroxide and water is still debated. Experimental studies suggest that $1000\ln\alpha_{\text{OH}^- - \text{H}_2\text{O}}$ is between -45 to -49‰ at 15°C, and $\sim -42.5\text{‰}$ at 25°C (Green and Taube, 1963; Bajnai and Herwartz, 2021), while theoretical calculations suggest much smaller values of -19.1 to -23.5‰ at 25°C, depending on the number of water molecules involved in the reactions (Zeebe, 2020). This $\sim 20\text{‰}$ offset between experimental and theoretical studies is cause for concern when applying these values to quantitative problems and is in need of further study.

Some researchers postulate a $1000\ln\alpha_{\text{OH}^- - \text{H}_2\text{O}} \approx 0\text{‰}$, based on the observation that there is little difference in the oxygen isotopic fractionations between several calcium-bearing minerals and water, compared to the corresponding dissolved species and water (e.g. CO_3^{2-} -water and $\text{CaCO}_3(\text{s})$ -water, or SO_4^{2-} -water and $\text{CaSO}_4(\text{s})$ -water) and that if this trend holds true for portlandite then $1000\ln\alpha_{\text{OH}^- - \text{H}_2\text{O}} \approx 0$ because $1000\ln\alpha_{\text{Ca}(\text{OH})_2(\text{s}) - \text{H}_2\text{O}}$ is small (Böttcher et al., 2018). Zeebe (2020) disagrees, citing that for carbonate and sulfate minerals, the covalent bonds of both the aqueous species (CO_3^{2-} and SO_4^{2-}) and solid minerals are similar in nature and dominate the isotopic fractionation, with differences between the aqueous and solid environments being more minor. Zeebe (2020) explains that the O-H bond of H_2O and OH^- is considerably weaker than the O-C bond of dissolved and solid carbonate, and is expected to exhibit larger isotopic differences between the aqueous and solid phases.

5 Isotopic composition of calcite

5.1 Oxygen isotopes: $\delta^{18}\text{O-T}$

The oxygen isotopic composition of calcite exhibits a strong temperature-dependence (Urey, 1947; McCrea, 1950; Kim and O’Neil, 1997; Coplen, 2007; Watkins et al., 2013; Daëron et al., 2019) and is commonly used in paleoclimate studies to reconstruct past sea surface temperatures. Equilibrium oxygen isotope partitioning between calcite and water is found only in extremely slowly grown natural calcites (Coplen, 2007; Daëron et al., 2019). Previous calibrations based on both natural and experimental calcite that have precipitated at or near isotopic equilibrium are systematically one to several permil isotopically lighter than the extremely slowly grown natural subaqueous calcites grown in Devils Hole cave (Coplen, 2007) and Laghetto Basso lake within Corchia Cave (Daëron et al., 2019). Laghetto Basso calcite is a lower temperature (7.9°C) parallel to the previously well-established Devils Hole calcite (33.7°C), creating a more robust equilibrium oxygen isotopic temperature calibration (Daëron et al., 2019), of which has nearly the same slope ($\sim 0.2\text{‰}$ decrease per unit Kelvin) as the calibration from experimental and common natural calcites (Kim and O’Neil, 1997) but which is offset $\sim 1.5\text{‰}$ to lower values. This experimental calibration using Devils Hole and Laghetto Basso cave calcites is indistinguishable from both the equation of Watkins et al. (2013) and the original prediction made in Coplen (2007) based solely on the Devils Hole calcite (Fig. 4).

Most natural and experimental calcite grows too quickly to maintain equilibrium between the $\text{CaCO}_3\text{-DIC-H}_2\text{O}$ reservoirs, in which case factors including growth rate, pH, degree of supersaturation (Ω), and solution composition affect the oxygen isotope signature recorded in the mineral. Most natural calcites record kinetic oxygen isotope effects of at least 1-2‰ (Daëron et al., 2019). Despite these strong pervasive kinetic effects, calcite-water oxygen isotope thermometry works reasonably well because many natural carbonates precipitate under narrow ranges in pH and growth rates (Watkins et al., 2014).

Higher degrees of supersaturation correspond to faster growth rates (Nielsen et al., 2012), which in turn leads to lower oxygen isotope composition (Dietzel et al., 2009) as isotopic fractionation moves away from equilibrium partitioning and towards the kinetic limit (Lemarchand et al., 2004; Tang et al., 2008; Nielsen et al., 2012). Coplen (2007) suggested that rapid growth rates result in the preferential incorporation of isotopically light CO_3^{2-} , while very low degrees of supersaturation ($\Omega=0.16\text{-}0.21$) correlated with very slow growth rates.

Gabitov et al (2012) systematically changed growth rate and found that slow growth allowed the crystal surface to reach equilibrium with the bulk calcite lattice, but that fast growth “captured” disequilibrium crystal surface isotopic signatures that were isotopically lighter than the bulk lattice. These experiments suggest that the near-surface region of calcite may be depleted in ^{18}O relative to the bulk lattice under equilibrium conditions (Gabitov et al, 2012). Increasing growth rate resulting in isotopically lighter calcite supports the Watson (2004) growth entrapment model (GEM). While Watson (2004) models calcite growth by the diffusivity of the near-surface layers competing with

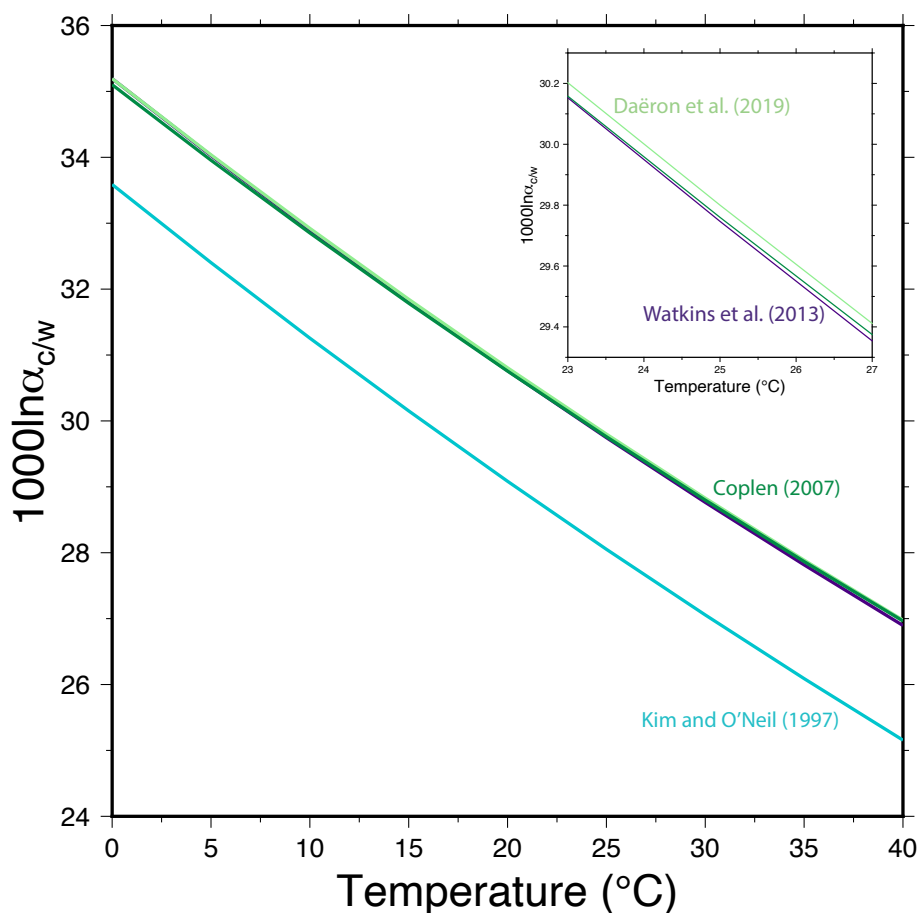


Figure 4: Compilation of $\delta^{18}\text{O}$ vs. temperature calibrations for a range of natural and synthetic, inorganic and biogenic CaCO_3 . The calibrations of Coplen (2007), Watkins et al. (2013), and Daëron et al. (2019) are in agreement (see inset), and are generally accepted in the low temperature carbonate community to represent equilibrium oxygen isotope fractionation between calcite and water. The calibration of Kim and O'Neil (1997) has the same slope as the above calibrations with an approximately 2 ‰ offset to isotopically lower values. Many natural and synthetic calcites do not achieve isotopic equilibrium due to a variety of factors, and often record isotopic compositions along the Kim and O'Neil (1997) calibration.

crystal growth rate, another growth model treats the isotopic signature of a mineral as a reflection of the competition between attachment and detachment rates at the crystal surface, yielding isotopic compositions ranging from equilibrium to fully kinetic (DePaolo, 2011).

Impurity ions in the calcite lattice may also affect the $\delta^{18}\text{O}$ of the calcite. Experiments carried out over a range in temperature (25 – 80°C) and solution Mg/Ca found that increasing Mg content of the calcite resulted in heavier $\delta^{18}\text{O}$ such that at 25°C, 5 mol% MgCO_3 increased $1000\ln\alpha_{c/w}$ by 0.88‰ (Mavromatis et al., 2012).

Chapter III explores the effect of ionic strength on isotopic fractionation in inorganic calcite, while Chapter IV investigates the role of solution pH.

5.2 Clumped isotopes: Δ_{47} -T

Clumped isotopologues are molecules in which heavy isotopes are bonded, or “clumped”, together. In carbonates, ^{18}O and ^{13}C result in a mass 47 CO_2 molecule of $^{13}\text{C}^{18}\text{O}^{16}\text{O}$, or a mass 63 CO_3^{2-} molecule of $^{13}\text{C}^{18}\text{O}^{16}\text{O}^{16}\text{O}$. The clumping of heavy isotopes is temperature-dependent, with a greater degree of clumping occurring at lower temperatures and fading to a stochastic distribution with increasing temperature (Ghosh et al., 2006; Eiler, 2007). This is a self-contained isotopic thermometer in calcite, not requiring isotopic analysis (or estimation) of the water the calcite grew from, unlike the oxygen isotope thermometer (Eiler, 2007).

The first Δ_{47} -temperature calibration was presented in Ghosh et al. (2006) based on analysis of mass 47 CO_2 produced from phosphoric acid digestion of synthetic calcite and biogenic aragonite. In less than two decades, the clumped isotope carbonate community has exploded with dozens of revised Δ_{47} -T calibrations based on theoretical models and calculations (Guo, 2009; Passey and Henkes, 2012), experimentally-grown carbonates (Zaarur et al., 2013; Tang et al., 2014; Kluge et al., 2015; Levitt et al., 2018), slowly-grown natural inorganic calcite (Daëron et al., 2019), a wide variety of biogenic carbonates including from otoliths (Ghosh et al., 2007), foraminifera (Wacker et al., 2014 – also brachiopod, bivalve, ostrich egg) and even separate mineral-specific calibrations such as for siderite (van Dijk et al., 2019) (Figure 5).

Despite the abundance of slightly different proposed equilibrium Δ_{47} -T calibrations (Fig. 5), the clumped isotope community seems to be converging on a single equilibrium calibration resulting from efforts in cross-correlating results between laboratories and accounting for how slight differences in methods may affect the calibration equations (e.g. acid digestion temperature, CO_2 purification process, selection of reference frame, selection of standards, use or lack of carbonic anhydrase when growing synthetic calcites, etc.) (Tripathi et al., 2015; Kelson et al., 2017).

As the community nears an equilibrium Δ_{47} -T calibration, studies have begun to tease apart KIEs in Δ_{47} of carbonate minerals. Solution pH is expected to influence isotope clumping in fast-growing carbonates (Hill et al., 2014; Watkins and Hunt, 2015; Tripathi et al., 2015; Kluge et al., 2018; Daëron et al., 2019). While I do not report Δ_{47} values in this dissertation, experiments of both Chapters IV and V grew CaCO_3 across a range of pH. Growth rates for calcite in Chapter IV are fast, but unlikely to record particularly large KIEs in Δ_{47} . CaCO_3 of Chapter V, however, mimicked processes occurring at hyperalkaline springs from which travertines have recorded large Δ_{47} enrichments up to 0.2‰ above expected equilibrium values (Falk et al., 2016). We therefore expect our experimental CaCO_3 from Chapter V to preserve significant KIEs in Δ_{47} as well, which is an avenue of continued study.

6 Paleoenvironment applications

The isotopic composition of major elements in calcite, as well as the concentration and isotopic composition of trace elements, has been an important topic of study over the last several decades. Some studies quantify trace element incorporation and isotopic fractionation using natural inorganic

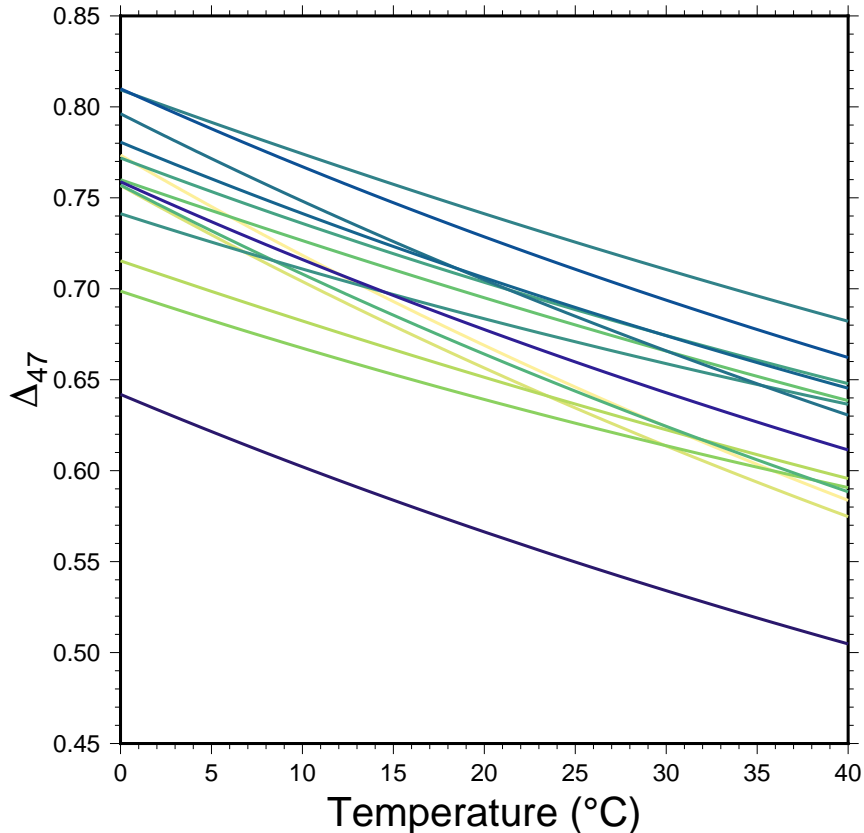


Figure 5: Compilation of Δ_{47} vs. temperature calibrations for a range of natural and synthetic, inorganic and biogenic CaCO_3 . Arranged from light yellow to dark blue: Ghosh et al., 2006; Ghosh et al., 2007; Guo, 2009; Dennis and Schrag, 2010; Passey and Henkes, 2012; Zaarur et al., 2013; Tang et al., 2014; Wacker et al., 2014; Kluge et al., 2015; Tripathi et al., 2015; Kelson et al., 2017; Levitt et al., 2018; Peral et al., 2018; Daëron et al., 2019; van Dijk et al., 2019. Notably, the outlying calibration at lower Δ_{47} values is the van Dijk et al., 2019 calibration for siderite, while all other calibrations are for CaCO_3 . Earlier calibrations (yellow to light green colors) tend to report lower Δ_{47} values, with more recent calibrations (dark green to blue colors) trending towards higher Δ_{47} . The slopes of the Δ_{47} -T calibrations are generally consistent.

or biogenic calcite, while other studies experimentally precipitate calcite under controlled laboratory conditions. Many paleoproxies involving the isotopic and/or trace element concentration of calcite have been recognized and quantified, with additional potential proxies being a continuing forefront of research in the low temperature geochemistry community.

Shifts in the isotopic composition of speleothem calcite in caves along the South African coast were interpreted as climate signals, with lower $\delta^{18}\text{O}$ values signaling weaker summer rains and stronger winter rains, and lower $\delta^{13}\text{C}$ values corresponding with more C3 grasses, which are isotopically lighter than C4 grasses (Table 1) (Bar-Matthews et al., 2010). Biogenic lacustrine calcite

was found to have the highest $\delta^{18}\text{O}$ and $\delta^{13}\text{C}$ when it was deposited along with gypsum, interpreted as low lake levels and an arid climate, and the lowest $\delta^{18}\text{O}$ and $\delta^{13}\text{C}$ when it was deposited along with clay sediments during higher lake levels with a moister climate (Escobar et al., 2012). Mg/Ca and Sr/Ca concentrations of calcite from veins in mid-ocean ridge flank basalts were used to reconstruct past seawater composition (Coggon et al., 2010). Veins that formed at low temperatures ($<6^\circ\text{C}$) were found to be reliable records of seawater chemistry due to minimal seawater-basalt interaction at that temperature, while veins that formed at warmer temperatures required calculation of the evolved fluid back to pre-basalt interaction in order to tease out the seawater signal (Coggon et al., 2010).

6.1 Trace elements

Trace element partitioning between calcite and solution is commonly affected by factors such as temperature, precipitation rate, solution ionic strength, impurity ion concentration, or the concentration of other ions in solution. While solid solution incorporation with the impurity ion replacing Ca^{2+} in the calcite lattice is commonly assumed, there are several other mechanisms of trace element incorporation including surface adsorption, occlusion, and separate phase formation (Pingitore et al., 1988). Some impurity ions are smaller than Ca^{2+} , such as Mg^{2+} and Mn^{2+} , while others such as Sr^{2+} and Ba^{2+} , are larger.

Both Mg/Ca and Sr/Ca in calcite are widely used to reconstruct past sea surface temperatures. Cl eroux et al. (2008) report Mg/Ca and Sr/Ca temperature calibrations derived from foraminiferal calcite, with both Mg and Sr uptake into calcite increasing with temperature. Lopez et al. (2009) also found an increase in [Mg] with temperature that was mostly insensitive to precipitation rate and degree of supersaturation, and suggested that temperature-dependence of Mg incorporation may be related to the changes in calcite growth mechanisms they observed with temperature. Other studies of Mg partitioning found increased Mg uptake as both growth rate and degree of supersaturation increased (Mavromatis, et al., 2013). Despite the strong Sr/Ca temperature relationship, Sr incorporation into calcite is also affected by growth rate, solution composition ($[\text{Sr}]$, $[\text{Ca}]$, $[\text{CO}_3^{2-}]$), ionic strength, and the Mn and Mg content of the calcite (Ichikuni, 1973; Carpenter and Lohmann, 1992; Cl eroux et al., 2008). The uptake of smaller trace elements (i.e. Mn^{2+} , Mg^{2+} , Fe^{2+}) may distort the calcite lattice and subsequently allow for greater incorporation of larger ions such as Sr^{2+} (Ichikuni, 1973), as the co-variation of trace element concentrations is commonly observed (Carpenter and Lohmann, 1992; Cl eroux et al., 2008).

Carbonate mineral growth rate commonly affects trace element partitioning, as well as the isotopic composition of the trace element incorporation. Sr incorporation is primarily affected by growth rate, with a lesser dependence on ionic strength (Tang et al., 2012). While biogenic and inorganic marine calcites incorporate similar concentrations of Mg, the [Sr] of biogenic calcite is consistently offset to higher values compared to inorganic calcite due to high growth rates (Carpenter and Lohmann, 1992). Experimental calcite and biogenic calcite were found to have similar Sr partition coefficients, suggesting they precipitate at similar rapid rates, while slowly-grown, natural

inorganic calcite is a better candidate for calculating Sr partition coefficients that approach equilibrium (Carpenter and Lohmann, 1992). Sr isotope fractionation in calcite has also been demonstrated to be strongly dependent on growth rate, and that equilibrium $\Delta^{88/86}\text{Sr}_{\text{CaCO}_3-\text{Sr}^{2+}} \approx 0$ (Böhm et al., 2012).

Trace element uptake also affects calcite crystal growth morphology. Mg^{2+} incorporation into calcite has also been shown to affect the morphology of the crystals by differential step interaction, which leads to roughened step edges and the development of pseudofacets that alter overall crystal shape (Davis et al., 2004). Folk (1974) found that high Mg/Ca solutions resulted in more elongate to acicular calcite crystals, while low Mg/Ca solutions yielded more equant to rhombic crystal morphologies. Intrasectoral zoning of trace element concentrations has been observed for Mg, Sr, and Mn in calcite, indicating that certain step geometries preferentially incorporate these trace elements (Paquette and Reeder, 1995; Davis et al., 2004). Li^+ incorporation into calcite has also been experimentally demonstrated to stabilize the basal (0001) face, thereby modifying crystal shape (Wang et al., 2011).

Trace elements may also affect the cathodoluminescence (CL) of a calcite crystal, which provides insight into textures and zoning that are not visible on an optical microscope. Mn^{2+} and trivalent REE (Sm^{3+} , Eu^{3+}) are the main CL activators in carbonates, while Fe^{2+} is the main CL quencher (Budd et al., 2000; Habermann, 2002; Major and Wilber, 1991; Mason, 1987; Richter et al., 2003). Mg and Sr do not demonstrate a relationship with CL in carbonates (Mason, 1987).

Cathodoluminescence (CL) has primarily been applied to diagenetic calcite cements to infer pH and redox potential of diagenetic environments, though stalagmites and biogenic calcifiers have also been imaged (Machel, 1985). A few studies on synthetic doped calcite have been conducted. Since Mn incorporation depends inversely on growth rate, natural calcites precipitated more slowly in cooler, deeper marine environments or recrystallized at slower rates may contain more Mn and be cathodoluminescent, in contrast to quickly precipitated calcite in shallow, warm seawater (Major and Wilber, 1991). Growth banding in diagenetic carbonates has been interpreted to be due to shifts in pH and redox conditions since Mn and Fe, the primary activator and quencher, have multiple valence states and their incorporation into calcite is most favored in less oxidizing waters where a greater portion of the ions are present in the 2+ valence state (Major and Wilber, 1991; Mason, 1987).

The $\delta^{11}\text{B}$ of calcite is used as a paleo-pH proxy (Zeebe and Wolf-Gladrow, 2001; Mavromatis et al., 2015; Uchikawa et al., 2015). While $\delta^{18}\text{O}$, $\delta^{13}\text{C}$, and Mg/Ca in calcite are strongly affected by diagenesis, $\delta^{11}\text{B}$ does not appear to be, which suggests that the boron isotopic composition of calcite may be a reliable paleo-pH indicator for even diagenetically altered calcic sediments (Edgar et al., 2015; Fantle, 2015). Boron in the oceans is present as both boric acid, $\text{B}(\text{OH})_3$, and borate ion, $\text{B}(\text{OH})_4^-$, characterized by pH-dependent speciation in which $[\text{B}(\text{OH})_3] = [\text{B}(\text{OH})_4^-]$ at \sim pH 8.6. Assuming that the $\delta^{11}\text{B}$ of average seawater does not substantially change over time, then the consistent isotopic offset between the two boron species and the hypothesis that only $\text{B}(\text{OH})_4^-$ is incorporated into calcite allow for solution pH to be reconstructed from $\delta^{11}\text{B}$ of calcite (Zeebe

and Wolf-Gladrow, 2001; Mavromatis et al., 2015; Uchikawa et al., 2015). However, experiments indicate kinetic effects primarily due to calcite growth rate and solution $[B]/[DIC]$ which may affect validity of this paleo-proxy (Uchikawa et al., 2015).

7 Bridge

In the preceding Chapter (II), I introduced important concepts including equilibrium and kinetic isotopic fractionation, the $\text{CaCO}_3\text{-DIC-H}_2\text{O}$ system and its reactions, and factors affecting the trace element and isotopic composition of carbonate minerals. While the oxygen isotope composition of calcite exhibits a strong temperature dependence, most natural and experimental carbonates precipitate too rapidly to maintain isotopic equilibrium between the mineral and the growth solution, and therefore factors other than temperature may affect the isotopic composition of the resulting carbonate. In Chapter III, we conduct well-controlled calcite growth experiments to isolate non-equilibrium kinetic isotope effects caused by the solution ionic strength. Many past studies conduct experiments in low ionic strength solutions, with conclusions that may not be as directly applicable to carbonates from saline settings. This work has significant implications for natural inorganic and biogenic calcite growing in seawater or even more saline environments.

CHAPTER III

OXYGEN ISOTOPES OF CALCITE PRECIPITATED AT HIGH IONIC STRENGTH: CaCO_3 -DIC FRACTIONATION AND CARBONIC ANHYDRASE INHIBITION

From Olsen, E.K., Watkins, J.M., and Devriendt, L.S. (2022). Oxygen isotopes of calcite precipitated at high ionic strength: CaCO_3 -DIC fractionation and carbonic anhydrase inhibition. *Geochimica et Cosmochimica Acta* 325, 170-186.

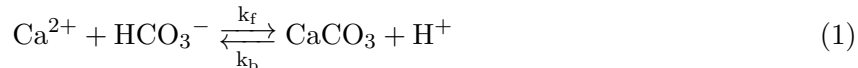
1 Introduction

Laboratory-controlled calcite and aragonite precipitation experiments have been used to determine isotopic fractionation factors between carbonate minerals and dissolved carbonate species or water. When crystals grow slowly, near chemical equilibrium conditions, oxygen isotope partitioning is expected to depend solely on temperature, providing a theoretical foundation for oxygen isotope thermometry (Bigeleisen and Mayer, 1947; Urey, 1947). It is often the case, however, that crystals grow fast enough that isotopic exchanges between phases do not reach equilibrium, leading to kinetic isotopic effects (KIEs) that depend on variables other than temperature and arise from either or both of the following: (1) a dissolved inorganic carbon ($\text{DIC} = \text{CO}_2 + \text{HCO}_3^- + \text{CO}_3^{2-}$) pool that is not fully equilibrated with water (Uzdowski et al., 1991; Zeebe and Wolf-Gladrow, 2001; Devriendt et al., 2017b) and/or (2) transport of ions to and from the mineral surface and reaction of ions at the mineral surface (DePaolo, 2011; Watkins et al., 2014, 2017).

Until recently, it was difficult to separate these two different sources of KIEs. The enzyme carbonic anhydrase from bovine erythrocytes (bCA) is commercially available and can be used in carbonate precipitation experiments to reduce or eliminate KIEs arising from homogeneous chemical reactions between DIC species and water (Uchikawa and Zeebe, 2012; Watkins et al., 2013, 2014). Addition of bCA in calcite growth experiments is useful for investigating isotopic fractionations under conditions that mimic the secretion of biogenic carbonates and for isolating surface reaction-controlled KIEs.

In the few calcite growth experiments where bCA has been employed for the purpose of equilibrating the DIC pool, there is a resolvable pH- and growth rate-dependence to the KIEs (Watkins et al., 2013, 2014). This suggests that surface reaction-controlled kinetic effects may be sensitive to the proportion of HCO_3^- versus CO_3^{2-} participating in growth (pH effect) and there is a mass

dependence to the reaction rate constants (growth rate effect) for the reactions:



where the k_f 's and k_b 's are forward (precipitation) and backward (dissolution) rate constants, respectively. Previous experiments with bCA were done in low ionic strength solutions, but background electrolytes are known to affect the solubility product of calcite (Mucci, 1983), calcite growth and dissolution kinetics (Ruiz-Agudo et al., 2010, 2011; Hong and Teng, 2014), calcite growth morphology (Wang et al., 2011), and solution speciation (e.g. Millero et al., 2006, 2007). Hence, solution composition may influence KIEs and be partly responsible for oxygen isotope variability in natural carbonates.

Here, we performed calcite-growth experiments under constant temperature (25°C) and pH (8.3) but with distinct salinities ($0.0 < [\text{NaCl}] < 1.4 \text{ M}$; $I = 0.1\text{-}1.6$) to assess the effect of ionic strength on calcite-DIC oxygen isotope fractionation and on the activity of bCA. We found no evidence for a salinity effect on the oxygen isotope fractionation between calcite and the DIC species up to a NaCl concentration of $\sim 0.35 \text{ M}$. However, NaCl significantly lowers the activity of the enzyme bCA, giving rise to highly variable isotopic results at higher NaCl concentrations. We use these well-controlled experiments to adapt and refine a previously published isotopic box model for kinetic isotope effects in the $\text{CaCO}_3\text{-DIC-H}_2\text{O}$ system (Chen et al., 2018; Christensen et al., 2021). The model is used to constrain the functional form for the salt effect on the enzyme-catalyzed rate constant for CO_2 hydration.

2 Methods

2.1 Calcite growth experiments

We use the same experimental setup as Watkins et al. (2013, 2014). Although the methods were described previously, we review them here because the details are used to develop a quantitative model reflecting our experimental conditions (Section 4). We measured the $\delta^{18}\text{O}$ of input CO_2 , which matters if the DIC pool is not fully isotopically equilibrated, and monitored [DIC] and total alkalinity 2-4 times per day.

Solutions were prepared by dissolving $\text{CaCl}_2 \cdot 2\text{H}_2\text{O}$ (30 mM), NH_4Cl (5 mM) and variable amounts of NaCl (0-1.4 M) in 1.7 L of deionized water. The beaker with the prepared solutions was submerged in a water bath containing both heating and cooling elements for precise temperature control ($25 \pm 0.2^\circ\text{C}$). The beaker was sealed by a lid that has ports for a pH probe, NaOH dripper, sampling syringe, and gas bubbler (Watkins et al., 2013). DIC was added to the solution by continuous bubbling of a $\text{CO}_2\text{-in-N}_2$ gas mixture through a diffusion stone at 0.5 standard cubic feet per hour using a SmartTrak100 gas flow controller (Sierra Instruments). The pCO_2 of the headspace

was recorded by a K-30 USB CO₂ Probe Data Logger (CM0039 from CO₂meter.com).

Prior to the start of an experiment, the gas was fluxed through the solution for 1-6 hours, during which time the headspace pCO₂ decreased from ~500 ppm to 240-280 ppm as the lab air was replaced by the gas tank mixture.

To begin an experiment, the autotitrator was activated and between 0.3-1.2 mL of 1 M NaOH was dispensed to bring the pH up to a setpoint of 8.3 ± 0.02 . The increase in pH caused CO₂ from the bubbles to partition into solution, which led to an abrupt decrease in the pCO₂ of the headspace. Variable amounts of bCA (0-3 μ M) were added after the solution had reached a pH of 8.3. The total alkalinity (TA) as measured by Gran titration increased from 0 to ~0.2-0.7 mEq/L following the addition of NaOH. The TA was measured each time samples were collected for [DIC] during the course of an experiment. From 22 titrations of the same solution carried out over the course of one week, we determined a 95% confidence interval of ± 0.03 and a standard error of 0.003 for our reported TA values, which accounts for any error due to pH probe calibration drift, issues with the autotitrator dispensing HCl accurately, and subjectivity in the Gran method calculation.

All of our experiments behaved similarly to the example shown in Figure 1a. Each experiment had a pre-precipitation period (Stage I) during which DIC, TA, and pCO₂ of the headspace increased as CO₂ dissolved in solution. Eventually, enough DIC was added for calcite crystals to nucleate and grow on the beaker walls, marking the onset of the calcite precipitation period (Stage II). The duration of Stages I and II, as well as the rate of NaOH addition, varies somewhat between experiments (Fig. 1b), which we attribute to fluctuations in the average size of bubbles emanating from the diffusion stone and random nucleation processes leading to differences in the initial surface area of the first crystals. The growth rate of calcite (mmol/h) was calculated from the rate of NaOH addition during Stage II (cf. Watkins et al., 2013).

The TA and [DIC] were measured at regular intervals and results from all experiments are plotted together in Figs. 2a and 2b. Solution ionic strength and free activities of Ca²⁺ and CO₃²⁻ were calculated through the R-package of PHREEQC using the Pitzer database (Charlton and Parkhurst, 2011; De Lucia and Kühn, 2013). The degree of supersaturation (Fig. 2c, $\Omega = \alpha_{\text{Ca}^{2+}} * \alpha_{\text{CO}_3^{2-}} / K_{\text{sp}}$) was determined by using these ionic activities and the solubility product of calcite at 25°C ($K_{\text{sp}} = 10^{-8.42}$, Jacobson and Langmuir, 1974). Additional considerations regarding DIC speciation as a function of salinity and solution composition are provided in Appendix A. In all experiments, a short period of rapid crystal growth at high Ω (5-11) was followed by a long period of crystal growth under relatively steady conditions at $\Omega = 3.7 \pm 1.5$.

Following the final measurements, experimental solutions were discarded and crystals adhered to the beaker walls were rinsed 3 times with de-ionized water and allowed to air-dry. Precipitates from each experiment were imaged on the FEI Quanta 200 Environmental Scanning Electron Microscope (ESEM) at the Center for Advanced Materials Characterization (CAMCOR) at the University of Oregon (Appendix B). ESEM imaging found only rhombohedral to rhombo-scalenohedral CaCO₃ crystals present. Additionally, X-Ray Diffraction (XRD) analysis of select experiments spanning the range in [NaCl] conducted at the Oregon State University X-Ray Diffraction Facility confirmed

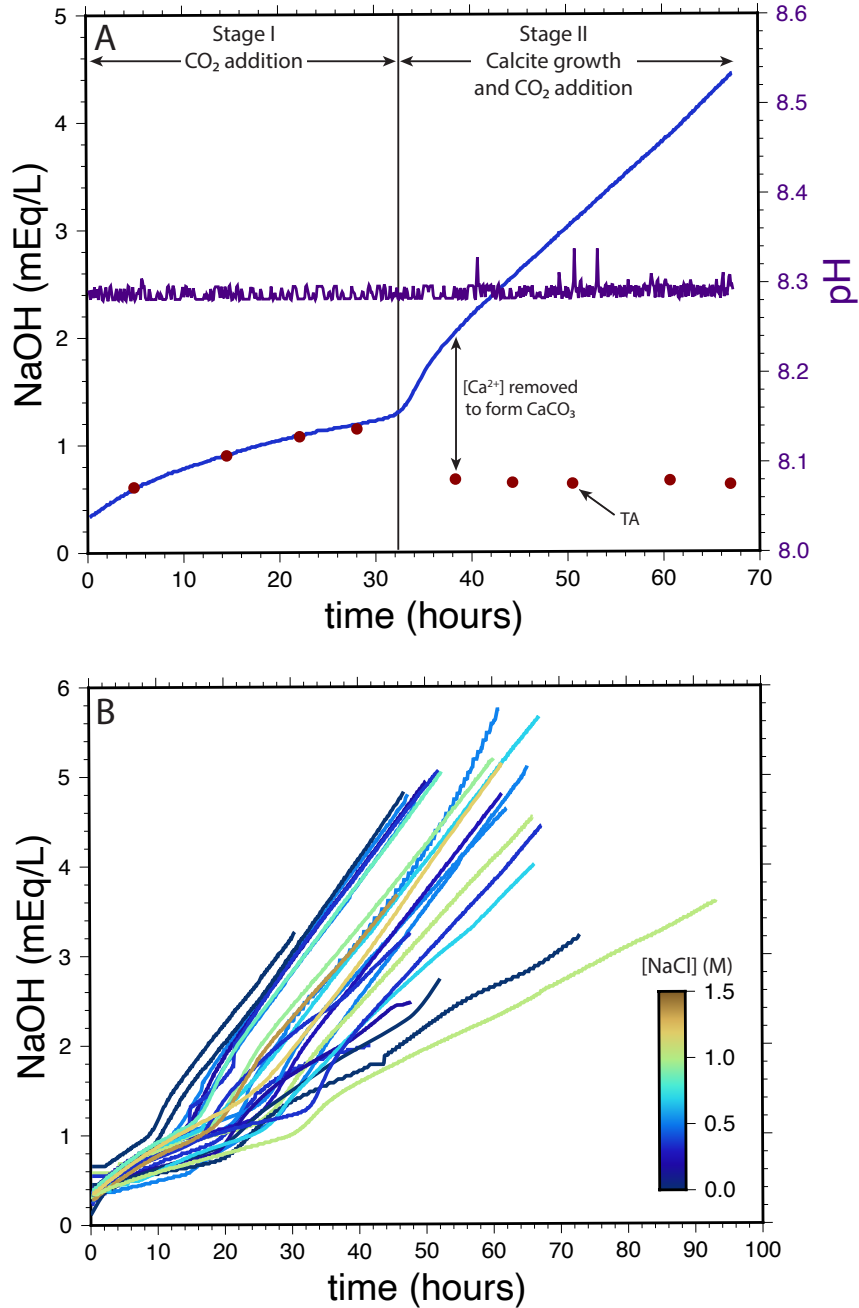


Figure 1: Behavior of the calcite growth experiments. (A) Example of an experimental run (S11). During Stage I, the increase in TA matches the amount of NaOH added to offset the addition of CO₂ to solution. At the onset of Stage II, the change in TA is due to addition of NaOH as well as removal of Ca²⁺ to CaCO₃. During Stage II, the difference between NaOH added and TA can be used to calculate the CaCO₃ flux (mmol/h). (B) Rate of NaOH addition for all experiments. The range of slopes during Stage II translates to a range in the CaCO₃ precipitation rate from 0.04 to 0.15 mmol/h.

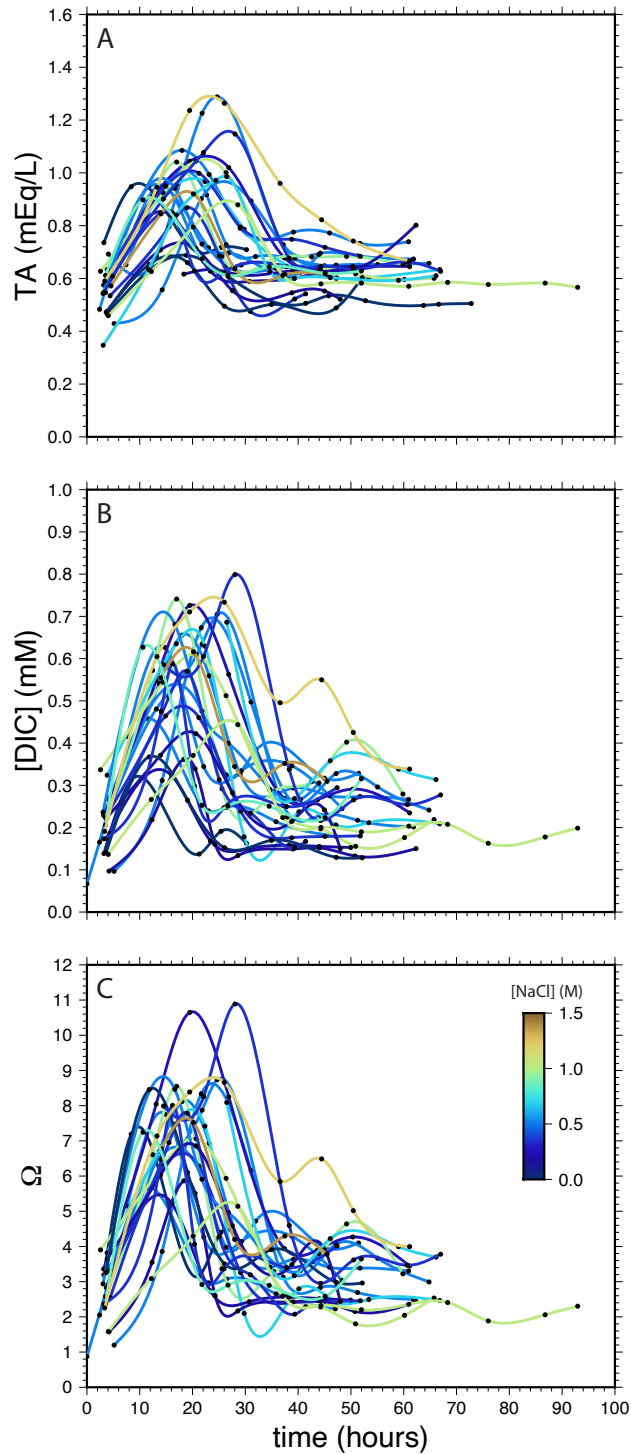


Figure 2: Variations in total alkalinity (TA, A), dissolved inorganic carbon (DIC, B) and calcite saturation state (Ω , C) during the course of each calcite growth experiment. Black dots are measured points (or calculated from measured points) and curves are splines. This figure shows the variabilities in TA, DIC and Ω are not related to the different NaCl concentrations. Typically, Ω increased to between 5 and 9 around the 15-20 hour mark before decreasing to a quasi-steady state value of $\Omega = 2$ to 4 after 30 hours.

that calcite is the only phase present.

2.2 $\delta^{18}\text{O}$, $\delta^{13}\text{C}$, and [DIC] measurements

Exetainers for all experimental water samples were prepared on a GasBench II in the Stable Isotope Laboratory at the University of Oregon, by flushing them with helium gas for five minutes. The isotopic composition of CO_2 in the CO_2 -in- N_2 mixtures (Table 1) was measured in the Stable Isotope Lab at the University of Oregon after cryogenic separation from the N_2 gas on a vacuum line that is otherwise and usually used for mineral fluorination. The gas tank with a regulator was connected to the inlet port of the vacuum line and set to 1 bar gauge pressure. Gas was allowed to flow into the line and atmospheric air was flushed out by cyclical opening and closing of valves at least three times to completely fill the line with the CO_2 -in- N_2 gas mixture and exclude air. Dewar flasks containing liquid nitrogen (LN_2) were placed at three traps along the line for at least 20 minutes to allow the small proportion of CO_2 in the gas mixture to freeze. The N_2 in the line was pumped away, and then LN_2 dewars at the two upstream traps were removed and heated to allow the CO_2 to collect at the yield measurement trap that was still submerged in LN_2 . Yield was obtained by heating the last and third trap that was isolated between valves, and observing the pressure on a digital manometer. An initial low digital gauge pressure reading was common due to the small fraction of CO_2 present in the gas (typically 200 ppm), often necessitating multiple cycles of gas mixture inlet and freezing of CO_2 at the traps. After all the upstream valves were closed, the last LN_2 dewar was removed, the trap heated, and downstream valve opened, allowing the purified CO_2 to flow from the vacuum line to a Thermo-Finnigan MAT 253 mass spectrometer.

The isotopic composition of the sample CO_2 gas was measured using the mass spectrometer dual inlet system, and a CO_2 reference gas of known composition. Though the standard analytical error (1σ) is $\pm 0.010\text{‰}$ for $\delta^{18}\text{O}$ and $\pm 0.005\text{‰}$ for $\delta^{13}\text{C}$, we suggest that our analyses may have greater uncertainty for several other reasons. Isotopic fractionation could be occurring at the gas tank regulator as the gas flows from the tank into the fluorination line, as well as during the preferential freezing of isotopically heavy CO_2 . Additionally, cryogenic separation procedures and mass spectrometer analyses suggest that some of our CO_2 -in- N_2 gas tanks contained a small amount of H_2O , which decreases our confidence in the measurements. Taking these uncertainties into account, we conclude the isotopic analysis of our CO_2 gas to be within $\pm 1\text{‰}$, which is sufficiently accurate for our purposes.

The isotopic composition of calcite, aqueous solution, and DIC were analyzed at the Stable Isotope Laboratory in the College of Earth, Ocean, and Atmospheric Sciences (CEOAS) at Oregon State University. Data are presented in standard delta notation. Water samples for DIC and $\delta^{13}\text{C}$ were taken 2-4 times per day during an experiment, while water for $\delta^{18}\text{O}$ was taken only at the end of most experiments since previous work showed constant $\delta^{18}\text{O}$ values over the course of an experiment (Baker, 2015).

For DIC analysis, 3.5 mL of water was injected through rubber septa into He-flushed exetainers. At CEOAS, 0.1 mL of 85% orthophosphoric acid was added to the exetainers. After equilibrating

for 4 hours, the gas headspace was analyzed by continuous-flow mass spectrometry on a GasBench-DeltaV system. A known concentration in-house NaHCO_3 standard was analyzed with the samples, from which a calibration curve was determined and DIC concentration in our samples was approximated. Data are reported in standard delta notation relative to VPDB (Appendix A, Table 2). The standard analytical error (1σ) is $\pm 0.15\text{‰}$ for $\delta^{13}\text{C}$ of DIC.

Water samples for $\delta^{18}\text{O}$ were collected in He-flushed exetainers and filled almost completely (~ 11 mL) to minimize headspace and allow for replicate analyses. The $\delta^{18}\text{O}$ was analyzed using the CO_2 -equilibration method whereby the CO_2 headspace is equilibrated with 5 mL of water while agitated in an 18°C water bath. The CO_2 was then analyzed by dual inlet mass spectrometry on a DeltaPlus XL and data are reported in standard delta notation relative to VSMOW (Table 1). The standard analytical error (1σ) is $\pm 0.05\text{‰}$ for $\delta^{18}\text{O}$ of H_2O .

Calcite samples were reacted with 105% orthophosphoric acid in a Kiel III preparation device for 8 minutes at 70°C . Evolved CO_2 and H_2O gases were condensed and CO_2 was separated and transferred into a MAT 252 mass spectrometer for analysis via dual inlet mass spectrometry. Data are reported in standard delta notation relative to VPDB (Table 1). The $\delta^{18}\text{O}$ data were converted to the VSMOW scale by the following relationship: $\delta^{18}\text{O}_{\text{VSMOW}} = 1.03091 \cdot \delta^{18}\text{O}_{\text{VPDB}} + 30.91$ (Coplen et al., 1983). The standard analytical error (1σ) is $\pm 0.05\text{‰}$ for $\delta^{18}\text{O}$ and $\pm 0.03\text{‰}$ for $\delta^{13}\text{C}$.

3 Results

3.1 Oxygen isotope fractionation

The fractionation factor between two phases or compounds, for example calcite (c) and water (w), are related to delta values as follows:

$$\alpha_{c/w} = \frac{(^{18}\text{O}/^{16}\text{O})_c}{(^{18}\text{O}/^{16}\text{O})_w} = \frac{\delta^{18}\text{O}_c + 1000}{\delta^{18}\text{O}_w + 1000} \quad (3)$$

With $[\text{NaCl}] = 0$ and $[\text{bCA}] \geq 0.2 \mu\text{M}$, the data form a tight cluster ($1000\ln\alpha_{c/w} = 28.0 \pm 0.1\text{‰}$, $n = 4$, Table 1, Fig. 3) that agrees with previous results from calcite growth experiments carried out at 25°C , pH 8.3 and with bCA (Watkins et al., 2013, 2014; Baker, 2015). These experiments indicate $0.2 \mu\text{M}$ bCA is sufficient to maintain an isotopically equilibrated DIC pool in low salinity experiments.

Results from experiments with added NaCl (0.2-1.4 M) and $[\text{bCA}] \sim 0.2 \mu\text{M}$ vary from 25.2 to 27.6‰ in $1000\ln\alpha_{c/w}$ (Table 1, Fig. 3) and are comparatively lower than results from the low salinity experiments.

Repeat NaCl experiments but with higher bCA concentrations (up to $2.9 \mu\text{M}$) display $1000\ln\alpha_{c/w}$ values consistently higher than those from experiments with $[\text{bCA}] \sim 0.2 \mu\text{M}$, indicating higher $[\text{bCA}]$ are required for isotopic equilibration of the DIC pool in solutions of high ionic strength. Specifically, experiments with $[\text{NaCl}]$ from 0.18 to 0.35 M and $[\text{bCA}] \sim 1 \mu\text{M}$ resulted in $1000\ln\alpha_{c/w}$

Table 1: Experimental parameters and isotopic data for all experiments of this study.

Experiment	[NaCl] (M)	Salinity ^a (g/kg)	bCA (mg)	[bCA] (μ M)	R (mmol/h)	$\log_{10}R$ (mol/m ² /s)	$\delta^{18}O_{\text{gas}}$ CO ₂ (VSMOW)	$\delta^{18}O_w$ (VSMOW)	$\delta^{18}O_c$ (VPDB)	$\delta^{18}O_c$ (VSMOW)	1000ln $\alpha_{c/w}$ (VSMOW)
S2 ^b	0.52	35	11.35	0.22	-	-	12.89	-11.65	-16.39	14.02	25.64
S3 ^b	0.52	35	10.48	0.21	-	-	12.89	-11.52	-16.43	13.98	25.47
S4 ^b	0.18	15	10.06	0.20	-	-	12.89	-11.42	-14.24	16.23	27.59
S5	0.35	25	10.89	0.21	0.053	-6.10	12.89	-11.32	-14.34	16.13	27.38
S6	0	3.5	10.6	0.21	0.044	-6.45	12.74	-11.31	-13.66	16.83	28.06
S7	0.18	15	10.04	0.20	0.057	-6.20	12.74	-11.34	-14.34	16.13	27.40
S8	0	3.5	10.48	0.21	0.053	-6.27	12.74	-11.39	-13.84	16.65	27.96
S9	0.35	25	10.21	0.20	0.070	-6.24	12.74	-11.40	-15.95	14.47	25.83
S10	0.69	45	10	0.20	0.071	-6.34	12.74	-11.39	-16.52	13.88	25.24
S11	0.35	25	10.01	0.20	0.093	-6.27	12.74	-11.62	-16.51	13.89	25.48
S12	1.37	85	10.03	0.20	0.094	-6.17	22.20	-11.57	-16.06	14.36	25.89
S13	1.03	65	10.27	0.20	0.040	-6.54	22.20	-11.72	-15.61	14.82	26.50
S14	0.86	55	10.24	0.20	0.103	-6.30	22.20	-11.82	-16.62	13.78	25.57
S15	1.20	75	10.41	0.20	0.101	-6.31	22.20	-11.82	-16.21	14.20	25.99
CA1	0.52	35	0	0.00	0.101	-6.31	24.30	-11.83	-16.01	14.41	26.20
CA2	0.52	35	20.35	0.40	0.102	-6.26	24.30	-11.86	-15.84	14.58	26.40
CA3	0.52	35	0.97	0.02	0.102	-6.27	24.30	-11.91	-16.43	13.98	25.86
CA4	0	3.5	0	0.00	0.101	-6.07	24.30	-11.68	-16.72	13.68	25.33
CA5	0.52	35	50.13	0.98	0.090	-6.31	24.30	-11.17	-14.18	16.29	27.39
CA6	0.52	35	100	1.96	0.105	-6.34	24.30	-11.18	-14.16	16.31	27.42
CA7	0.26	20	50	0.98	0.095	-6.30	24.30	-11.33	-13.67	16.82	28.07
CA9	0.95	60	100	1.96	0.089	-6.37	13.45	-11.57	-15.93	14.49	26.02
CA12	0.69	45	75.82	1.49	0.085	-6.44	13.45	-11.76	-14.91	15.54	27.24
CA13	1.03	65	150	2.94	0.082	-6.35	13.45	-11.65	-15.21	15.24	26.84
CA14	0.18	15	49.01	0.96	0.101	-6.29	13.45	-11.85	-14.16	16.31	28.09
CA15	0.35	25	50	0.98	0.100	-6.31	13.45	-11.86	-14.16	16.31	28.11
CA18 ^c	0	3.5	20	0.39	0.152	-6.28	23.50	-11.88	-14.26	16.21	28.03
CA20	0	3.5	10.12	0.20	0.089	-6.34	13.63	-11.95	-14.34	16.12	28.02

^a Salinities given are approximate.

^b Calcite growth rate could not be calculated for early experiments due to use of an unreliable NaOH autotitrator.

^c CA18 used an 800 ppm CO₂-in-N₂ gas tank, while all other experiments used 200 ppm CO₂-in-N₂ tanks. Flow rate was scaled back so that all experiments have a constant flux of 0.12-0.13 mmol CO₂/h.

values ($28.1 \pm 0.05\%$) indistinguishable from the low salinity experiments ($28.0 \pm 0.1\%$). These results suggest that, for these experiments, (1) the DIC pool remained isotopically equilibrated with $\sim 1 \mu\text{M}$ of bCA and (2) $[\text{NaCl}]$ of up to 0.35 M has no significant effect on $1000\ln\alpha_{c/w}$. However, experiments with $[\text{NaCl}] > 0.35 \text{ M}$ resulted in $1000\ln\alpha_{c/w}$ values significantly lower than 28.0% despite very high $[\text{bCA}]$ (up to $2.9 \mu\text{M}$). The cause of the lower $1000\ln\alpha_{c/w}$ values at high ionic strength is investigated in Section 6.2.

4 Model for calcite growth from a DIC pool with variable level of isotopic equilibration

The variability in $1000\ln\alpha_{c/w}$ as a function of $[\text{bCA}]$ is a manifestation of kinetic effects arising from a variably equilibrated DIC pool. Recent progress has been made on the development of numerical models that quantify kinetic isotope effects in the CaCO_3 -DIC- H_2O system (Chen et al., 2018; Christensen et al., 2021; Uchikawa et al., 2021). In this section, we present a model adapted from that of Chen et al. (2018), and use it to evaluate the oxygen isotopic variations observed. This is aided by the constraints we have on the CO_2 flux, $\delta^{18}\text{O}$ of CO_2 gas, and carbonate growth rates.

We begin with a 1.7 L solution at 25°C , $\text{pH} = 8.3$, $[\text{Ca}^{2+}] = 30 \text{ mM}$ and $[\text{DIC}] \sim 0.01 \text{ mM}$. The DIC is initially isotopically equilibrated. Equilibrium fractionation factors used in the model are provided in Table 2. As CO_2 bubbles through, some of it partitions into solution, constituting a net flux of $\text{CO}_2(\text{aq})$ (i.e., DIC). The incoming $\text{CO}_2(\text{g})$ has the isotopic composition of the gas tank, which is out of equilibrium with the dissolved $\text{CO}_2(\text{aq})$ and water. We assume there is no isotopic fractionation of CO_2 as it gets converted from the gaseous to dissolved state (equilibrium fractionation between $\text{CO}_2(\text{g})$ and $\text{CO}_2(\text{aq}) < 0.2\%$, Brenninkmeijer et al., 1983; Beck et al., 2005; diffusive isotope effects $< 0.7\%$; O’Leary, 1984). The CO_2 that enters solution undergoes hydration and hydroxylation reactions to produce HCO_3^- , a fraction of which deprotonates to form CO_3^{2-} . As the concentration of CO_3^{2-} increases, the degree of supersaturation (Ω) also increases, and calcite grows at a rate that depends on the degree of supersaturation. Fast calcite growth draws down $[\text{DIC}]$, thus slowing calcite growth in a negative feedback.

For the model to be informative, it should: (1) capture the behavior that a quasi-steady state is reached in the system whereby the influx of DIC from CO_2 (F_{CO_2}) is balanced by the outflux

Table 2: Compilation of equilibrium fractionation factors (EFFs; T in Kelvin).

Compounds	Equation	α (25 °C)	References
$\text{CO}_2(\text{g})\text{-H}_2\text{O}$	$17.611 T^{-1} + 0.9821$	1.0412	Zeebe (2007)
$\text{CO}_2(\text{aq})\text{-H}_2\text{O}$	$\exp(2520 T^{-2} + 0.01212)$	1.0413	Beck et al. (2005)
$\text{HCO}_3^-\text{-H}_2\text{O}$	$\exp(2590 T^{-2} + 0.00189)$	1.0315	Beck et al. (2005)
$\text{CO}_3^{2-}\text{-H}_2\text{O}$	$\exp(2390 T^{-2} - 0.00270)$	1.0245	Beck et al. (2005)
Calcite- H_2O	$\exp((\frac{17747}{T} - 29.777)/1000)$	1.0302	Coplen (2007), Watkins et al. (2013)
$\text{OH}^-\text{-H}_2\text{O}$	$(1 + [-4.4573 + \frac{10.3255 \cdot 10^3}{T} - \frac{0.5976 \cdot 10^6}{T^2}]/1000)^{-1}$	0.9771	Zeebe (2020)

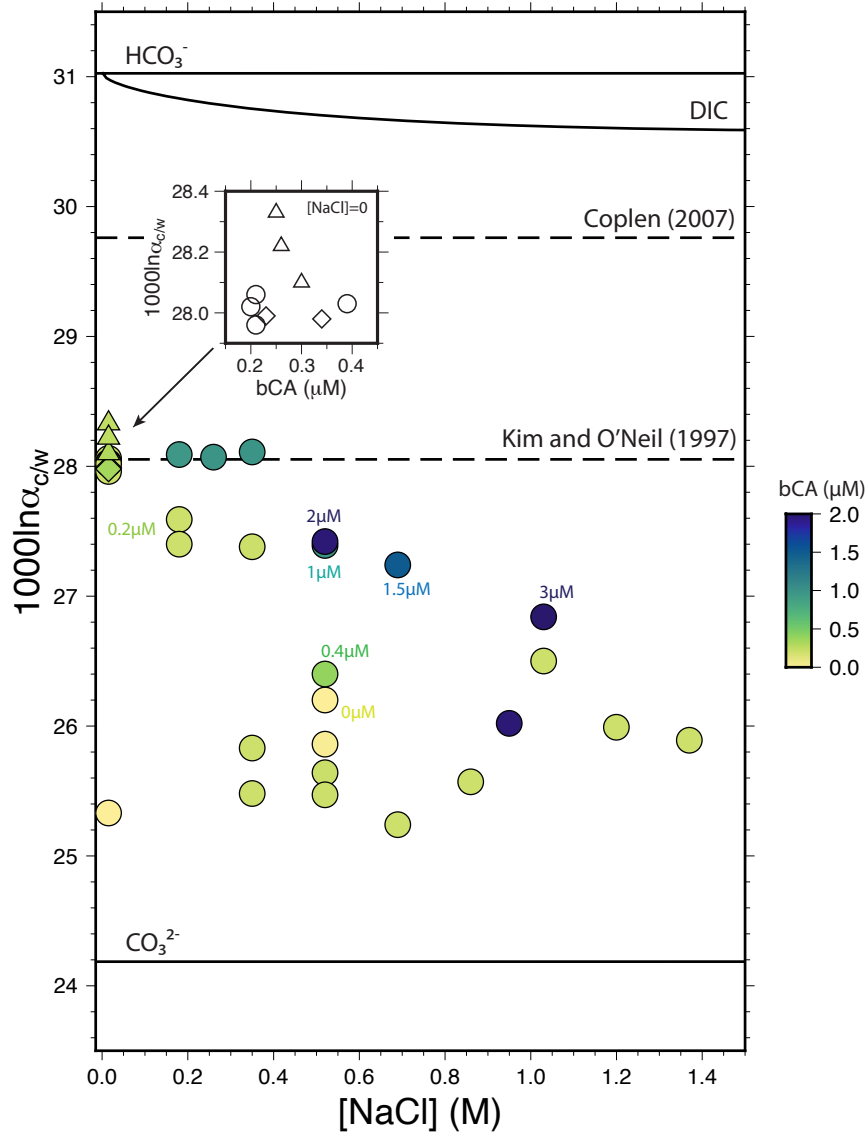
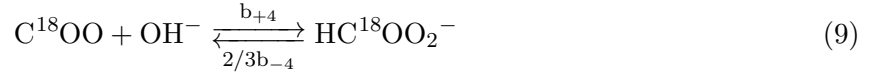
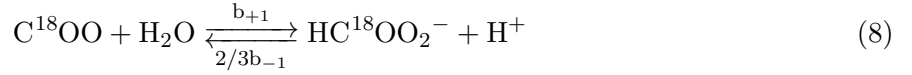
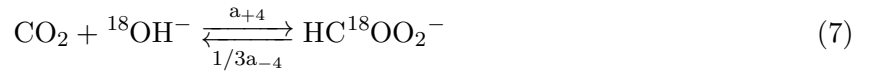
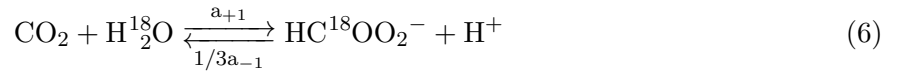
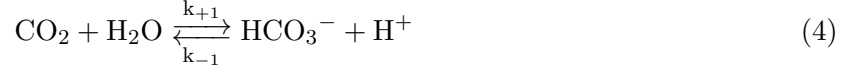


Figure 3: Calcite-water oxygen isotope fractionation expressed as $1000\ln\alpha_{c/w}$. Results from this study's experiments (circles) at low salinity ($[\text{NaCl}]=0$, $n=4$) agree with previous calcite growth experiments conducted at pH 8.3 and 25°C with bovine carbonic anhydrase (Watkins et al., 2014 – triangles; Baker, 2015 – diamonds), as well as with the expected value obtained using the Kim and O'Neil (1997) calibration. Experiments with $[\text{NaCl}] > 0.35$ M show lower and variable $1000\ln\alpha_{c/w}$ despite the use of high bovine carbonic anhydrase concentrations. Equilibrium fractionation factors are listed in Table 2 (Beck et al., 2005; Coplen, 2007). We use the Zeebe (2007) expression to calculate oxygen isotope fractionation between the sum of DIC and water, substituting Millero et al. (2007) pK values for simple NaCl solutions and equilibrium fractionation factors from Beck et al. (2005).

of DIC to calcite (F_{CaCO_3}), (2) reach steady state fluxes that agree with the inferred growth rate (mmol/h), and (3) provide insights into the isotopic results. For this latter point, we specifically seek to explain the 3‰ variability among the experiments despite the use of high [bCA].

4.1 Chemical reactions

The model tracks the following chemical and isotope exchange reactions (Chen et al., 2018; Christensen et al., 2021):



The k 's are rate constants for the (de)hydration and (de)hydroxylation reactions. Rate constants for the ^{18}O -substituted species are denoted a or b , with a representing substitution on H_2O or OH^- , and b representing substitution on CO_2 . The ratio of these rate constants is equal to the equilibrium constant for each reaction, as given in Table 3. We solve numerically these five coupled ordinary differential equations:

$$\frac{d[\text{CO}_2]}{dt} = -k_{+1}[\text{CO}_2] + k_{-1}[\text{EIC}]\chi[\text{H}^+] - k_{+4}[\text{CO}_2][\text{OH}^-] + k_{-4}[\text{EIC}]\chi^+ \frac{F_{\text{CO}_2}}{V} \quad (10)$$

$$\frac{d[\text{EIC}]}{dt} = k_{+1}[\text{CO}_2] - k_{-1}[\text{EIC}]\chi[\text{H}^+] + k_{+4}[\text{CO}_2][\text{OH}^-] - k_{-4}[\text{EIC}]\chi^- \frac{F_{\text{CaCO}_3}}{V} \quad (11)$$

$$\begin{aligned} \frac{d[\text{C}^{18}\text{OO}]}{dt} = & -b_{+1}[\text{C}^{18}\text{OO}] + \frac{2}{3}b_{-1}[^{18}\text{EIC}]^{18}\chi[\text{H}^+] - b_{+4}[\text{C}^{18}\text{OO}][\text{OH}^-] \\ & + \frac{2}{3}b_{-4}[^{18}\text{EIC}]^{18}\chi^+ \frac{F_{\text{CO}_2}^{18}\text{RCO}_2}{V} \quad (12) \end{aligned}$$

$$\begin{aligned} \frac{d[^{18}\text{EIC}]}{dt} = & a_{+1}[\text{CO}_2]r_w - \frac{1}{3}a_{-1}[^{18}\text{EIC}]^{18}\chi[\text{H}^+] + a_{+4}[\text{CO}_2][^{18}\text{OH}^-] - \frac{1}{3}a_{-4}[^{18}\text{EIC}]^{18}\chi \\ & + b_{+1}[\text{C}^{18}\text{OO}] - \frac{2}{3}b_{-1}[^{18}\text{EIC}]^{18}\chi[\text{H}^+] + b_{+4}[\text{C}^{18}\text{OO}][\text{OH}^-] - \frac{2}{3}b_{-4}[^{18}\text{EIC}]^{18}\chi \\ & - \frac{F_{\text{CaCO}_3}}{V} \frac{[^{18}\text{EIC}]}{[\text{EIC}]} \alpha_{\text{c/EIC}} \end{aligned} \quad (13)$$

and

$$\frac{d[\text{Ca}^{2+}]}{dt} = - \frac{F_{\text{CaCO}_3}}{V} \quad (14)$$

where F_{CO_2} and F_{CaCO_3} are fluxes (moles s^{-1}), V is volume (L), and HCO_3^- and CO_3^{2-} are written together as EIC (short for “equilibrated inorganic carbon”), assuming instantaneous equilibrium between these two species (Chen et al., 2018). The factors of 1/3 and 2/3 are needed for oxygen isotope mass balance; for every mole of $\text{HC}^{18}\text{OO}_2^-$ that undergoes dehydrations, $\sim 2/3$ goes to C^{18}OO and $\sim 1/3$ goes to H_2^{18}O .

Kinetic isotope fractionation between calcite and EIC (i.e., $\alpha_{\text{c/EIC}}$) is dependent on pH and growth rate, as described by the ion-by-ion model (Watkins et al., 2014) and a parameterized analytical expression (Devriendt et al., 2017b). Here, we adopt the ion-by-ion model of Watkins et al. (2014) but note that the Devriendt et al. (2017b) formulation produces nearly identical outputs at pH 8.3 and calcite growth rate = $10^{-6.3 \pm 0.3} \text{ mol m}^{-2} \text{ s}^{-1}$.

The free parameters of the model are F_{CO_2} and F_{CaCO_3} , and constraints on the functional form of each are discussed below.

4.2 CaCO_3 flux

The surface area normalized growth rate of CaCO_3 (moles $\text{m}^{-2} \text{ s}^{-1}$) is dependent on the degree of supersaturation through a commonly used rate law (Nancollas and Reddy, 1971; Berner and Morse, 1974; Morse, 1978):

$$R = k(\Omega - 1)^n \quad (15)$$

or in logarithmic form

$$\log_{10} R = \log_{10} k + n \log_{10}(\Omega - 1) \quad (16)$$

Zuddas and Mucci (1998) performed seeded calcite growth experiments using CaCl_2 - NaCl solutions that closely match our solution compositions. Their data, which span a wide range of ionic strengths, are shown in Figure 4. A linear regression using all of the Zuddas and Mucci (1998) data yields $n = 1.6$ and $k = 10^{-7.38}$. These values are used as a starting point, but the values can be adjusted to some degree, as permitted by the scatter of the data in Figure 4.

Table 3: Constants and parameters used in the model.

Symbol	Meaning	Value	Reference/Note
<i>Part I: Model Parameters</i>			
V	Volume of solution (L)	1.7	-
F_{CO_2}	CO ₂ flux into solution	$F_{\text{CO}_2} = mF_{\text{CaCO}_3} + b$	m and b to fit [DIC] data
R_{CaCO_3}	Carbonate precipitation rate (mol/m ² /s)	$R_{\text{CaCO}_3} = k(\Omega - 1)^n$	Zuddas and Mucci (1998)
		$n = 1.6$	
		$k = 10^{-7.38}$	
		$\Omega = \frac{[\text{Ca}^{2+}][\text{CO}_3^{2-}]}{K_{\text{sp}}}$	
Sp	Specific surface area (m ² /mol)	30	Tang et al. (2008)
SA	Total reactive surface area (m ²)	$\text{Sp} \cdot n_{\text{CaCO}_3}$	-
F_{CaCO_3}	Carbonate precipitation flux (mol/s)	$\text{SA} \cdot R_{\text{CaCO}_3}$	-
<i>Part II: Reaction rate constants</i>			
χ	Fraction of HCO ₃ ⁻ in EIC	$\chi = (1 + \frac{K_2}{[\text{H}^+]})^{-1}$	K_2 from Millero et al. (2006)
k_{+1}	Rate const. CO ₂ hydration (s ⁻¹)	$\log_{10} k_{+1} = 329.85 - 110.541 \log_{10}(TK) - \frac{17265.4}{TK}$	Pinsent et al. (1956) and Uchikawa and Zeebe (2012)
k_{-1}	Rate const. CO ₂ dehydration (M ⁻¹ s ⁻¹)	$k_{-1} = k_{+1}/K_1$	K_1 from Millero et al. (2007)
k_{+4}	Rate const. CO ₂ hydrox (M ⁻¹ s ⁻¹)	$\log_{10} k_{+4} = 13.635 - \frac{2895}{TK}$	Pinsent et al. (1956) and Uchikawa and Zeebe (2012)
k_{-4}	Rate const. CO ₂ dehydrox (s ⁻¹)	$k_{-4} = k_{+4} (\frac{K_w}{K_1})$	K_w from DOE (1994)
<i>Part III: Isotopic parameters</i>			
r_{CO_2}	¹⁸ O/ ¹⁶ O ratio of CO ₂	-	Isotope ratio
r_{EIC}	¹⁸ O/ ¹⁶ O ratio of EIC	-	Isotope ratio
R_{CO_2}	$[\text{C}^{18}\text{OO}]/[\text{CO}_2]$	$2r_{\text{CO}_2}$	Isotopologue ratio
R_{EIC}	$[\text{EIC}^{18}]/[\text{EIC}]$	$3r_{\text{EIC}}$	Isotopologue ratio
$^{18}\chi$	Fraction of HC ¹⁸ OO ₂ in EIC	$^{18}\chi = (1 + \frac{K_2 \cdot \alpha_{\text{CO}_3^{2-}/\text{HCO}_3^-}}{[\text{H}^+]})^{-1}$	K_2 from Millero et al. (2007)
a_{+1}, b_{+1}	Rate const for hydration (s ⁻¹)	$a_{+1}/k_{+1} = 1.0000^a$	Yumol et al. (2020)
		$b_{+1}/k_{+1} = 0.9812^a$	
a_{-1}, b_{-1}	Rate const for dehydration (M ⁻¹ s ⁻¹)	$a_{-1}/k_{-1} = K_1 \cdot \alpha_{\text{HCO}_3^-/\text{H}_2\text{O}}$	Equilibrium constant
		$b_{-1}/k_{-1} = K_1 \cdot \alpha_{\text{HCO}_3^-/\text{CO}_2}$	Equilibrium constant
a_{+4}, b_{+4}	Rate const for hydrox. (M ⁻¹ s ⁻¹)	$a_{+4}/k_{+4} = 0.9988^b$	Christensen et al. (2021)
		$b_{+4}/k_{+4} = 1.0000^b$	
a_{-4}, b_{-4}	Rate const for dehydrox. (s ⁻¹)	$\frac{a_{+4}}{k_{+4}} = \frac{K_1}{K_w} \cdot \frac{\alpha_{\text{HCO}_3^-/\text{H}_2\text{O}}}{\alpha_{\text{OH}^-/\text{H}_2\text{O}}}$	Equilibrium constant
		$b_{+4}/k_{+4} = \frac{K_1}{K_w} \cdot \alpha_{\text{HCO}_3^-/\text{CO}_2}$	Equilibrium constant
$\alpha_{\text{c/EIC}}$	Growth rate-dependent isotopic fractionation	$f(T, \text{pH}, [\text{Ca}^{2+}], [\text{HCO}_3^-], [\text{CO}_3^{2-}])$	Ion-by-ion model of Watkins et al. (2014)

^a These values yield a bulk KFF that is consistent with Yumol et al. (2020).

^b These values yield a bulk KFF that is consistent with Christensen et al. (2021).

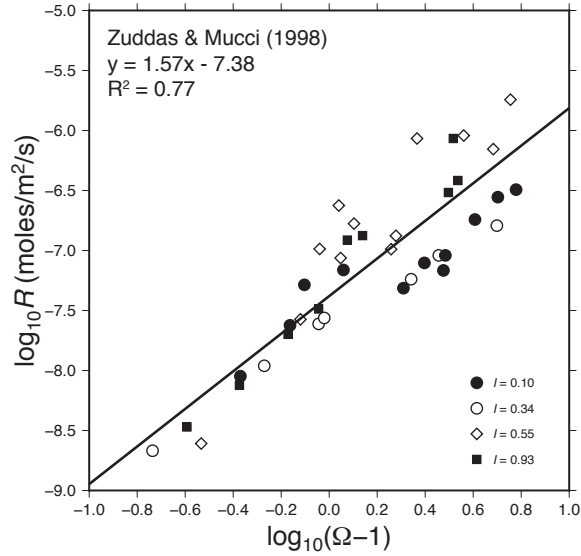


Figure 4: Effect of the solution saturation (Ω) on calcite growth rate (R) in simple $\text{CaCl}_2\text{-NaCl}$ solutions (data from Zuddas and Mucci, 1998). Seeded calcite precipitation experiments at varying ionic strength provide an empirical relationship between Ω and the surface area normalized growth rate R used in the model.

The CaCO_3 flux is related to the growth rate through the relationship:

$$F_{\text{CaCO}_3} = \text{SA} \cdot R \quad (17)$$

where SA is the reactive surface area (m^2). At the onset of an unseeded experiment, $\text{SA} = 0$ and then it increases as calcite nucleates and grows. To calculate SA , we use a specific surface area, Sp , which is the surface area of calcite crystals at the end of an experiment ($28 \pm 5 \text{ m}^2/\text{mol}$ for an average particle size of $\sim 10 \mu\text{m}$ as determined from SEM images; Tang et al., 2008).

Using the model, we estimate that 35% of the mass of crystals forms during the period of fast growth and 65% forms during the period of steady-state growth. The growth rate values in Table 1 are based on the steady state growth rate and thus represent minimum estimates.

4.3 CO_2 flux

The flux of CO_2 (moles s^{-1}) into solution is expressed as

$$F_{\text{CO}_2} = k_p ([\text{CO}_2]_{\text{eq}} - [\text{CO}_2]) \quad (18)$$

where $[\text{CO}_2]_{\text{eq}}$ is calculated from Henry's constant and the pCO_2 of the gas tank ($200 \mu\text{atm}$ in most experiments). The parameter k_p (kg-soln s^{-1}) describes the efficiency of gas transfer to solution, which varies between experiments depending on fluid dynamics (stirring) and the variable average bubble size produced by the diffusion stone. We therefore adjust k_p as needed to satisfy

the constraint that the CO_2 influx matches the DIC outflux (i.e., the calcite growth rate) at steady state. For experiment S8, a value for $k_p = 0.0026 \text{ kg-soln s}^{-1}$ satisfies this constraint.

5 Model results

Model outputs are compared to data from two low salinity experiments (exp. S8 and CA4 with no NaCl) in Figure 5. For the curves labeled “Model 1,” the reactive surface area increases monotonically (Fig. 5a), which leads to a steadily decreasing [DIC] and Ω during Stage II. For the curves labeled “Model 2,” the surface area of crystals is constant after the period of rapid nucleation and growth. This is akin to a seeded crystallization experiment where the reactive surface area is determined by the size distribution of seed crystals and assumed to be unchanging as overgrowth is added (e.g. Zuddas and Mucci, 1998). The different treatments of reactive surface area between Models 1 and 2 have little effect on the resulting isotopic composition of calcite.

The F_{CO_2} and F_{CaCO_3} curves (Fig. 5b and 5c) illustrate the negative feedback that leads to steady state behavior. The flux of CO_2 is at a maximum value initially because $[\text{CO}_2(\text{aq})] \sim 0$ and it decreases steadily during Stage I as $[\text{CO}_2(\text{aq})]$ accumulates in solution (Eq. 18). The accumulation of $[\text{CO}_2(\text{aq})]$ leads to an increase in F_{CaCO_3} into Stage II. This acts to draw down the $[\text{CO}_2(\text{aq})]$, which is then compensated by an increase in F_{CO_2} at the beginning of Stage II. A few hours into Stage II, F_{CaCO_3} and F_{CO_2} are nearly in balance. The model k_p parameter that yields a match to the steady state growth rate (Fig. 5c) also matches the evolution of [DIC] (Fig. 5d), suggesting that the rate law derived from the seeded experiments of Zuddas and Mucci (1998) is valid for our unseeded experiments.

In the absence of bCA enzyme (i.e. uncatalyzed experiment), the $1000\ln\alpha$ of $\text{CO}_2(\text{aq})$ begins at the equilibrium value and then steeply drops (Fig. 5e) because of the input of bubbled $\text{CO}_2(\text{g})$ with $\delta^{18}\text{O} \sim 24.3\text{‰}$ vs VSMOW ($\sim 5\text{‰}$ lower than the equilibrium value). The light CO_2 undergoes hydration and hydroxylation to form isotopically light EIC initially (Fig. 5f), but as the DIC residence time in solution increases due to increasing [DIC], the CO_2 hydration reaction becomes increasingly bi-directional ($\text{Rb/Rf} \rightarrow 1$, where Rb is the backward rate and Rf is the forward rate; Fig. 5g), leading to a progressively isotopically heavier EIC pool during Stage I that approaches the EIC equilibrium value. Around the 21-hour mark, the CaCO_3 flux is sufficiently high, leading to higher Rf/Rb for the hydration reaction and isotopically lighter EIC pool until steady state is reached during Stage II. Without any enzyme added, the time-integrated $1000\ln\alpha_{\text{c/w}}$ values are 25.3 for Model 1 and 25.6 for Model 2, which agree well with the measured 25.3 value.

With a [bCA] of 0.2 μM , the rate constant of CO_2 hydration (k_{+1}) is increased by a factor of 200 (Uchikawa and Zeebe, 2012) and the $1000\ln\alpha_{\text{EIC/w}}$ is equilibrated for all but the first couple hours of the simulated experiments (Fig. 5f). The $1000\ln\alpha_{\text{c/w}}$ values are 28.0 for Model 1 and 27.9 for Model 2 (Fig. 5h), which match the measured value of 28.0 and is $\sim 1.5\text{-}2\text{‰}$ lower than the equilibrium value due to the growth rate-dependent calcite- CO_3^{2-} and calcite- HCO_3^- fractionation.

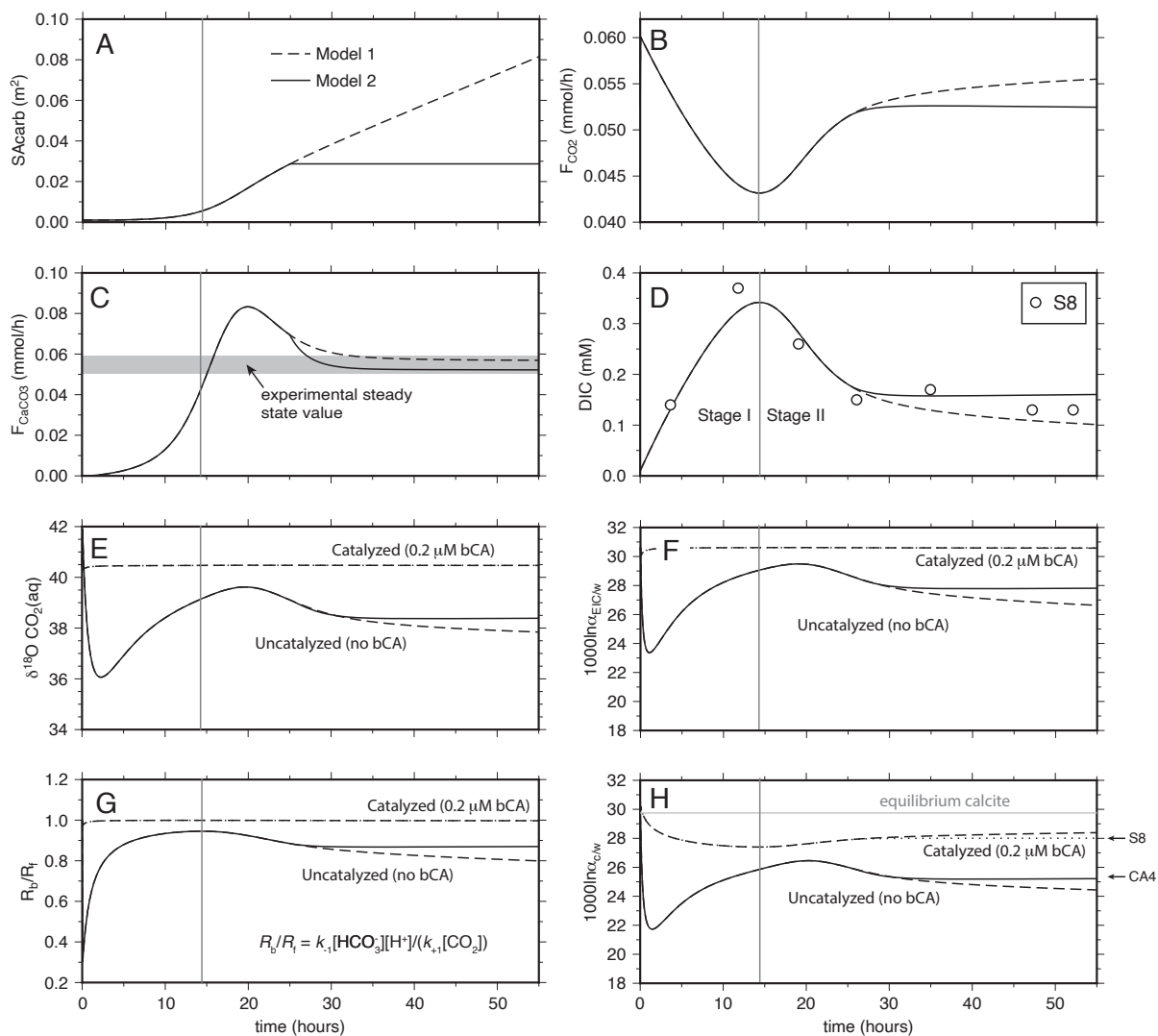


Figure 5: Model for the time-dependent behavior in experiments S8 and CA4 at $T = 25^\circ\text{C}$, $\text{pH} = 8.3$ and $[\text{NaCl}] = 0 \text{ M}$. Model 1 assumes that the reactive surface area of carbonate crystals is proportional to the mass of carbonate precipitated whereas Model 2 treats the steady state portion of Stage II as a seeded experiment with fixed reactive surface area. The two different approaches yield similar isotopic outputs and are in good agreement with measured $1000\ln\alpha_{\text{c/w}}$ values.

6 Discussion

6.1 The effect of ionic strength on the oxygen isotope fractionation between calcite and the EIC

Mineral-anion KFFs may be dependent on solution composition. The kinetics of calcite growth and dissolution have been postulated to depend NaCl concentration (Zuddas and Mucci, 1998). Hence it could be expected that ionic strength affects the calcite dissolution/precipitation ratio and by extension the isotopic fractionation between calcite and CO_3^{2-} (and HCO_3^-) (Devriendt et al., 2017b). The observation that the maximum measured $1000\ln\alpha_{c/w}$ for a given $[\text{NaCl}]$ does not vary up to $[\text{NaCl}]$ of 0.35 M suggests that the calcite- CO_3^{2-} (and possibly calcite- HCO_3^-) KFF(s) is/are independent of change in ionic strength caused by Na^+ and Cl^- ions, contrary to the hypothesis proposed by Devriendt et al. (2017b). The decrease in the maximum $1000\ln\alpha_{c/w}$ above $[\text{NaCl}] = 0.35$ M could be attributed to a changing calcite-EIC KFF but that would require an abrupt change in crystal growth mechanism or surface speciation for which there is no independent evidence.

6.2 The origin of $\delta^{18}\text{O}_{\text{calcite}}$ variability at high ionic strength

Experiments with $[\text{NaCl}] > 0.35$ M display lower and more variable $1000\ln\alpha_{c/w}$ values despite the very high $[\text{bCA}]$ (up to 3 μM) used in these experiments. In the following subsections, we consider the possible explanations for this variability, including the $\delta^{18}\text{O}$ of free water, the effect of ion pairs, the effect of NaCl on DIC speciation, and the effect of dissolved salts on the enzyme kinetics.

6.2.1 Effect of dissolved ions on $\delta^{18}\text{O}_w$

Isotopically heavy oxygen is concentrated in the hydration spheres of some cations or anions in solution, resulting in an oxygen isotope composition of free water that is potentially lighter than the $\delta^{18}\text{O}$ of the overall solution (Taube, 1954). However, the hydration spheres of Na^+ and Cl^- do not fractionate oxygen isotopes, regardless of solution molality (Taube, 1954). The other cations in our solutions exhibit opposing behavior, with Ca^{2+} ions having isotopically heavy hydration spheres (Sofer and Gat, 1972) and NH_4^+ ions having isotopically light hydration spheres (Taube, 1954). Although we use Ca^{2+} and NH_4^+ , our solutions are far too dilute with respect to these ions to expect a resolvable effect. A salt effect on hydration spheres is therefore not responsible for the $1000\ln\alpha_{c/w}$ variations.

6.2.2 Effect of ion pairing on oxygen isotope fractionation between DIC species and H_2O

The equilibrium fractionation factors in the $\text{CO}_2\text{-H}_2\text{O}$ system ($\alpha_{\text{CO}_2\text{-H}_2\text{O}}$, $\alpha_{\text{HCO}_3^-\text{-H}_2\text{O}}$, and $\alpha_{\text{CO}_3^{2-}\text{-H}_2\text{O}}$) are based on freshwater solutions (Beck et al., 2005). The addition of dissolved salts can lead to significant fractions of bicarbonate and carbonate ions existing as cation- CO_3^{2-} complexes such as

NaHCO_3^0 and NaCO_3^- , which may shift the isotopic composition of the HCO_3^- and CO_3^{2-} compounds reacting with Ca^{2+} to form CaCO_3 . Kim et al. (2014) showed that variable amounts of dissolved NaCl ($I = 0$ to 0.7) have a negligible effect on the equilibrium fractionation factors in the Na-Cl- CO_2 - H_2O system. Similarly, Uchikawa and Zeebe (2013) found no discernible effects of MgCO_3^0 on oxygen isotope equilibrium in the Mg-Cl- CO_2 - H_2O system over a large range of MgCO_3^0 abundances (0 to 40% of total CO_3^{2-}). Hence, isotope partitioning among ion pairs is not responsible for the $1000\ln\alpha_{c/w}$ variations.

6.2.3 Effect of DIC speciation on $\delta^{18}\text{O}_{\text{calcite}}$

The relative proportions of CO_3^{2-} and HCO_3^- within the EIC may affect $\delta^{18}\text{O}_{\text{calcite}}$ where HCO_3^- attachment to the calcite surface is significant (Wolthers et al., 2012; Watkins et al., 2014). This is because CO_3^{2-} and HCO_3^- have distinct oxygen isotope compositions (Fig. 3; Beck et al., 2005). Increasing salinity shifts the solution to higher $\text{CO}_3^{2-}/\text{DIC}$ (e.g. Millero et al., 2007), which decreases the $\delta^{18}\text{O}$ of the EIC. Moreover, the DIC equilibration time increases at higher $\text{CO}_3^{2-}/\text{DIC}$ due to lower $[\text{CO}_2]$ (Uzdowski et al., 1991; Uchikawa and Zeebe, 2012).

In simple NaCl solutions, the $\text{CO}_3^{2-}/\text{DIC}$ ratio increases from 1.8% to 5.3% between $[\text{NaCl}] = 0$ and 0.5 M, with very little change above $[\text{NaCl}] = 0.5$ M (Millero et al., 2007, Fig. S1.1e). However, this increase in $\text{CO}_3^{2-}/\text{DIC}$ only lowers the $\delta^{18}\text{O}$ of isotopically equilibrated DIC by about 0.3‰ (Fig. 3). In addition, the change in speciation translates to a minor increase in the DIC equilibration time that is accounted for in our model. Hence, a salt effect on solution speciation and equilibration time is not responsible for the $1000\ln\alpha_{c/w}$ variations.

6.2.4 Effect of NaCl on the kinetics of catalyzed CO_2 (de)hydration

The enzyme bCA increases the CO_2 (de)hydration rate constants k_{+1} and k_{-1} . According to the Michaelis-Menten kinetic model, the expression for the enzyme-catalyzed rate constant for CO_2 hydration is:

$$k_{+1}^* = k_{+1} \cdot \frac{k_{\text{cat}}}{K_{\text{M}}} \cdot [\text{CA}] \quad (19)$$

where k_{cat} is the turnover number and K_{M} is the Michaelis-Menten constant. Uchikawa and Zeebe (2012) determined $k_{\text{cat}}/K_{\text{M}} = 2.7 \times 10^7 \text{ M}^{-1} \text{ s}^{-1}$ for bCA in NaCl-free solutions. In the absence of an inhibitor, addition 0.2 μM of bCA is expected to increase k_{+1} by a factor of 200 in freshwater solutions. We performed assays after Uchikawa and Zeebe (2012) in an effort to directly measure any inhibitory effect of NaCl on bCA, but discovered many complications and inconsistencies with the procedure (Appendix C).

Many inorganic and organic compounds are known to inhibit the activity of various forms of carbonic anhydrase (Bertucci et al., 2009, 2011a; De Simone and Supuran, 2012; Del Prete et al., 2014). Previous studies have found that several anions (including Cl^- , Br^- , and NO_3^-) affect the activity of CA. Nielsen and Frieden (1972) found these anions to have an inhibitory effect on the

activity of both oyster CA and bovine CA, while Dionisio-Sese and Miyachi (1992) studied a variety of marine algae and found that the inhibitory or catalytic effects of these anions on CA activity was species-dependent, with a proposed mechanism for inhibition being that these anions may displace the hydroxyl group bound to the zinc at the enzyme active site. Enzyme inhibition is typically expressed in terms of an inhibition constant, K_I (mM), which is the concentration of inhibitor at which the rate of the uninhibited reaction is reduced by a factor of 2. The larger the value of K_I , the weaker the inhibitor.

Nielsen and Frieden (1972) carried out pH-stat assays and reported $K_I = 170$ mM for bCA at $T = 6^\circ\text{C}$ and $\text{pH} = 7.5$. They showed the CO_2 (de)hydration reaction velocity (V) decreases exponentially with increasing $[\text{NaCl}]$ (Figure 6). They define V as the difference between the catalyzed versus uncatalyzed reaction velocity, which in turn, we infer to be directly proportional to k_{cat}/K_M . Their results can be used to write an equation for k_{cat}/K_M that depends explicitly on $[\text{NaCl}]$:

$$\frac{k_{\text{cat}}}{K_M} = \left(\frac{k_{\text{cat}}}{K_M}\right)_{[\text{NaCl}]=0} \exp(A \cdot [\text{NaCl}]) \quad (20)$$

where the exponent A describes the strength of inhibition. Our fit to the data from Nielsen and Frieden (1972) gives $A = -3.82$ (Fig. 6).

To assess whether NaCl as a mild inhibitor can account for our observations, Figure 7 shows model outputs using the functional form for k_{cat}/K_M from Eq. 20. Model outputs are obtained using the same parameters from experiment S8 and CA4 (Fig. 5) but with k_{+1}^* (Eq. 19 and 20) instead of k_{+1} in reactions (4), (6) and (8), and by varying $[\text{bCA}]$ and $[\text{NaCl}]$. Model results using $A = -3.82$ ($K_I = 170$ mM, based on data from Nielsen and Frieden, 1972) are shown on the left panels of Fig. 7 (panels a to d). Measured data and model outputs are compared in two separate panels

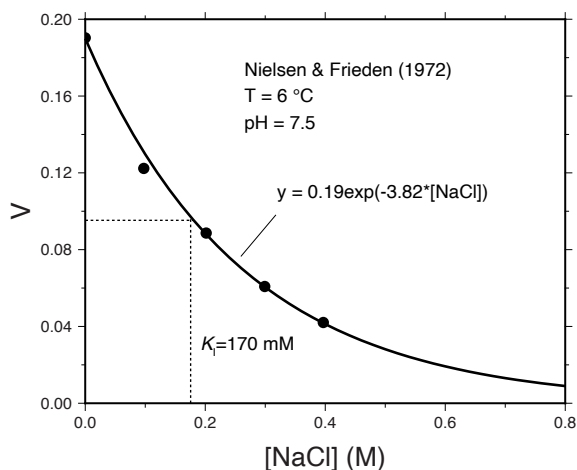


Figure 6: The pH-stat assays of Nielsen and Frieden (1972) conducted at $\text{pH} 7.5$ and a temperature of 6°C suggest an exponential dependence of CO_2 (de)hydration reaction velocity (V) on $[\text{NaCl}]$. The data gives an exponent of -3.82 and an inhibition constant $K_I = 170$ mM.

(Fig. 7b and 7c) because the $\delta^{18}\text{O}$ of DIC species under non-equilibrium conditions depends on the $\delta^{18}\text{O}$ of bubbled CO_2 (Appendix A, Section 2): (1) experiments with high $\delta^{18}\text{O}_{\text{CO}_2(\text{g})}$ (22.2-24.3‰, Fig. 7b) and (2) experiments with low $\delta^{18}\text{O}_{\text{CO}_2(\text{g})}$ (12.27-13.45‰, Fig. 7c). Model outputs shown in Fig. 7b and 7c involve no free parameters and yet can explain several first-order features of the dataset: (1) The range of measured $1000\ln\alpha_{c/w}$ values in the high $\delta^{18}\text{O}_{\text{CO}_2(\text{g})}$ experiments is about 3‰. (2) About 1 μM bCA is required to maintain an isotopically equilibrated the DIC pool up to $[\text{NaCl}] \sim 0.35 \text{ M}$. (3) Maintaining DIC at isotopic equilibrium with bCA becomes increasingly difficult above $[\text{NaCl}] = 0.35 \text{ M}$ even with 2-3 μM of bCA added. (4) There is a general decrease, for a given [bCA], in the $1000\ln\alpha_{c/w}$ values with increasing [NaCl]. However, the model $1000\ln\alpha_{c/w}$ values are systematically higher than the measured values for all experiments with bCA, implying that the modeled NaCl inhibition is too weak and that the modeled DIC pool is more equilibrated than suggested by the data (Fig. 7d).

The data-model agreement is improved using $A = -5.5$ ($K_1 = 120 \text{ mM}$, Fig. 7e to 7h). There are a couple of possible reasons why the inhibitory effect of NaCl on bCA may be stronger in our experiments than suggested by the data of Nielsen and Frieden (1972). First, the Nielsen and Frieden (1972) parameters were derived from a solution with a lower temperature and pH than our experiments and it is conceivable that NaCl inhibition varies with either or both of these parameters. Second, it is possible that they used a different isozyme of bCA, and different isozymes can have a substantially different K_1 values (De Simone and Supuran, 2012).

Overall, these results suggest that the most up-to-date values for the kinetic fractionation factors (Table 3) and functional form of the salt effect on bCA from Nielsen and Frieden (1972) are an accurate quantitative description of our calcite growth experiments and should be useful for modeling the $\delta^{18}\text{O}$ of CaCO_3 in other experiments and natural environments.

7 Implications

7.1 Towards a general model for kinetic oxygen isotope effects

The current work builds on a large number of studies, each contributing to the development of a general model of kinetic oxygen isotope fractionation in the CaCO_3 -DIC- H_2O system (e.g. Clark et al., 1992; Usdowski and Hoefs, 1993; Zeebe and Wolf-Gladrow, 2001; Beck et al., 2005; Kim et al., 2006; DePaolo, 2011; Nielsen et al., 2012; Watkins et al., 2013, 2014, 2017; Zeebe, 2014; Devriendt et al., 2017b; Sade and Halevy, 2017; Chen et al., 2018; Yumol et al., 2020; Zeebe, 2020; Guo and Zhou, 2019; Guo, 2020; Christensen et al., 2021). This study presents the first attempt to model kinetic oxygen isotope effects recorded in laboratory grown calcite with a fully reversible isotopic box model (Chen et al., 2018; Christensen et al., 2021) and provides a functional form for the inhibitory effect of NaCl on the catalytic effect of bovine carbonic anhydrase. The success of the model applied to our experiments with variably equilibrated DIC pools (Fig. 7f to 7h) suggests that the community is converging towards an accurate set of equilibrium and kinetic fractionation factors in the CaCO_3 -DIC- H_2O system that will be useful for improving models of

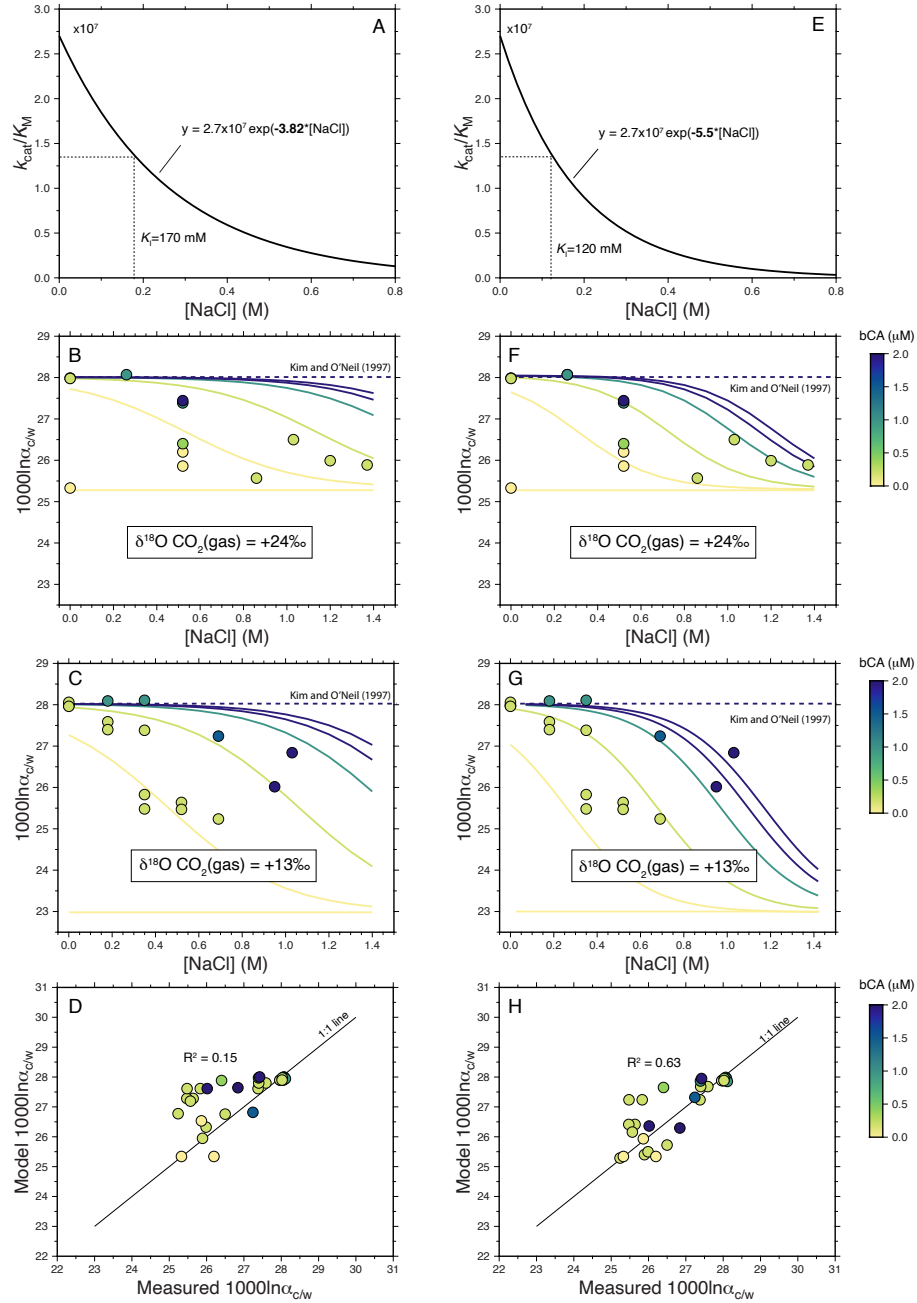


Figure 7: Data-model comparison for the calcite-water oxygen isotope fractionation ($1000\ln\alpha_{c/w}$) in solutions with different NaCl concentrations (0-1.4 M). Model outputs were obtained using Eq. (19) and (20) for the NaCl dependence of the catalyzed CO_2 (de)hydroxylation reaction kinetic (as in Figure 6). Left panels (A-D) show results using an exponent of -3.82 (Nielsen and Frieden, 1972). Right panels (E-H) show results using an exponent of -5.5. For panels (B) and (F), the input gas has high $\delta^{18}\text{O}$ (22.2-24.3‰). For panels (C) and (G), the input gas has low $\delta^{18}\text{O}$ (12.27-13.45‰). The NaCl dependence of Nielsen and Frieden (1972) is weaker than indicated by our experiments, leading to model $1000\ln\alpha_{c/w}$ values that are systematically higher (i.e., more equilibrated DIC) than the measured values (panel D). A stronger inhibition by NaCl yields better overall agreement between model and data (panel H).

isotopic disequilibrium and biological ‘vital effects’ in other settings.

7.2 Application to marine calcifiers

Carbonic anhydrase (CA) is present at or near the site of calcification of many (if not all) biological organisms, including urchins (e.g. Mitsunaga et al., 1986), crustaceans (e.g. Henry, 2001), corals (e.g. Furla et al., 2000; Moya et al., 2008; Tambutté et al., 2011; Bertucci et al., 2011b; Mass et al., 2014), coccolithophores (e.g. Zhang et al., 2021), and foraminifera (e.g. de Goeyse et al., 2021). Despite the presence of CA, all of these organisms produce CaCO_3 skeletons or tests that exhibit deviations from isotopic equilibrium (e.g., McConnaughey, 1989; Spero et al., 1997; Adkins et al., 2003; Kimball et al., 2014; Hermoso et al., 2014; Devriendt et al., 2017a; Chen et al., 2018).

The pervasiveness of KIEs in the marine carbonate record has motivated efforts to develop isotopic biomineralization models. Recent approaches for coral and coccolith calcification invoke a CO_2 -fed fluid and explicitly account for carbonic anhydrase activity on KIEs in the DIC-water system (Devriendt et al., 2017b; Chen et al., 2018; Zhang et al., 2021). For both organisms, the parameter $k_{\text{cat}}/K_{\text{M}}$ has been treated as a constant. Given that the composition of the calcifying fluid is likely to have higher pH and lower salinity than ambient seawater due to proton pumping and cation selectivity, respectively, the treatment of constant $k_{\text{cat}}/K_{\text{M}}$ may warrant relaxation in future refinements. An obvious caveat is that the bCA used herein may not be representative of CA found in marine organisms. For example, it is possible that marine varieties of CA are less sensitive to salt inhibition, either through modifications to the enzyme structure or by screening inhibitors from the calcifying fluid (e.g. Dionisio-Sese and Miyachi, 1992; Bertucci et al., 2009).

8 Summary

Calcite crystals were precipitated at 25°C in solutions of variable NaCl and bovine carbonic anhydrase (bCA) concentrations to investigate the effect of a solution ionic strength on the oxygen isotope fractionation between calcite and an isotopically equilibrated DIC pool (EIC). The experimental results indicate no significant ionic strength effects on calcite-EIC oxygen isotope fractionation but revealed the inhibitory effect of NaCl on the catalyzed CO_2 (de)hydration reaction. This led to DIC pools that were not isotopically equilibrated and variable $1000\ln\alpha_{\text{c/w}}$ values in high ionic strength solutions ($[\text{NaCl}] > 0.35 \text{ M}$). Using an updated isotopic box model and accurate measurements of solution parameters ($[\text{TA}]$, $[\text{DIC}]$ and $\delta^{18}\text{O}$ of input $\text{CO}_2(\text{g})$), we successfully modeled the measured variability in $1000\ln\alpha_{\text{c/w}}$ values at high $[\text{NaCl}]$ and quantified the inhibitory effect of NaCl on bCA. The new parameterization of the dependence of bCA activity on $[\text{NaCl}]$ can be used in biochemical models of calcification with the caveat that other isozymes of CA may be less sensitive to inhibition by dissolved salts and solution pH. This is a subject that warrants further investigation for understanding vital effects in biogenic calcite and for finding an alternative to bCA for equilibrating the DIC pool in experiments that involve seawater-like compositions.

9 Bridge

In the preceding Chapter (III), I investigated the effect of solution composition and ionic strength on DIC-CaCO₃ oxygen isotopic fractionation and found no significant effect, but a significant NaCl inhibition of the enzyme carbonic anhydrase that is used to catalyze CO₂ (de)hydration. Another factor that has been proposed to affect the oxygen isotope signature of carbonates during non-equilibrium growth is the pH of the growth solution. In Chapter IV, I perform calcite growth experiments to examine the oxygen and carbon isotopic fractionation between calcite and the aqueous solution over a range of solution pH common in many natural waters from which calcite precipitates, from pH 7.5 to 9.3. I utilize the enzyme carbonic anhydrase to help facilitate equilibration of the DIC pool, but in these low ionic strength solutions any inhibitory effect of NaCl should be negligible.

CHAPTER IV

EFFECT OF pH ON THE ISOTOPIC COMPOSITION OF CALCITE GROWN FROM CO₂-FED SOLUTIONS: EXPERIMENTS AND MODELING

This chapter is in preparation for submission to *Geochemistry, Geophysics, Geosystems*, co-authored with J.M. Watkins and L.S. Devriendt. The experiments were performed by E.K. Olsen. The model was a code from an earlier paper of J.M. Watkins, with parameters adjusted and run by E.K. Olsen. The writing is by E.K. Olsen, with editorial assistance from J.M. Watkins.

1 Introduction

The oxygen isotope composition of calcite exhibits a strong temperature dependence, and is commonly used in paleoenvironment reconstructions to estimate the temperature of the oceans (Elderfield & Ganssen, 2000; Strassen et al., 2009; Van Geldern et al., 2006; Zachos et al., 2001), lakes (Lacey et al., 2018; Leng & Marshall, 2004; Leng et al., 2001), or caves (Bar-Matthews et al., 1997; Feng et al., 2014; Gascoyne, 1992) in which it formed. This $\delta^{18}\text{O}$ “thermometer” is based on principles of isotopic equilibrium between the mineral and its host solution (McCrea, 1950; Urey, 1947). When calcite grows too quickly to maintain isotopic equilibrium with the solution, however, non-equilibrium kinetic isotope effects (KIEs) that depend on factors such as solution pH, precipitation rate, source(s) of dissolved inorganic carbon (DIC), and solution composition affect the calcite $\delta^{18}\text{O}$ (Baker, 2015; Dietzel et al., 2009; Gabitov et al., 2012; Kim & O’Neil, 1997; Levitt et al., 2018; Watkins et al., 2013, 2014).

This study focuses on the effect of solution pH on the oxygen isotope composition of low temperature inorganic calcite. Calcite grows in a variety of geologic settings that span a range in pH, from fresh water lakes and rivers (pH \sim 6-8), to alkaline lakes (pH \sim 9-11), and seawater systems. While the modern surface ocean pH generally falls within a narrow range (pH 8.1-8.3), the full oceanic water column displays considerably greater pH-variation, from pH 7.6-8.4 (Beck et al., 2005). The pH of the ocean has also been proposed to vary significantly over geologic time. Some studies argue for a high pH (9-11), “soda ocean” with (bi)carbonate present in greater abundance than even chloride during the Archean (Kempe & Degens, 1985), while other studies suggest the Archean ocean pH was lower than that of the modern ocean. Calculations using projected Archean atmospheric CO₂ concentrations suggest an ocean pH of 6.5-7.0 (Grotzinger & Kasting, 1993;

Halevy & Bachan, 2017).

In contrast to the inorganic calcic sediments of the Precambrian, Phanerozoic calcic seafloor sediments are dominated by biogenic CaCO_3 (Grotzinger & Kasting, 1993; Zeebe & Wolf-Gladrow, 2001). Biocalcifiers do not typically create their skeletons directly from seawater, but from a calcifying fluid modified from seawater composition via preferential pumping of Ca^{2+} in and H^+ out of the calcifying space, creating an environment of higher pH and higher CaCO_3 saturation state (Chen et al., 2018). Biogenic CaCO_3 is always depleted in ^{18}O and ^{13}C relative to inorganic CaCO_3 from similar environments, which has been hypothesized to result from kinetic isotope effects during $\text{CO}_2\text{-HCO}_3^-$ interconversion, or due to pH-dependent DIC speciation within the calcifying fluid (Chen et al., 2018; McConnaughey, 1989). The $\delta^{18}\text{O}$ of foraminiferal calcite has been observed to vary with seawater carbonate ion concentration, recording isotopically lower values with increasing $[\text{CO}_3^{2-}]$ or pH (Spero et al., 1997; Zeebe, 1999). Increasing ocean pH by 0.2-0.3 would correspondingly result in a decrease of $\delta^{18}\text{O}$ of calcite by $\sim 0.22\text{-}0.33\text{‰}$, which would typically be interpreted as an increase in ocean temperature (Coplen, 2007; Zeebe, 1999).

In addition to being observed in biogenic calcite (Zeebe, 1999), the pH effect on oxygen isotope partitioning between calcite and water has also been studied experimentally (Baker, 2015; Dietzel et al., 2009; Watkins et al., 2014) with consistent findings that as solution pH increases, the oxygen isotope composition of calcite decreases. This shift in calcite $\delta^{18}\text{O}$ mimics the shift in the $\delta^{18}\text{O}$ of the DIC pool over the same pH range, as the CO_3^{2-} proportion of DIC increases, which is depleted in ^{18}O relative to HCO_3^- (Beck et al., 2005; Millero et al., 2006, 2007; Zeebe, 2007). Thus, researchers have postulated that the relative contribution to the mineral lattice from each DIC species is pH-dependent. To investigate the effect of solution pH on the isotopic composition of calcite, we perform well-controlled inorganic calcite growth experiments at 25°C over a range in solution pH from 7.5-9.3 that are characterized by relatively constant $\text{HCO}_3^-/\text{CO}_3^{2-}$, degree of supersaturation (Ω), growth rate, and with time series for both total alkalinity (TA) and DIC concentration. Kinetic isotope effects (KIEs) in our CaCO_3 are attributed to attachment and detachment of ions at the mineral surface, since use of the enzyme carbonic anhydrase (bCA) to speed up isotopic equilibration of the DIC pool reduces or eliminates KIEs arising due to aqueous DIC disequilibrium. We then adapt the ion-by-ion model of Watkins et al. (2014) and Watkins and Devriendt (2022) and report modified kinetic fractionation factors (KFFs) for calcite precipitation and dissolution reactions due to the KIEs recorded in the $\delta^{18}\text{O}$ of our experimental CaCO_3 .

2 Methods

We use the same experimental set-up as Watkins et al. (2013, 2014), and more recently, Olsen et al. (2022) (Chapter III). Of note for comparison to previous studies of inorganic calcite precipitation, we measure the isotopic composition of the input CO_2 gas, which becomes important if the DIC pool is not fully equilibrated, and utilize the enzyme carbonic anhydrase (bCA), which catalyzes CO_2 hydration and dehydration reactions and thus promotes equilibration of the DIC pool. Bovine

carbonic anhydrase (MP Biomedicals #153879) dissolved in distilled, deionized (DDI) water was added immediately after the start of the experiment when the solution was brought to the pH of interest. For low ionic strength solutions of $\text{pH} \leq 8.3$, $[\text{bCA}]$ of $\sim 0.2 \mu\text{M}$ is sufficient to equilibrate the DIC pool (Olsen et al., 2022; Uchikawa & Zeebe, 2012; Watkins et al., 2013, 2014). At high pH, bCA becomes ineffective at establishing an equilibrated DIC pool due to low $\text{CO}_2(\text{aq})$ activity. CO_2 (de)hydroxylation reactions take over moderating isotopic exchange between DIC and water at high pH, which are also slow, rate-limiting reactions but which are not catalyzed by carbonic anhydrase. To mitigate the lower bCA efficacy and longer DIC equilibration time, our solutions from pH 8.65 - 9.3 were carried out at $[\text{bCA}] \sim 0.5\text{-}1.5 \mu\text{M}$ (Table 1).

Experimental solutions were prepared by dissolving $\text{CaCl}_2 \cdot 2\text{H}_2\text{O}$ (30 mM) and NH_4Cl (5 mM) in 1.7 L of DDI water. Solutions were held at 25°C (± 0.2) in a temperature-controlled water bath. CO_2 -in- N_2 mixtures (200 - 2000 ppm CO_2) were bubbled through our solutions for several hours prior to the start of an experiment until the headspace CO_2 concentration leveled off at approximately the gas tank value. Rate of gas flow ranged from 0.1 - 0.5 SCF/H (standard cubic feet per hour), which corresponds to a range of 0.025 - 1.264 mmol CO_2 per hour, with lower pH solutions requiring higher CO_2 flow in order to precipitate CaCO_3 (Table 1). The CO_2 concentration of the headspace was continuously recorded (Fig. 1a) using a K-30 USB CO_2 Probe Data Logger (CM0039 from CO2meter.com).

Experiments were maintained at constant pH through use of a Titronic 3000 autotitrator dispensing 1 M NaOH when solution pH measured 0.02 below its set point. Total alkalinity was measured by titration of a solution sample by 0.01 M HCl, and then calculated using the Gran method. Solution samples for DIC and TA were taken 2-3 times per day. Samples for measuring the $\delta^{18}\text{O}$ of the experimental solution were taken at the end of each experiment.

Ionic activities for our solutions are calculated using the R-package of PHREEQC with the Minteq.v4 database (Charlton & Parkhurst, 2011; De Lucia & Kühn, 2013). The degree of supersaturation with respect to calcite ($\Omega = \frac{a_{\text{Ca}^{2+}} \times a_{\text{CO}_3^{2-}}}{K_{\text{sp}}}$) is calculated using those ionic activities and a solubility product of calcite that accounts for ion pairs in solution ($K_{\text{sp}} = 10^{-8.48}$, Charlton & Parkhurst, 2011; De Lucia & Kühn, 2013; Jacobsen & Langmuir, 1974).

Imaging of precipitates was performed on an FEI Quanta 200 Environmental Scanning Electron Microscope (ESEM) at the Center for Advanced Materials Characterization (CAMCOR) at the University of Oregon (Appendix D).

Isotopic analysis methods are the same as detailed in Chapter III.

3 Experimental results

In many of our experiments, both the TA and DIC (Fig. 1b, e) increase at the beginning of the experiment, peak at or near the onset of calcite precipitation, and then decrease to a steady state value for the remainder of the experiment. Some experiments record a very high initial value, which might reflect peaks near the onset of calcite precipitation since calcite began growing quickly

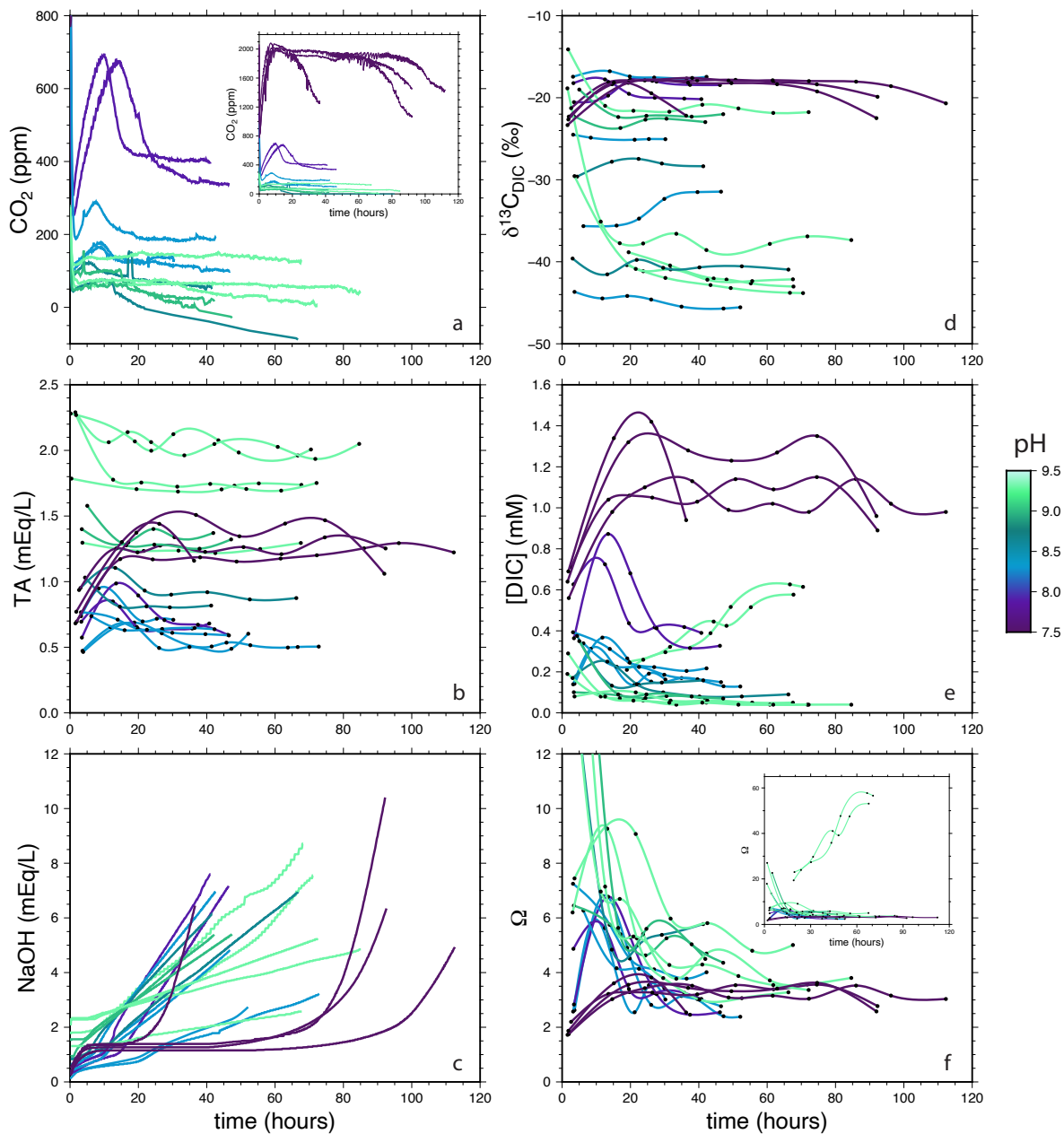


Figure 1: (a) Experiment headspace CO₂ concentration (ppm), (b) total alkalinity (TA), (c) NaOH added (mEq/L), (d) DIC δ¹³C (‰ VPDB), (e) DIC concentration (mM), and (f) calculated degree of supersaturation (Ω) for each experiment. The inset of panel (a) depicts the high CO₂ concentration experiments carried out at pH 7.5. The inset of panel (f) depicts the high Ω values early on in some experiments carried out at pH 8.65-9.3, as well as two experiments (CA10, CA11) with anomalously high Ω that we interpret as experimental error and should be disregarded.

Table 1: Experimental parameters

Experiment	pH	bCA (mg)	[bCA] (μ M)	CO ₂ flow (mmol/h)	Exp duration (h)	Precip (h)	R (mmol/h)	log ₁₀ R (mol/m ² /s)
S6	8.30	10.6	0.208	0.126	72.77	52.55	0.0440	-6.45
S8	8.30	10.48	0.205	0.126	52.15	34.15	0.0533	-6.27
CA4	8.30	0	0.000	0.126	30.55	21.55	0.1010	-6.07
CA10	9.30	50	0.980	0.025	68.29	60.29	0.0984	-6.51
CA11	9.30	75	1.471	0.038	71.11	64.11	0.0735	-6.54
CA16	7.90	10	0.196	0.253	41.19	31.69	0.1858	-6.23
CA17	7.90	10	0.196	0.202	46.42	33.02	0.1694	-6.25
CA18	8.30	20	0.392	0.126	42.68	35.48	0.1521	-6.28
CA20	8.30	10.1	0.198	0.126	46.82	40.35	0.0893	-6.34
CA21	8.65	25	0.490	0.126	41.69	37.69	0.1206	-6.31
CA22	9.00	25	0.490	0.126	42.28	40.78	0.0932	-6.34
CA23	9.30	0	0.000	0.038	67.82	61.82	0.0176	-6.52
CA24	9.30	0	0.000	0.038	85.19	79.69	0.0299	-6.63
CA25	8.65	50	0.980	0.101	66.77	55.77	0.0925	-6.48
CA26	7.50	20	0.392	1.264	92.66	66.26	0.0429	-6.25
CA27	7.50	10	0.196	0.758	112.69	63.99	0.0326	-6.17
CA28	9.00	50	0.980	0.076	47.43	42.93	0.0810	-6.37
CA29	9.30	50	0.980	0.038	72.51	71.01	0.0419	-6.58
CA30	7.50	20	0.392	1.264	92.24	55.38	0.1440	-6.08
CA31	7.50	10	0.196	1.264	36.68	21.51	0.2109	-6.03

in many of our higher pH solutions. In other experiments, the TA and DIC stay fairly constant throughout. Two experiments at pH 9.3 (CA10, CA11) record anomalously high [DIC] for their pH value (and therefore calculated Ω) that continues to increase throughout the experiment duration, which we attribute to human error during sampling for DIC measurements (e.g. not filtering the solution properly, improper sample storage conditions) since none of the other experimental values (TA, isotopic composition of calcite or solution) seem to be outliers for those experiments. We therefore exclude the values from CA10 and CA11 when fitting trends to Ω and ion activity $a_{\text{Ca}^{2+}}/a_{\text{CO}_3^{2-}}$ ratios later in this study.

Though there is a wide spread in $\delta^{13}\text{C}$ of DIC (Figure 1d) that primarily reflects the range in $\delta^{13}\text{C}$ of our CO₂-in-N₂ gas sources, within each experiment the carbon isotopic composition of the overall DIC pool remains fairly constant throughout the duration. The average DIC for an experiment is typically ~ 3 -8 ‰ isotopically heavier than its source gas.

DIC speciation is primarily a function of pH. HCO₃⁻ is the most abundant DIC species across our entire experimental range, with an increasing [CO₃²⁻] from ~ 0.3 to 16% of the total DIC pool (Charlton & Parkhurst, 2011; De Lucia & Kühn, 2013; Millero et al., 2007). We calculated DIC speciation using the PHREEQC Minteq.v4 database, which is approximately equivalent to the HCO₃⁻/CO₃²⁻ ratio of Millero et al. (2007) for simple NaCl solutions over this pH range.

Our solutions are supersaturated with respect to calcite at all times, with changes in Ω being governed by changes in [DIC] (Figure 1f). We precipitate calcite without the use of seed crystals,

so the peak in Ω values for many experiments at the onset of calcite precipitation reflects the critical degree of supersaturation necessary to initiate calcite growth. Both the $[\text{HCO}_3^-/\text{CO}_3^{2-}]$ and $a_{\text{HCO}_3^-}/a_{\text{CO}_3^{2-}}$ ratios decrease exponentially with increasing pH, though the ion activity ratio is consistently ~ 2.1 times greater than the concentration ratio due to ions of greater charge magnitude having lower effective activity in solution relative to ions of smaller charge or neutral species. Since the proportion of CO_3^{2-} of total DIC increases with pH while our starting $[\text{Ca}^{2+}]$ was constant, both the concentration and ion activity ratios for $\text{Ca}^{2+}/\text{CO}_3^{2-}$ decrease with pH. In all solutions, $a_{\text{Ca}^{2+}} \gg \gg a_{\text{CO}_3^{2-}}$, ranging from $\sim 6,000$ to $14,000$ (Fig. 2c). As a consequence of DIC speciation shifts, the degree of supersaturation increases with pH (Figure 2a) since it is calculated from the ion activities of Ca^{2+} and CO_3^{2-} , and does not consider any contribution from HCO_3^- .

In contrast to the stable $\{10\bar{1}4\}$ rhombohedral calcite face, scalenohedral faces in calcite are polar and unstable in stoichiometric solutions. These faces may be stabilized by the adsorption of charged species, which is promoted at high pH and high $a_{\text{HCO}_3^-}/a_{\text{CO}_3^{2-}}$ (Ruiz-Agudo et al., 2011). Our solutions are characterized by particularly high $a_{\text{HCO}_3^-}/a_{\text{CO}_3^{2-}}$ ($\sim 6,000$ - $14,000$), which could explain the range in crystal morphology present in our precipitates. Some experiments were dominated by rhombohedral crystals, while others had an abundance of more equant, rhombo-scalenohedral morphologies.

The slope of NaOH addition serves as a rough visual proxy for growth rate, with faster growth rates resulting in steeper slopes (Figure 1c). We hold our solutions at constant pH by use of an autotitrator that dispenses NaOH in response to processes occurring that acidify the solution: dissolution of CO_2 gas and calcite precipitation. The NaOH addition curves often have change in slope at the onset of calcite precipitation, which helps in determining when growth began while early calcite crystals are too small to be directly observed. Experiments from pH 7.9 to 9.3 have mostly linear NaOH slopes, sometimes with a slightly steeper initial slope that corresponds to a more rapid growth rate at precipitation onset before reaching a steady state.

The experiments at pH 7.5 are clear outliers among the NaOH curves, having a slope of zero for up to multiple days, followed by sudden exponential increase. Direct observation of these experiments reveal a few calcite grains precipitate during the slope of zero, but that calcite was not abundant until a while after NaOH addition began again. For these experiments, a uniform growth rate over the entire precipitation period is not a reasonable approximation. Instead, we adjust the growth periods of these experiments to reflect when growth rate was substantial. However the true rates at pH 7.5 are likely faster than our calculated values.

As pH increased from 7.5 to 9.3, the growth rate decreased from $\log_{10}R \sim -6.1$ to ~ -6.5 mol/m²/s (Figure 2b, Table 1). The NaOH added over experiment duration serves as a pseudo-growth rate proxy (Fig. 1c), as both CO_2 dissolution and CaCO_3 precipitation act to lower pH and therefore drive NaOH addition because the autotitrator and software hold the pH to set value of ± 0.02 . The overall trend of decreasing growth rate with increasing pH is an unexpected result due to the fact that growth rate often co-varies with degree of supersaturation (Dietzel et al., 2009; Nielsen et al., 2012), but we observe an inverse relationship between growth rate and Ω instead

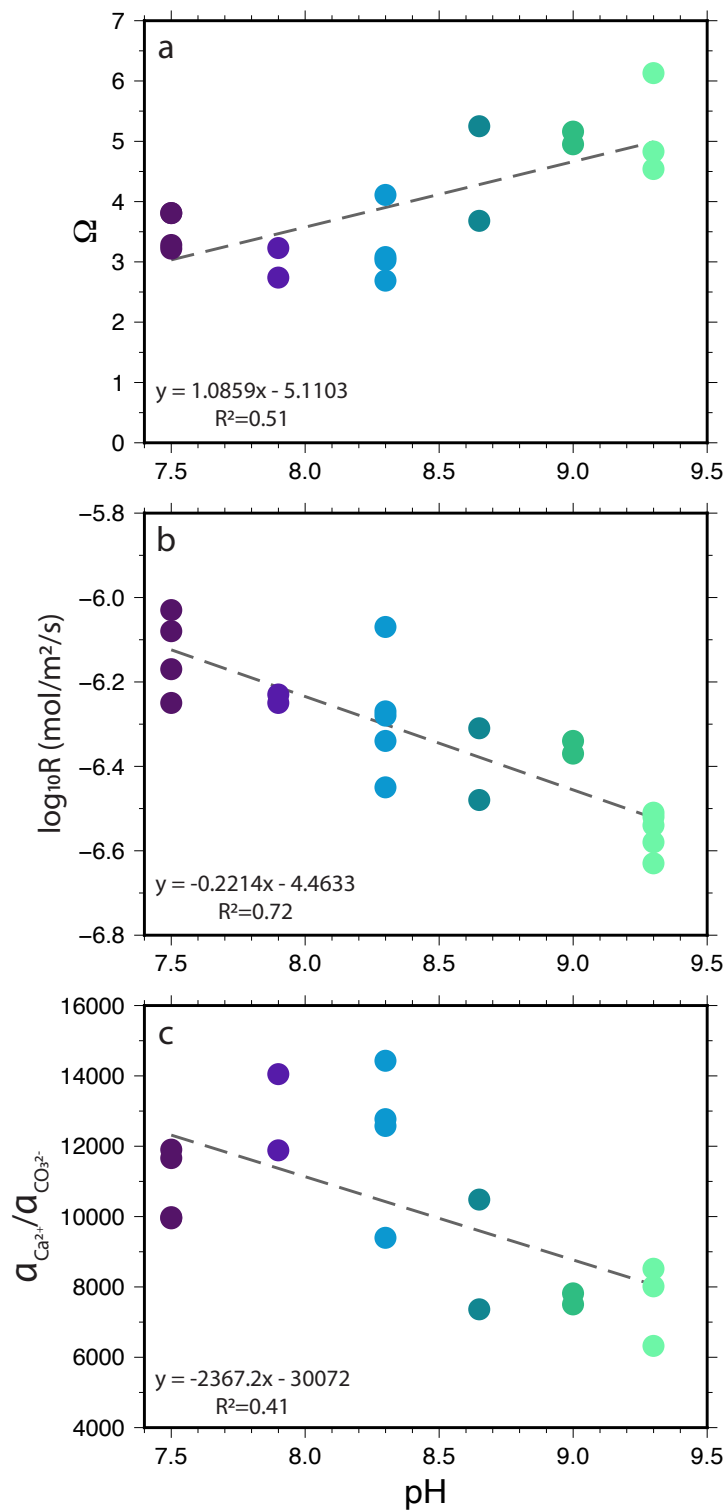


Figure 2: Over the pH range 7.5-9.3, (a) Ω increases, (b) growth rate decreases, and (c) $a_{\text{Ca}^{2+}}/a_{\text{CO}_3^{2-}}$ decreases.

(Fig. 2a).

3.1 Carbon isotopic fractionation

It is difficult to distinguish between contributions to the calcite mineral from HCO_3^- and CO_3^{2-} using carbon isotopes over the pH range of many natural waters (pH 7-10) due to the very small ($\sim 0.4\text{‰}$) equilibrium isotope fractionation between HCO_3^- - CO_3^{2-} resulting in the sum of DIC $\delta^{13}\text{C}$ varying minimally (Fig. 3; Millero et al., 2007; Mook, 1986; Zeebe, 2007). This is despite the fact that DIC speciation shifts significantly within this pH range, from 95% HCO_3^- and $\sim 0.3\%$ CO_3^{2-} to 84% HCO_3^- and 16% CO_3^{2-} at pH 7.5 and 9.3, respectively (Charlton & Parkhurst, 2011; De Lucia & Kühn, 2013; Millero et al., 2007). The HCO_3^- fraction of the DIC pool reaches its maximum of 97.6% at pH 8.1, while $[\text{CO}_3^{2-}]$ increases continuously over the pH range studied.

We expected $1000\ln\alpha_{\text{c-DIC}}$ to either be similar to that of the sum of DIC, or a few permil isotopically heavier. Seeded calcite growth experiments conducted at 10-30°C and pH 6.3-7.0 under chemo-stat conditions found the carbon fractionation between calcite and HCO_3^- to be a temperature-independent value of 1.6‰ (Levitt et al., 2018). They suggested this temperature-independence may be a reflection of the temperature-independent CO_3^{2-} carbon isotope composition, since calcite primarily forms from carbonate ions, or that “oxygen isotopes control isotope partitioning between DIC and calcite, and carbon isotopes have little to no influence” (Levitt et al., 2018). When calculated as fractionations from the DIC pool, the fractionations from Levitt et al. (2018) are larger and temperature-dependent; 4.51‰ at 10°C, 3.72‰ at 20°C, and 4.14‰ at 30°C. Baker (2015) found $\Delta^{13}\text{C}_{\text{c-DIC}}$ to be between -0.2 and 0.9‰. Over half of our experiments yield $1000\ln\alpha_{\text{c-DIC}}$ values between -1 and 1‰, but many experiments yield calcite that is isotopically lighter than DIC by 1.5 to 9‰ (Fig. 3, Table 2).

These low negative carbon isotope fractionations are beyond even what is hypothesized as the kinetic limit for carbon isotope calcite-DIC fractionation. Our $\delta^{13}\text{C}_{\text{DIC}}$ values used in these calculations are averages of several DIC water samples taken over the course of the experiment. Often, $\delta^{13}\text{C}$ and concentration of DIC reaches and maintains a steady state shortly after the onset of calcite precipitation (Fig. 1E). In some of our experiments, however, the $\delta^{13}\text{C}$ of DIC continually increases or decreases throughout an experiment, but still not of a magnitude that would cause the very large negative isotope fractionation discrepancy we observe in the data. Due to the many replicable DIC water samples, we conclude that the calcite samples from these experiments may have experienced contamination from isotopically light organic carbon.

Importantly, the oxygen isotope fractionations seem unaffected by the anomalous carbon isotope fractionations. For example, the two experiments at pH 9.0 record very different $1000\ln\alpha_{\text{c-DIC}}$ values, one being within the expected range (-0.15‰) and the other puzzlingly low (-9.21‰) (Fig. 3). Their oxygen isotope fractionations between calcite and water, however, are approximately equal (27.46‰ and 27.54‰) (Fig. 4, Table 2). Therefore, we feel confident in our oxygen isotope data despite harboring concerns regarding the carbon isotope data.

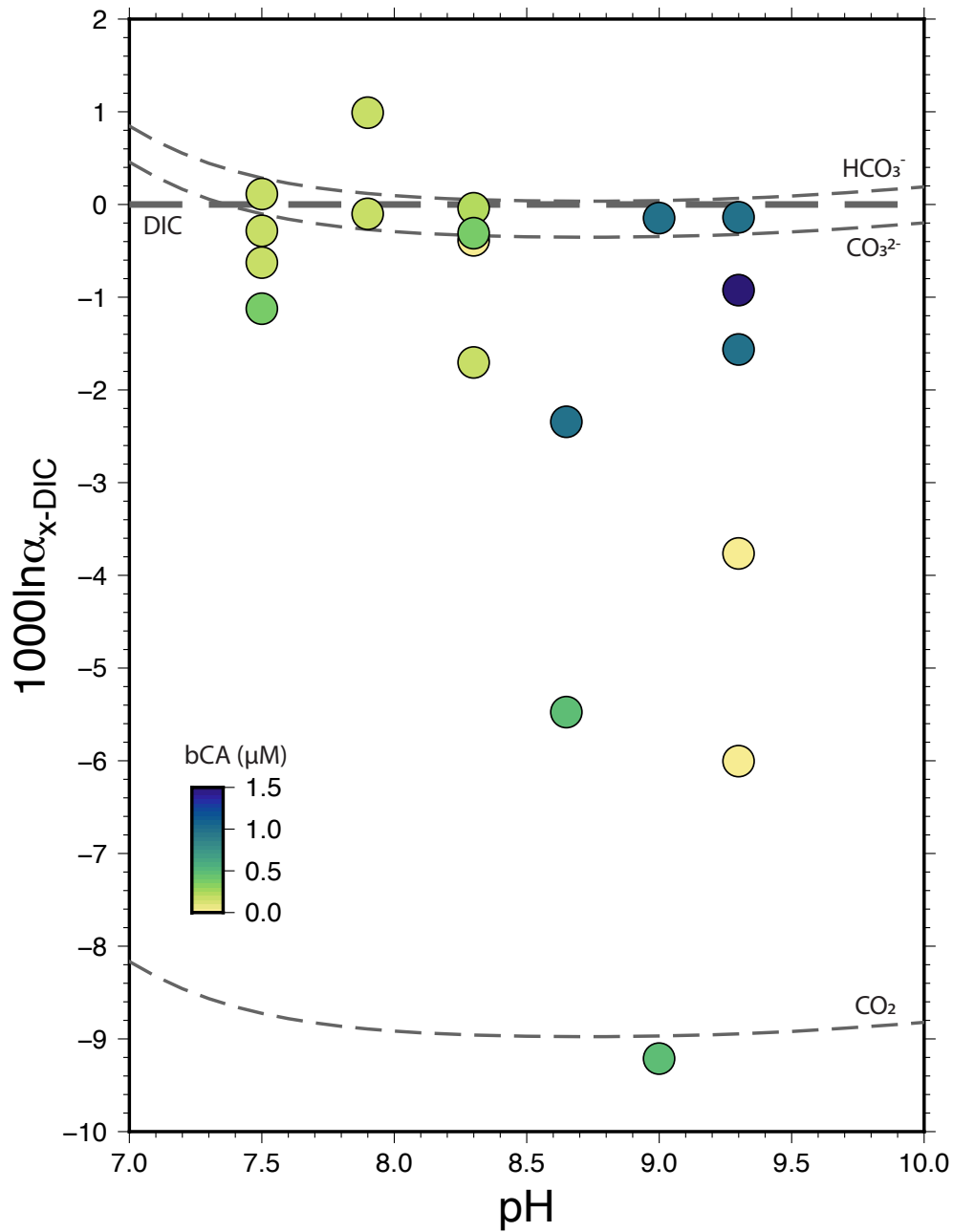


Figure 3: Calcite-DIC carbon isotope fractionation expressed as $1000\ln\alpha_{c-DIC}$. Carbon isotope results from this study's experiments are highly variable and inconsistent with expected fractionations due to the complementary oxygen isotope fractionations. Values for $1000\ln\alpha_{\text{CO}_2-DIC}$, $1000\ln\alpha_{\text{HCO}_3-DIC}$, and $1000\ln\alpha_{\text{CO}_3-DIC}$ are calculated using the Zeebe (2007) expression modified for carbon isotopes, Millero et al. (2007) DIC pK values for simple NaCl solutions, and equilibrium fractionation factors reported in Mook (1986) and Zhang et al. (1995).

Table 2: Isotopic data

Exp	[DIC] (mM)	Ω	$\delta^{13}\text{C}_c$ (VPDB)	$\delta^{18}\text{O}_c$ (VSMOW)	$\delta^{18}\text{O}_w$ (VSMOW)	$\delta^{13}\text{C}_{\text{DIC}}$ (VPDB)	$1000\ln^{13}\alpha_{c-\text{DIC}}$	$1000\ln^{18}\alpha_{c-w}$
S6	-	-	-46.06	16.83	-11.31	-	-	28.057
S8	0.1451	2.69	-45.37	16.65	-11.39	-45.33	-0.042	27.961
CA4	0.1638	3.03	-25.44	13.68	-11.68	-25.07	-0.385	25.334
CA10	0.4223	38.92	-43.02	15.62	-11.83	-41.52	-1.565	27.396
CA11	0.4158	38.37	-43.34	15.66	-11.80	-42.45	-0.923	27.412
CA16	0.4157	3.23	-18.98	16.31	-11.85	-19.95	0.992	28.097
CA17	0.4340	2.74	-18.28	16.23	-11.84	-18.18	-0.101	28.009
CA18	0.2402	4.11	-17.67	16.21	-11.88	-17.36	-0.309	28.030
CA20	0.1895	3.08	-34.77	16.12	-11.95	-33.12	-1.705	28.018
CA21	0.1440	5.25	-33.22	16.29	-11.52	-27.91	-5.476	27.740
CA22	0.0816	4.95	-31.79	15.64	-11.87	-22.83	-9.213	27.457
CA23	0.0661	6.13	-47.43	8.30	-10.65	-41.70	-6.003	18.975
CA24	0.0521	4.83	-40.85	3.24	-10.85	-37.23	-3.763	14.148
CA25	0.1010	3.68	-42.79	16.89	-10.91	-40.54	-2.344	27.717
CA26	1.0581	3.28	-18.52	17.08	-10.96	-18.24	-0.285	27.961
CA27	1.0374	3.22	-18.93	16.98	-11.15	-18.32	-0.626	28.050
CA28	0.0802	5.16	-22.36	16.32	-11.28	-22.22	-0.146	27.537
CA29	0.0490	4.54	-21.57	16.25	-11.36	-21.43	-0.137	27.540
CA30	1.2360	3.81	-20.21	17.11	-10.86	-19.11	-1.123	27.891
CA31	1.2330	3.81	-19.82	16.89	-11.23	-19.93	0.113	28.044

3.2 Oxygen isotopic fractionation

Our oxygen isotope fractionations between calcite and water at lower pH (7.5 – 8.3) are in approximate agreement with the $\delta^{18}\text{O}$ - T calibration of Kim and O’Neil (1997), but at higher pH our fractionations become smaller and fall off this calibration to lower values (Fig. 4). As many previous studies have concluded, the Kim and O’Neil (1997) calibration seems to be a good representative of oxygen isotope fractionation in many natural and synthetic calcites, but likely does not reflect true oxygen isotope equilibrium (Coplen, 2007; Daëron et al., 2019; Dietzel et al., 2009; Levitt et al., 2018; Watkins et al., 2013). The very slowly-grown cave calcites studied at Devils Hole and Corsica Cave together provide a better $\delta^{18}\text{O}$ - T equilibrium calibration (Coplen, 2007; Daëron et al., 2019). Equilibrium oxygen isotope partitioning between calcite and water is strongly temperature-dependent, while kinetic isotope effects depend on mineral growth rate, solution pH, and degree of supersaturation, rather than temperature.

Several experimental studies have aimed to quantify the $1000\ln\alpha_{c-w}$ dependence on mineral growth rate, solution pH, and degree of supersaturation. We compare our results to that of other experiments where calcite precipitated from an equilibrated DIC pool. The experiments of Watkins et al. (2014), Baker (2015), and this study used sufficient carbonic anhydrase (bCA) to ensure isotopic equilibration of the DIC pool (Uchikawa & Zeebe, 2012). While experiments of Levitt et al. (2018) did not utilize bCA, the low pH of their solutions and slower growth rates suggests that isotopic equilibration of the DIC pool was achieved. Other studies, including Kim et al. (2006), Dietzel et al. (2009), and Gabitov et al. (2012) suffer from a nonequilibrated DIC pool, which

complicates interpretations of KIEs occurring at the mineral surface.

This study systematically controlled solution pH, and calculated growth rate and degree of supersaturation for all experiments. As pH increases from 7.5 to 9.3, $1000\ln\alpha_{c-w}$ decreases from ~ 28.0 to $\sim 27.4\%$ (Figure 4). Similar trends but with slightly different slopes and intercepts were found in Baker (2015) ($1000\ln\alpha_{c-w} \approx 28.3$ to 27.7%) and Watkins et al. (2014) ($1000\ln\alpha_{c-w} \approx 28.7$ to 27.0%) (Fig. 4, see inset) using the same experimental methods and set-up.

The decrease in $1000\ln\alpha_{c-w}$ observed due to increasing pH has previously been attributed to shifts in the proportions of different DIC species contributing to the calcite mineral lattice (Zeebe, 1999). As pH increases from 7.5 to 9.3, the relative proportion of CO_3^{2-} increases while HCO_3^- and CO_2 decrease, leading to an isotopically lighter DIC pool because equilibrium CO_3^{2-} is 6.8‰ depleted in ^{18}O relative to HCO_3^- . We predict that as pH increases, the HCO_3^- contribution to calcite decreases, as the observed decreasing $1000\ln\alpha_{c-w}$ trend would be in agreement with a decreasing contribution from the isotopically heavier species, HCO_3^- .

We observe smaller isotopic fractionations at pH 7.5 than we would expect based on the approximately linear trend of our $1000\ln\alpha_{c-w}$ values at higher pH. These smaller fractionations at pH 7.5 could be due to the elevated growth rate we observed in these experiments (see steep NaOH addition curve - Fig. 1c). Fast growth has previously been found to result in isotopically lighter calcite (Dietzel et al., 2009; Gabitov et al., 2012). A contrasting explanation of the pH 7.5 data is that the trend in $1000\ln\alpha_{c-w}$ is not expected to continue mimicking the slope of the DIC pool isotopic composition at lower pH values with larger proportions of $\text{CO}_2(\text{aq})$ since $\text{CO}_2(\text{aq})$ is not inferred to contribute to the calcite lattice, while both HCO_3^- and CO_3^{2-} do (Watkins & Devriendt, 2022).

4 Updating the ion-by-ion model

We use our new experimental CaCO_3 oxygen isotope fractionation data to update the ion-by-ion model from Watkins et al. (2013, 2014) and Watkins and Devriendt (2022). The Watkins model modified that of Wolthers et al. (2012), which combined the simple cubic ionic crystal growth model of Zhang and Nancollas (1998) with the calcite surface speciation and complexation model of Wolthers et al. (2008).

The ion-by-ion model assumes calcite growth is proceeding via the spiral growth of hillocks. Many previous atomic force microscopy (AFM) studies suggest that spiral growth, in which calcite grows by step flow at surface defects including screw dislocations, is favored at lower degrees of supersaturation ($\Omega \leq 2.2$) and at increased Ω the 2D nucleation mechanism becomes increasingly important and then dominates (Larsen et al., 2010; Teng et al., 2000). Some studies are at odds with this, and observe spiral growth even in solutions of high supersaturation ($\Omega \approx 6.9$, Gratz et al., 1993; $\Omega \approx 8-20$, Paquette and Reeder, 1995). This discrepancy may be reconciled by a recent study modeling AFM experimental data from Teng et al. (2000) which found that spiral growth is favored for sufficiently large calcite crystals ($\geq 1 \mu\text{m}$) regardless of Ω (Darkins et al., 2022), as

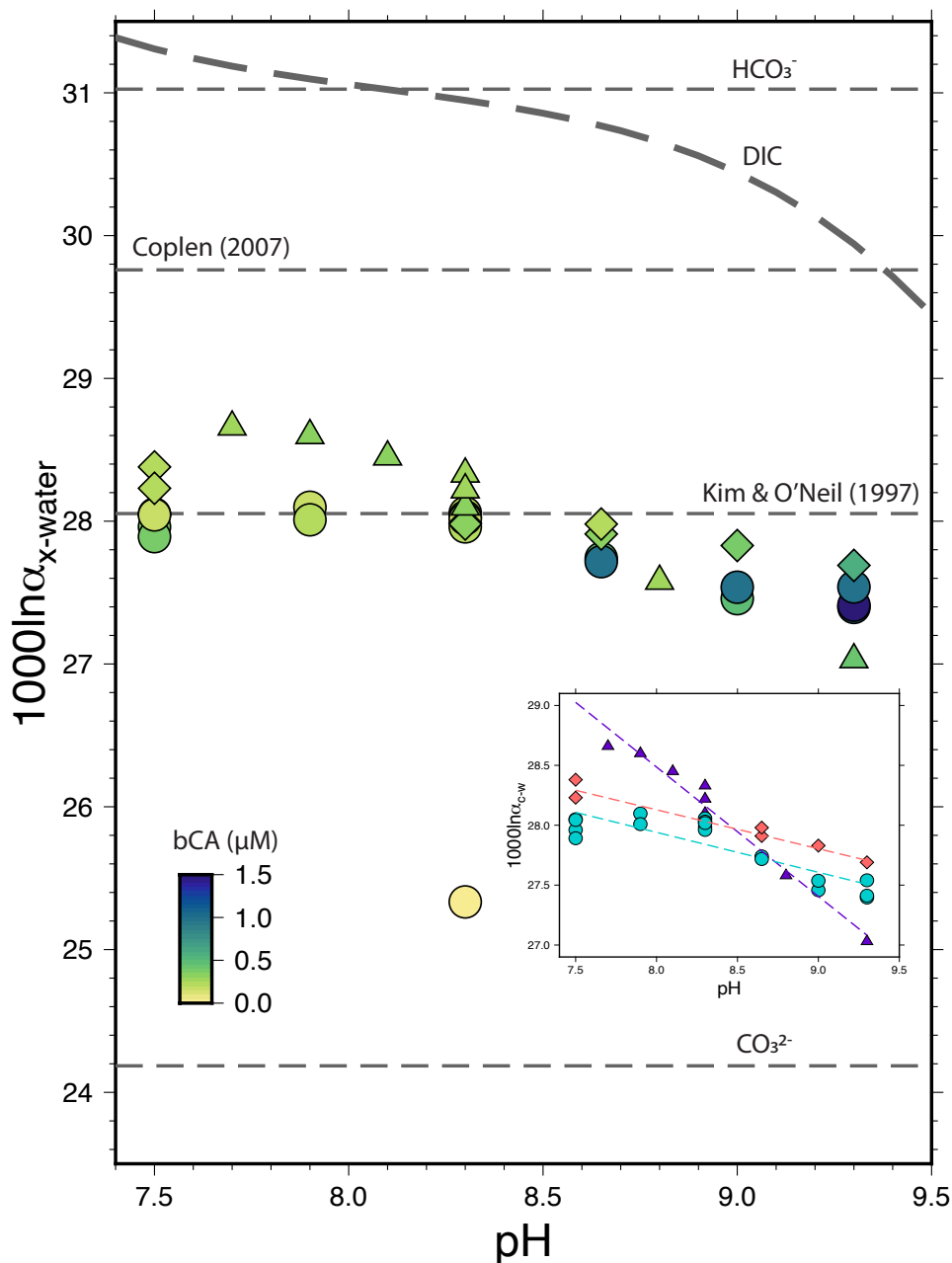


Figure 4: Oxygen isotope fractionation between calcite and experimental solution expressed as $1000\ln\alpha_{c-w}$. At higher pH, greater [bCA] should be necessary to ensure isotopic equilibration of the DIC pool. Oxygen isotope results from this study's experiments (circles) are consistent with that of similar experiments from past studies (triangles - Watkins et al., 2014; diamonds - Baker, 2015). Oxygen isotope fractionations of this study from pH 7.5-8.3 are in agreement with the Kim and O'Neil (1997) value for 25°C, but trend to lower fractionations above pH 8.3. Inset depicts the slope of $1000\alpha_{c-w}$ vs. pH for each set of experiments. The DIC isotopic composition is calculated using the Zeebe (2007) expression, Millero et al. (2007) DIC pK values for simple NaCl solutions, and equilibrium fractionation factors reported in Beck et al. (2005).

the experiments at high Ω observed spiral growth on sufficiently large calcite crystals (Gratz et al., 1993; Paquette and Reeder, 1995).

Darkins et al. (2022) noted the importance of the supersaturation at the calcite surface being lower than the supersaturation in the bulk solution, and that while growth kinetics are determined by surface supersaturation, it is difficult to measure and that growth can be reasonably characterized by a combination of bulk supersaturation and average crystal size. The majority of crystals from our experiments are sufficiently large, and therefore despite the high bulk supersaturation (average $\Omega > 2.5$ in our experiments), the spiral growth mechanism should be reasonably applicable. We do note that newly nucleated crystals are likely dominated by the 2D island nucleation growth mechanism until the crystal has grown to the critical length scale at which spiral growth takes over (Darkins et al., 2022).

DIC speciation at the calcite surface differs significantly from that of the bulk solution (Andersson et al., 2016b; Wolthers et al., 2008; Wolthers et al., 2012). In all of our experimental solutions, $[\text{HCO}_3^-] > [\text{CO}_3^{2-}]$ in the bulk solution, while the same may not be true for calcite surface speciation. The $\text{p}K_a$ for HCO_3^- - CO_3^{2-} interconversion is 10.35 - 10.5 in the bulk solution, while it is approximately 3 pH units lower for a $\text{p}K_a \sim 7.5$ when adsorbed onto the mineral surface (Andersson et al., 2016b; Plummer and Busenberg, 1982). Bicarbonate in the calcite lattice has even lower $\text{p}K_a$ values, meaning that bicarbonate readily deprotonates upon incorporation into the mineral (Andersson et al., 2016b). The ion-by-ion model considers separately the DIC speciation on the mineral surface compared to the bulk solution, and modifies the bulk solution speciation to account for temperature and the effect of background electrolytes (Millero et al., 2007; Watkins et al., 2014; Wolthers et al., 2012). How DIC speciation at the calcite surface is affected by temperature, background electrolytes, and factors other than pH is not known.

In updating the model, we modified some of the initial parameters and fractionation factors employed in past iterations. We calculate DIC speciation in the bulk solution (ϕ) using the $\text{p}K$ values of Millero et al. (2007) for simple CaCl_2 solutions (Table 3). We update the ratio of $\text{HCO}_3^-/\text{CO}_3^{2-}$ adsorbed on the calcite surface (θ) to reflect the density functional theory modeling of HCO_3^- and CO_3^{2-} adsorption energies to relevant calcite surface site geometries (i.e. the $\{10\bar{1}4\}$ cleavage surface and acute and obtuse steps) (Table 3; Andersson et al., 2016b). Model parameters in Table 4 are calculated using the initial parameters given in Table 3. Tables 3 and 4 use a shorthand notation for the constituent ions where A is Ca^{2+} and B is (bi)carbonate, with B_1 as CO_3^{2-} and B_2 as HCO_3^- , and A_1 as Ca^{2+} associated with CO_3^{2-} and A_2 as Ca^{2+} associated with HCO_3^- . The oxygen and carbon fractionation factors used in the model calculations are presented in Table 5.

The calcite growth ion-by-ion model predicts the $1000\ln^{18}\alpha_{\text{c-w}}$ and $1000\ln^{13}\alpha_{\text{c-DIC}}$ as functions of temperature, solution pH, and growth rate. Results at 25°C are shown over a range of pH and growth rate ($\log_{10}R = -4$ to -10 mol/m²/s) (Fig. 5). When calcite grows from an isotopically equilibrated DIC pool, KIEs recorded in the mineral may be attributed to processes occurring at the mineral surface (i.e. attachment and detachment of ions). We compare the calcite isotopic

Table 3: Model input parameters

Parameter	Symbol ¹	Value	Units
Kink formation energy	ϵ	$6.7 \cdot 10^{-21}$	J
Edge work	γ	$1.2 \cdot 10^{-19}$	J
Adsorbed $\text{HCO}_3^-/\text{CO}_3^{2-}$ ratio	θ	$\approx 10^{7.5-\text{pH}}$	no units
Bulk $\text{HCO}_3^-/\text{CO}_3^{2-}$ ratio	ϕ	$\frac{[\text{B}_2]}{[\text{B}_1]}$	no units
Attachment frequencies	k_{A_1}	$3.0 \cdot 10^6$	s^{-1}
	k_{A_2}	$\approx k_{A_1}$	s^{-1}
	k_{B_1}	$= 2k_{A_1} \cdot \frac{1+\theta}{1+\phi}$	s^{-1}
	k_{B_2}	$\approx k_{B_1}$	s^{-1}
Detachment frequencies	ν_{A_1}	$2 \cdot 10^3$	s^{-1}
	ν_{A_2}	$\approx \nu_{A_1}$	s^{-1}
	ν_{B_1}	$= \frac{K_s k_A k_B}{\bar{\nu}_A (1+\theta)}$	s^{-1}
	ν_{B_2}	$\approx \nu_{B_1}$	s^{-1}

¹ $\text{B}_1 = \text{CO}_3^{2-}$ and $\text{B}_2 = \text{HCO}_3^-$, while $\text{A}_1 = \text{Ca}^{2+}$ associated with CO_3^{2-} and $\text{A}_2 = \text{Ca}^{2+}$ associated with HCO_3^- .

Table 4: Model parameters calculated from input parameters

Parameter	Symbol ¹	Value	Units
Fraction of kink sites suitable for growth	χ	1	no units
Closest spacing between A and B sites	a	3.199×10^{-10}	m
Molar density of calcite	d	27,100	moles/m ³
Solubility product for calcite	K_{sp}	$\approx 10^{-8.48}$	no units
Saturation ratio for calcite	S	$(\frac{[\text{A}][\text{B}_1]}{K_{\text{sp}}})^{1/2}$	no units
Rate coefficient for A attachment	\bar{k}_A	$k_{A_1} + \theta k_{A_2}$	s^{-1}
Rate coefficient for B ₁ and B ₂ attachment	\bar{k}_B	$k_{B_1} + \phi k_{B_2}$	s^{-1}
Rate coefficient for A detachment	$\bar{\nu}_A$	$\nu_{A_1} + \nu_{A_2}$	s^{-1}
Rate coefficient for B ₁ and B ₂ detachment	$\bar{\nu}_B$	$\nu_{B_1} + \theta \nu_{B_2}$	s^{-1}
Probability that a given site is a B ₁ site	P_{B_1}	$\frac{\bar{k}_B [\text{B}_1] + \bar{\nu}_A}{\bar{k}_A [\text{A}] + \bar{\nu}_B + (1+\theta)(\bar{k}_B [\text{B}_1] + \bar{\nu}_A)}$	no units
Probability that a given site is an A site	P_A	$1 - (1 + \theta) P_{B_1}$	no units
Probability that a given site is a B ₂ site	P_{B_2}	$1 - P_A - P_{B_1}$	no units
Net incorporation rate of A ions	u_A	$\bar{k}_A [\text{A}] P_{B_1} - \bar{\nu}_A P_A$	s^{-1}
Net incorporation rate of B ions	u_B	$\bar{k}_B [\text{B}_1] P_A - \bar{\nu}_B P_{B_1}$	s^{-1}
Kink propagation rate	u_c	$u_A + u_B$	s^{-1}
Rate of kink formation on B sites	i_B	$2 \exp(\frac{-2\epsilon}{kT})(S^2 - 1)(\frac{\bar{\nu}_B \bar{k}_A [\text{A}]}{\bar{k}_A [\text{A}] + \bar{\nu}_B})$	s^{-1}
Rate of kink formation on A sites	i_A	$2 \exp(\frac{-2\epsilon}{kT})(S^2 - 1)(\frac{\bar{\nu}_A \bar{k}_B [\text{B}_1]}{\bar{k}_B [\text{B}_1] + \bar{\nu}_A})$	s^{-1}
Net rate of kink formation	i_c	$\frac{i_A + i_B}{2}$	s^{-1}
Steady state kink density	ρ_c	$(\frac{2i_c}{u_A + u_B})^{1/2}$	no units
Step spacing	y_0	$\frac{19a\gamma}{kT \ln S_2}$	m
Calcite growth rate	R_c	$\frac{\rho_c u_c a^2 d}{y_0}$	moles/m ² /s

¹ $\text{A} = \text{Ca}^{2+}$, $\text{B}_1 = \text{CO}_3^{2-}$, and $\text{B}_2 = \text{HCO}_3^-$.

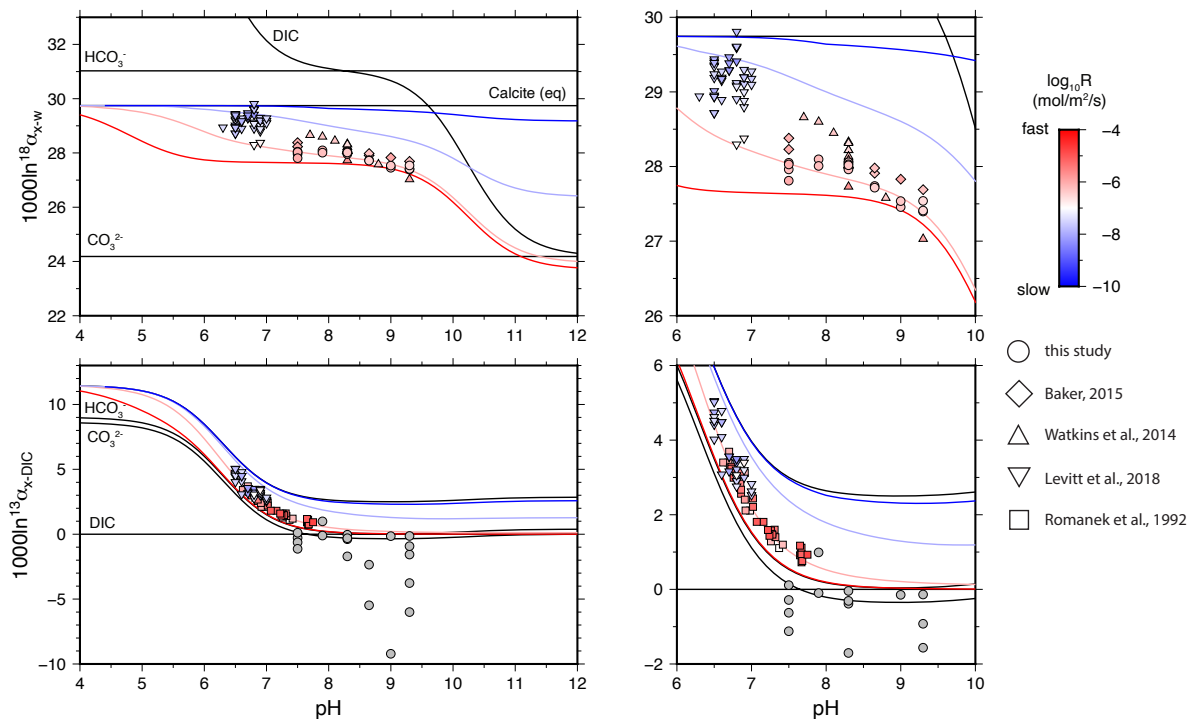


Figure 5: Updated ion-by-ion model of calcite growth at 25°C in 30 mM CaCl₂ solutions. The model predicts $1000\ln^{18}\alpha_{c-w}$ (upper panels) and $1000\ln^{13}\alpha_{c-DIC}$ (lower panels) as functions of temperature, solution pH, and growth rate (curves for $\log_{10}R = -4, -6, -8,$ and -10 mol/m²/s). Experiments plotted from this study (circles) and other studies (Baker, 2015 - diamonds; Levitt et al., 2018 - inverted triangles; Romanek et al., 1992 - squares; Watkins et al., 2014 - upright triangles) in which calcite grew from an equilibrated DIC pool, so that KIEs may be attributed to attachment and detachment of (bi)carbonate ions at the calcite surface.

fractionations of this study's experiments with that of other studies that reasonably assume calcite grew from an isotopically equilibrated DIC pool (Baker, 2015; Levitt et al., 2018; Romanek et al., 1992; Watkins et al., 2014). Since KIEs in $1000\ln^{18}\alpha_{c-w}$ should be a direct result of ion attachment/detachment, we modify the forward and backward KFFs attending calcite precipitation and dissolution reactions (Table 5) to fit the experimental CaCO₃ data of this study. Due to concerns about our carbon isotope data, we did not use our $1000\ln^{13}\alpha_{c-DIC}$ to adjust the model results (Fig. 5 - gray circles). We instead use the carbon KFFs postulated by Watkins and Hunt (2015), which are in agreement with carbon isotope fractionations from Romanek et al. (1992) and Levitt et al. (2018) (Table 5; Fig. 5).

This ion-by-ion model is a process-based model that fits experimental isotopic data rather well, despite many necessary assumptions. The model assumes a cubic mineral lattice, which does not account for the differential step and kink geometries of the acute and obtuse sites, which propagate at different rates depending on a variety of factors (i.e. $[Ca^{2+}]/[CO_3^{2-}]$, Ω ; Andersson et al., 2016a; Larsen et al., 2010; Perdikouri et al., 2009; Ruiz-Agudo & Putnis, 2012; Sand et al., 2016). Calcite growth is modeled by the attachment and detachment of free Ca²⁺, HCO₃⁻, and CO₃²⁻ ions to the

Table 5: Oxygen and carbon fractionation factors used to generate the ion-by-ion model curves

Fractionation factor	Equation	α (25°C)	Notes
Oxygen			
$\alpha_{\text{CO}_2(\text{g})-\text{w}}^{\text{eq}}$	17.611/ T_K +0.9821	1.0412	Zeebe (2007)
$\alpha_{\text{CO}_2(\text{aq})-\text{w}}^{\text{eq}}$	$\exp(\frac{2520}{T_K^2}+0.01212)$	1.0413	Beck et al. (2005)
$\alpha_{\text{HCO}_3-\text{w}}^{\text{eq}}$	$\exp(\frac{2590}{T_K^2}+0.00189)$	1.0315	Beck et al. (2005)
$\alpha_{\text{CO}_3-\text{w}}^{\text{eq}}$	$\exp(\frac{2390}{T_K^2}-0.00270)$	1.0245	Beck et al. (2005)
$\alpha_{\text{c}-\text{w}}^{\text{eq}}$	$\exp((\frac{17747}{T_K} - 29.777)/1000)$	1.0302	Coplen (2007); Watkins et al. (2013)
$\alpha_{\text{c}-\text{HCO}_3}^{\text{f}}$	-	0.9966	Model parameter
$\alpha_{\text{c}-\text{CO}_3}^{\text{f}}$	-	0.9995	Model parameter
$\alpha_{\text{c}-\text{HCO}_3}^{\text{eq}}$	$\alpha_{\text{c}-\text{w}}^{\text{eq}}/\alpha_{\text{HCO}_3-\text{w}}^{\text{eq}}$	0.9987	Beck et al. (2005); Copen (2007); Watkins et al. (2013)
$\alpha_{\text{c}-\text{CO}_3}^{\text{eq}}$	$\alpha_{\text{c}-\text{w}}^{\text{eq}}/\alpha_{\text{CO}_3-\text{w}}^{\text{eq}}$	1.0056	Beck et al. (2005); Copen (2007); Watkins et al. (2013)
$\alpha_{\text{c}-\text{HCO}_3}^{\text{b}}$	$\alpha_{\text{c}-\text{HCO}_3}^{\text{f}}/\alpha_{\text{c}-\text{HCO}_3}^{\text{eq}}$	0.9979	Beck et al. (2005); Copen (2007); Watkins et al. (2013)
$\alpha_{\text{c}-\text{CO}_3}^{\text{b}}$	$\alpha_{\text{c}-\text{CO}_3}^{\text{f}}/\alpha_{\text{c}-\text{CO}_3}^{\text{eq}}$	0.9940	Beck et al. (2005); Copen (2007); Watkins et al. (2013)
Carbon			
$\alpha_{\text{CO}_2(\text{g})-\text{HCO}_3}^{\text{eq}}$	$1/((-0.1141*T_C + 10.78)/1000 + 1)$	0.9921	Zhang et al. (1995)
$\alpha_{\text{CO}_2(\text{aq})-\text{CO}_2(\text{g})}^{\text{eq}}$	$(0.0049*T_C - 1.31)/1000 + 1$	0.9988	Zhang et al. (1995)
$\alpha_{\text{CO}_3-\text{HCO}_3}^{\text{eq}}$	$(\frac{-867}{T_K} + 2.52)/1000 + 1$	0.9996	Mook (1986)
$\alpha_{\text{CO}_2(\text{aq})-\text{HCO}_3}^{\text{eq}}$	$(\frac{-9866}{T_K} + 24.12)/1000 + 1$	0.9910	Mook (1986)
$\alpha_{\text{CO}_2(\text{g})-\text{c}}^{\text{eq}}$	$\exp((-2.4612 + \frac{7666.3}{T_K} - \frac{2988000}{T_K^2})/1000)$	0.9897	Bottinga (1968)
$\alpha_{\text{c}-\text{HCO}_3}^{\text{f}}$	-	1.000	Model parameter
$\alpha_{\text{c}-\text{CO}_3}^{\text{f}}$	-	1.000	Model parameter
$\alpha_{\text{c}-\text{HCO}_3}^{\text{eq}}$	$1/(\alpha_{\text{CO}_2(\text{g})-\text{c}}^{\text{eq}}/\alpha_{\text{CO}_2(\text{g})-\text{HCO}_3}^{\text{eq}})$	1.0025	Bottinga (1968); Zhang et al. (1995)
$\alpha_{\text{c}-\text{CO}_3}^{\text{eq}}$	$\alpha_{\text{c}-\text{HCO}_3}^{\text{eq}}/\alpha_{\text{CO}_3-\text{HCO}_3}^{\text{eq}}$	1.0029	Bottinga (1968); Mook (1986); Zhang et al. (1995)
$\alpha_{\text{c}-\text{HCO}_3}^{\text{b}}$	$\alpha_{\text{c}-\text{HCO}_3}^{\text{f}}/\alpha_{\text{c}-\text{HCO}_3}^{\text{eq}}$	0.9975	Bottinga (1968); Zhang et al. (1995)
$\alpha_{\text{c}-\text{CO}_3}^{\text{b}}$	$\alpha_{\text{c}-\text{CO}_3}^{\text{f}}/\alpha_{\text{c}-\text{CO}_3}^{\text{eq}}$	0.9972	Bottinga (1968); Mook (1986); Zhang et al. (1995)

calcite surface, assuming constant attachment (\bar{k}_A, \bar{k}_B) and detachment ($\bar{\nu}_A, \bar{\nu}_B$) frequencies, as well as equal frequencies for HCO_3^- and CO_3^{2-} ions ($k_{B_2} = k_{B_1}, \nu_{B_2} = \nu_{B_1}$) all of which might not be a realistic description of processes occurring at the mineral surface. The importance of ion pairs and polynuclear complexes in calcite growth processes is a continued avenue of research, as ion pairs tend to have faster dehydration rates than free ions and can therefore attach more readily at the mineral surface (Andersson et al., 2016a; Ruiz-Agudo & Putnis, 2012; Ruiz-Agudo et al., 2011). The model assumes that calcite growth proceeds via spiral growth mechanism, which until recently was understood to be unrealistic at our high supersaturations, but a new study highlighting the importance of the critical length scale of calcite crystals suggests spiral growth takes over for crystals $\geq 1 \mu\text{m}$ (Darkins et al., 2022). However, our experiments are unseeded and therefore processes such as 2D island nucleation are dominant for newly nucleated crystals until they grow sufficiently large. Despite these limitations, the model still constitutes a physics-based parameterization that describes $1000\ln\alpha_{c-w}^{18}$ and $1000\ln\alpha_{c-DIC}^{13}$ over a broad range of T, pH, and growth rate.

5 Summary

Most natural CaCO_3 grows at rates by which the solution pH may result in kinetic isotope effects, even when the DIC is isotopically equilibrated (Baker, 2015; Daëron et al., 2019; Watkins et al., 2013, 2014). We report a decrease in $1000\ln^{18}\alpha_{c-w}$ over the pH range 7.5-9.3, with a slope of $\sim 0.33\text{‰}$ per pH unit that is in agreement with the experiments of Baker (2015), but which exhibit a higher y-intercept by $\sim 0.12\text{‰}$ than experiments of this study (Fig. 4). Our use of the enzyme carbonic anhydrase to facilitate isotopic equilibration of the DIC pool allows us to isolate KIEs that result from attachment and detachment of ions at the calcite surface (Uchikawa & Zeebe, 2012; Watkins et al., 2013). We update the ion-by-ion model of Watkins et al. (2014) with improved constraints on equilibrium fractionation between DIC species and water, and DIC speciation on the calcite surface, and report updated oxygen KFFs attending CaCO_3 precipitation and dissolution reactions.

Quantifying the inorganic DIC- CaCO_3 isotopic fractionations and better understanding the mechanisms and processes leading to these KIEs gives insight into separating vital effects from mass-dependent kinetic fractionations in biogenic CaCO_3 . Understanding biocalcification processes is of high priority since the vast majority of calcic seafloor sediments are biogenic and constitute an important global paleoenvironmental archive (Zachos, 2001; Zeebe & Wolf-Gladrow, 2001).

6 Bridge

The prior two chapters examine the effect of ionic strength (Chapter III) and solution pH (Chapter IV) on kinetic isotopic effects recorded in nonequilibrium inorganic calcite, but under growth conditions that result in relatively small magnitude KIEs ($\sim 2\text{-}5\text{‰}$). In Chapter V, I conduct exper-

iments investigating extreme kinetic isotopic effects during far-from-isotopic-equilibrium carbonate precipitation. These experiments simulate processes occurring at hyperalkaline springs upwelling through ultramafic ophiolitic bodies, where CaCO_3 travertines precipitate at the air-water interface as the high pH, DIC-free spring water interacts with atmospheric CO_2 . This work quantifies the kinetic fractionation factors attending CO_2 hydroxylation, and contributes valuable insights into understanding the isotopic signatures of carbonates from these environments that helps lay the groundwork for their use as paleoenvironmental archives.

CHAPTER V

EXTREME ISOTOPIC FRACTIONATIONS IN CaCO_3 FROM A HYPERALKALINE SPRING ANALOG: QUANTIFYING KINETIC FRACTIONATIONS ATTENDING CO_2 HYDROXYLATION

This chapter is in preparation for submission to *Geochemistry, Geophysics, Geosystems*, co-authored with J.M. Watkins and L.S. Devriendt. The experiments were performed by E.K. Olsen. J.M. Watkins modeled the results and compared them to a previous study. All other writing is by E.K. Olsen, with editorial assistance from J. M. Watkins.

1 Introduction

Hyperalkaline springs upwelling through ultramafic ophiolite formations commonly result in travertine precipitation upon contact with atmospheric CO_2 . Carbonate precipitated in this environment records large kinetic isotope effects that are not fully understood, but likely reflect kinetic fractionations during CO_2 hydroxylation. The isotopic composition of carbonates formed in this environment is a potential paleoproxy to reconstruct the isotopic composition of atmospheric CO_2 and meteoric water from which it grew (Christensen et al., 2021). However, to utilize natural travertines as a paleoenvironmental archive, we must more fully understand and quantify the kinetic isotopic fractionations that occur during their precipitation.

The spring waters typically originate as meteoric water seeping downward into the peridotite, reacting with olivine and pyroxene to form serpentine, brucite, iron hydroxides, and other hydrated secondary minerals (Chavagnac et al., 2013; Falk et al., 2016; Mervine et al., 2014; Palandri & Reed, 2004). During serpentinization, the groundwaters become isolated from the atmosphere and evolve with progressive reactions. Calcium silicate minerals are generally unstable in high Mg serpentine systems, so the breakdown of clinopyroxene results in increased Ca^{2+} in the groundwater (Morrill et al., 2013; Palandri & Reed, 2004). The dissolved carbon content is precipitated at depth in the form of carbonate minerals, commonly magnesite (MgCO_3) (Falk et al., 2016). Overall, serpentinization of the peridotite shifts water composition from its Mg- HCO_3 meteoric origin to increased pH, increased Ca^{2+} , decreased Mg^{2+} , and decreased dissolved inorganic carbon (DIC) (Chavagnac et al., 2013; Falk et al., 2016; Morrill et al., 2013). These high pH (up to pH 11.7, Chavagnac et al., 2013; Christensen et al., 2021; up to pH 12-12.1, Falk et al., 2016; Giampouras et al., 2019; Morrill et al., 2013) spring waters then upwell at the surface as Ca-OH waters, with atmospheric

CO₂ dissolving into solution and being rapidly precipitated out as CaCO₃.

1.1 CO₂ captured as CaCO₃

As CO₂ gas diffuses from the atmosphere into the Ca-OH pools, it dissolves into solution by the reaction:



during which the isotopes fractionate according to mass-dependent processes. CO₂ exchange at the gas-solution interface is rapid, so we assume isotopic equilibrium is achieved between gaseous and aqueous CO₂ (Clark et al., 1992). During equilibrium isotopic fractionation, the heavier isotopes tend to be enriched in the phase in which they are more strongly bound, and in this case carbon and oxygen have opposite fractionation effects where ¹³C prefers CO₂(g) and ¹⁸O prefers CO₂(aq). At 25°C, the resulting CO₂(aq) is depleted in ¹³C by ~1.1-1.4‰ (Vogel et al., 1970; Yumol et al., 2020; Zhang et al., 1995), and enriched in ¹⁸O by ~0.3‰ (Barkan and Luz, 2012; Beck et al., 2005).

Reactions involving molecules containing ¹³C or ¹⁸O proceed more slowly than reactions involving molecules containing only the light isotopes, thereby enriching the product species in light carbon and oxygen if the reactions are unidirectional, or mostly unidirectional. Upon dissolving into solution, the CO₂ undergoes primarily unidirectional hydroxylation:



producing HCO₃⁻ that is depleted in both heavy carbon and oxygen relative to the reacting CO₂(aq). CO₂ hydration and hydroxylation are the slowest DIC exchange reactions, and are also the only reactions through which DIC exchanges oxygen with water (Sade & Halevy, 2017; Zeebe & Wolf-Gladrow, 2001). In disequilibrium systems, the kinetic isotope effects attending these reactions are more likely to be recorded in carbonate minerals compared to the other, more rapid DIC exchange reactions. The relative production of HCO₃⁻ from CO₂ hydration versus hydroxylation depends on solution pH. In low ionic strength solutions at 25°C, the contribution from CO₂ hydration is negligible at pH 10.5 or higher (Bajnai and Herwartz, 2021; Devriendt et al., 2017).

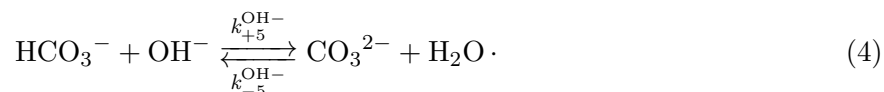
The isotopic composition of the HCO₃⁻ should reflect the CO₂ hydroxylation kinetic fractionation factors (KFFs) for both oxygen and carbon, provided that the amount of back-reaction is negligible as we reasonably expect for our solutions. The dissolved CO₂ is the only source of carbon, while oxygen comes from both the dissolved CO₂ and OH⁻. A single KFF can describe the carbon kinetic fractionation, while two KFFs are required to fully explain the oxygen isotope signature of the resulting precipitate: the KFF for CO₂(aq)-HCO₃⁻ and the KFF for OH⁻-HCO₃⁻. However, previous studies have been unable to tease apart the KFFs for CO₂ and OH⁻ separately during CO₂ hydroxylation, and instead report ¹⁸O/¹⁶O fractionation using a single bulk oxygen KFF that is weighted according to the number of oxygen atoms each source contributes to the

HCO_3^- (Christensen et al., 2021; Dietzel et al., 1992).

HCO_3^- then converts to CO_3^{2-} either via deprotonation:



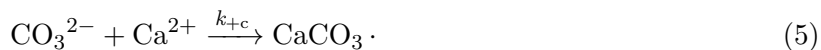
or by reacting with OH^- :



$\text{HCO}_3^- - \text{CO}_3^{2-}$ exchange is many orders of magnitude faster than hydroxylation over our pH range of interest, so therefore instantaneous isotopic equilibration of $\text{HCO}_3^- - \text{CO}_3^{2-}$ may be assumed (Eigen, 1964; Christensen et al., 2021; Pinsent et al., 1956; Sade & Halevy, 2017; Zeebe & Wolf-Gladrow, 2001). Equilibrium CO_3^{2-} is 0.4‰ and 6.8‰ isotopically lighter than HCO_3^- for carbon and oxygen, respectively (Beck et al., 2005; Christensen et al., 2021; Mook, 1986). However, no net isotopic fractionation would be expected during quantitative conversion of HCO_3^- to CO_3^{2-} , which is a reasonable assumption for $\text{pH} > 12$ where $\text{HCO}_3^-/\text{DIC} < 1\%$ (Christensen et al., 2021).

With unidirectional CO_2 hydroxylation, the full kinetic fractionation is expressed in the EIC (equilibrated inorganic carbon = $\text{HCO}_3^- + \text{CO}_3^{2-}$) prior to CaCO_3 precipitation. Assuming near quantitative conversion of EIC to CaCO_3 , then the CaCO_3 precipitates would reflect the CO_2 hydroxylation KFFs. Previous studies have addressed the isotopic composition of travertines from natural hyperalkaline springs as well laboratory experiments in an effort to quantify the KFFs for CO_2 hydroxylation. Many studies agree that the ^{13}C KFF is quite large, approximately -17‰ with little to no temperature dependence, while the bulk ^{18}O KFF appears to have a stronger temperature-dependence, and an approximate value at 25°C of -7.2‰ when expressed relative to the weighted sum of $\text{CO}_2(\text{aq}) + \text{OH}^-$, or -13.9‰ when expressed relative to the weighted sum of $\text{CO}_2(\text{aq}) + \text{H}_2\text{O}$ (Böttcher et al., 2018; Christensen et al., 2021; Clark et al., 1992; Falk et al., 2016; Mervine et al., 2014; Zeebe, 2020).

If the EIC is not quantitatively precipitated as CaCO_3 , then we would expect isotopic fractionation to occur based on the degree of EIC distillation, but also based on the extent the CaCO_3 precipitation reactions are unidirectional or bidirectional. At low supersaturation, CaCO_3 precipitation reactions would be bi-directional. However, in our high supersaturation solutions ($\Omega > 5$), negligible back-reaction is expected:



Unidirectional precipitation of CaCO_3 from CO_3^{2-} should result in calcite with $\delta^{13}\text{C} \sim 0.5\%$ heavier and of $\delta^{18}\text{O} \sim 0.5\%$ lighter than the reacting CO_3^{2-} (Devriendt et al., 2017; Kim et al., 2006; Sade et al., 2020).

1.2 OH⁻-H₂O fractionation

The dissociation of water:



is a relatively rapid reaction, with equilibration timescales akin to the bicarbonate-carbonate exchange, and therefore is regarded as having attained equilibrium when dealing with the DIC system, which equilibrates much slower due to the rate-limiting CO₂ hydration and hydroxylation reactions through which DIC exchanges oxygen with H₂O.

There is considerable disagreement as to the equilibrium oxygen fractionation between OH⁻ and H₂O. Experimental studies suggest that at 25°C, $1000\ln\alpha_{\text{OH}^- - \text{H}_2\text{O}} \sim -42.5\text{‰}$ (Bajnai & Herwartz, 2021; Green & Taube, 1963), while theoretical calculations suggest much smaller values of -19.1 to -23.5‰, depending on the number of water molecules involved in the reactions (Zeebe, 2020). This ~20‰ offset between experimental and theoretical studies introduces a significant degree of uncertainty into our fractionation factor calculations. Therefore, we choose to present bulk oxygen KFFs from CO₂+H₂O, in addition to the KFFs from CO₂+OH⁻ which would be the true contributing source of the oxygen.

1.3 Motivation

Past studies have addressed the isotopic composition of travertines from natural hyperalkaline springs and carbonate precipitation experiments conducted at high pH, with the aim of quantifying the kinetic isotope fractionations attending CO₂ hydroxylation and/or the equilibrium oxygen isotope fractionation between H₂O and OH⁻. However, separating the kinetic fractionation factors attending CO₂ hydroxylation from equilibrium isotopic fractionations between OH⁻ and H₂O have proved difficult, and past studies have failed to do so definitively (Zeebe, 2020). The isotopic composition of the carbonate mineral may be described by minimal OH⁻-H₂O fractionation and a large CO₂ hydroxylation KFF (Böttcher et al., 2018), or by a large OH⁻-H₂O fractionation and a small to negligible CO₂ hydroxylation KFF (Clark et al., 1992), or anywhere in between those end-member scenarios.

We conducted well-controlled laboratory experiments in simple CaCl₂ solutions at high pH in an attempt to simulate what occurs naturally at hyperalkaline springs such as The Cedars, California, and the Samail Ophiolite, Oman, in order to better understand how these large isotopic fractionations arise. We sought to recreate the (1) mineralogy, (2) morphology, and (3) isotopic fractionations observed in natural travertines, with the goal of isolating and quantifying the KFFs attending CO₂ hydroxylation (¹³C/¹²C on CO₂(aq), ¹⁸O/¹⁶O on CO₂(aq), and ¹⁸O/¹⁶O on OH⁻).

2 Methods

Our initial experimental design (Figure 1) consists of a sealed beaker containing 1.3 L distilled, deionized (DDI) water with 10 millimolar (mM) or 30 mM $\text{CaCl}_2 \cdot 2\text{H}_2\text{O}$ sitting in a temperature-controlled water bath, held at 10°C or 25°C (Table 1). Initially, pure N_2 gas is fluxed into a rapidly-stirring solution until the CO_2 concentration of the headspace drops to < 30 ppm CO_2 , typically over 1-1.5 hours. N_2 was bubbled for at least 1.5 hours to minimize the amount of remnant DIC in the experimental solution so that experimental precipitates can be reasonably expected to form from the CO_2 introduced later. For experiments CH2 - CH10, a mixture of 3 M KCl and 1 M NaOH was added to the solution to raise the pH to ~ 12.4 , with the final solution containing 50 mM KCl and 12 mM NaOH. For experiments CH1, CH11 - CH27, 1 M NaOH was added to reach the desired pH (11 - 12.6), with the final solution containing 1 - 18 mM NaOH (Table 1). The gas bubbler was moved above the solution into the headspace, with N_2 still flowing. Stirring was turned down to a very slow rate (~ 6 -12 rpm) or off entirely and the gas was then switched to a mixture of CO_2 in N_2 (200 ppm or 2000 ppm CO_2). As CO_2 diffuses into the high pH, DIC-free solution, calcium carbonate precipitates on the surface of the water, forming a mineral crust. Solution pH decreases slightly throughout an experiment (Figure 2, Table 1) as both CO_2 diffusion and CaCO_3 precipitation act to lower pH, but remains high enough in the majority of our experiments so that kinetic isotope effects from CO_2 hydration reactions are assumed to be negligible.

We found that in many of our early experiments, the CO_2 concentration of the experimental headspace was lower than that of the gas tank, which can complicate interpretation of results. To mitigate this, we adjusted our experimental design (Figure 1b) to maximize the headspace volume to solution surface area where CO_2 was being taken up into solution. Experiments CH14-15, 18-19, 21, and 23 were experiments in which a smaller beaker of experimental solution was positioned within the larger experimental beaker that sat in the temperature-controlled water bath. These experiments were entirely unstirred even during the N_2 flow period because the smaller beaker had to sit elevated from the magnetic stir bar for the probe and bubbler to reach the solution.

We also adjusted our experimental routine to carry out experiments that grew CaCO_3 from laboratory air CO_2 rather than from a gas tank. These experiments (CH13, 17, 20, 22, 24-27) still follow the original experimental design (Figure 1) and start enclosed with pure N_2 gas fluxing through the experimental solution until the CO_2 concentration of the headspace is minimized, but then the experiment lid is removed to expose the solution to the laboratory atmosphere. These particular experiments were carried out during weekends and other periods of time in which human presence in the lab air space was minimized to lessen the impact of human CO_2 exhalation on the isotopic composition of the CO_2 in the lab air.

Solution samples for DIC and $\delta^{18}\text{O}$ were collected at the end of each experiment (Table 2). Mid-experiment DIC samples were also collected for a few experiments (CH5, CH7, CH20) to assess whether the DIC concentration or isotopic composition was evolving over time. Experiments CH22, 24, and 25 were conducted as time series, with mid-experiment water sampling for DIC and $\delta^{18}\text{O}$. For later experiments, total alkalinity (TA) was also measured by Gran titration using an

Table 1: Experimental parameters, solution composition and pH for all experiments of this study.

Exp	Temp (°C)	CO ₂ (ppm)	Volume (mL)	I	CaCl ₂ ·2H ₂ O (g)	Ca ²⁺ (mM)	KCl (mM)	NaOH (mM)	N ₂ (h)	Exp dur. (h)	CO ₂ flow (SCF/H)	pH max	pH end	pH unstirred
CH1	25	200	1300	0.031	1.922	10.06	0	1.23	2.12	166.93	0.5, 0.25, 0.15	11.029	8.43	
CH2	25	200	1300	0.152	5.735	30.01	50	12	2.08	96.27	0.5, 0.2	12.528	12.28	
CH3	25	2000	1300	0.152	5.733	30.00	50	12	1.65	70.4	0.5, 0.2	11.93	11.82	
CH4	25	2000	1300	0.152	5.735	30.01	50	12	3.6	44.2	0.5, 0.2	12.25	12.03	
CH5	25	200	1300	0.152	5.734	30.00	50	12	1.6	117.53	0.5, 0.2	12.426	12.154	
CH6	10	2000	1300	0.152	5.738	30.03	50	12	4.12	97.33	0.5, 0.2	12.225	11.87	11.8
CH7	25	2000	1300	0.152	5.734	30.00	50	12	1.68	46.07	0.5	12.444	12.016	8.89
CH8	10	2000	1300	0.152	5.737	30.02	50	12	3	48.67	0.5	12.769	12.355	
CH9	25	200	1300	0.092	1.913	10.01	50	12	2.5	66.47	0.5	12.669	12.371	
CH10	10	200	1300	0.152	5.735	30.01	50	12	4.83	70.73	0.5	12.238	12.051	
CH11	25	2000	1300	0.031	1.913	10.01	0	1.08	5.35	14.47	0.5	11.404	9.443	
CH12	25	2000	1300	0.039	1.916	10.03	0	9.23	5.42	17.93	0.5	12.535	12.147	
CH13	25	lab air	1300	0.040	1.917	10.03	0	10	4.13	40.53	lab air	12.606	12.254	
CH14	25	2000	130	0.042	0.196	10.27	0	10.77	3.48	21.07	0.5	12.528	11.91	11.55
CH15	25	2000	130	0.045	0.197	10.33	0	13.85	4.02	36.53	0.5	12.105	11.305	10.42
CH17	25	lab air	1300	0.034	1.918	10.03	0	3.85	2.07	41.47	lab air	11.735	10.615	9.036
CH18	25	2000	130	0.035	0.192	10.05	0	4.62	1.63	27.87	0.5	11.873	10.46	8.737
CH19	25	2000	130	0.034	0.194	10.17	0	3.08	1.67	18.67	0.5	11.606	10.52	
CH20	25	lab air	1300	0.032	1.916	10.03	0	2	2.9	23.93	lab air	11.429	10.617	10.117
CH21	25	2000	130	0.034	0.193	10.07	0	3.85	2.62	25.40	0.5	11.813	11.027	
CH22	25	lab air	1300	0.035	1.917	10.03	0	4.62	2.48	30.77	lab air	12.076	10.993	
CH22_1												12.076	11.96	
CH22_2												11.96	10.993	
CH23	25	2000	130	0.033	0.191	10.02	0	3.08	2.67	19.77	0.5	11.868	10.973	9.253
CH24	25	lab air	1300	0.036	1.912	10.01	0	6.15	3.20	39.12	lab air	12.317	10.976	
CH24_1												12.317	12.08	
CH24_2												12.08	11.78	
CH24_3												11.78	10.976	
CH25	10	lab air	1300	0.039	1.914	10.01	0	8.46	2.38	72.50	lab air	12.323	11.267	
CH25_1												12.323	12.169	
CH25_2												12.169	11.853	
CH25_3												11.853	11.267	
CH26	10	lab air	1300	0.043	1.913	10.01	0	17.69	2.93	43.63	lab air	12.599	12.465	
CH27	10	lab air	1300	0.039	1.914	10.01	0	10	2.75	37.73	lab air	12.367	12.143	

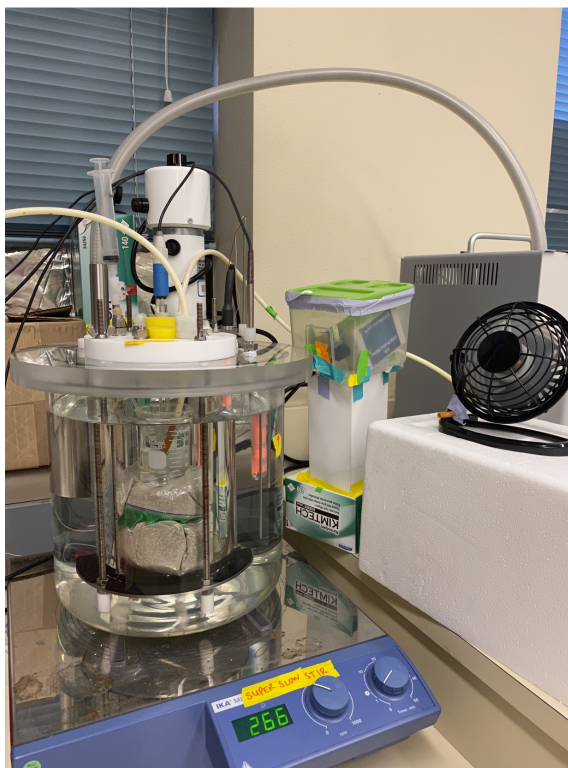
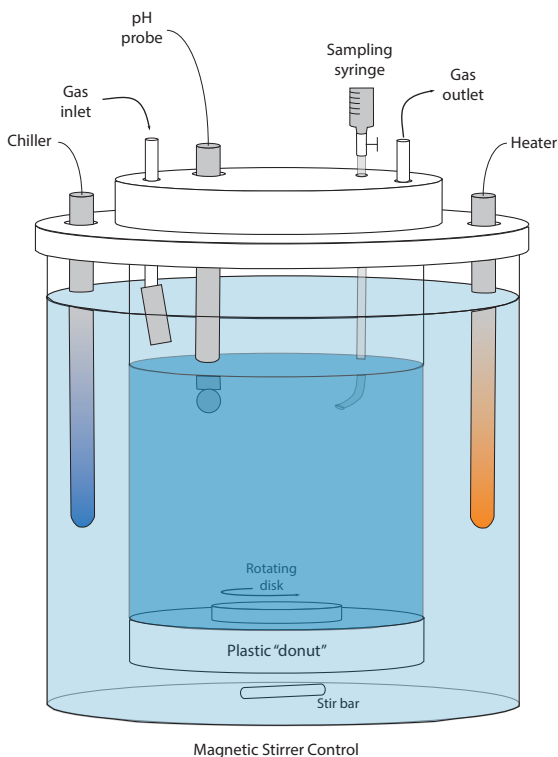


Figure 1: Experimental apparatus schematic (left) modified from Watkins et al. (2013) showing the set-up for our 1300 mL experiments where we pulled the gas inlet bubbler above the solution surface into the headspace before turning on the CO_2 -in- N_2 gas, resulting in CaCO_3 precipitating and remaining at the air-water interface. Open air experiments used the same design with the lid removed. A photo of our apparatus (right) in the early N_2 bubbling stages of a 130 mL experiment with the gas inlet below the solution surface, and the water bath actively heating up.

autotitrator dispensing 0.01 M HCl (Table 2). Solution ionic strength and free activities of Ca^{2+} and CO_3^{2-} were calculated through the R-package of PHREEQC using the Minteq.v4 database (Charlton & Parkhurst, 2011; De Lucia & Kühn, 2013). The degree of supersaturation ($\Omega = (\alpha_{\text{Ca}^{2+}} \times \alpha_{\text{CO}_3^{2-}}) / K_{\text{sp}}$) was determined by using these ionic activities and the solubility product of calcite at 25°C ($K_{\text{sp}} = 10^{-8.48}$, Charlton & Parkhurst, 2011; De Lucia & Kühn, 2013; Jacobson & Langmuir, 1974).

The measured solution pH of unstirred experiments decreases rapidly upon water sampling at the end of the experiment (Fig. 2g). The pH probe measures solution pH below the air-water interface to ensure the probe remains fully submerged and functioning properly, and solutions of unstirred experiments developed evident pH stratification of the near-surface region, with the true surface pH commonly being much lower than was being measured by the probe. After all water samples were taken, with care to minimize disturbance of the floating precipitates, the solutions were removed from the water bath and precipitates were skimmed off the surface. Skimmed precipitates, as well as the remaining solution, were filtered through $2.5 \mu\text{m}$ filter paper and rinsed with DDI.

Table 2: Direct experimental solution measurements

Experiment	[DIC] (mM)	$\delta^{13}\text{C}_{\text{DIC}}$ (VPDB)	TA (mEq/L)	$\delta^{18}\text{O}_w$ (VSMOW)
CH1	0.179	-35.778	-	-11.290
CH2	0.067	-33.317	-	-11.289
CH3	0.036	-34.781	-	-11.193
CH4	0.073	-36.665	-	-11.003
CH5_1	0.125	-27.203	-	-
CH5_2	0.091	-32.954	-	-10.484
CH6	0.136	-41.978	-	-10.769
CH7_1	0.071	-29.039	-	-
CH7_2	0.101	-34.104	-	-10.642
CH8	0.207	-42.305	-	-10.524
CH9	0.113	-36.810	-	-10.680
CH10	0.173	-38.061	-	-10.806
CH11	0.138	-47.870	0.313	-11.260
CH12	0.077	-43.807	3.947	-11.187
CH13	0.070	-24.813	5.141	-10.365
CH14	0.133	-47.476	2.629	-10.823
CH15	0.337	-49.015	2.546	-10.548
CH17	0.064	-26.695	0.627	-10.544
CH18	0.274	-44.418	0.936	-10.955
CH19	0.254	-37.191	0.448	-10.913
CH20_1	0.041	-19.491	-	-
CH20_2	0.038	-24.674	0.466	-10.577
CH21	0.687	-33.210	0.700	-10.478
CH22_1	0.125	-26.660	2.906	-10.904
CH22_2	0.095	-15.891	0.646	-10.107
CH23	0.258	-35.351	0.602	-10.360
CH24_1	0.213	-27.925	4.107	-10.664
CH24_2	0.184	-23.007	2.156	-10.409
CH24_3	0.076	-27.272	0.660	-9.728
CH25_1	0.099	-27.945	5.318	-10.787
CH25_2	0.221	-31.791	2.823	-10.797
CH25_3	0.086	-28.783	0.989	-10.745
CH26	0.120	-27.199	11.975	-10.879
CH27	0.180	-26.294	5.991	-10.993

During the time series experiments (CH22, CH24, CH25), each time after the mid-experiment water sampling, all floating crystal precipitates were also skimmed, filtered, and stored separately. Most experiments also resulted in tiny crystals encrusted on the bottom of the experimental beaker, which were also rinsed with DDI and later gently scraped from the beaker.

Imaging of precipitates was performed on an FEI Quanta 200 Environmental Scanning Electron Microscope (ESEM) at the Center for Advanced Materials Characterization (CAMCOR) at the University of Oregon.

Isotopic analyses methods are the same as detailed in Chapter III. In this contribution, all isotopic analyses are reported with respect to VPDB unless otherwise specified.

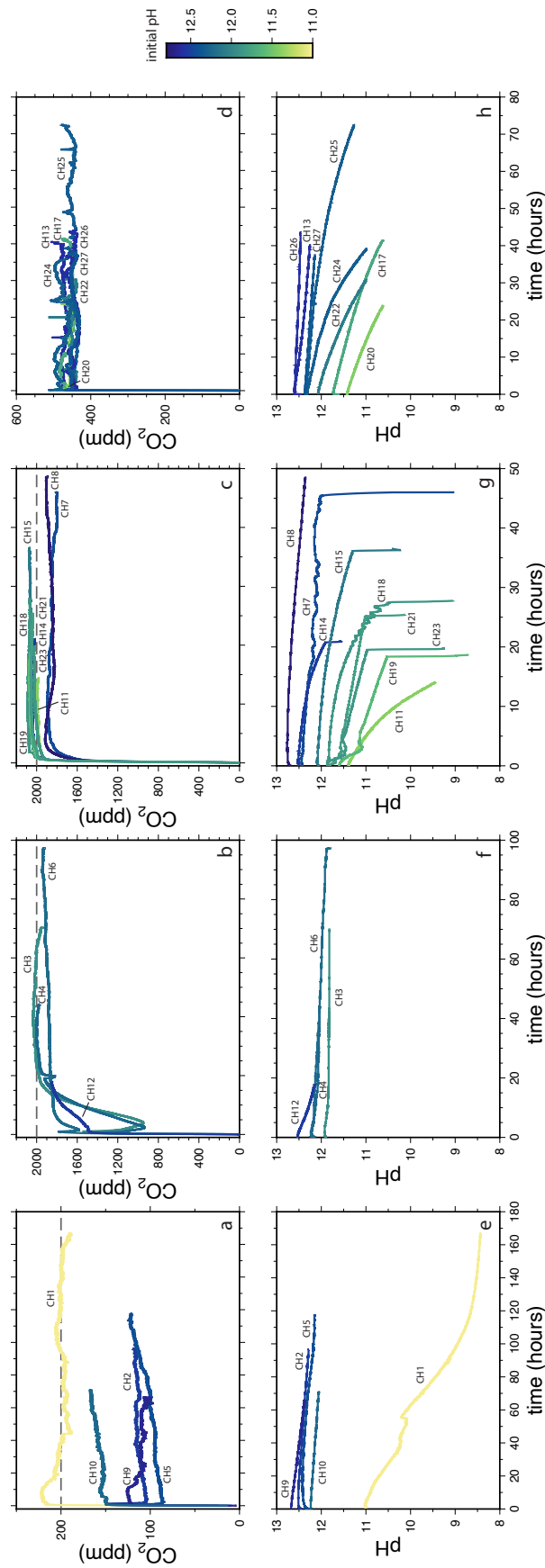


Figure 2: Experimental headspace CO₂ concentration (ppm) (panels a-d) and solution pH (panels e-h) over the course of each experiment. The gray dashed lines (panels a-c) represent the gas tank concentration of CO₂ (ppm). The left-most panels are the 200 ppm CO₂ experiments, the left-middle panels are 2000 ppm CO₂ experiments in which the headspace CO₂ took a long time to reach the gas tank value, the right-middle panels are 2000 ppm CO₂ experiments in which the headspace quickly reached the gas tank value, and the right-most plots are open, laboratory air experiments.

3 Results and Discussion

3.1 Experiment results

3.1.1 CaCO₃ precipitates

SEM images of precipitates from several experiments illustrate the range in both CaCO₃ crystal morphology and polymorphs present, and indicate the experimental design achieved our aim of simulating CaCO₃ crusts on the surface of hyperalkaline springs (Figure 3). Additional SEM images of precipitates are presented in Appendix E. Rhombohedral calcite, as well as both disaggregated and radiating acicular aragonite needles are common morphologies produced. Many crystals show a less well-defined habit. Early experiments that contained 30mM Ca²⁺ tended to produce cohesive, rigid carbonate crusts on the water surface characterized by a flat top side and a hummocky underside, with crystals stemming from the flat top and extending into the solution below. Our CaCO₃ crust flakes look remarkably similar to those of natural carbonate crusts from hyperalkaline springs, which also consist of a mixture of calcite and aragonite (see Christensen et al., 2021: Figure 4).

Travertines from natural hyperalkaline springs have a variety of mineralogies based on several different factors, including water composition, temperature, water turbulence, and degree of mixing with surface or other groundwaters. Atmospheric CO₂ dissolution into the hyperalkaline Ca-OH type spring waters with little to no surface water mixing typically results in precipitation of calcite, aragonite, or a mixture of the two polymorphs. Increased mixing of hyperalkaline spring water with Mg-HCO₃ type surface waters tends to result in precipitation of hydroxide minerals in addition to the much more abundant CaCO₃ (Chavagnac et al., 2013). Rhombohedral calcite is more likely to form from slower flowing discharge, while more dynamic flows result in aragonite precipitation of a variety of morphologies including needle, dumbbell, and spheroidal (Chavagnac et al., 2013).

In our simple CaCl₂ solutions, we do not allow for mixing with additional water types (i.e. surface Mg-HCO₃⁻ type waters) as might occur at natural hyperalkaline spring systems. We maintained a low degree of water turbulence with a very slow stirring rate or even unstirred, in an effort to keep the CaCO₃ floating at the air-water interface. We do not observe systematic differences in polymorph prevalence between our stirred and unstirred experiments.

The dominant factors influencing CaCO₃ polymorph formation are water temperature and aqueous Mg/Ca ratio (Chavagnac et al., 2013; Folk, 1994). Findings from a combination of experiments and studies of natural spring samples suggest that only calcite forms at temperatures <25°C, a mixture of calcite and aragonite precipitates from 30-60°C, and only aragonite grows at elevated temperatures >70°C (Chavagnac et al., 2013; Folk, 1994; Kitano, 1962). However, another main control in addition to water temperature on CaCO₃ polymorph formation is the Mg/Ca ratio of the springs. Aragonite dominates at Mg/Ca = 1, superseding the effect of water temperature and precipitating aragonite in cold springs that would otherwise be favored to grow calcite (Chavagnac et al., 2013; Folk, 1994). Some studies agree, finding calcite dominated springs at low temperatures and low Mg/Ca (<25°C and Mg/Ca ~ 0, Chavagnac et al., 2013; <40°C and Mg/Ca < 0.5, Gi-

ampouras et al., 2019), while others are at odds. Despite the low temperature and Mg/Ca ratio of the springs, Christensen et al. (2021) found that aragonite was the dominant CaCO_3 polymorph, with minor calcite, which suggests that while temperature and solution Mg/Ca are important, CaCO_3 polymorph formation is influenced by additional environmental and/or geochemical factors. Our experimental solutions contain no Mg, and CaCO_3 precipitated in the temperature range where calcite is favored, and yet, all experiments yielded mixtures of calcite and aragonite.

In many hyperalkaline springs, carbonate minerals precipitate as a crust on the surface of the water, with additional unconsolidated material either growing or collecting at the bottom of the pools. Different studies use different terms for each of these mineralizations: the surface material has been referred to as carbonate crusts (Chavagnac et al., 2013), surface films (Falk et al., 2016) or floes (Christensen et al., 2021) while the unconsolidated bottom material has been called bottom floc (Falk et al., 2016) or snow (Christensen et al., 2021). Falk et al. (2016) found calcite to be more common in surface crusts, and aragonite more common in unconsolidated deposits at the bottom of spring pools. Christensen et al. (2021) attributes the snow at the bottom of the pool to be sunken surface floe material, whereas other studies of natural springs do not speculate on where the bottom material originally precipitated. In this study, we report isotopic analyses of CaCO_3 crusts precipitated at the air-water interface, and, for our open-air experiments, analyses of CaCO_3 crystals that are reasonably interpreted as having precipitated at the bottom of the experimental beaker (“beaker crystals”: “_b”, Table 3) rather than be sunken surface crystals.

3.1.2 Impact of varying experimental parameters

We varied key experimental parameters to determine the effect on the morphology, mineralogy, and isotopic composition of the resulting carbonate crusts. The key variables at play are temperature (10°C or 25°C), $[\text{Ca}^{2+}]$ (10 mM or 30 mM), CO_2 gas source and isotopic composition (200 ppm or 2000 ppm CO_2 gas tanks, and laboratory air ~ 450 ppm CO_2), the CO_2 concentration of the experiment headspace relative to the CO_2 concentration of the gas source, the presence or absence of a NaOH/KCl mixture to help control solution pH, the initial starting pH of the solution, the final solution pH of the solution, and whether the solution was stirred or not.

The solution pH and headspace CO_2 (ppm) of each experiment was continuously measured (Figure 2). In many early experiments, the concentration of CO_2 in the experiment headspace was lower than the CO_2 concentration of the gas tank source for the majority of the experiment duration (Fig. 2a). Each gas tank experiment began with an initial 0.5 SCF/H (standard cubic feet per hour) flux of the CO_2 -in- N_2 mixture. For CH2-6 the gas flow rate was lowered to 0.2 SCF/H once the CO_2 concentration of the headspace reached the gas tank value, which then resulted in a sudden drop in headspace CO_2 early on in those experiments (Fig. 2a, b). The flow rate of CH1 was lowered ~ 44 hours into the experiment, which seems to have had minimal impacts on the headspace CO_2 and precipitates as solution pH was already fairly low. For all gas tank experiments CH7 and onward, the flow rate remained at 0.5 SCF/H throughout the entire experiment. The rate of CO_2 flow at 0.5 SCF/H for 200 ppm and 2000 ppm CO_2 -in- N_2 gas tanks corresponds to

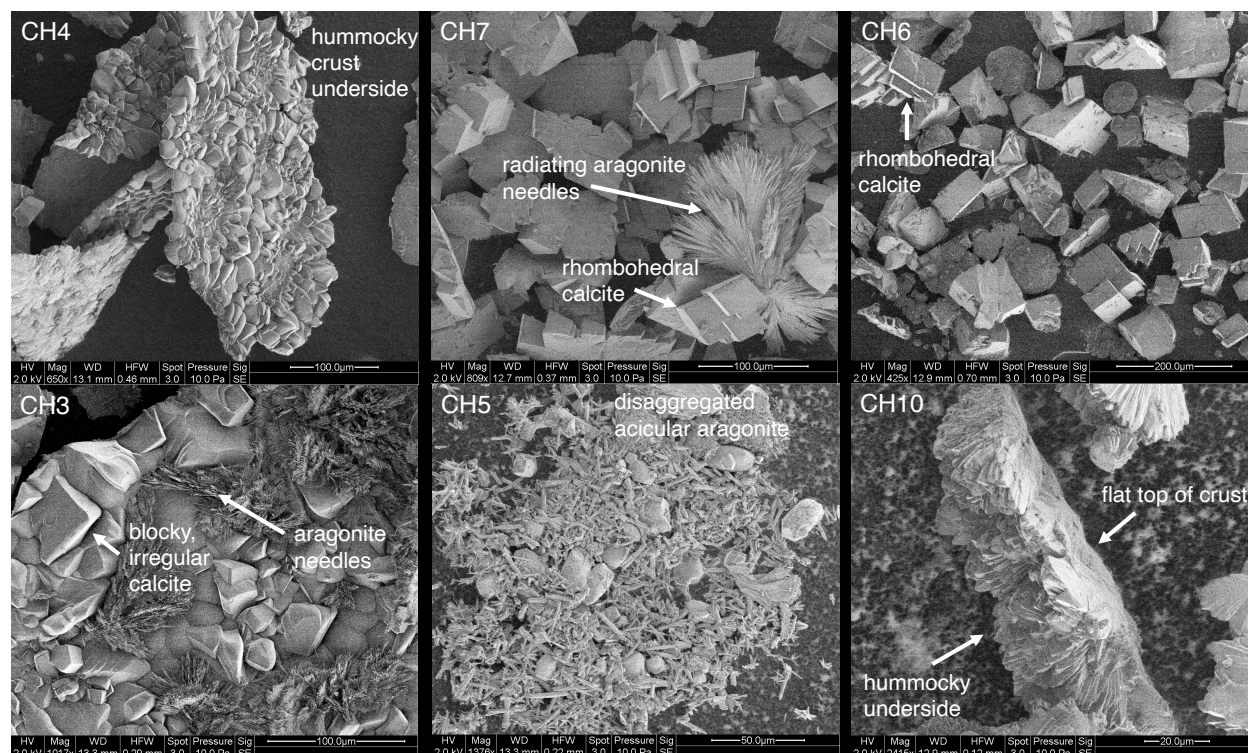


Figure 3: SEM images of CaCO_3 precipitates from several experiments. Some experiments produced flaky, cohesive carbonate crusts with a flat top and hummocky underside (CH3, CH4, CH10) while others resulted in less cohesive, disaggregated crystals (CH5, CH6, CH7). Calcite is present ranging from rhombohedral crystals with distinct crystal faces to blocky, irregular masses with poorly defined to absent crystal faces. Aragonite is present as radiating acicular clusters to disaggregated needles.

0.126 and 1.264 mmol CO_2 per hour.

Even without manually lowering the CO_2 flow rate, most early gas tank experiments did not reach their gas source CO_2 concentration until far into the experiment. CH1 is the only 200 ppm CO_2 experiment in which the headspace is approximately 200 ppm CO_2 for the experiment duration, while the other experiments conducted on that gas tank have headspace values that range from ~ 100 -150 ppm CO_2 (Figure 2a). We were concerned that the experimental headspace having a lower CO_2 concentration than the source gas meant that $\text{CO}_2(\text{g})$ distillation was occurring. We use the term CO_2 distillation to describe the chemical and isotopic evolution of the CO_2 reservoir that would occur when the rate of CO_2 uptake by the solution outpaces the replenishment of the gas to the headspace. During this gaseous CO_2 reservoir distillation, the concentration of CO_2 in the headspace would be less than that of the gas tank source. Its isotopic composition would also be affected, though minimally so, due to small KFFs attending CO_2 dissolution (Vogel et al., 1970; Zhang et al., 1995).

Experiments with higher starting pH (12-12.5) consistently had headspace CO_2 concentrations lower than their gas source, while CH1 (initial pH 11) did not, so to mitigate potential $\text{CO}_2(\text{g})$

reservoir distillation effects we carried out experiments with lower initial pH and tried to avoid solution pH dropping too low while still precipitating enough CaCO_3 for analysis. CH1 started with 10 mM Ca^{2+} rather than the 30 mM Ca^{2+} used in most of our other early experiments, so we began using 10 mM Ca^{2+} instead. This is still much more concentrated than that of most natural hyperalkaline springs, which have a $[\text{Ca}^{2+}] \sim 1\text{-}2$ mM (Christensen et al., 2021; Falk et al., 2016; Morrill et al., 2013).

While differences in experimental behavior or CaCO_3 crust traits were observed, our experiments do not show significant differences in the carbon and oxygen isotopic composition of carbonate precipitates due to differences in temperature, $[\text{Ca}^{2+}]$, or presence or absence of the NaOH/KCl control mixture. Solutions with 30 mM Ca^{2+} resulted in precipitation of an interlocking, more cohesive carbonate crust on the surface of the experimental solution, in contrast to the smaller precipitate yields of the 10 mM Ca^{2+} solutions. Precipitates also grew more slowly in 10°C solutions compared to 25°C solutions. CH24 and CH25 had the same starting pH ~ 12.3 , but CH25 (at 10°C) took much longer for pH to decrease due to CO_2 uptake and CaCO_3 precipitation than CH24 (at 25°C). Experiments CH2-CH10 consisted of a mixture of NaOH and KCl to maintain a high solution pH throughout. Initial solutions were 12 mM NaOH and 50 mM KCl, with slightly variable starting pH values from 11.9-12.8. Experiments CH1 and CH11-CH27 had 1 M NaOH added until reaching the pH of interest, with starting solutions ranging from 1-18 mM NaOH. The solution pH of experiments with the NaOH + KCl control mixture tended to record slightly slower decreases in pH over experiment duration. For example, CH3 and CH4 are characterized by a slower pH decrease than other 25°C, slowly stirred, 2000 ppm CO_2 experiments that did not contain KCl, such as CH12.

Stirring or not stirring an experiment affects the pH recorded with the probe, as well as the pH at the gas-solution interface. Not stirring an experiment causes the solution to become pH-stratified, with lower pH nearer to the air-water interface and higher pH deeper into the solution because both CO_2 dissolution and CaCO_3 precipitation reactions act to lower pH. We discovered this pH stratification in unstirred experiments when the pH as measured by the probe drops significantly when water samples are taken due to sufficient lowering of the water level so that the probe tip is now approaching the gas-solution interface. By not stirring, the pH-stratified solution has a lower surface pH, which may mean that there is a greater contribution from CO_2 hydration reactions than would be otherwise expected based on the higher solution pH values measured by the probe.

We experimented with variably stirring or not stirring a few of our early gas tank experiments, in addition to all small beaker experiments (0.13 L solution; CH14, CH15, CH18, CH19, CH21, CH23) being unstirred due to the necessary alterations of the experimental design not allowing for a magnetic stir bar. CH6 and CH7 were unstirred throughout the entire experiment, whereas CH5 was stirred only for the first half. Experiments at 25°C that were unstirred for their entire duration had a significantly lower pH boundary layer at the water surface in contrast to the higher pH that the probe was recording a couple centimeters below the water line. The unstirred 10°C experiment, however, had a surface pH much closer to that of where the probe was measuring (fully below the

air-water interface) when compared to the steep pH decreases recorded in 25°C solutions, which could be due to the observed slower CaCO₃ growth rate in the 10°C solutions.

In our high pH solutions, CO₃²⁻ is the dominant DIC species, with variable amounts of HCO₃⁻ and always negligible CO₂. At pH 11, ~10 % of the DIC is HCO₃⁻, whereas the HCO₃⁻ portion decreases to ~ 0.2% of the DIC pool at pH 12. CO₃²⁻ was >99% of the total DIC pool at the start of all experiments except CH1, CH11, CH20, CH21, and CH23, and it makes up >98% of the total DIC pool for the entire experiment duration for experiments CH2-CH10, CH12-CH14 and CH26-CH27.

Several experiments dropped into the pH range in which we predict CO₂ hydration would be contributing to HCO₃⁻ production. At 25°C and low ionic strength (I = 0.05), the contribution from CO₂ hydration is negligible at or above a solution pH of 10.5 (Bajnai & Herwartz, 2021; Devriendt et al., 2017).

3.2 Isotopic results

3.2.1 CO₂, DIC, and CaCO₃

This study includes experimental travertines grown from three isotopically distinct CO₂ gas sources (Figure 4 - pentagons). All 200 ppm CO₂ experiments were performed using a single gas tank, as well as for the 2000ppm CO₂ experiments, and their measured isotopic compositions are reported in Table 3. We assume the isotopic composition of the laboratory air to be the same as estimates of modern atmospheric CO₂ for our open-air experiments. One study of the isotopic composition of atmospheric CO₂ that spanned several years found that seasonal variability for both oxygen and carbon isotopes stayed within a range of a few permil, from -8.5 to -7.5‰ VPDB-CO₂ for δ¹³C and -2 to +1‰ VPDB-CO₂ for δ¹⁸O (Troler et al., 1996). Atmospheric CO₂ monitoring from NOAA agrees with those values (Global Monitoring Laboratory Data Viewer: <https://gml.noaa.gov/dv/iadv/>). For this study, we approximate the isotopic composition of modern atmospheric CO₂ and the laboratory air that contributed CO₂ for our open-air experiments to be δ¹³C = -8 ‰ VPDB-CO₂ and δ¹⁸O = -0.5‰ VPDB-CO₂. For carbon, there is no offset between the VPDB-CO₂ and VPDB scales, but for oxygen there is an approximately 10‰ offset and requires conversion using the equation (Srivastava and Verkouteren, 2018; Swart et al., 1991):

$$\delta^{18}\text{O}_{\text{VPDB-CO}_2} = (\delta^{18}\text{O}_{\text{VPDB}} - 10.25)/1.01025 \quad (7)$$

so the δ¹⁸O of modern atmospheric CO₂ is 9.75‰ VPDB.

Despite the δ¹⁸O of all our experimental solutions being tightly clustered at -10.8 ± 0.5 ‰ VSMOW (-40.5 ‰ VPDB), the drastically different isotopic compositions of the CO₂ sources results in each suite of CaCO₃ recording very different isotopic compositions (Figure 4). This supports the notion that these carbonates reflect extreme kinetic processes, and are quite far from isotopic equilibrium with the experimental solution, since equilibrium CaCO₃ would be expected to record δ¹⁸O ~ -11.6 ‰ VPDB according to the Coplen (2007) δ¹⁸O-T calibration at 25°C. Overall,

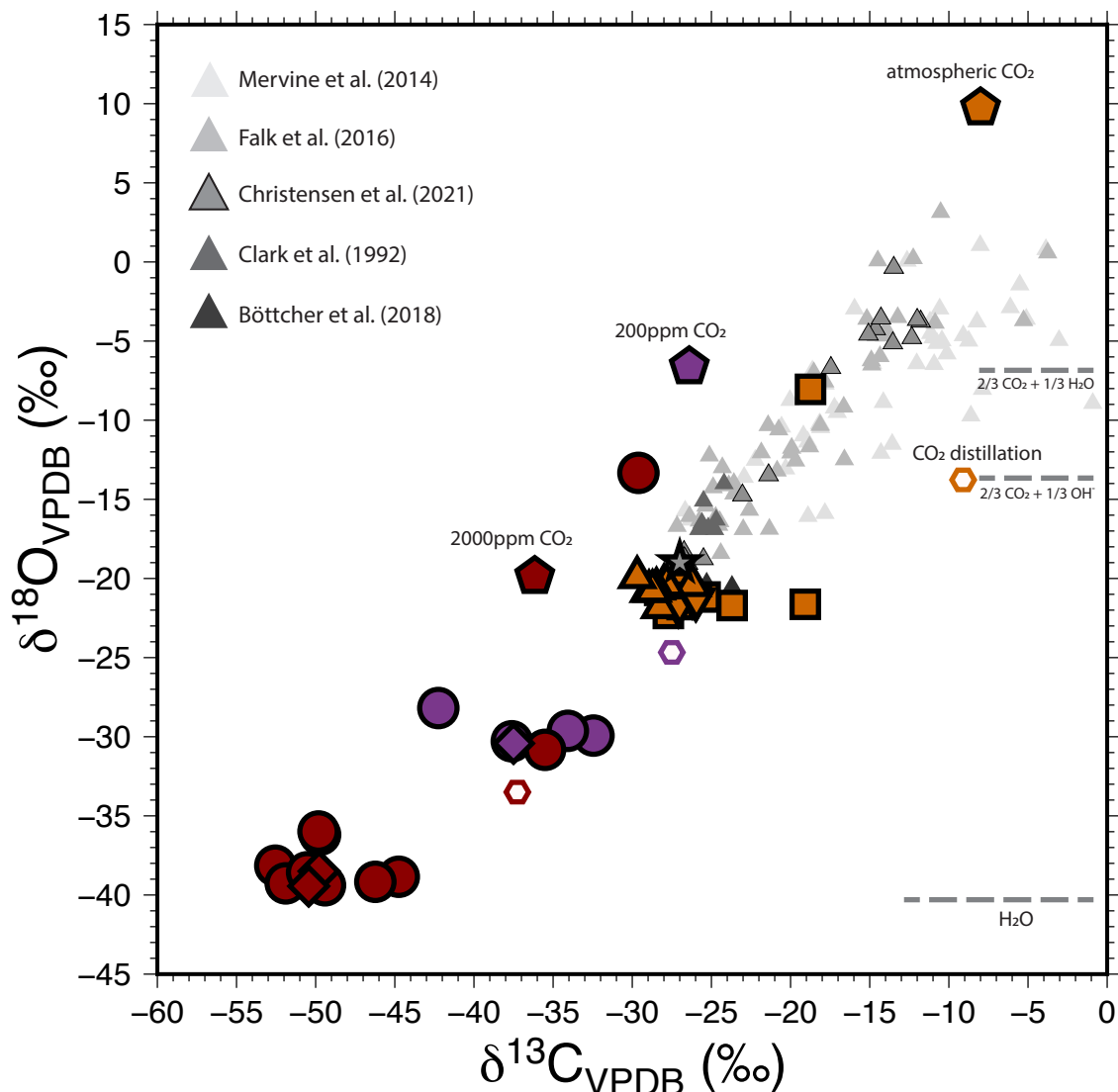


Figure 4: Isotopic compositions of precipitated carbonates and gas sources. The data are grouped by gas source, with the 200 ppm CO₂ experiments in purple, 2000 ppm CO₂ experiments in red, and open air experiments using the modern CO₂ atmosphere in orange. Pentagons are the gas sources, circles are 25°C gas tank experiments, diamonds are 10°C gas tank experiments, upright triangles are 25°C open air experiments, inverted triangles are 10°C experiments, and squares are open air experiment crystals from the bottom of the beaker. The isotopic outliers are CH21 and CH23 (red circles), and CH22 beaker crystals (orange square). The hexagons represent where the data would trend towards if experiencing CO₂ distillation. The gray triangles are the isotopic compositions of natural and experimental travertines, in order of increasingly dark shade of gray: Mervine et al. (2014), Falk et al. (2016), Christensen et al. (2021), Clark et al. (1992), and Böttcher et al. (2018), with the gray star representing the most highly fractionated travertine from The Cedars (Christensen et al., 2021).

Table 3: Isotopic data for all experiments

Experiment	$\delta^{13}\text{C}_{\text{CaCO}_3}$ (VPDB)	$\delta^{18}\text{O}_{\text{CaCO}_3}$ (VPDB)	$\delta^{13}\text{C}_{\text{CO}_2(\text{g})}$ (VPDB)	$\delta^{18}\text{O}_{\text{CO}_2(\text{g})}$ (VPDB)	$\delta^{18}\text{O}_{\text{w}}$ (VSMOW)	$\delta^{18}\text{O}_{\text{w}}$ (VPDB)
CH1	-42.24	-28.18	-26.40	-6.61	-11.29	-40.93
CH2	-32.44	-29.93	-26.40	-6.61	-11.28	-40.92
CH3	-44.75	-38.84	-36.16	-19.86	-11.19	-40.84
CH4	-46.23	-39.17	-36.16	-19.86	-11.00	-40.65
CH5	-34.07	-29.62	-26.40	-6.61	-10.48	-40.15
CH6	-49.78	-38.50	-36.16	-19.86	-10.74	-40.40
CH7	-50.47	-38.88	-36.16	-19.86	-10.62	-40.29
CH8	-50.44	-39.44	-36.16	-19.86	-10.52	-40.19
CH9	-37.61	-30.28	-26.40	-6.61	-10.65	-40.31
CH10	-37.50	-30.42	-26.40	-6.61	-10.80	-40.46
CH11	-52.55	-38.15	-36.16	-19.86	-11.26	-40.91
CH12	-49.41	-39.39	-36.16	-19.86	-11.19	-40.83
CH13	-26.21	-20.42	-8	9.75	-10.37	-40.04
CH13_b	-25.40	-21.17	-8	9.75	-10.37	-40.04
CH14	-51.89	-39.27	-36.16	-19.86	-10.82	-40.48
CH15	-50.54	-38.56	-36.16	-19.86	-10.55	-40.22
CH17	-28.24	-21.82	-8	9.75	-10.54	-40.21
CH17_b	-27.72	-22.21	-8	9.75	-10.54	-40.21
CH18	-49.72	-36.18	-36.16	-19.86	-10.95	-40.61
CH19	-49.82	-35.98	-36.16	-19.86	-10.91	-40.57
CH20	-27.99	-20.42	-8	9.75	-10.58	-40.24
CH20_b	-27.40	-20.53	-8	9.75	-10.58	-40.24
CH21	-29.61	-13.32	-36.16	-19.86	-10.48	-40.15
CH22_1	-27.84	-20.40	-8	9.75	-10.90	-40.56
CH22_2	-28.47	-20.64	-8	9.75	-10.11	-39.79
CH22_b	-18.74	-8.05	-8	9.75	-10.11	-39.79
CH23	-35.51	-30.82	-36.16	-19.86	-10.36	-40.03
CH24_1	-28.94	-20.80	-8	9.75	-10.66	-40.33
CH24_2	-28.72	-20.78	-8	9.75	-10.41	-40.08
CH24_3	-29.69	-19.92	-8	9.75	-9.73	-39.42
CH24_b	-28.27	-20.75	-8	9.75	-9.73	-39.42
CH25_1	-26.20	-21.20	-8	9.75	-10.79	-40.45
CH25_2	-27.08	-21.75	-8	9.75	-10.80	-40.46
CH25_3	-28.19	-20.94	-8	9.75	-10.74	-40.41
CH25_b	-26.85	-21.65	-8	9.75	-10.74	-40.41
CH26	-25.99	-21.38	-8	9.75	-10.88	-40.54
CH26_b	-19.07	-21.63	-8	9.75	-10.88	-40.54
CH27	-25.94	-21.31	-8	9.75	-10.99	-40.65
CH27_b	-23.69	-21.71	-8	9.75	-10.99	-40.65

there is a relatively consistent offset in $\delta^{18}\text{O}$ between $\text{CO}_2(\text{g})$ and CaCO_3 for all gas compositions, whereas we observe up to 10‰ variability in $\delta^{13}\text{C}$ of CaCO_3 for a given $\delta^{13}\text{C}$ of CO_2 gas.

We plotted the isotopic compositions of natural (Clark et al., 1992; Mervine et al., 2014; Falk et al., 2016; Christensen et al., 2021) and experimental (Böttcher et al., 2018) travertines from past studies on Figure 4 (gray triangles). The natural travertines record a wide array of co-varying $\delta^{13}\text{C}$ and $\delta^{18}\text{O}$ compositions. Our open-air experiments overlap with the most isotopically depleted natural travertines. This suggests that human exhalation in the laboratory space had minimal

impact on the isotopic composition of the overall CO₂ reservoir from which our carbonates grew because the isotopic composition of human CO₂ exhalation is distinctively isotopically lighter ($\delta^{13}\text{C}$: -18.7 to -23.5‰ VPDB, $\delta^{18}\text{O}$: 2.8 to 5.9‰ VPDB; Epstein & Zeiri, 1988) than atmospheric CO₂. We conclude that our laboratory-air CaCO₃ precipitates may be directly compared to natural hyperalkaline spring travertines and also may reflect the kinetic fractionation factors attending CO₂ hydroxylation, as both natural and laboratory travertines precipitated in this manner have been interpreted to reflect (Böttcher et al., 2018; Christensen et al., 2021; Clark et al., 1992).

The hexagons on Figure 4, color coded by gas source, represent where the CaCO₃ isotopic compositions would trend towards if experiencing gaseous CO₂ distillation, which notably, our CaCO₃ does not seem to be trending toward for any of the gas sources. For carbon, the trend would go to the $\delta^{13}\text{C}$ of CO₂(aq) in equilibrium with the CO₂ gas source. For oxygen, the trend would go towards the sum of 2/3 CO₂(aq) + 1/3 OH⁻. The CaCO₃ isotopic compositions would be expected to trend towards the isotopic compositions of its constituent reservoirs because there is no net isotopic fractionation during quantitative conversion, which would occur in the most extreme case of CO₂ distillation where all CO₂(g) is converted to CO₂(aq) and subsequently CaCO₃. For these calculations, equilibrium fractionations of CO₂(g)-CO₂(aq) of -1.1‰ (Vogel et al., 1970) and +0.3‰ (Barkan and Luz, 2012; Beck et al., 2005) for carbon and oxygen, respectively, were used, as well as the OH-H₂O equilibrium fractionation of -21.5‰ (Zeebe, 2020).

In the majority of our experiments, the $\delta^{13}\text{C}$ of the CaCO₃ is isotopically lighter than that of the DIC in the solutions from which they precipitated. This is unexpected, because CaCO₃ is typically isotopically heavier than the DIC it grew from (Sade et al., 2020). With the exception of isotopic outliers described in the following section (CH21, CH23), the 2000 ppm CO₂ experiments consistently produce DIC $\delta^{13}\text{C}$ isotopically heavier (from around 1 - 10+ ‰) than its CaCO₃ (Figure 5B). The 200 ppm CO₂ and open air experiments, however, seem to mostly straddle the 1:1 line where $\delta^{13}\text{C}_{\text{CaCO}_3} \approx \delta^{13}\text{C}_{\text{DIC}}$. The 25°C open air experiments result in CaCO₃ that is slightly isotopically lighter than the DIC, while the 10°C open air experiments produce CaCO₃ that is slightly isotopically heavier (Figure 5C).

When most of the CO₃²⁻ is converted to CaCO₃, then the CaCO₃ records the KFF and the remaining CO₃²⁻ is pushed to lighter values, while conversely, when only a small fraction of the CO₃²⁻ is converted to CaCO₃ then the KFF is recorded in the EIC and the CaCO₃ is heavier (Christensen et al., 2021). However, this offset is expected to be small based on the proposed KFF of +0.5‰ where CaCO₃ is just slightly isotopically heavier than the CO₃²⁻ it grew from (Sade et al., 2020).

3.2.2 Outliers

There are several clear isotopic outliers (Figure 4), as well as experiments in which solution pH dropped low enough that there is reason to expect that processes other than unidirectional CO₂ hydroxylation (e.g. CO₂ hydration, DIC equilibration) may be contributing to the isotopic signature of the CaCO₃ minerals.

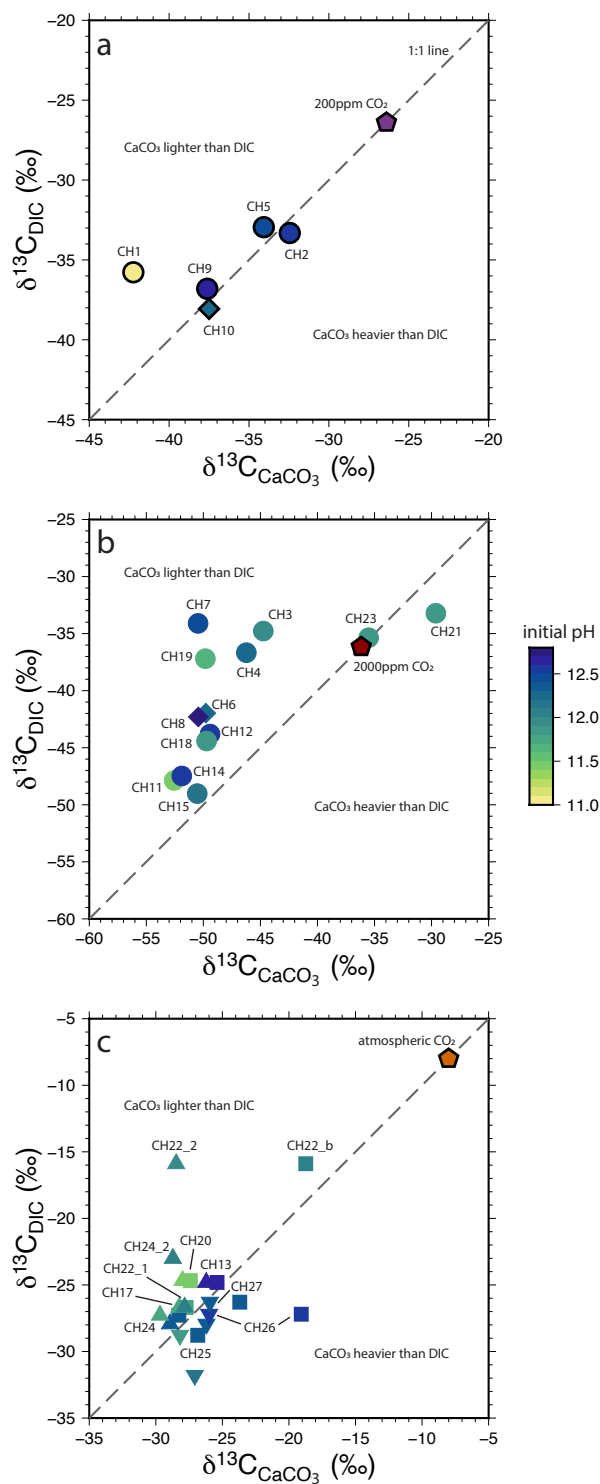


Figure 5: The $\delta^{13}\text{C}$ of CaCO_3 and $\delta^{13}\text{C}$ of DIC in the solutions in which the CaCO_3 precipitated. (A) Experiments on the 200 ppm CO₂ tank ($\delta^{13}\text{C} = -26.40\text{‰}$ VPDB), (B) experiments on the 2000 ppm CO₂ gas tank ($\delta^{13}\text{C} = -36.16\text{‰}$ VPDB), and (C) open air experiments using atmospheric CO₂ ($\delta^{13}\text{C} = -8\text{‰}$ VPDB).

CaCO₃ from CH21 and CH23 (red circles), and CH22 and CH26 beaker crystals (orange squares) record unusual isotopic fractionations relative to our other experiments (Figure 4). CH23 is depleted from its reservoirs with respect to oxygen but very slightly enriched with respect to carbon. CH21 is the only experiment that records enrichments in both of the heavy isotopes relative to its reservoirs. Both CH21 and CH23 are unstirred, resulting in a pH-stratified solution with a lower pH surface. The final pH values near the surface are 9.25 and 10.1 respectively, which are low enough that there might be some contribution from CO₂ hydration. However, CH18 and CH19 are also unstirred experiments that have a lower surface pH of 9.0 and 8.7, respectively, and precipitates from those experiments have similar isotopic compositions as the earlier 2000 ppm CO₂ experiments, with a slight caveat that the oxygen isotope compositions of CH18 and CH19 are noticeably isotopically heavier by about 2‰ compared to earlier 2000 ppm CO₂ experiments. CH18, CH19, CH21, and CH23 are the last four experiments conducted on the 2000ppm CO₂ gas tank, which had in total 13 experiments conducted on it. This suggests that something regarding the gas tank source itself might be confounding interpretation of the CaCO₃ isotopic compositions, such as that the isotopic composition of the tank might be changing substantially as it gets emptier, or at least that the gas delivered to the experiment headspace might be getting fractionated as the tank approaches empty.

The “beaker crystals” are the tiny crystals that grew at the bottom of the experimental beakers, which we analyzed for each of our open air experiments. These crystals were adhered to the beaker, in contrast to sunken surface floes, which did not adhere to the beaker surface. CH22 beaker crystals (CH22_b) record a depletion in ¹³C that is not as extreme as similar experiments, and an enrichment in ¹⁸O relative to its reservoirs, possibly reflecting partial equilibration of the DIC. CH22_b plots on an array between the most extremely fractionated precipitates and the isotopic composition of the atmospheric CO₂ gas source, among CaCO₃ from natural hyperalkaline springs (Figure 4). CH26 beaker crystals record the same ¹³C depletion as CH22_b, but notably the δ¹⁸O matches that of the rest of the open air experiments.

Some of the experiments with lower initial starting pH (closer to pH 11-11.5 - CH1, CH11) record smaller oxygen fractionations, which may reflect partial equilibration of the DIC, and/or small contributions from CO₂ hydration rather than only CO₂ hydroxylation.

3.2.3 CaCO₃ precipitated via CO₂ hydroxylation

Since this study includes experimental travertines grown from three isotopically distinct CO₂ gas sources (Figure 4 - pentagons), we therefore must compare calculated isotopic fractionations between phases rather than the standalone isotopic values of the CaCO₃ in order to make meaningful comparisons across all of our experiments. We effectively removed any existing DIC from our experimental solutions prior to the start of each experiment by bubbling pure N₂ gas for > 1.5 hours, so we may conclude that the carbon atoms in CaCO₃ come from one source: the dissolved CO₂. For oxygen, we calculate a weighted sum because dissolved CO₂ contributes two oxygen atoms and OH⁻ contributes one oxygen atom to CaCO₃ that precipitates as a result of CO₂ hydroxylation:

$$\delta^{18}\text{O}_{\text{CO}_2(\text{aq})+\text{OH}^-} = \frac{2}{3} \cdot \delta^{18}\text{O}_{\text{CO}_2(\text{aq})} + \frac{1}{3} \cdot \delta^{18}\text{O}_{\text{OH}^-} \quad (8)$$

However, due to uncertainty in the OH^- - H_2O oxygen isotope fractionation factor (Bajnai & Herwartz, 2021; Green & Taube, 1963; Zeebe, 2020), we also present our fractionations using H_2O rather than OH^- :

$$\delta^{18}\text{O}_{\text{CO}_2(\text{aq})+\text{H}_2\text{O}} = \frac{2}{3} \cdot \delta^{18}\text{O}_{\text{CO}_2(\text{aq})} + \frac{1}{3} \cdot \delta^{18}\text{O}_{\text{H}_2\text{O}}, \quad (9)$$

since $\delta^{18}\text{O}$ of our experimental H_2O is a measured value. Quantifying kinetic isotope fractionations for oxygen from $\text{CO}_2(\text{aq})+\text{OH}^-$ or $\text{CO}_2(\text{aq})+\text{H}_2\text{O}$ both constitute a “bulk oxygen” fractionation because at this point we are unable to quantify the fractionations independently for oxygen on $\text{CO}_2(\text{aq})$ and OH^- . We present isotopic fractionations as epsilon (ϵ) values (Table 4, Figure 6), where:

$$\epsilon_{\text{A/B}} = (\alpha_{\text{A/B}} - 1) \cdot 1000 \quad (10)$$

and the fractionation between phases A and B (α) is equal to:

$$\alpha_{\text{A/B}} = \frac{\delta^{18}\text{O}_{\text{A}} + 1000}{\delta^{18}\text{O}_{\text{B}} + 1000}. \quad (11)$$

From the isotopic fractionations between CaCO_3 and $\text{CO}_2(\text{aq})$ for carbon and $\text{CO}_2(\text{aq})+\text{H}_2\text{O}$ for oxygen (Figure 6), we found that in experiments with CO_2 from a gas tank:

1. The carbon and oxygen isotope fractionations are smaller than at The Cedars.
2. The carbon isotope variability is much larger than the oxygen isotope variability.
3. The slope of the $\delta^{13}\text{C}$ - $\delta^{18}\text{O}$ relationship is lower than what would be expected from isotopic distillation of $\text{CO}_{2(\text{g})}$.
4. In open-air experiments, the $\delta^{13}\text{C}$ of carbonates is lower than in gas tank experiments. Hence, the possibility of variable amounts of air getting into the apparatus cannot explain the variability and trend towards heavier $\delta^{13}\text{C}$ in gas tank experiments.

These observations led us to postulate that the hydroxylation KFF on oxygen isotopes may be near unity whereas the KFF for carbon isotopes is large. If so, the carbon isotope composition of $\text{CO}_{2(\text{aq})}$ would get isotopically distilled during conversion to HCO_3^- , leading to heavy compositions in $\delta^{13}\text{C}$ with little to no effect on the $\delta^{18}\text{O}$ of $\text{CO}_{2(\text{aq})}$. Such a scenario would imply that CO_2 exchange at the air-water interface is not replenishing the $\text{CO}_{2(\text{aq})}$ fast enough to keep it at the equilibrium concentration or equilibrium isotopic composition relative to the $\text{CO}_{2(\text{g})}$ in the headspace.

In the model described below, we test this hypothesis and show that the $\delta^{13}\text{C}$ - $\delta^{18}\text{O}$ variations can be used to separate the two oxygen isotope KFFs acting on the reactants $\text{CO}_{2(\text{aq})}$ and OH^- .

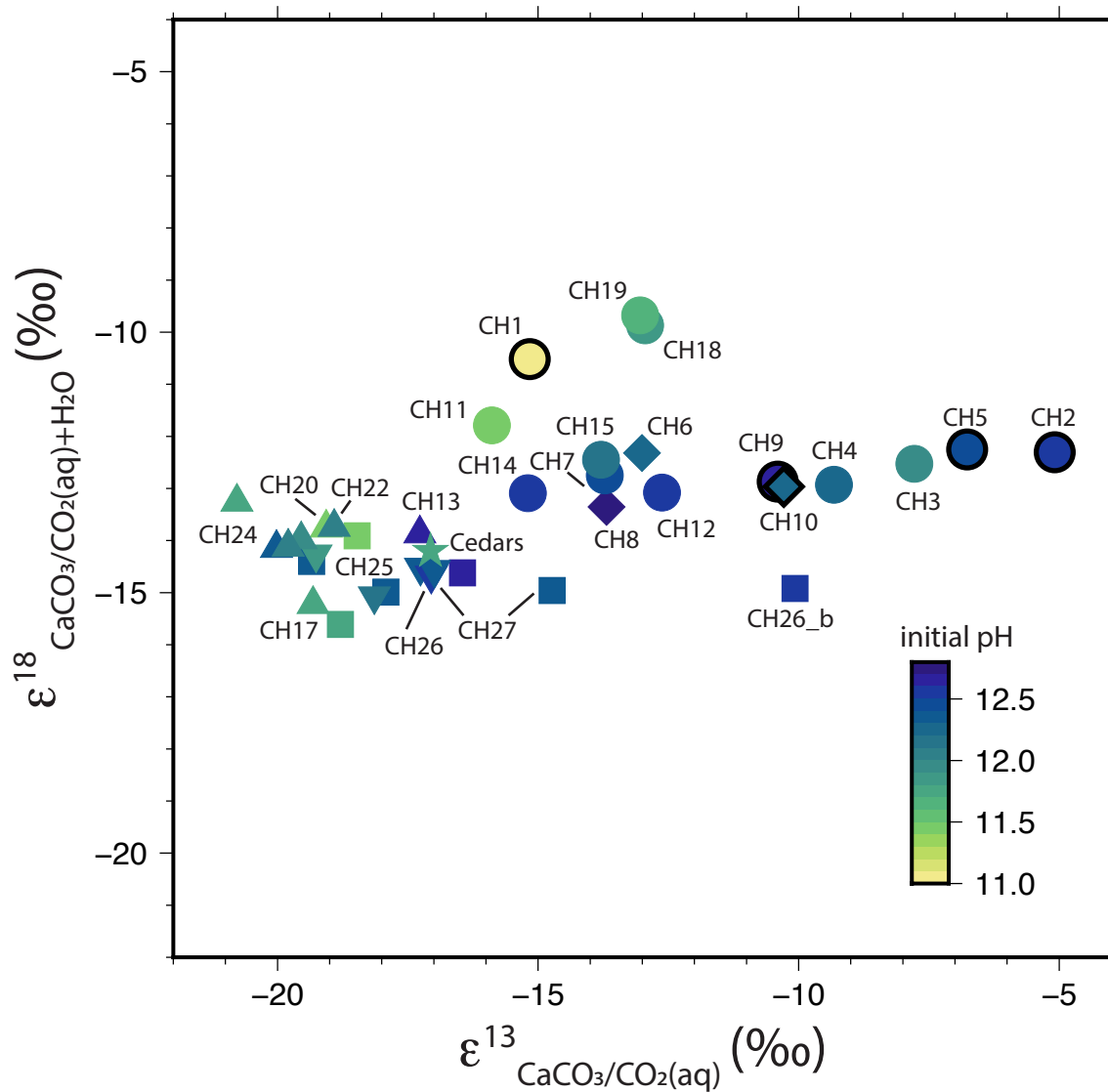


Figure 6: Carbon and bulk oxygen kinetic isotope fractionations (KIFs) for all experiments of this study, calculated as $\epsilon = (\alpha - 1) \cdot 1000$. Gas tank experiments (25°C - circles; 10°C - diamonds) on 200 ppm CO₂ (black outline) or 2000 ppm CO₂ (no outline). Open air experiments (25°C - upright triangles; 10°C - inverted triangles) with crystals from the bottom of those beakers (squares). The star represents the KIFs determined from The Cedars, California (Christensen et al., 2021).

Table 4: Carbon and bulk oxygen kinetic isotope fractionations

Experiment	^{13}C	^{18}O	^{18}O
	$\epsilon_{\text{CaCO}_3-\text{CO}_2\text{aq}}$	$\epsilon_{\text{CaCO}_3-(\text{CO}_2\text{aq}+\text{OH})}$	$\epsilon_{\text{CaCO}_3-(\text{CO}_2\text{aq}+\text{H}_2\text{O})}$
CH1	-15.16	-3.46	-10.52
CH2	-5.09	-5.26	-12.30
CH3	-7.78	-5.42	-12.53
CH4	-9.32	-5.83	-12.93
CH5	-6.76	-5.21	-12.25
CH6	-13.01	-5.22	-12.32
CH7	-13.72	-5.65	-12.75
CH8	-13.69	-6.26	-13.36
CH9	-10.40	-5.83	-12.87
CH10	-10.28	-5.93	-12.96
CH11	-15.88	-4.68	-11.79
CH12	-12.62	-5.99	-13.08
CH13	-17.27	-6.92	-13.87
CH13_b	-16.45	-7.67	-14.62
CH14	-15.19	-5.99	-13.09
CH15	-13.79	-5.35	-12.45
CH17	-19.32	-8.28	-15.22
CH17_b	-18.79	-8.67	-15.61
CH18	-12.94	-2.75	-9.87
CH19	-13.04	-2.55	-9.68
CH20	-19.07	-6.84	-13.79
CH20_b	-18.47	-6.96	-13.91
CH21	7.94	20.75	13.46
CH22.1	-18.91	-6.72	-13.68
CH22.2	-19.55	-7.22	-14.17
CH22_b	-9.73	5.54	-1.49
CH23	1.82	2.60	-4.56
CH24.1	-20.02	-7.21	-14.16
CH24.2	-19.80	-7.27	-14.21
CH24.3	-20.78	-6.62	-13.57
CH24_b	-19.34	-7.45	-14.40
CH25.1	-17.26	-7.57	-14.52
CH25.2	-18.14	-8.13	-15.07
CH25.3	-19.26	-7.32	-14.26
CH25_b	-17.92	-8.04	-14.99
CH26	-17.05	-7.73	-14.67
CH26_b	-10.07	-7.98	-14.92
CH27	-16.99	-7.61	-14.56
CH27_b	-14.73	-8.02	-14.96

4 Box model approach

We are going to get an expression for the steady state concentration and isotopic composition of $\text{CO}_2(\text{aq})$ that depends on (a) the KFFs attending hydroxylation and (b) the forward and backward exchange rate at the air-water interface (Fig. 7). Parameters for the model are listed in Table 5.

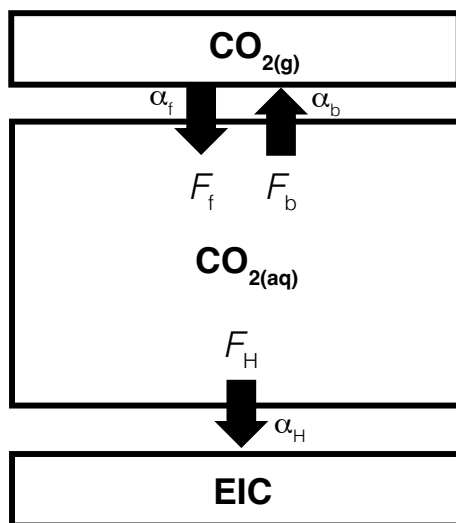


Figure 7: Schematic denoting the carbon reservoirs in our box model, and the fluxes and fractionations between them. The flux between gaseous and aqueous CO_2 is bidirectional, whereas we assume no back-reaction between EIC and aqueous CO_2 .

Table 5: Model parameters

Parameter	Value	Reference/Note
F_f	$\geq F_H$	CO_2 dissolution flux: $\text{CO}_2(\text{g}) \rightarrow \text{CO}_2(\text{aq})$
F_b	$F_f - F_H$	CO_2 degassing flux: $\text{CO}_2(\text{g}) \leftarrow \text{CO}_2(\text{aq})$
F_H	$k_{+4}[\text{CO}_2][\text{OH}^-]$	CO_2 hydroxylation flux: $\text{CO}_2(\text{aq}) + \text{OH}^- \rightarrow \text{HCO}_3^-$
k_p	2000	Isotope results not sensitive to this
k_{+4}	$10^{(13.635 - \frac{2895}{T_K})}$	Pinsent et al. (1956); Uchikawa and Zeebe (2012)
$^{18}\alpha_{\text{eq}}$	1.0003	$\text{CO}_2(\text{g})$ is lighter than $\text{CO}_2(\text{aq})$
$^{18}\alpha_f$	1.000	Results not sensitive to this
$^{18}\alpha_b$	$^{18}\alpha_f / ^{18}\alpha_{\text{eq}}$	Equilibrium constraint
$^{18}\alpha_H$	variable	Depends on the KFF assigned to OH^-
$^{13}\alpha_{\text{eq}}$	0.9989	$\text{CO}_2(\text{g})$ is heavier than $\text{CO}_2(\text{aq})$
$^{13}\alpha_f$	1.000	Results not sensitive to this
$^{13}\alpha_b$	$^{13}\alpha_f / ^{13}\alpha_{\text{eq}}$	Equilibrium constraint
$^{13}\alpha_H$	0.9814	Christensen et al. (2021)

4.1 Model assumptions

- $\text{CO}_2(\text{g})$ does not get isotopically distilled. Although there is evidence of $\text{CO}_2(\text{g})$ depletion in the headspace of many experiments, the influence on the isotopic composition of residual $\text{CO}_2(\text{g})$ should be negligible because the $^{13}\text{C}/^{12}\text{C}$ and $^{18}\text{O}/^{16}\text{O}$ isotopic fractionations attending the $\text{CO}_2(\text{g}) \rightarrow \text{CO}_2(\text{aq})$ reaction are small (Vogel et al., 1970; Zhang et al., 1995).
- The dehydroxylation reaction is negligible, implying that HCO_3^- is isotopically fractionated from $\text{CO}_2(\text{aq})$ by the forward hydroxylation reaction only. This is convenient because it means we can calculate the isotopic composition of EIC directly from that of $\text{CO}_2(\text{aq})$.

3. The $\text{CO}_2(\text{aq})$ is a well-mixed reservoir. This is a necessary simplification that ignores the chemical stratification of the fluid near the air-water interface.

4.2 Concentrations

At steady state, the influxes must balance the outfluxes:

$$\underbrace{F_f - F_b}_{\text{net flux in}} = F_H, \quad (12)$$

where F_f is the CO_2 dissolution flux, F_b is the CO_2 degassing flux, and F_H is the CO_2 hydroxylation flux. The value of F_H is known as a function of pH and [DIC]. The values of F_f and F_b are not known, but since F_b cannot be negative, F_f must be greater than or equal to F_H . Hence, we treat F_f as an adjustable parameter from which the value of F_b can be calculated. The hydroxylation flux is given by:

$$F_H = k_{+4}[\text{CO}_2][\text{OH}^-], \quad (13)$$

Following Olsen et al. (2022), the net influx can be written as:

$$F_f - F_b = k_p ([\text{CO}_2]_{\text{eq}} - [\text{CO}_2]), \quad (14)$$

where k_p is akin to a ‘piston velocity’ that describes the efficiency of CO_2 exchange across the air-water interface. From Eqs. 12, 13, and 14, the steady state CO_2 concentration is given by:

$$[\text{CO}_2]_{\text{ss}} = \frac{k_p[\text{CO}_2]_{\text{eq}}}{k_{+4}[\text{OH}^-] + k_p}. \quad (15)$$

For isotopes, it doesn’t really matter what value we use for k_p , but as you might expect, as k_p increases, $[\text{CO}_2]_{\text{ss}} \rightarrow [\text{CO}_2]_{\text{eq}}$.

4.3 Isotopes

The formula for a changing oxygen isotope ratio (R_{CO_2}) with time is:

$$N_{16} \frac{dR_{\text{CO}_2}}{dt} = \frac{dN_{18}}{dt} - R_{\text{CO}_2} \frac{dN_{16}}{dt}, \quad (16)$$

which comes from taking the time derivative of the expression for the ratio, $R_{\text{CO}_2} = ({}^{18}\text{O}/{}^{16}\text{O})_{\text{CO}_2}$. The number of moles of ${}^{16}\text{O}$ in CO_2 (N_{16}) changes with time according to the equation:

$$\frac{dN_{16}}{dt} = F_f - F_b - F_H. \quad (17)$$

The number of moles of ^{18}O in CO_2 (N_{18}) changes with time according to the equation

$$\frac{dN_{18}}{dt} = R_g \alpha_f F_f - R_{\text{CO}_2} \alpha_b F_b - R_{\text{CO}_2} \alpha_H F_H, \quad (18)$$

where the fluxes refer to ^{16}O but are multiplied by the isotope ratio to get the relevant ^{18}O fluxes. Combining Eqs. 17 and 18 with 16 leads to:

$$N_{16} \frac{dR_{\text{CO}_2}}{dt} = F_f (R_g \alpha_f - R_{\text{CO}_2}) - F_b (R_{\text{CO}_2} \alpha_b - R_{\text{CO}_2}) - F_H (R_{\text{CO}_2} \alpha_H - R_{\text{CO}_2}). \quad (19)$$

At steady state, we have:

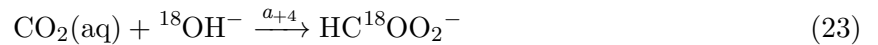
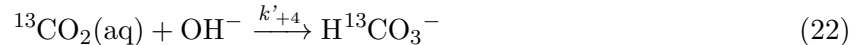
$$F_f (R_g \alpha_f - R_{\text{CO}_2}) = F_b (R_{\text{CO}_2} \alpha_b - R_{\text{CO}_2}) + F_H (R_{\text{CO}_2} \alpha_H - R_{\text{CO}_2}), \quad (20)$$

which leads to an equation for R_{CO_2} :

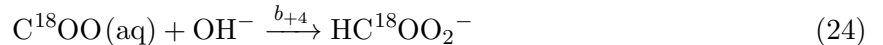
$$R_{\text{CO}_2} = \frac{F_f R_g \alpha_f}{F_f + F_b (\alpha_b - 1) + F_H (\alpha_H - 1)}. \quad (21)$$

The box model tracks how the kinetic isotope effects (KIEs) recorded in the EIC change as the rate of CO_2 dissolution (F_f) shifts relative to a fixed CO_2 hydroxylation rate (F_H) (Figure 8). At $\log_{10}(F_f/F_H) = 0$, $F_f = F_H$ and all dissolved CO_2 undergoes hydroxylation, no longer preserving the isotopic depletion from unidirectional CO_2 hydroxylation in the EIC, and therefore the CaCO_3 . At $\log_{10}(F_f/F_H) = 2$, $F_f \gg F_H$, meaning the rate of CO_2 dissolution far outpaces the rate of CO_2 hydroxylation so there is no isotopic distillation of $\text{CO}_2(\text{aq})$, so the EIC and therefore CaCO_3 are expected to record large isotopic depletions due to CO_2 hydroxylation, up to the full KFFs. Distillation of $\text{CO}_2(\text{aq})$ has a larger effect on carbon KIEs than oxygen (Fig. 8), which is consistent with the large range in $^{13}\epsilon_{\text{EIC}/\text{CO}_2}$ and relatively small range in $^{18}\epsilon_{\text{EIC}/\text{CO}_2}$ observed in many of our small headspace experiments (Figure 6).

Keeping with the assumption that there is negligible back-reaction, we consider the following hydroxylation reactions that are occurring simultaneously but at different reaction rates:



and



in addition to Eq. 2 (k_{+4}), which involves only light carbon and oxygen isotopes. The same KFF for ^{13}C is used for all model curves (k'_{+4}). We test out different KFF values for oxygen between $\text{HCO}_3^- - \text{CO}_2$ (b_{+4}/k_{+4}), with corresponding shifts to $\text{HCO}_3^- - \text{OH}^-$ (a_{+4}/k_{+4}) (Table 6) to maintain the overall bulk oxygen KFF, to see if we can recreate the slope of $^{18}\epsilon_{\text{CaCO}_3/\text{CO}_2 + \text{H}_2\text{O}}/^{13}\epsilon_{\text{CaCO}_3/\text{CO}_2}$ observed in the experiments that experienced $\text{CO}_2(\text{aq})$ distillation (Figure 9). The CO_2 gas tank

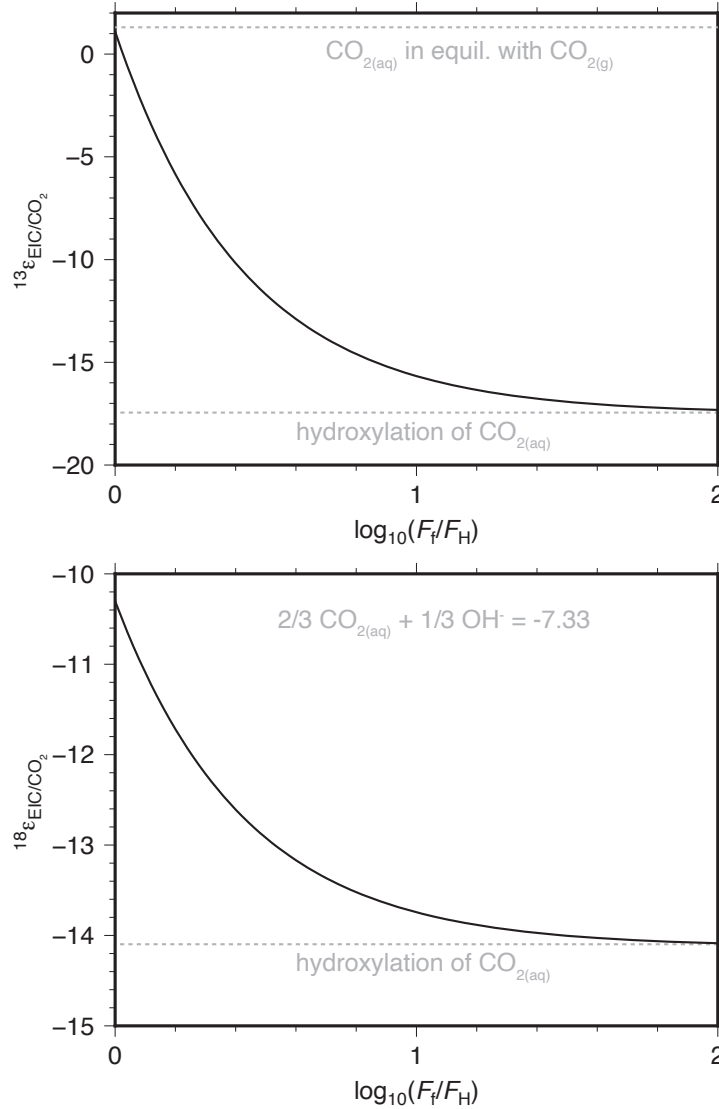


Figure 8: Model outputs showing how the KIEs change with increasing F_f relative to a fixed hydroxylation flux F_H . At $\log_{10}(F_f/F_H) = 0$, $F_f = F_H$ so all dissolved CO_2 undergoes hydroxylation. When $F_f \gg F_H$, there is no distillation of the $\text{CO}_2(\text{aq})$ reservoir.

experiments seem to fall along the model curve of $b_{+4}/k_{+4} = 0.996$ and $a_{+4}/k_{+4} = 0.986$, which corresponds to KFFs of -4% for $\text{HCO}_3^- - \text{CO}_2$ and -14% for $\text{HCO}_3^- - \text{OH}^-$.

4.4 Comparison to previous work

There is one study in the literature that is relevant to the present discussion. Clark et al. (1992) carried out an experiment where they connected five beakers in series to a $\text{CO}_2\text{-N}_2$ tank with known isotopic composition. Each beaker contained a BaCl_2 solution that was brought to high pH (12.8) by addition of NaOH . Between each beaker there was a sampling port that enabled them to measure the CO_2 partial pressure and its isotopic composition. Their results show that the $\text{CO}_2(\text{g})$ gets

Table 6: Model curves varying KFFs for CO₂ hydroxylation with ¹⁸O on CO₂ (b_{+4}) and OH⁻ (a_{+4})

b_{+4}/k_{+4}	a_{+4}/k_{+4}
0.992	0.994
0.994	0.990
0.996	0.986
0.998	0.982
1	0.978

distilled to heavier isotopic compositions as it exchanges with CO₂(aq) in the fluid (Fig. 10; Clark et al., 1992, Table 3). Since the CO₂(g)-CO₂(aq) isotope effects are relatively small, the results can be used to get an estimate of the hydroxylation KFFs (Fig. 10). Clark et al. (1992) modeled their data using a simple Rayleigh model equation:

$$\frac{R_r}{R_o} = f^{(\alpha-1)}, \quad (25)$$

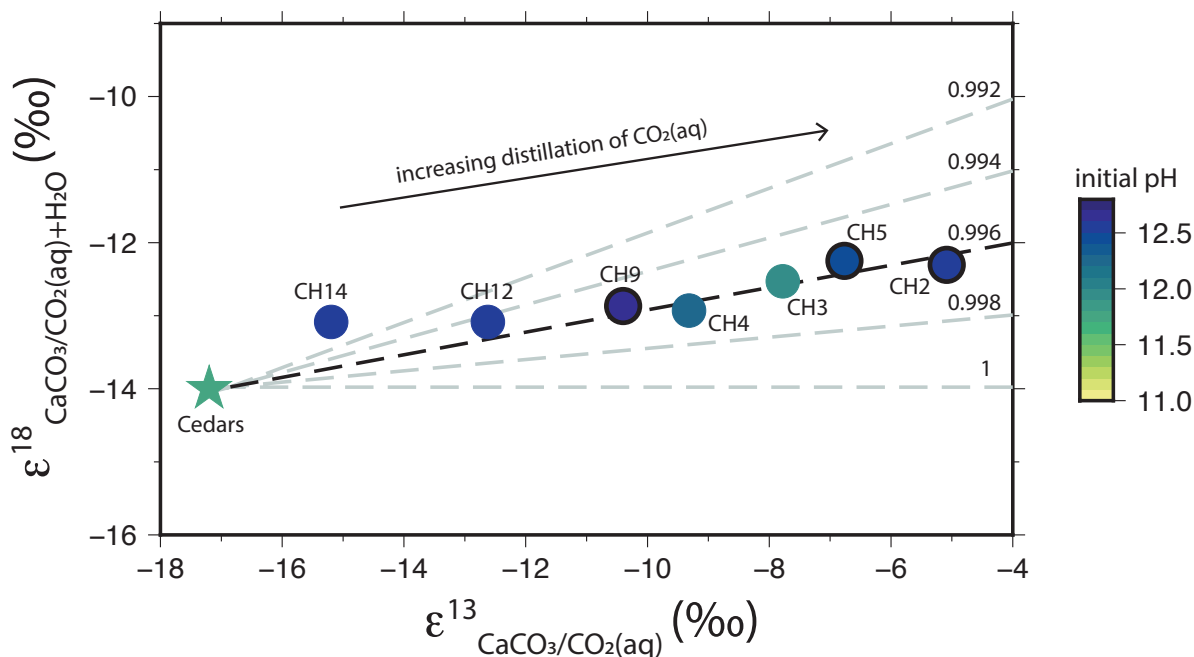


Figure 9: Box model results of $\epsilon_{\text{EIC}/\text{CO}_2+\text{H}_2\text{O}}^{18}/\epsilon_{\text{EIC}/\text{CO}_2}^{13}$ slopes using different KFF values for ¹⁸O on CO₂, and correspondingly on OH⁻, during CO₂ hydroxylation with increasing degrees of CO₂(aq) distillation. Numerical line labels correspond to HCO₃⁻-CO₂ KFFs in Table 6. We plot our 25°C gas tank experiments during which solution pH always remained higher than pH = 10.5, and find the slope of the experiments suggests there is a -4‰ KFF for oxygen on HCO₃⁻-CO₂ (black dashed line).

where R_r is the isotopic ratio of the residual CO_2 , R_o is the initial isotopic ratio of CO_2 , f is the fraction of CO_2 remaining, and α is the net fractionation factor. The results, presented as a set of curves in Figure 10, suggest a carbon KFF of $\epsilon \approx -17\text{‰}$, which is consistent with what we obtained in our experiments. Applying the same model to the oxygen isotope results indicates $\epsilon \approx -2\text{‰}$, which is somewhat lower than the value we obtained above (Fig. 9), but supports the overall conclusion that the hydroxylation KFF on $\text{CO}_2(\text{aq})$ is much smaller for oxygen isotopes than for carbon isotopes (Fig. 10).

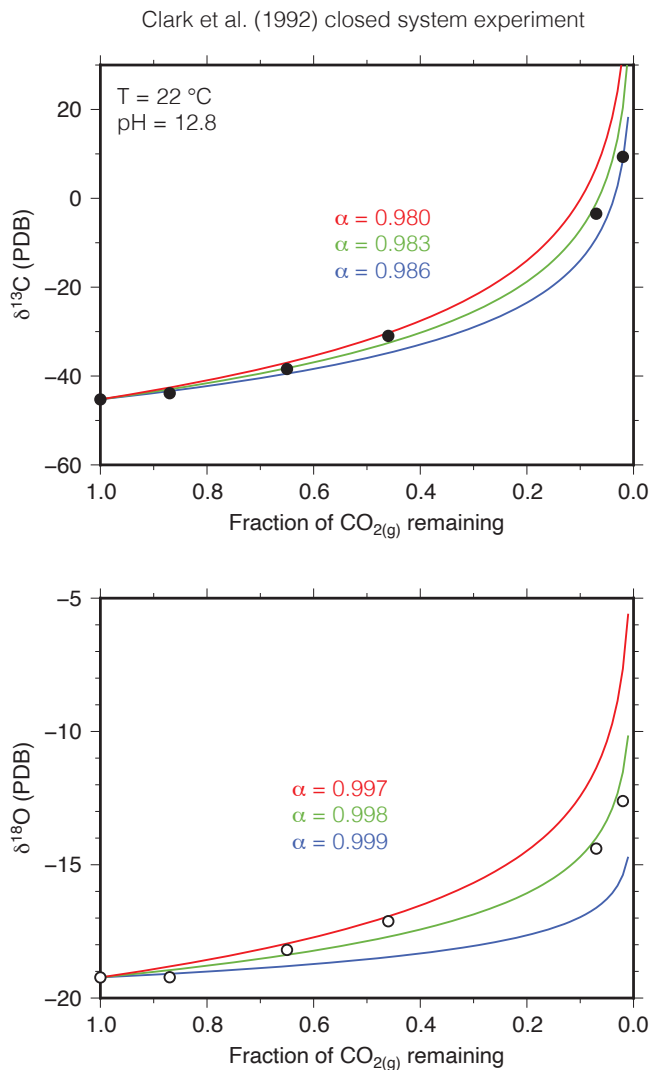


Figure 10: Results from Clark et al. (1992) showing isotopic distillation of headspace CO_2 during hydroxylation. The effects are much larger for $\delta^{13}\text{C}$ than for $\delta^{18}\text{O}$, consistent with a small KIE on CO_2 as it undergoes hydroxylation to form HCO_3^- . Results suggest a carbon KFF of about -17‰ and an oxygen KFF of about 2‰ . These are approximate because (a) there is large uncertainty in f for the rightmost data points, (b) the Rayleigh calculations assume a single fractionation factor even though there are multiple steps involved, and (c) it's not really a closed system experiment because gas was continually flowing through five beakers connected in series.

5 CO₂ hydroxylation KFFs

The largest isotopic fractionations from this study were observed in our open-air experiments, which appear to recreate the extreme isotopic fractionations recorded in natural travertines such as the Cedars. Our largest carbon and oxygen fractionations are not from the same experimental CaCO₃. CH24 records the largest carbon fractionation of $\epsilon_{\text{CaCO}_3-\text{CO}_2(\text{aq})} = -20.8$ ‰, while the largest oxygen fractionation is recorded in CH17 as $\epsilon_{\text{CaCO}_3-(\text{CO}_2(\text{aq})+\text{OH}^-)} = -8.3$ ‰, or $\epsilon_{\text{CaCO}_3-(\text{CO}_2(\text{aq})+\text{H}_2\text{O})} = -15.2$ ‰ (Table 4). However, these values are highly sensitive to our selection of the $\delta^{13}\text{C}$ and $\delta^{18}\text{O}$ of atmospheric CO₂, which has been shown to have both regional and seasonal variability (Trolier et al., 1996), in addition to the complication that our laboratory air likely has a slightly different isotopic composition than atmospheric CO₂ anyways.

We add our open-air experiment data to the CO₂ hydroxylation KFF vs. temperature literature compilation from Christensen et al. (2021, 2023), presented in Table 7 and Figure 11. The carbon KFFs do not show a clear overall temperature dependence, while the bulk oxygen KFFs do, with larger kinetic fractionations occurring at lower temperature (Fig. 11).

Of note, the isotopic compositions of our experimental CaCO₃ support $1000\ln\alpha_{\text{OH}^--\text{H}_2\text{O}} = -21.5$ ‰ of Zeebe (2020) rather than the larger $1000\ln\alpha_{\text{OH}^--\text{H}_2\text{O}} = -42.53$ ‰ determined by Bajnai and Herwartz (2021), because if ~ -42.53 ‰ is used, then the bulk oxygen isotopic fractionations ($\epsilon_{\text{CaCO}_3-(\text{CO}_2(\text{aq})+\text{OH}^-)}$) of the overwhelming majority of experiments would be positive rather than negative.

5.1 Complications and possible causes of variability

Here we briefly list some confounding factors and possible causes of variability in this study:

- Variable contribution of CO₂ hydration in some experiments where the solution pH dropped

Table 7: Literature compilation¹ of KFFs during CO₂ hydroxylation

Study	Temp (°C)	¹³ C/ ¹² C KFF from CO ₂ (aq)	¹⁸ O/ ¹⁶ O KFF from CO ₂ (aq)+OH ⁻	¹⁸ O/ ¹⁶ O KFF from CO ₂ (aq)+H ₂ O	pH
Usdowski and Hoefs 1986	18	-17	-	-	10
Clark et al. 1992	22	-13.9	-8.5	-15	11.5
Clark et al., 1992	22	-16.3	-7.9	-14.5	12.8
Dietzel et al., 2009	5	-	-10	-16.8	10.5
Böttcher et al., 2018	4	-11.8	-9.7	-16.6	12.4
Böttcher et al., 2018	21	-15.8	-8.4	-14.9	12.4
Clark et al., 1992	28	-17	-6.5	-13	11.5
Clark et al., 1992	28	-16.9	-7.2	-13.6	11.5
Mervine et al., 2014	28	-17	-6.4	-12.9	11.0
Falk et al., 2016	27	-17.2	-6.9	-13.4	11.7
Christensen et al., 2021	17	-17.1	-7.3	-14	11.0
This study	10	-17.74	-7.67	-14.62	12.26
This study	25	-19.34	-7.14	-14.08	12.0

¹ Data from Christensen et al. (2021, 2023) Table 7.

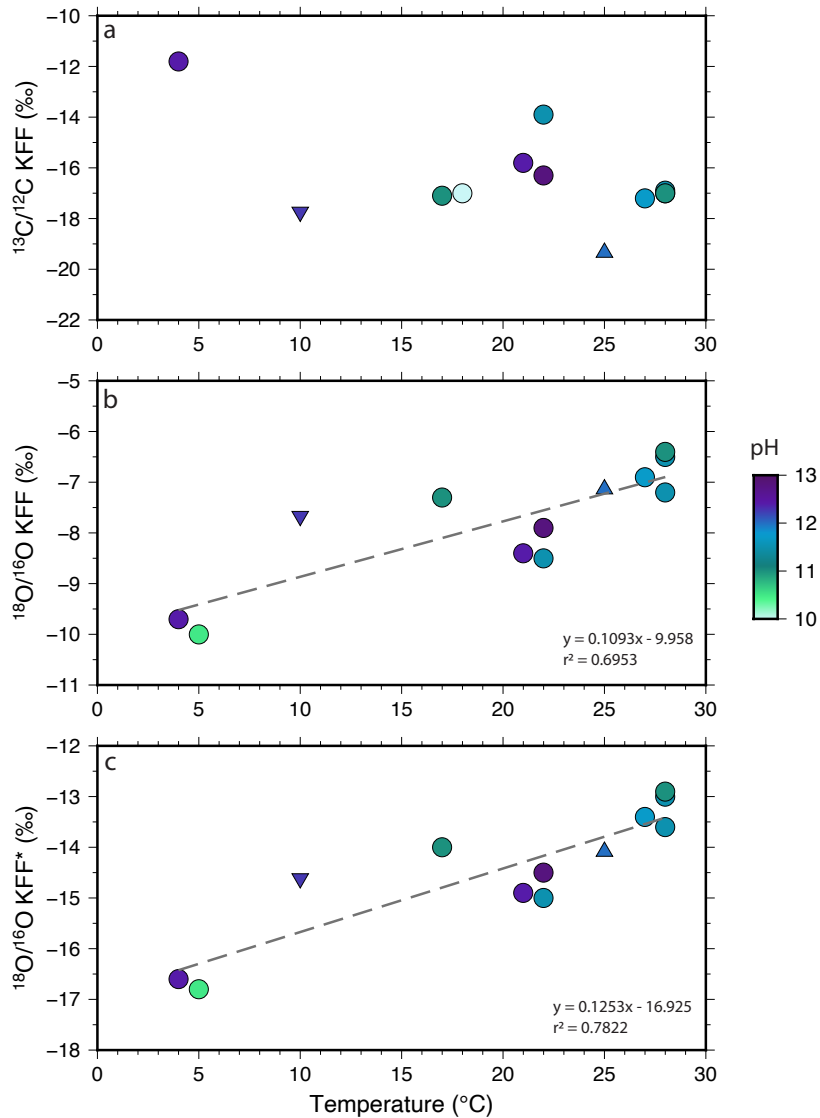


Figure 11: Carbon and bulk oxygen KFFs vs. temperature, plotting the average KFFs from our open-air experiments (10°C - inverted triangle, 25°C - upright triangle) with data from past studies (circles) (Table 7, from Christensen et al., 2021, 2023, Table 7). $^{18}\text{O}/^{16}\text{O}$ KFF is expressed from $\text{CO}_2(\text{aq})+\text{OH}^-$, while $^{18}\text{O}/^{16}\text{O}$ KFF* is expressed from $\text{CO}_2(\text{aq})+\text{H}_2\text{O}$. The bulk oxygen KFF shows a significant temperature-dependence, while the carbon KFF does not.

below pH 10.5, which is difficult to quantify because we do not know the KFFs for CO_2 hydration for each reactant independently

- It is unclear why the $\text{CO}_2(\text{aq})$ is not being replenished efficiently during gas tank experiments but is being replenished fine during our open air experiments, despite many of the gas tank experiments being conducted at higher CO_2 concentrations
- The gas tank experiments could be affected by the humidity of the experimental headspace,

as opposed to the open air experiments which are not enclosed

- There might be isotopic fractionation occurring during transfer of the CO₂-in-N₂ gas from the gas tank to the experimental headspace, so that the measured gas tank value is not an accurate reflection of the actual CO₂ reaching the experimental solution
- The last few experiments conducted on the 2000 ppm CO₂ gas tank resulted in abnormal CaCO₃ isotopic values, which could be due to the isotopic composition of the gas tank evolving as it becomes progressively emptier, or that the gas tank is isotopically stratified
- Our modeled curves on Figure 9 represent EIC not CaCO₃
- In every experiment we were able to obtain DIC analyses, which suggests that the DIC is not quantitatively precipitated and there should be some offset between our modeled EIC curves and precipitated CaCO₃
- We precipitated multiple CaCO₃ polymorphs in our experiments (as occurs at natural hyperalkaline springs), but having both calcite and aragonite present in variable proportions might obscure some of the quantitative results if the polymorphs have different fractionations attending their precipitation reactions
- At the beginning of very high pH experiments (>12), we observed a surface sheen not present for solutions at lower starting pH, and hypothesize this might be an amorphous calcium carbonate (ACC) precursor, which may affect the isotopic composition of the analyzed CaCO₃ in ways that are not fully understood

6 Summary

In summary:

1. We performed open air and small headspace experiments that successfully reproduce the natural process of high pH travertine formation, including mineralogy, morphology, and isotopic composition.
2. The largest isotopic fractionations occurred during our open air experiments, which mimic the most isotopically depleted natural travertines. We used these experiments to determine the carbon and bulk oxygen kinetic fractionation factors (KFFs) attending CO₂ hydroxylation.
3. Smaller and more variable fractionations occurred in small headspace experiments. We used these experiments to separate, for the first time, the KFFs for CO₂-HCO₃⁻ and OH⁻-HCO₃⁻ based on a box model of CO₂(aq) distillation during hydroxylation.
4. We compared our results to Clark et al. (1992) and found them to be broadly consistent.

5. We add our KFFs to those of past studies and present equations for the temperature dependence of the bulk oxygen KFFs.

CO₂ sequestration in the form of stable carbonate minerals is a promising avenue through which significant quantities of CO₂ may be removed from the atmosphere. Studies of carbon capture and storage assess carbonation rates in-situ within lithologic units that have high carbonation potential (e.g. ultramafic to mafic ophiolite bodies, Kelemen and Matter, 2008) and ex-situ in industrial settings (Kelly et al., 2011; Kemache et al., 2016), and weight those against the costs, required energy, space, materials, and waste generated. Understanding and quantifying the isotopic evolution of CO₂ gas injected for sequestration is being developed as a technique to assess the degree of success of the CO₂ capture processes (Flude et al., 2017). In a similar vein, understanding and quantifying the isotopic composition of the product CaCO₃ may be able to give a comparable evaluation since its isotopic composition reflects the CO₂ hydroxylation KFFs at low uptake fractions, trending towards that of the initial injected CO₂ at high levels of reservoir distillation.

CHAPTER VI

SUMMARY

This dissertation explores how non-equilibrium isotopic partitioning between calcium carbonate minerals and water is affected by environmental parameters through a combination of experiments and modeling. Equilibrium oxygen isotope fractionation between calcite and water exhibits a strong temperature dependence, and as a result is used in paleoclimate and paleoenvironment reconstructions to estimate the water temperatures of caves, lakes, surface oceans, and hydrothermal systems in which the calcite grew. Commonly, however, isotopic equilibrium is not achieved and the carbonate minerals record kinetic isotope effects (KIEs) that may depend on growth rate, source(s) of DIC, pH and solution composition.

Non-equilibrium isotopic fractionation may be characterized by small departures from equilibrium, or, in contrast, reflect the kinetic fractionation factors (KFFs). I investigate the effect of ionic strength and pH on isotopic partitioning in calcite under relatively near-isotopic equilibrium growth conditions characterized by reasonably small KIEs in Chapters III and IV, respectively. Experiments from Chapter IV and low ionic strength (up to $[\text{NaCl}] = 0.35 \text{ M}$) experiments from Chapter III result in calcite grown from an isotopically equilibrated DIC pool, so that KIEs recorded in the CaCO_3 may be attributed to processes occurring at the mineral surface during mass-dependent attachment and detachment of ions. We ensure isotopic equilibration of the DIC pool by utilizing sufficient concentrations of the enzyme carbonic anhydrase (bCA). Due to salt inhibition of bCA, calcite from experiments of Chapter III precipitated in solutions of higher ionic strength ($[\text{NaCl}] \geq 0.52 \text{ M}$) grew from a not fully isotopically equilibrated DIC pool, so resulting KIEs are due to a combination of DIC- H_2O and DIC- CaCO_3 disequilibrium. Experiments from Chapter V are characterized by a DIC pool that is far-from-isotopically equilibrated, as our experimental conditions promote unidirectional CO_2 hydroxylation with negligible back-reaction, thus hindering isotopic exchange between DIC- H_2O .

In Chapter II, I provide background information regarding the chemical reactions and isotopic fractionations of the CaCO_3 -DIC- H_2O system, factors affecting isotopic partitioning in carbonates, and an overview of several proxies based on trace element uptake and/or isotopic partitioning and their corresponding paleoenvironment applications. This chapter outlines core concepts of the stable isotope systematics of calcite which may prove beneficial to understanding the experimental and modeling studies of the subsequent chapters.

In Chapter III, I investigated the effect of ionic strength on the isotopic composition of inorganic calcite, finding no significant effect on CaCO_3 -DIC fractionation, but a significant inhibition of the

enzyme carbonic anhydrase (bCA) by NaCl. This enzyme inhibition prevented isotopic equilibration of the DIC pool above $[\text{NaCl}] = 0.35 \text{ M}$, and as a result lower and more variable $1000\ln\alpha_{c/w}$. This finding is important because biocalcifiers use carbonic anhydrase during their calcification processes, and while the composition of the calcifying fluid is poorly constrained and likely species-dependent, the inhibition of bCA may be applied to biochemical models to help understand vital effects in biogenic calcite.

In Chapter IV, I performed inorganic calcite experiments designed to isolate the effect of solution pH and subsequently $\text{HCO}_3^-/\text{CO}_3^{2-}$ ratio of solution on the resulting calcite isotopic composition, finding a decrease in $1000\ln\alpha_{c/w}$ with increasing pH consistent with past studies. Using my experimental data, I then updated the ion-by-ion model of calcite growth, which is a generalizable model with a wide range of applications to natural and experimental carbonates. This study helps to further constrain DIC- CaCO_3 isotopic fractionations, which in turn gives insight into separating vital effects from mass-dependent kinetic fractionations in biogenic CaCO_3 .

In Chapter V, I investigate far-from-isotopic equilibrium carbonate growth proceeding via near unidirectional CO_2 hydroxylation and characterized by large KIEs and probing the KFFs attending CO_2 hydroxylation. These experiments simulate the direct air capture of CO_2 via CO_2 hydroxylation and subsequent travertine formation at hyperalkaline springs, which are characterized by large isotopic depletions in both carbon and oxygen. Our open-air experiments mimic the isotopic compositions of the most depleted natural travertines, likely reflecting the KFFs attending CO_2 hydroxylation. The small headspace experiments resulted in overall smaller isotopic fractionations, as well as more variable carbon isotopic fractionations, leading us to model the effect of $\text{CO}_2(\text{aq})$ distillation on the isotopic composition of the EIC (Equilibrated Inorganic Carbon). Modeling $\epsilon_{\text{EIC}/\text{CO}_2}^{13}$ and $\epsilon_{\text{EIC}/\text{CO}_2+\text{H}_2\text{O}}^{18}$ over increasing degrees of $\text{CO}_2(\text{aq})$ distillation using different oxygen KFF values for $\text{HCO}_3^- - \text{CO}_2$, we found the slope of our experiments suggests oxygen KFFs of -4% for $\text{HCO}_3^- - \text{CO}_2$ and -14% for $\text{HCO}_3^- - \text{OH}^-$. This is the first experimental study to report separate oxygen KFFs attending CO_2 hydroxylation, which is a valuable contribution to the CaCO_3 -DIC- H_2O stable isotope systematics and may aid in the development of isotopic paleoproxies for carbonates precipitated in this geologic setting.

APPENDIX A

CHAPTER III SUPPLEMENTARY MATERIAL

Supplementary material of Olsen, E.K., Watkins, J.M., and Devriendt, L.S. (2022). Oxygen isotopes of calcite precipitated at high ionic strength: CaCO₃-DIC fractionation and carbonic anhydrase inhibition. *Geochimica et Cosmochimica Acta* **325**, 170-186.

1 DIC speciation

Although DIC speciation is primarily a function of pH, factors such as temperature, pressure, and solution composition are also important. DIC speciation is well known for seawater solutions (Millero et al., 2006), but our solutions (CaCl₂ + NH₄Cl + NaCl) are substantially simpler in composition. The stoichiometric equilibrium constants (pK) have been determined for similar NaCl solutions (Millero et al., 2007), and while this may provide an accurate description of DIC speciation in our system, the stoichiometric solubility product (K_{sp}) for simple NaCl solutions is unknown. Hence, even with an accurate description of solution speciation, it is not straightforward to relate speciation to the degree of supersaturation with respect to calcite in non-seawater solutions. Consequently, we chose to use PHREEQC to model our solution speciation and degree of supersaturation in a self-consistent way using the Pitzer ionic activity database and our exact solution compositions as inputs (Charlton and Parkhurst, 2011; De Lucia and Kühn, 2013).

Differences in speciation between seawater solutions and NaCl solutions are shown in Fig. S1.1 for three different [NaCl] (0, 0.52, 1.37 M). For both seawater and NaCl solutions, increasing salinity shifts pK1 and pK2 to lower pH so that at a fixed pH of 8.3 the [CO₃²⁻] increases while [HCO₃⁻] and [CO₂] decrease. Increasing salinity has a greater effect on pK2 than on pK1 for both solution types. Overall DIC speciation differs between seawater and NaCl solutions, as increasing salinity in seawater dramatically shifts speciation so that CO₃²⁻ becomes the dominant DIC species at approximately 1 M NaCl (salinity ~75 g/kg) at a pH of 8.3 (Fig. S1.1b). Speciation shifts in NaCl solutions are more moderate, with CO₃²⁻ increasing from 1.8% of total DIC in freshwater solutions to 6.7% of total DIC in highly saline solutions. It is important to note that the PHREEQC speciation for our solution closely matches the DIC speciation based on pure NaCl solutions (Fig S1.1e, Millero et al., 2007).

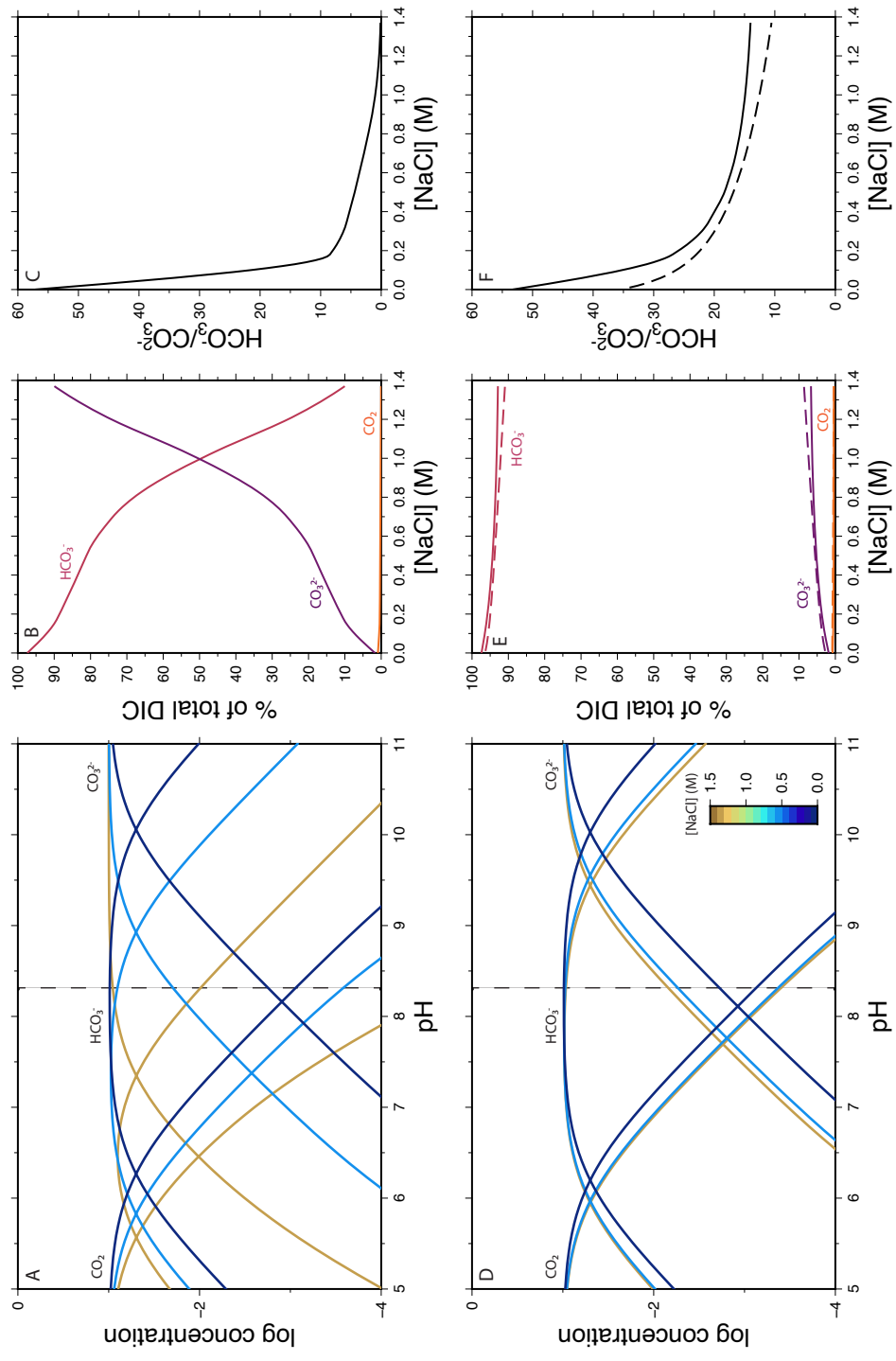


Figure 1: Solution speciation in seawater solutions (a-c; Millero et al., 2006) versus NaCl solutions (d-f; solid lines: Millero et al., 2007; dashed lines: PHREEQC, R-package Pitzer database) at 25°C. [NaCl] 0, 0.52, and 1.37 M span the range of this study (a, d). Proportion of each DIC species and $\text{HCO}_3^-/\text{CO}_3^{2-}$ for solutions at pH 8.3 (b-c, e-f).

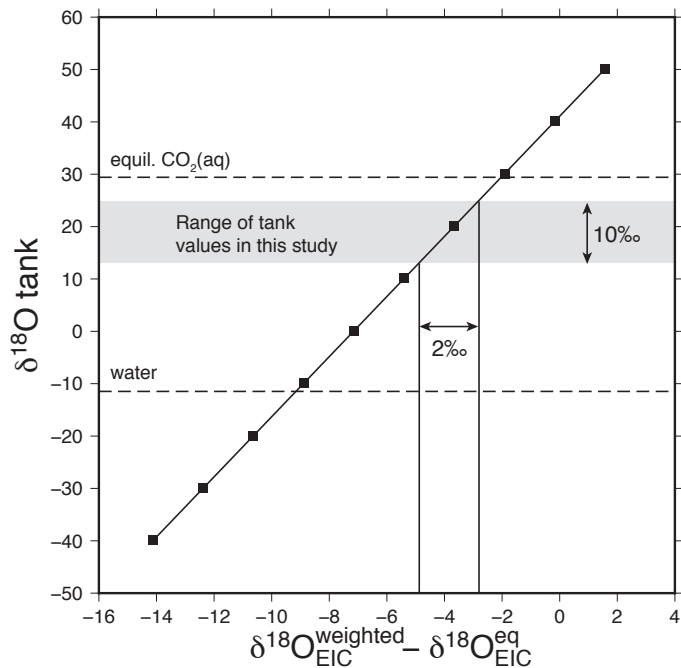


Figure 2: Modeled sensitivity of the steady state EIC composition to the $\delta^{18}\text{O}$ of CO_2 gas.

2 Sensitivity of the kinetic isotope effects to the $\delta^{18}\text{O}$ of CO_2 gas

To assess the sensitivity of $1000\ln\alpha_{c/w}$ to the isotopic composition of gas used, we simulated the uncatalyzed case ($[\text{bCA}] = 0$) for different $\delta^{18}\text{O}$ values of input CO_2 . The results shown in Fig. S2.1 reveal a simple linear relationship between the $\delta^{18}\text{O}$ of CO_2 and $\delta^{18}\text{O}$ of EIC at steady state (all other parameters fixed) and show that a large 10‰ shift in the $\delta^{18}\text{O}$ of CO_2 translates to a much smaller 2‰ shift in the $\delta^{18}\text{O}$ of EIC (and calcite). This is attributed to the hydration reaction being bi-directional ($R_b/R_f \sim 0.8$; Fig. 5g of Chapter II). The sensitivity of $1000\ln\alpha_{c/w}$ to $\delta^{18}\text{O}$ of CO_2 decreases as more bCA is added, because bCA pushes R_b/R_f closer to unity.

3 Research data

Table 1: Additional parameters and isotopic data for experiments of this study

Experiment	Salinity (g/kg)	Molality	I^a	Time (total) (h)	Time (precip) (h)	$\delta^{13}\text{C}_{\text{CaCO}_3}$ (VPDB)	$1000\text{ln}\alpha_{\text{CaCO}_3-\text{DIC}}$ (VPDB)	Ω_{peak}^a	Ω_{ss}^a
S2	35	0.5542	0.633	51.9	28.4	-44.00	-0.16	5.59	4.20
S3	35	0.5542	0.633	44.3	27.9	-45.56	-0.42	8.46	4.02
S4	15	0.2134	0.274	62.4	42.9	-46.26	-0.97	5.86	2.38
S5	25	0.3843	0.452	41.6	23.3	-45.08	-0.47	7.78	2.52
S6 ^b	3.5	-	-	72.8	52.6	-46.06	-	-	-
S7	15	0.2132	0.274	47.7	29.4	-45.29	-0.40	6.85	3.61
S8	3.5	0.0365	0.094	52.2	34.2	-45.37	-0.59	8.46	3.34
S9	25	0.3854	0.453	47.6	32.0	-45.22	-0.40	8.01	3.71
S10	45	0.7275	0.820	66.0	40.7	-45.28	-0.13	8.09	3.70
S11	25	0.3852	0.452	66.9	34.8	-44.32	0.31	10.89	3.68
S12	85	1.4121	1.603	45.9	27.7	-24.00	0.61	7.52	4.09
S13	65	1.0692	1.203	93.2	64.2	-25.13	-0.02	5.14	2.22
S14	55	0.8992	1.010	52.4	36.6	-24.25	-0.33	7.24	2.99
S15	75	1.2414	1.401	61.3	37.5	-23.35	0.41	8.66	5.34
CA1	35	0.5566	0.634	65.2	37.6	-23.78	0.06	8.34	3.48
CA2	35	0.5565	0.634	48.5	33.9	-23.79	-0.05	7.76	3.93
CA3	35	0.5566	0.634	47.5	34.5	-24.29	-0.19	5.66	2.73
CA4	3.5	0.0368	0.094	30.6	21.5	-25.44	-0.54	7.19	3.77
CA5	35	0.5565	0.634	62.2	37.5	-22.86	0.62	8.74	2.79
CA6	35	0.5570	0.634	61.2	40.5	-22.38	0.55	8.12	3.55
CA7	20	0.2999	0.363	61.5	37.1	-21.59	0.61	10.65	3.89
CA9	60	0.9847	1.106	60.3	43.3	-43.55	0.41	8.55	3.62
CA12	45	0.7280	0.820	66.9	51.0	-43.52	-0.38	7.49	2.46
CA13	65	1.0697	1.203	66.0	41.0	-43.35	0.09	7.06	2.25
CA14	15	0.2143	0.274	50.2	36.1	-43.24	-0.44	5.23	2.54
CA15	25	0.3856	0.453	52.0	37.5	-42.59	0.05	6.33	2.64
CA18	3.5	0.0387	0.095	42.7	35.5	-17.67	-0.30	9.03	5.11
CA20	3.5	0.0376	0.094	46.8	40.3	-34.77	-1.27	7.80	3.82

^a Ionic strength (I), Ω_{peak} , and Ω_{ss} were calculated using the PHREEQC R-package Pitzer database. Ω_{peak} represents the highest degree of supersaturation during an experiment, which occurs at the onset of calcite precipitation. Ω_{ss} represents the average degree of supersaturation for an experiment during the “steady state” calcite growth period.

^b S6 lacks DIC measurements

Table 2: Experiment measurements

Experiment	Time (h)	TA (mEq/L)	[DIC] (mM)	$\delta^{13}\text{C}_{\text{DIC}}$ (VPDB)	$\delta^{18}\text{O}_w$ (VSMOW)	pCO ₂ (ppm)
S2	0.00	-	0.07	-35.52	-	206
-	7.40	0.65	0.36	-43.65	-	141
-	22.65	0.92	0.45	-43.49	-	192
-	26.40	0.73	0.32	-43.16	-11.65	170
-	31.97	0.68	0.38	-43.61	-	148
-	44.98	0.65	0.32	-44.52	-	140
-	51.45	0.65	0.33	-44.64	-	142
S3	3.05	0.54	0.24	-44.45	-	70
-	16.65	0.94	0.68	-44.93	-	129
-	21.78	0.73	0.48	-44.78	-	102
-	26.78	0.70	0.40	-45.13	-	97
-	40.47	0.62	0.27	-45.86	-	92
-	43.97	0.69	0.31	-45.81	-11.52	93
S4	4.18	-	0.10	-44.77	-	60
-	12.33	-	0.22	-45.37	-	76
-	18.35	0.62	0.36	-45.73	-	91
-	20.50	-	0.34	-45.37	-	90
-	24.28	0.63	0.16	-45.02	-	70
-	28.60	0.61	0.13	-44.90	-	66
-	39.02	0.63	0.15	-44.54	-	67
-	44.02	0.63	0.15	-46.07	-	68
-	50.77	0.64	0.13	-45.85	-	65
-	62.33	0.80	0.15	-45.80	-11.42	60
S5	4.38	0.53	0.24	-43.30	-	79
-	15.55	0.80	0.51	-44.66	-	131
-	18.98	0.87	0.57	-44.81	-	141
-	25.05	0.69	0.31	-44.04	-	165
-	30.97	0.48	0.23	-45.28	-	194
-	39.35	0.52	0.15	-45.50	-	210
-	41.42	0.54	0.17	-44.81	-11.32	209
S6	3.85	0.46	-	-	-	-
-	18.82	0.69	-	-	-	-
-	26.83	0.61	-	-	-	-
-	41.45	0.51	-	-	-	-
-	45.78	0.53	-	-	-	-
-	52.75	0.52	-	-	-	-

Table 2 continued

Experiment	Time (h)	TA (mEq/L)	[DIC] (mM)	$\delta^{13}\text{C}_{\text{DIC}}$ (VPDB)	$\delta^{18}\text{O}_w$ (VSMOW)	pCO ₂ (ppm)
-	63.75	0.50	-	-	-	-
-	66.63	0.50	-	-	-	-
-	72.78	0.50	-	-	-11.31	-
S7	3.83	0.48	0.22	-44.33	-	67
-	13.92	0.71	0.37	-45.16	-	105
-	20.65	0.71	0.42	-44.65	-	117
-	27.57	0.55	0.28	-44.80	-	83
-	38.83	0.55	0.21	-44.47	-	82
-	45.00	0.55	0.24	-45.50	-	89
-	48.00	0.52	0.15	-45.47	-11.34	184
S8	3.65	0.47	0.14	-43.66	-	97
-	11.80	0.65	0.37	-44.47	-	142
-	19.07	0.66	0.26	-44.18	-	143
-	26.07	0.49	0.15	-44.60	-	103
-	34.97	0.50	0.17	-45.47	-	104
-	47.22	0.49	0.13	-45.70	-	102
-	52.15	0.60	0.13	-45.55	-11.39	91
S9	3.22	0.55	0.17	-44.63	-	72
-	14.05	0.85	0.48	-44.68	-	172
-	16.22	0.85	0.59	-44.25	-	179
-	20.40	0.63	0.30	-44.18	-	123
-	25.95	0.62	0.25	-45.22	-	118
-	37.83	0.64	0.25	-45.47	-	124
-	47.38	0.60	0.29	-45.48	-11.40	118
S10	3.08	0.35	-	-	-	78
-	11.67	0.63	-	-	-	142
-	16.90	0.84	-	-	-	171
-	24.42	0.97	-	-	-	198
-	26.50	0.99	0.69	-44.22	-	192
-	34.65	0.63	0.29	-44.45	-	136
-	39.30	0.60	0.27	-45.24	-	129
-	46.10	0.60	0.36	-45.53	-	128
-	59.03	0.59	0.34	-45.76	-	136
-	66.13	0.61	0.31	-45.74	-11.39	132
S11	4.83	0.61	-	-	-	107
-	14.50	0.90	0.59	-44.36	-	189

Table 2 continued

Experiment	Time (h)	TA (mEq/L)	[DIC] (mM)	$\delta^{13}\text{C}_{\text{DIC}}$ (VPDB)	$\delta^{18}\text{O}_{\text{w}}$ (VSMOW)	pCO ₂ (ppm)
-	22.10	1.08	0.61	-43.72	-	218
-	28.07	1.15	0.80	-43.03	-	235
-	38.32	0.68	0.34	-43.34	-	139
-	44.27	0.65	0.22	-45.10	-	130
-	50.52	0.63	0.27	-45.51	-	130
-	60.68	0.66	0.25	-45.85	-	131
-	66.98	0.63	0.28	-46.02	-11.62	127
S12	4.55	0.57	-	-	-	131
-	14.03	0.85	0.56	-24.53	-	171
-	20.20	0.92	0.62	-23.87	-	176
-	28.00	0.64	0.34	-24.38	-	127
-	37.50	0.61	0.35	-24.94	-	127
-	45.50	0.62	0.31	-25.23	-11.57	124
S13	4.05	0.46	0.14	-24.15	-	194
-	12.20	0.63	0.27	-24.89	-	221
-	20.13	0.80	0.37	-24.76	-	226
-	28.58	0.88	0.44	-24.53	-	237
-	37.10	0.61	0.22	-24.18	-	219
-	44.32	0.58	0.20	-24.71	-	216
-	51.98	0.58	0.19	-25.08	-	217
-	60.97	0.57	0.20	-25.35	-	210
-	68.32	0.59	0.21	-25.74	-	208
-	76.02	0.58	0.16	-25.83	-	209
-	86.78	0.58	0.18	-26.05	-	204
-	92.95	0.57	0.20	-26.00	-11.72	206
S14	3.52	0.61	0.21	-23.69	-	89
-	10.62	0.90	0.63	-23.82	-	138
-	21.80	0.67	0.25	-23.74	-	98
-	26.72	0.61	0.25	-24.53	-	94
-	34.52	0.64	0.25	-24.39	-	96
-	45.13	0.62	0.22	-24.83	-	95
-	52.00	0.63	0.32	-22.45	-11.82	98
S15	3.37	0.59	0.19	-24.27	-	85
-	13.27	0.95	0.60	-24.32	-	142
-	19.47	1.24	0.71	-23.73	-	172
-	26.03	1.26	0.73	-23.00	-	178

Table 2 continued

Experiment	Time (h)	TA (mEq/L)	[DIC] (mM)	$\delta^{13}\text{C}_{\text{DIC}}$ (VPDB)	$\delta^{18}\text{O}_{\text{w}}$ (VSMOW)	pCO ₂ (ppm)
-	36.60	0.96	0.50	-22.96	-	136
-	44.47	0.82	0.55	-23.34	-	122
-	50.45	0.74	0.43	-23.84	-	111
-	61.12	0.67	0.34	-24.53	-11.82	97
CA1	5.15	0.43	0.10	-23.32	-	54
-	14.25	0.56	0.31	-23.96	-	83
-	21.65	0.90	0.67	-23.73	-	148
-	31.08	0.89	0.50	-22.91	-	149
-	39.38	0.68	0.26	-23.68	-	110
-	47.20	0.65	0.33	-24.26	-	108
-	55.07	0.65	0.30	-24.36	-	109
-	64.80	0.66	0.24	-24.49	-11.83	106
CA2	7.63	0.72	0.42	-23.58	-	127
-	14.78	0.95	0.63	-22.89	-	162
-	22.12	0.67	0.34	-23.30	-	105
-	29.22	0.65	0.33	-23.96	-	101
-	38.82	0.64	0.35	-24.20	-	93
-	48.33	0.63	0.24	-24.49	-11.86	97
CA3	2.40	0.48	0.17	-24.53	-	76
-	11.70	0.95	0.46	-23.61	-	146
-	23.03	0.72	0.24	-23.30	-	103
-	26.47	0.65	0.25	-24.24	-	102
-	35.83	0.64	0.21	-24.38	-	99
-	47.05	0.65	0.18	-24.54	-11.91	96
CA4	3.22	0.74	0.14	-24.50	-	134
-	8.38	0.95	0.31	-24.88	-	165
-	21.25	0.70	0.14	-25.12	-	121
-	25.38	0.72	0.19	-25.04	-	138
-	30.22	0.71	0.16	-25.05	-11.68	124
CA5	4.07	0.69	0.24	-23.50	-	94
-	13.15	-	0.48	-23.32	-	159
-	21.82	1.23	0.64	-22.53	-	195
-	24.68	1.29	0.71	-22.26	-	200
-	37.20	0.73	0.25	-23.27	-	131
-	44.22	0.70	0.23	-24.03	-	132
-	51.25	0.69	0.22	-24.25	-	130

Table 2 continued

Experiment	Time (h)	TA (mEq/L)	[DIC] (mM)	$\delta^{13}\text{C}_{\text{DIC}}$ (VPDB)	$\delta^{18}\text{O}_w$ (VSMOW)	pCO ₂ (ppm)
-	61.87	0.67	0.20	-24.58	-11.17	128
CA6	4.00	0.60	0.27	-23.19	-	85
-	13.68	-	0.54	-22.54	-	169
-	18.03	1.09	0.66	-21.94	-	191
-	23.15	0.99	0.56	-21.49	-	167
-	29.03	0.79	0.33	-22.30	-	118
-	39.12	0.78	0.29	-23.36	-	107
-	45.95	0.77	0.28	-23.63	-	103
-	51.73	0.73	0.27	-23.75	-	105
-	60.92	0.74	0.27	-24.00	-11.18	102
CA7	3.17	0.58	0.23	-23.19	-	81
-	13.12	0.92	0.55	-22.00	-	173
-	19.50	1.04	0.73	-21.09	-	203
-	26.85	1.02	0.56	-20.41	-	191
-	37.43	0.68	0.27	-22.09	-	113
-	43.67	0.64	0.27	-22.66	-	112
-	50.35	0.65	0.29	-22.87	-	109
-	61.13	0.65	0.23	-23.20	-11.33	104
CA9	3.52	0.55	0.22	-44.09	-	34
-	12.45	0.91	0.57	-43.99	-	126
-	16.98	1.04	0.74	-43.55	-	154
-	25.58	0.68	0.29	-43.29	-	97
-	35.37	0.67	0.29	-44.15	-	95
-	42.58	0.68	0.31	-44.13	-	94
-	49.20	0.68	0.40	-44.03	-	92
-	59.87	0.65	0.28	-44.27	-11.57	90
CA12	3.83	0.63	0.32	-42.02	-	102
-	16.93	0.96	0.64	-42.92	-	184
-	22.37	0.97	0.63	-42.54	-	168
-	29.78	0.79	0.18	-42.25	-	128
-	40.15	0.63	0.24	-43.45	-	96
-	47.15	0.60	0.21	-43.67	-	87
-	53.40	0.60	0.21	-43.93	-	84
-	66.82	0.63	0.21	-44.46	-11.76	83
CA13	2.57	0.63	0.34	-43.70	-	67
-	14.40	0.93	0.54	-43.22	-	171

Table 2 continued

Experiment	Time (h)	TA (mEq/L)	[DIC] (mM)	$\delta^{13}\text{C}_{\text{DIC}}$ (VPDB)	$\delta^{18}\text{O}_{\text{w}}$ (VSMOW)	pCO ₂ (ppm)
-	20.68	1.05	0.61	-42.61	-	194
-	26.35	1.00	0.51	-42.13	-	184
-	37.92	0.61	0.22	-43.38	-	103
-	44.25	0.63	0.20	-43.82	-	103
-	50.88	0.62	0.16	-43.87	-	102
-	60.17	0.60	0.18	-43.89	-	105
-	65.75	0.60	0.22	-44.36	-11.65	106
CA14	3.67	0.59	0.17	-42.28	-	87
-	16.05	0.84	0.32	-41.79	-	155
-	23.38	0.63	0.17	-42.22	-	96
-	30.77	0.59	0.15	-43.02	-	94
-	38.28	0.60	0.16	-43.29	-	98
-	44.03	0.62	0.16	-43.66	-	100
-	49.97	0.64	0.15	-43.43	-11.85	97
CA15	4.40	0.63	0.19	-42.63	-	98
-	14.92	0.95	0.46	-42.75	-	179
-	21.23	1.00	0.46	-41.89	-	169
-	29.10	0.79	0.24	-41.90	-	112
-	38.80	0.75	0.18	-42.91	-	98
-	45.10	0.72	0.18	-43.19	-	95
-	51.80	0.68	0.18	-43.19	-11.86	88
CA18	3.20	0.77	0.39	-17.44	-	220
-	13.93	0.71	0.31	-16.77	-	214
-	19.78	0.64	0.24	-17.40	-	192
-	26.93	0.64	0.22	-17.53	-	186
-	36.45	0.65	0.20	-17.66	-	188
-	42.28	0.64	0.22	-17.45	-11.88	191
CA20	6.22	0.74	0.34	-35.65	-	161
-	15.95	0.63	0.23	-35.59	-	127
-	22.50	0.63	0.22	-34.74	-	124
-	29.92	0.61	0.19	-32.34	-	115
-	39.62	0.60	0.16	-31.50	-	102
-	46.50	0.59	0.15	-31.45	-11.95	99

APPENDIX B
CHAPTER III SUPPLEMENTARY MATERIAL:
EXPERIMENT DATA AND SEM IMAGES OF PRECIPITATES

1 Experiment data

For each experiment, we periodically took water samples that were sent for [DIC] and $\delta^{13}\text{C}$ analysis, which are depicted by black circles, with curves interpolated between the data measurements (dark green and light green, respectively). We continuously monitored the concentration of CO_2 (ppm) of the experimental headspace (light blue line). The CO_2 concentrations of early experiments (S2-S8) were measured with a less reliable software and are not reported. We continuously measured solution pH (purple line) and amount of added NaOH (dark blue line), in addition to the periodic water samples we titrated to calculate the total alkalinity of the solution (red squares). The vertical gray line represents the onset of calcite precipitation for each experiment.

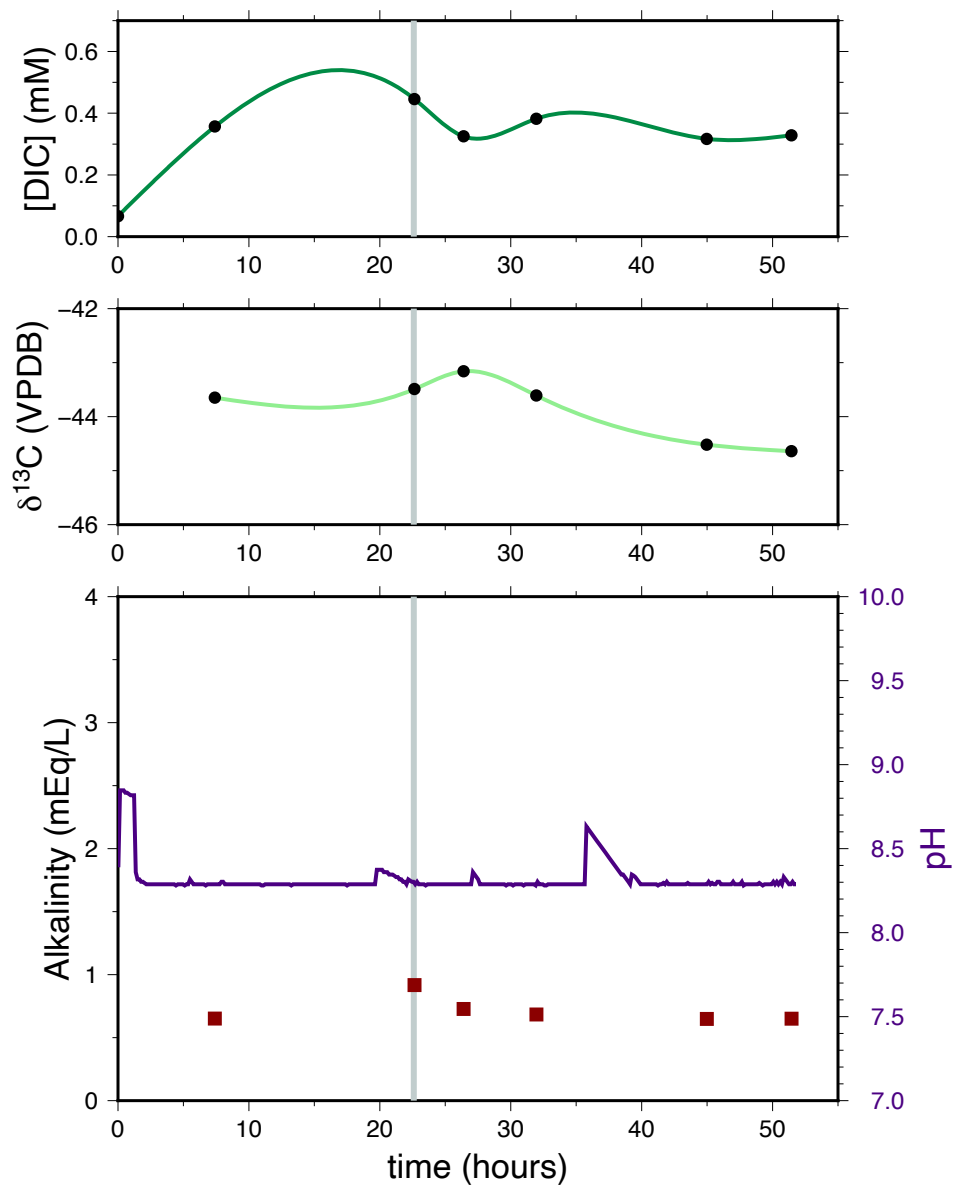


Figure 1: S2, [NaCl] = 0.52 M, salinity = 35 g/kg

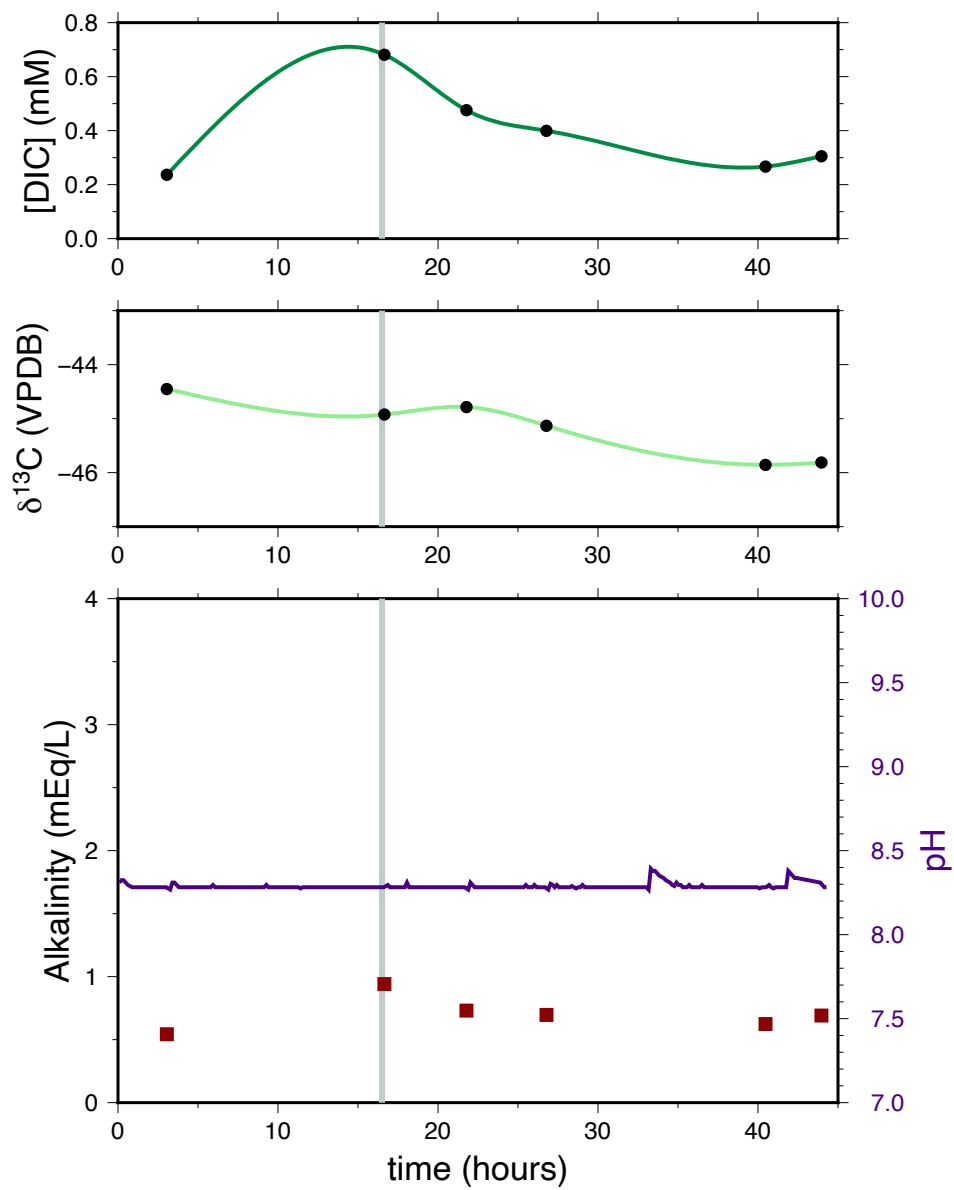


Figure 2: S3, $[\text{NaCl}] = 0.52 \text{ M}$, salinity = 35 g/kg

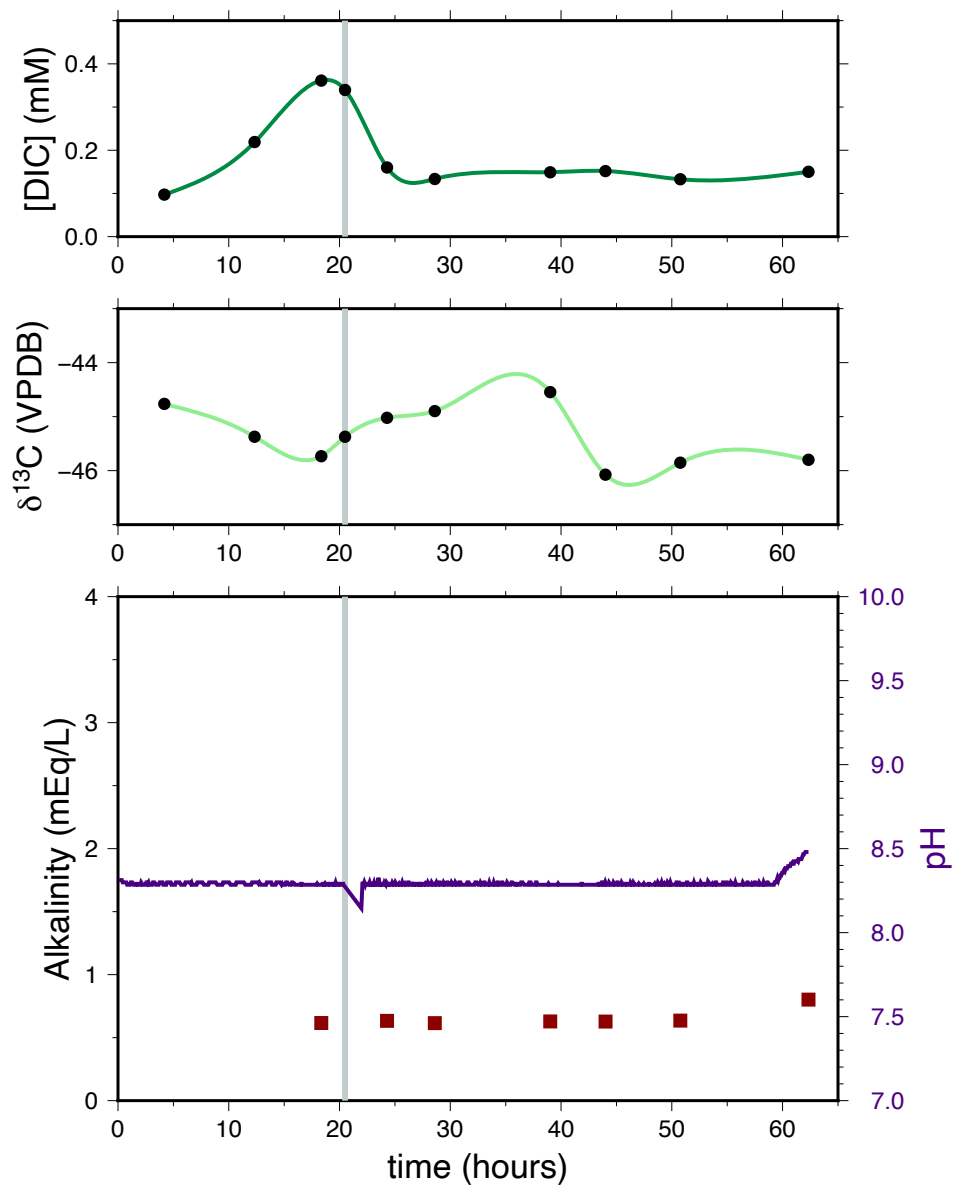


Figure 3: S4, $[\text{NaCl}] = 0.18 \text{ M}$, salinity = 15 g/kg

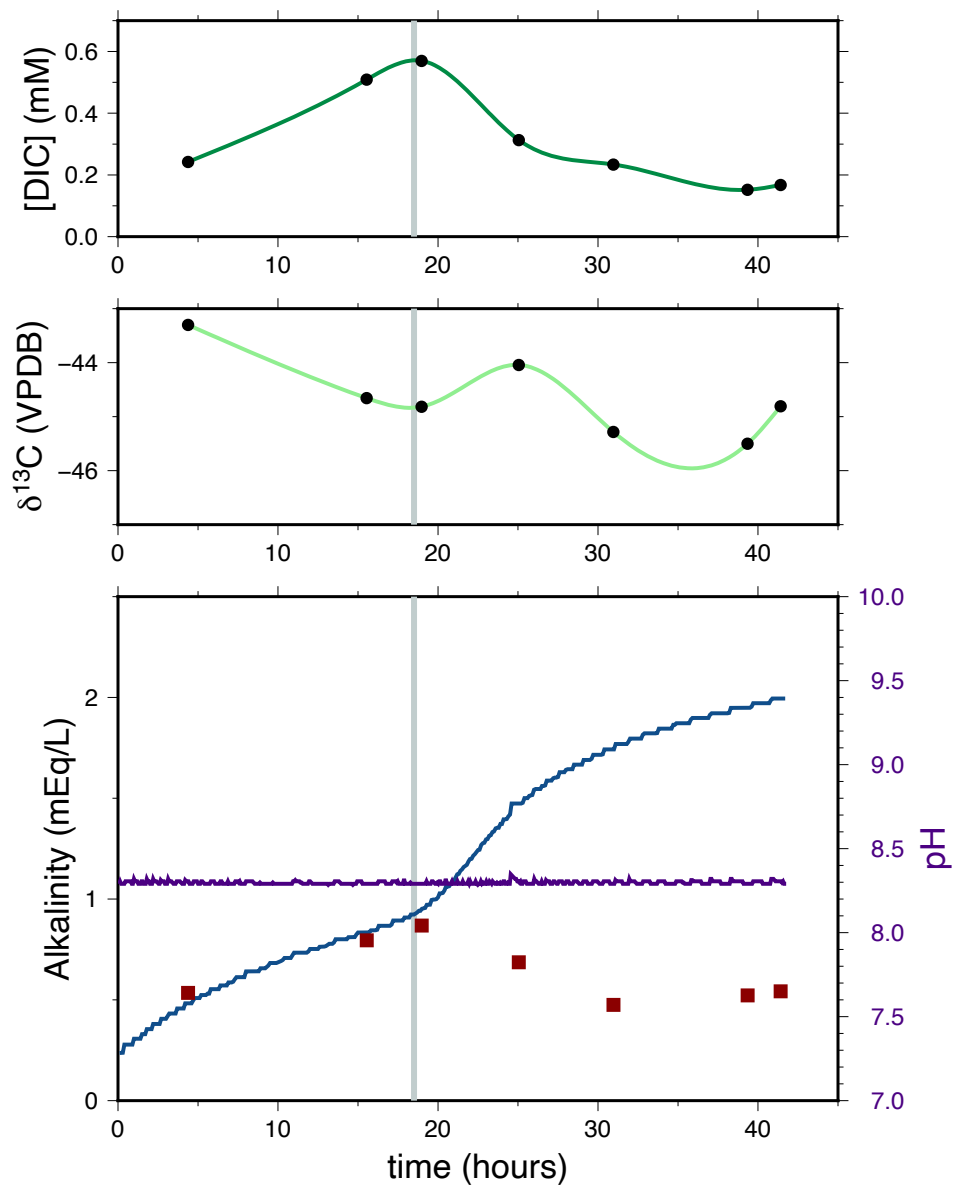


Figure 4: S5, $[\text{NaCl}] = 0.35 \text{ M}$, salinity = 25 g/kg

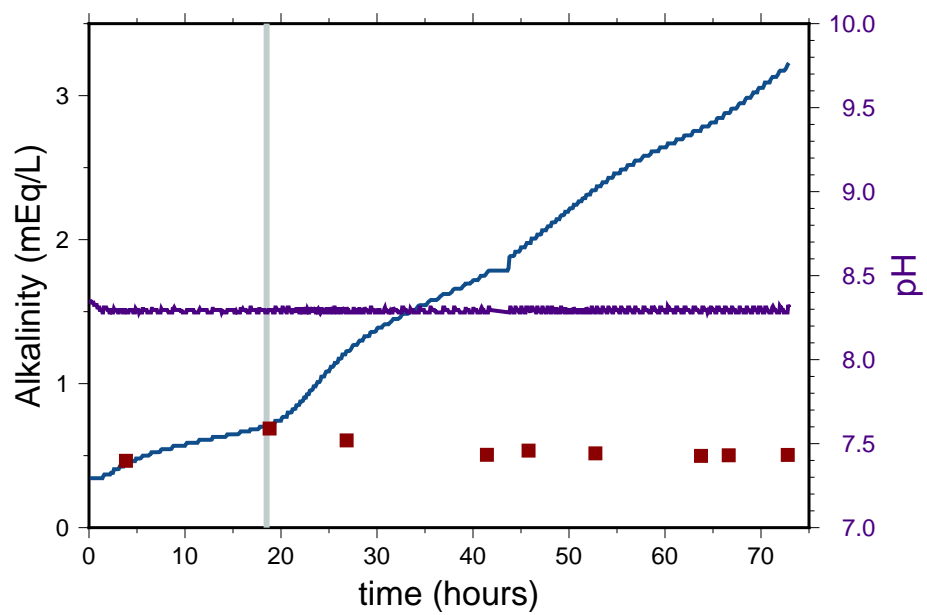


Figure 5: S6, $[\text{NaCl}] = \sim 0 \text{ M}$, salinity = 3.5 g/kg

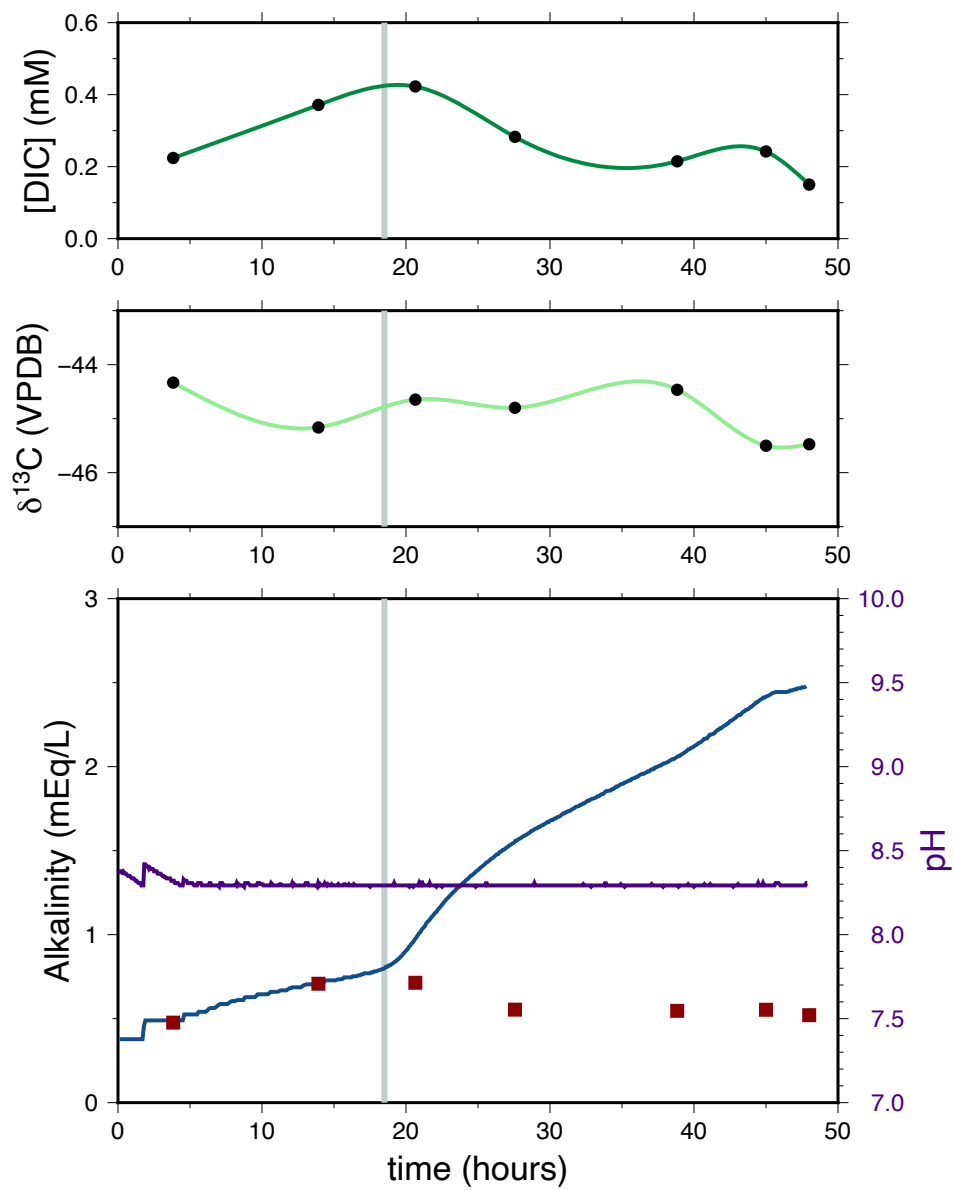


Figure 6: S7, [NaCl] = 0.18 M, salinity = 15 g/kg

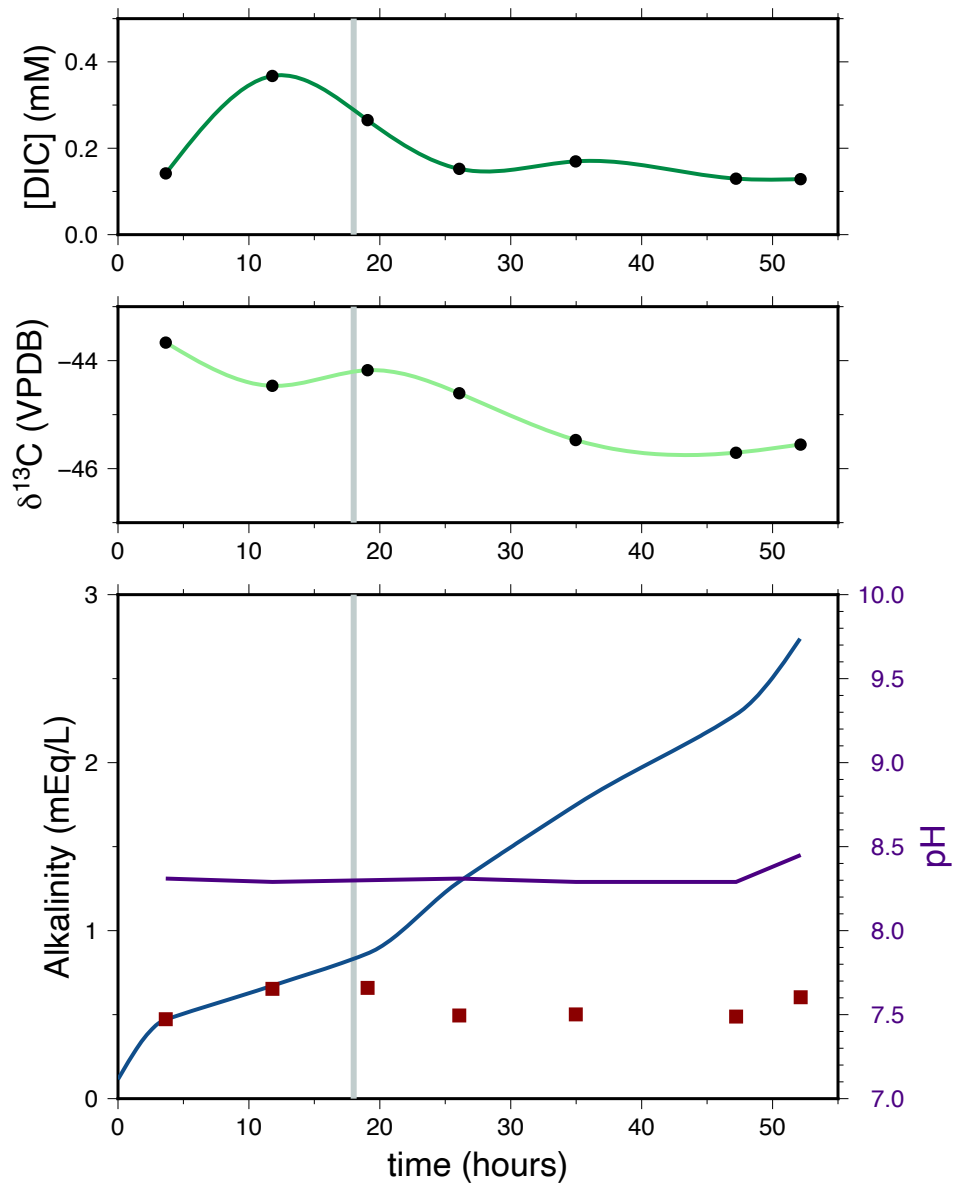


Figure 7: S8, $[\text{NaCl}] = \sim 0 \text{ M}$, salinity = 3.5 g/kg

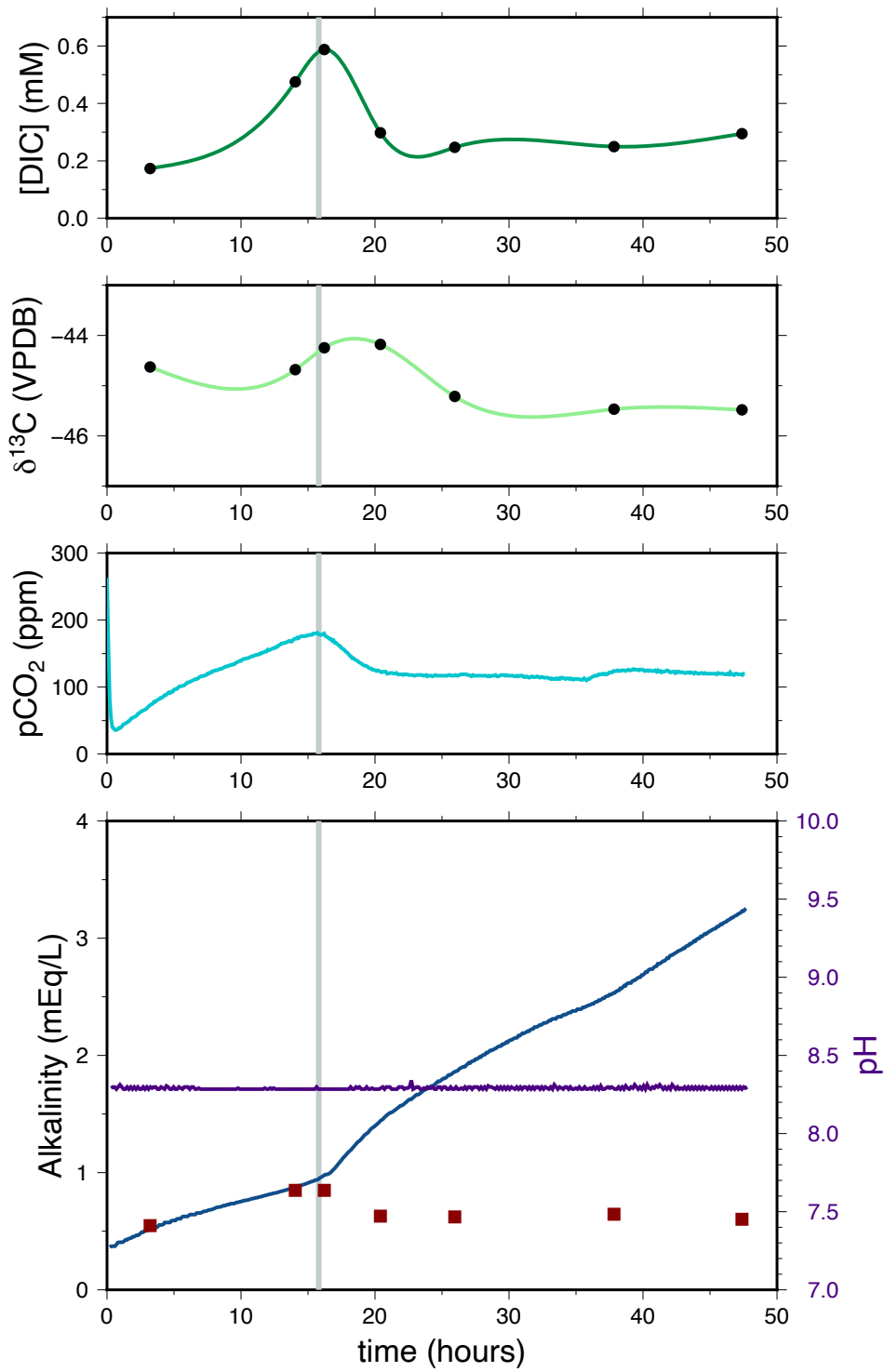


Figure 8: S9, $[\text{NaCl}] = 0.35 \text{ M}$, salinity = 25 g/kg

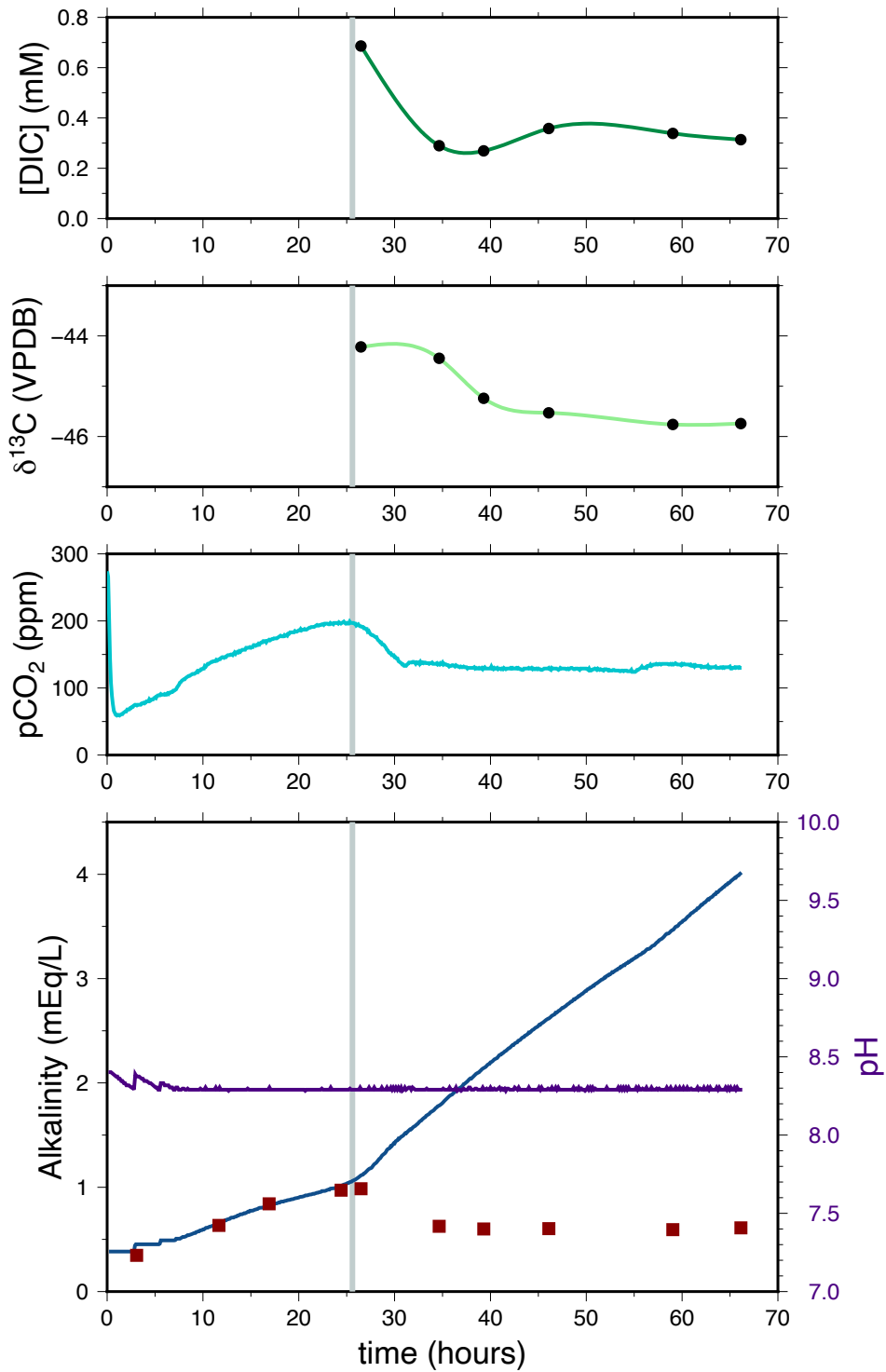


Figure 9: S10, $[\text{NaCl}] = 0.69 \text{ M}$, salinity = 45 g/kg

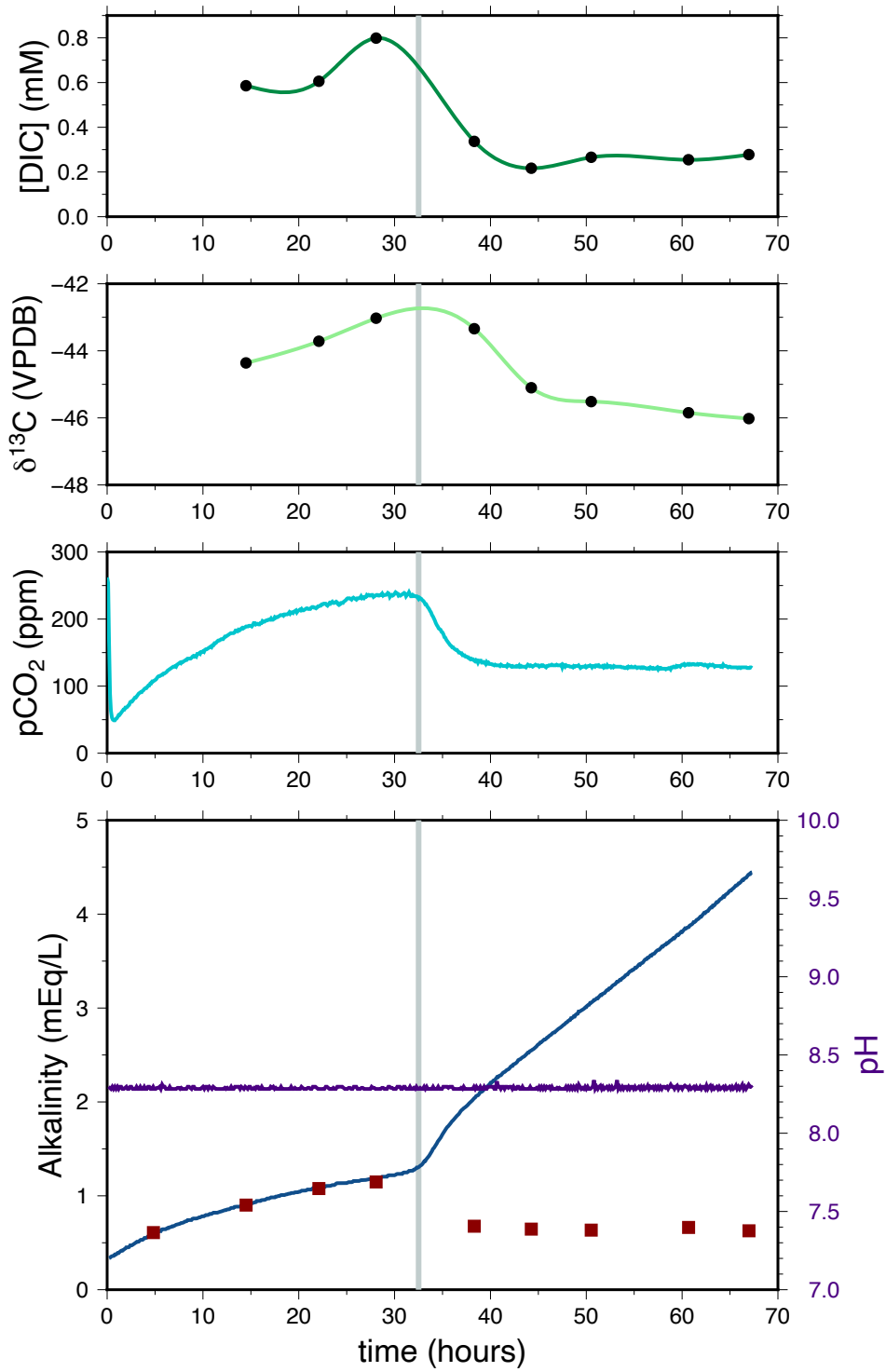


Figure 10: S11, $[\text{NaCl}] = 0.35 \text{ M}$, salinity = 25 g/kg

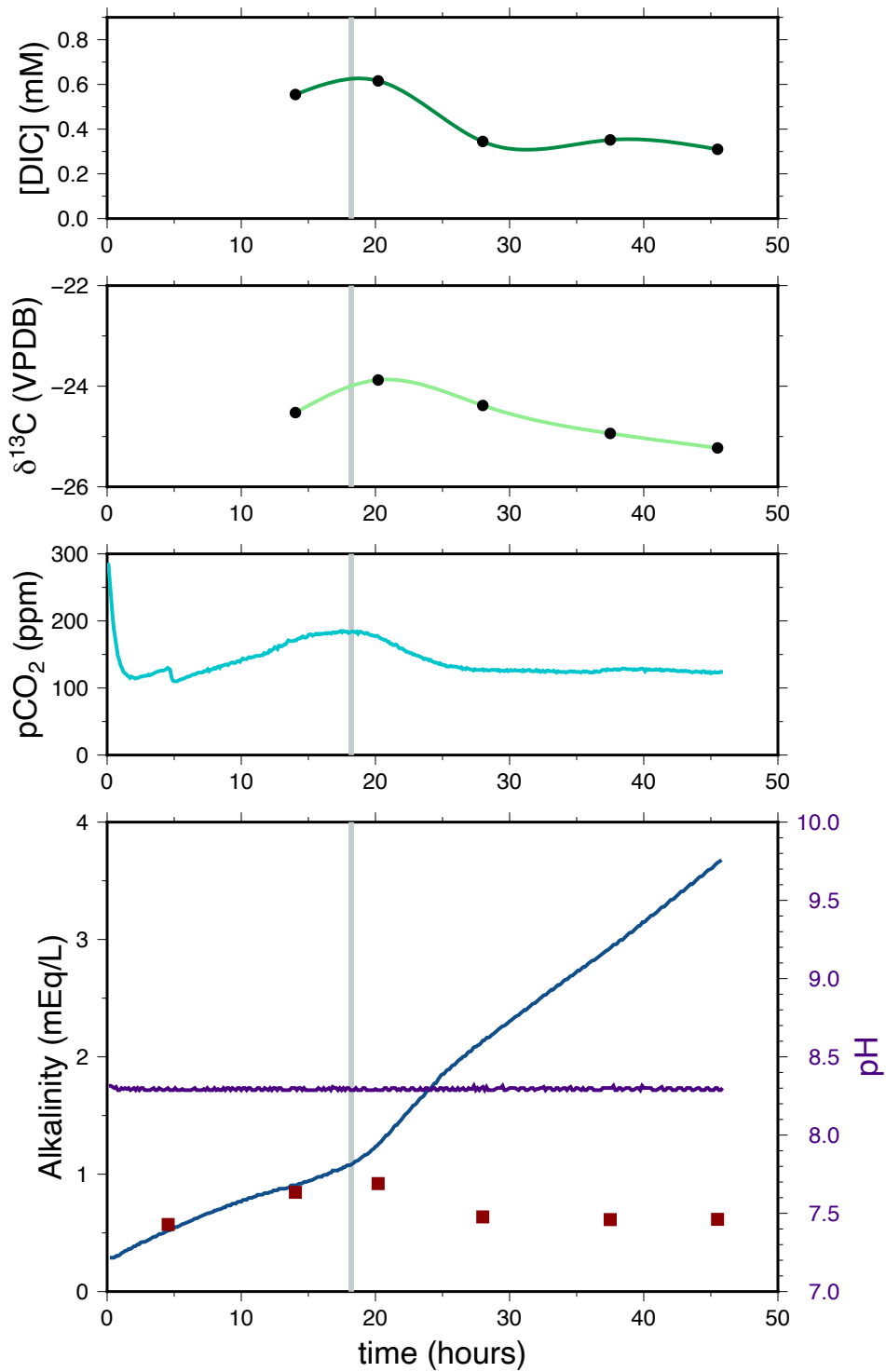


Figure 11: S12, $[\text{NaCl}] = 1.37 \text{ M}$, salinity = 85 g/kg

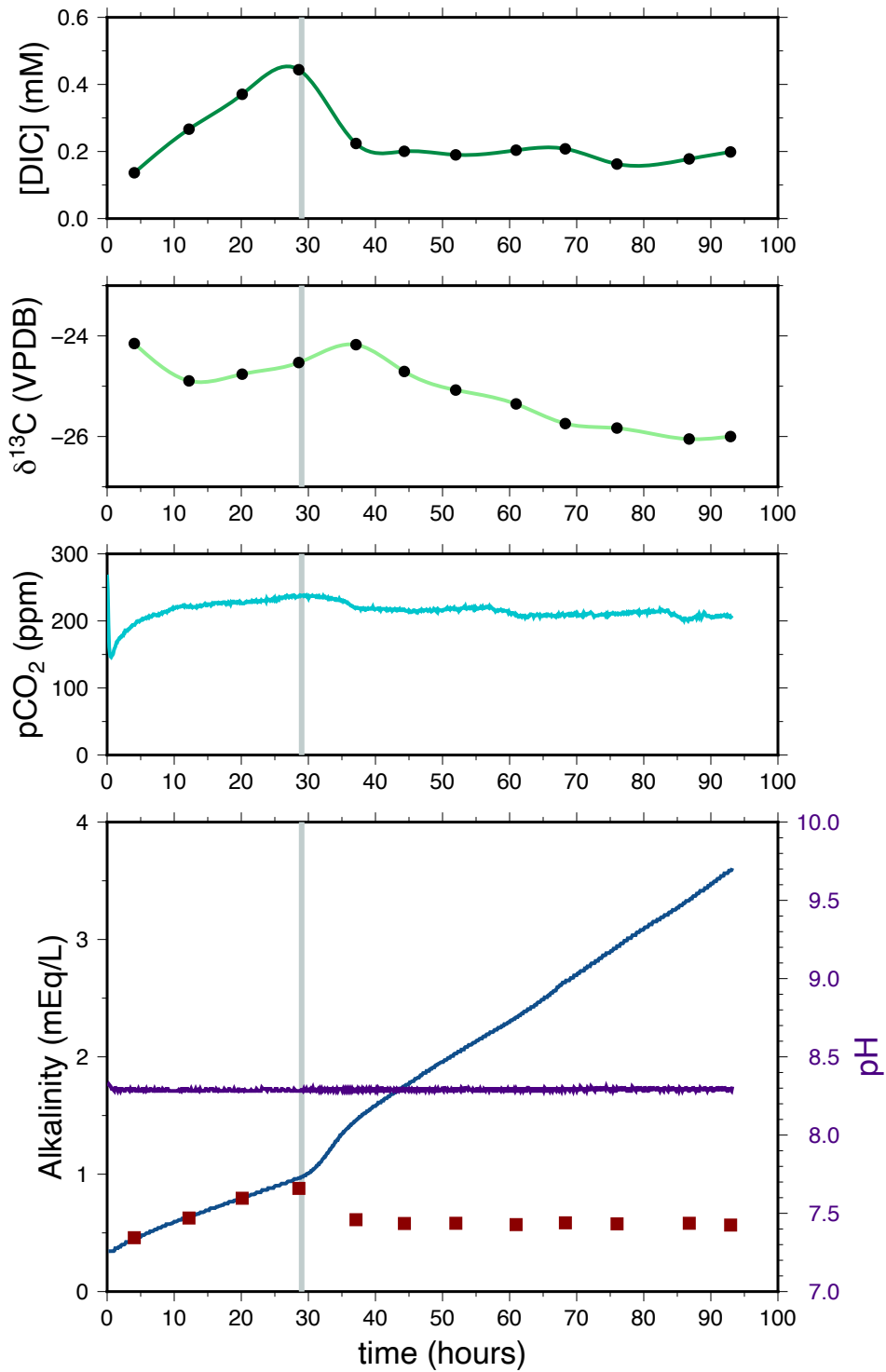


Figure 12: S13, [NaCl] = 1.03 M, salinity = 65 g/kg

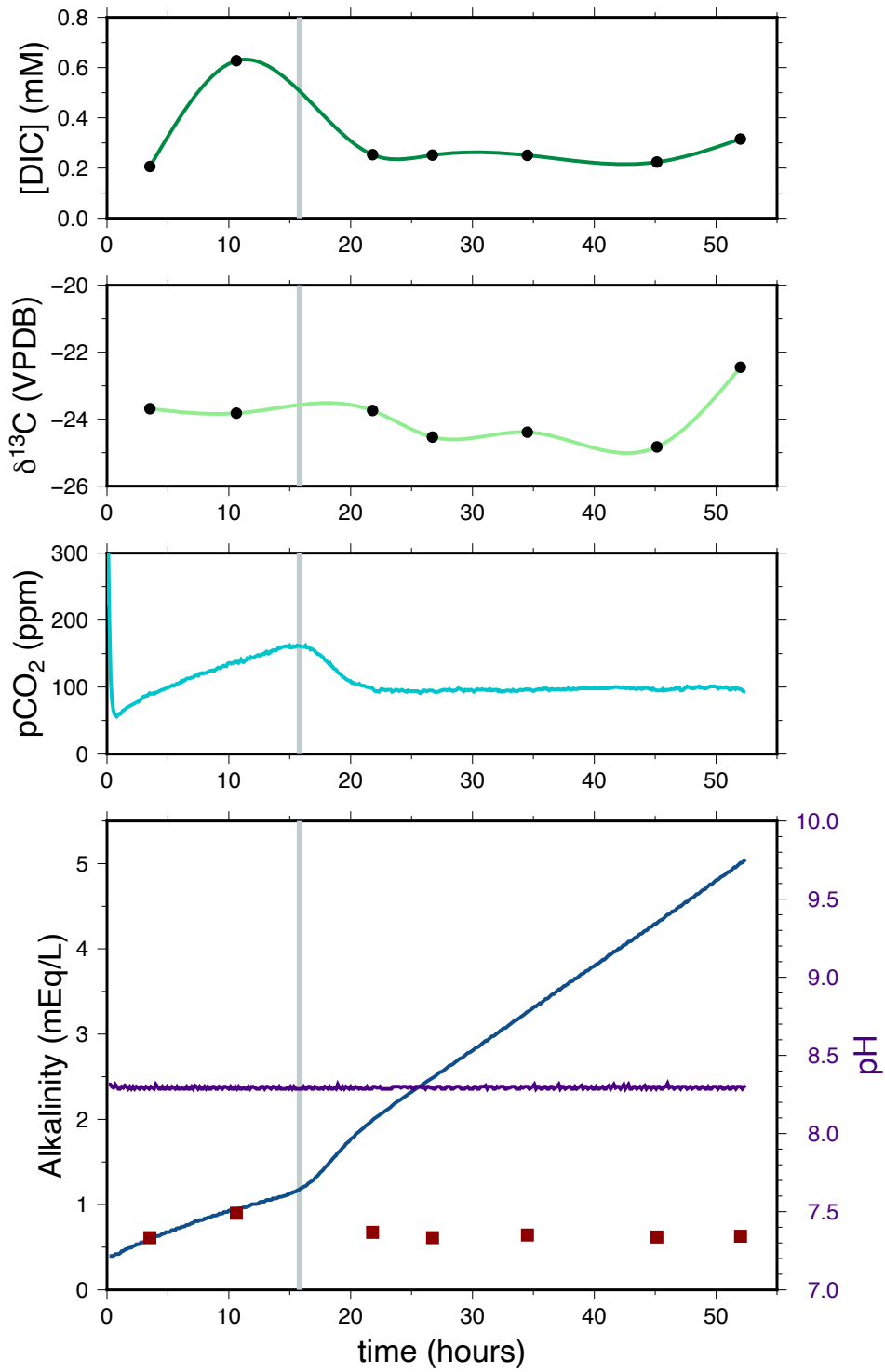


Figure 13: S14, $[\text{NaCl}] = 0.86 \text{ M}$, salinity = 55 g/kg

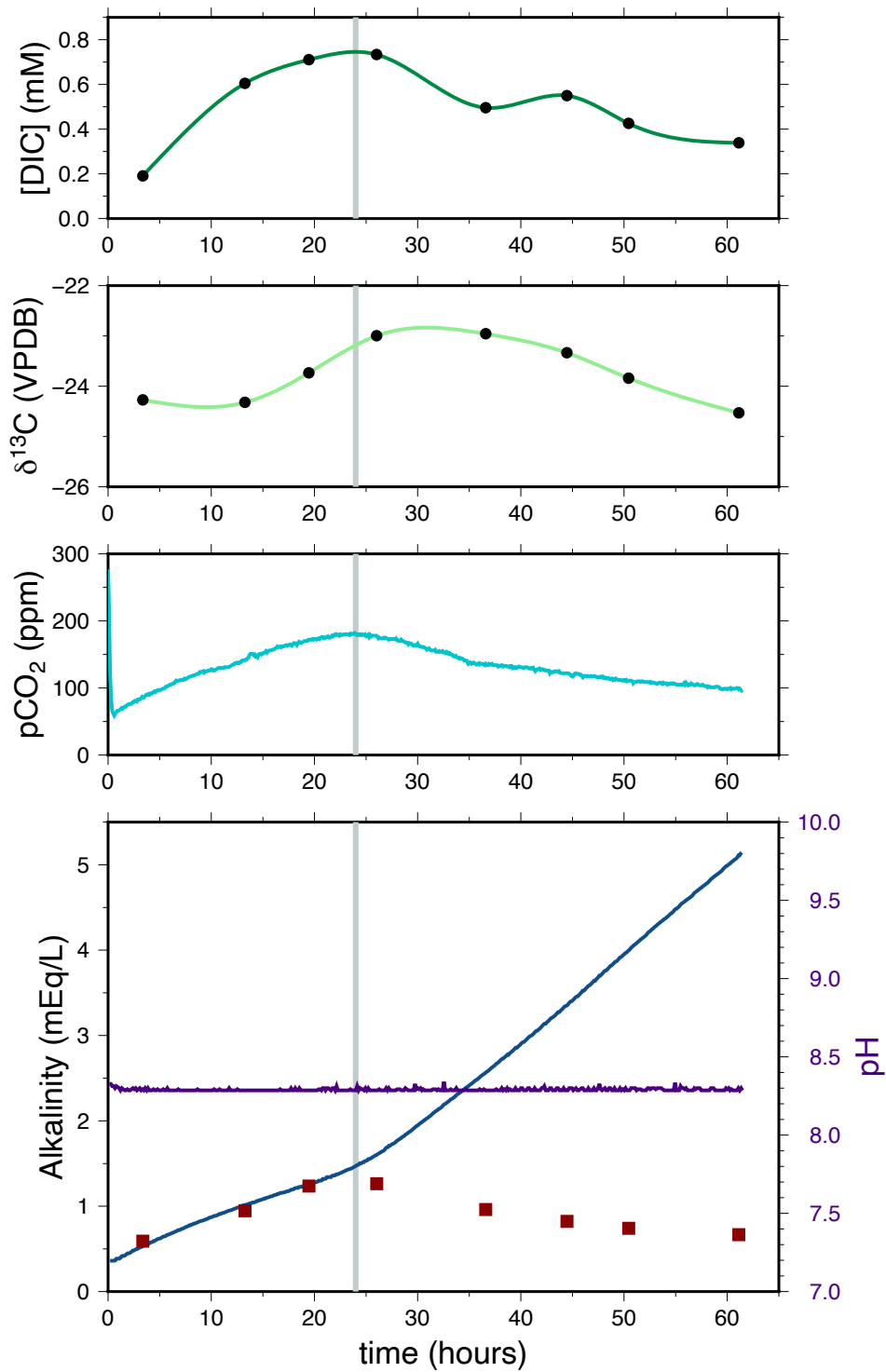


Figure 14: S15, $[\text{NaCl}] = 1.20 \text{ M}$, salinity = 75 g/kg

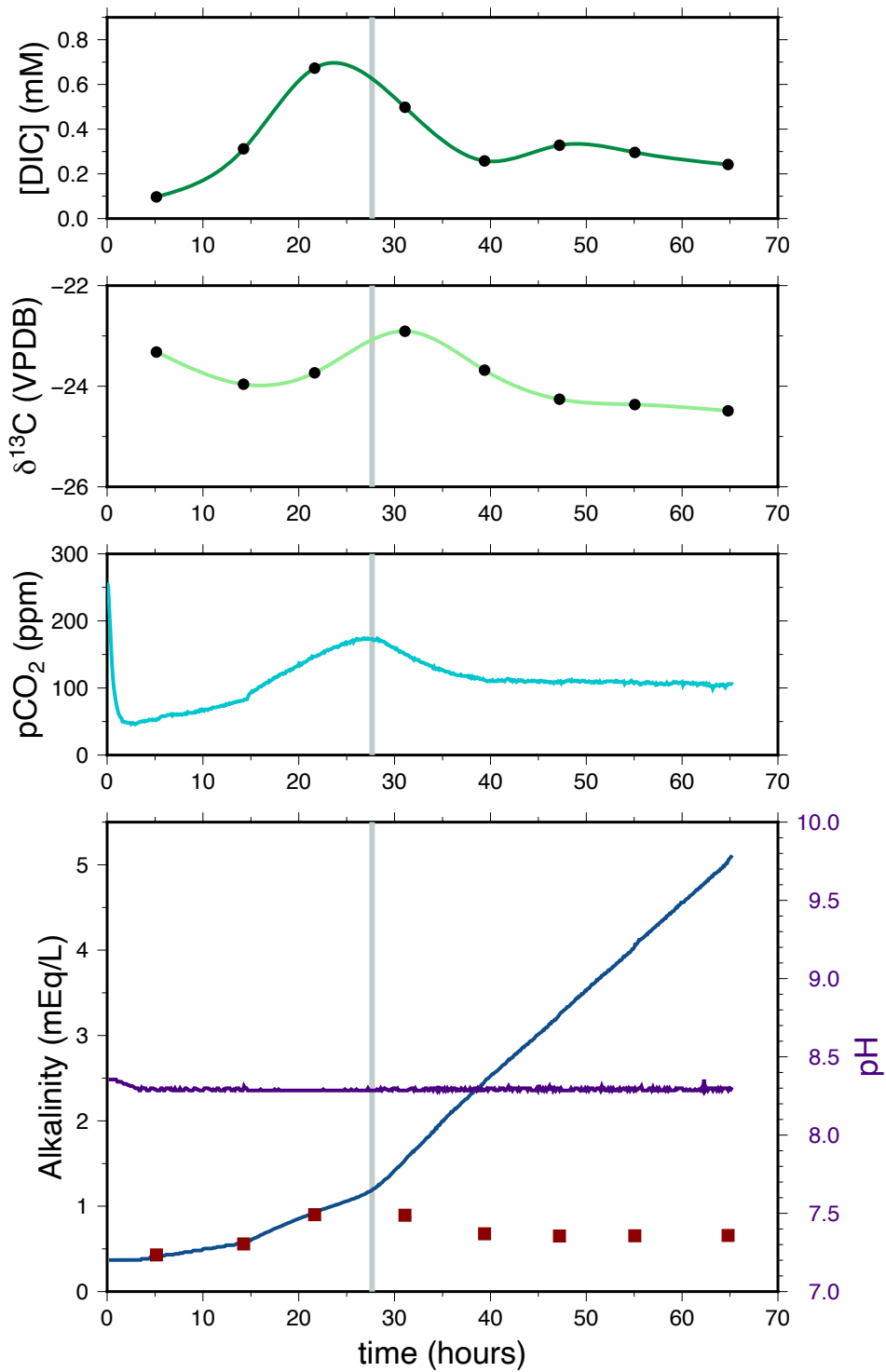


Figure 15: CA1, [NaCl] = 0.52 M, salinity = 35 g/kg

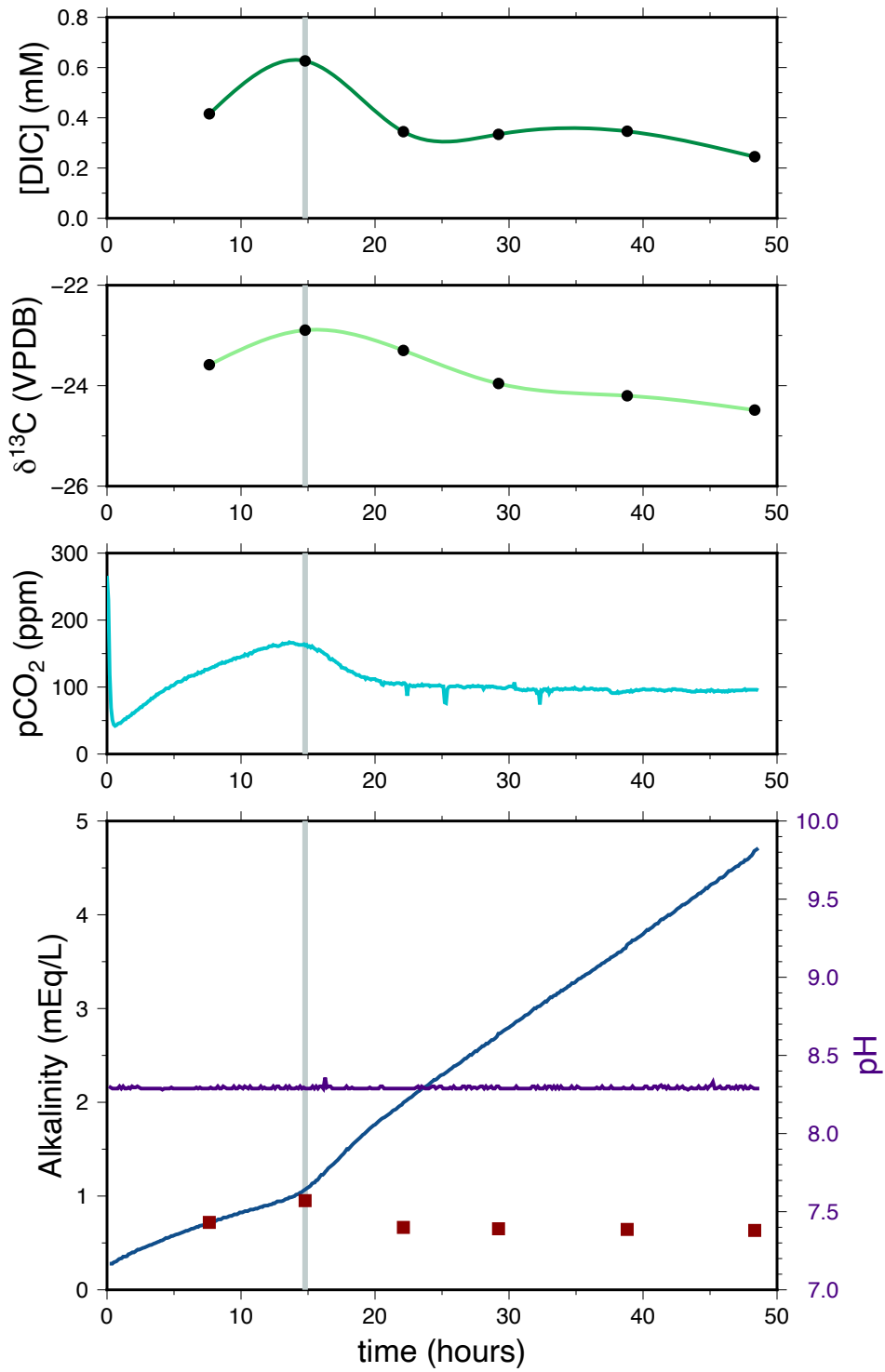


Figure 16: CA2, $[\text{NaCl}] = 0.52 \text{ M}$, salinity = 35 g/kg

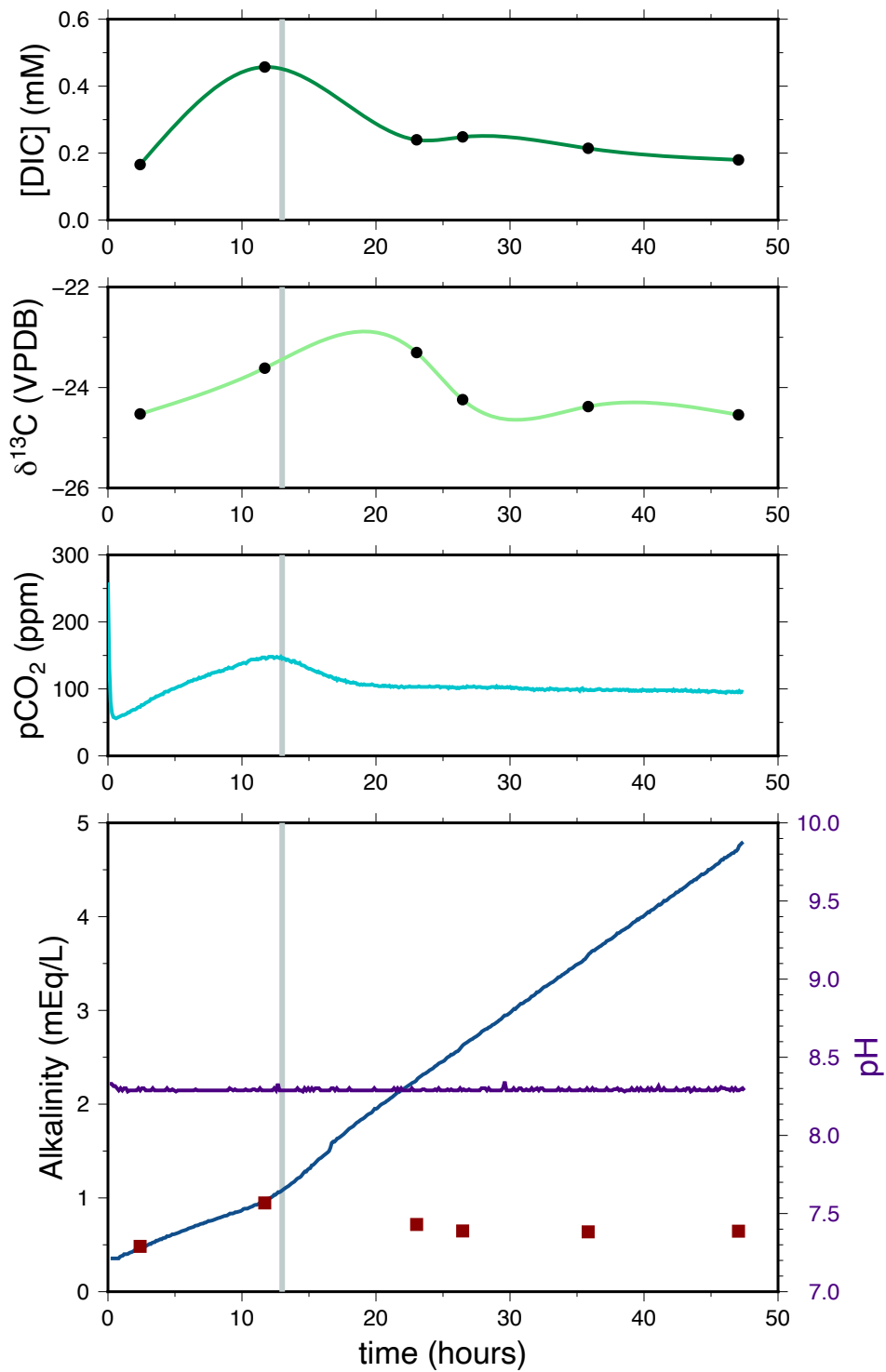


Figure 17: CA3, [NaCl] = 0.52 M, salinity = 35 g/kg

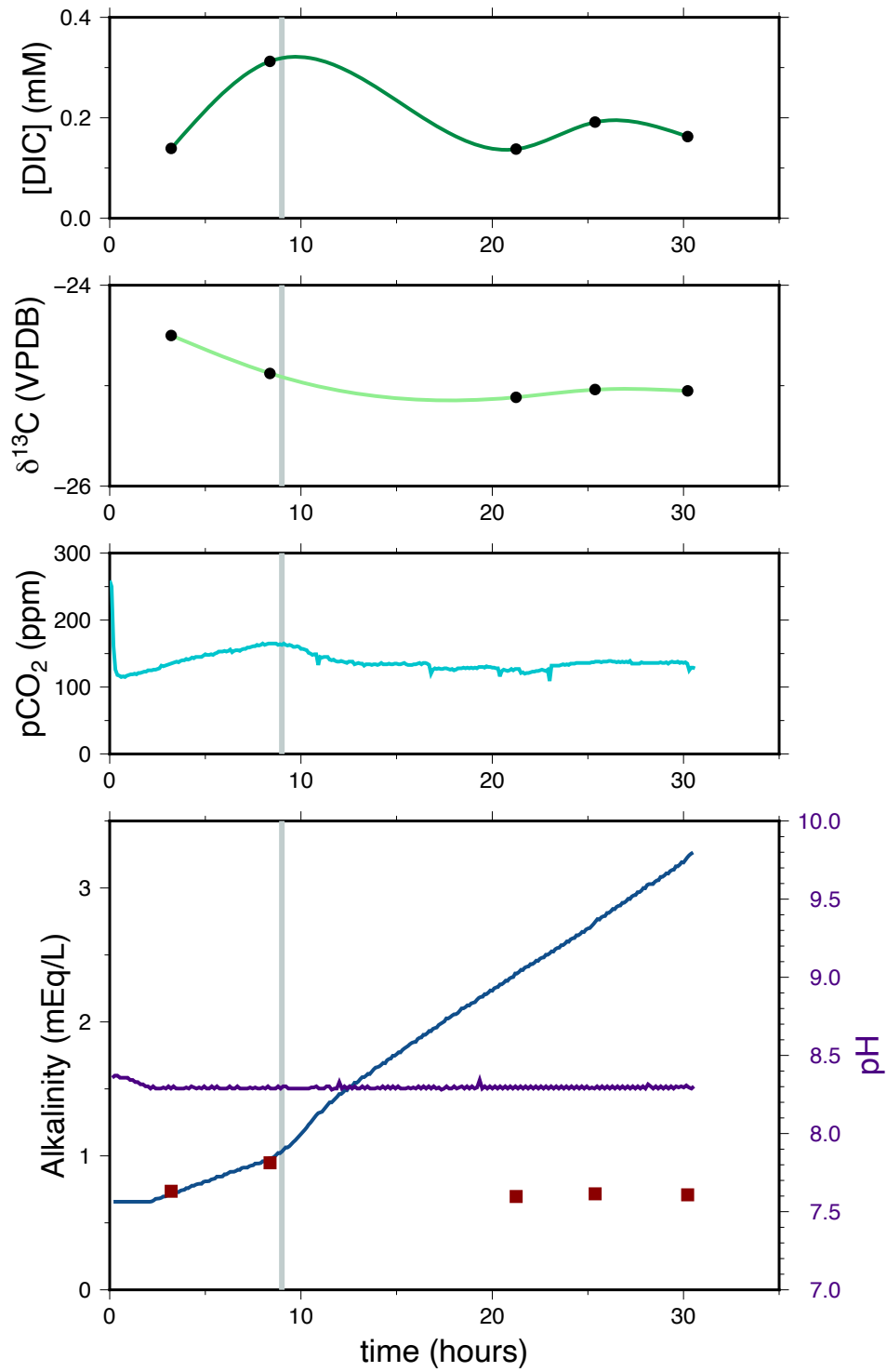


Figure 18: CA4, $[\text{NaCl}] = \sim 0 \text{ M}$, salinity = 3.5 g/kg

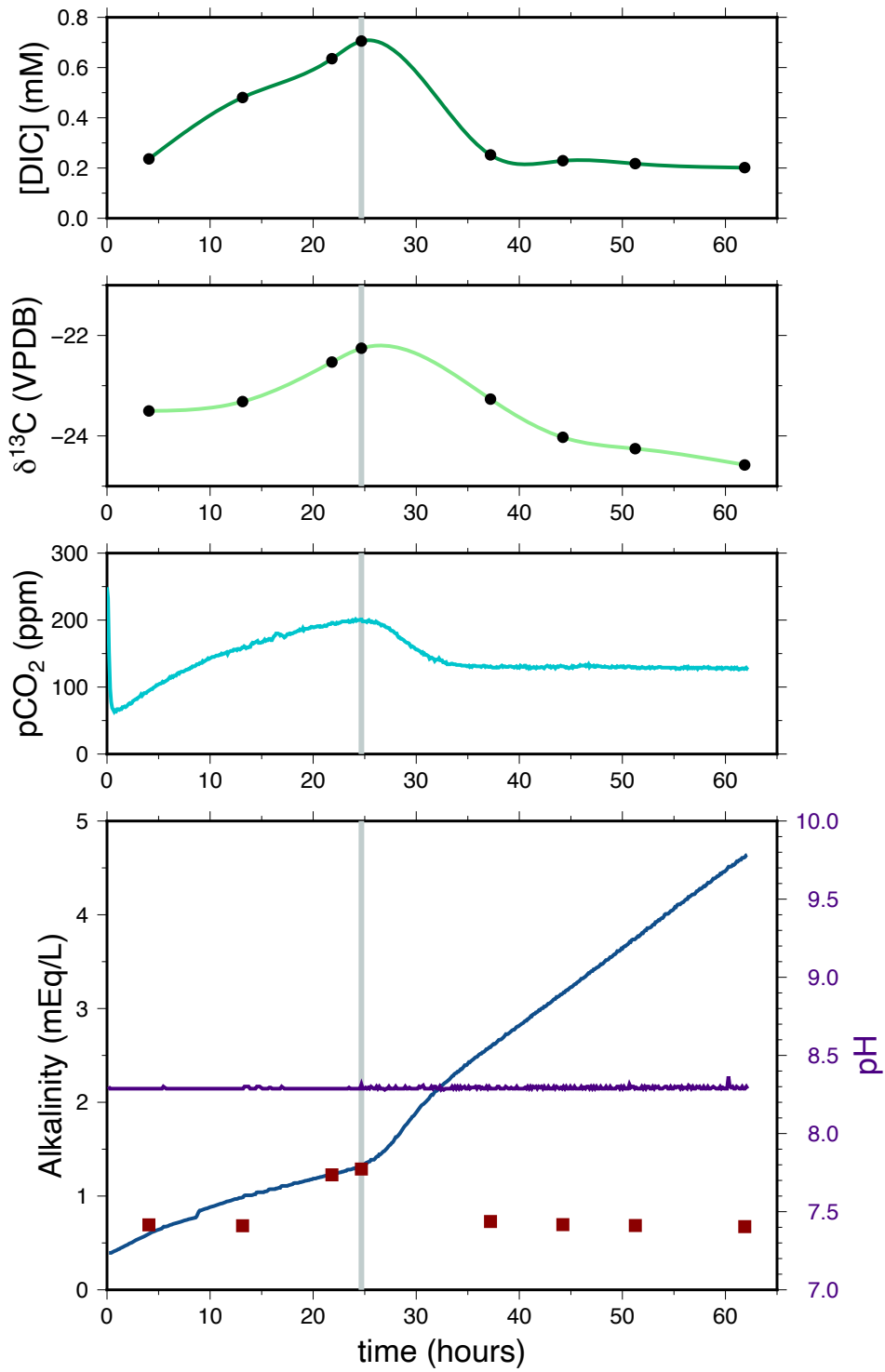


Figure 19: CA5, $[\text{NaCl}] = 0.52 \text{ M}$, salinity = 35 g/kg

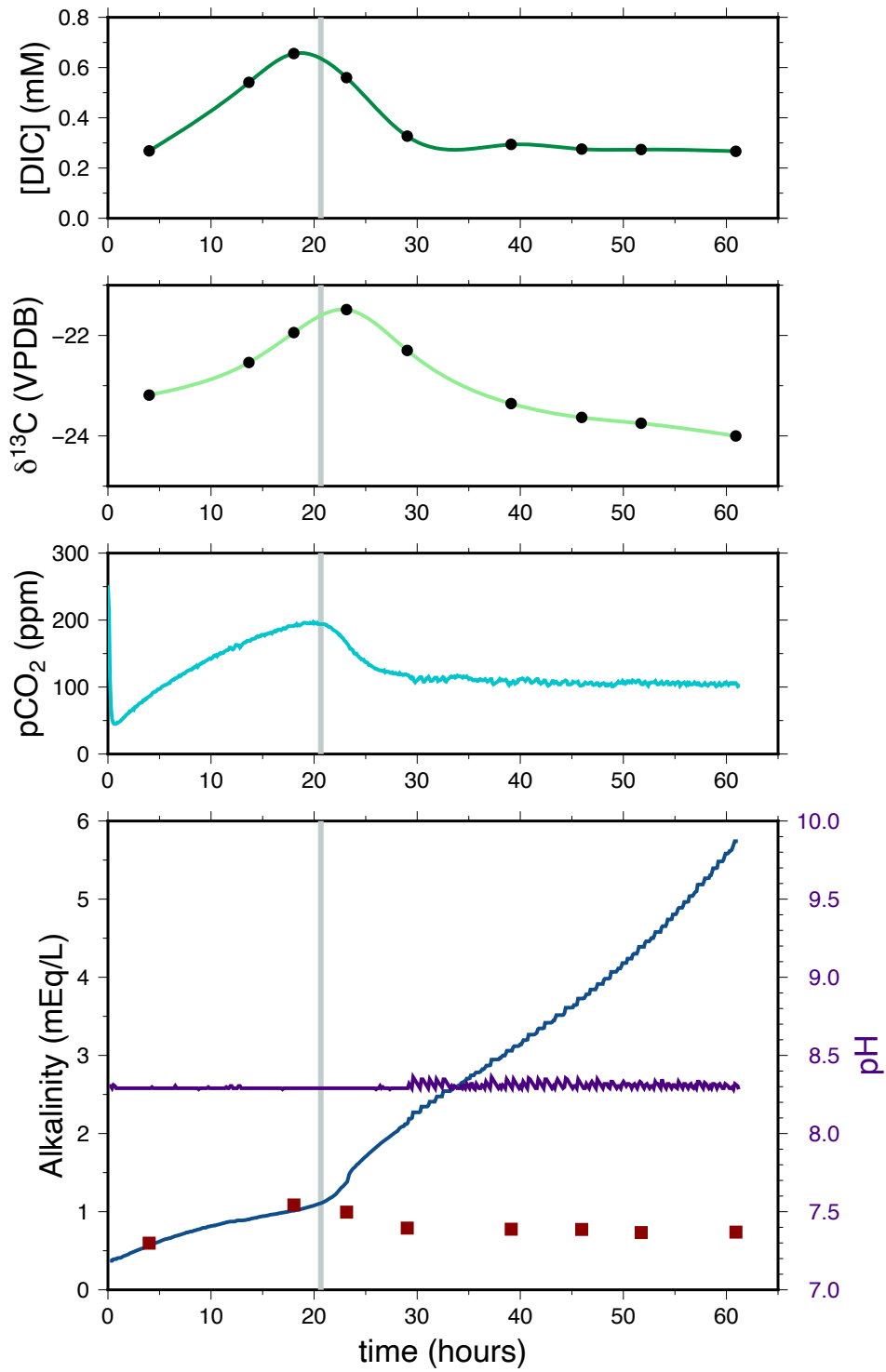


Figure 20: CA6, [NaCl] = 0.52 M, salinity = 35 g/kg

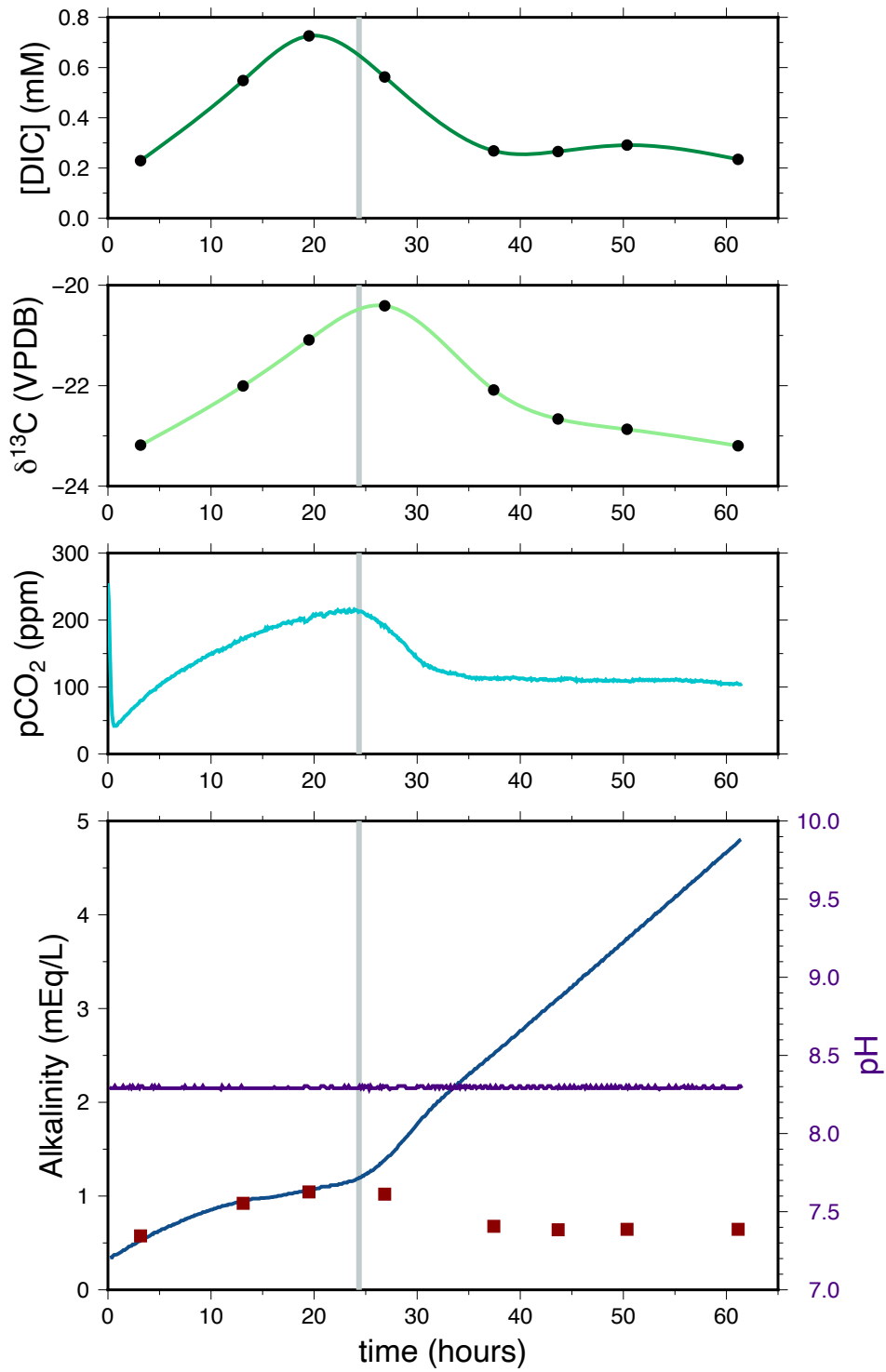


Figure 21: CA7, [NaCl] = 0.26 M, salinity = 20 g/kg

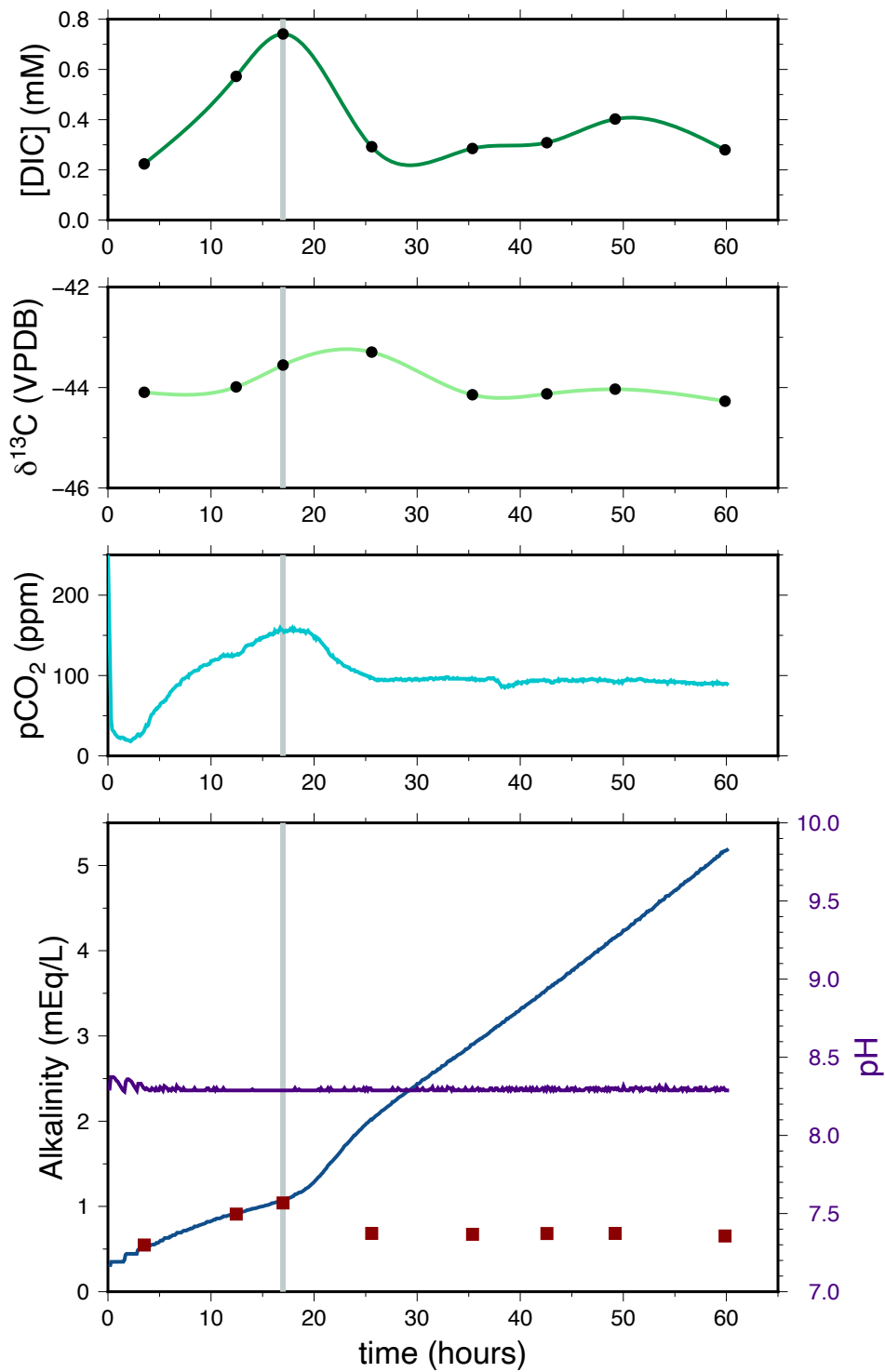


Figure 22: CA9, $[\text{NaCl}] = 0.95 \text{ M}$, salinity = 60 g/kg

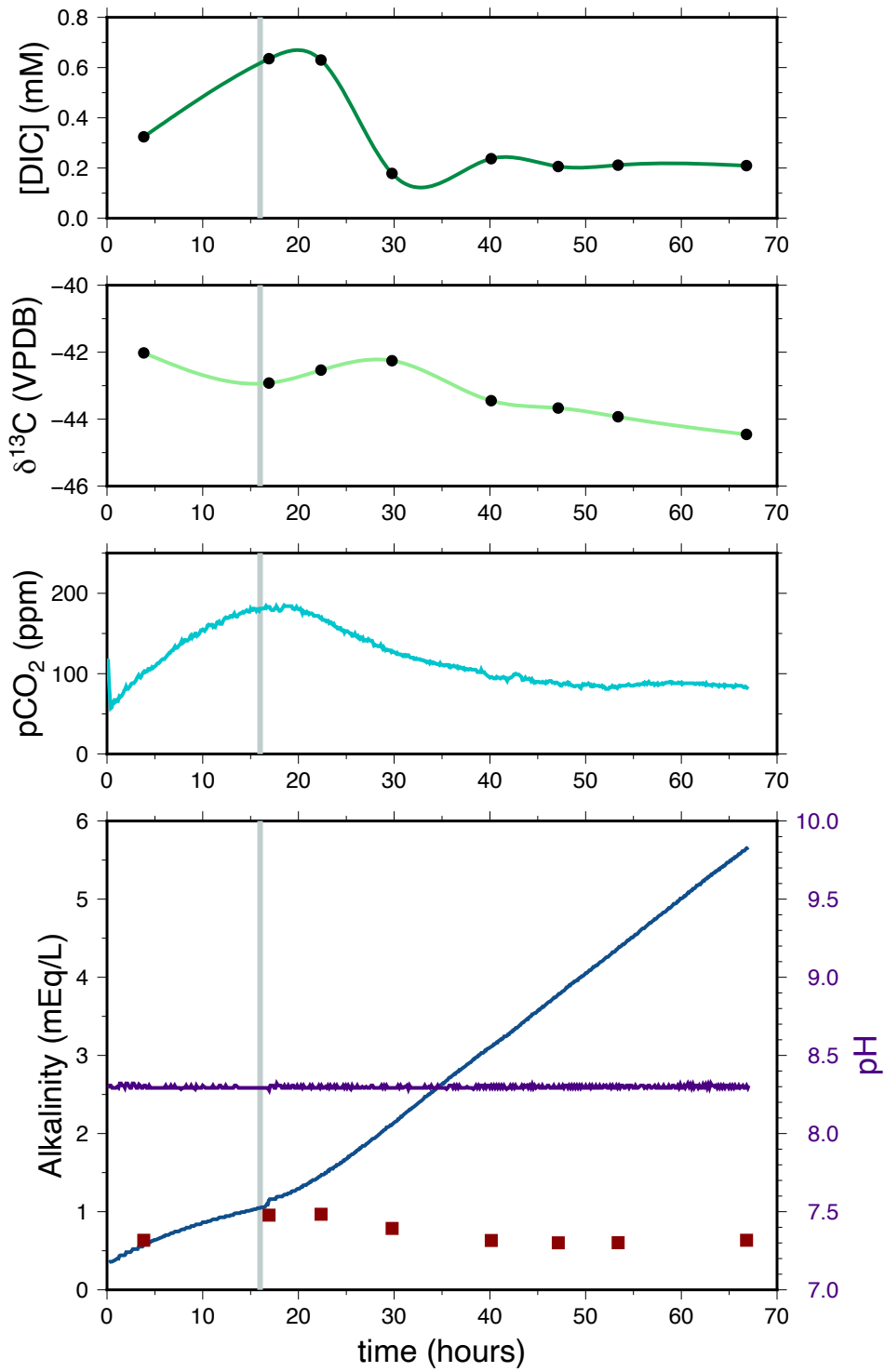


Figure 23: CA12, $[\text{NaCl}] = 0.69 \text{ M}$, salinity = 45 g/kg

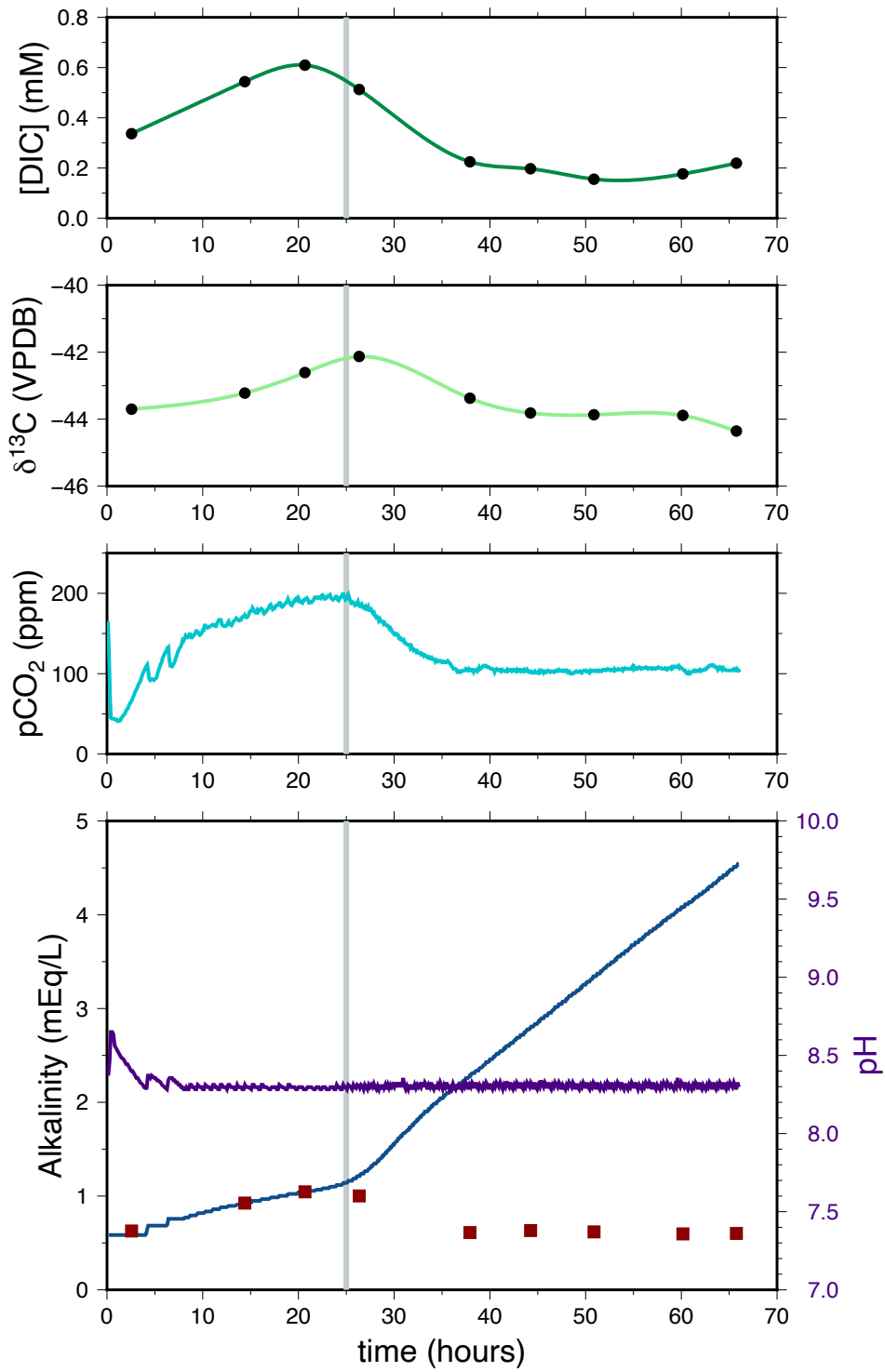


Figure 24: CA13, [NaCl] = 1.03 M, salinity = 65 g/kg

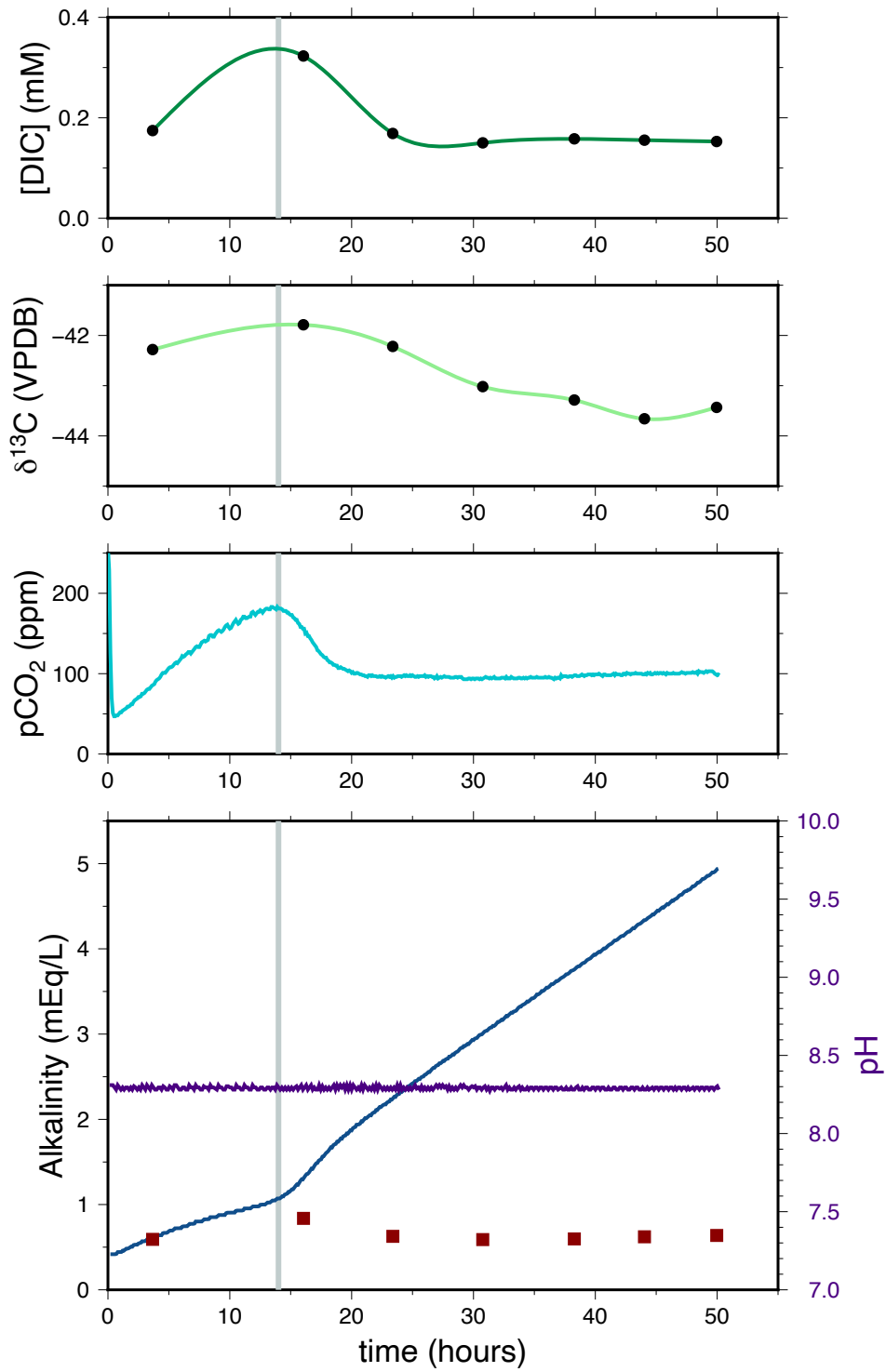


Figure 25: CA14, $[\text{NaCl}] = 0.18 \text{ M}$, salinity = 15 g/kg

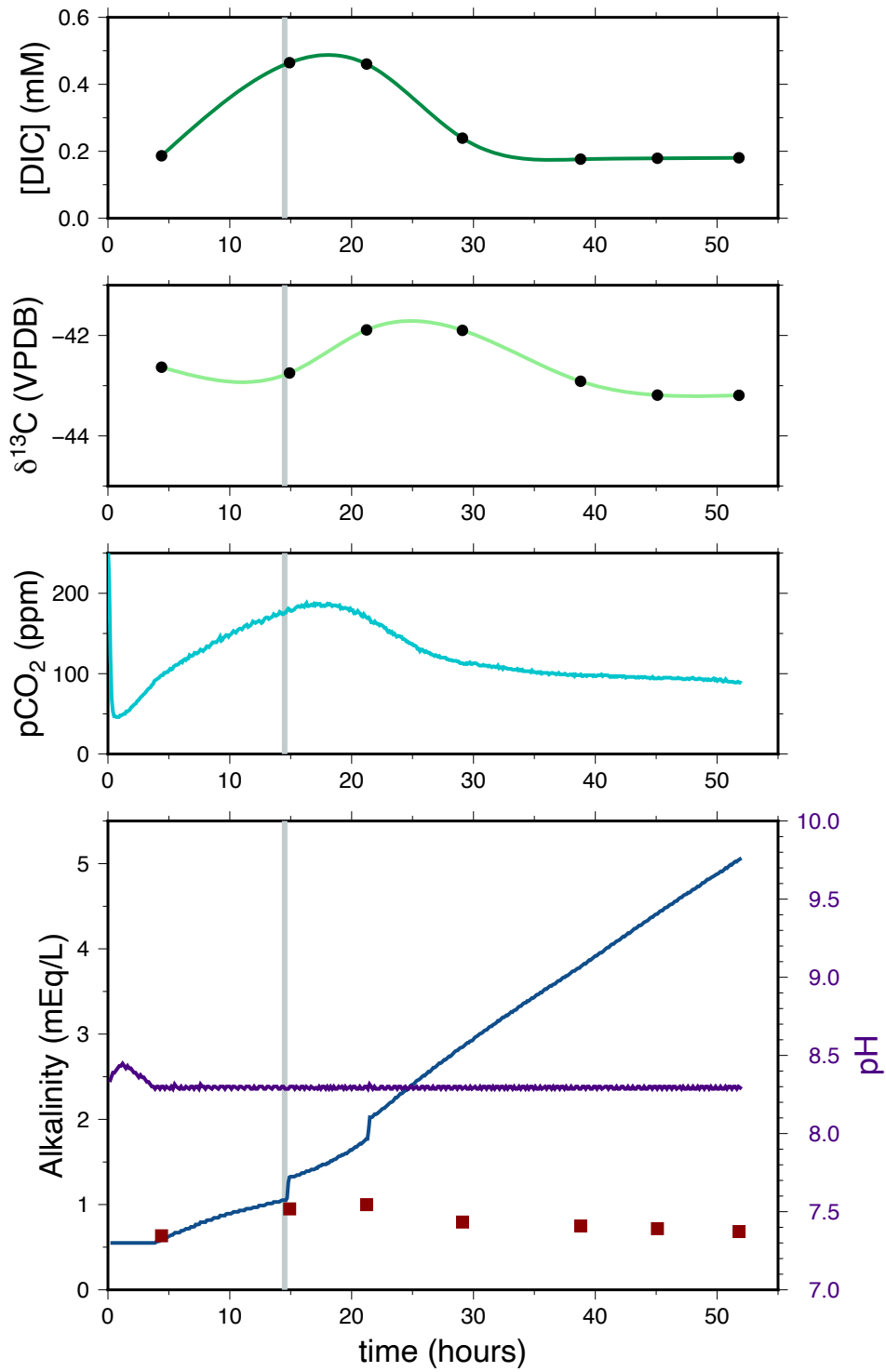


Figure 26: CA15, $[\text{NaCl}] = 0.35 \text{ M}$, salinity = 25 g/kg

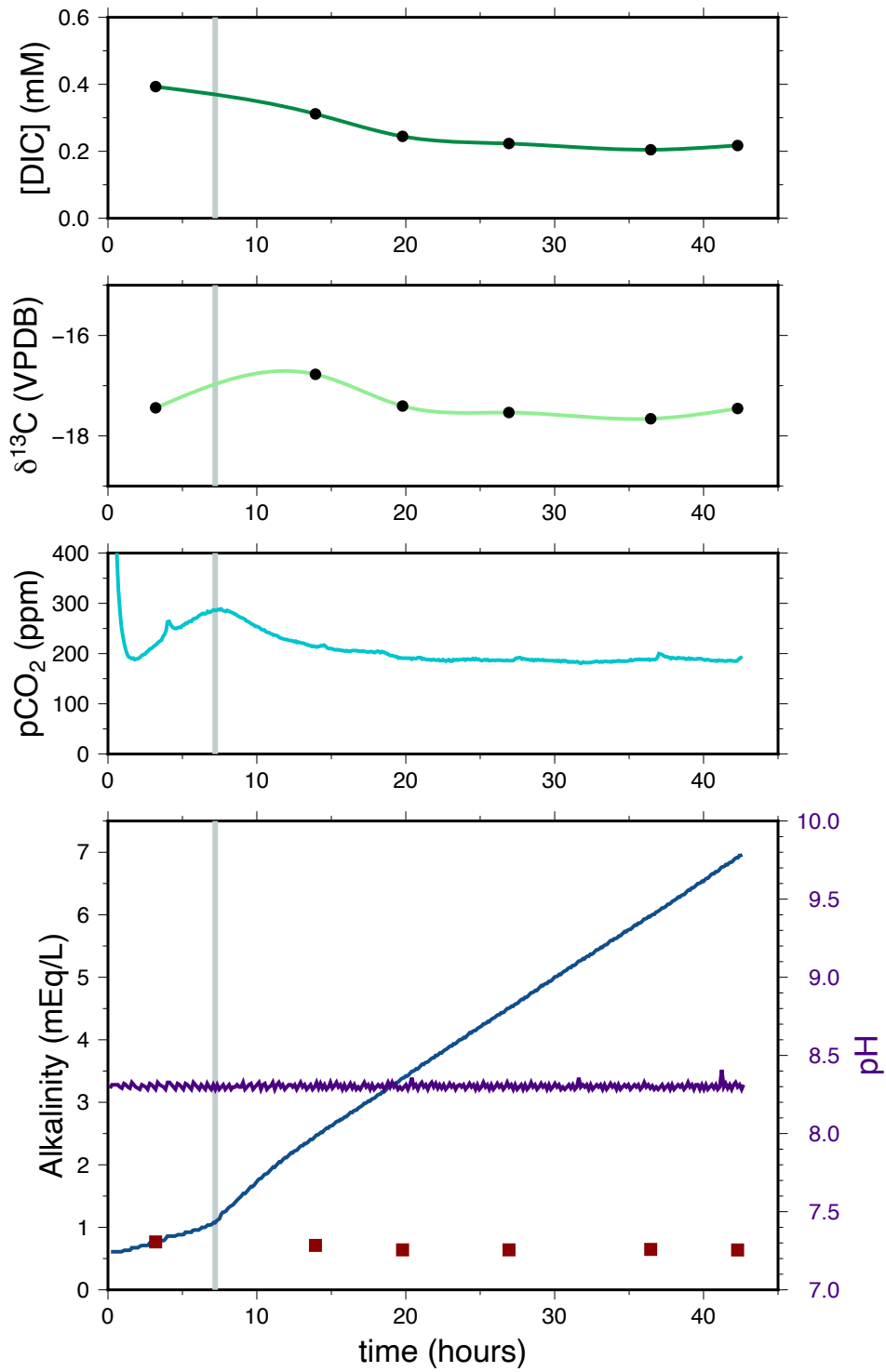


Figure 27: CA18, $[\text{NaCl}] = \sim 0 \text{ M}$, salinity = 3.5 g/kg

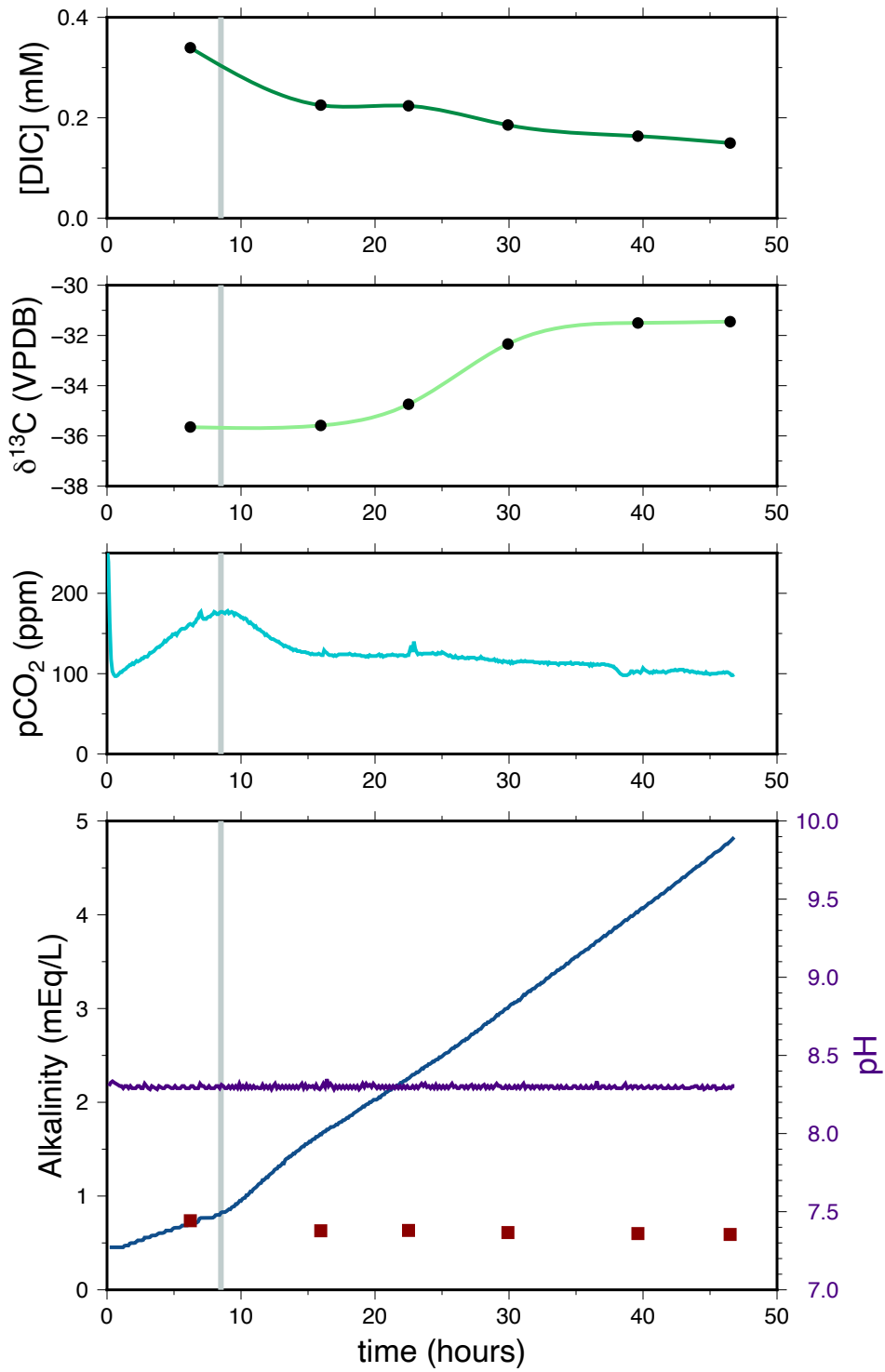


Figure 28: CA20, [NaCl] = ~0 M, salinity = 3.5 g/kg

2 SEM images

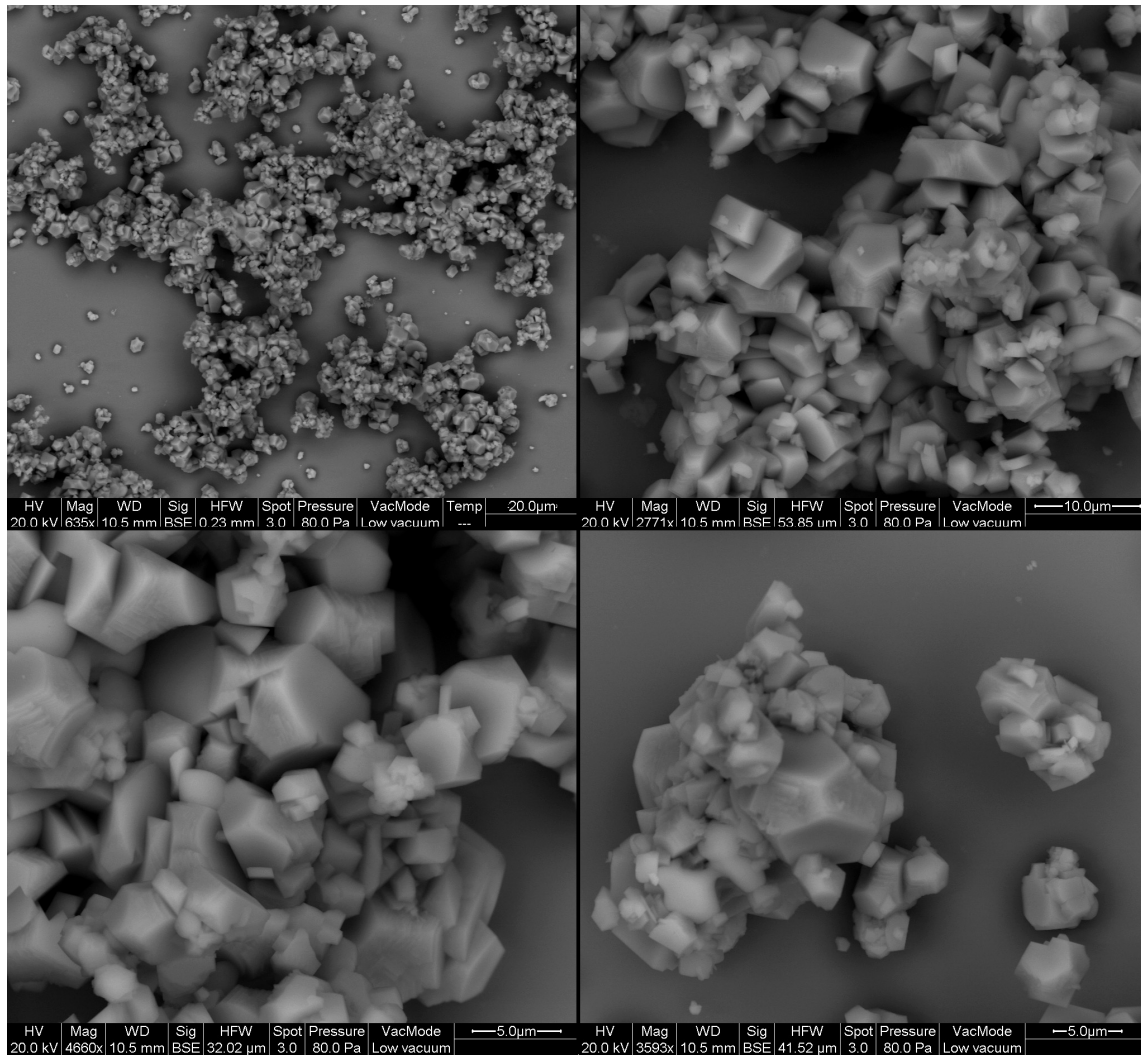


Figure 29: S2, $[\text{NaCl}] = 0.52 \text{ M}$, salinity = 35 g/kg

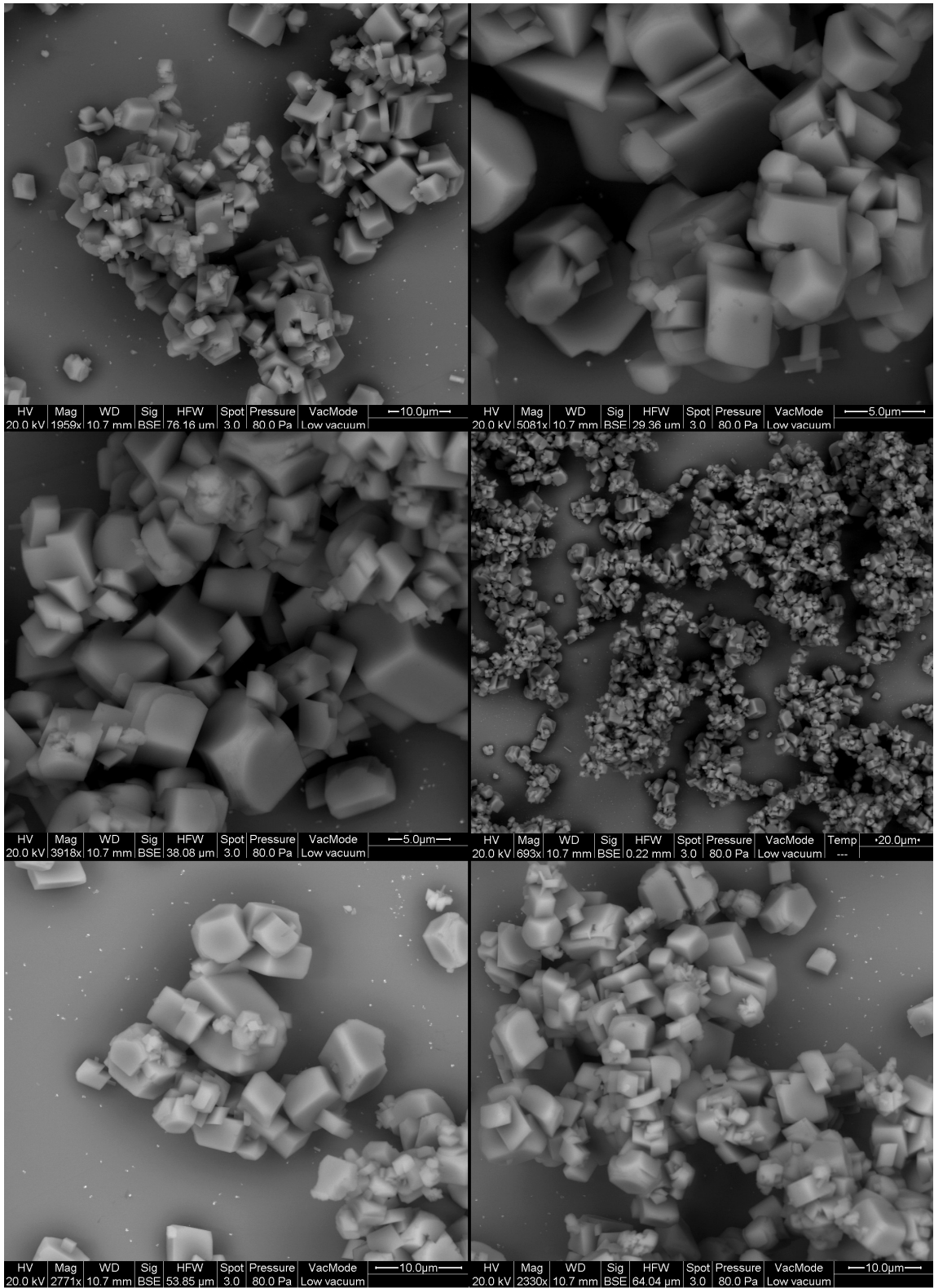


Figure 30: S3, [NaCl] = 0.52 M, salinity = 35 g/kg

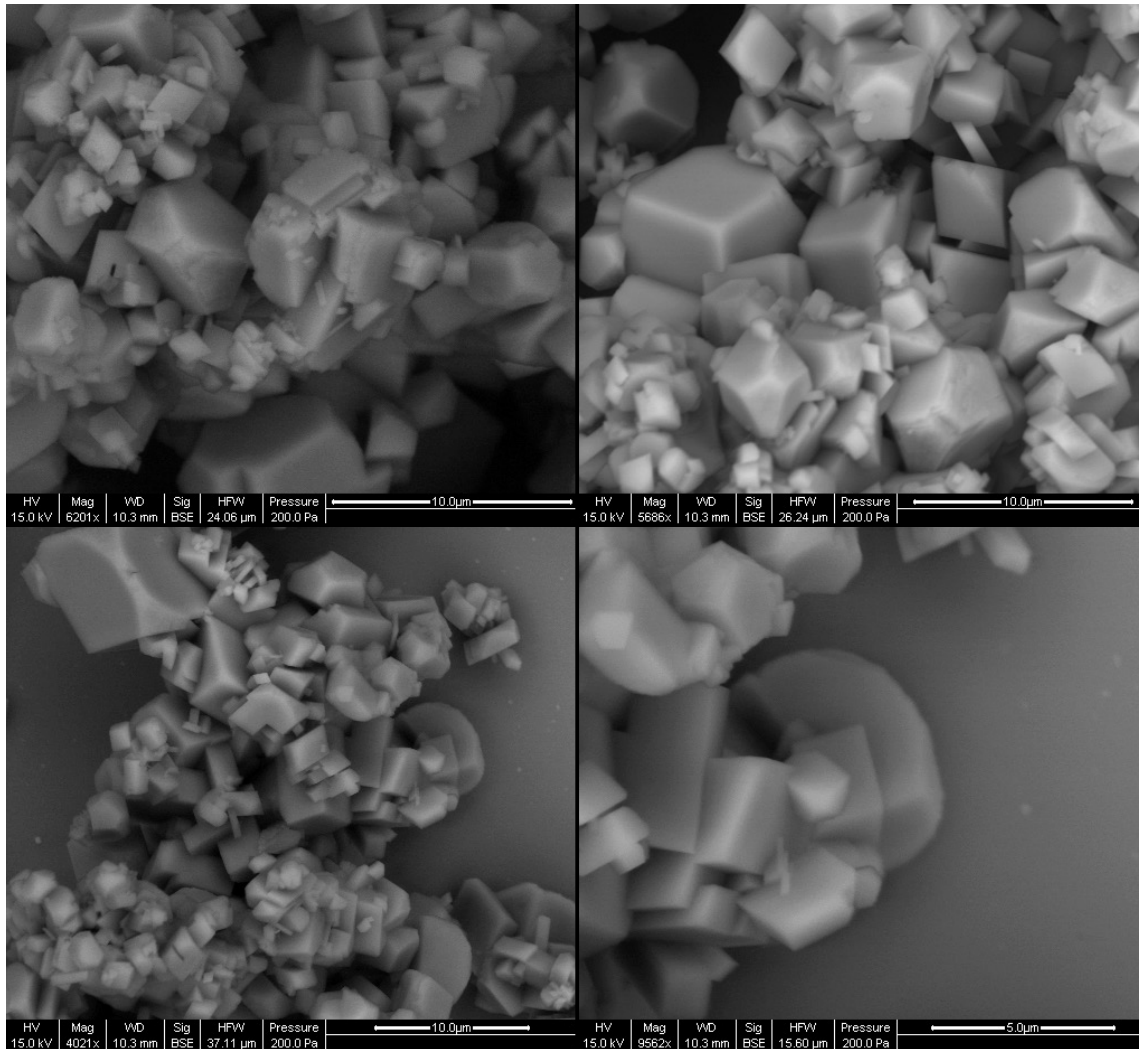


Figure 31: S4, $[\text{NaCl}] = 0.18 \text{ M}$, salinity = 15 g/kg

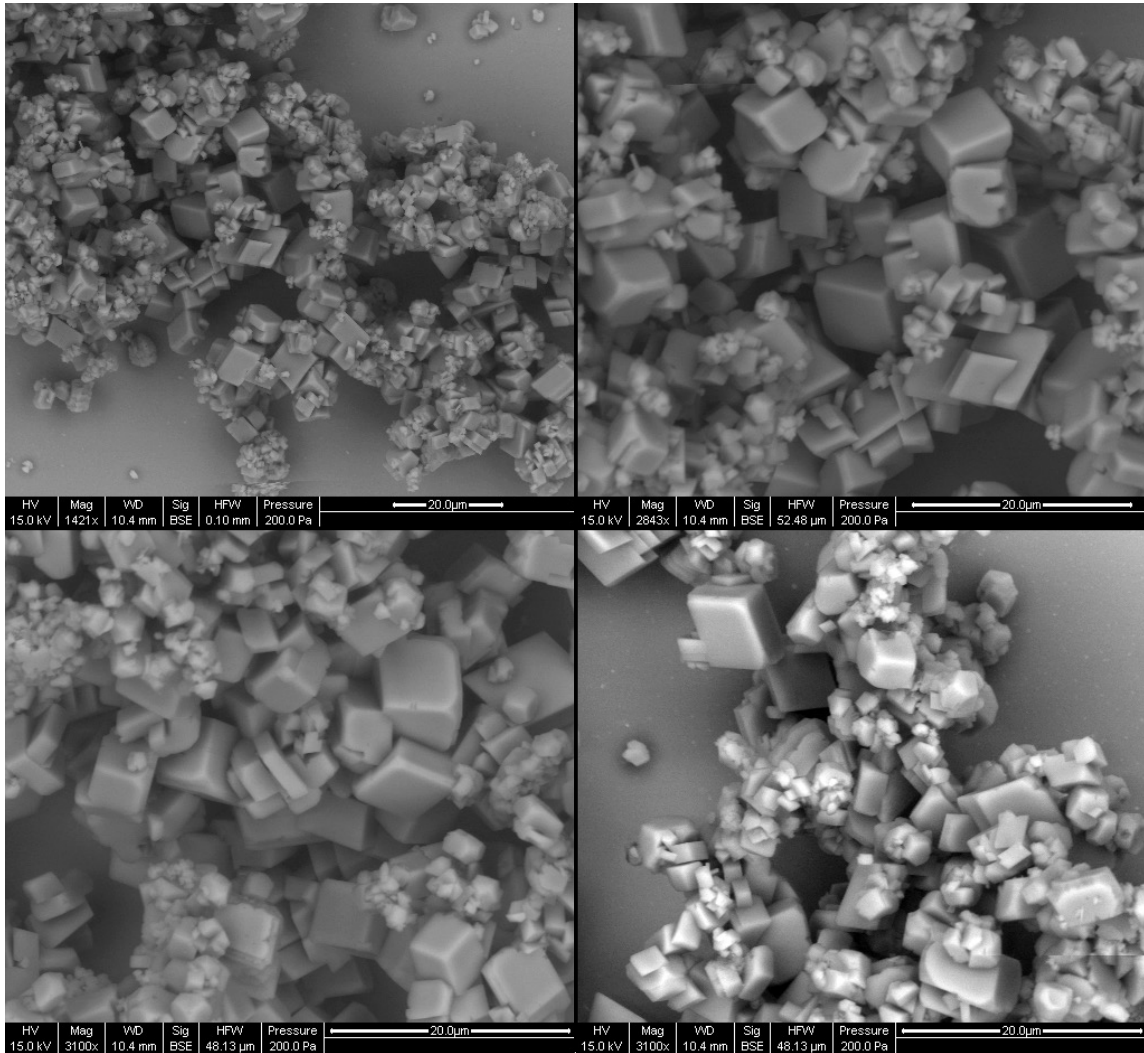


Figure 32: S5, [NaCl] = 0.35 M, salinity = 25 g/kg

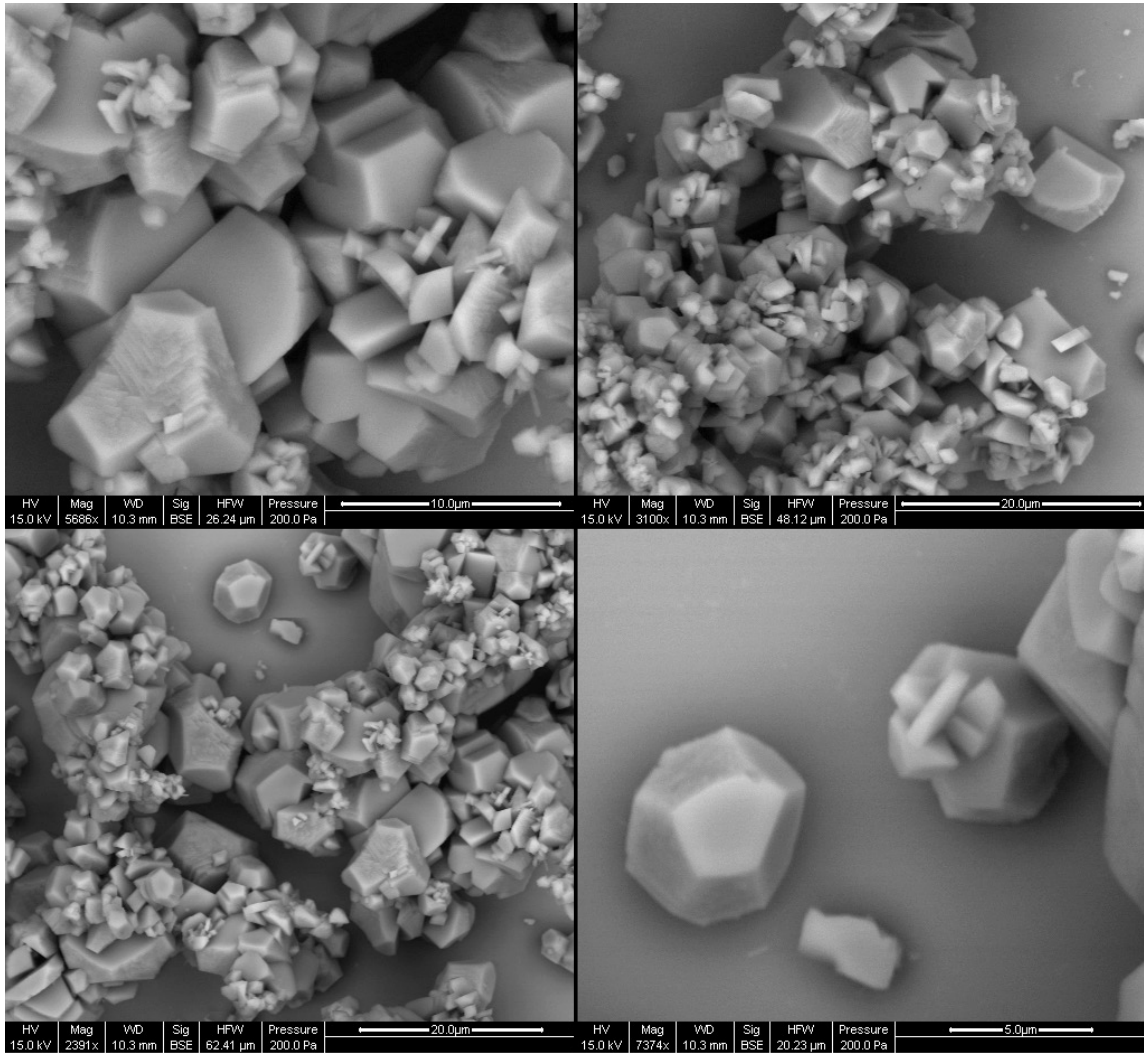


Figure 33: S6, $[\text{NaCl}] = \sim 0 \text{ M}$, salinity = 3.5 g/kg

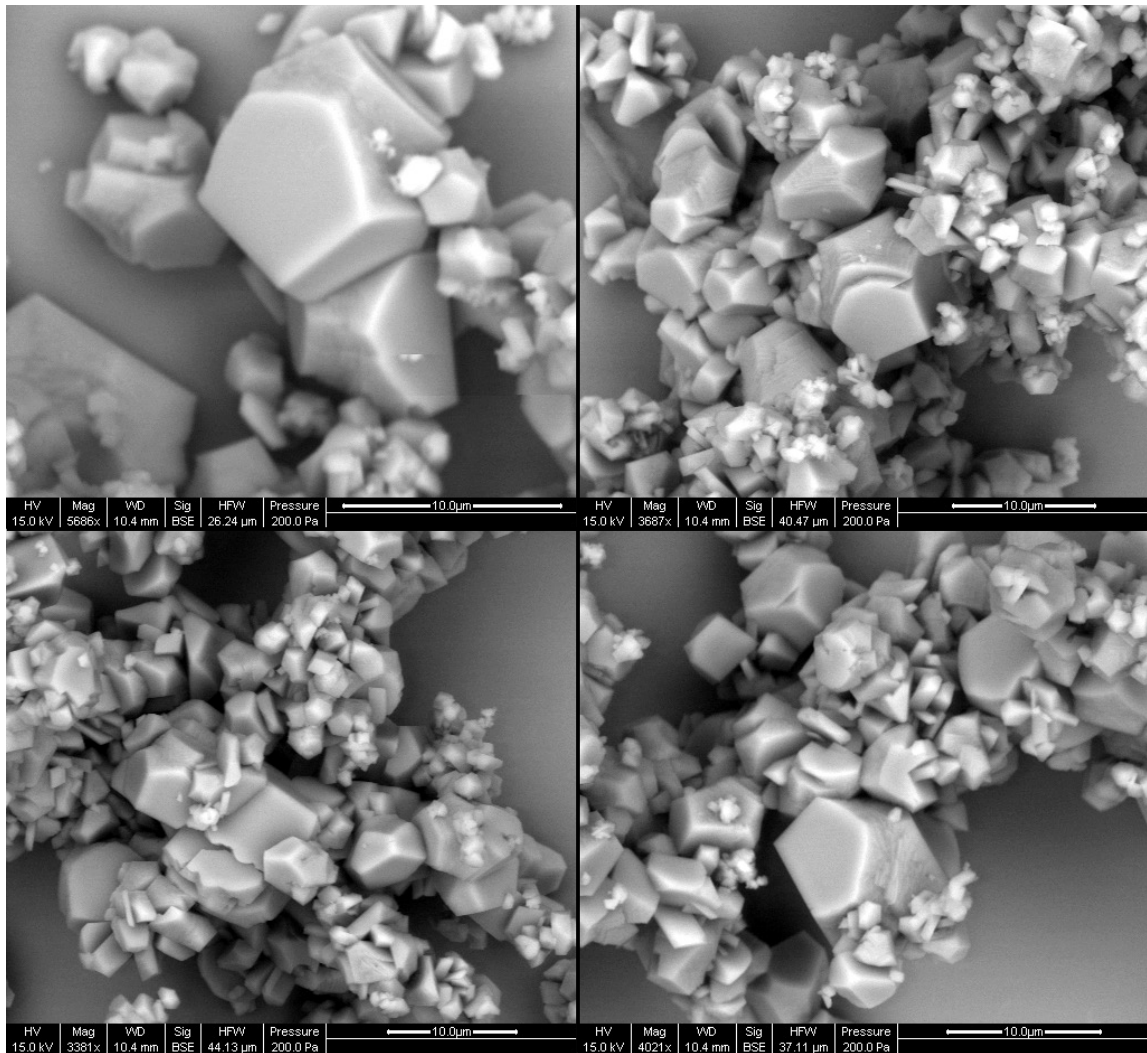


Figure 34: S7, [NaCl] = 0.18 M, salinity = 15 g/kg

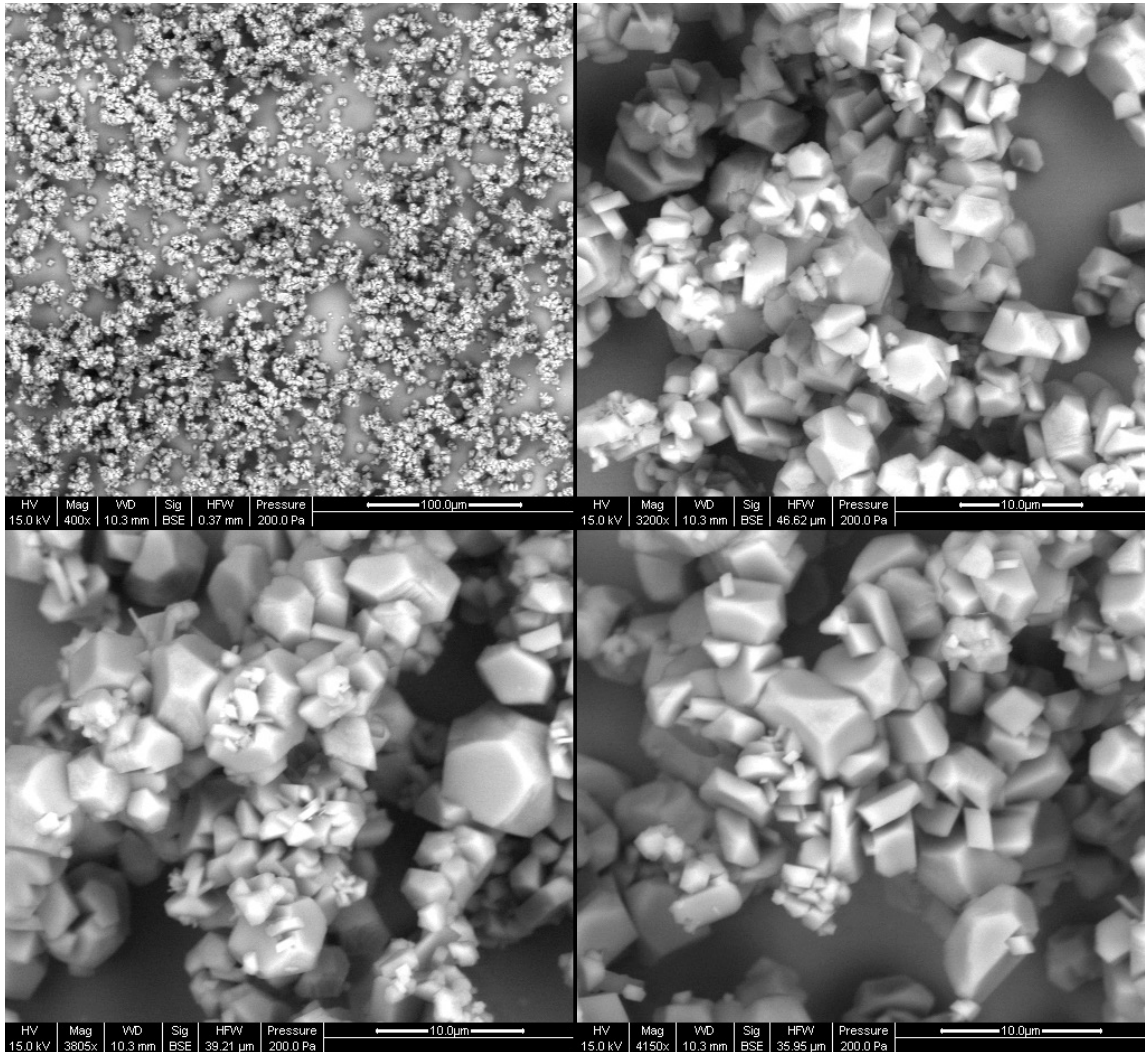


Figure 35: S8, $[\text{NaCl}] = \sim 0 \text{ M}$, salinity = 3.5 g/kg

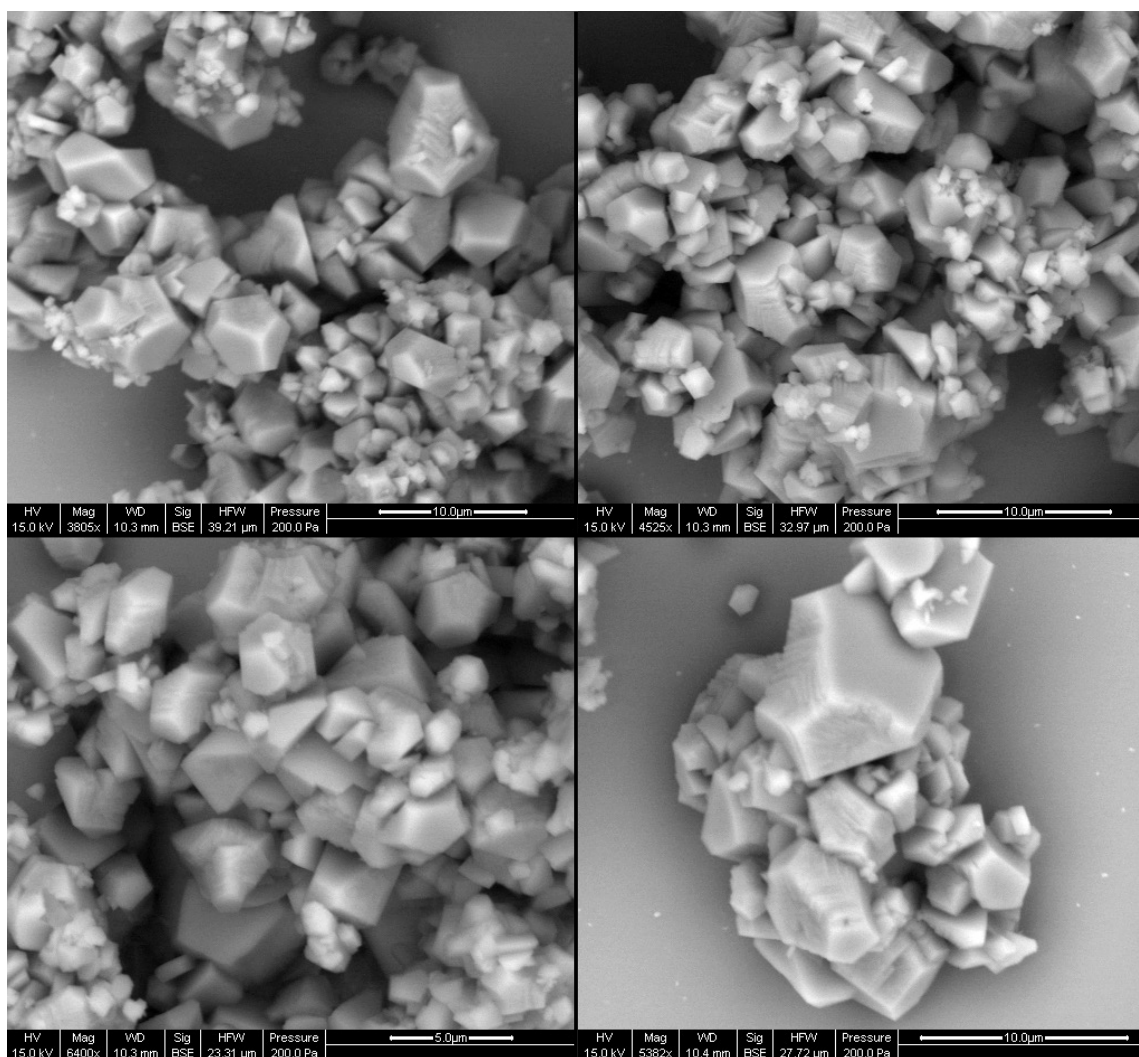


Figure 36: S9, [NaCl] = 0.35 M, salinity = 25 g/kg

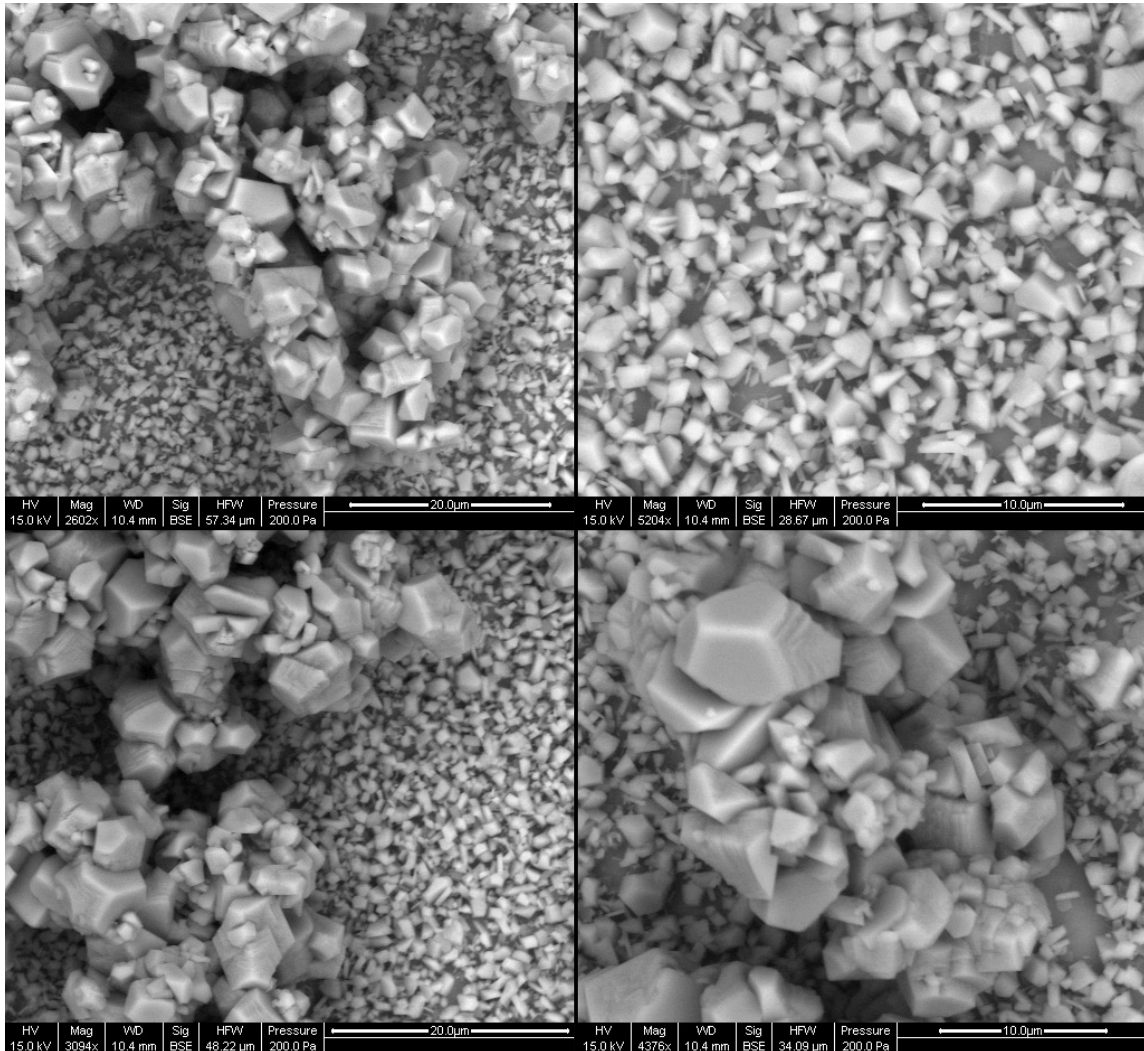


Figure 37: S10, [NaCl] = 0.69 M, salinity = 45 g/kg

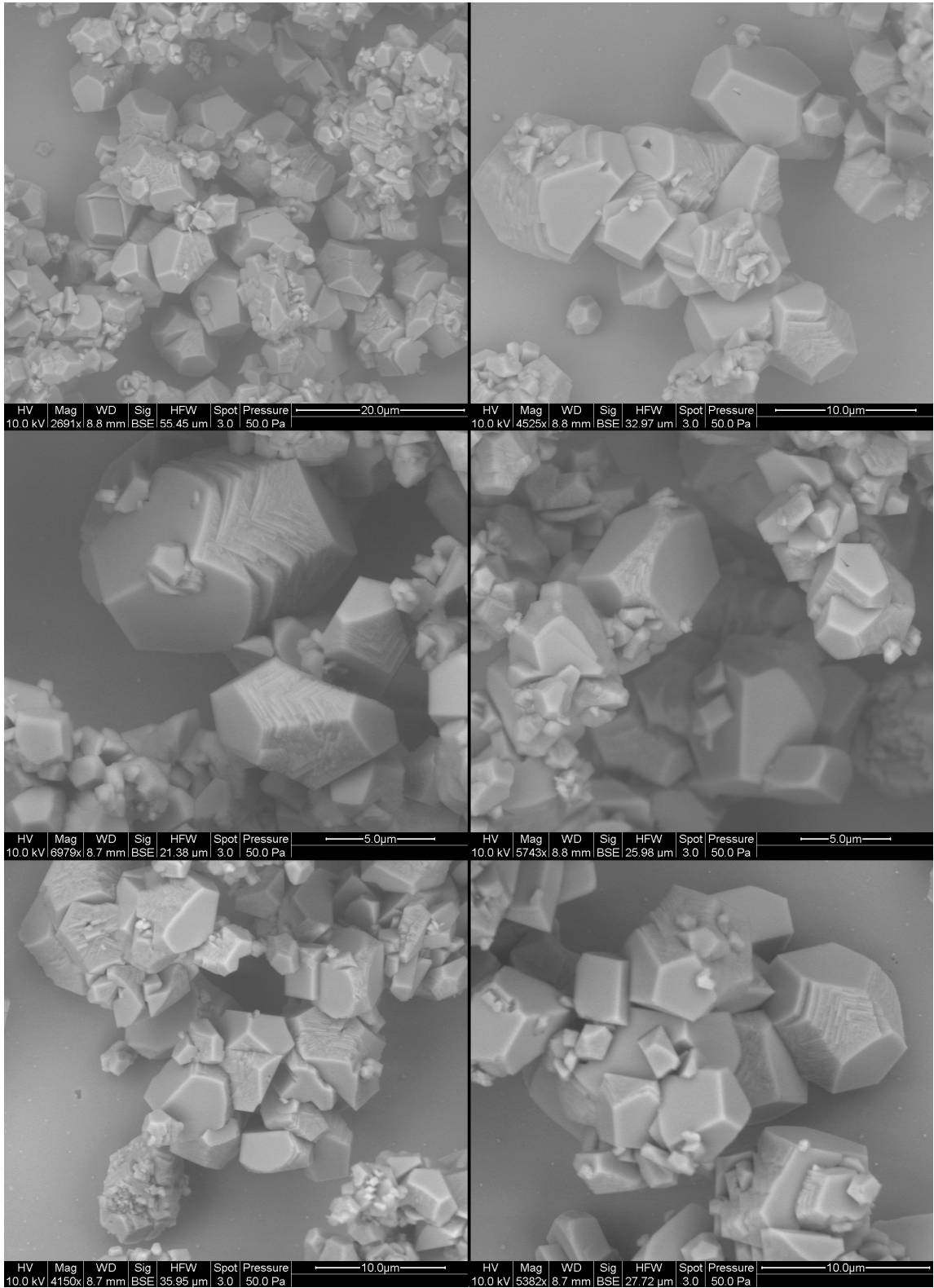


Figure 38: S11, [NaCl] = 0.35 M, salinity = 25 g/kg

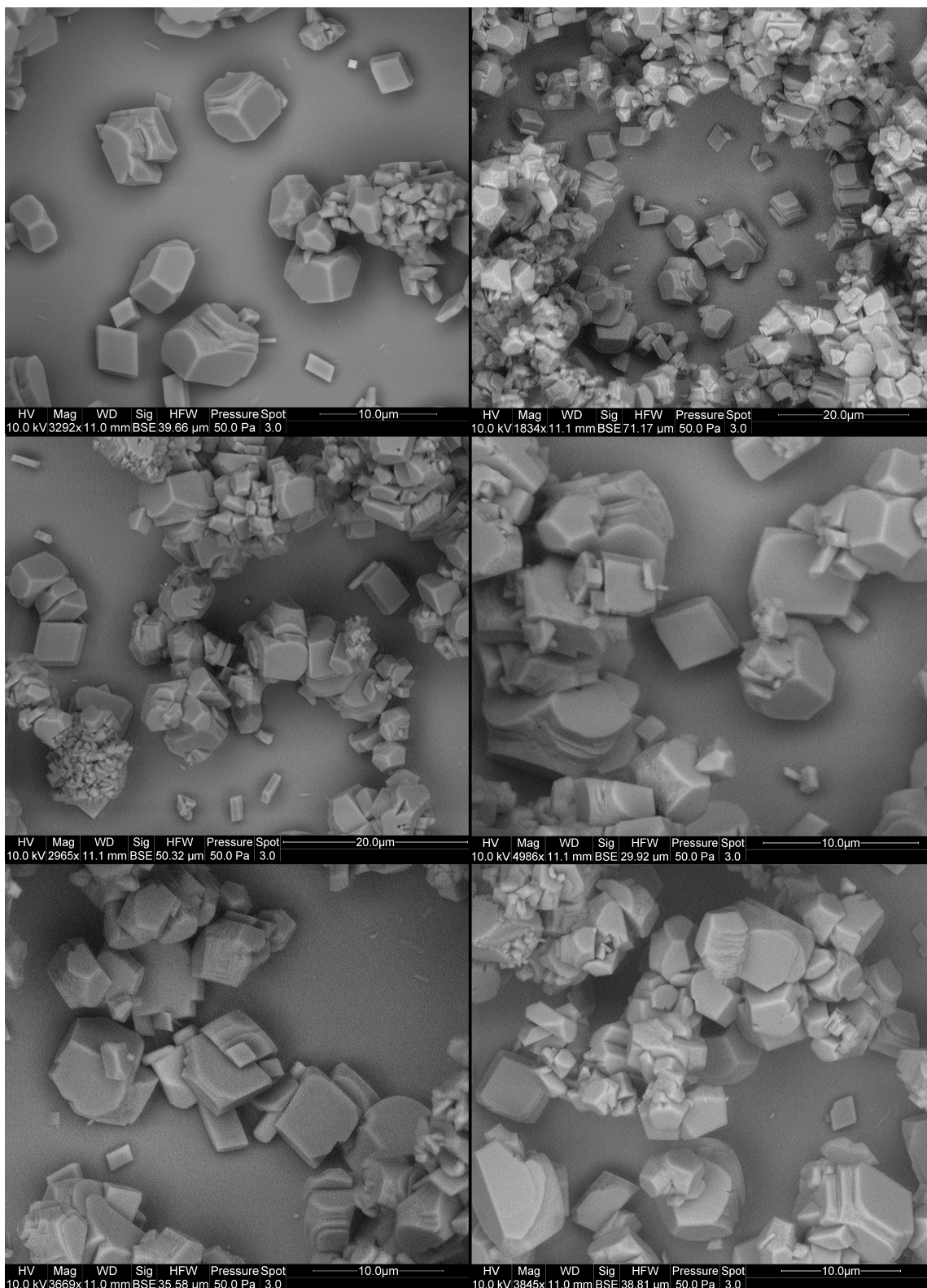


Figure 39: S12, [NaCl] = 1.37 M, salinity = 85 g/kg

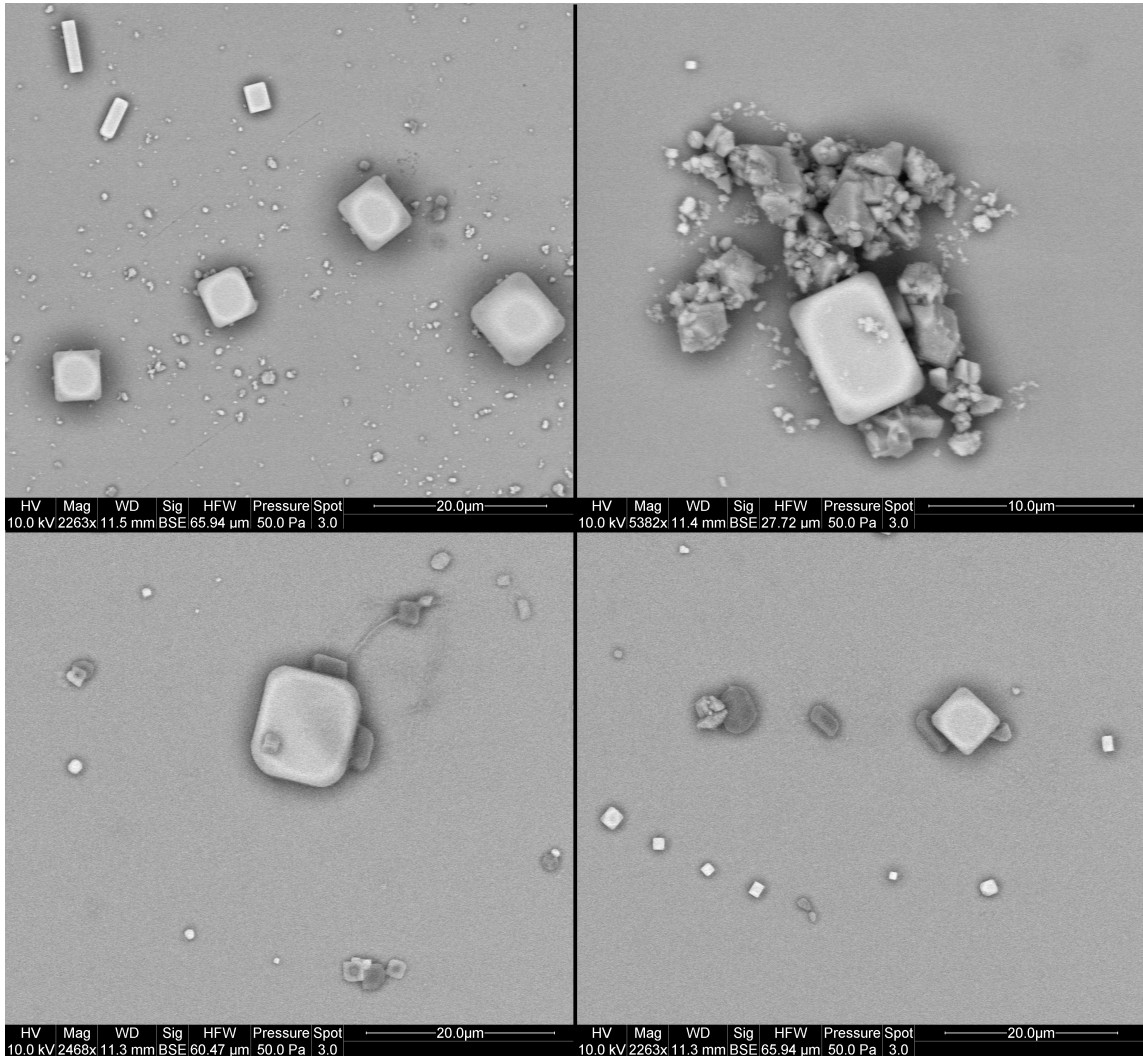


Figure 40: S13, [NaCl] = 1.03 M, salinity = 65 g/kg

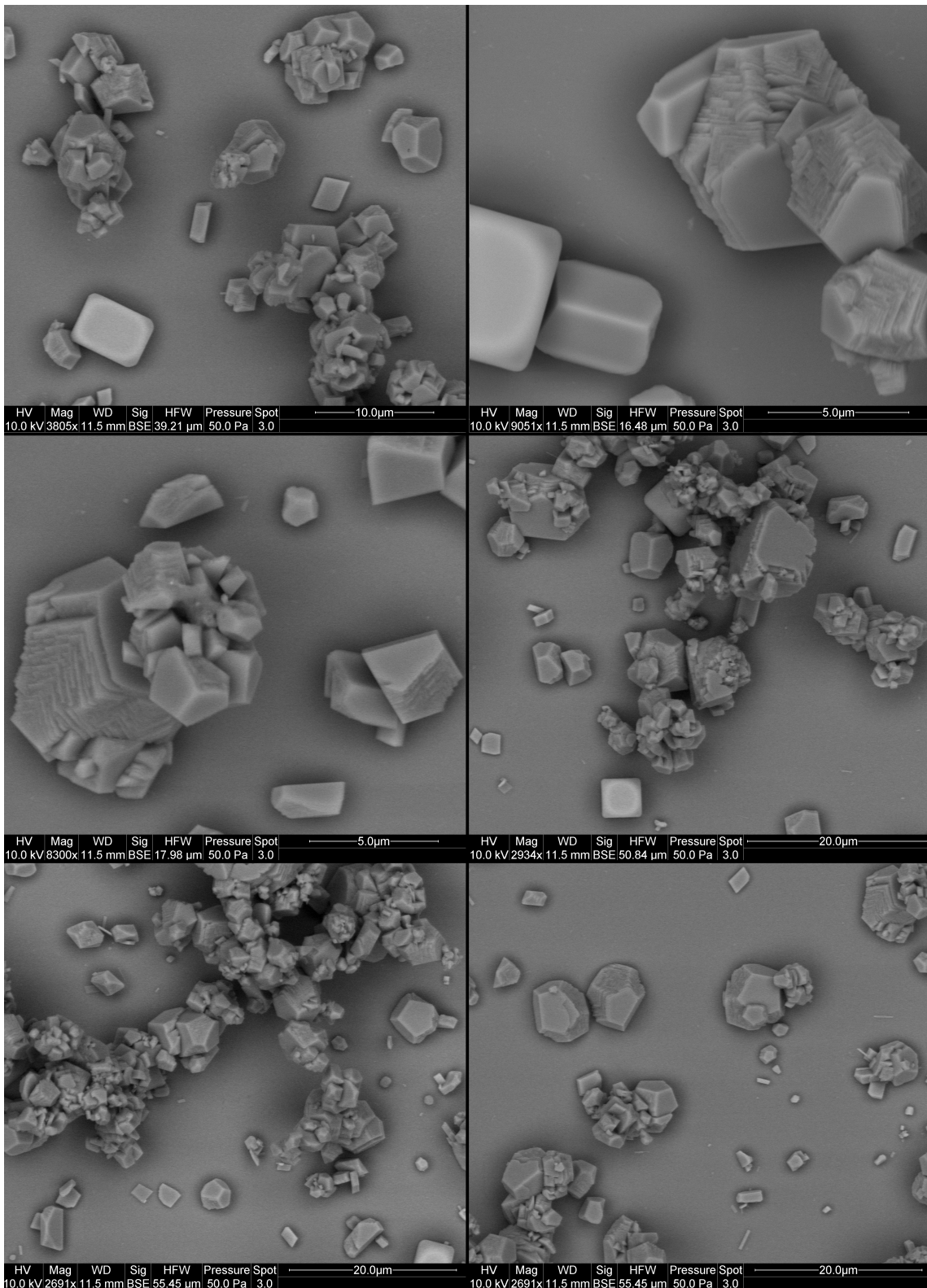


Figure 41: S14, $[\text{NaCl}] = 0.86 \text{ M}$, salinity = 55 g/kg

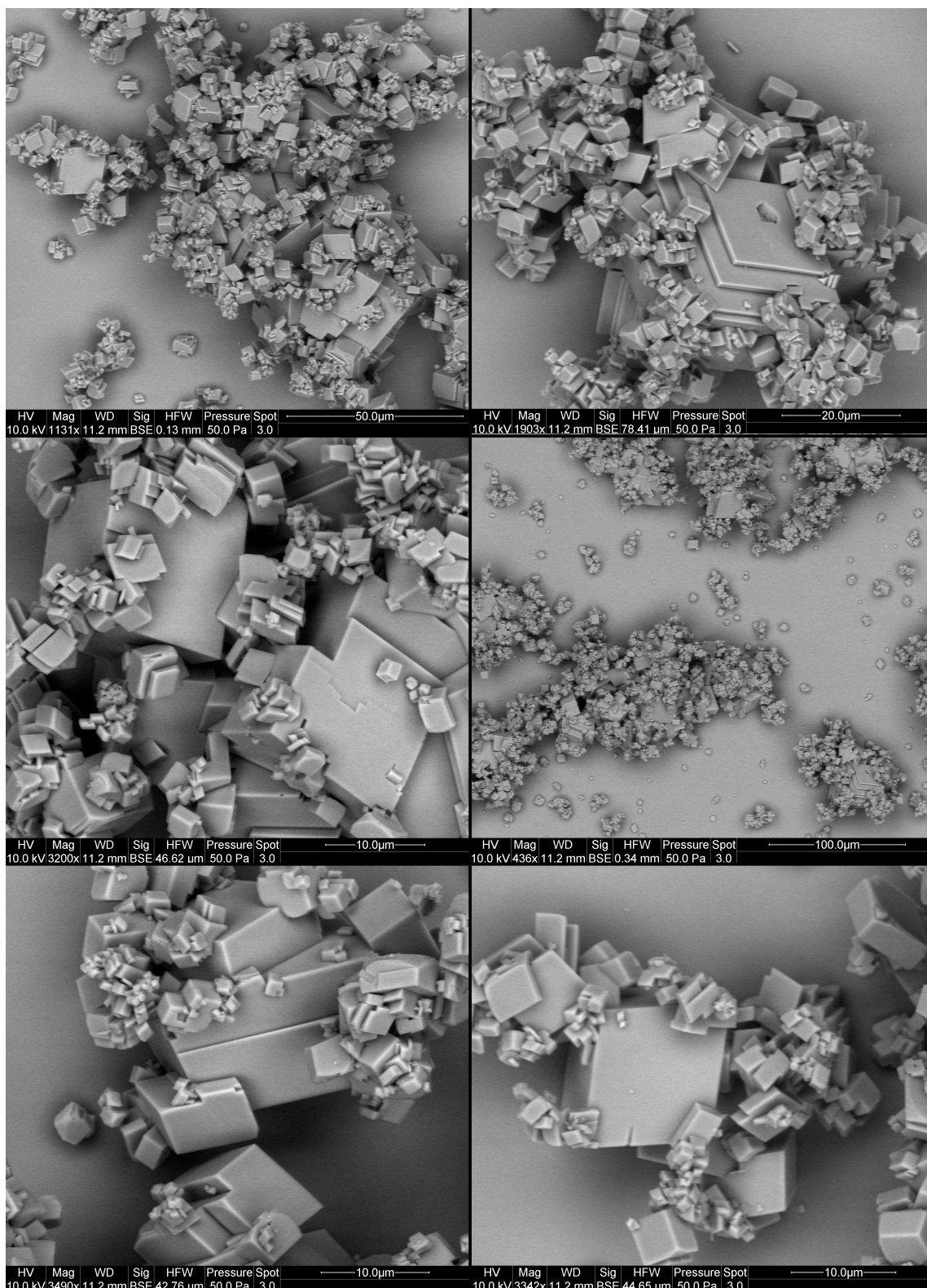


Figure 42: S15, [NaCl] = 1.20 M, salinity = 75 g/kg

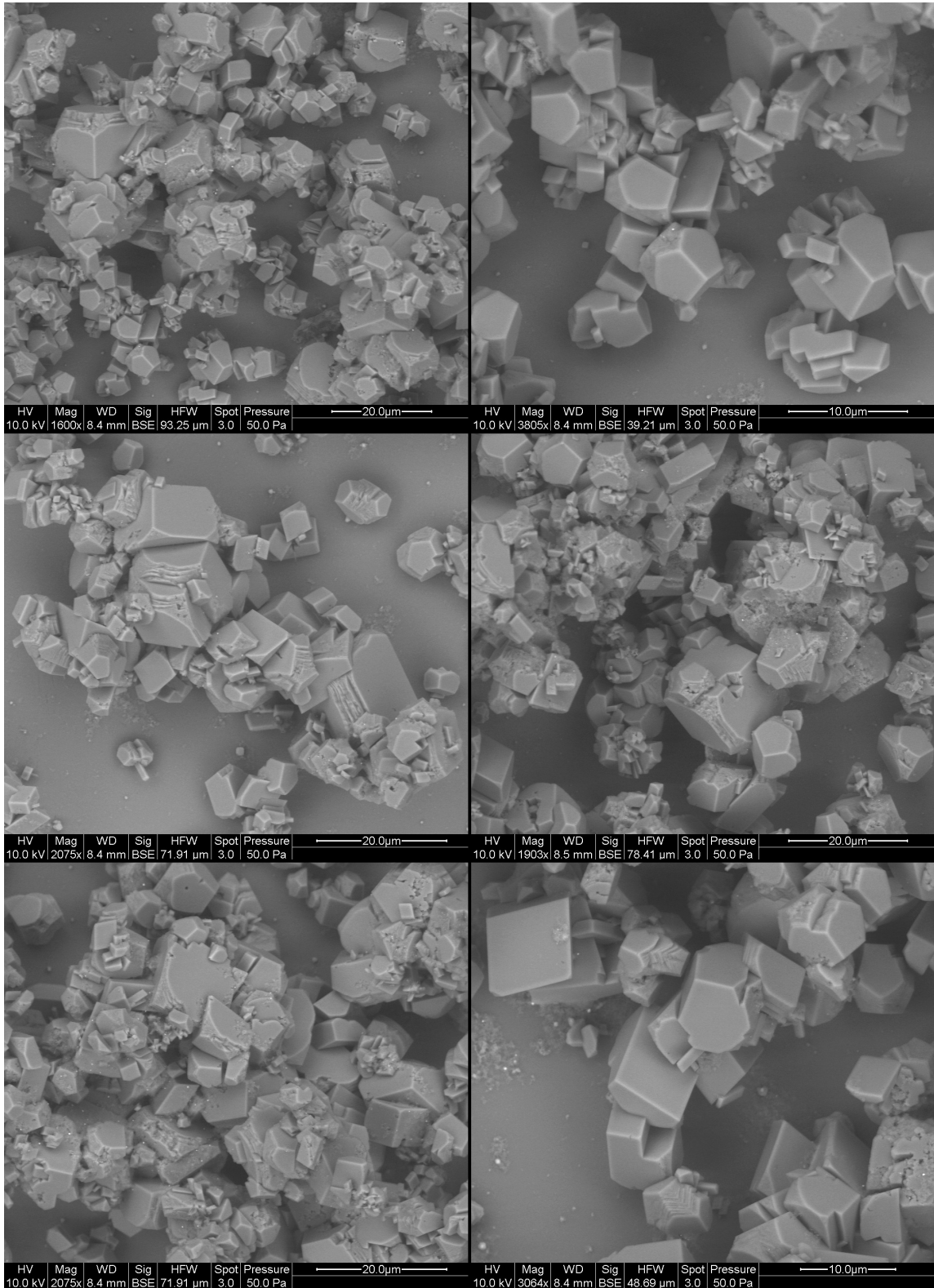


Figure 43: CA1, $[\text{NaCl}] = 0.52 \text{ M}$, salinity = 35 g/kg

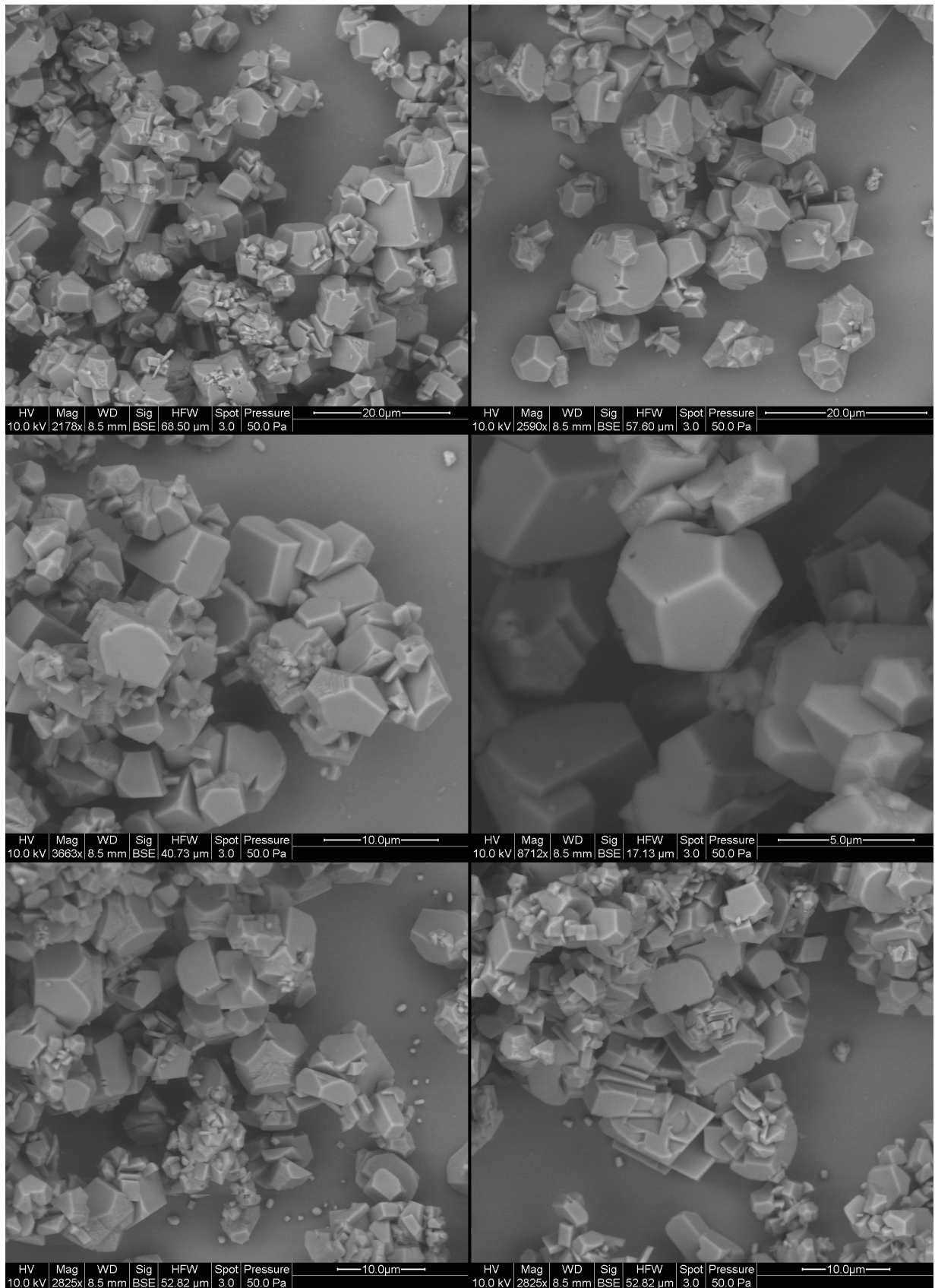


Figure 44: CA2, [NaCl] = 0.52 M, salinity = 35 g/kg

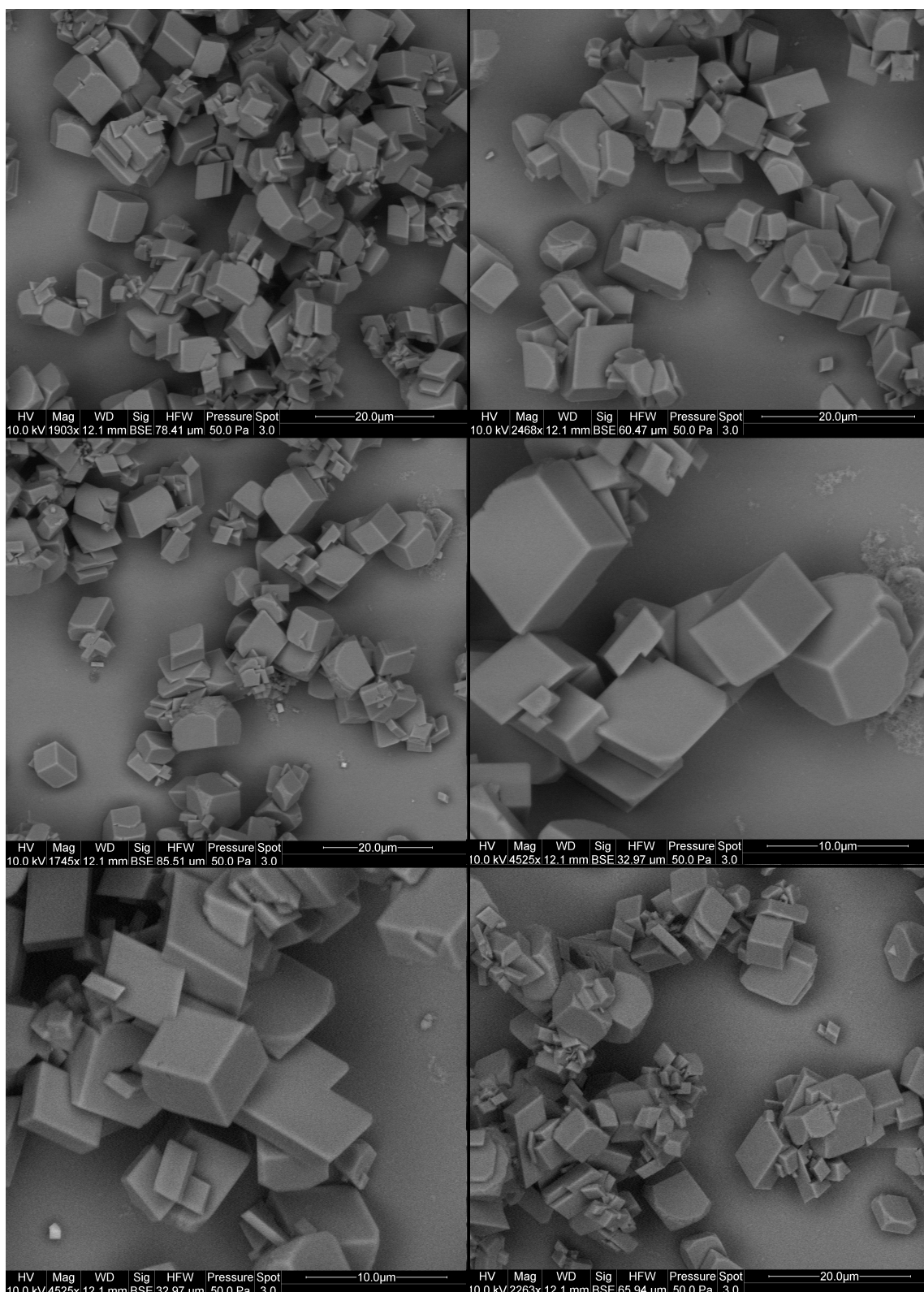


Figure 45: CA4, [NaCl] = \sim 0 M, salinity = 3.5 g/kg

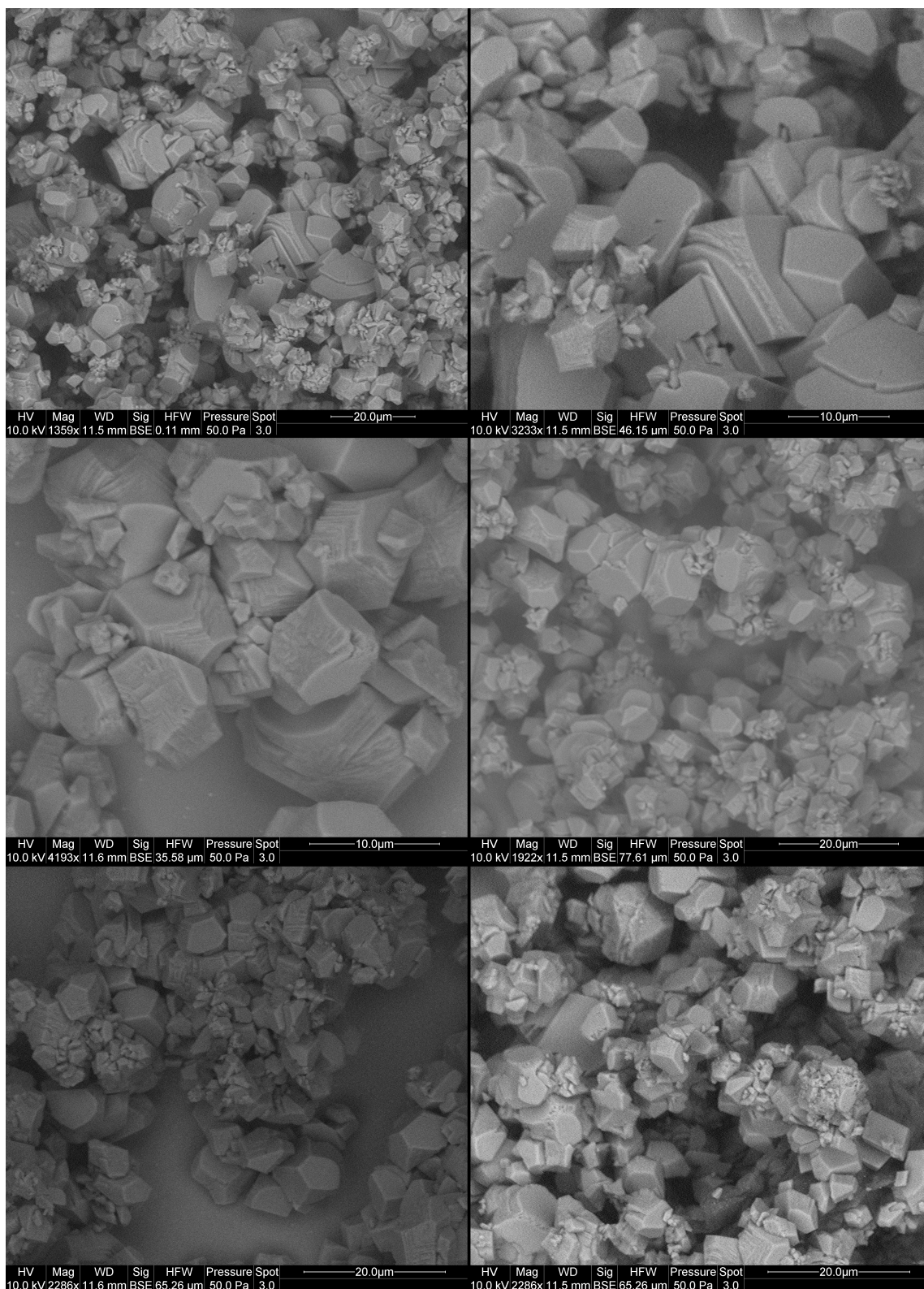


Figure 46: CA5, [NaCl] = 0.52 M, salinity = 35 g/kg

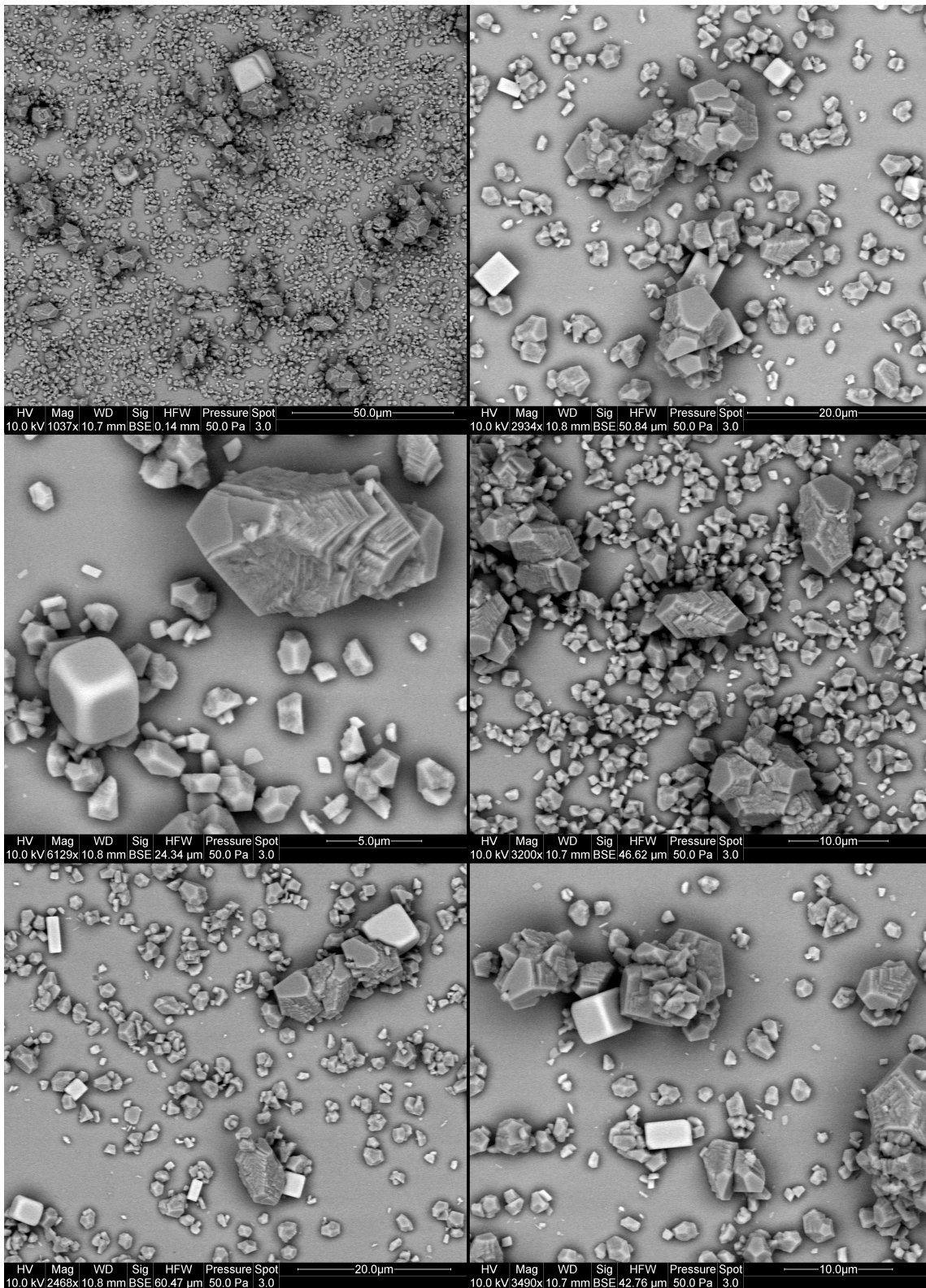


Figure 47: CA6, [NaCl] = 0.52 M, salinity = 35 g/kg

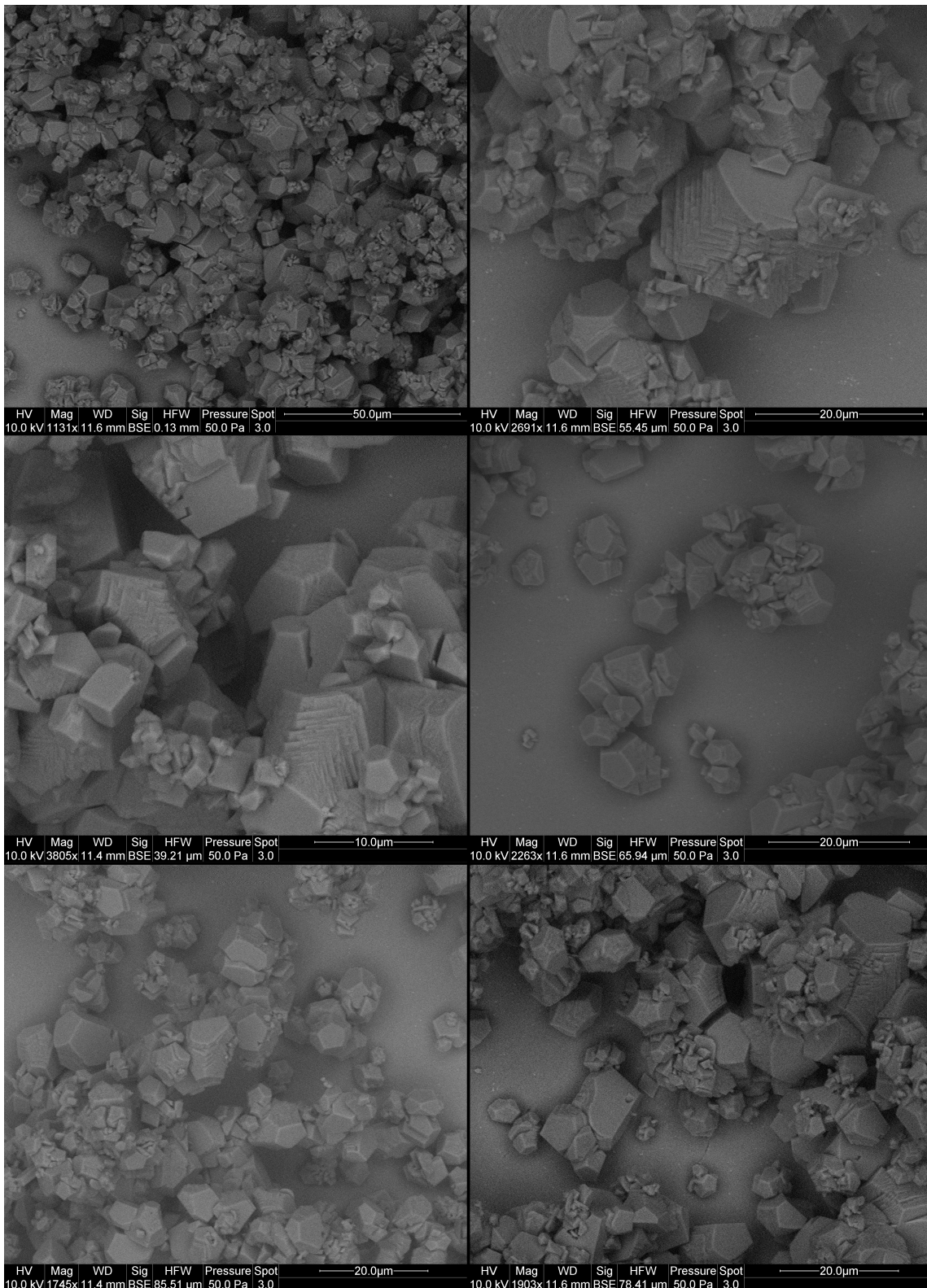


Figure 48: CA7, [NaCl] = 0.26 M, salinity = 20 g/kg

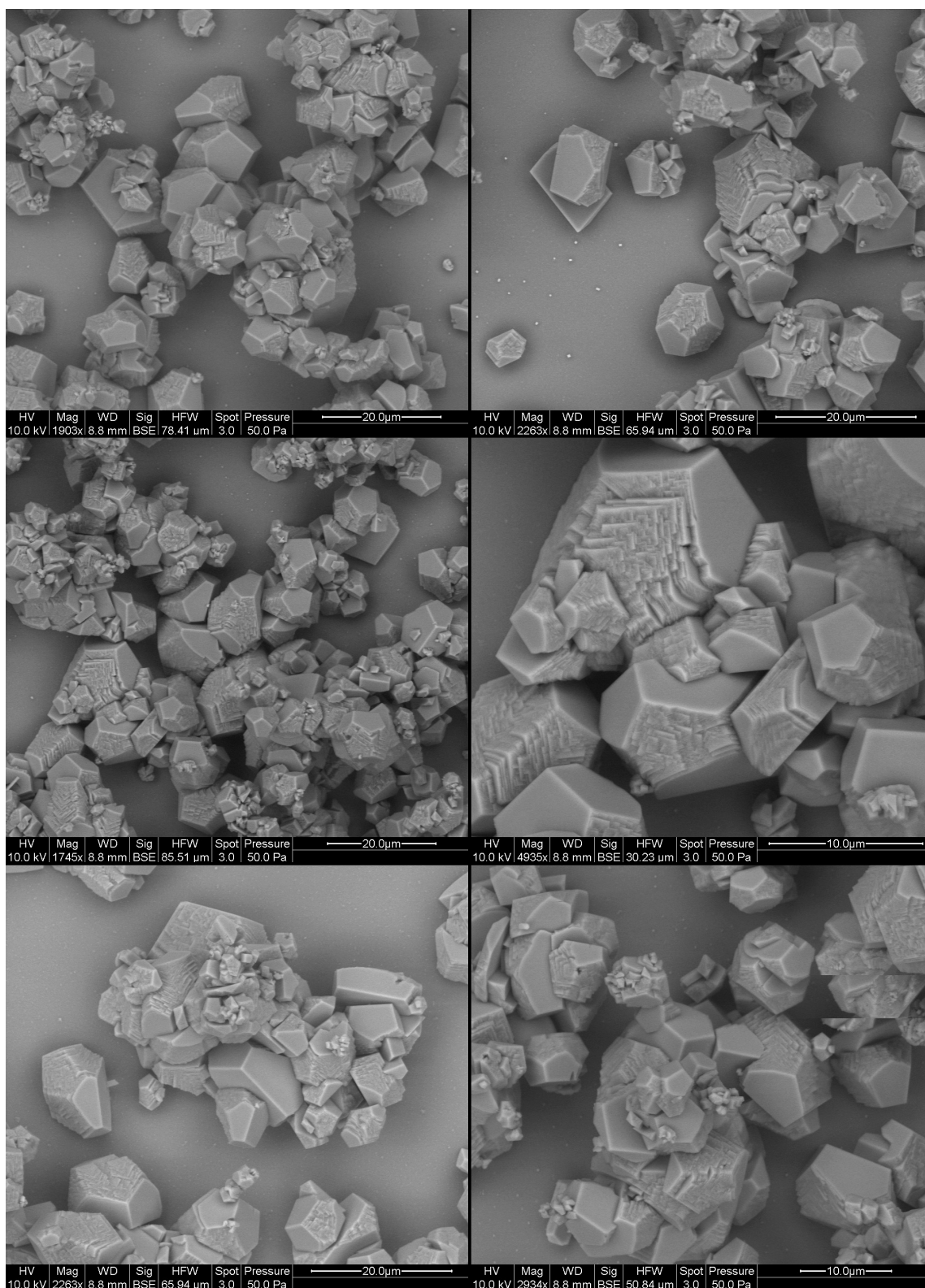


Figure 49: CA9, $[\text{NaCl}] = 0.95 \text{ M}$, salinity = 60 g/kg

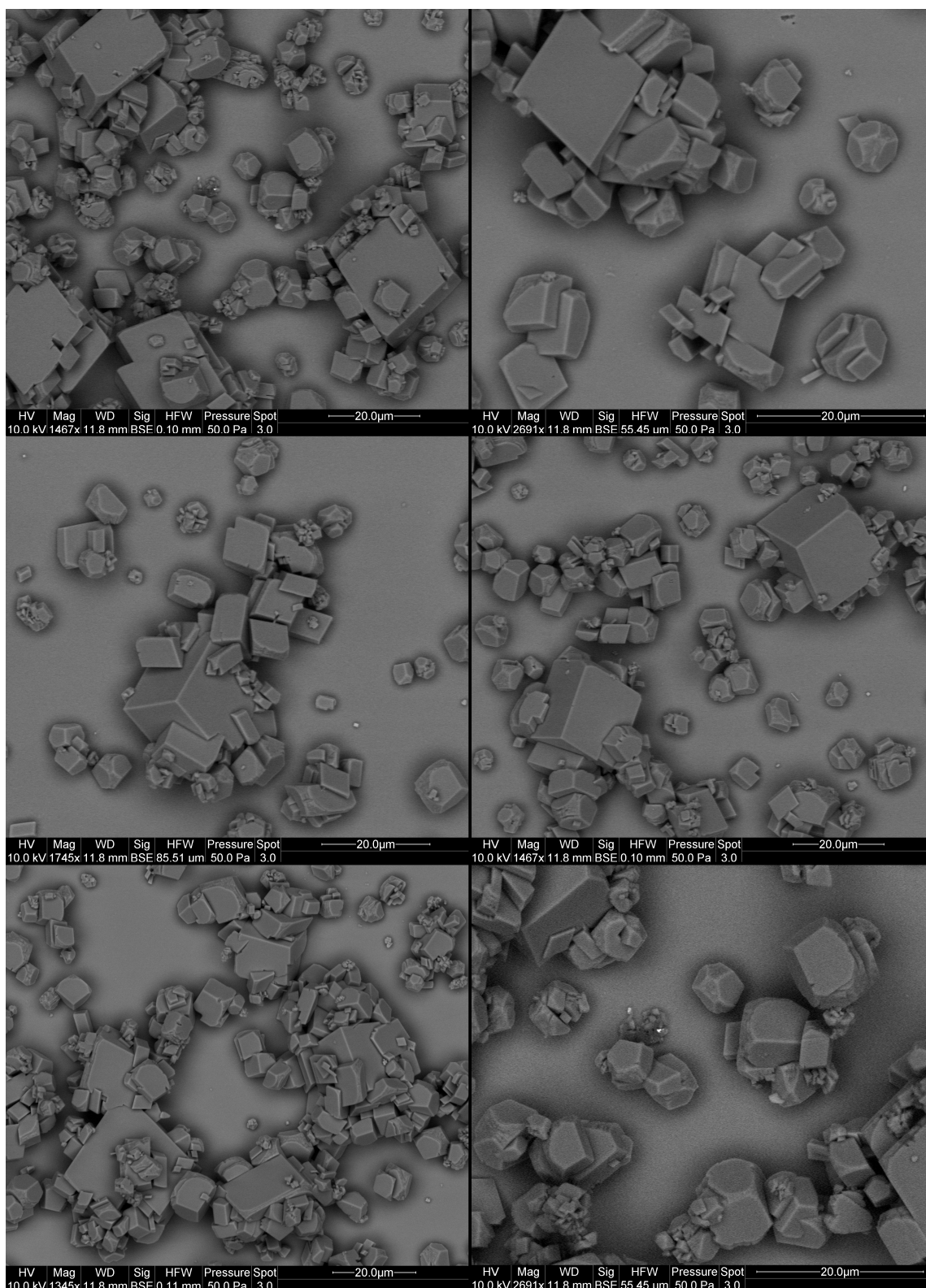


Figure 50: CA12, [NaCl] = 0.69 M, salinity = 45 g/kg

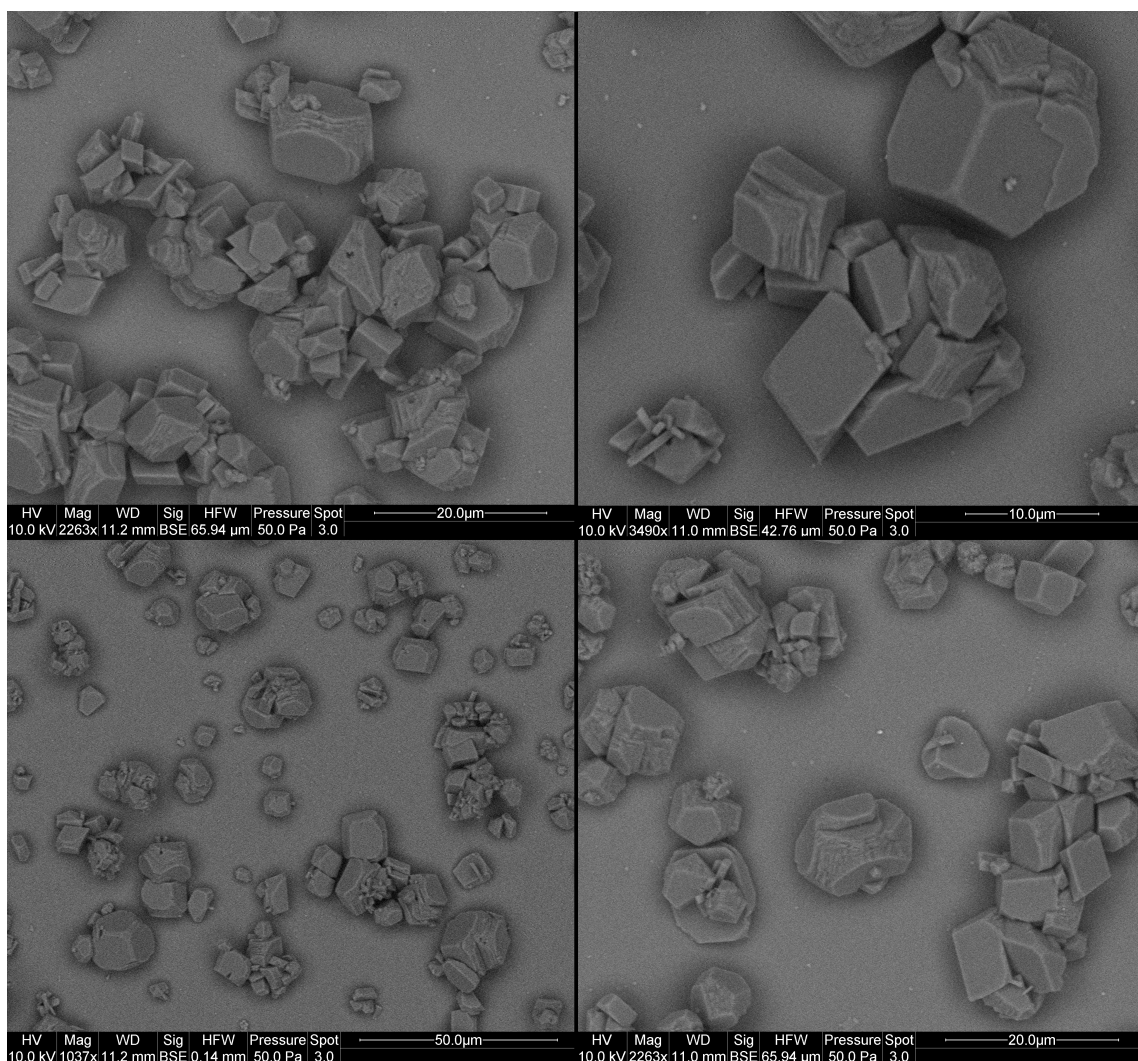


Figure 51: CA13, $[\text{NaCl}] = 1.03 \text{ M}$, salinity = 65 g/kg

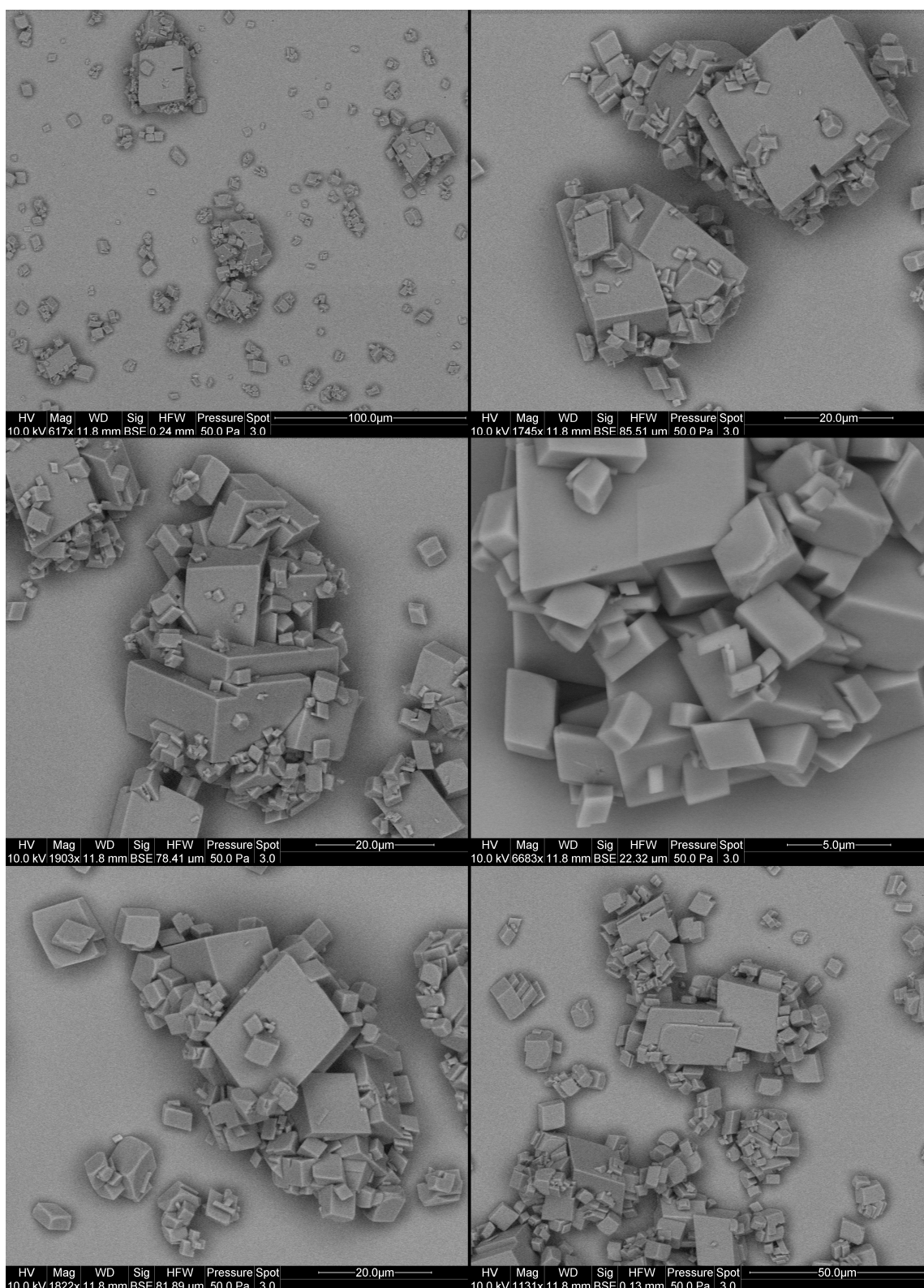


Figure 52: CA15, [NaCl] = 0.35 M, salinity = 25 g/kg

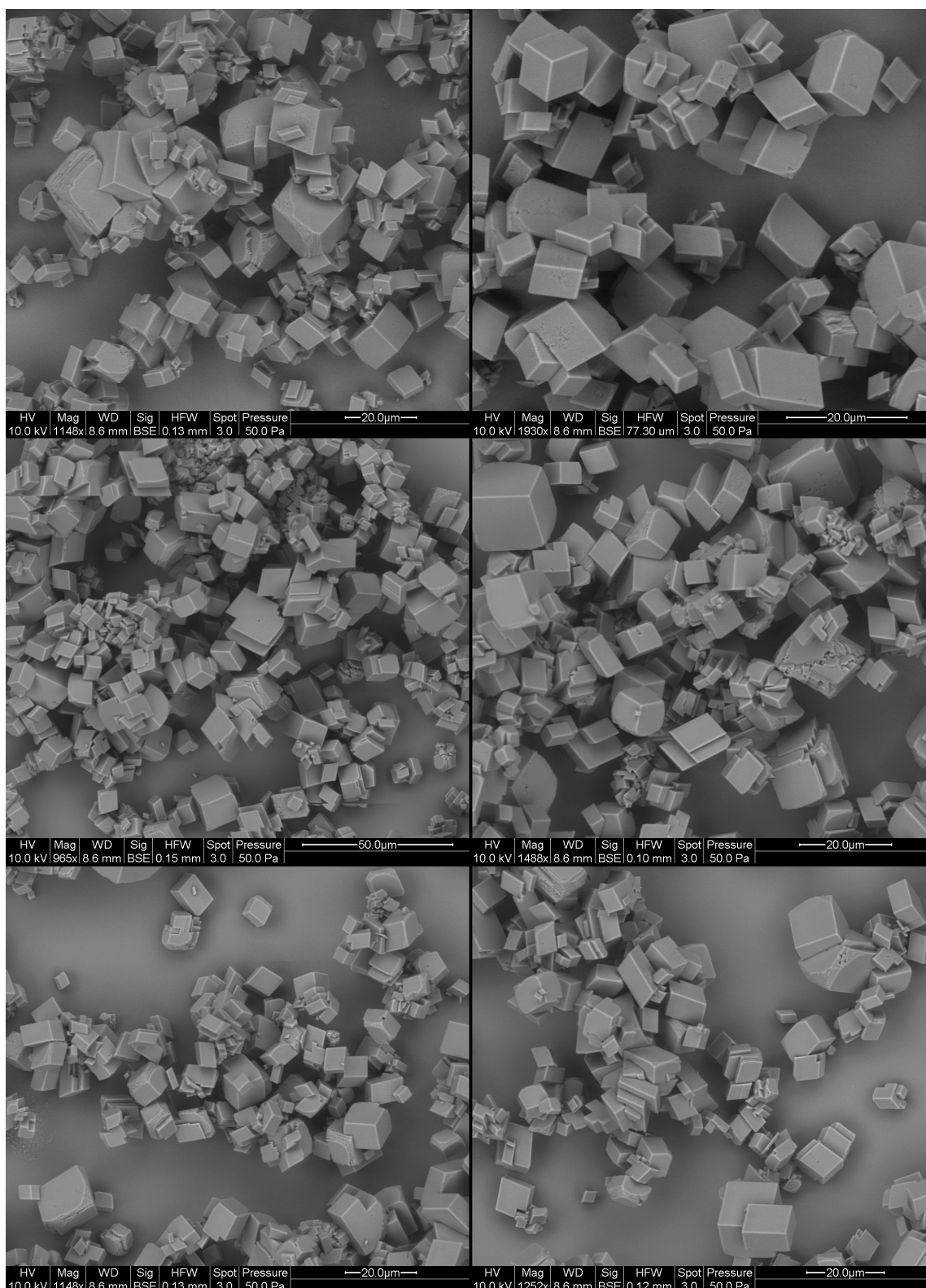


Figure 53: CA18, $[\text{NaCl}] = \sim 0 \text{ M}$, salinity = 3.5 g/kg. Time series experiment - 1st disc removed

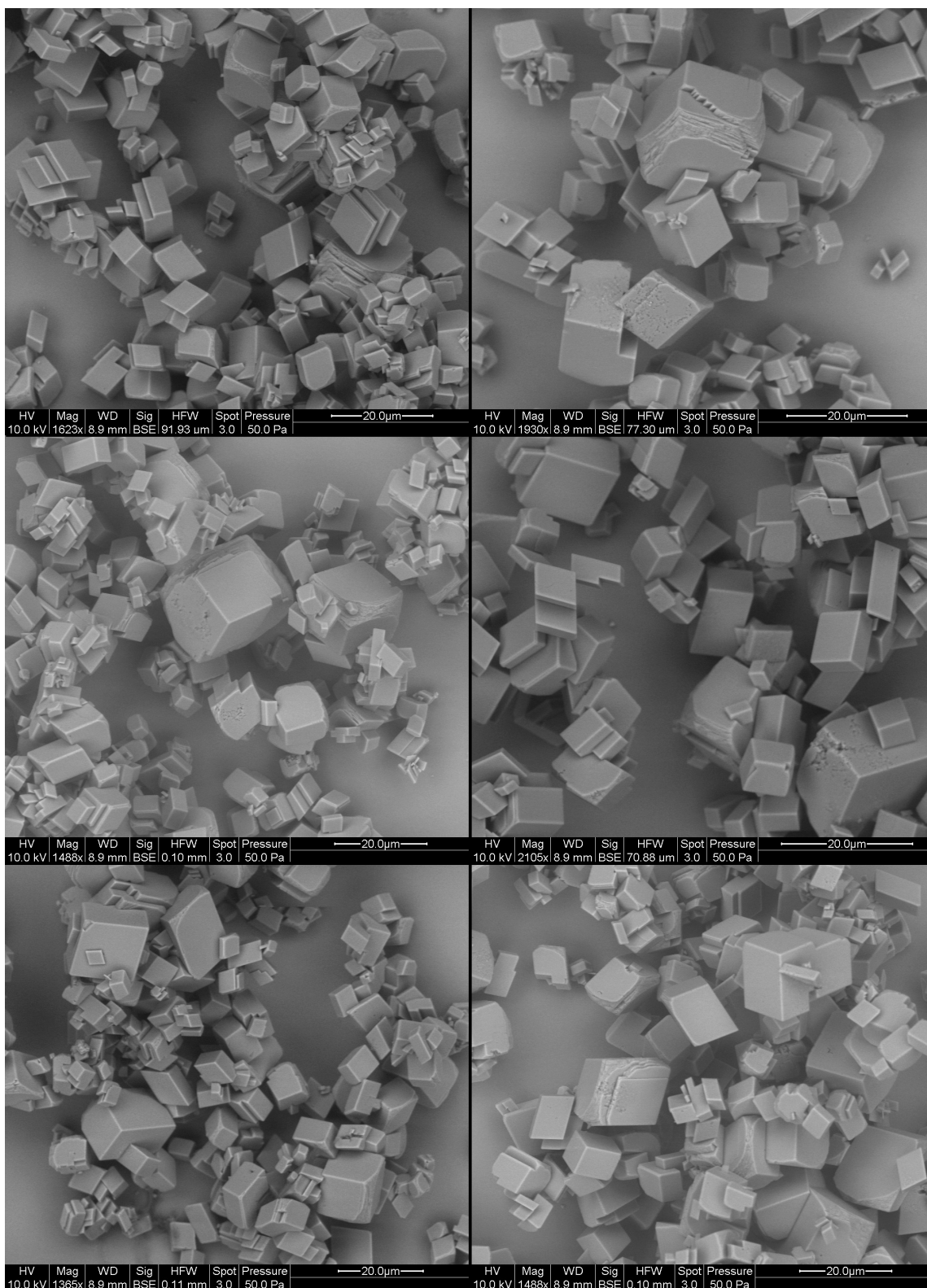


Figure 54: CA18, $[\text{NaCl}] = \sim 0 \text{ M}$, salinity = 3.5 g/kg. Time series experiment - 2nd disc removed

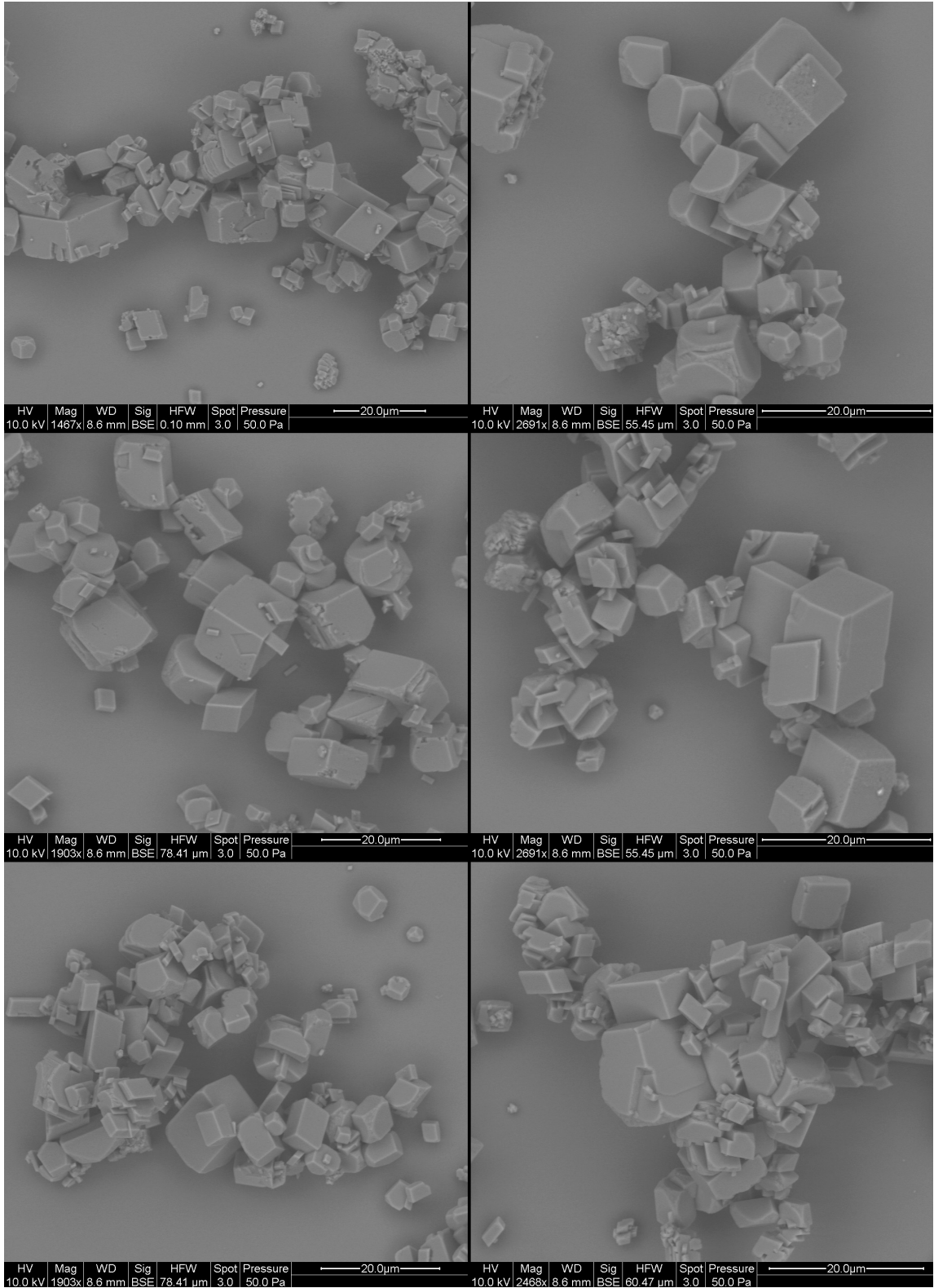


Figure 55: CA18, [NaCl] = ~0 M, salinity = 3.5 g/kg. Time series experiment - 3rd disc removed

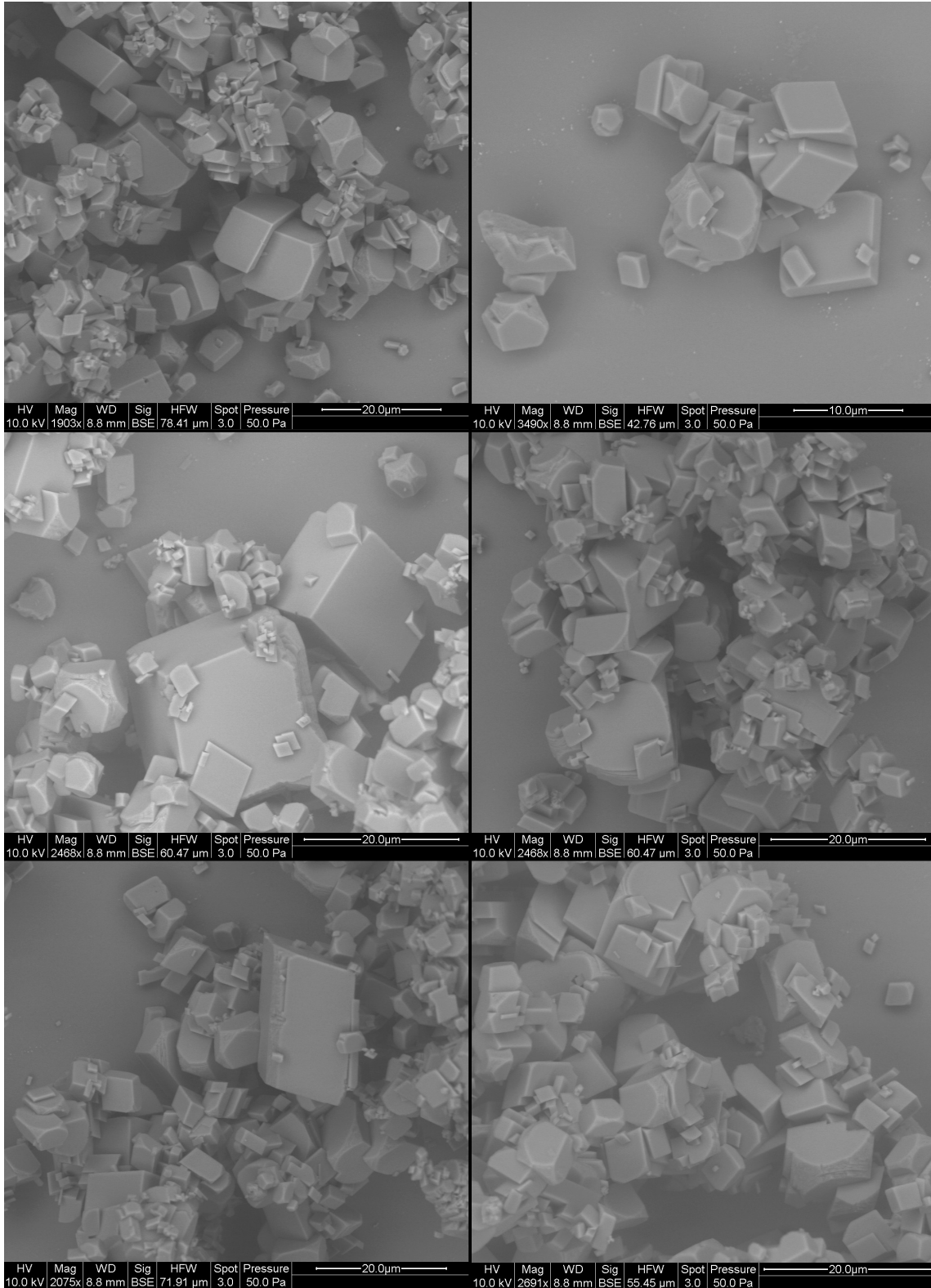


Figure 56: CA18, $[\text{NaCl}] = \sim 0 \text{ M}$, salinity = 3.5 g/kg. Time series experiment - disc in solution for the full experiment

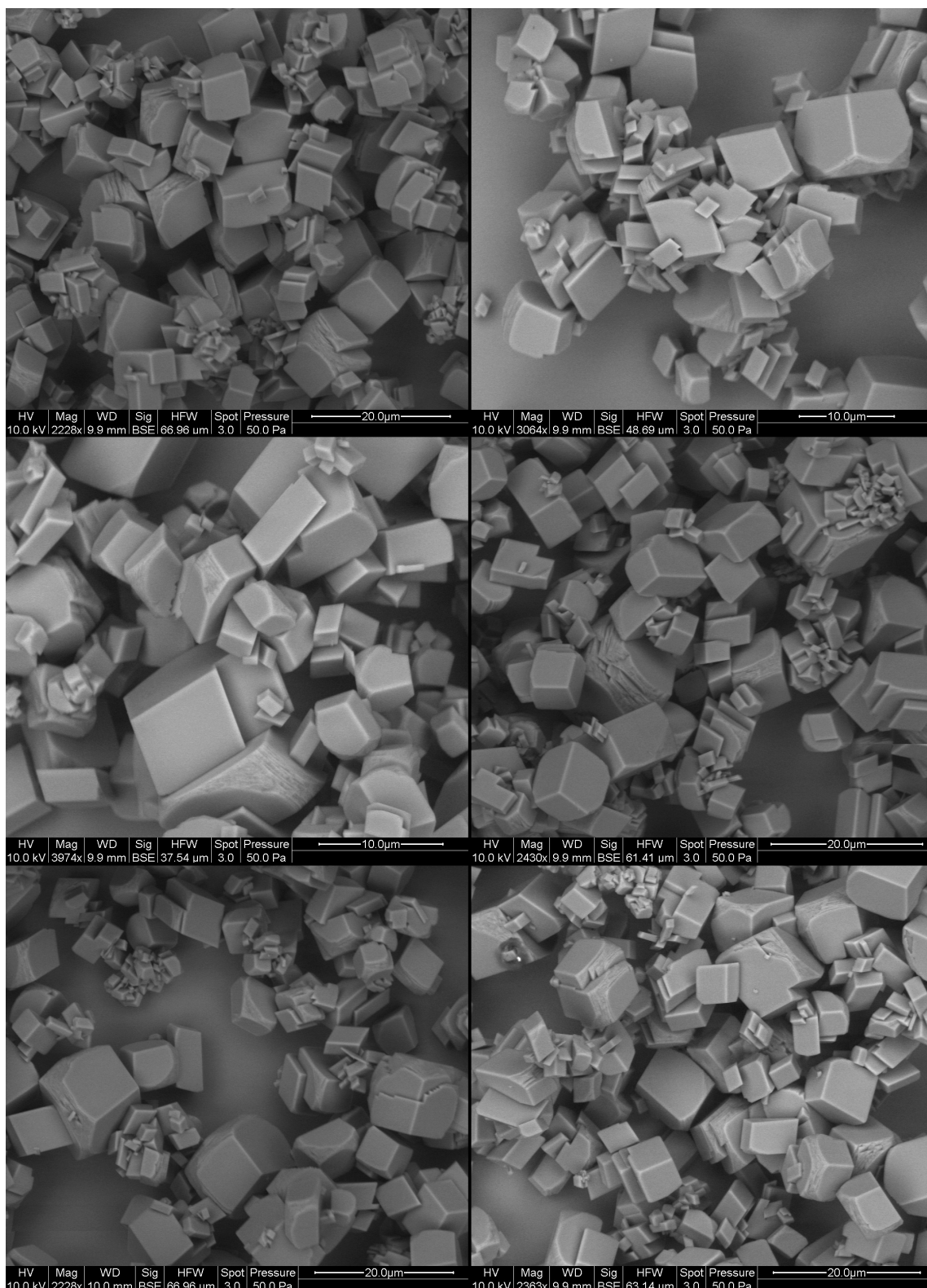


Figure 57: CA20, $[\text{NaCl}] = \sim 0 \text{ M}$, salinity = 3.5 g/kg. Time series experiment - 1st disc removed

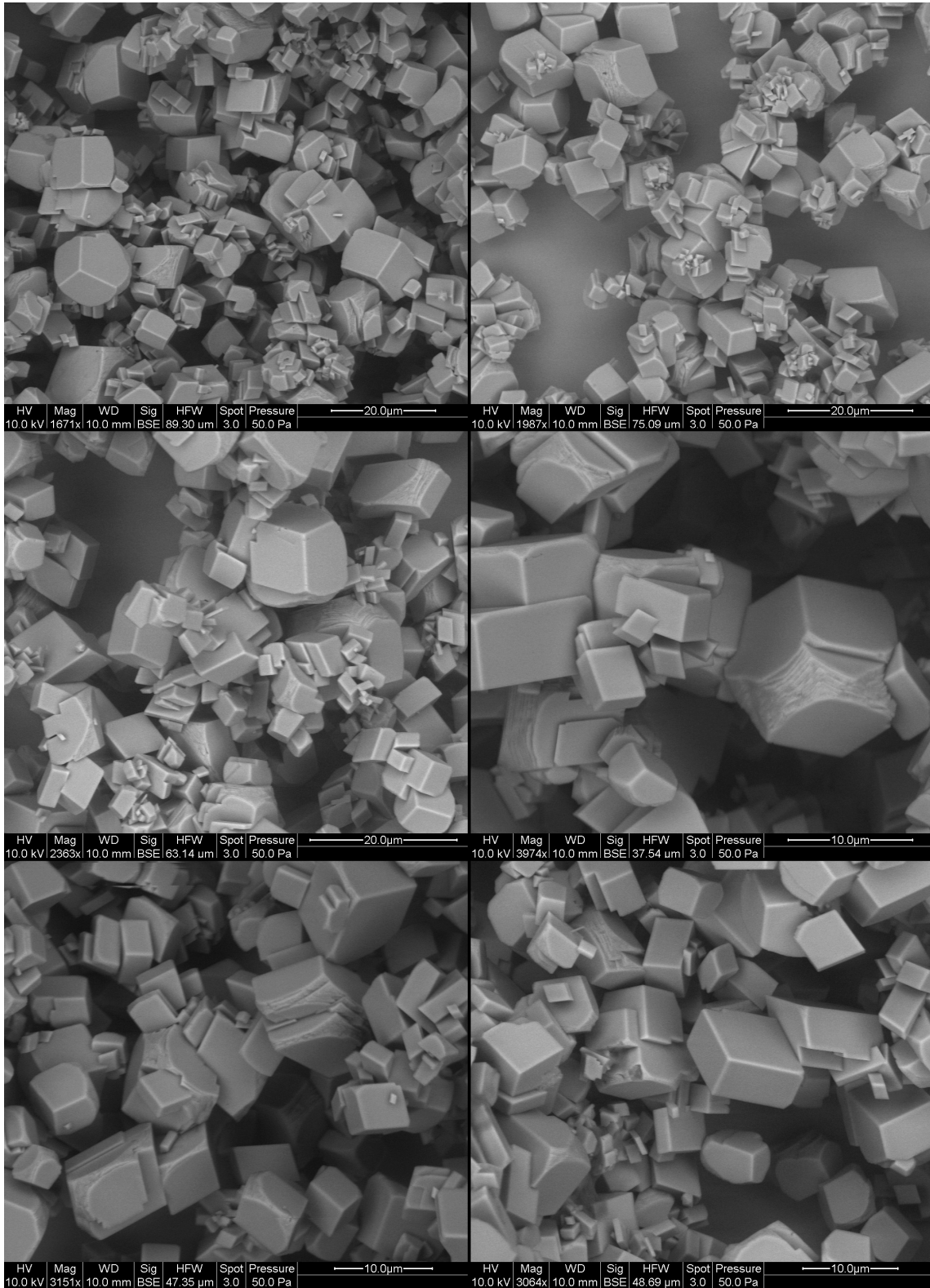


Figure 58: CA20, $[\text{NaCl}] = \sim 0 \text{ M}$, salinity = 3.5 g/kg. Time series experiment - 2nd disc removed

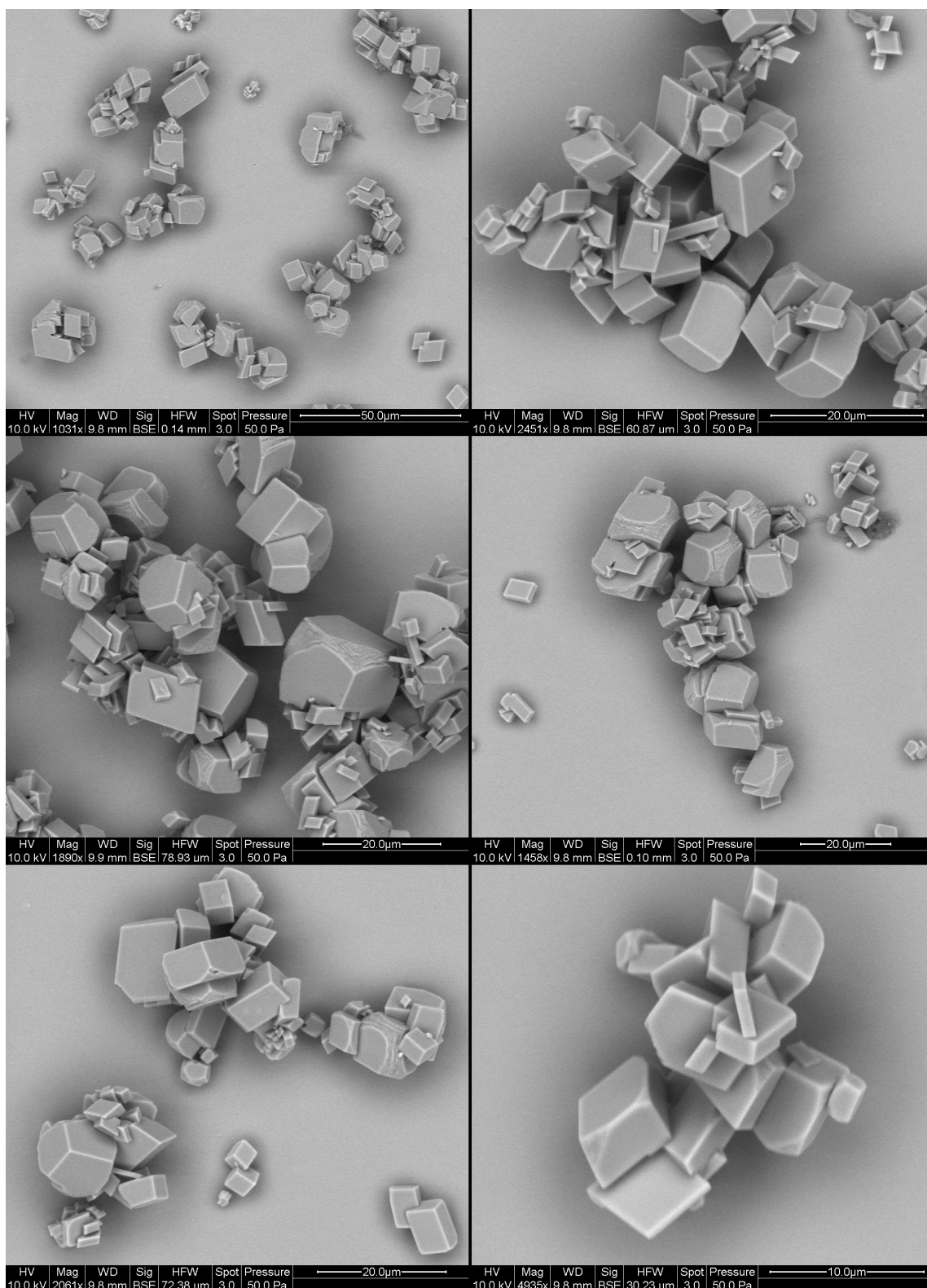


Figure 59: CA20, $[\text{NaCl}] = \sim 0 \text{ M}$, salinity = 3.5 g/kg. Time series experiment - 3rd disc removed

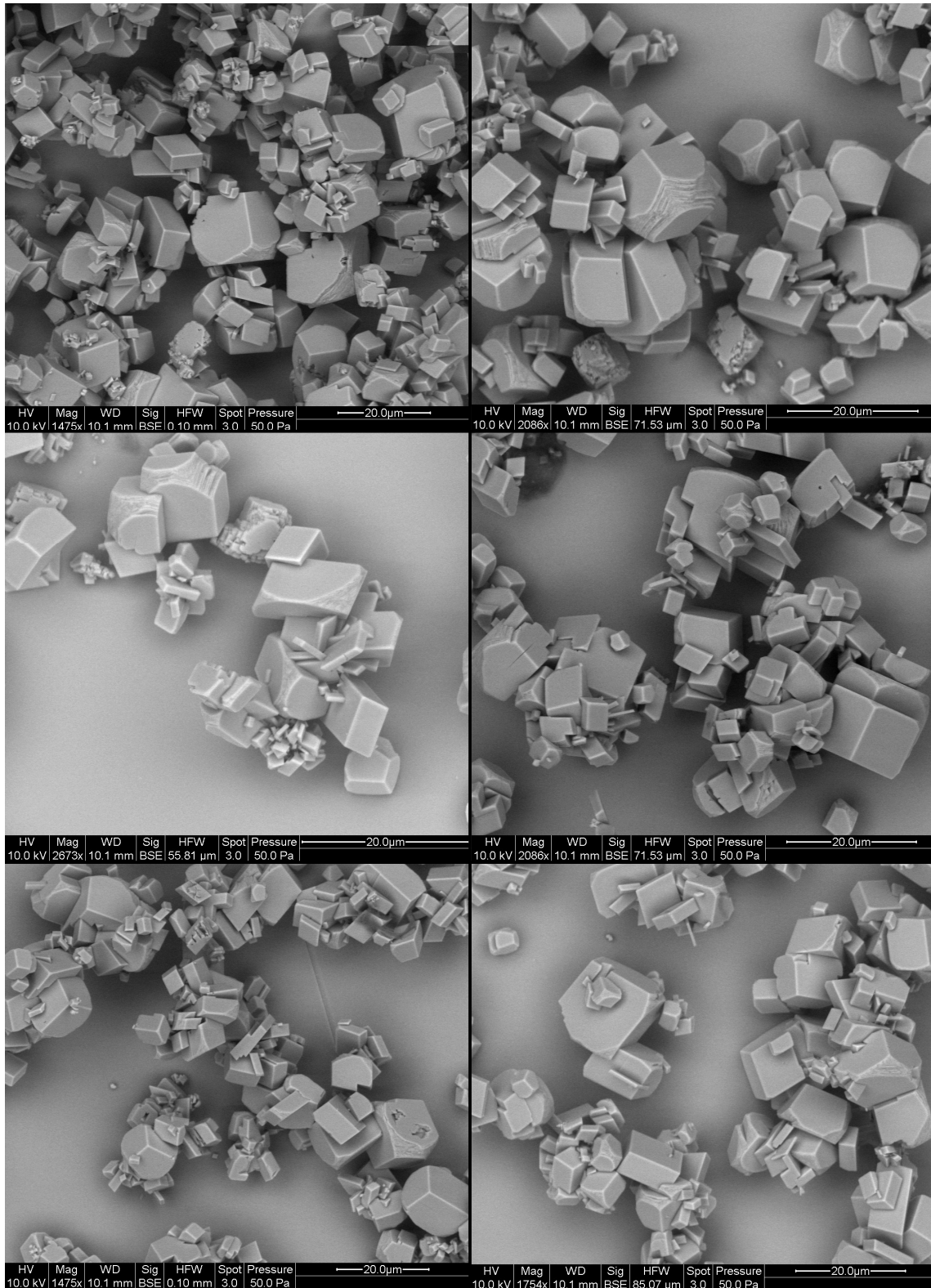


Figure 60: CA20, [NaCl] = ~0 M, salinity = 3.5 g/kg. Time series experiment - 4th disc removed

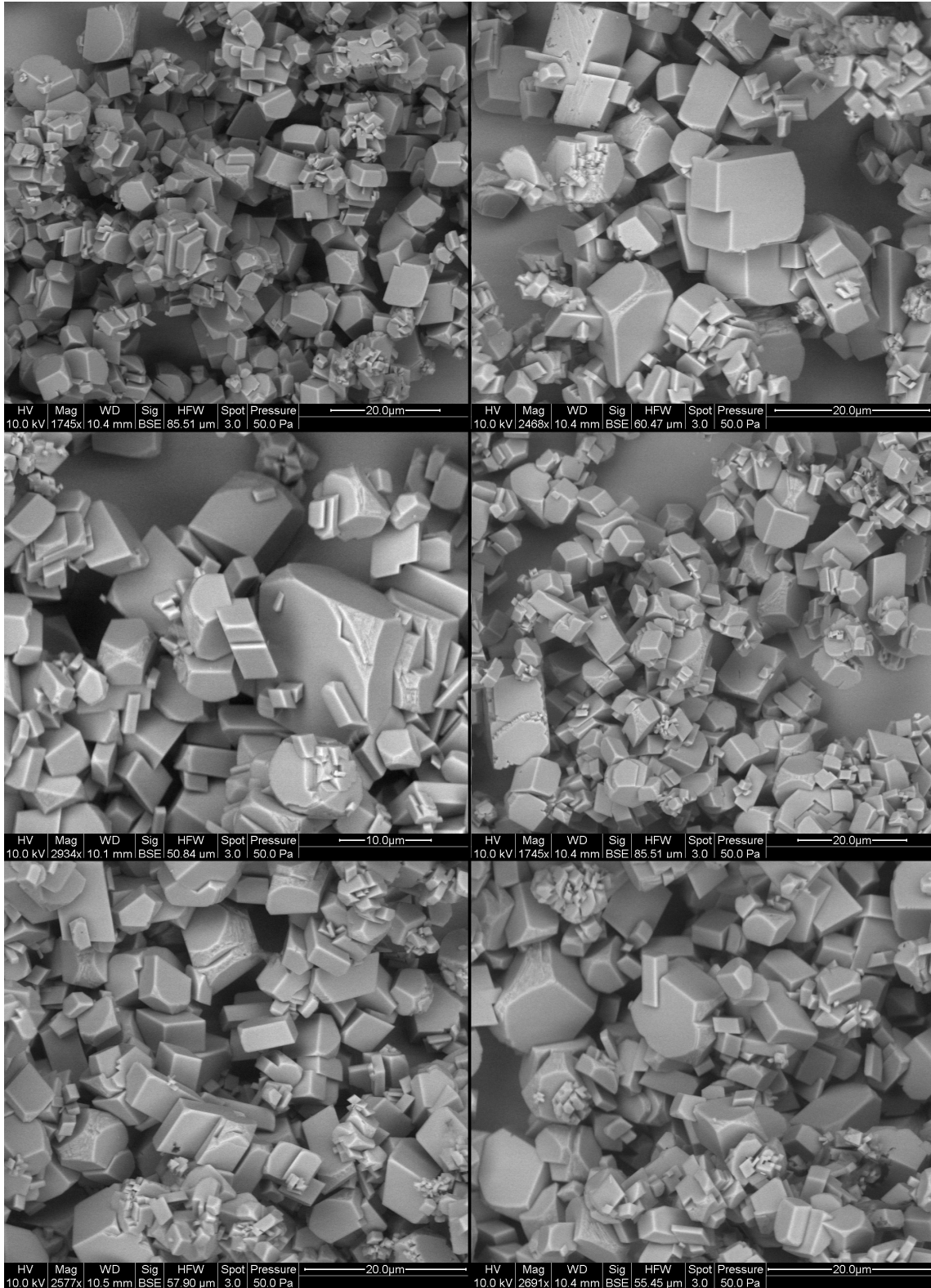


Figure 61: CA20, $[\text{NaCl}] = \sim 0 \text{ M}$, salinity = 3.5 g/kg. Time series experiment - disc in solution for the full experiment

3 Additional figures

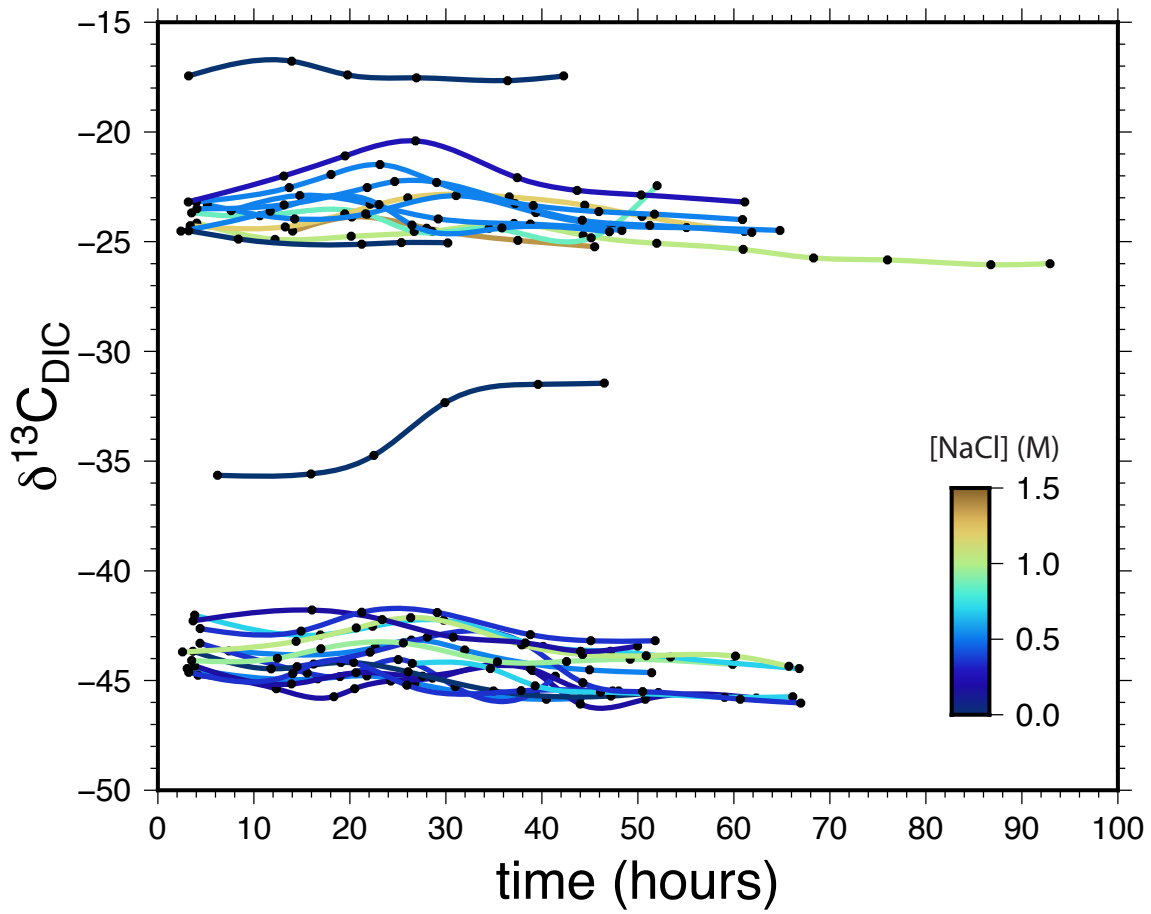


Figure 62: $\delta^{13}\text{C}$ of DIC (‰ VPDB) for all experiments.

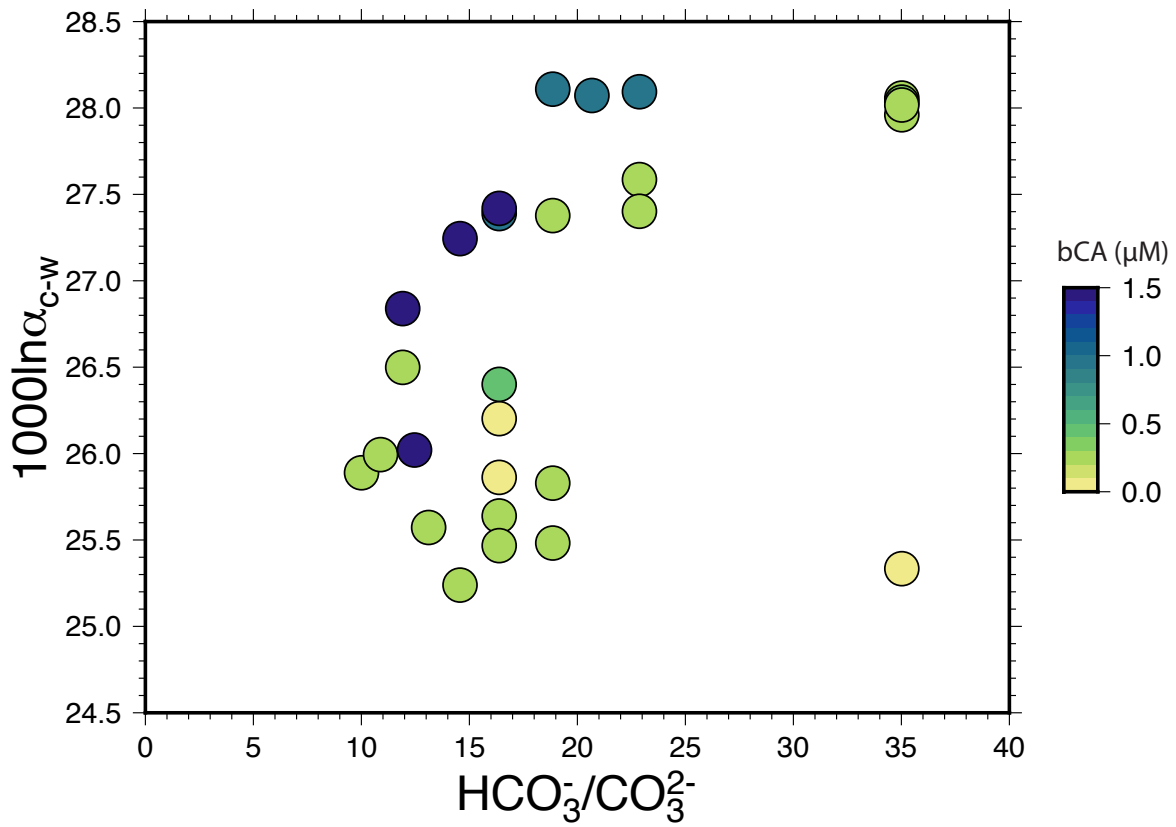


Figure 63: Oxygen isotope fractionation between calcite and experimental solution expressed as $1000\ln\alpha_{c-w}$, over the range of experimental solution $\text{HCO}_3^-/\text{CO}_3^{2-}$.

APPENDIX C
CHAPTER III SUPPLEMENTARY MATERIAL:
CARBONIC ANHYDRASE ENZYME ASSAYS

1 Carbonic anhydrase enzyme

Carbonic anhydrase is an enzyme that catalyzes CO₂ (de)hydration reactions, which are some of the slowest reactions in the DIC-H₂O system, in addition to being the only pathway (other than hydroxylation) through which DIC may exchange with H₂O (Zeebe and Wolf-Gladrow, 2001). At the pH of this study (pH 8.3), CO₂ (de)hydration reactions are several orders of magnitude slower than HCO₃⁻-CO₃²⁻ exchange, which may be assumed to achieve equilibrium instantaneously (Sade and Halevy, 2017). Catalyzing CO₂ (de)hydration therefore helps in establishing an isotopically equilibrated DIC pool, which is important when trying to separate kinetic isotope effects (KIEs) due to disequilibrium of CaCO₃-DIC during attachment and detachment of ions at the mineral surface, from KIEs due to disequilibrium of DIC-H₂O as a result of precipitating calcite from a not fully equilibrated DIC pool.

This enzyme has been used in a few prior studies of inorganic calcite precipitation (Uchikawa and Zeebe, 2012; Watkins et al., 2013, 2014; Baker, 2015), all of which were performed in solutions of low ionic strength. Since we use carbonic anhydrase in solutions of varying ionic strength, it was important at the outset of our study to assess whether the activity of carbonic anhydrase is affected by other ions in solution.

2 Assay methods

The enzyme carbonic anhydrase from bovine erythrocytes (bCA) used in our work was purchased from MP Biomedicals (#153879), with a reported molecular weight of 30,000 g/mol.

The standard method for determining bCA activity involves measuring the time required for a CO₂-saturated solution to lower the pH of a veronal buffer solution from 8.3 to 6.3 at 0-4°C, both in the presence and absence of bCA (Wilbur and Anderson, 1948; Worthington, 1993; Uchikawa and Zeebe, 2012). The enzyme activity is reported in Wilbur-Anderson enzyme units (EU):

$$\text{EU} = 2 \cdot \frac{t_{\text{blank}} - t_{\text{CA}}}{t_{\text{CA}}} \quad (1)$$

where t_{CA} and t_{blank} are the measured time interval for the pH decline with and without bCA, respectively. According to Eq. ??, two enzyme units corresponds to an uncatalyzed reaction time that is twice as long as the catalyzed reaction time.

For blank assays, a 30 mL beaker containing 12 mL of ice-cold Tris-HCl (0.02 M; pH = 8.6) was set in an ice bath on a magnetic stir plate. The temperature of the Tris-HCl was monitored to ensure that it stayed within 0-4°C during the assay. The reaction was initiated by pipetting 8 mL of (nearly) CO₂-saturated distilled, deionized H₂O (DDI), which was prepared by briefly bubbling pure CO₂ through 200 mL of ice-cold deionized water. The pH of this solution was found to be 3.96, in agreement with literature values (Peng et al., 2013). Upon addition of the CO₂ solution to the Tris-HCl, there is a relatively sharp decrease in pH to about 8.3, followed by a more gradual decrease to the pH endpoint.

For assays at high salinity, we prepared (nearly) CO₂-saturated solutions using DDI mixed with 87.5 g/kg and 175 g/kg NaCl, such that the final mixtures of Tris-HCl and CO₂-saturated solutions were 35 g/kg and 70 g/kg.

For CA assays, we added 0.04 mL of 0.1 mg/mL bCA (4×10^{-3} mg of bCA) to the Tris-HCl buffer immediately prior to addition of the (nearly) CO₂-saturated solution. This bCA solution was stored in a refrigerator and we noticed no significant drop in bCA activity over the course of several months.

3 Assay results

Results from freshwater and saltwater assays with essentially the same t_{blank} (~135-150 s) show a resolvable influence of NaCl on bCA activity (Fig. ??). The catalyzed time for freshwater is about 25 s, and about 40 s and 45 s for saltwater of 35 g/kg and 70 g/kg, respectively. From these results we calculate a bCA activity of ~2350 EU/mg for freshwater, which is consistent with the manufacturer's quote as well as the values determined by Uchikawa and Zeebe (2012). From the saltwater results we calculate a bCA activity of about 1340 EU/mg in 35 g/kg salinity solutions and 1070 EU/mg in 70 g/kg solutions, indicating that 35-70 g/kg of background NaCl inhibits the activity of bCA by a factor of 1.8-2.2. This should be regarded with caution because the assays are carried out at variable pH and ~0°C whereas our experiments are at fixed pH and 25°C.

4 Assay complications and challenges

We encountered a number of issues with the assay protocol that have not been adequately addressed in the literature. In the discussion that follows, we attempt to lay bare these issues so that future researchers can avoid the pitfalls that we encountered.

The standard method for determining the activity of CA involves measuring the time required for a CO₂-saturated solution to lower the pH of a veronal buffer solution from 8.3 to 6.3 at 0-4°C, both in the presence of, and absence of, CA (Wilbur and Anderson, 1948). A clear recipe for

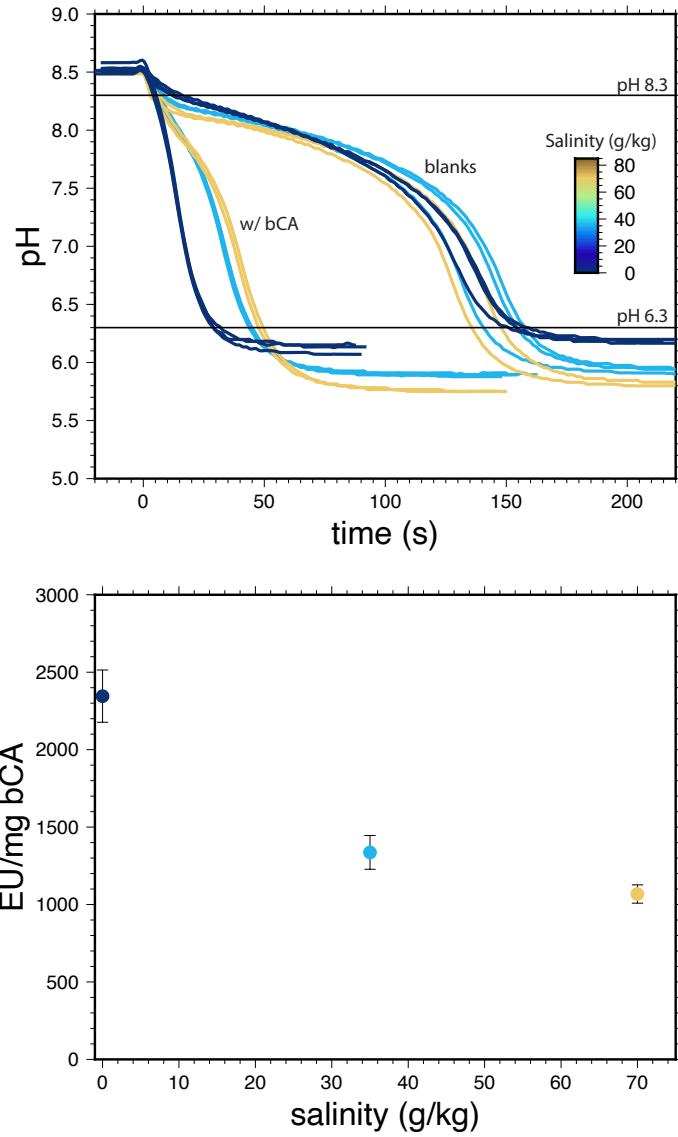


Figure 1: The activity of bovine CA is inhibited by NaCl. Freshwater assays yield 2150-2520 EU/mg. Saltwater assays yield 1240-1450 EU/mg at 35 g/kg and 1000-1100 EU/mg at 70 g/kg. Error bars represent one standard deviation from the mean.

carrying out the assay can be found in Worthington (1993), which was modified by Uchikawa and Zeebe (2012) who used different concentrations of reagents.

To prepare our veronal buffer solution, Tris-base (121.14 g/mol) was added to DDI and placed in an ice bath. The initial pH of the ice-cold 0.02 M Tris solution was 11-11.5. Between 1-2 mL concentrated HCl was added to reach the target pH of 8.6 for the Tris-HCl solution. An alternative approach is to use Tris-HCl base, which contains equal molar quantities of Tris and HCl, and requires addition of a base such as NaOH to reach the target pH.

Uchikawa and Zeebe (2012) bubbled pure CO₂ gas through DDI water for 30-60 minutes to ensure CO₂-saturation (Uchikawa and Zeebe, 2012; Worthington, 1993). When we bubbled CO₂ through DDI for this amount of time or longer, the resulting t_{blank} was much lower (~ 30 to 80 s) than the t_{blank} of ~ 160 s reported by Uchikawa and Zeebe (2012). Additionally, our blank runs had poor reproducibility whereas Fig. 2 in Uchikawa and Zeebe (2012) shows excellent reproducibility. The bCA activities that we obtained from these early runs were generally about a factor of two lower than those obtained by Uchikawa and Zeebe (2012), as well as the manufacturer's quote.

Setting aside the disagreement between our blanks and theirs, we investigated several possible causes for the lack of reproducibility, including changing the stirring rate, calibrating the pH probe at 0°C instead of room temperature, storing the probe in ice versus a room temperature solution between assays, using different batches of Tris, transferring the CO₂-saturated solution in a large pipette to minimize interaction with the air, and performing the assay in a round bottom flask instead of a beaker to minimize interaction with the air. None of these approaches improved the reproducibility. Ultimately, we concluded that the variable blank results were due to variably under- or over-saturated CO₂ solutions. This conclusion aligns with a careful reading of the Sigma-Aldrich assay protocol (<https://www.sigmaaldrich.com/technical-documents/protocols/biology/enzymatic-assay-of-carbonic-anhydrase.html>):

The general blank time after first opening [the CO₂ solution] is approximately 40 seconds. Record this time as "Blank-1". If this occurs, transfer [the CO₂ solution] back fourth between a 1 L beaker and the "Vess Seltzer" bottle a couple of times. Place [the CO₂ solution] back in ice. Repeat [the blank assay]. Record all blank times in seconds. The blank times tend to increase with each opening of the bottle containing [the CO₂ solution]. Once a blank time of 65 seconds is reached, proceed with [the CA assay]. After all test runs, the final blank average must be in the range of 70 to 100 seconds.

This text implies use of a partially degassed CO₂ solution, which is not mentioned elsewhere in the literature (Worthington, 1993; Uchikawa and Zeebe, 2012). By bubbling CO₂ and allowing the solution to partially degas, we managed to obtain blanks between 70-100 s but this still led to bCA activities that were a factor of two lower than the manufacturer's quote (Fig. ??). An important caveat is that we followed the Uchikawa and Zeebe (2012) protocol, and for direct comparison to their results, we tried bubbling CO₂ for shorter durations (<2 minutes) to obtain blank runs of ~ 140 -150 seconds to match their blank time. This led to a bCA activity in excellent agreement with their results in NaCl-free solutions (2325 ± 175 versus 2358 EU/mg).

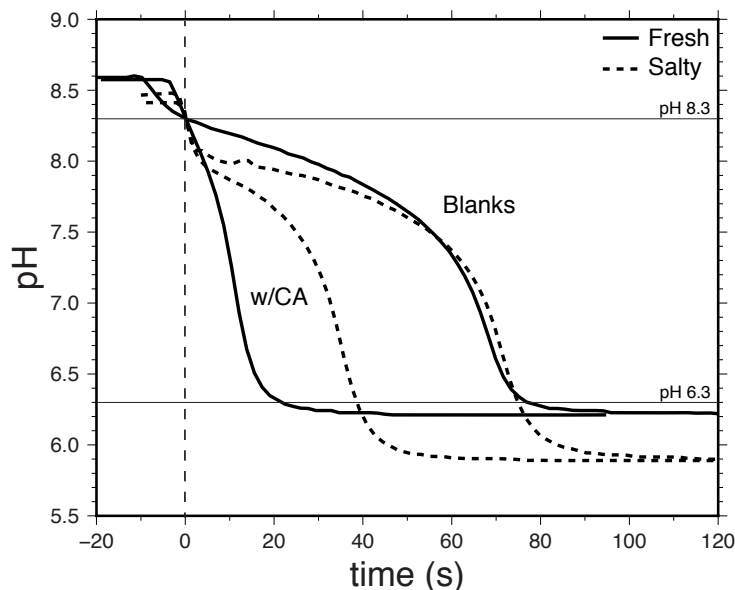


Figure 2: Assay results for a shorter t_{blank} of ~ 75 seconds. The freshwater assay yields a bCA activity of ~ 1375 EU/mg whereas the saltwater assay yields ~ 450 EU/mg. These values are significantly lower than the manufacturer's quote (~ 2000 EU/mg), which is why we accept the assays with longer t_{blank} in the main text. The choice of t_{blank} does not affect the main conclusion that there is a salt inhibition effect of about a factor of 2-3.

For saltwater assays, we adjusted the CO_2 bubbling time in order to obtain the same t_{blank} of ~ 140 - 150 seconds to facilitate direct comparison to freshwater results. Importantly, regardless of t_{blank} , whether it be 40, 80, or 150 seconds, we find that NaCl lowers bCA activity by about a factor of 2-3 in going from $[\text{NaCl}] = 0$ g/kg to 35 g/kg (Fig. ?? and Fig. ??).

Additional References

- Peng C., Crawshaw J. P., Maitland G. C., Martin Trusler J. P. and Vega-Maza D. (2013) The pH of CO_2 -saturated water at temperatures between 308 K and 423 K at pressures up to 15 MPa. *J. Supercrit. Fluids* **82**, 129–137.
- Wilbur K. M. and Anderson N. G. (1948) Electrometric and Colorimetric Determination of Carbonic Anhydrase. *J. Biol. Chem.* **176**, 147–154.
- Worthington V. (1993) Worthington Enzyme Manual. Worthington Biomedical Corporation, Lakewood, New Jersey.

APPENDIX D
 CHAPTER IV SUPPLEMENTARY MATERIAL:
 EXPERIMENT DATA AND SEM IMAGES OF PRECIPITATES

1 Experiment data table

Table 1: Experimental measurements

Experiment	Time (h)	TA (mEq/L)	[DIC] (mM)	$\delta^{13}\text{C}_{\text{DIC}}$ (VPDB)	$\delta^{18}\text{O}_w$ (VSMOW)	pCO ₂ (ppm)
S6	3.85	0.46	-	-	-	223
-	18.82	0.69	-	-	-	295
-	26.83	0.61	-	-	-	242
-	41.45	0.51	-	-	-	294
-	45.78	0.53	-	-	-	238
-	52.75	0.52	-	-	-	238
-	63.75	0.50	-	-	-	346
-	66.63	0.50	-	-	-	275
-	72.78	0.50	-	-	-11.31	
S8	3.65	0.47	0.14	-43.66	-	97
-	11.80	0.65	0.37	-44.47	-	142
-	19.07	0.66	0.26	-44.18	-	143
-	26.07	0.49	0.15	-44.60	-	103
-	34.97	0.50	0.17	-45.47	-	104
-	47.22	0.49	0.13	-45.70	-	102
-	52.15	0.60	0.13	-45.55	-11.39	91
CA4	3.22	0.74	0.14	-24.50	-	134
-	8.38	0.95	0.31	-24.88	-	165
-	21.25	0.70	0.14	-25.12	-	121
-	25.38	0.72	0.19	-25.04	-	138
-	30.22	0.71	0.16	-25.05	-11.68	124
CA10	0.40	1.78	-	-	-	130
-	19.47	1.70	0.25	-38.84	-	70

Table 1 continued

Experiment	Time (h)	TA (mEq/L)	[DIC] (mM)	$\delta^{13}\text{C}_{\text{DIC}}$ (VPDB)	$\delta^{18}\text{O}_{\text{w}}$ (VSMOW)	pCO ₂ (ppm)
-	31.58	1.69	0.32	-40.45	-	71
-	44.33	1.70	0.45	-42.03	-	71
-	48.10	1.73	0.42	-42.16	-	69
-	55.23	1.75	0.52	-42.63	-	68
-	67.72	1.74	0.58	-43.02	-11.825	67
CA11	0.20	2.28	-	-	-	151
-	18.97	2.07	0.21	-40.40	-	64
-	23.77	2.00	0.26	-41.16	-	64
-	30.25	2.12	0.30	-41.97	-	64
-	43.42	2.08	0.39	-42.84	-	64
-	49.37	1.98	0.52	-43.21	-	64
-	66.67	1.96	0.63	-43.79	-	59
-	70.50	2.01	0.61	-43.82	-11.8	58
CA16	3.30	0.69	0.63	-18.22	-	469
-	12.53	0.85	0.72	-17.77	-	576
-	19.55	0.65	0.44	-19.52	-	418
-	27.12	0.63	0.42	-20.00	-	411
-	35.77	0.64	0.42	-20.11	-	404
-	40.75	0.68	0.39	-20.17	-11.85	398
CA17	3.47	0.57	0.36	-20.54	-	374
-	13.48	0.99	0.87	-19.73	-	673
-	19.97	0.90	0.68	-17.80	-	531
-	27.62	0.71	0.41	-18.03	-	383
-	37.42	0.67	0.32	-18.44	-	341
-	46.18	0.59	0.33	-18.45	-11.84	339
CA18	3.20	0.77	0.39	-17.44	-	220
-	13.93	0.71	0.31	-16.77	-	214
-	19.78	0.64	0.24	-17.40	-	192
-	26.93	0.64	0.22	-17.53	-	186
-	36.45	0.65	0.20	-17.66	-	188
-	42.28	0.64	0.22	-17.45	-11.88	191
CA20	6.22	0.74	0.34	-35.65	-	161
-	15.95	0.63	0.23	-35.59	-	127
-	22.50	0.63	0.22	-34.74	-	124
-	29.92	0.61	0.19	-32.34	-	115
-	39.62	0.60	0.16	-31.50	-	102

Table 1 continued

Experiment	Time (h)	TA (mEq/L)	[DIC] (mM)	$\delta^{13}\text{C}_{\text{DIC}}$ (VPDB)	$\delta^{18}\text{O}_w$ (VSMOW)	pCO ₂ (ppm)
-	46.50	0.59	0.15	-31.45	-11.95	99
CA21	4.38	1.03	0.38	-29.62	-	121
-	14.57	0.81	0.13	-27.80	-	86
-	22.38	0.81	0.14	-27.46	-	71
-	29.20	0.80	0.15	-28.02	-	65
-	41.30	0.82	0.16	-28.35	-11.52	54
CA22	3.45	1.40	0.10	-22.25	-	100
-	17.07	1.30	0.08	-23.69	-	66
-	24.40	1.40	0.07	-22.68	-	36
-	30.57	1.34	0.08	-22.56	-	29
-	41.92	1.37	0.07	-22.97	-11.87	18
CA23	3.62	1.30	0.08	-29.56	-	127
-	21.55	1.23	0.10	-40.87	-	150
-	31.75	1.24	0.06	-40.94	-	141
-	42.52	1.22	0.06	-42.19	-	144
-	55.65	1.25	0.05	-42.35	-	133
-	67.55	1.29	0.05	-42.14	-10.65	122
CA24	1.57	2.29	0.19	-18.86	-	56
-	11.32	2.06	0.08	-35.10	-	67
-	16.85	2.14	0.07	-37.74	-	63
-	23.72	2.06	0.06	-37.77	-	64
-	33.43	1.96	0.04	-36.58	-	64
-	42.25	2.05	0.05	-38.57	-	65
-	60.78	2.03	0.04	-37.82	-	58
-	71.80	1.93	0.04	-36.91	-	56
-	84.62	2.05	0.04	-37.36	-10.85	39
CA25	3.07	0.95	0.17	-39.61	-	56
-	13.25	1.10	0.25	-41.53	-	41
-	21.83	0.93	0.14	-39.77	-	-4
-	29.60	0.90	0.10	-40.73	-	-20
-	40.18	0.92	0.08	-40.69	-	-38
-	52.60	0.86	0.08	-40.55	-	-64
-	66.25	0.87	0.09	-40.96	-10.91	-85
CA26	2.65	0.94	0.71	-21.27	-	1638
-	13.55	1.25	1.04	-18.10	-	2042
-	19.73	1.22	1.06	-17.89	-	1976

Table 1 continued

Experiment	Time (h)	TA (mEq/L)	[DIC] (mM)	$\delta^{13}\text{C}_{\text{DIC}}$ (VPDB)	$\delta^{18}\text{O}_{\text{w}}$ (VSMOW)	pCO ₂ (ppm)
-	26.38	1.27	1.05	-17.93	-	1983
-	39.55	1.23	1.03	-17.88	-	1962
-	50.77	1.26	1.14	-17.82	-	1934
-	61.87	1.21	1.09	-18.07	-	1888
-	74.55	1.34	1.15	-18.37	-	1787
-	92.33	1.25	0.89	-19.88	-10.96	1458
CA27	1.97	0.70	0.56	-22.30	-	1074
-	14.68	1.17	0.98	-18.35	-	2008
-	24.20	1.17	1.10	-17.88	-	1981
-	38.07	1.19	1.13	-17.59	-	1963
-	48.73	1.15	0.99	-17.92	-	1946
-	61.62	1.18	1.02	-17.87	-	1942
-	72.22	1.20	0.98	-17.97	-	1939
-	86.05	1.25	1.14	-18.04	-	1852
-	96.22	1.29	1.02	-18.59	-	1745
-	112.32	1.22	0.98	-20.68	-11.15	1434
CA28	5.03	1.58	0.35	-19.01	-	58
-	16.45	1.28	0.09	-22.35	-	63
-	24.67	1.28	0.09	-22.21	-	34
-	37.90	1.25	0.08	-22.31	-	-9
-	47.15	1.32	0.07	-22.00	-11.28	-26
CA29	1.77	2.27	0.29	-14.10	-	74
-	12.60	1.78	0.08	-20.98	-	75
-	20.87	1.76	0.06	-21.58	-	72
-	31.38	1.72	0.05	-21.70	-	66
-	41.02	1.74	0.05	-20.85	-	40
-	51.58	1.71	0.04	-21.30	-	31
-	61.80	1.69	0.04	-21.86	-	17
-	72.15	1.75	0.04	-21.76	-11.36	3
CA30	1.58	0.68	0.64	-23.33	-	1168
-	19.4	1.37	1.32	-18.18	-	1933
-	36.87	1.51	1.28	-18.17	-	1896
-	49.57	1.35	1.23	-18.22	-	1878
-	62.93	1.44	1.27	-18.35	-	1707
-	74.65	1.47	1.35	-19.23	-	1652
-	91.98	1.06	0.96	-22.48	-10.86	1069

Table 1 continued

Experiment	Time (h)	TA (mEq/L)	[DIC] (mM)	$\delta^{13}\text{C}_{\text{DIC}}$ (VPDB)	$\delta^{18}\text{O}_w$ (VSMOW)	pCO ₂ (ppm)
CA31	1.82	0.77	0.69	-22.66	-	1190
-	15.17	1.30	1.34	-18.15	-	1988
-	26.12	1.44	1.42	-19.46	-	1719
-	36.3	1.16	0.94	-22.18	-11.23	1286

2 Experiment data figures

For each experiment, we periodically took water samples that were sent for [DIC] and $\delta^{13}\text{C}$ analysis, which are depicted by black circles, with curves interpolated between the data measurements (dark green and light green, respectively). We continuously monitored the concentration of CO₂ (ppm) of the experimental headspace (light blue line). We continuously measured solution pH (purple line) and amount of added NaOH (dark blue line), in addition to the periodic water samples we titrated to calculate the total alkalinity of the solution (red squares). The vertical gray line represents the onset of calcite precipitation for each experiment.

Data figures for experiments S6, S8, CA4, CA18, and CA20 were included as part of the experimental suite for Chapter III and may be found in Appendix B.

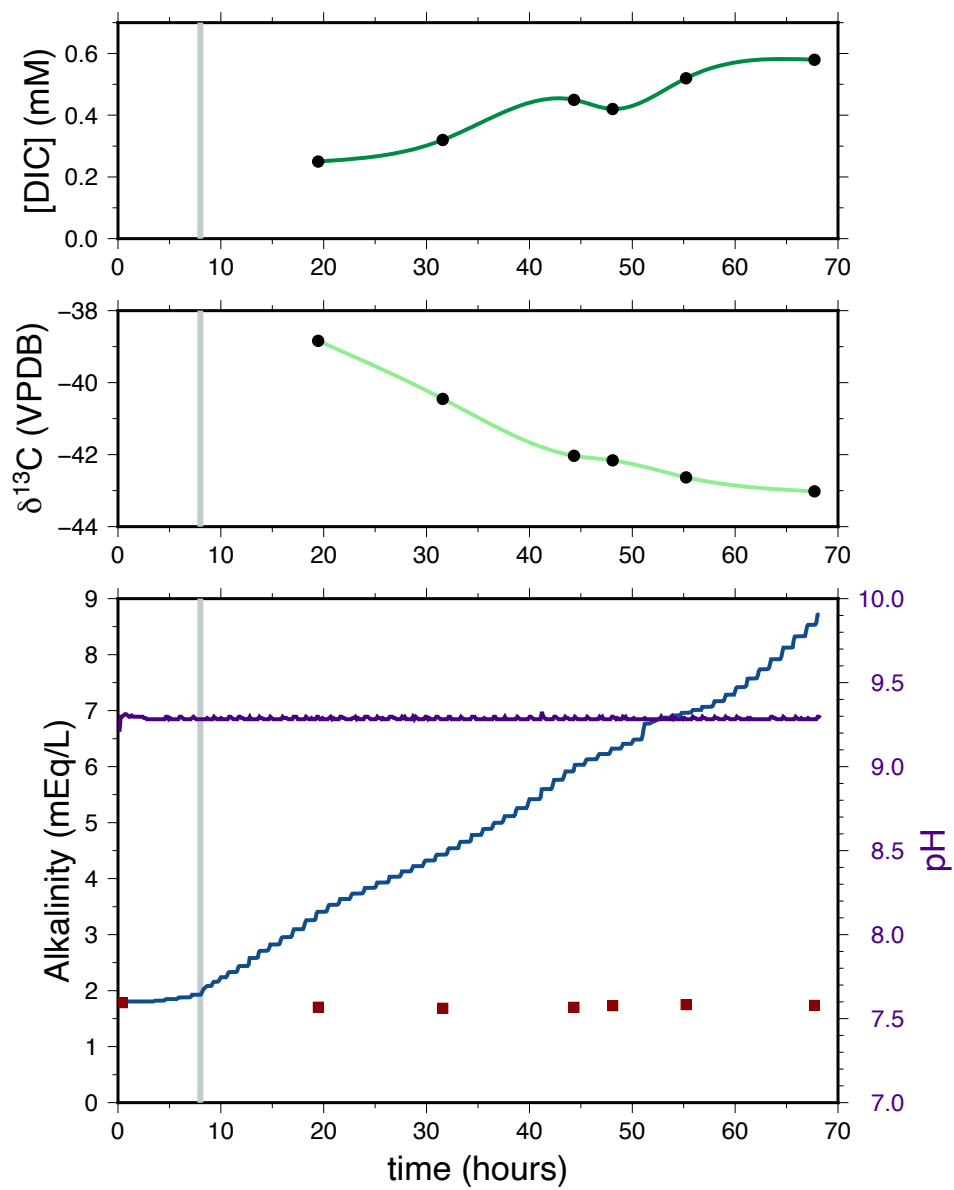


Figure 1: CA10, pH = 9.3

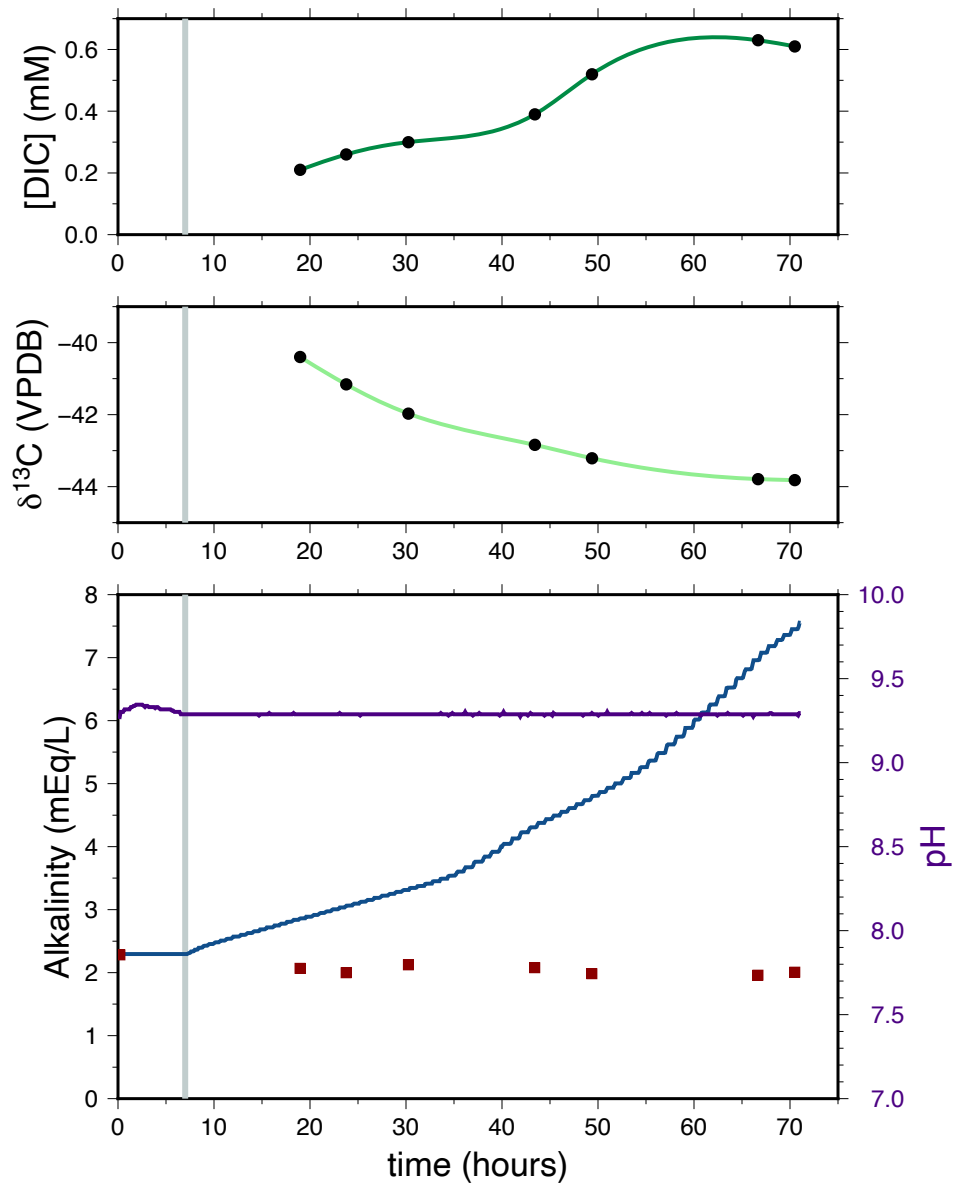


Figure 2: CA11, pH = 9.3

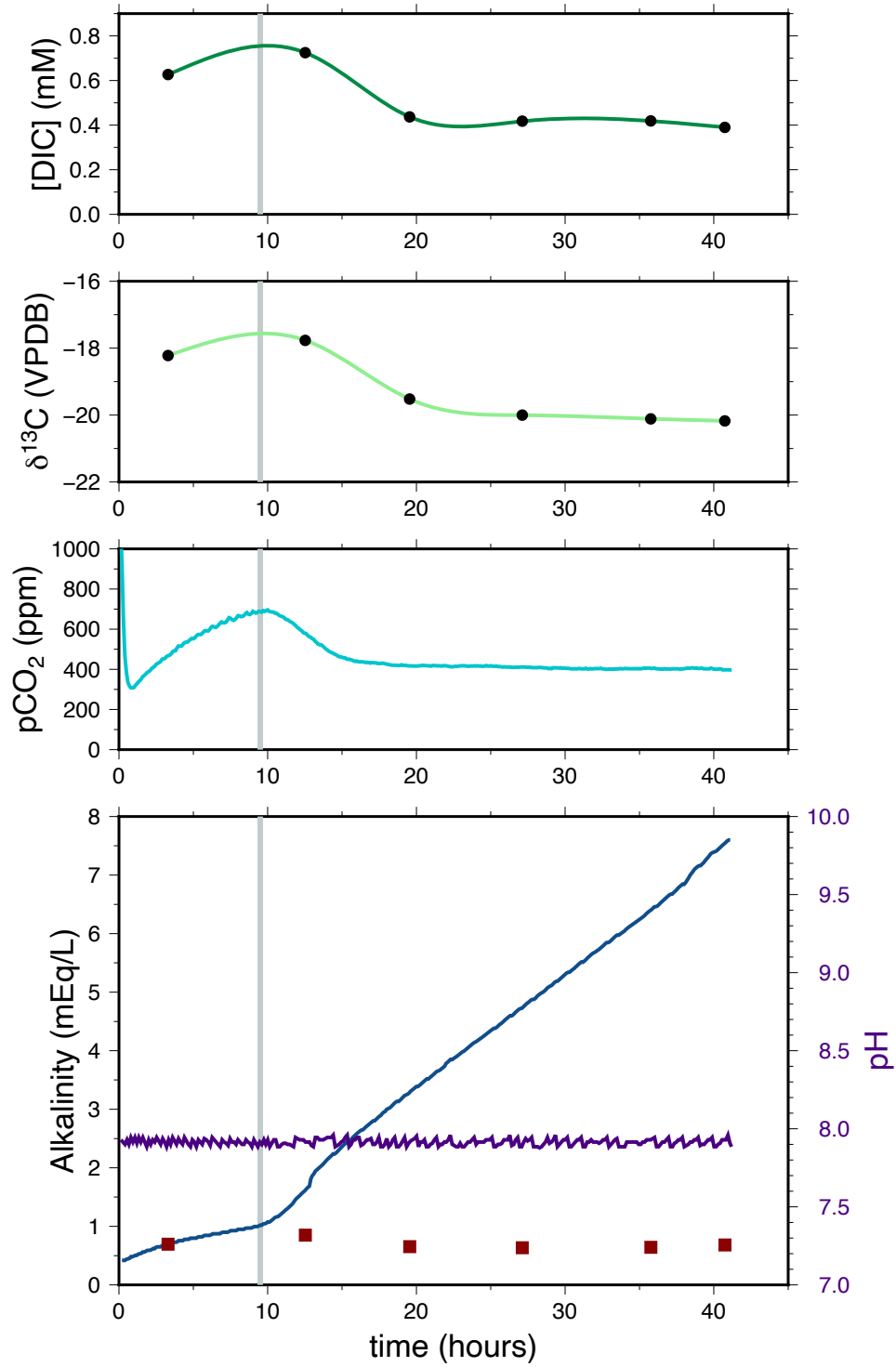


Figure 3: CA16, pH = 7.9

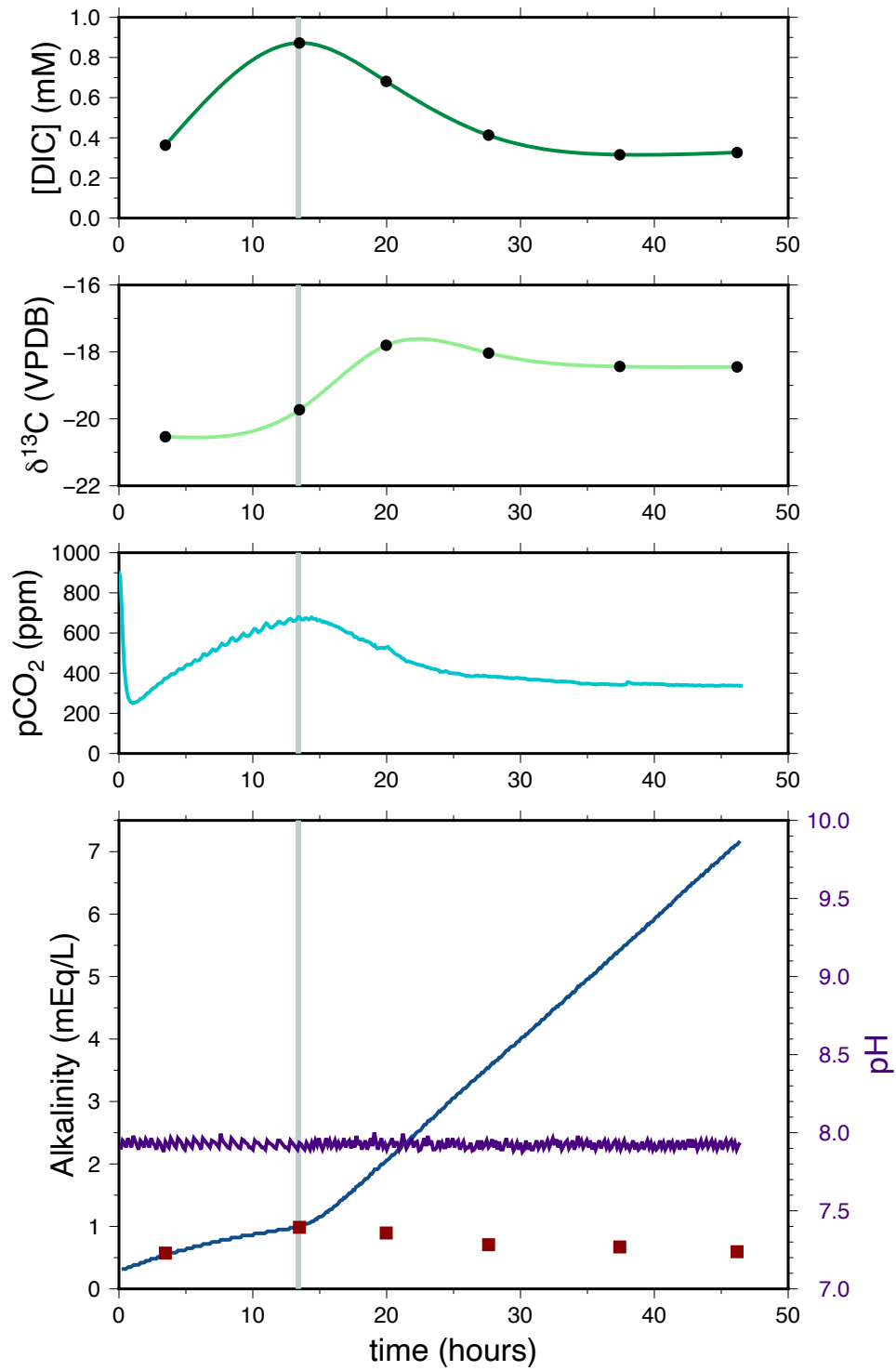


Figure 4: CA17, pH = 7.9

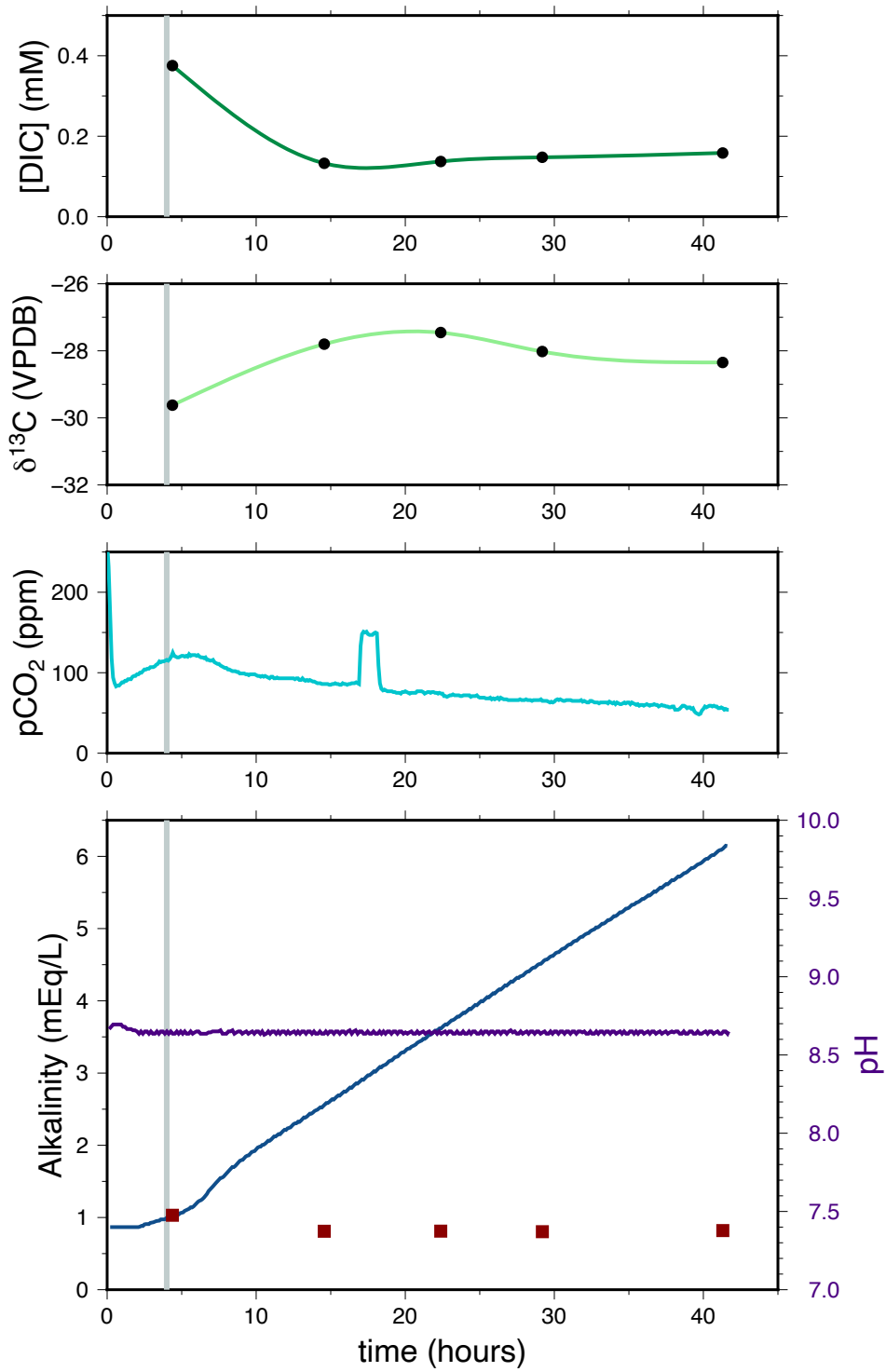


Figure 5: CA21, pH = 8.65

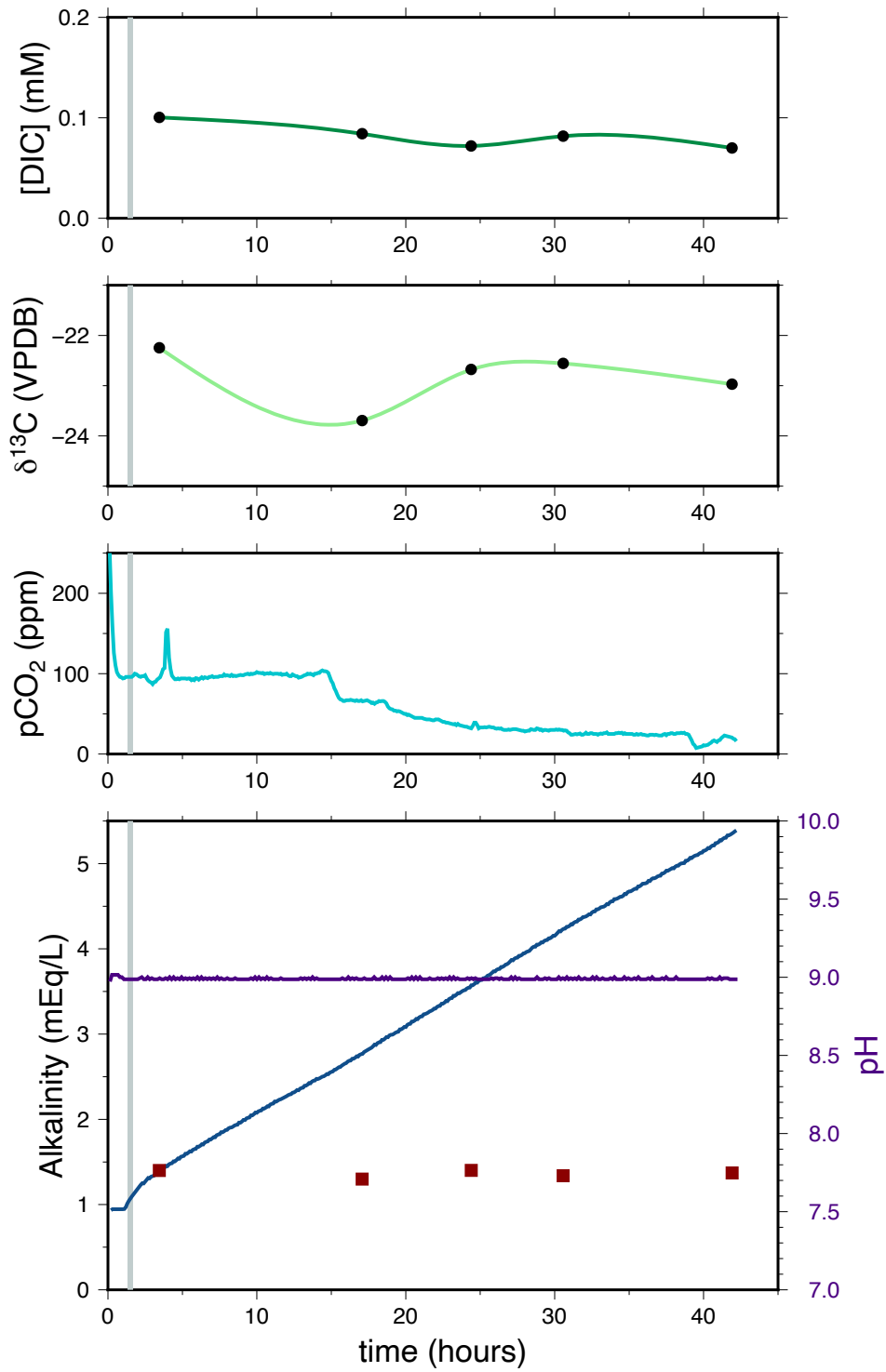


Figure 6: CA22, pH = 9.0

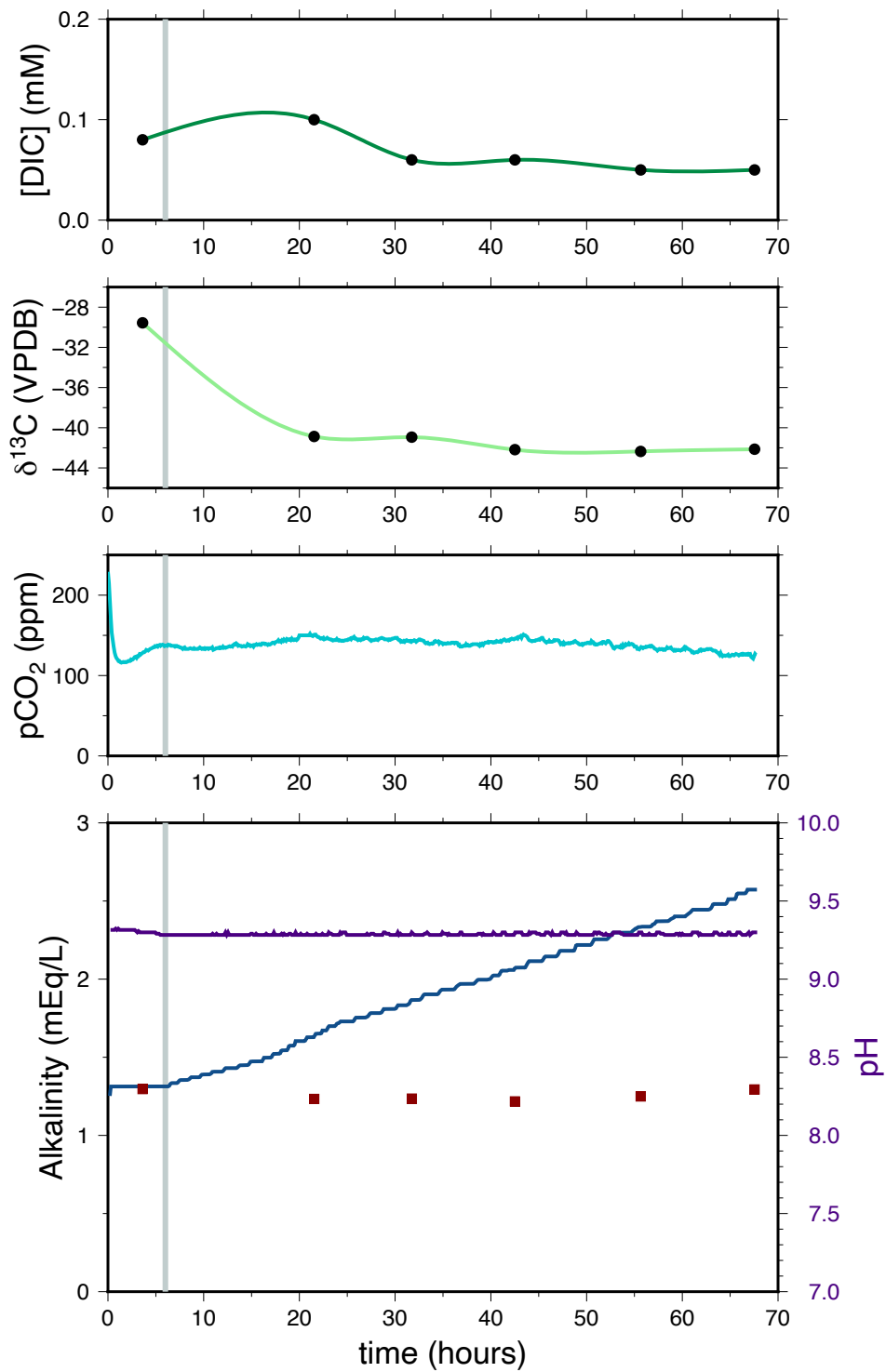


Figure 7: CA23, pH = 9.3

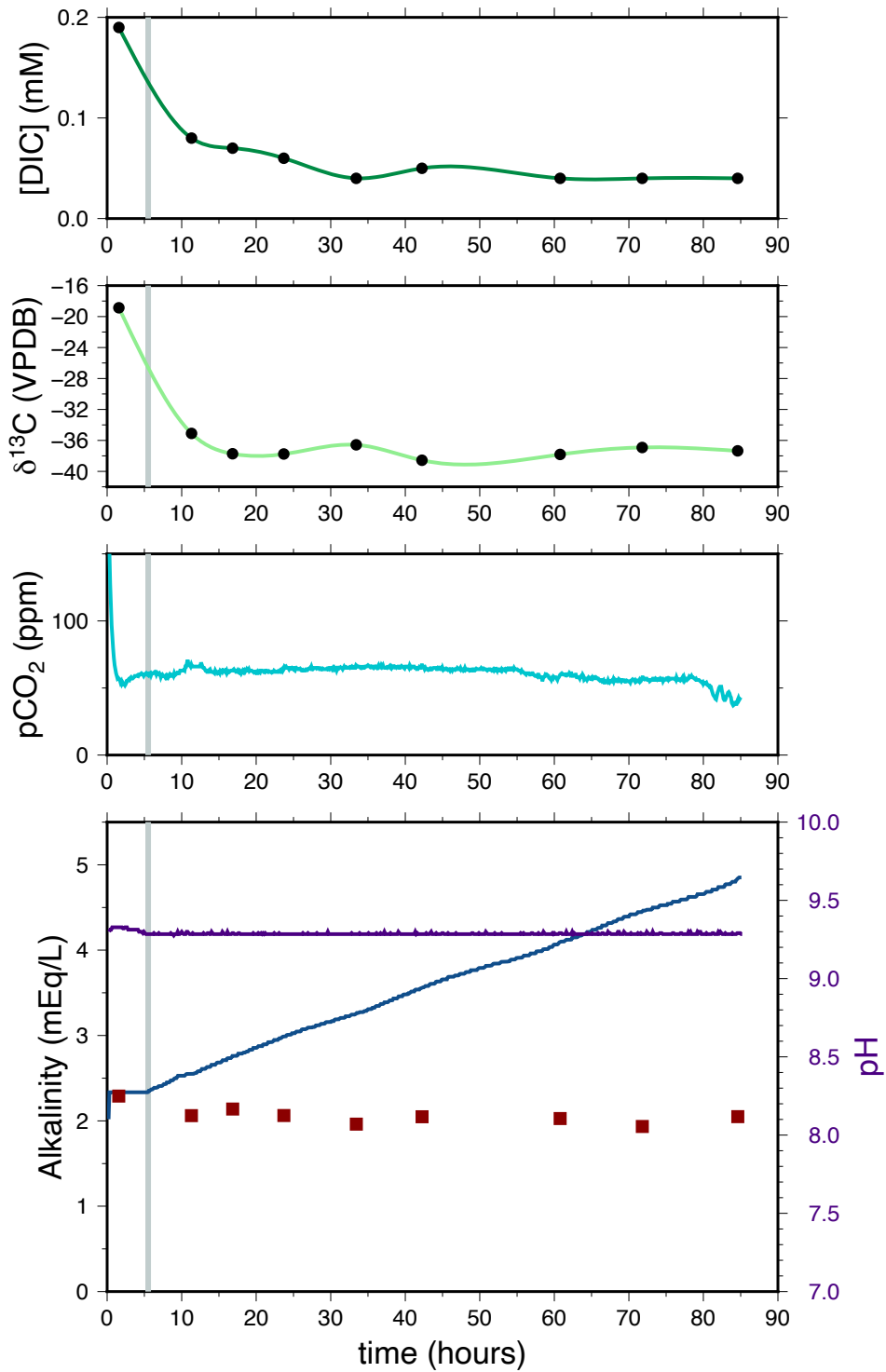


Figure 8: CA24, pH = 9.3

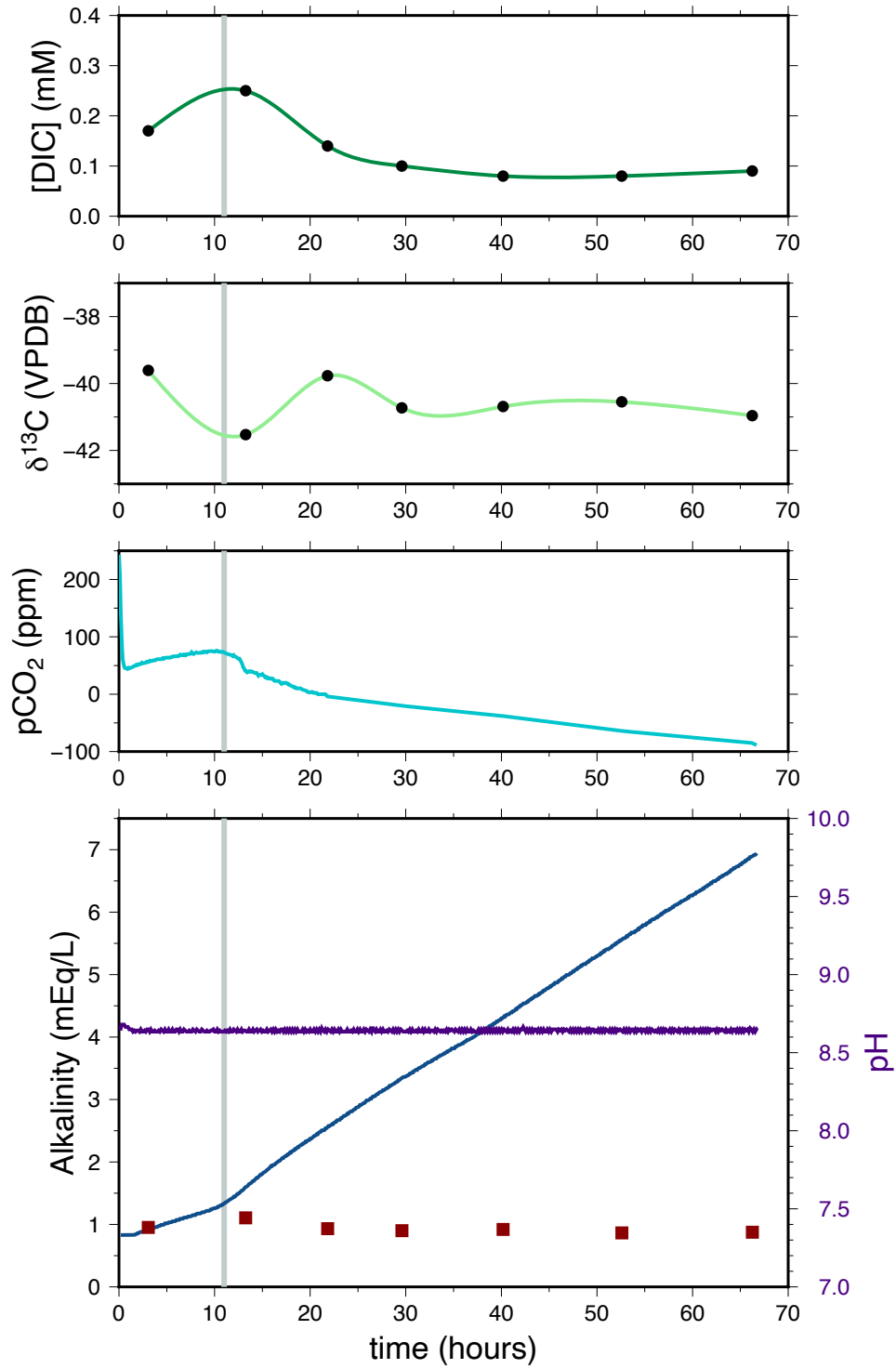


Figure 9: CA25, pH = 8.65

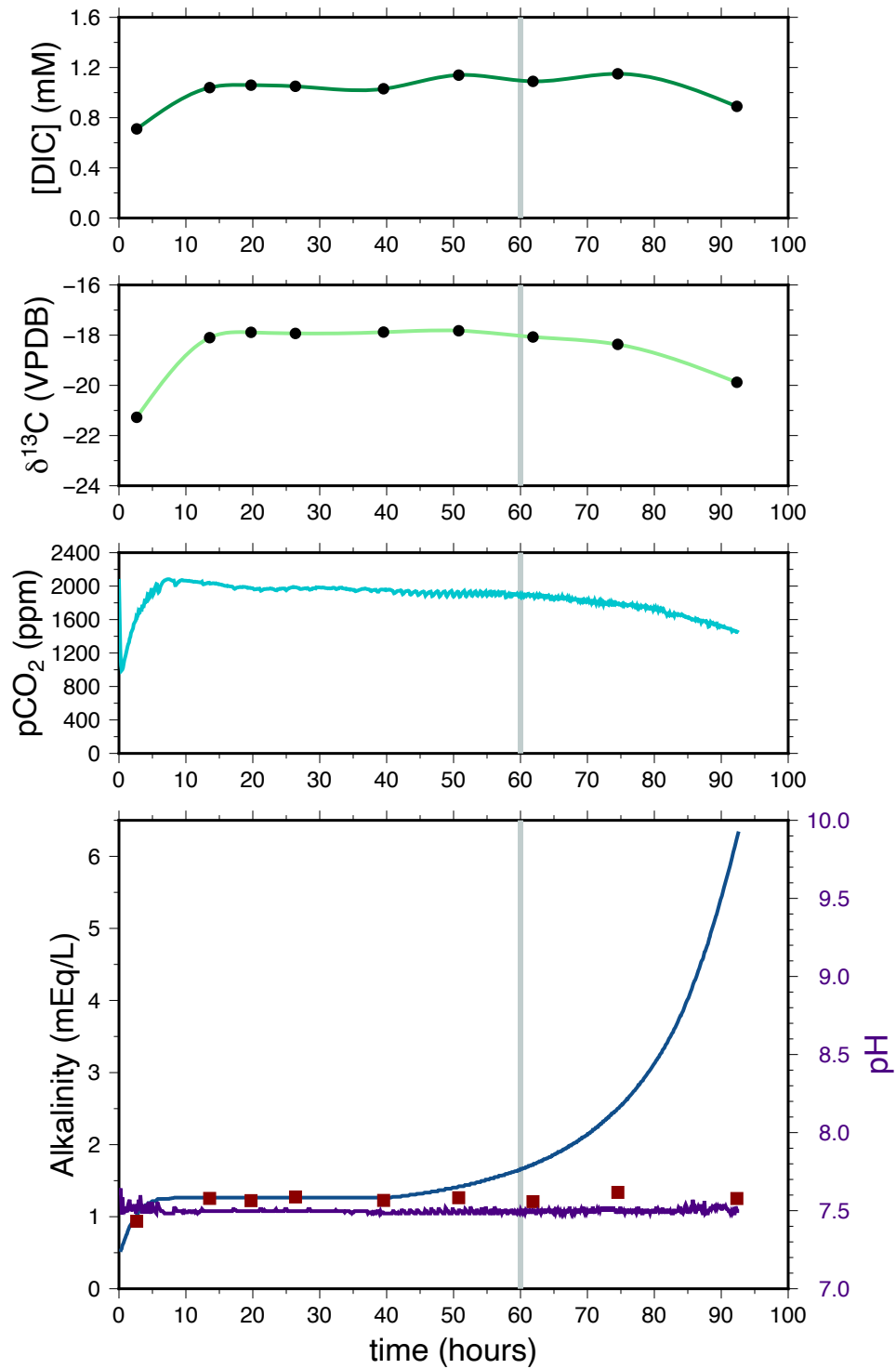


Figure 10: CA26, pH = 7.5

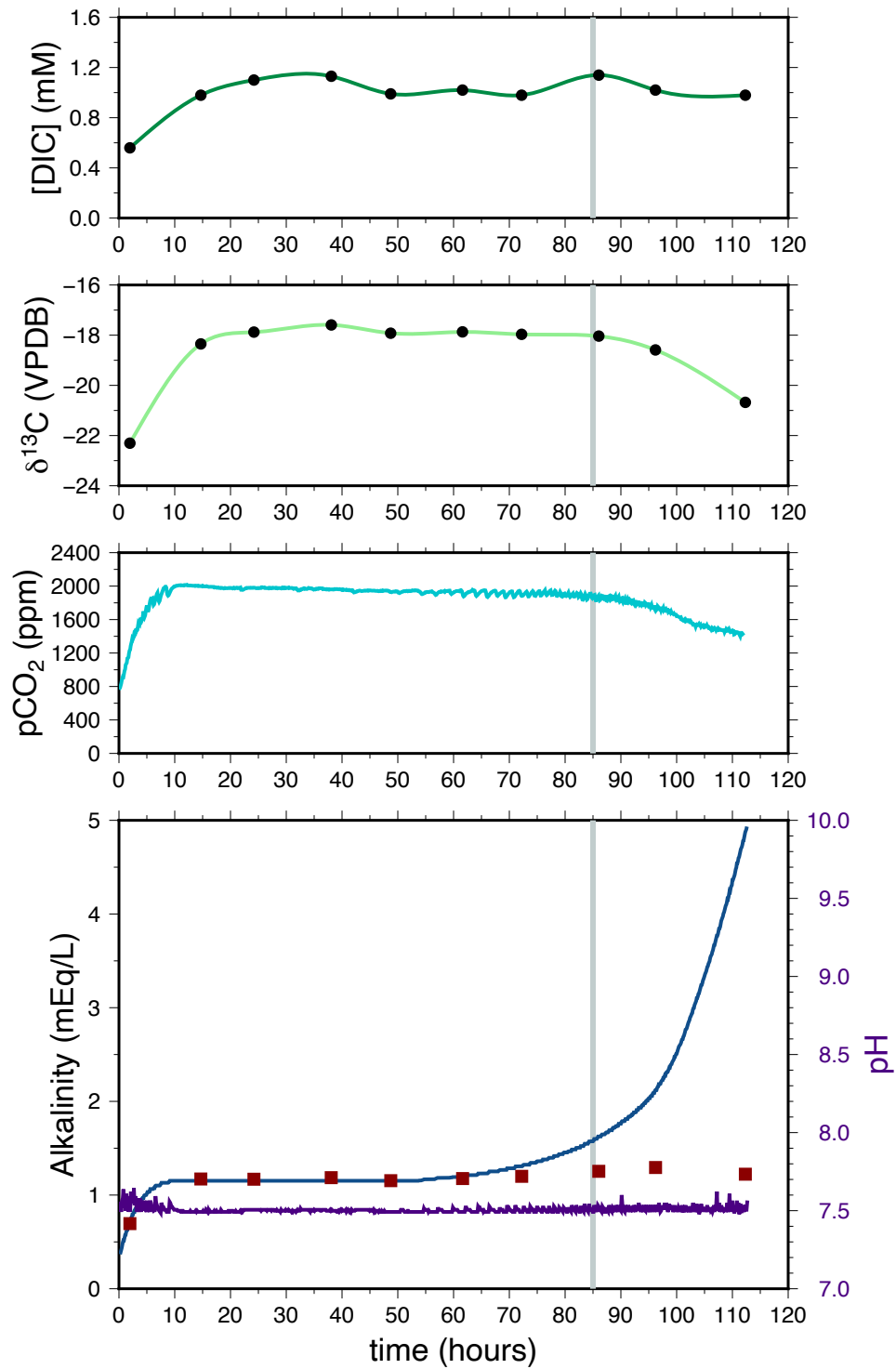


Figure 11: CA27, pH = 7.5

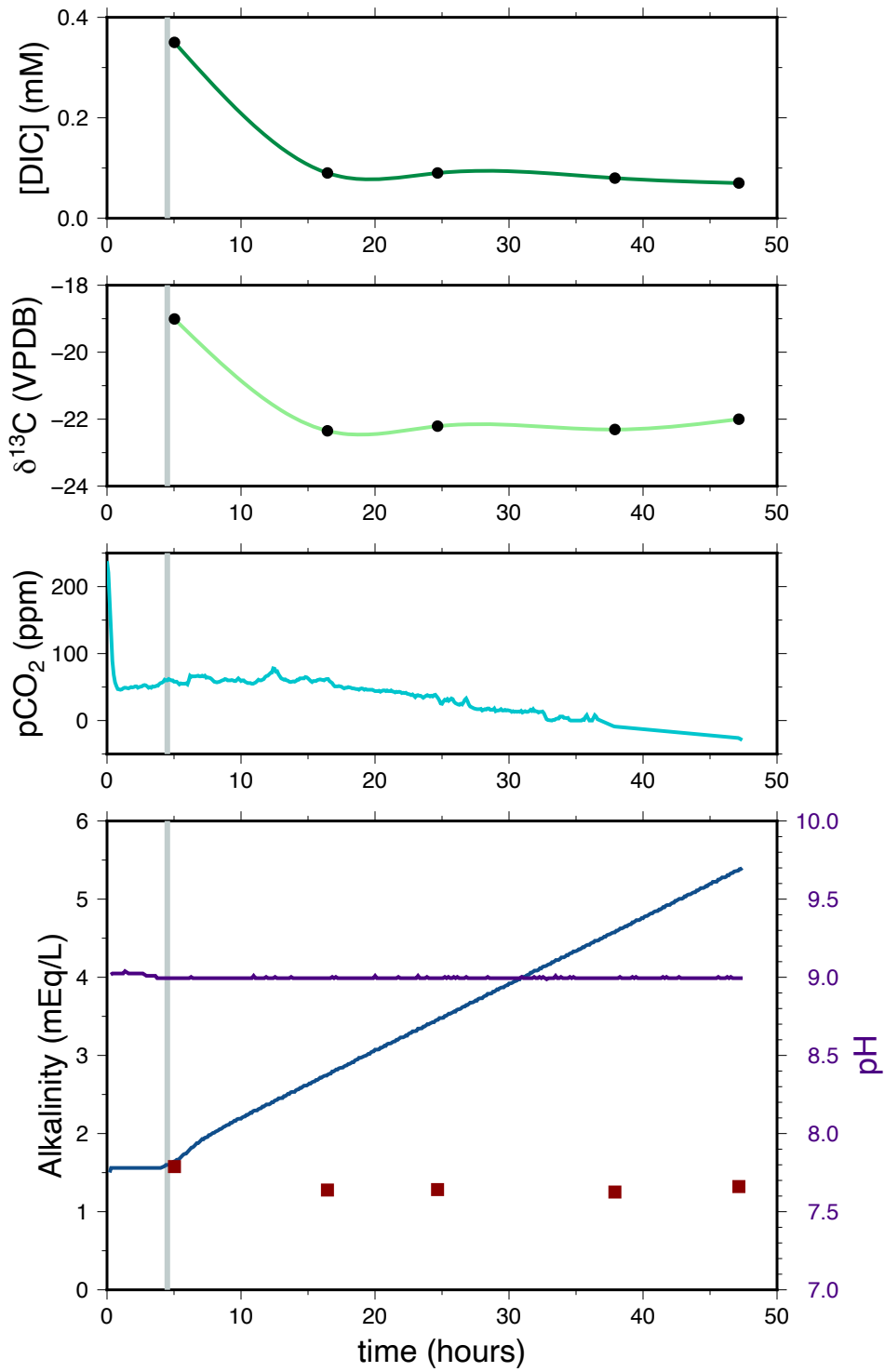


Figure 12: CA28, 9.0

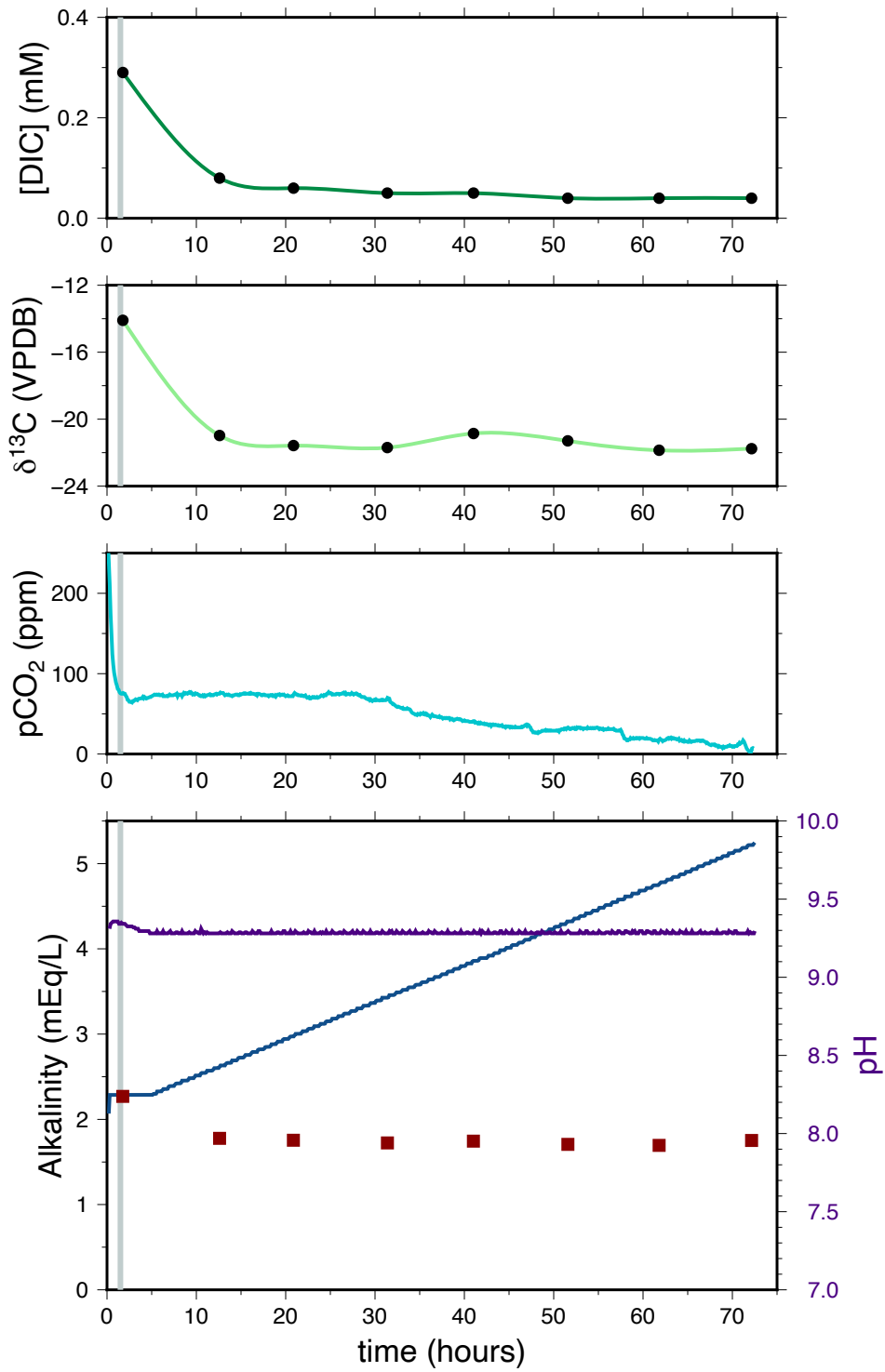


Figure 13: CA29, pH = 9.3

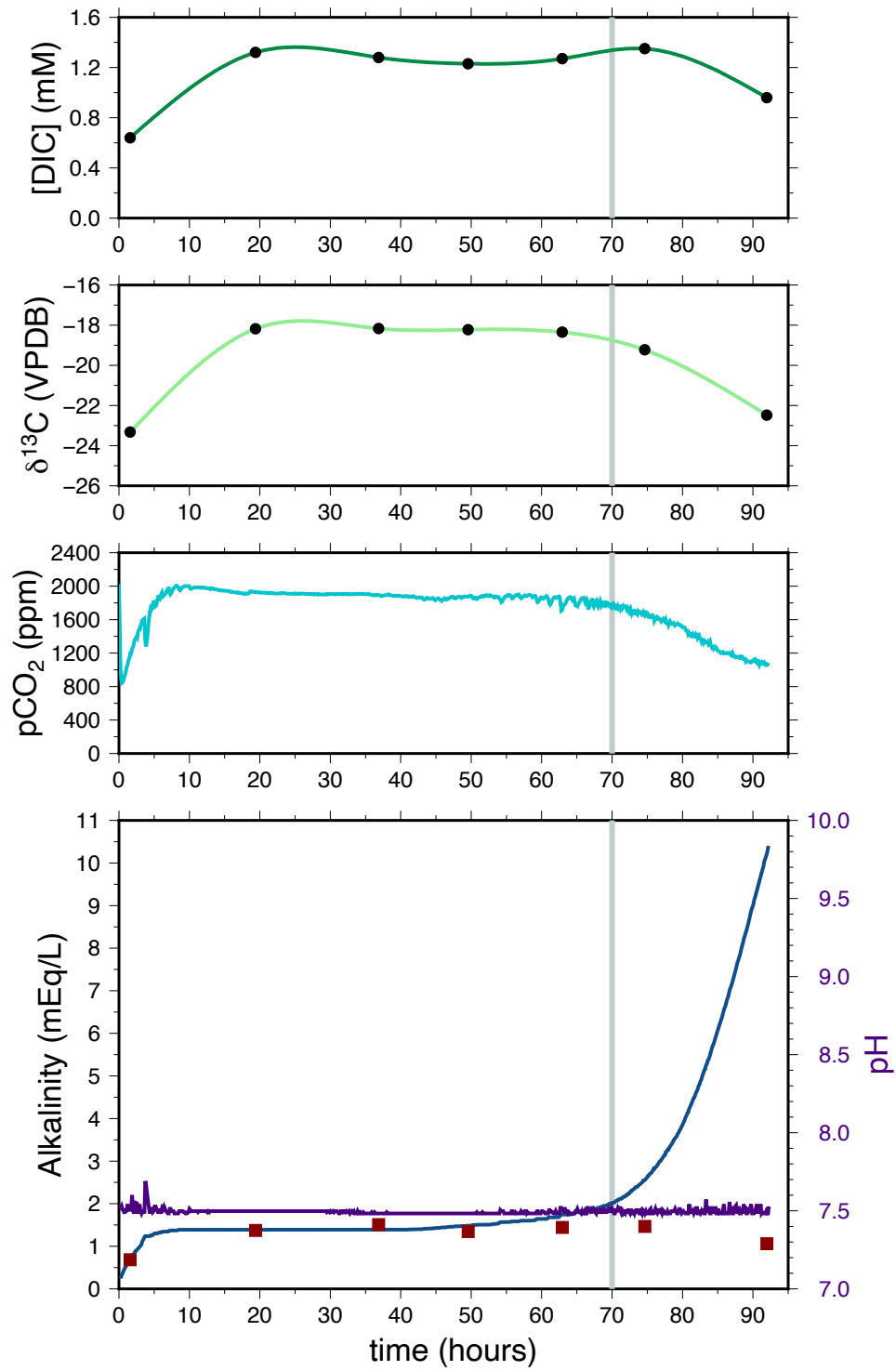


Figure 14: CA30, pH = 7.5

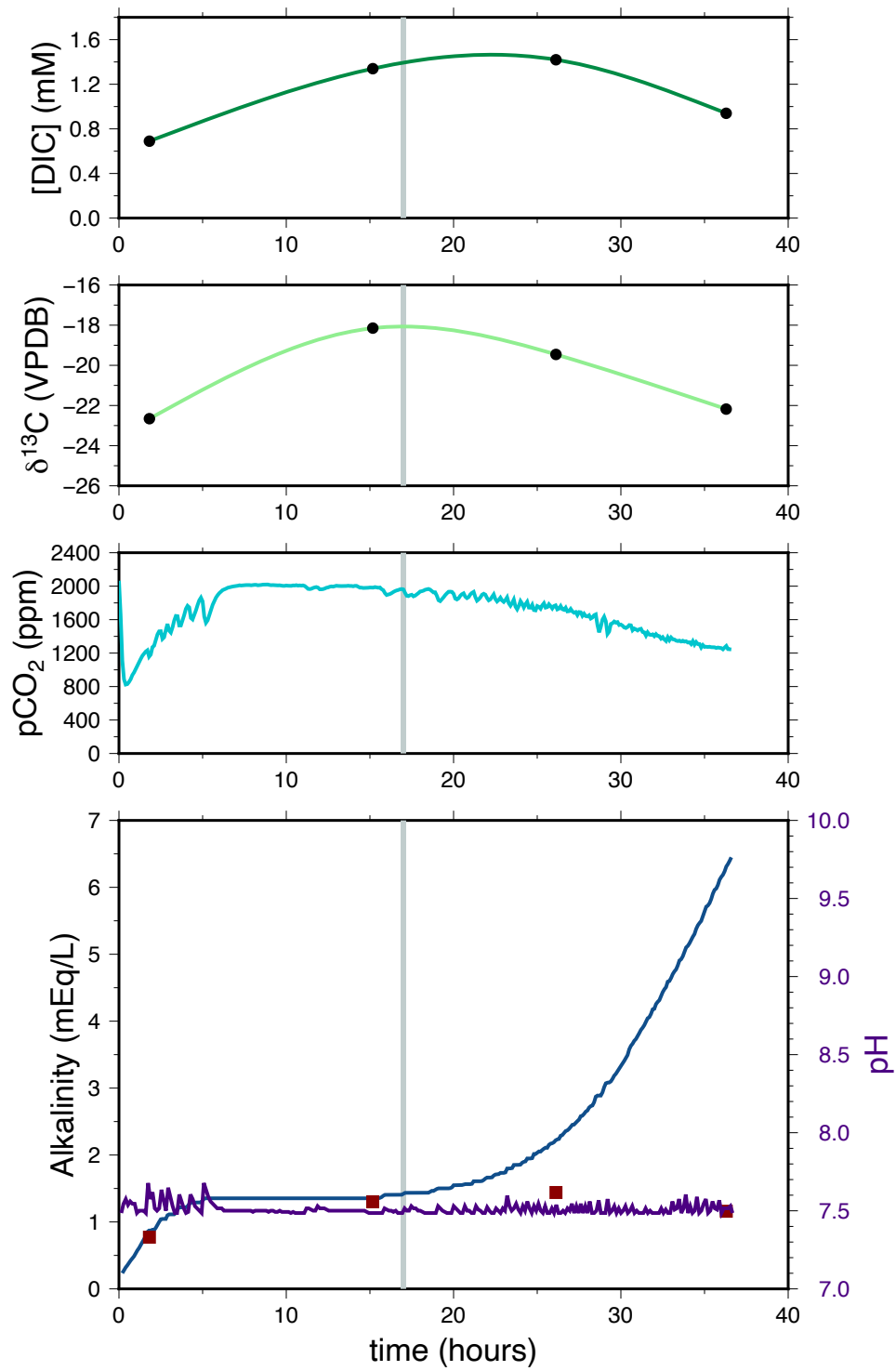


Figure 15: CA31, pH = 7.5

3 SEM images

SEM images for experiments S6, S8, CA4, CA18, and CA20 were included as part of the experimental suite for Chapter III and may be found in Appendix B.

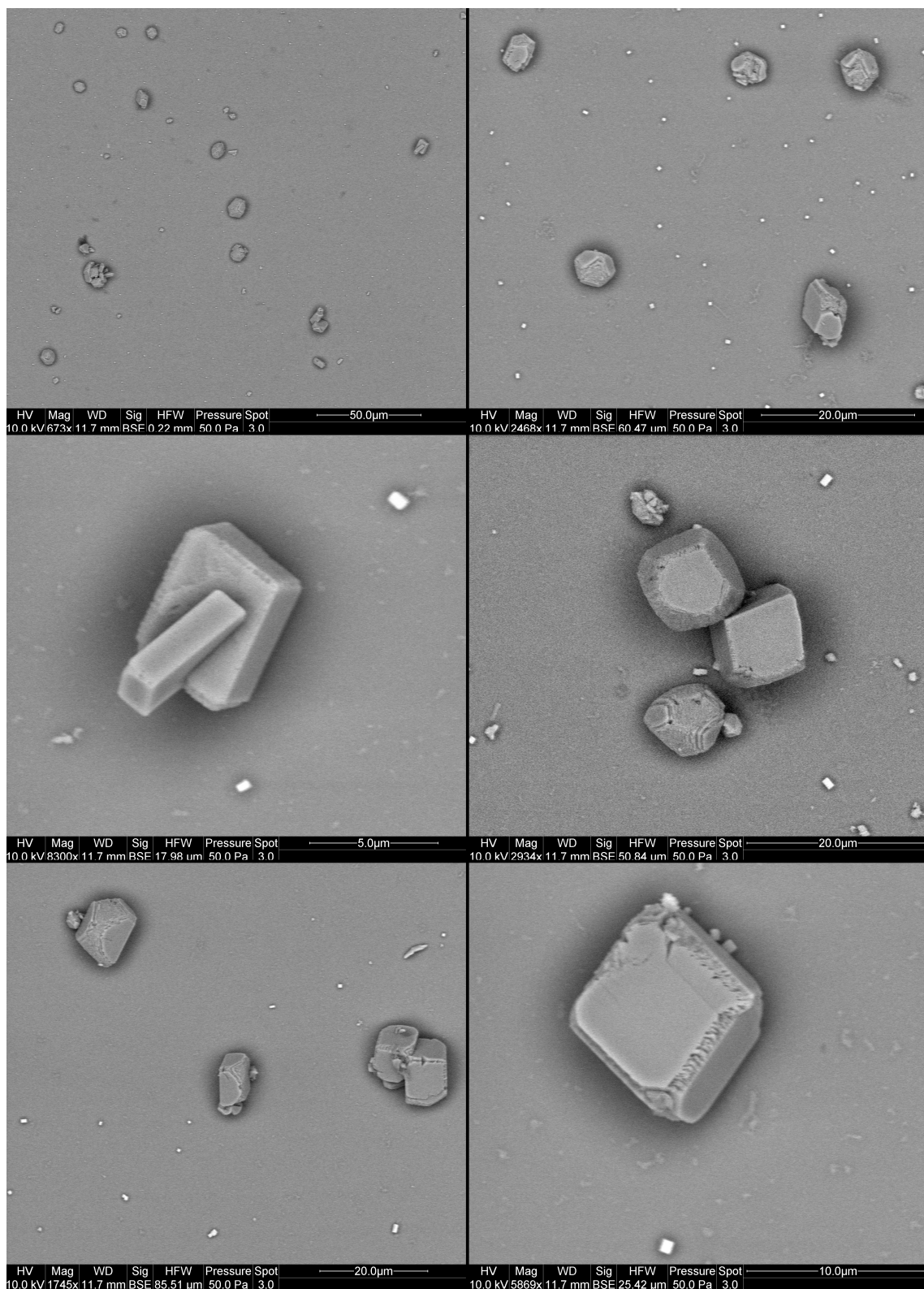


Figure 16: CA10, pH = 9.3

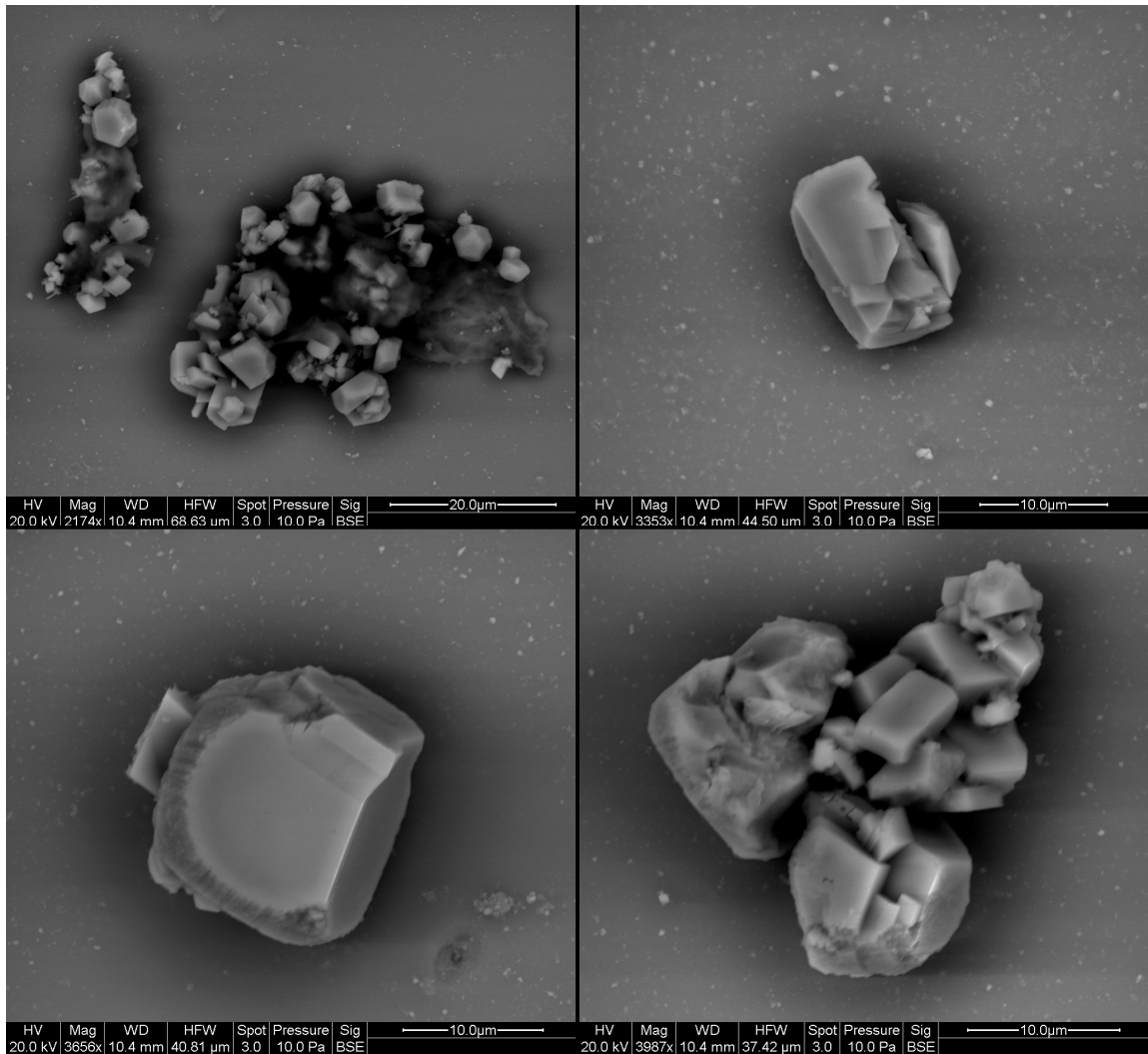


Figure 17: CA11, pH = 9.3

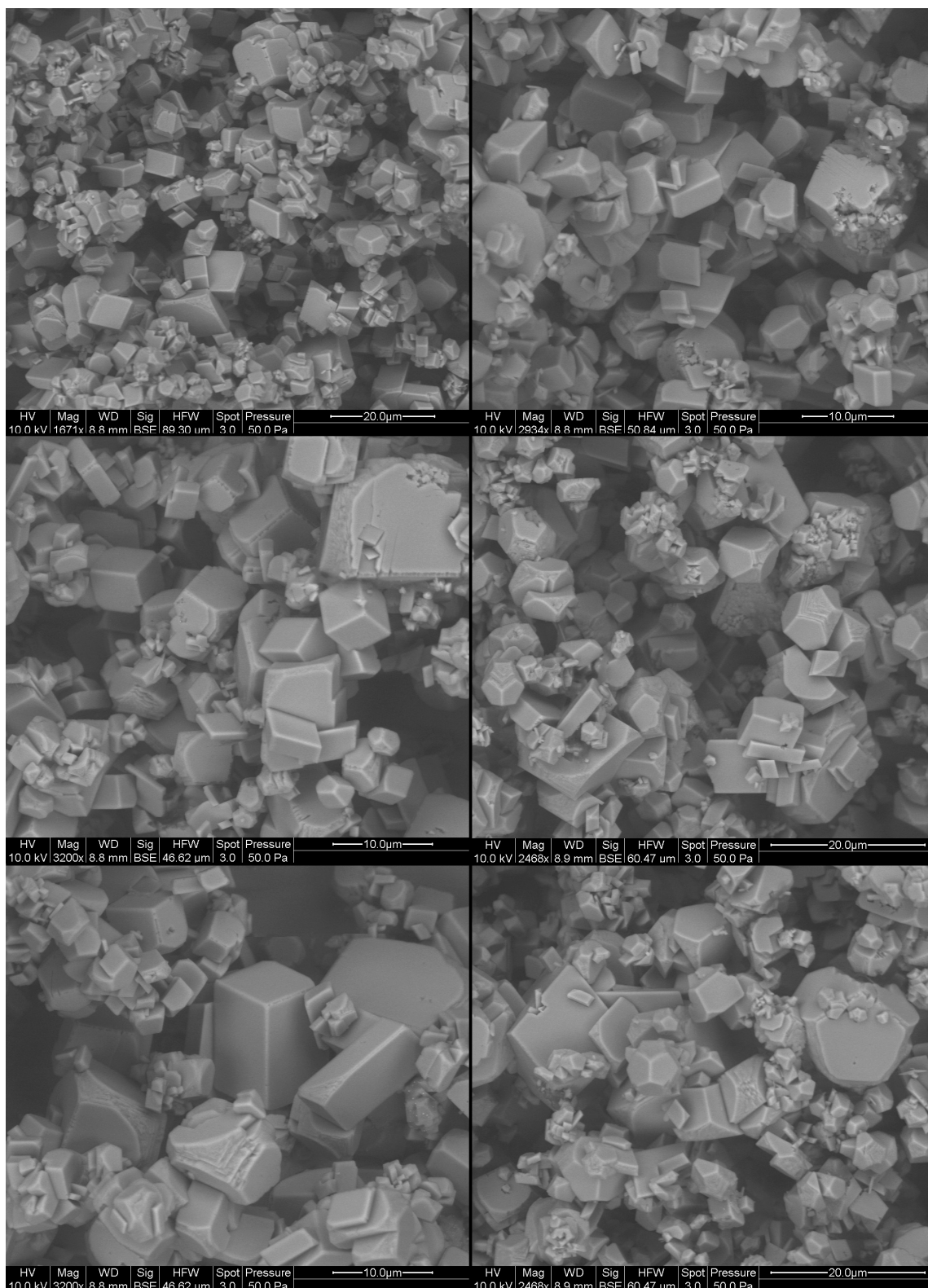


Figure 18: CA16, pH = 7.9

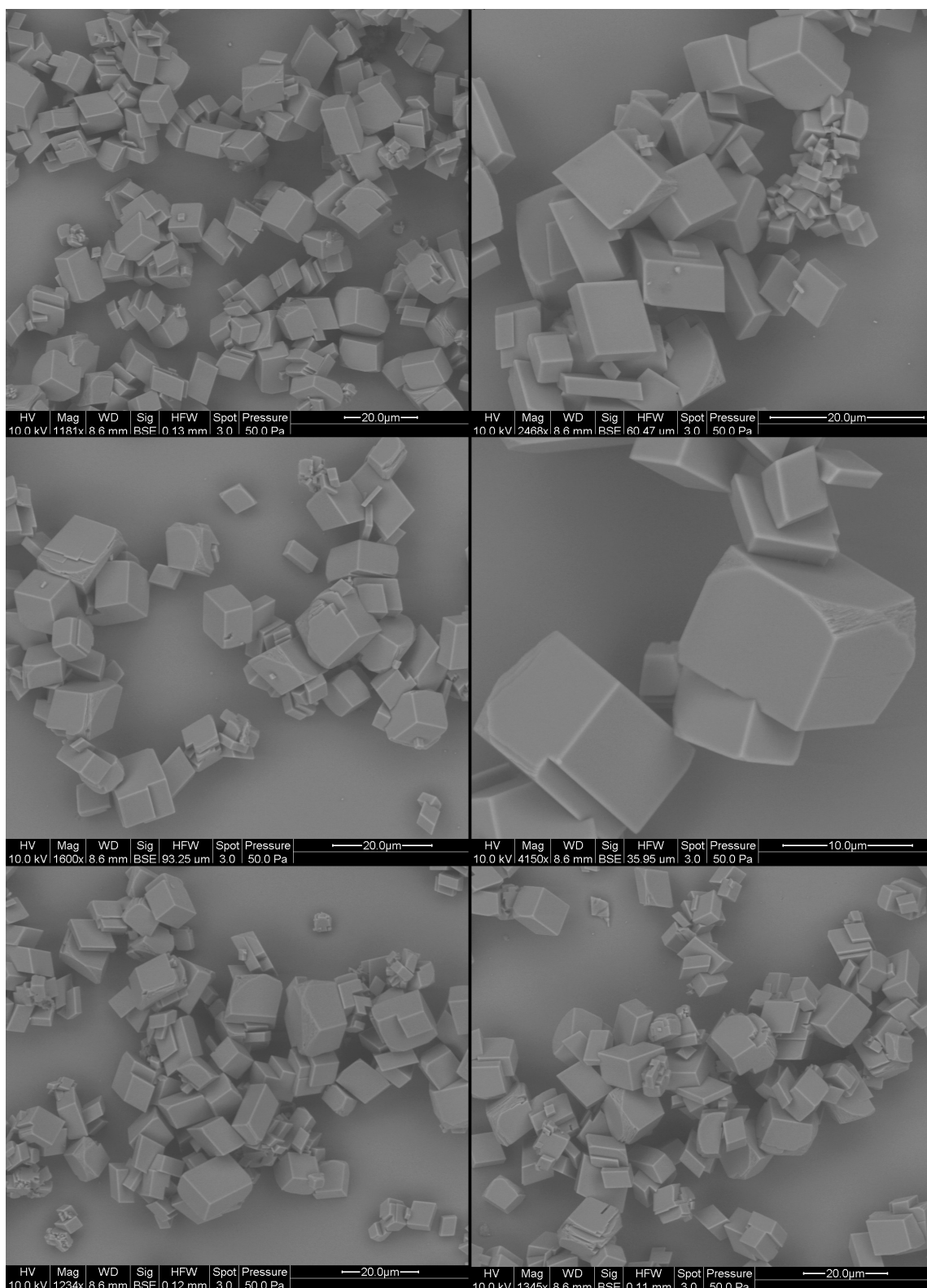


Figure 19: CA17, pH = 7.9. Time series experiment - 1st disc removed

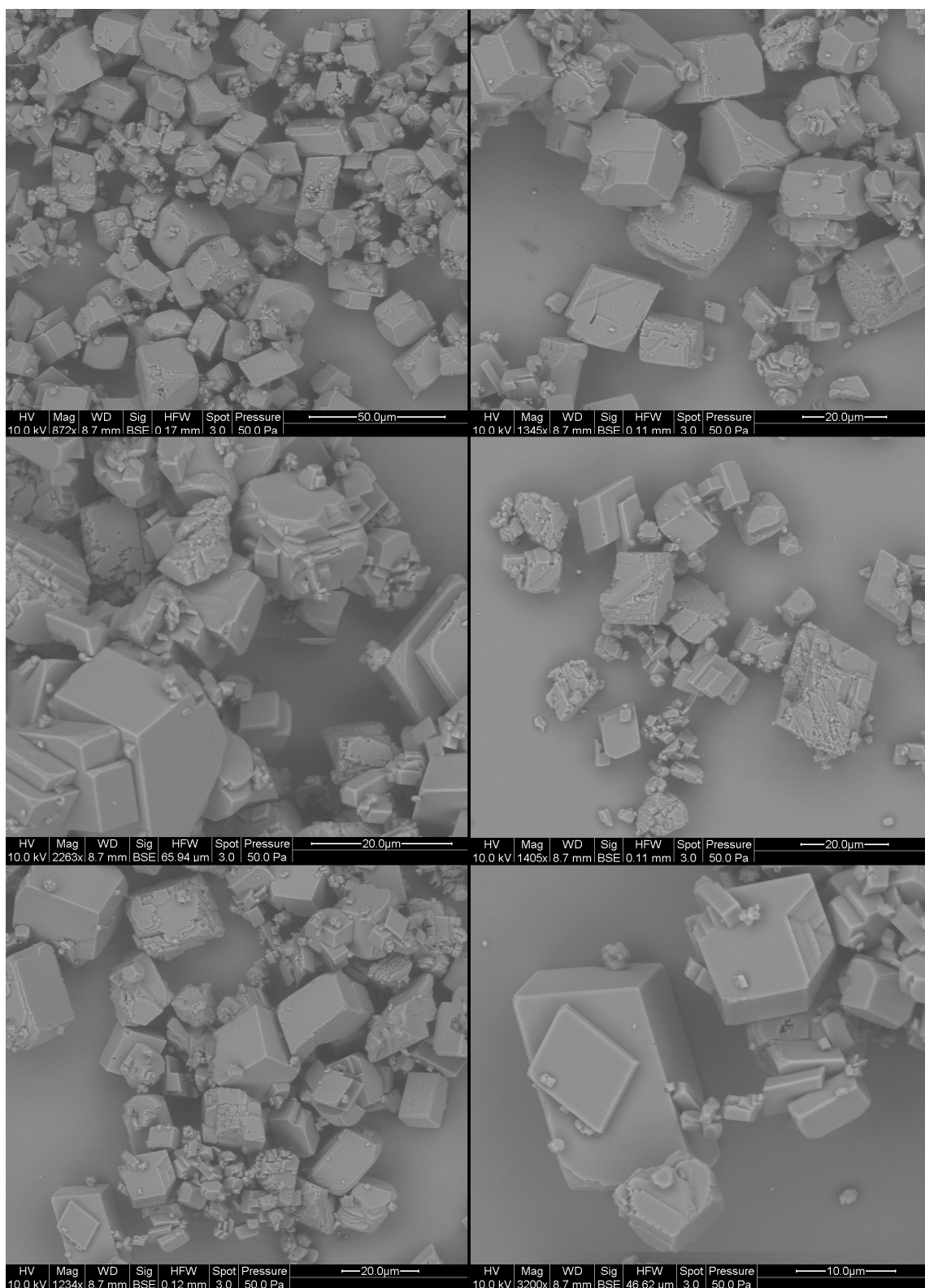


Figure 20: CA17, pH = 7.9. Time series experiment - 2nd disc removed

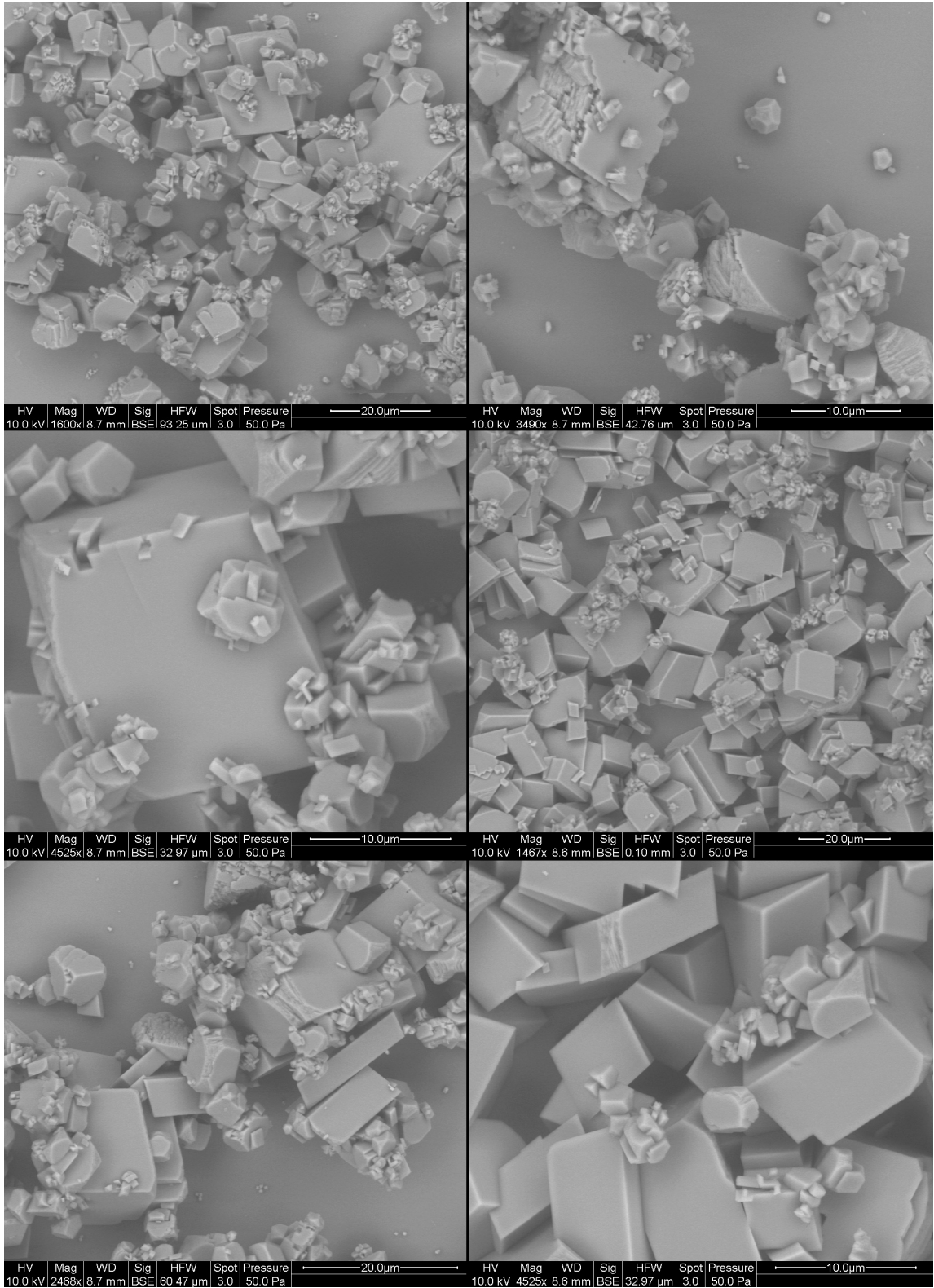


Figure 21: CA17, pH = 7.9. Time series experiment - disc in solution for the full experiment

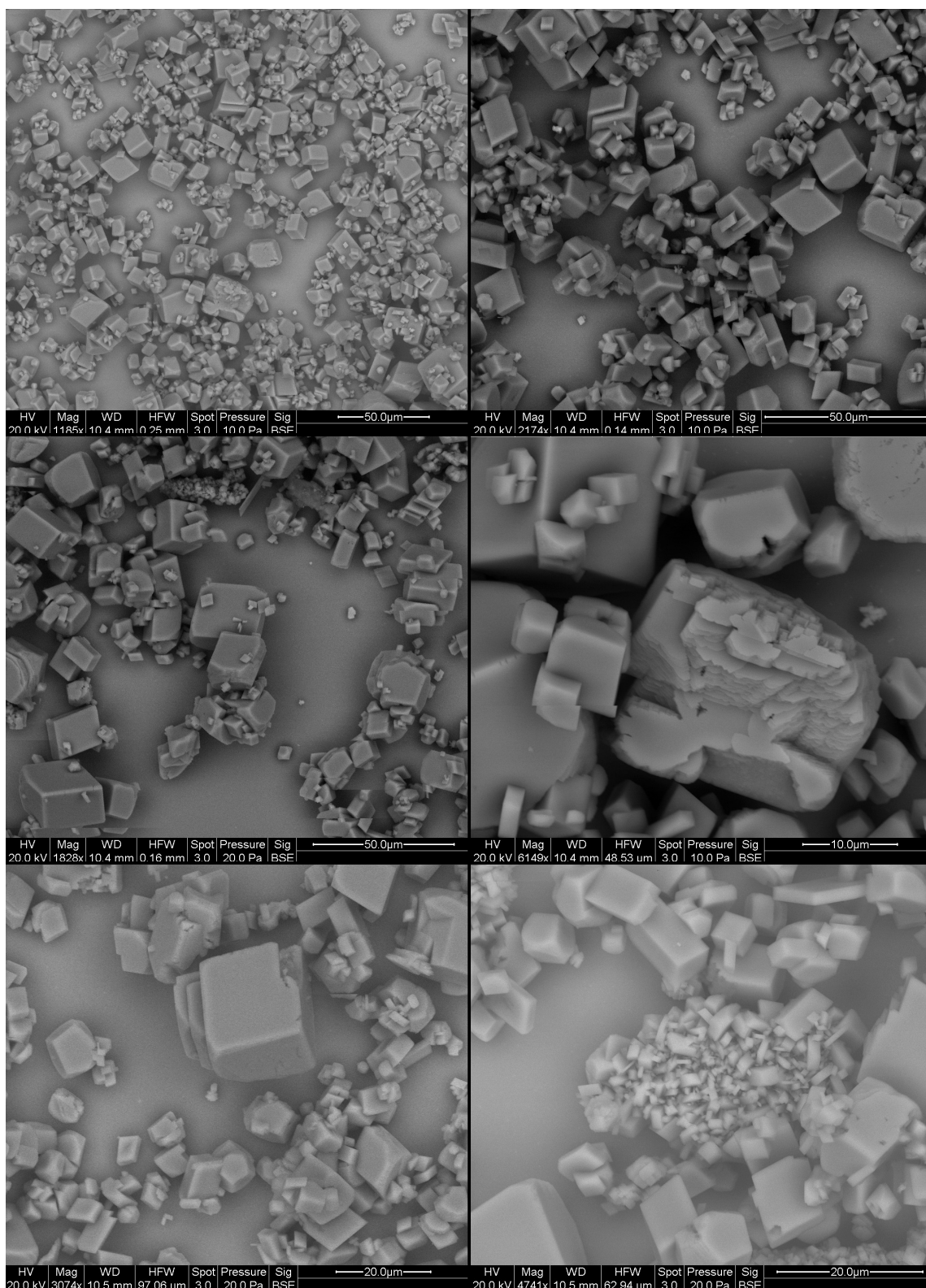


Figure 22: CA21, pH = 8.65

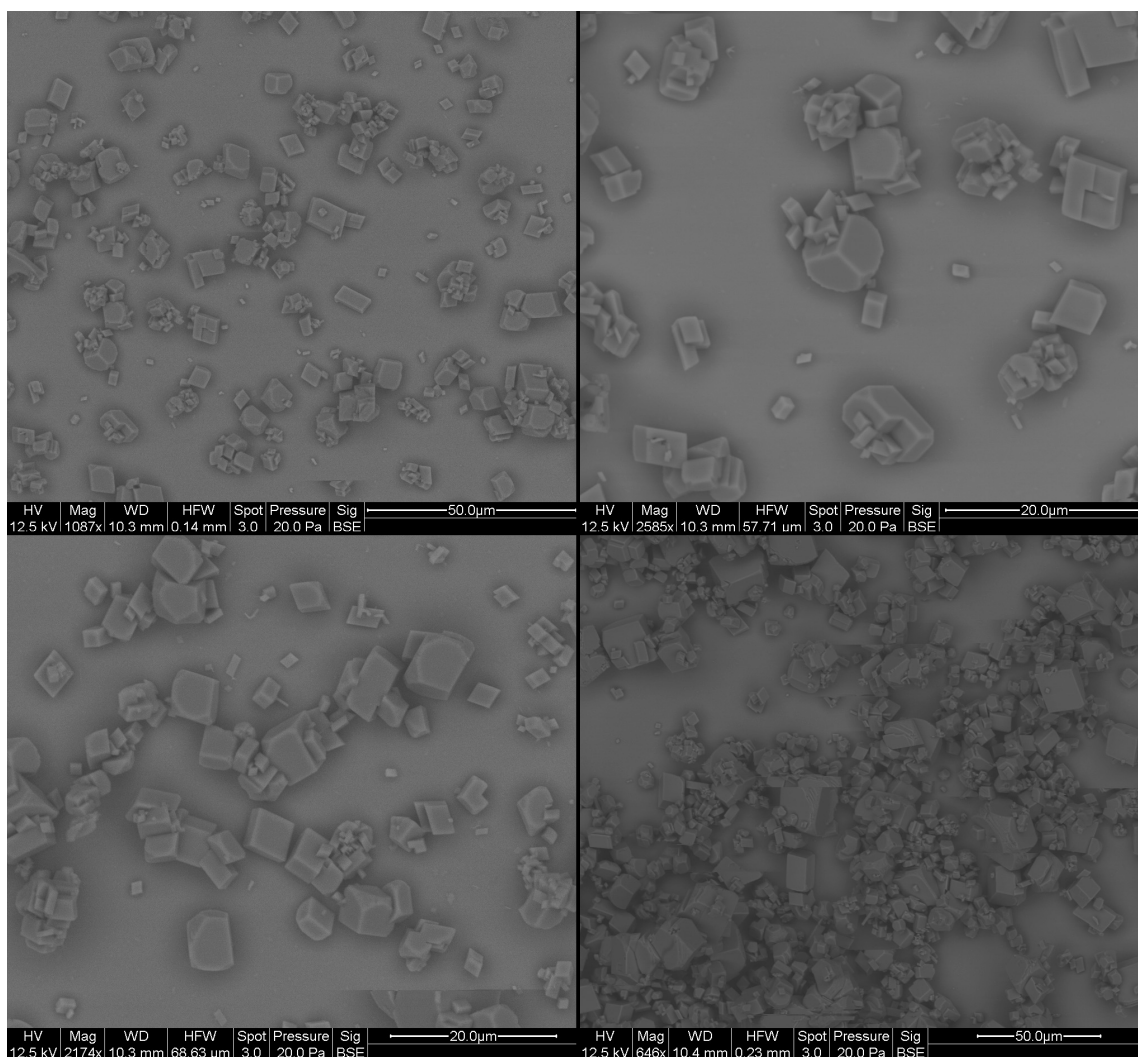


Figure 23: CA22, pH = 9.0

4 Additional figures

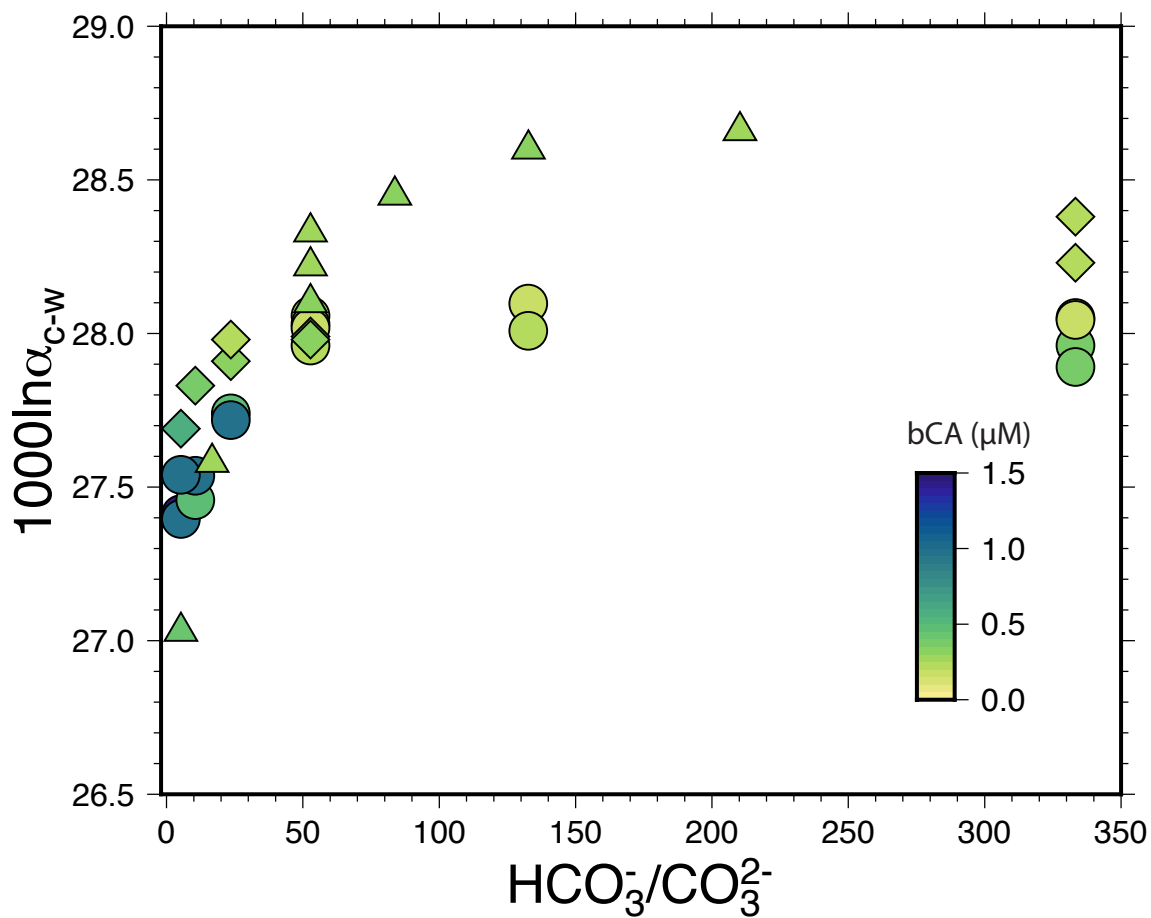


Figure 24: Oxygen isotope fractionation between calcite and experimental solution expressed as $1000\ln\alpha_{c-w}$, over the range of experimental solution $\text{HCO}_3^-/\text{CO}_3^{2-}$. Included are experiments from this study (circles), from Baker (2015) (diamonds), and from Watkins et al. (2014) (triangles).

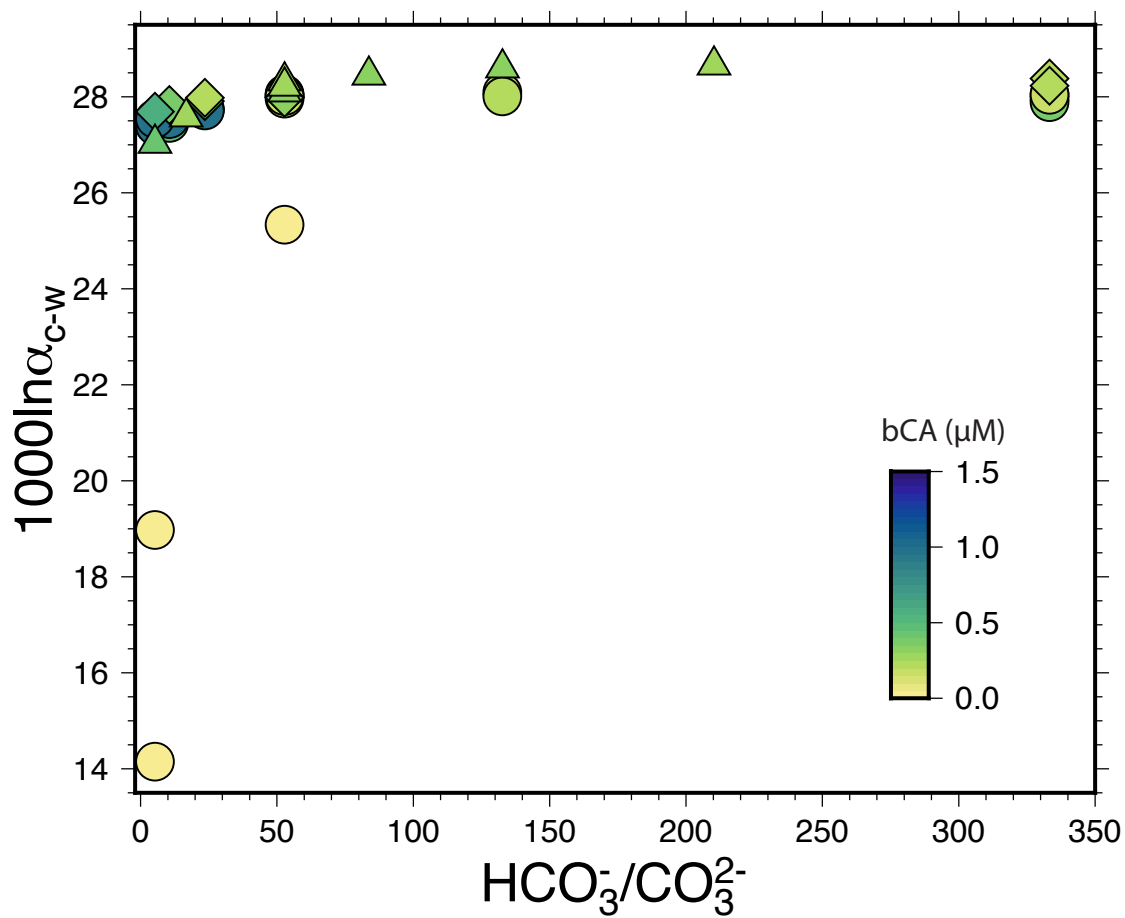


Figure 25: Oxygen isotope fractionation between calcite and experimental solution expressed as $1000\ln\alpha_{c-w}$, over the range of experimental solution $\text{HCO}_3^-/\text{CO}_3^{2-}$, including experiments that did not utilize the enzyme bCA. Included are experiments from this study (circles), from Baker (2015) (diamonds), and from Watkins et al. (2014) (triangles).

APPENDIX E
CHAPTER V SUPPLEMENTARY MATERIAL:
EXPERIMENT DATA AND SEM IMAGES OF PRECIPITATES

1 Experiment data

For each experiment, we continuously monitored the experimental solution pH and concentration of CO₂ (ppm) of the experiment headspace. For open-air experiments, the concentration of CO₂ reflects that of the laboratory air.

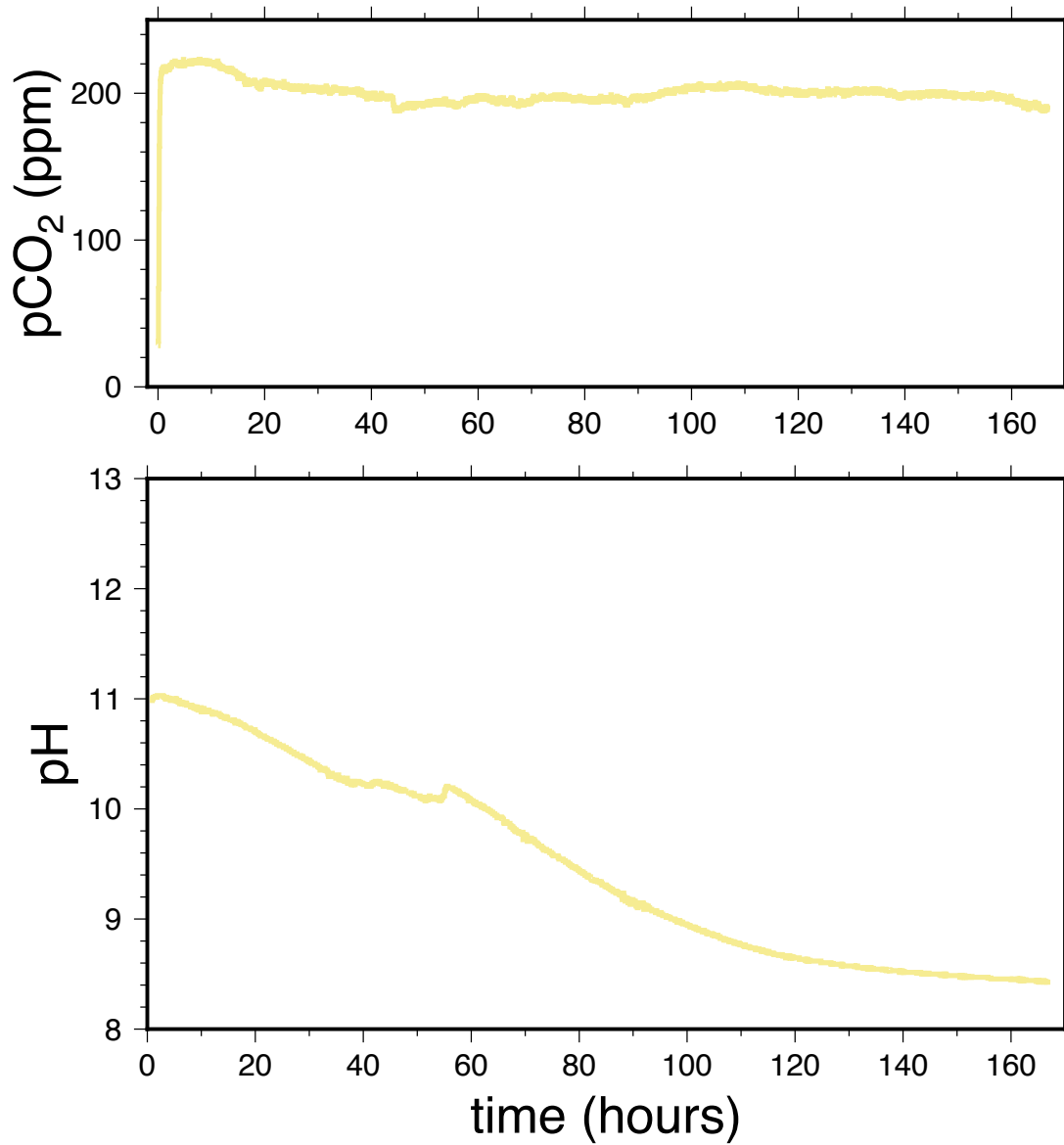


Figure 1: CH1. 200ppm CO₂, 25°C, 10mM Ca²⁺

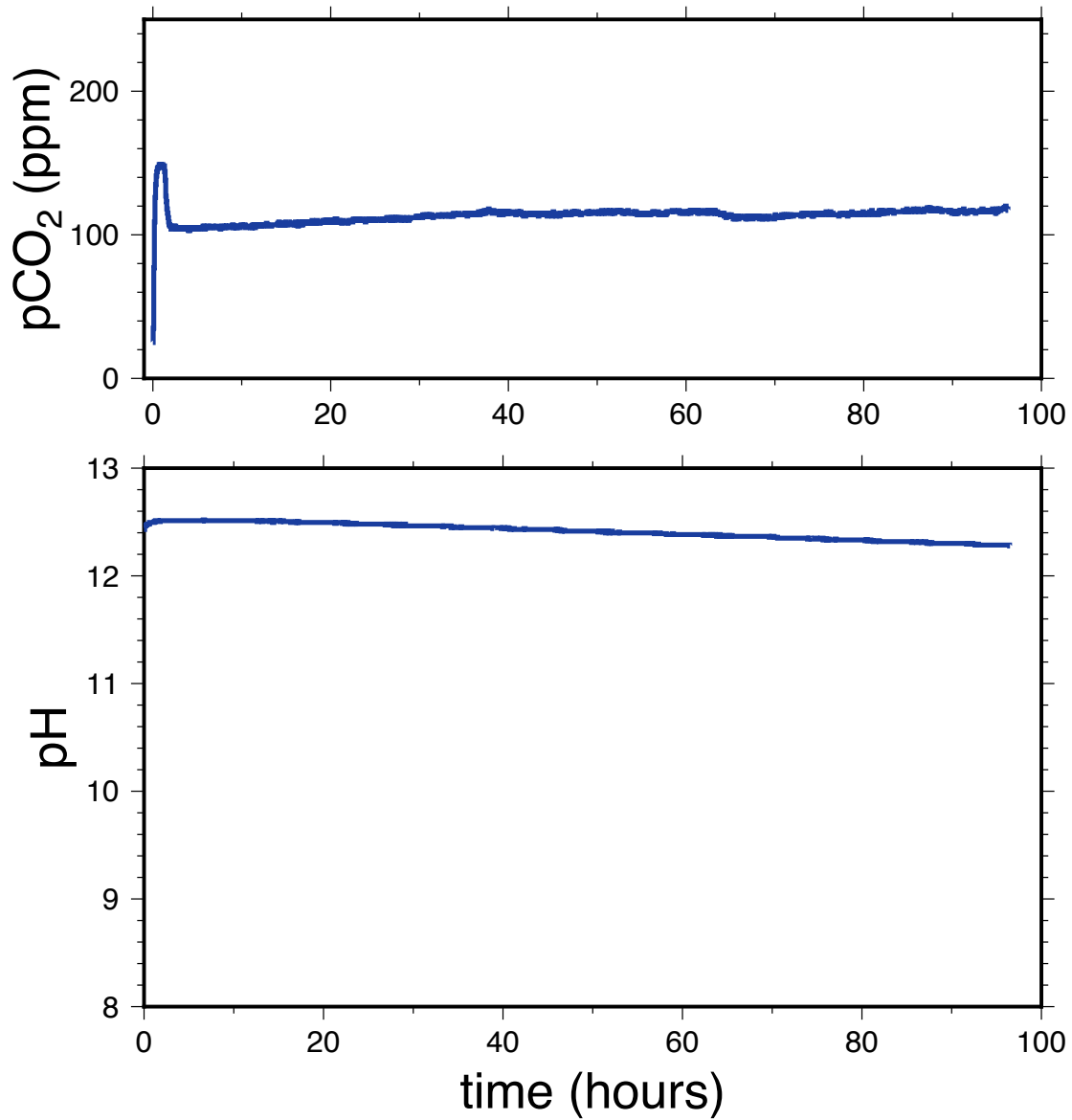


Figure 2: CH2. 200ppm CO₂, 25°C, 30mM Ca²⁺

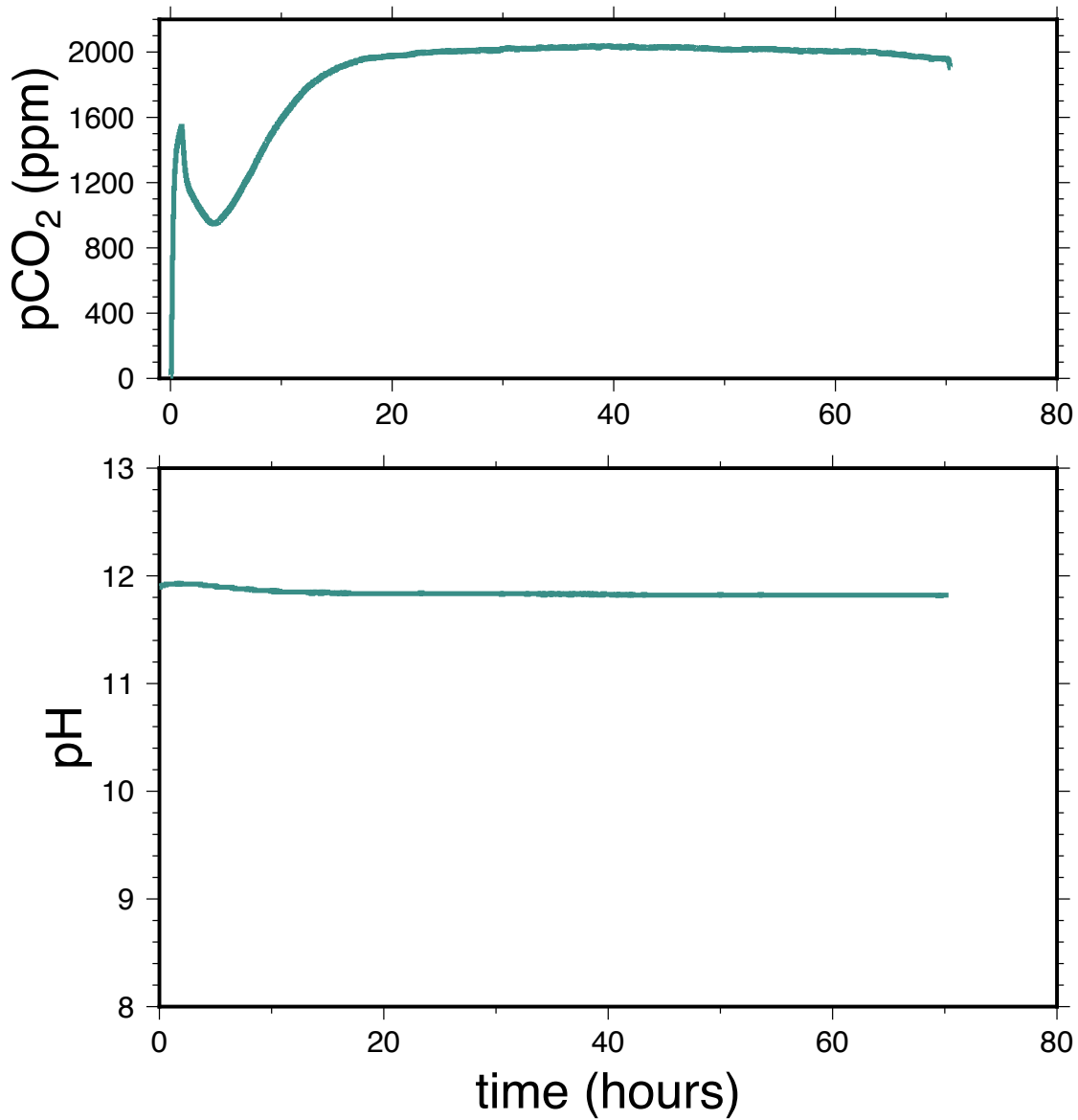


Figure 3: CH3. 2000ppm CO₂, 25°C, 30mM Ca²⁺

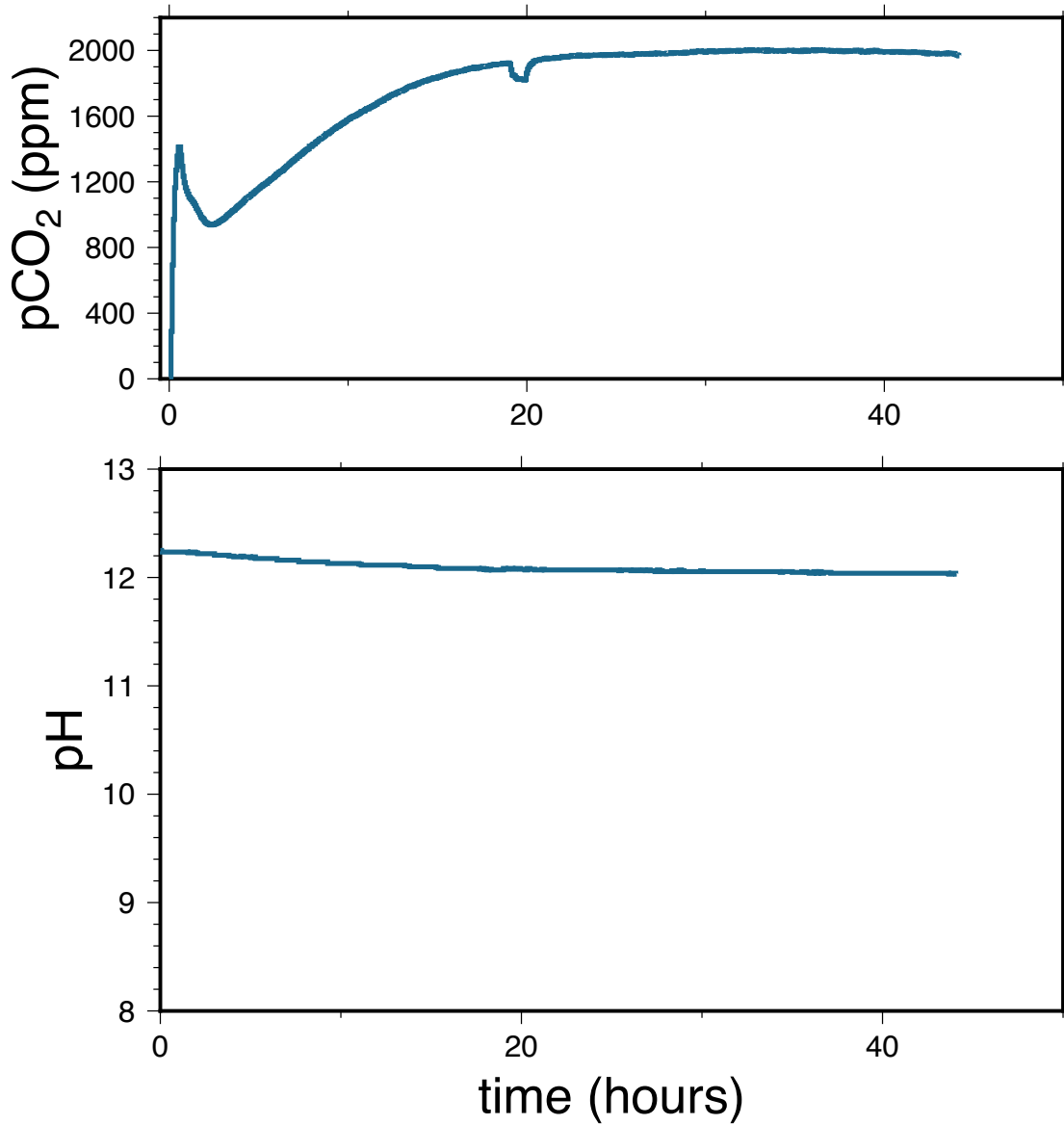


Figure 4: CH₄. 2000ppm CO₂, 25°C, 30mM Ca²⁺

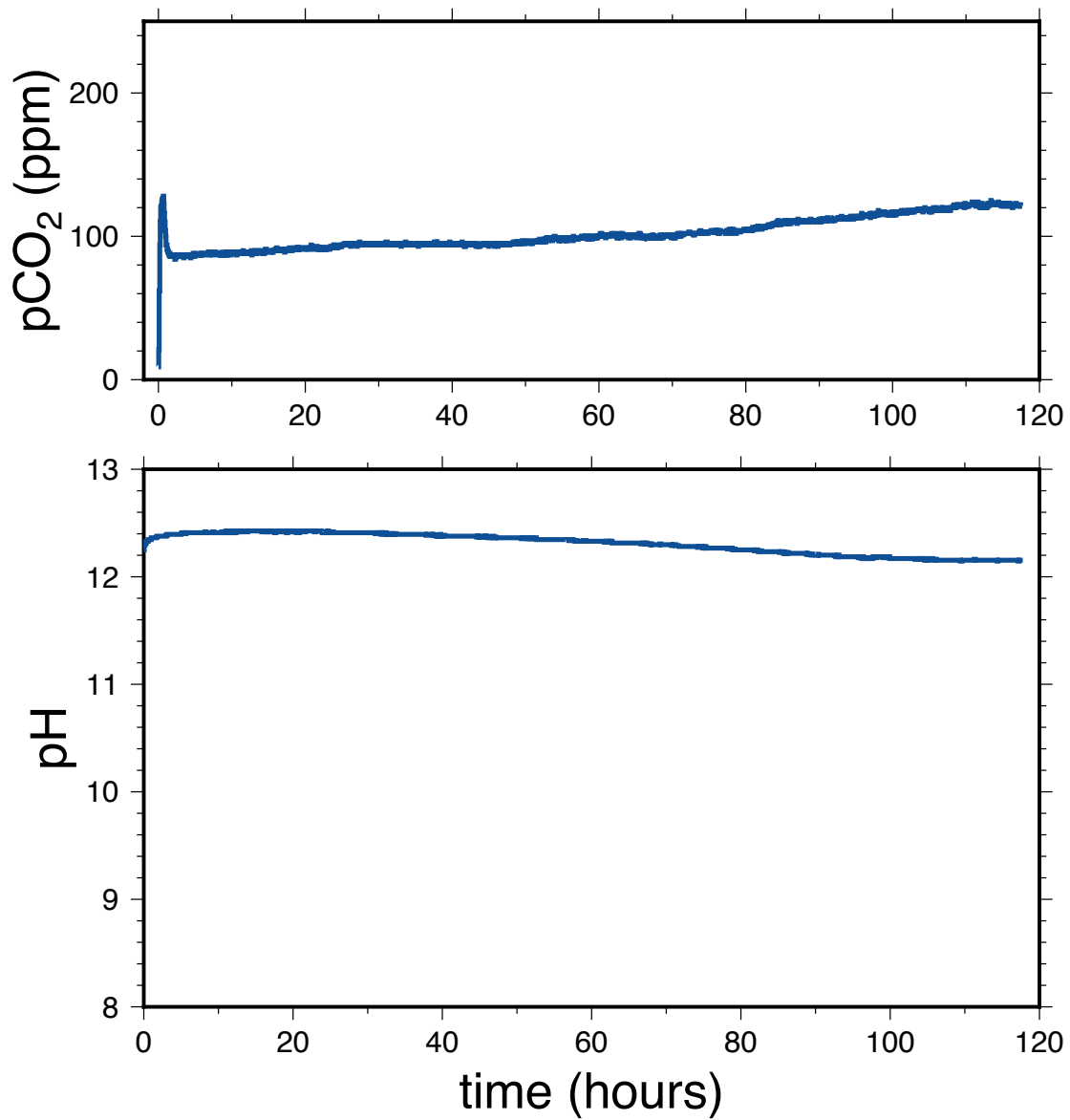


Figure 5: CH5. 200ppm CO₂, 25°C, 30mM Ca²⁺

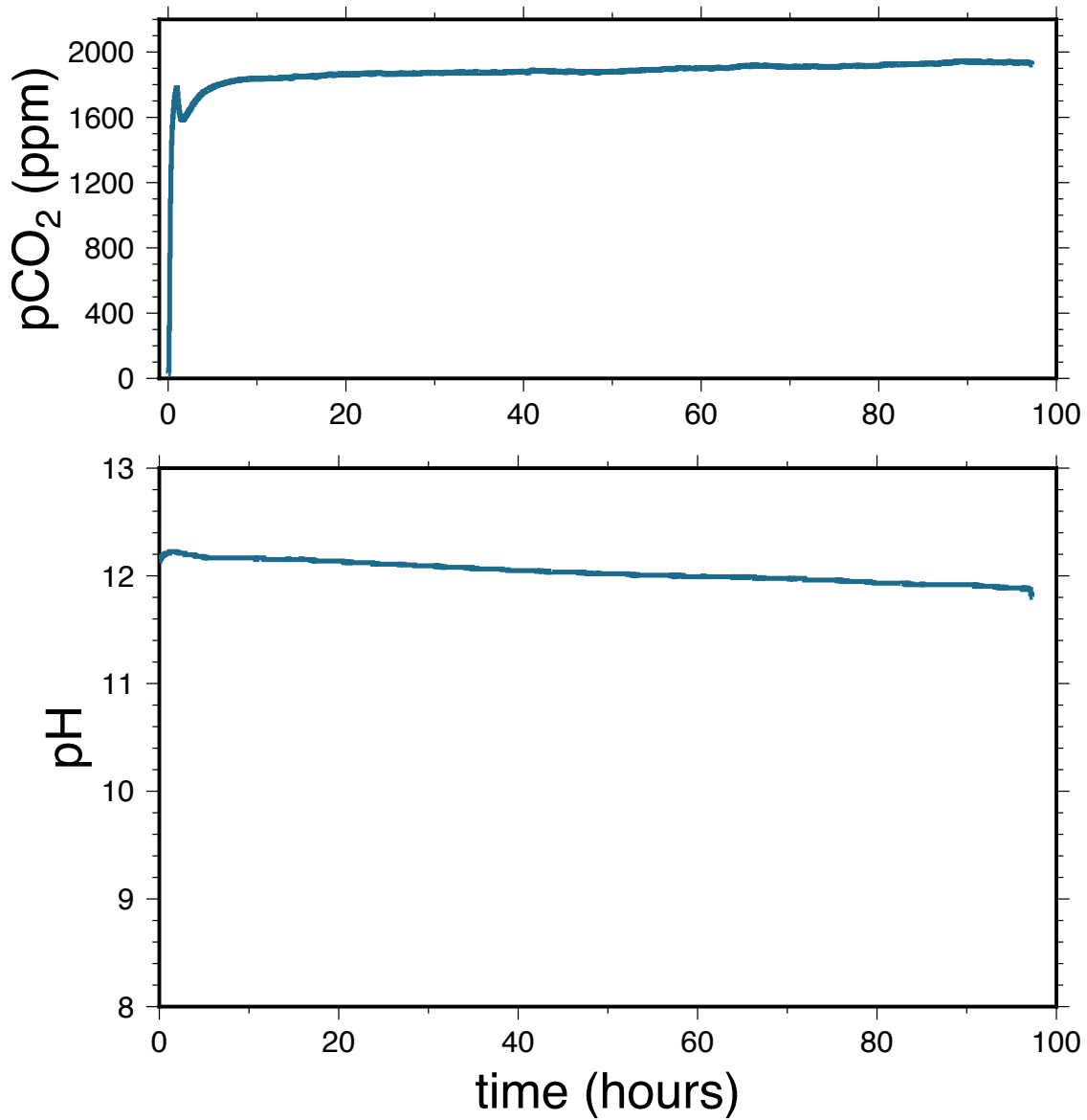


Figure 6: CH6. 2000ppm CO₂, 10°C, 30mM Ca²⁺

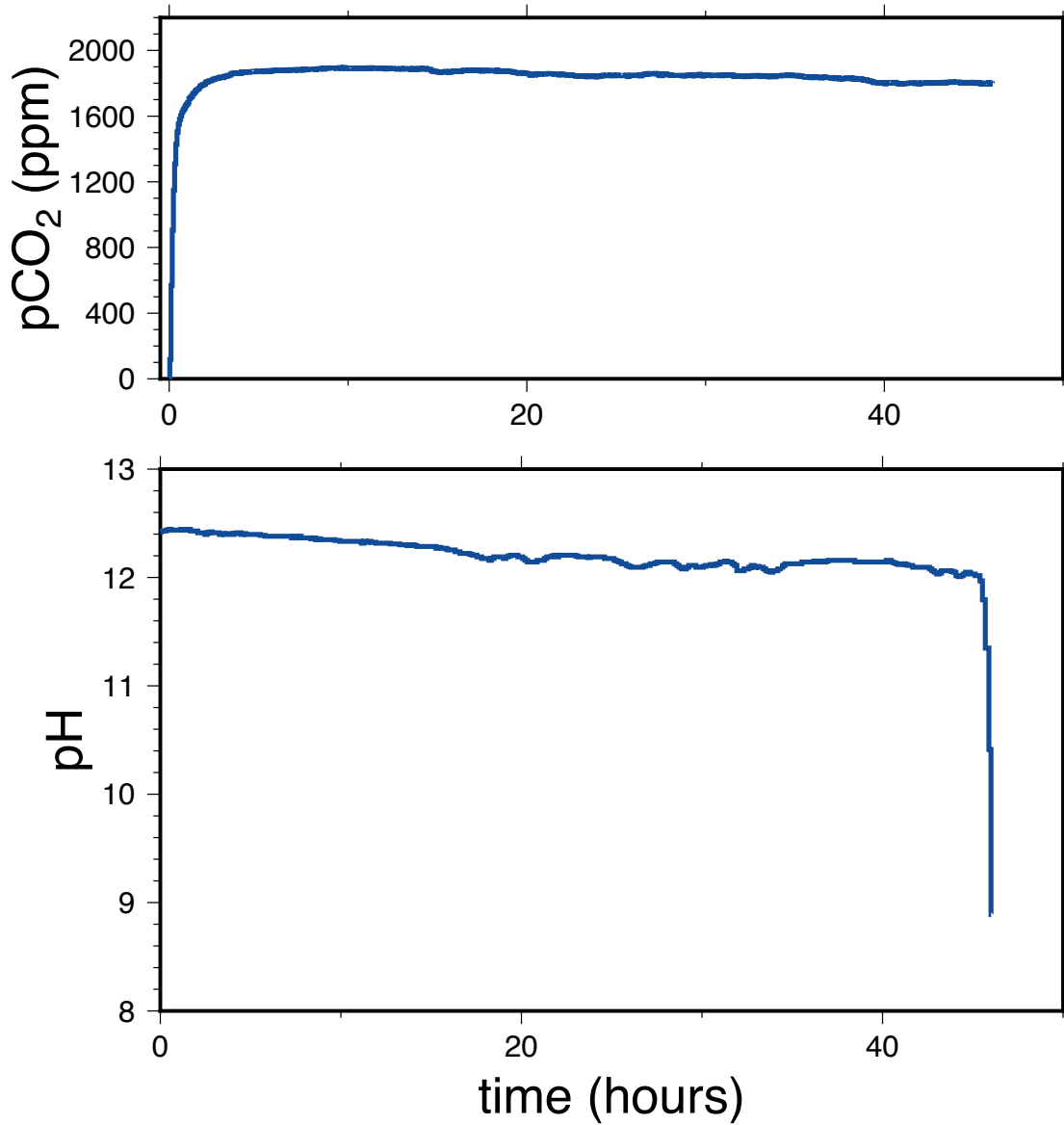


Figure 7: CH7. 2000ppm CO₂, 25°C, 30mM Ca²⁺. Unstirred

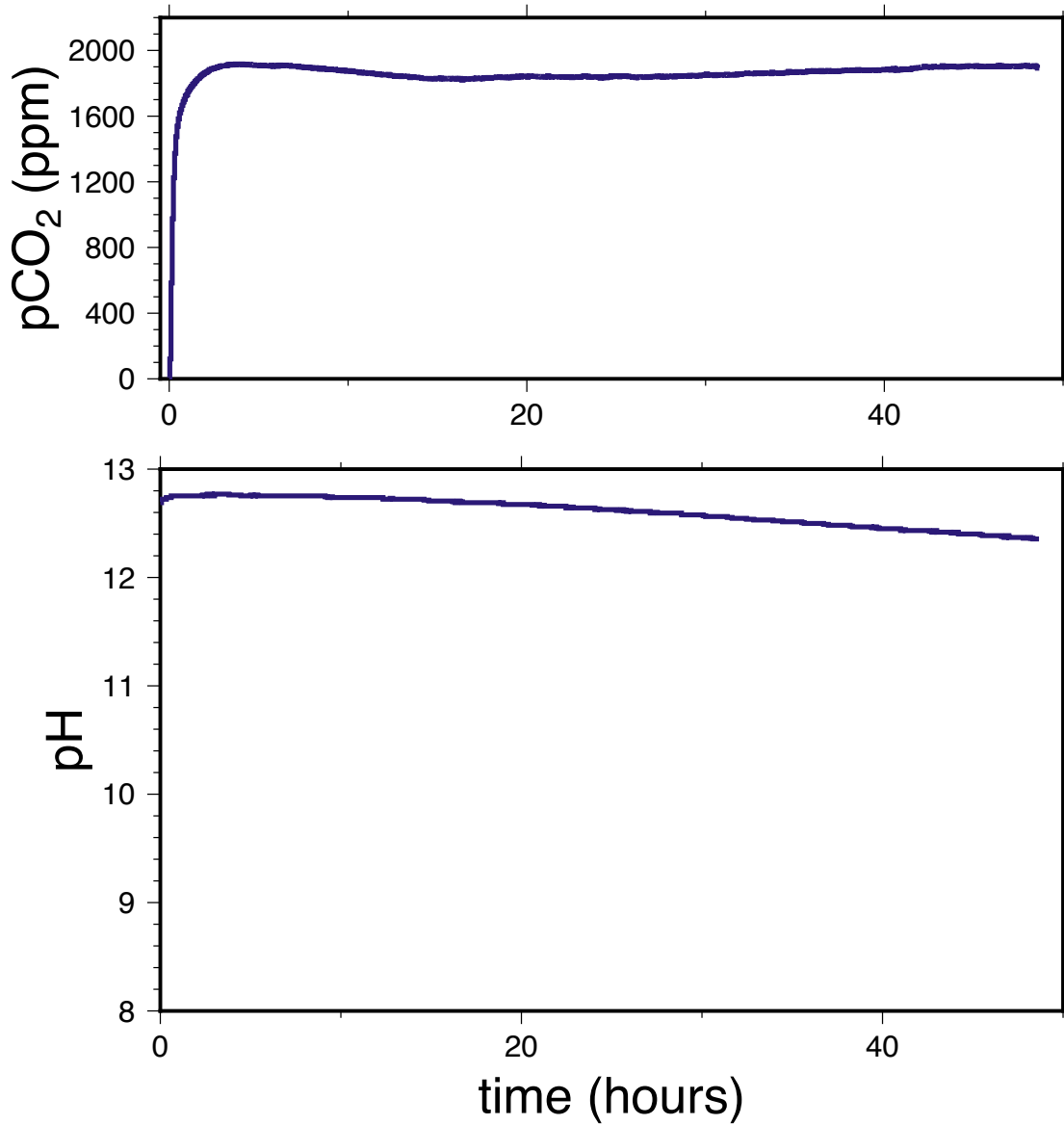


Figure 8: CH8. 2000ppm CO₂, 10°C, 30mM Ca²⁺

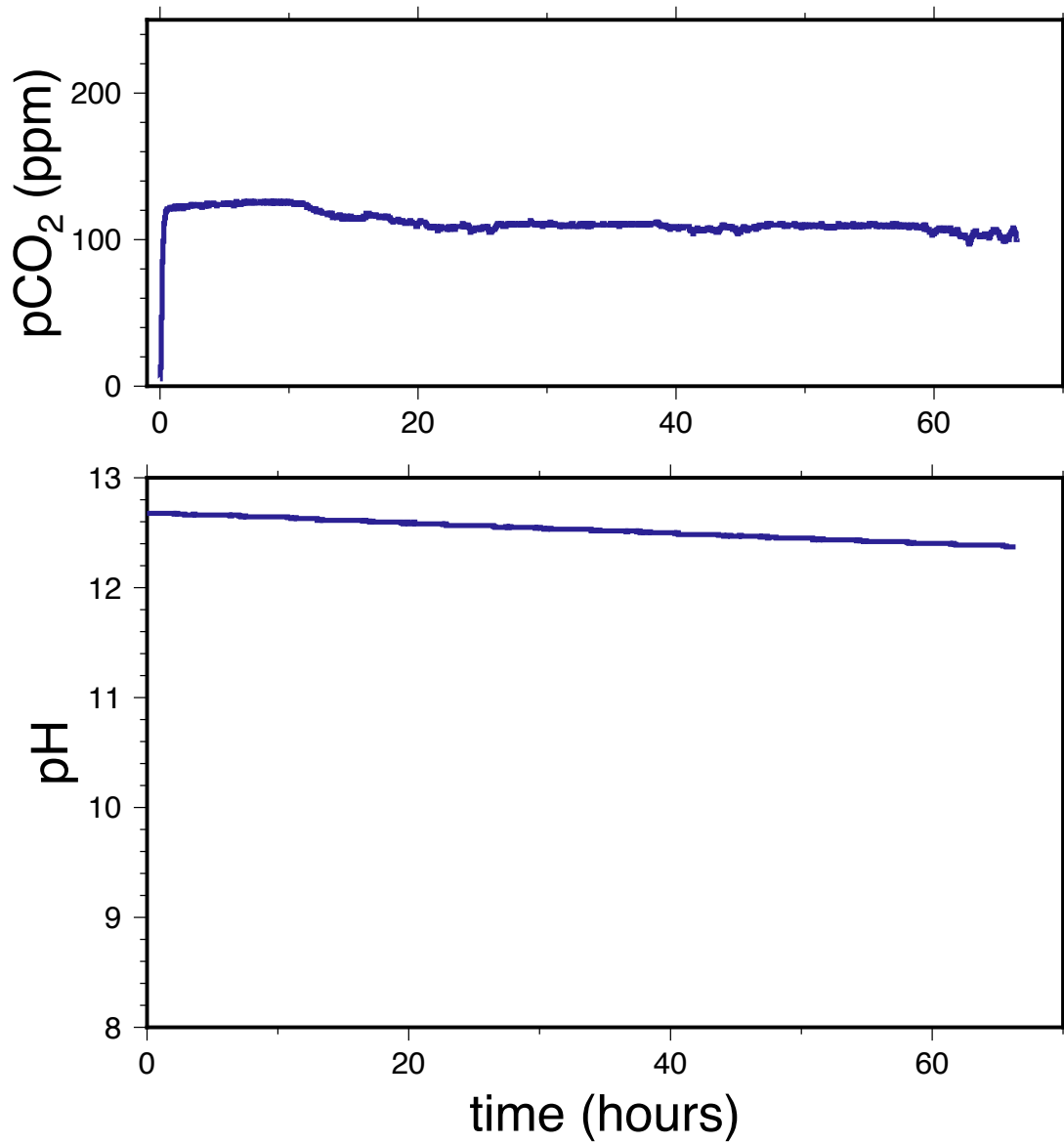


Figure 9: CH9. 200ppm CO₂, 25°C, 10mM Ca²⁺

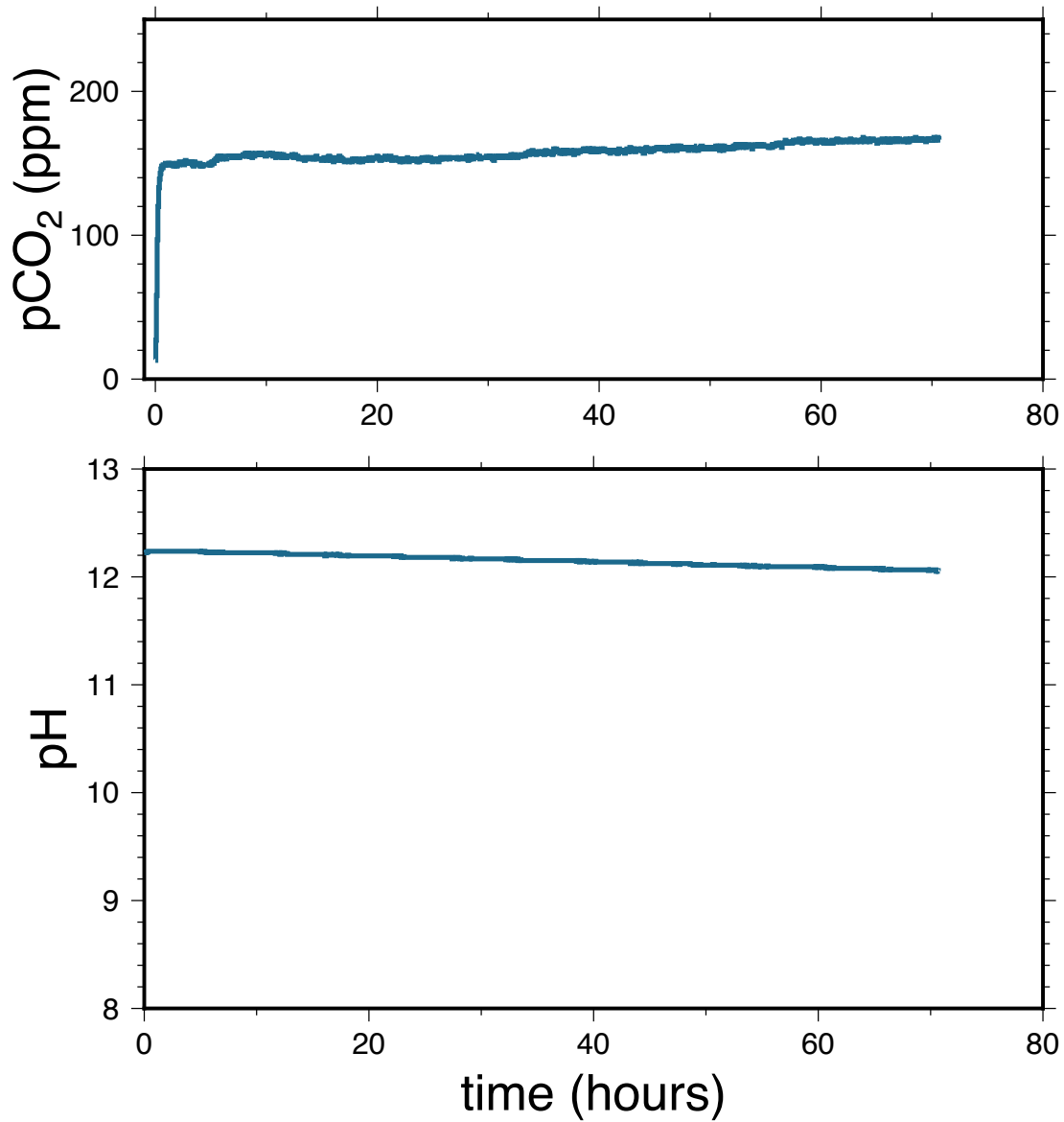


Figure 10: CH10. 200ppm CO₂, 10°C, 30mM Ca²⁺

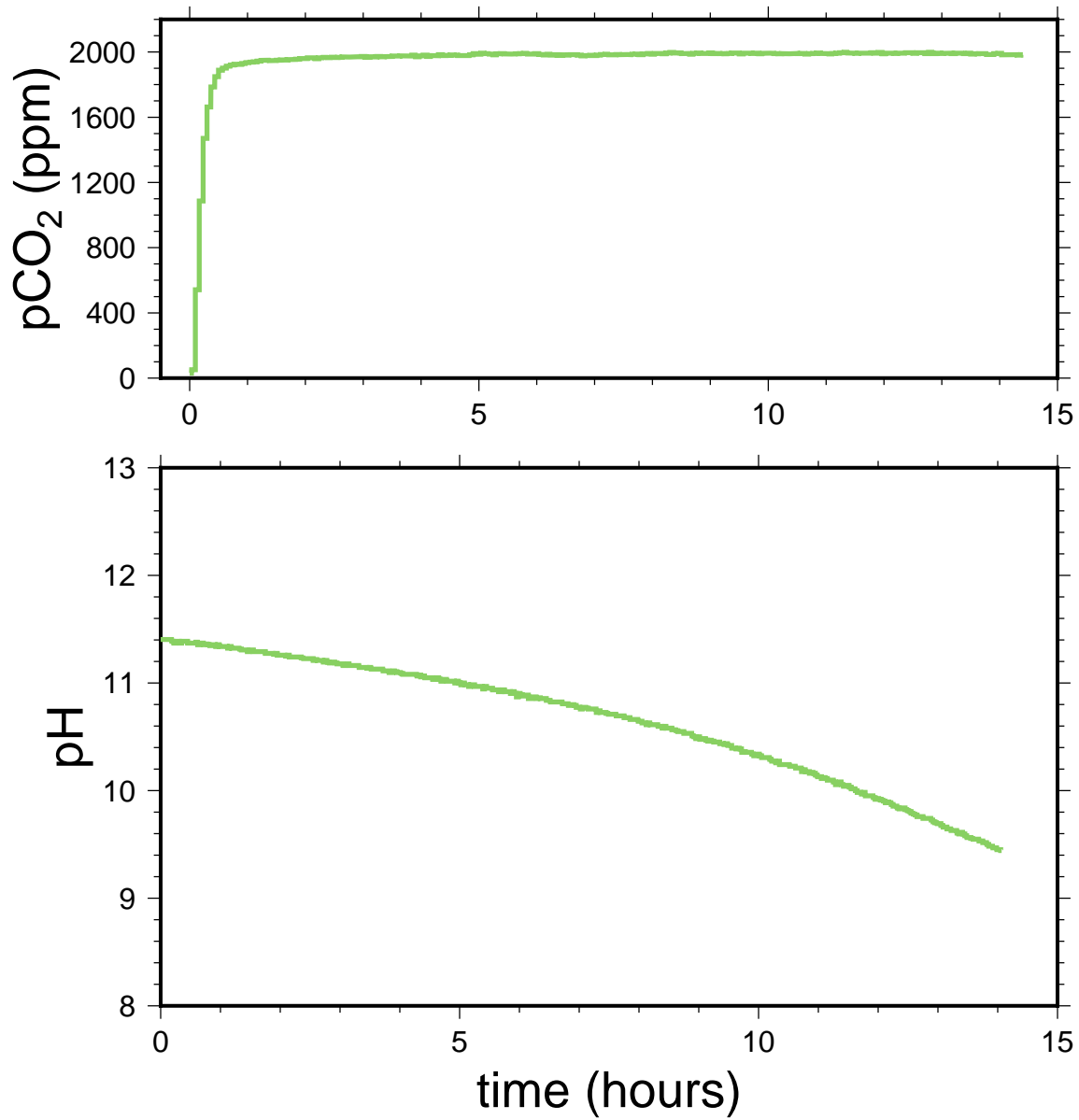


Figure 11: CH11. 2000ppm CO₂, 25°C, 10mM Ca²⁺

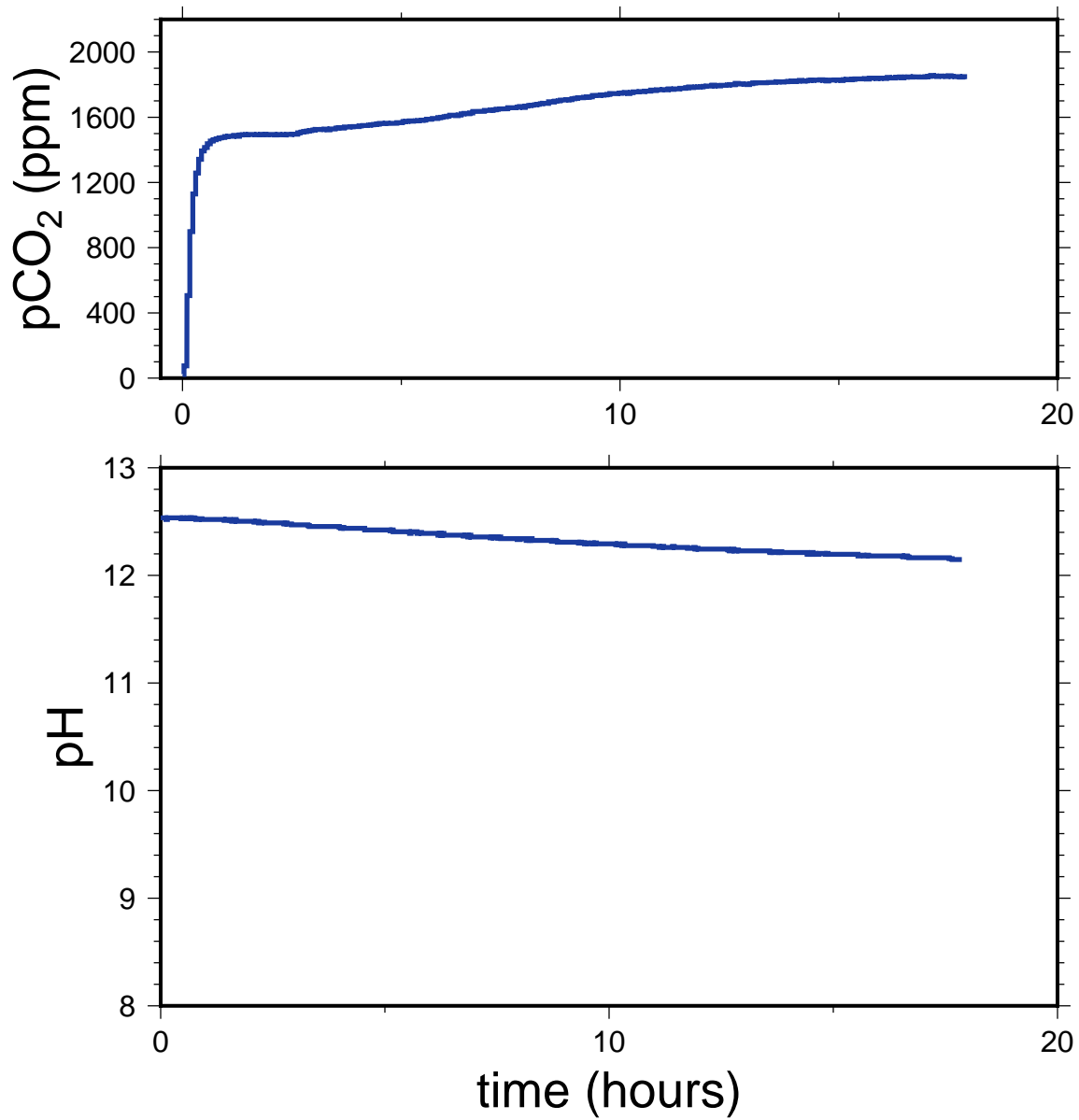


Figure 12: CH12. 2000ppm CO₂, 25°C, 10mM Ca²⁺

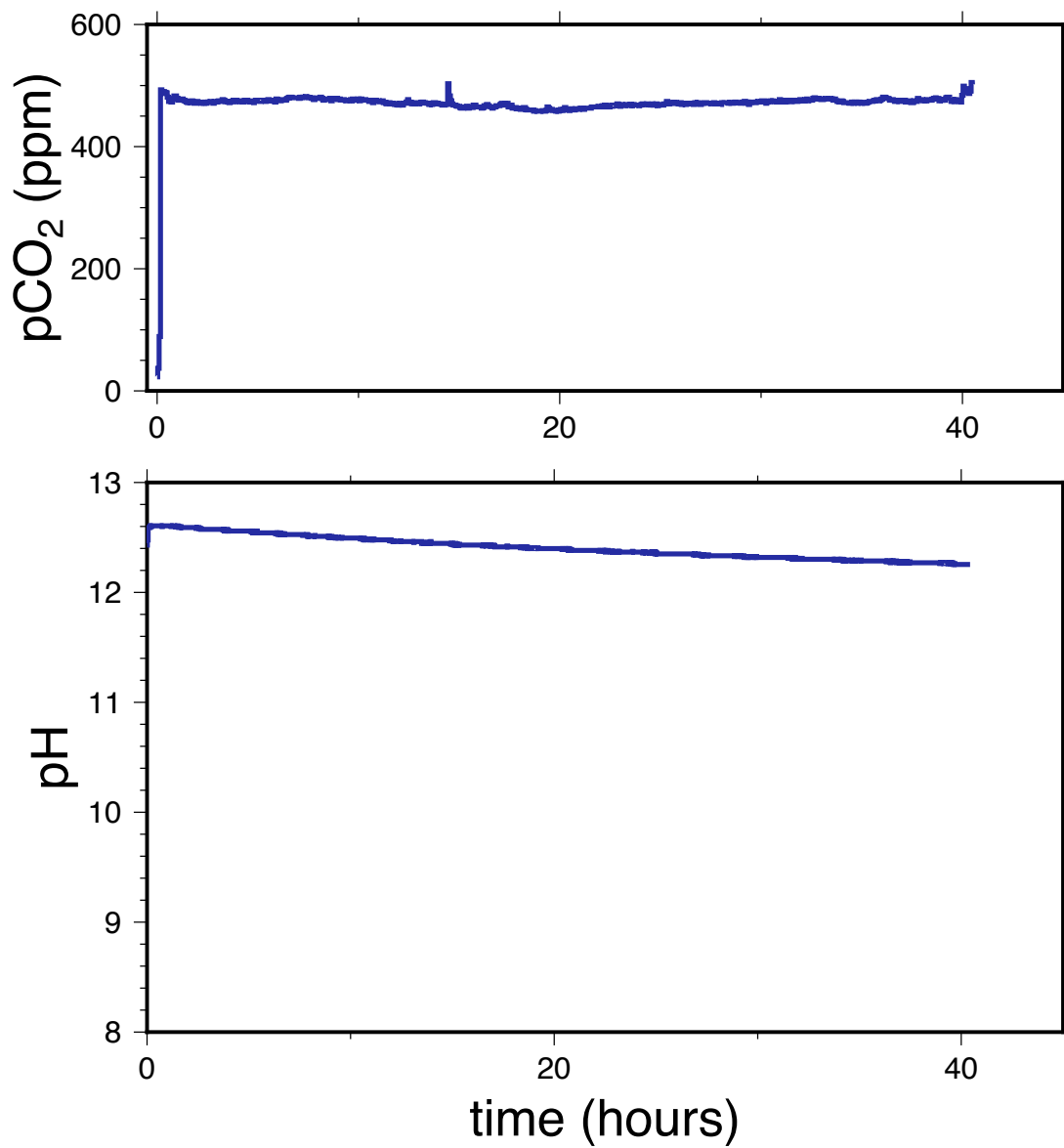


Figure 13: CH13. Lab air ~450ppm CO₂, 25°C, 10mM Ca²⁺

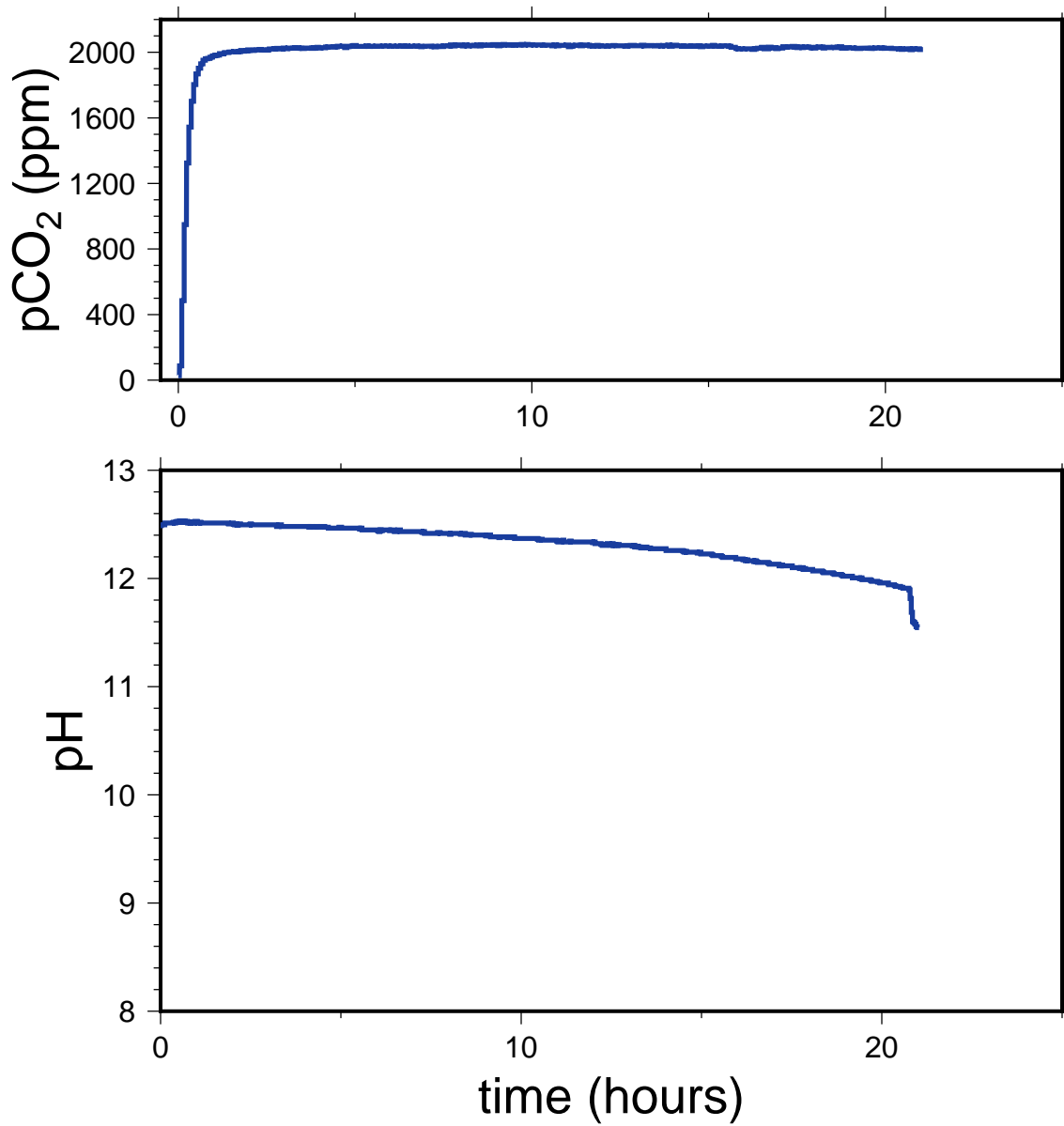


Figure 14: CH14. 2000ppm CO₂, 25°C, 10mM Ca²⁺. Mini-beaker, unstirred

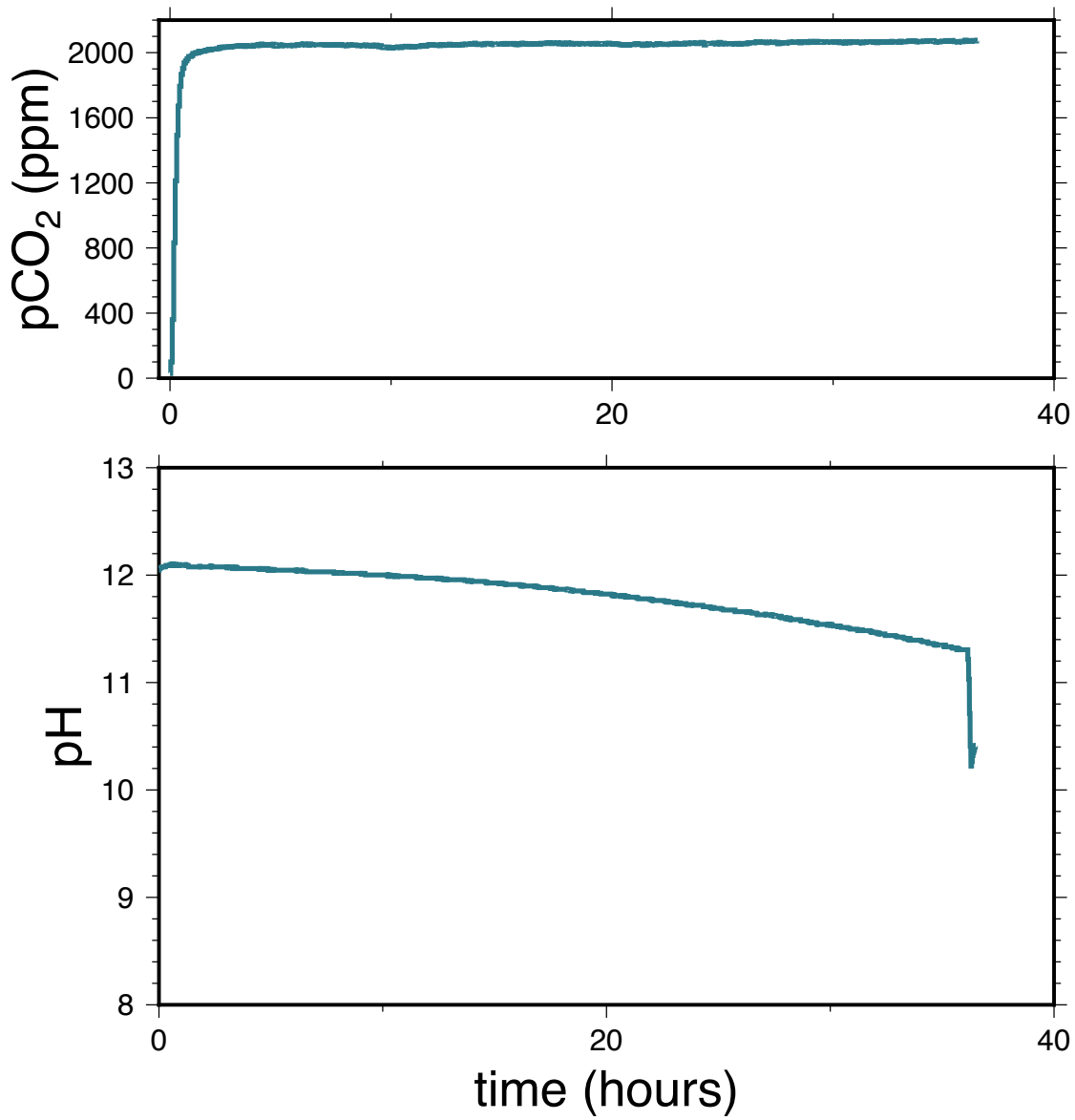


Figure 15: CH15. 2000ppm CO₂, 25°C, 10mM Ca²⁺. Mini-beaker, unstirred

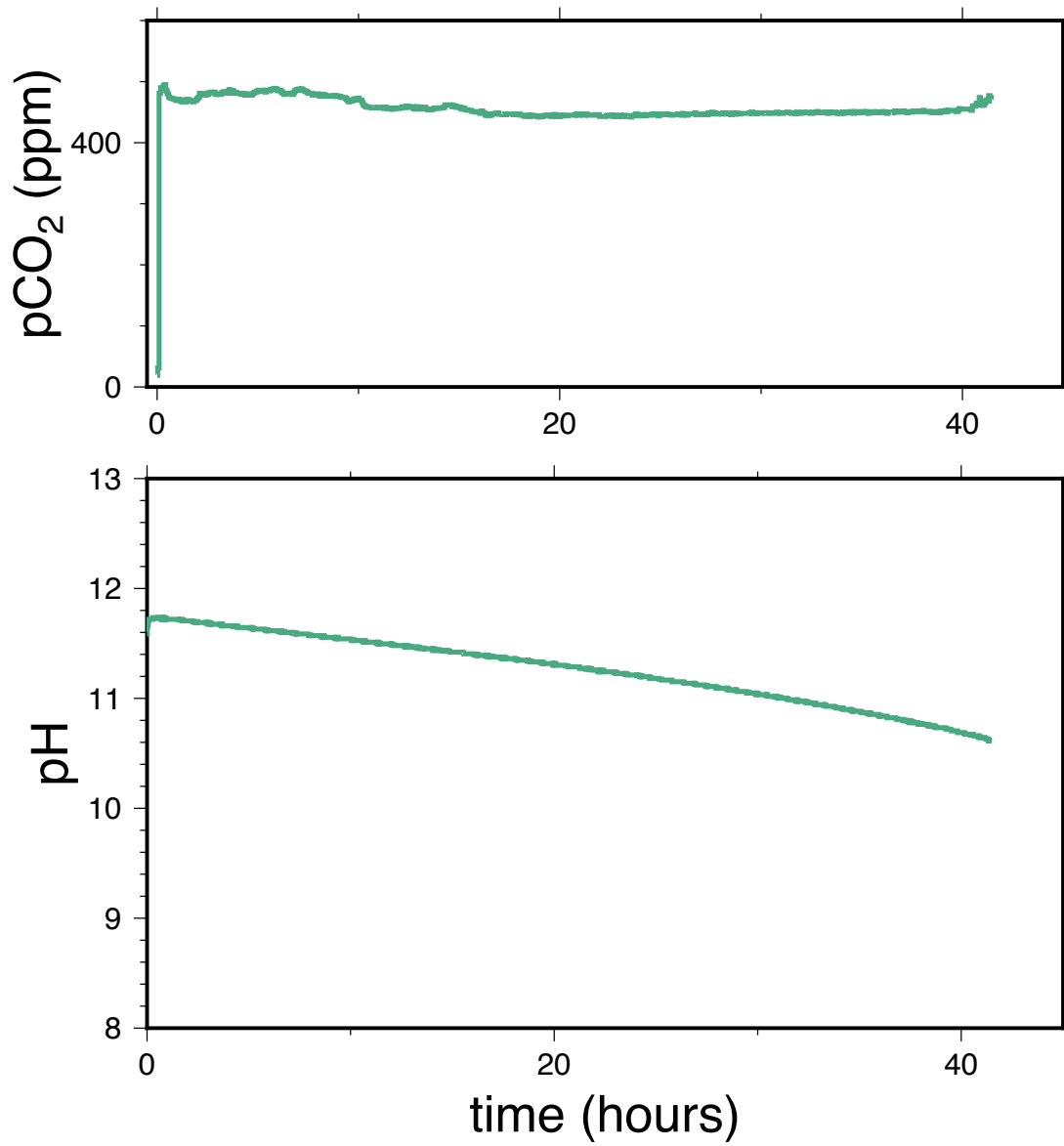


Figure 16: CH17. Lab air ~450ppm CO₂, 25°C, 10mM Ca²⁺

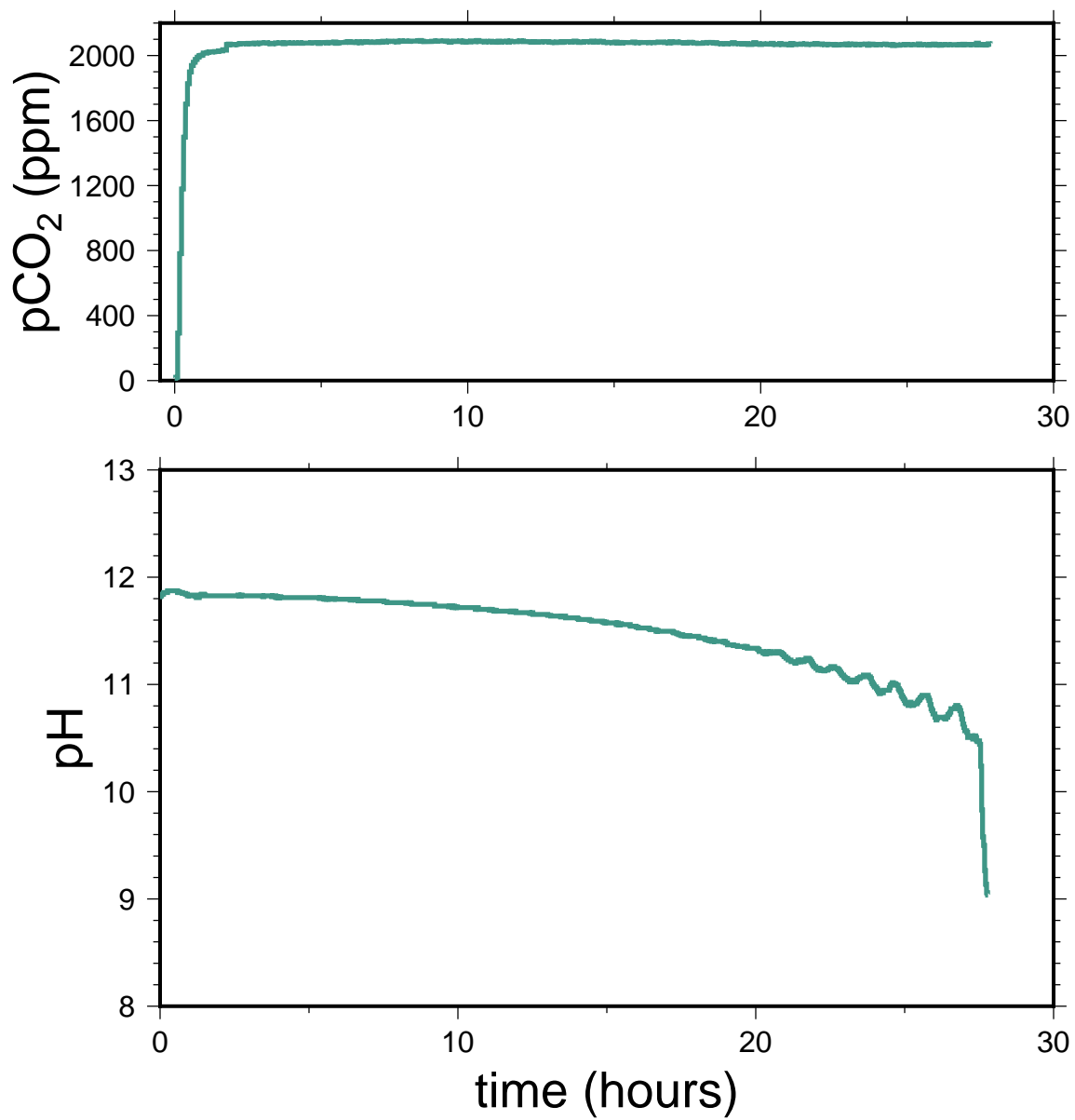


Figure 17: CH18. 2000ppm CO₂, 25°C, 10mM Ca²⁺. Mini-beaker, unstirred

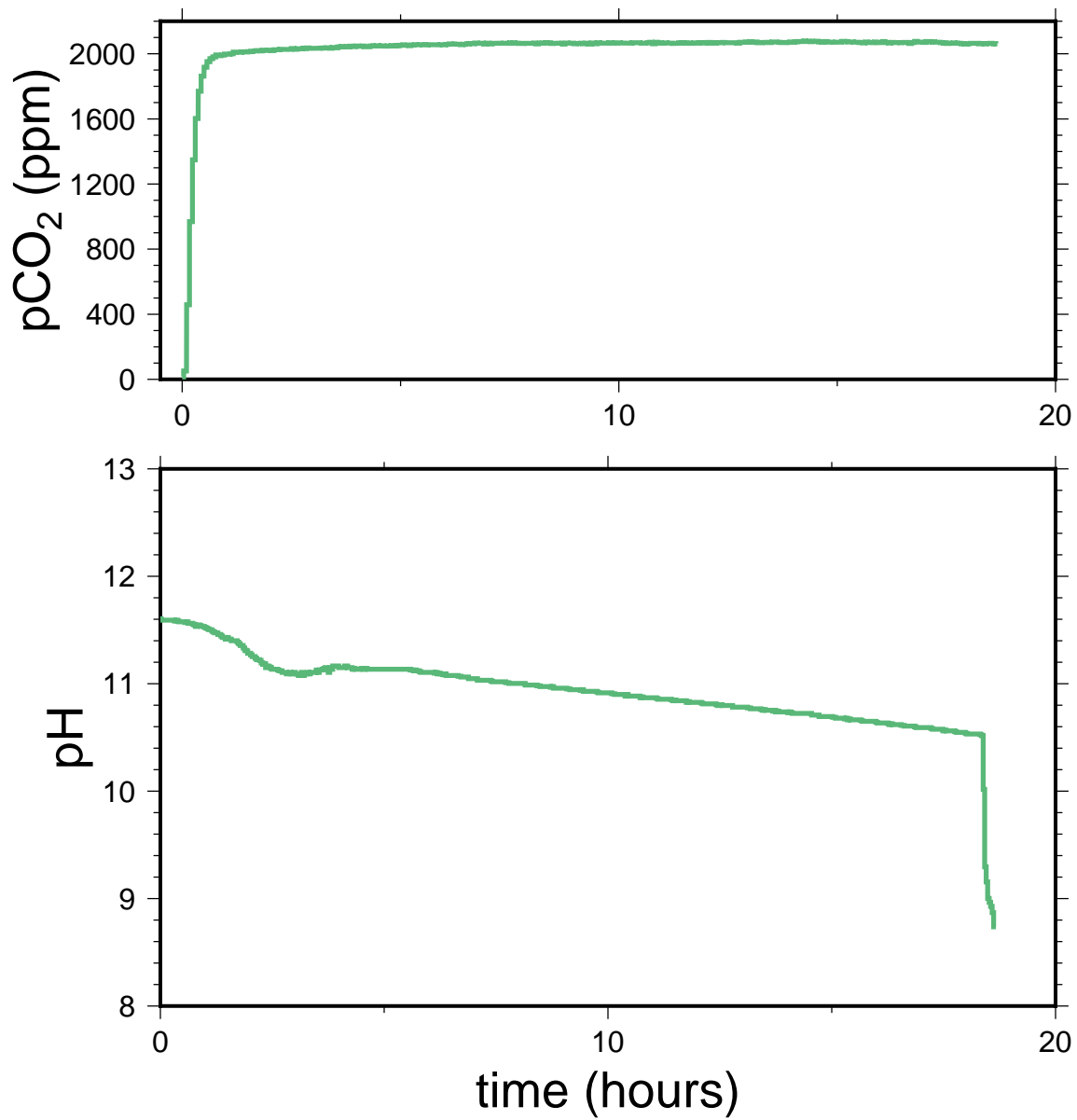


Figure 18: CH19. 2000ppm CO₂, 25°C, 10mM Ca²⁺. Mini-beaker, unstirred

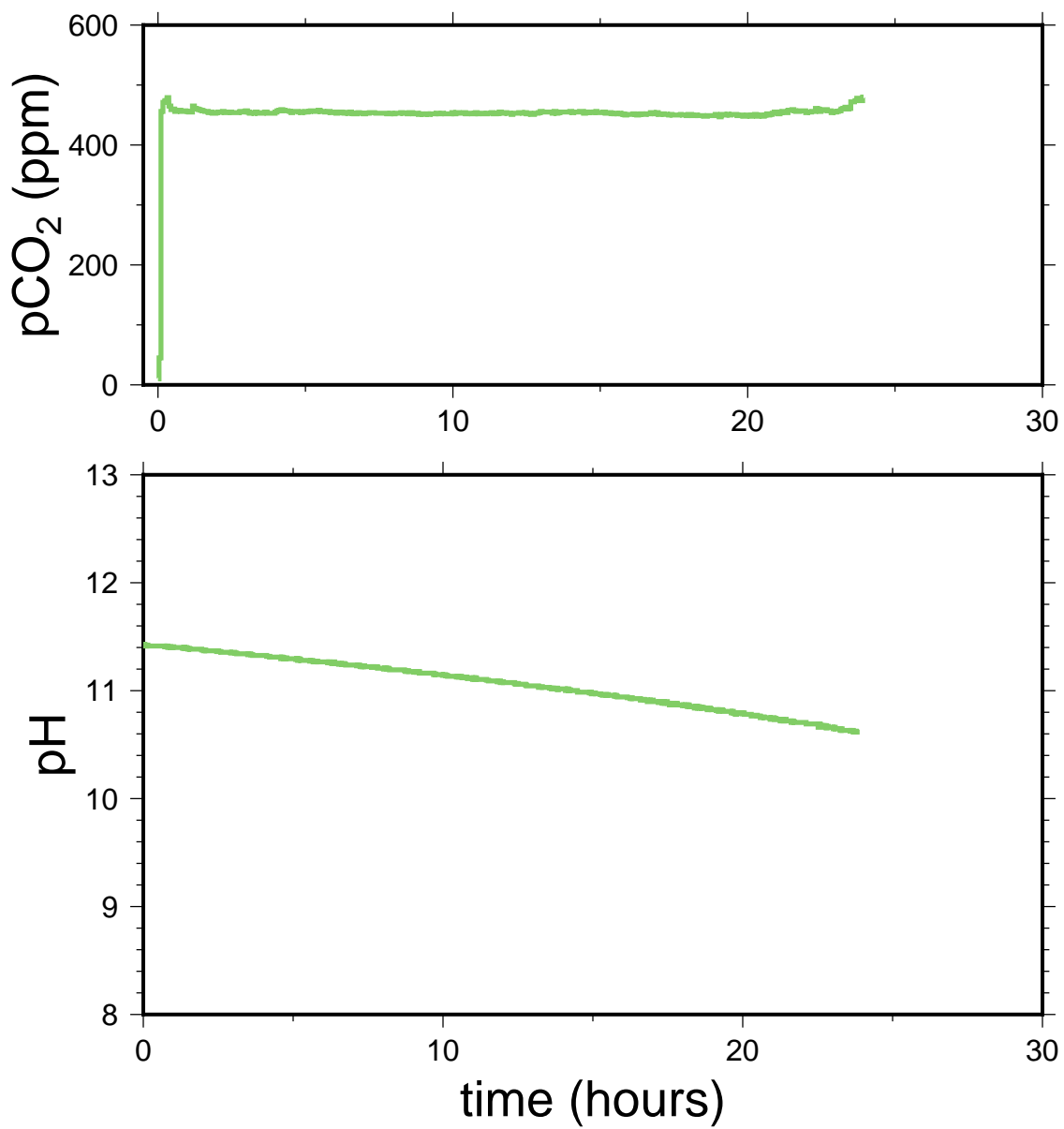


Figure 19: CH20. Lab air ~450ppm CO₂, 25°C, 10mM Ca²⁺

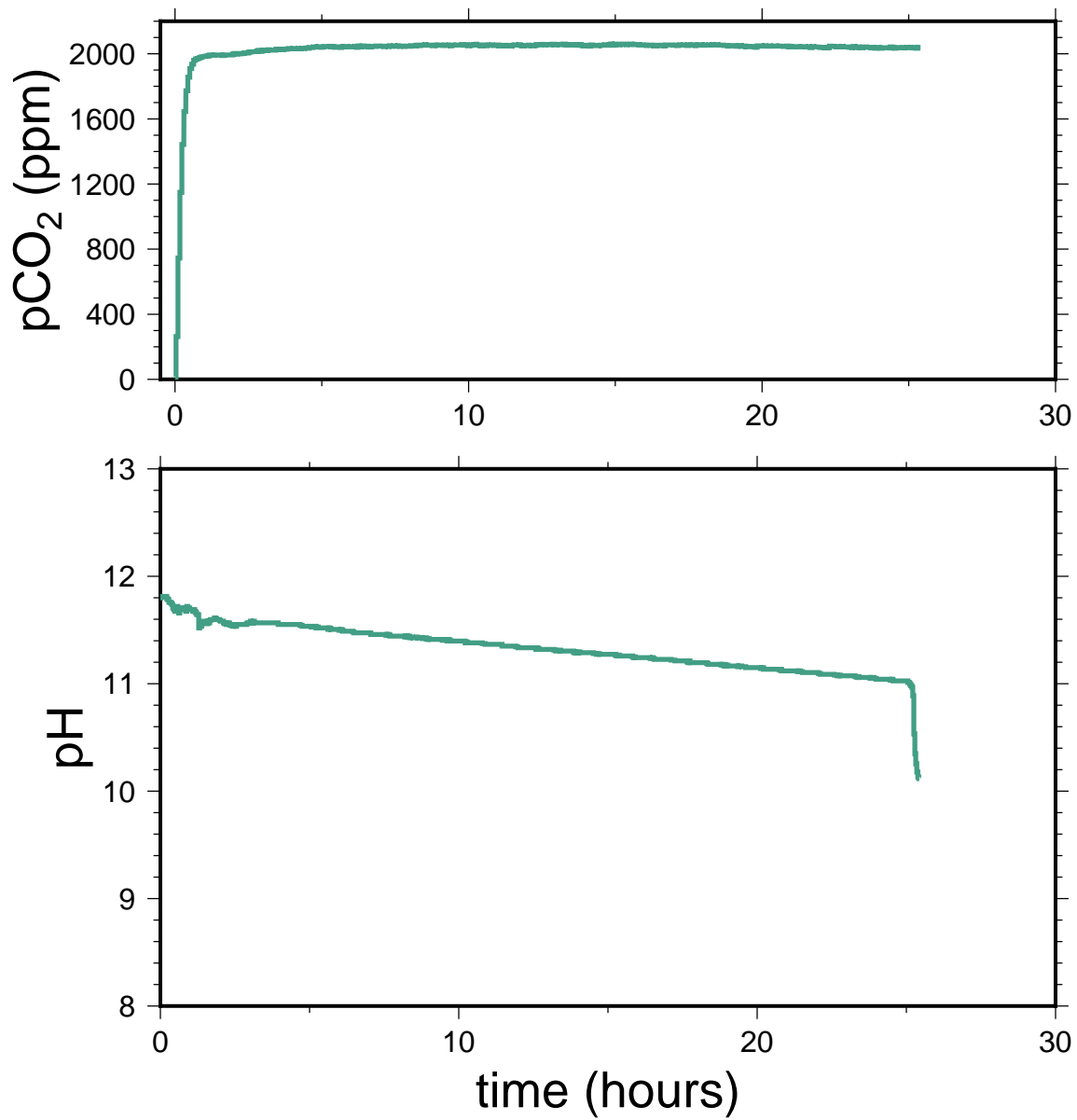


Figure 20: CH21. 2000ppm CO₂, 25°C, 10mM Ca²⁺. Mini-beaker, unstirred

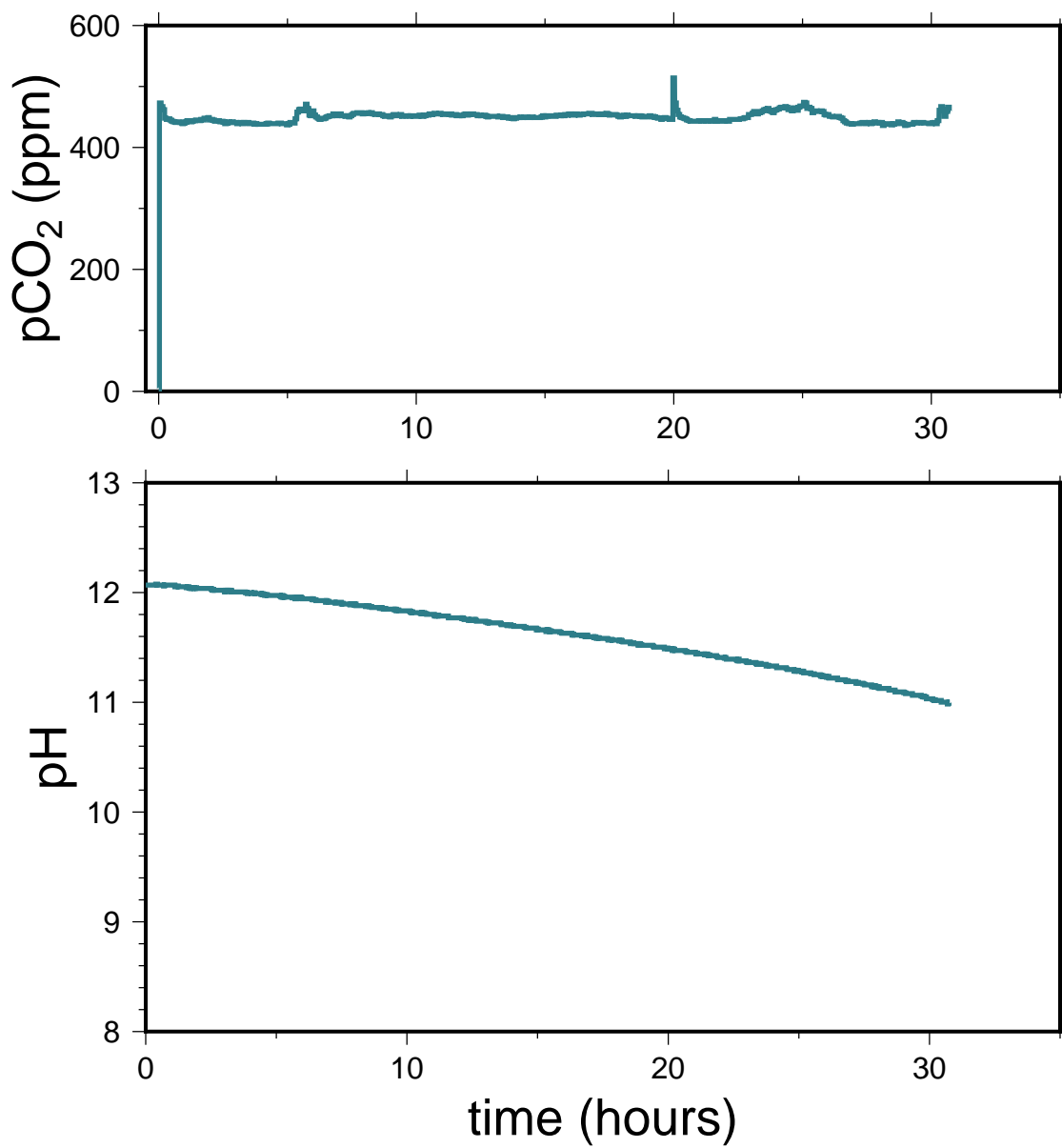


Figure 21: CH22. Lab air ~450ppm CO₂, 25°C, 10mM Ca²⁺. Time series (2 crystal skims)

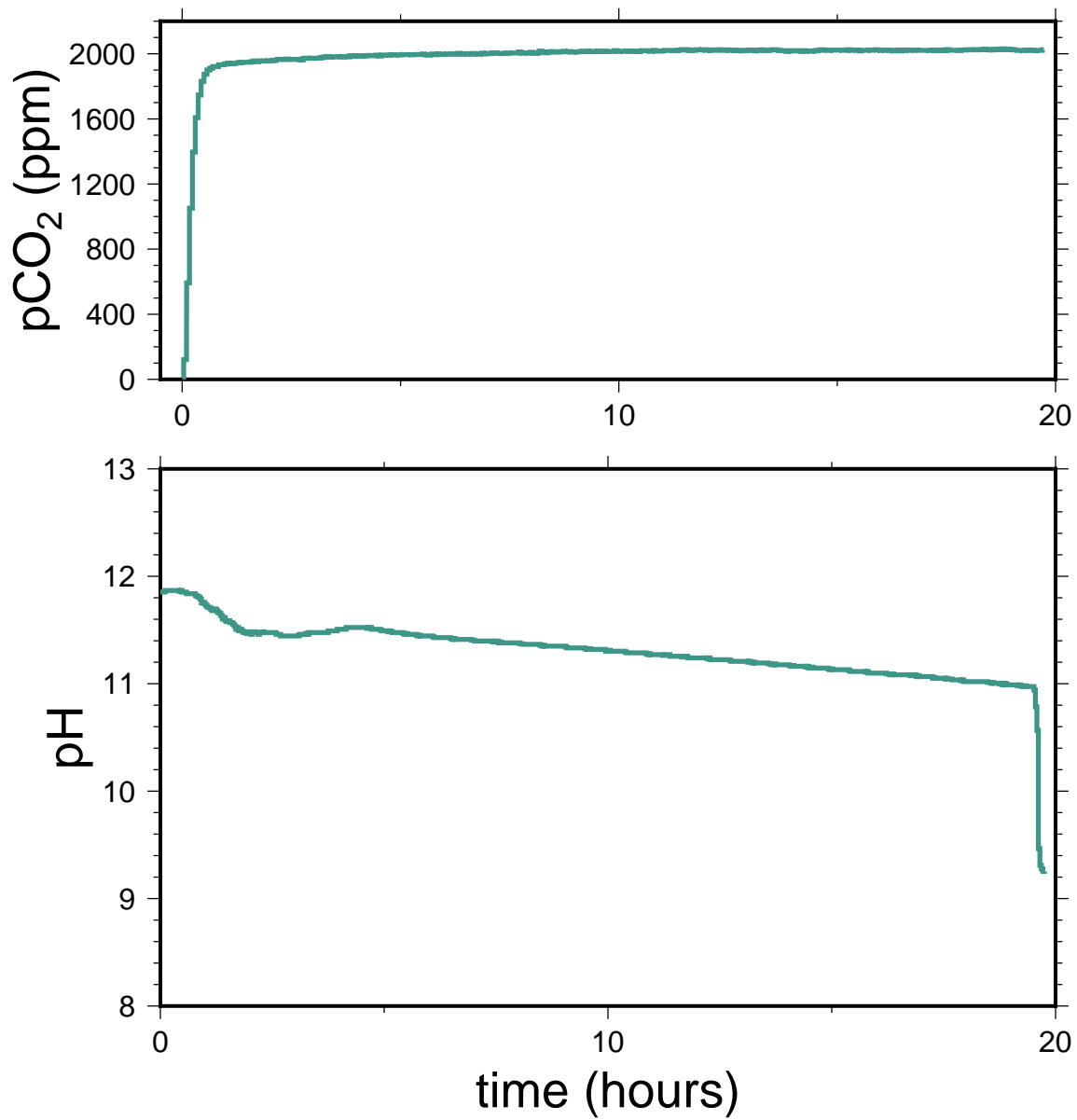


Figure 22: CH23. 2000ppm CO₂, 25°C, 10mM Ca²⁺. Mini-beaker, unstirred

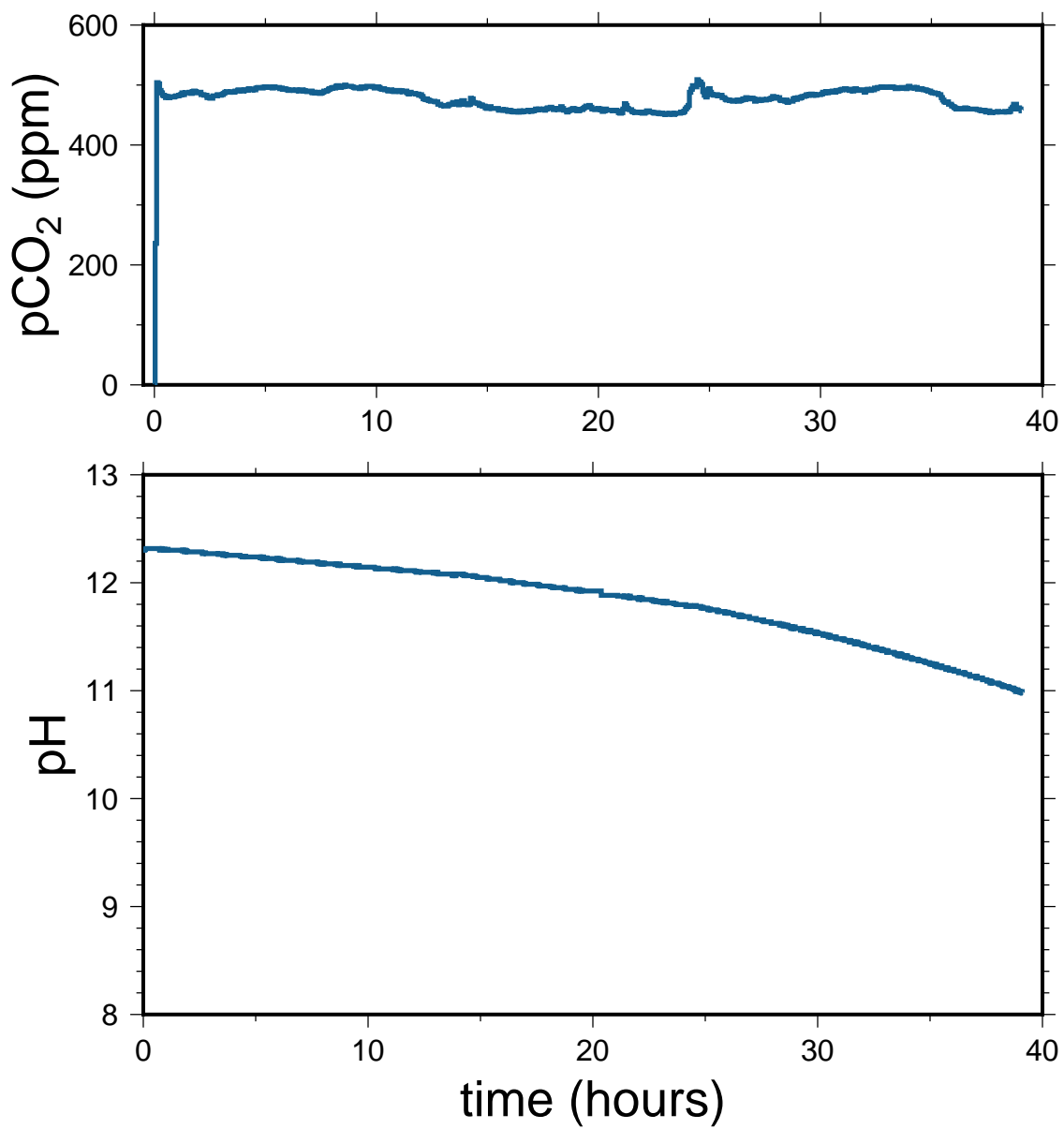


Figure 23: CH24. Lab air ~450ppm CO₂, 25°C, 10mM Ca²⁺. Time series (3 crystal skins)

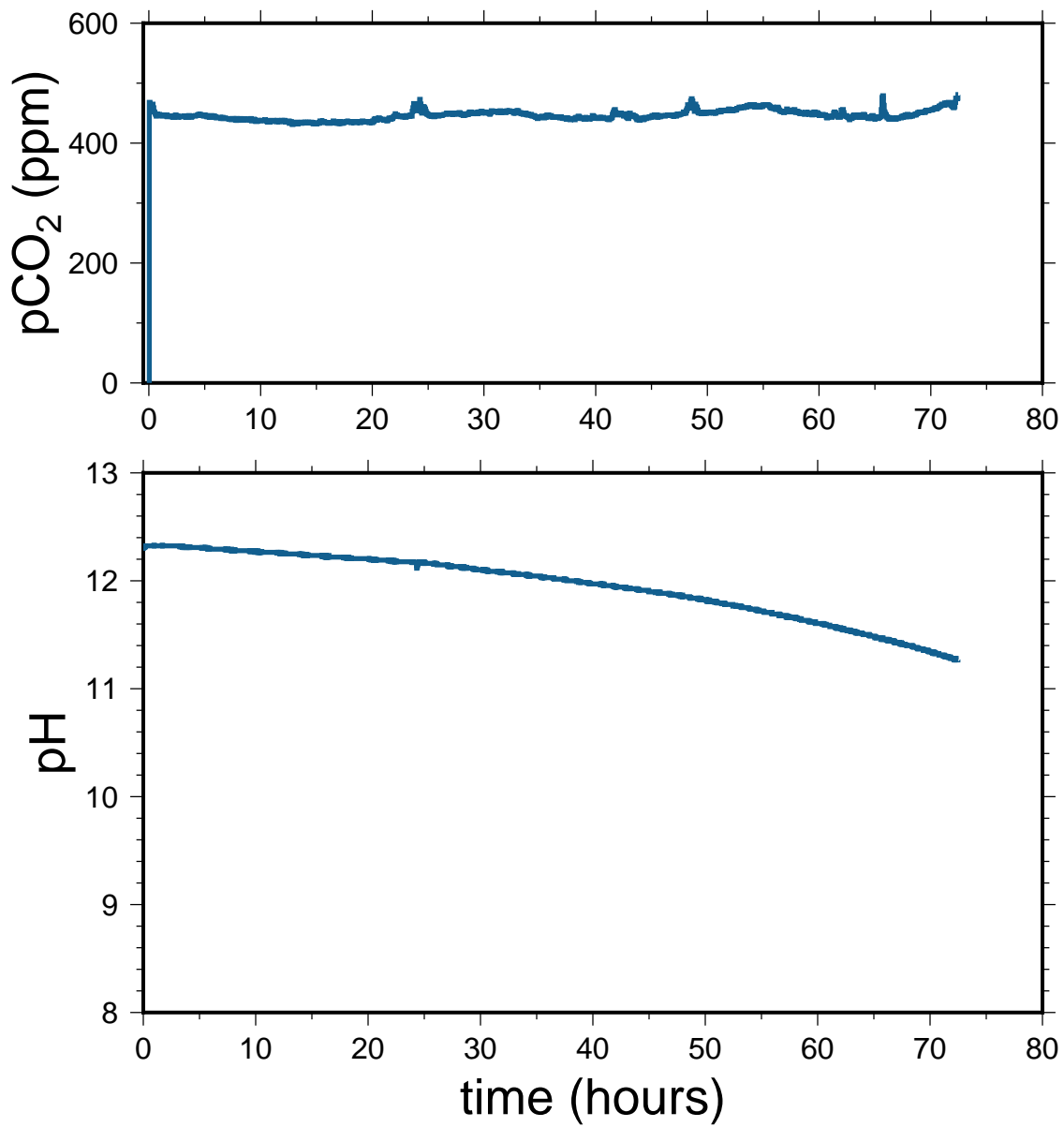


Figure 24: CH25. Lab air ~450ppm CO₂, 10°C, 10mM Ca²⁺. Time series (3 crystal skins)

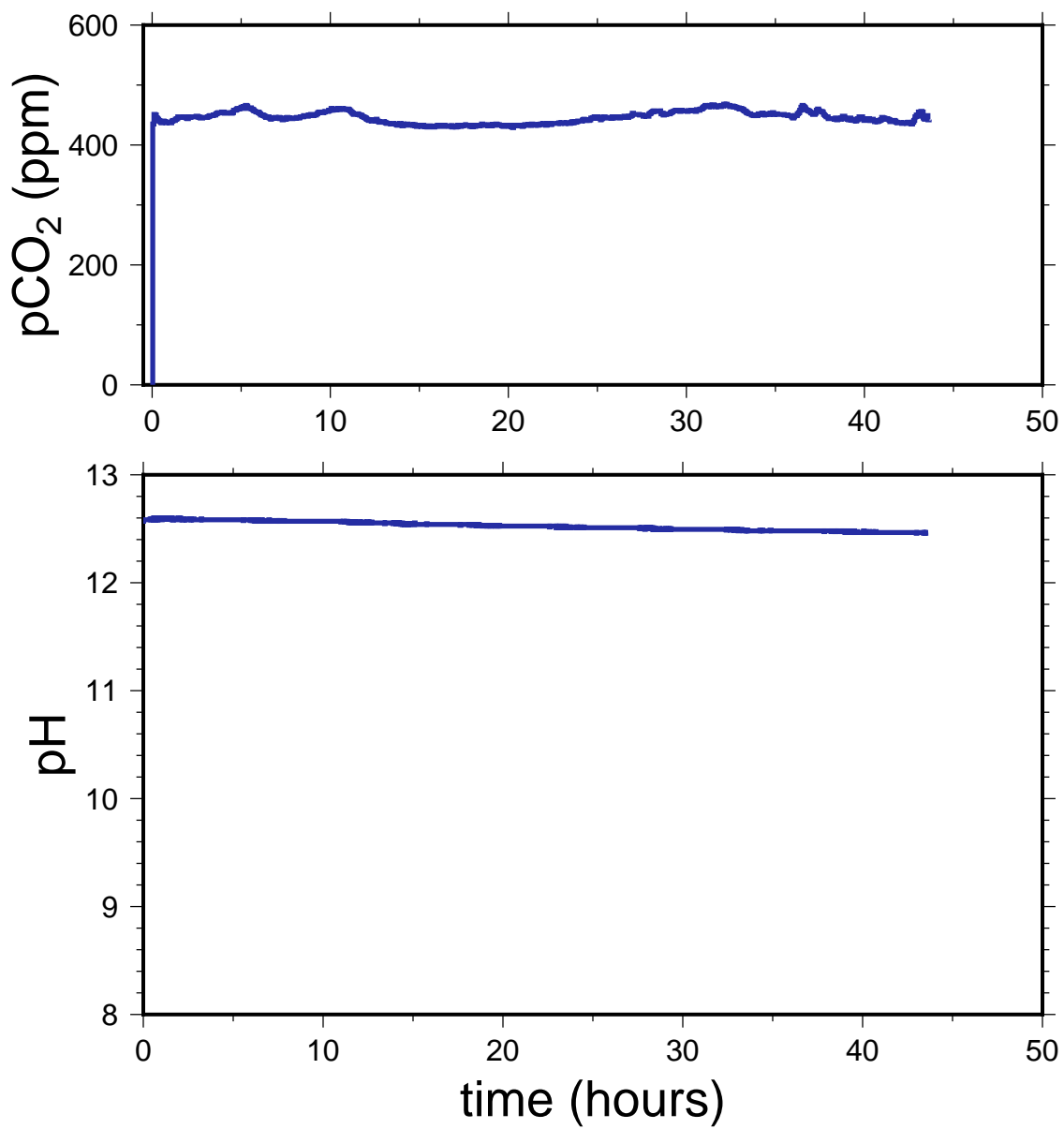


Figure 25: CH26. Lab air ~450ppm CO₂, 10°C, 10mM Ca²⁺.

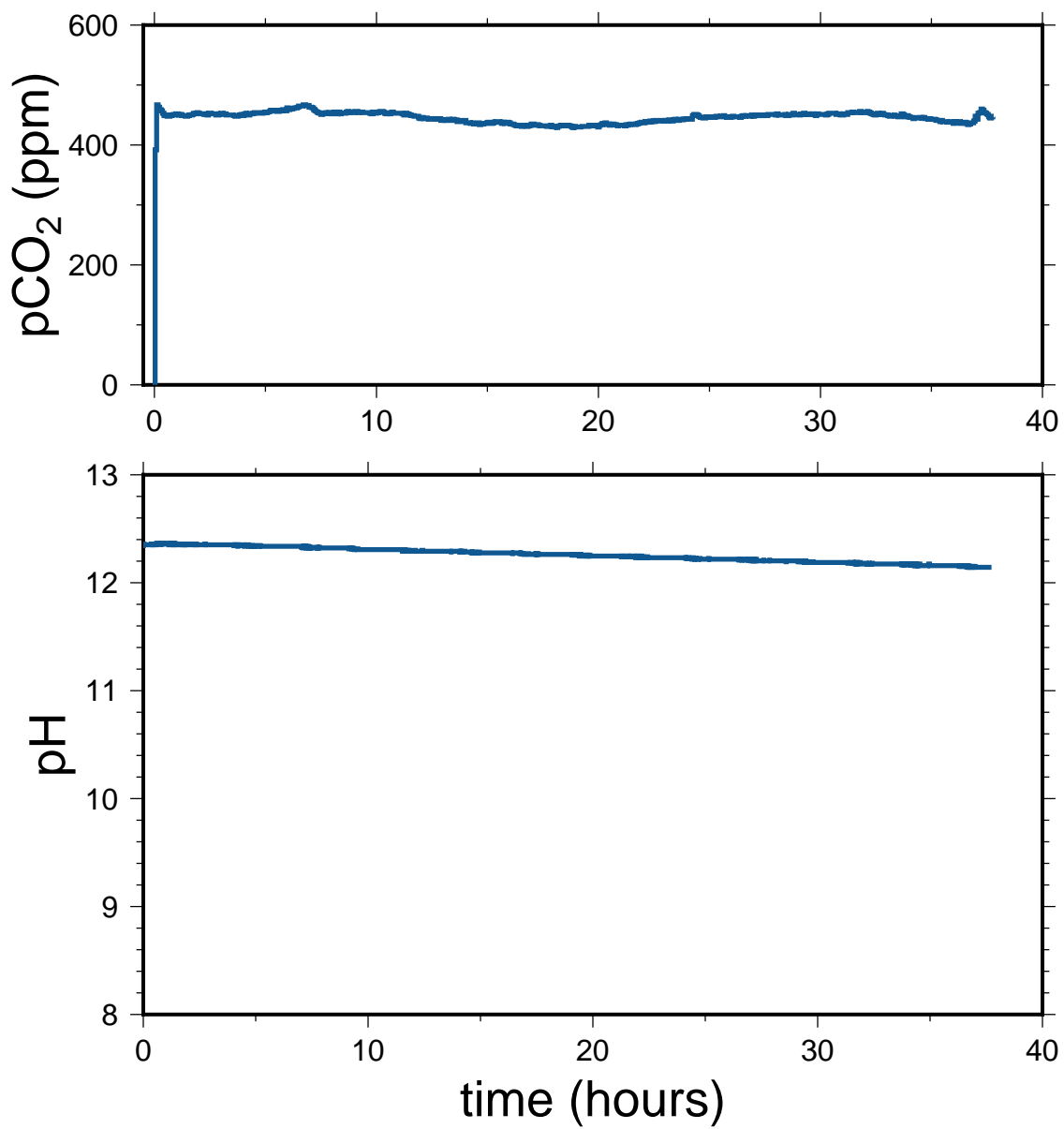


Figure 26: CH27. Lab air ~450ppm CO₂, 10°C, 10mM Ca²⁺.

2 SEM images

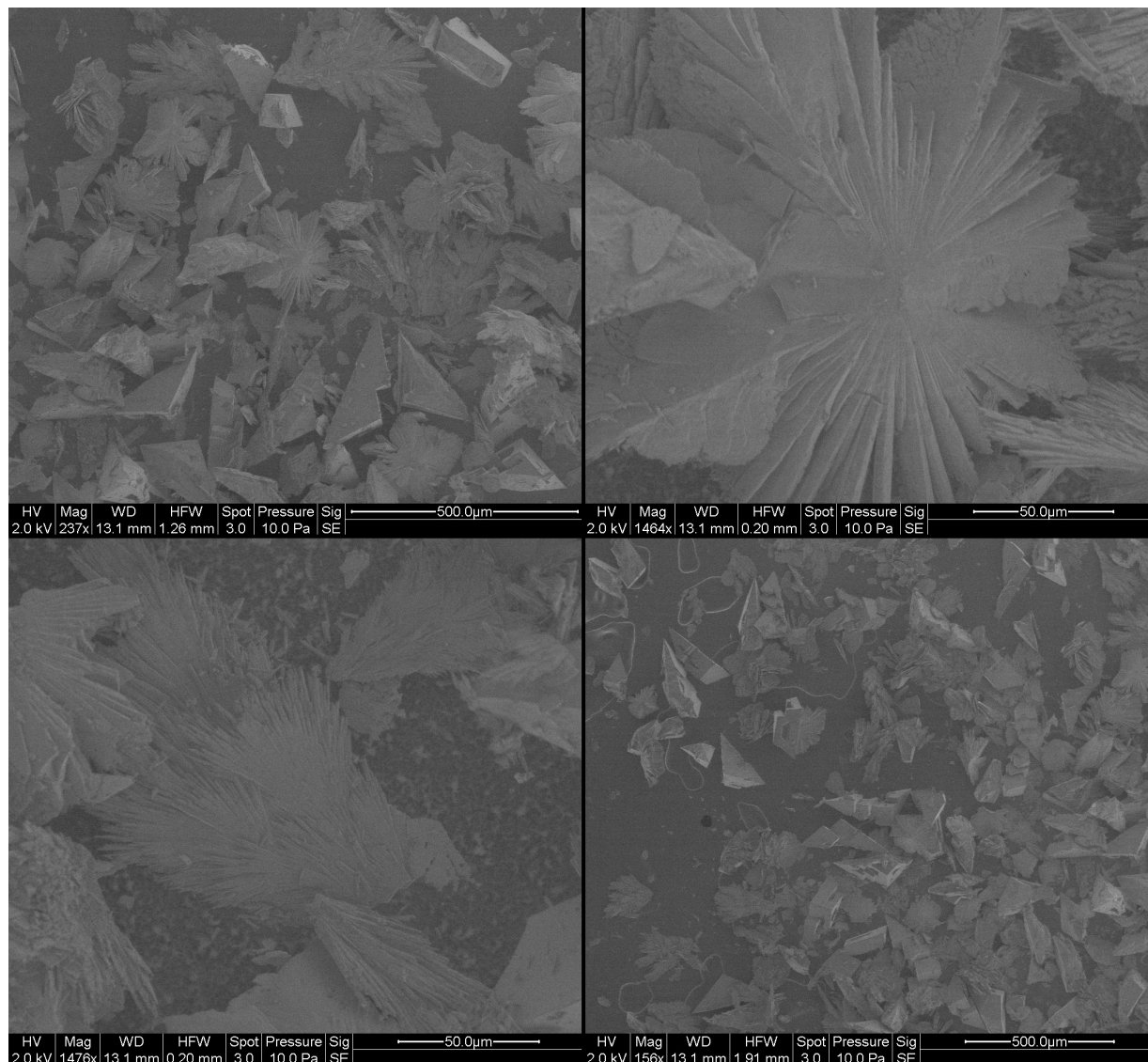


Figure 27: CH1. 200ppm CO₂, 25°C, 10mM Ca²⁺

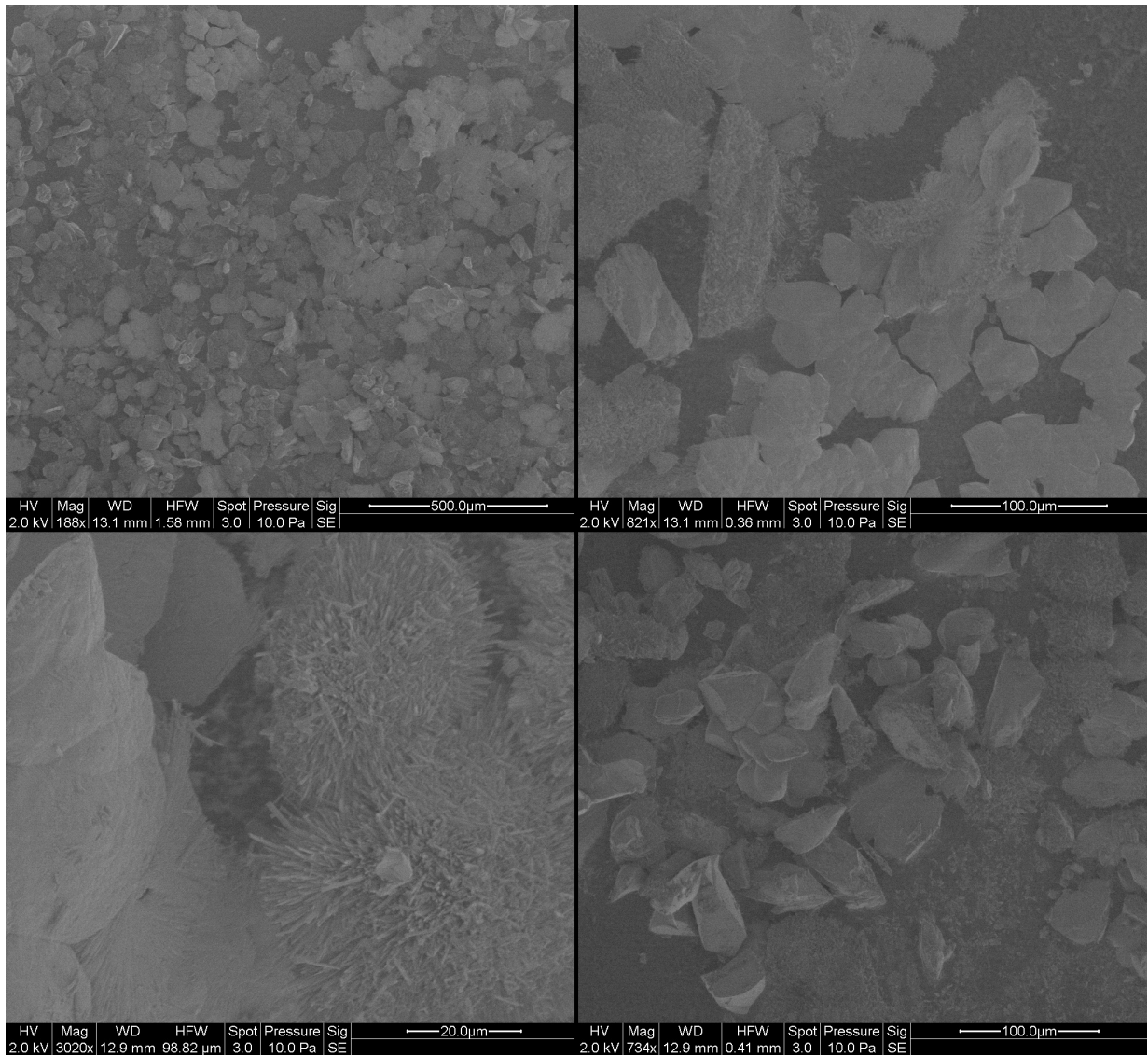


Figure 28: CH2. 200ppm CO₂, 25°C, 30mM Ca²⁺

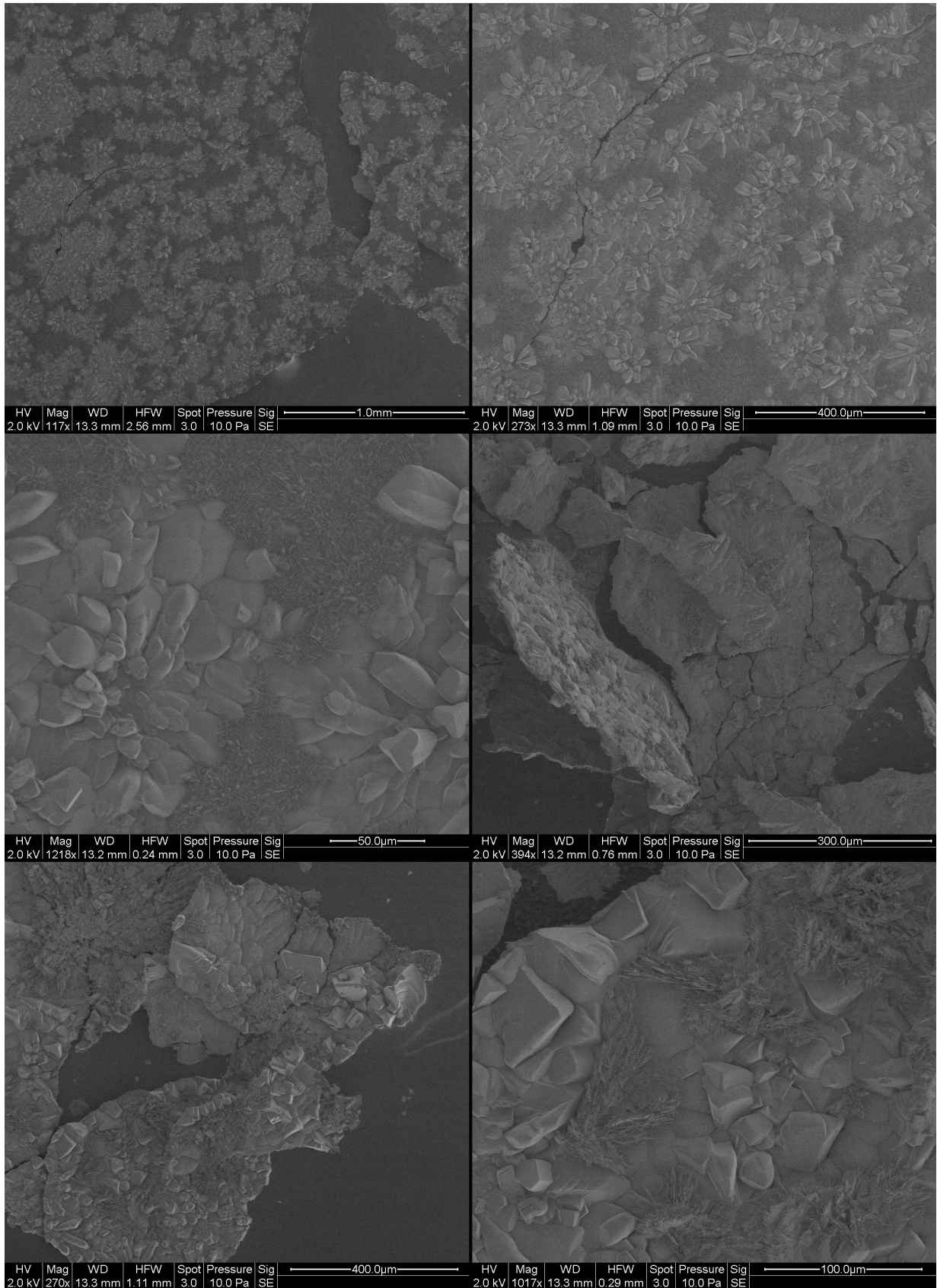


Figure 29: CH3. 2000ppm CO₂, 25°C, 30mM Ca²⁺

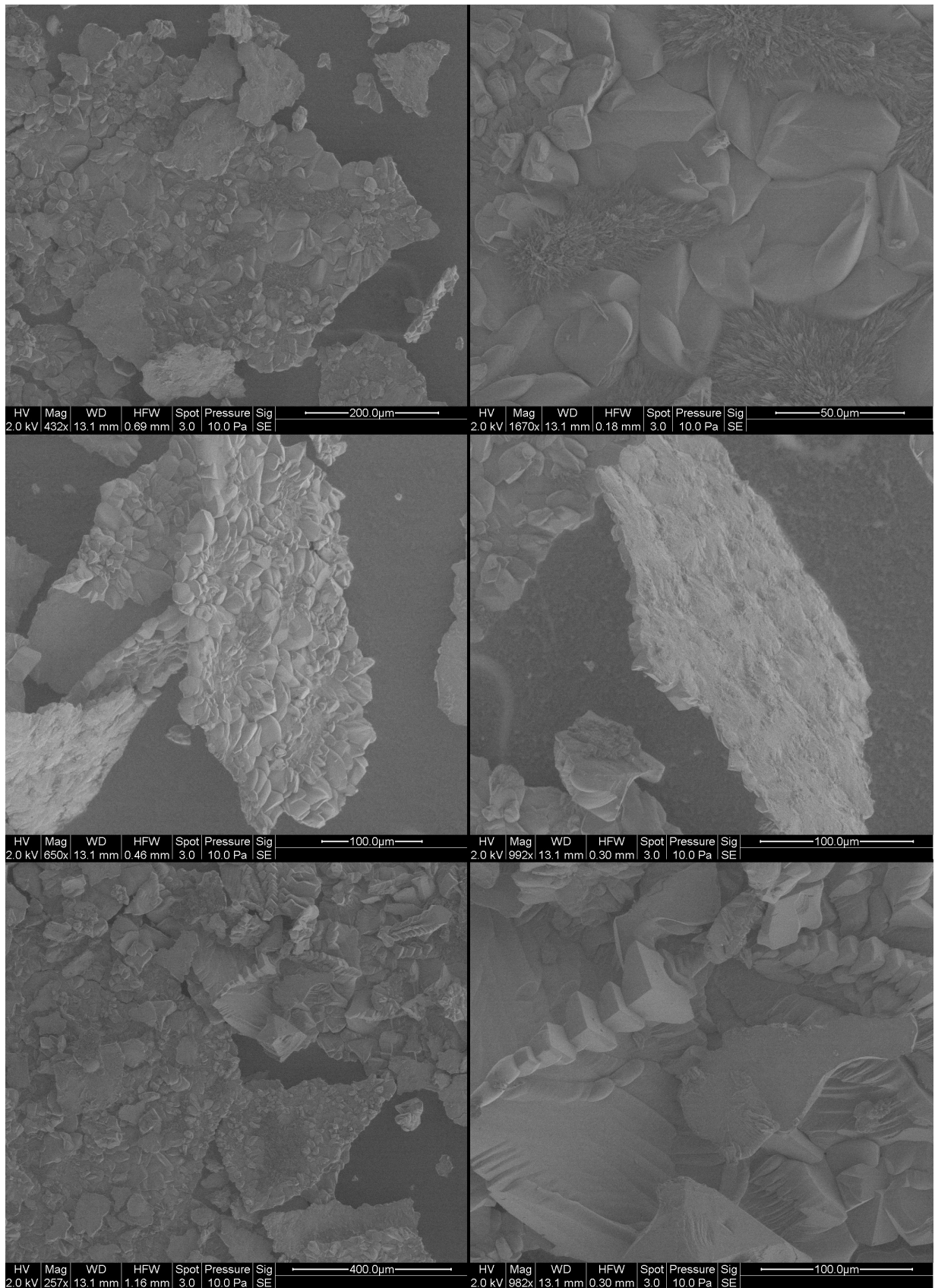


Figure 30: CH4. 2000ppm CO₂, 25°C, 30mM Ca²⁺

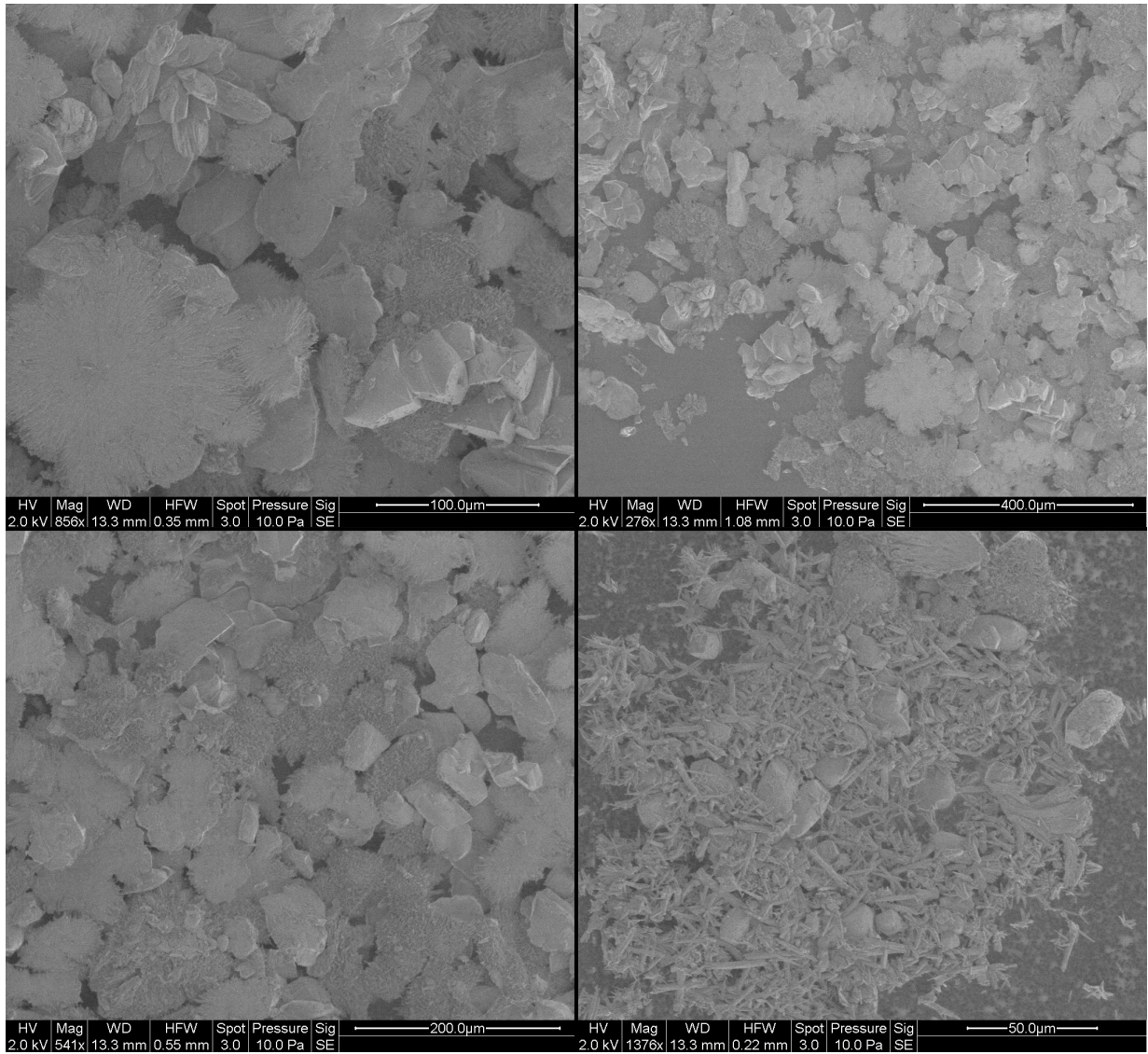


Figure 31: CH5. 200ppm CO₂, 25°C, 30mM Ca²⁺

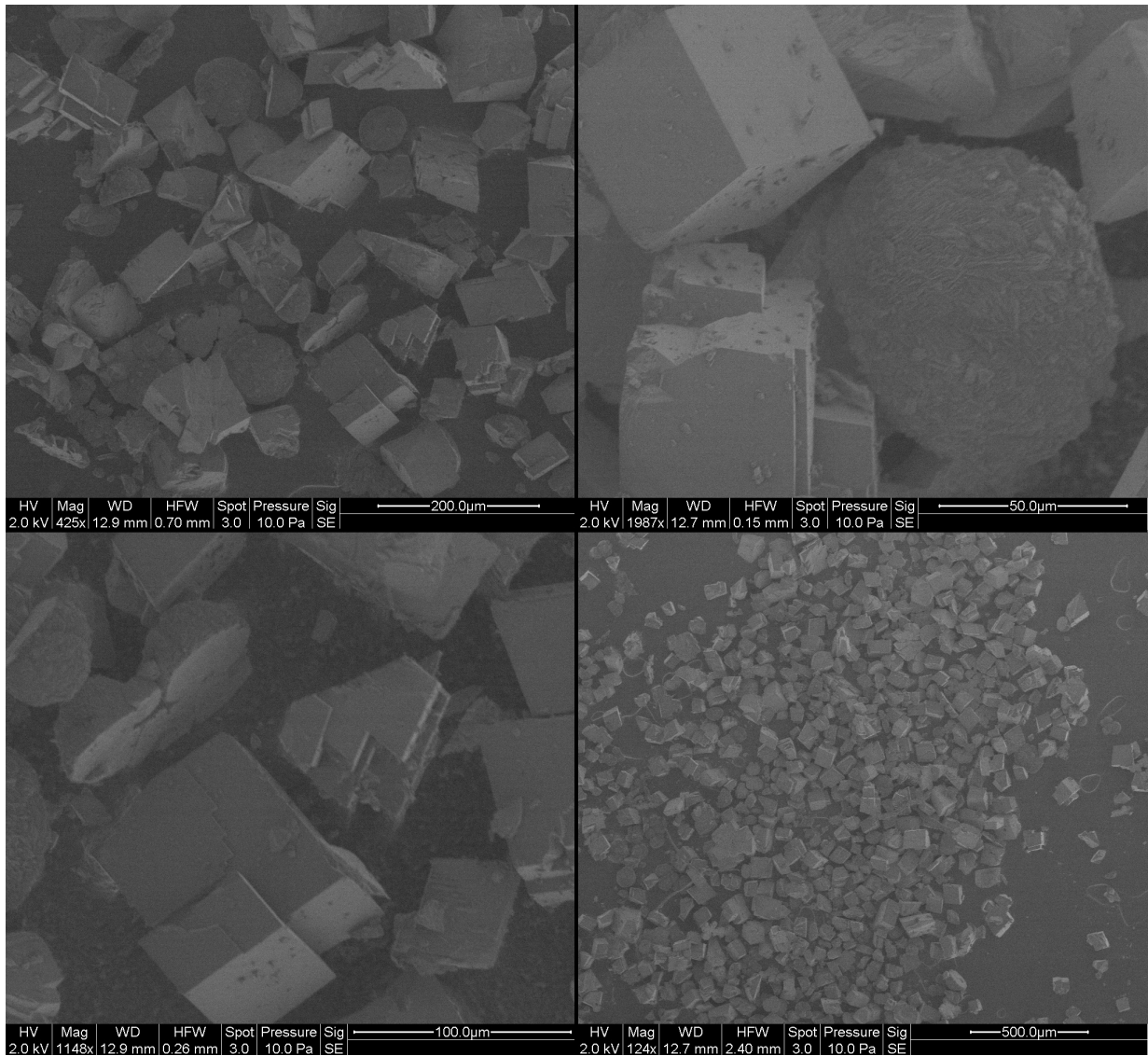


Figure 32: CH6. 2000ppm CO₂, 10°C, 30mM Ca²⁺

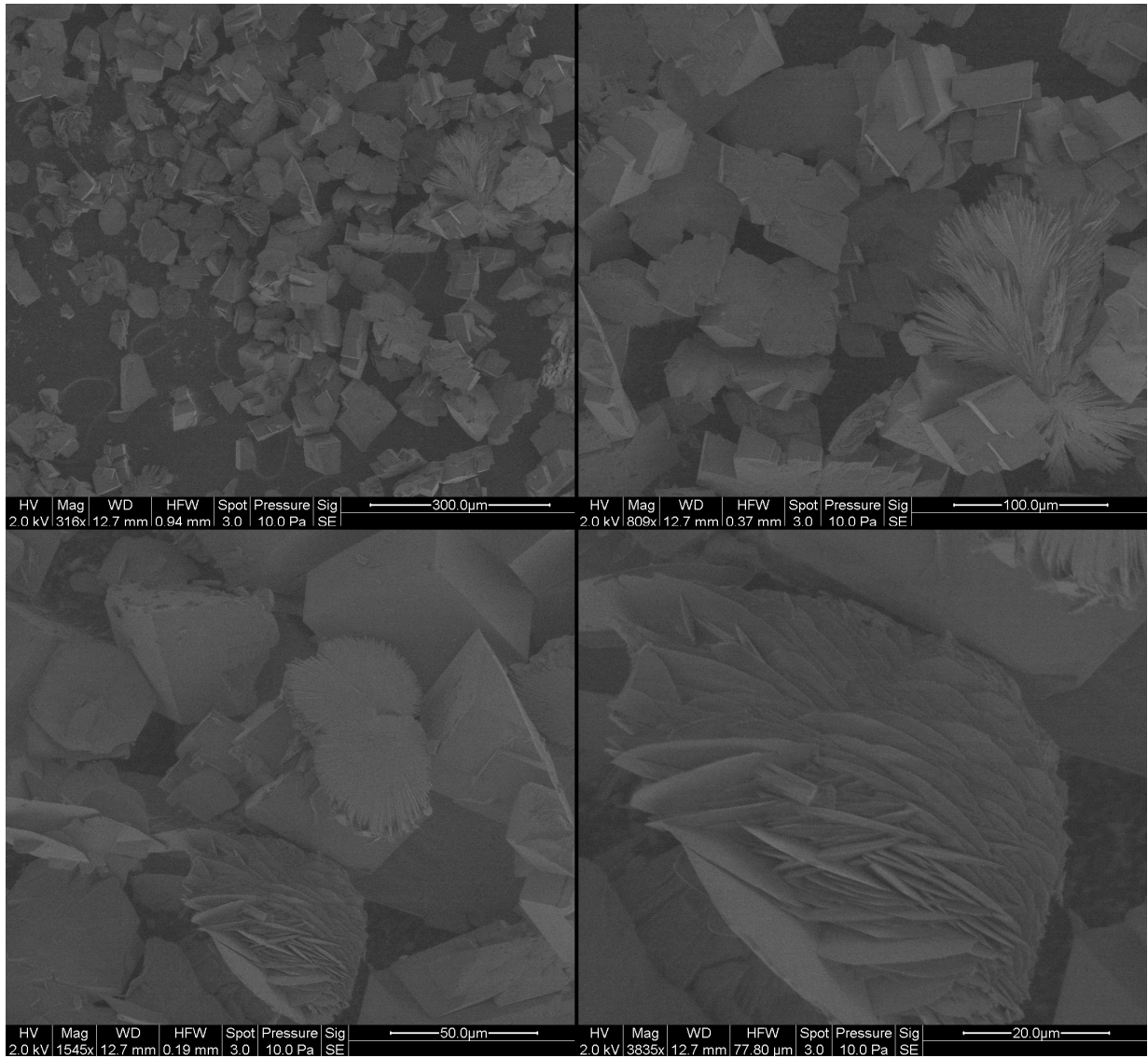


Figure 33: CH7. 2000ppm CO₂, 25°C, 30mM Ca²⁺. Unstirred

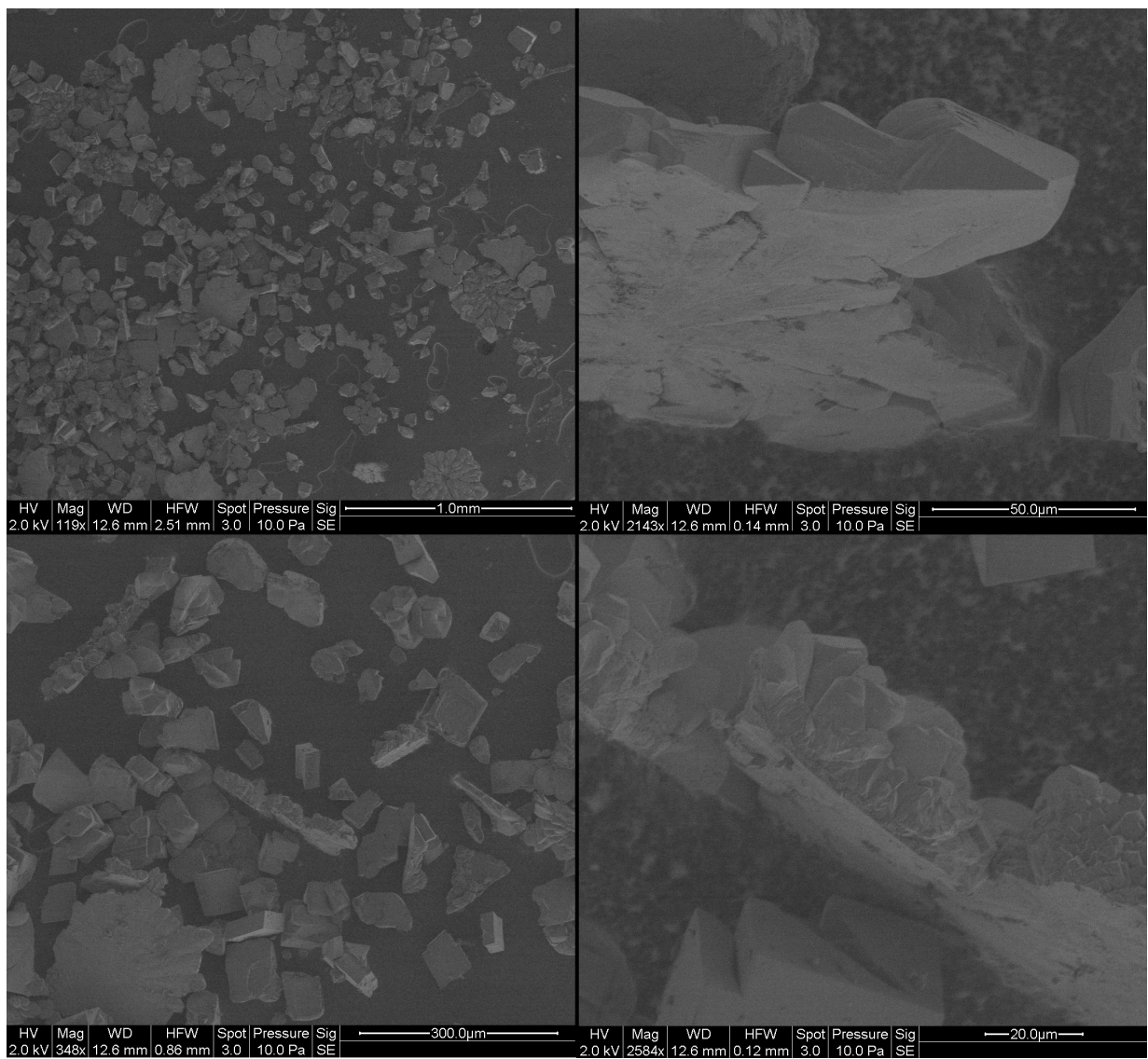


Figure 34: CH8. 2000ppm CO₂, 10°C, 30mM Ca²⁺

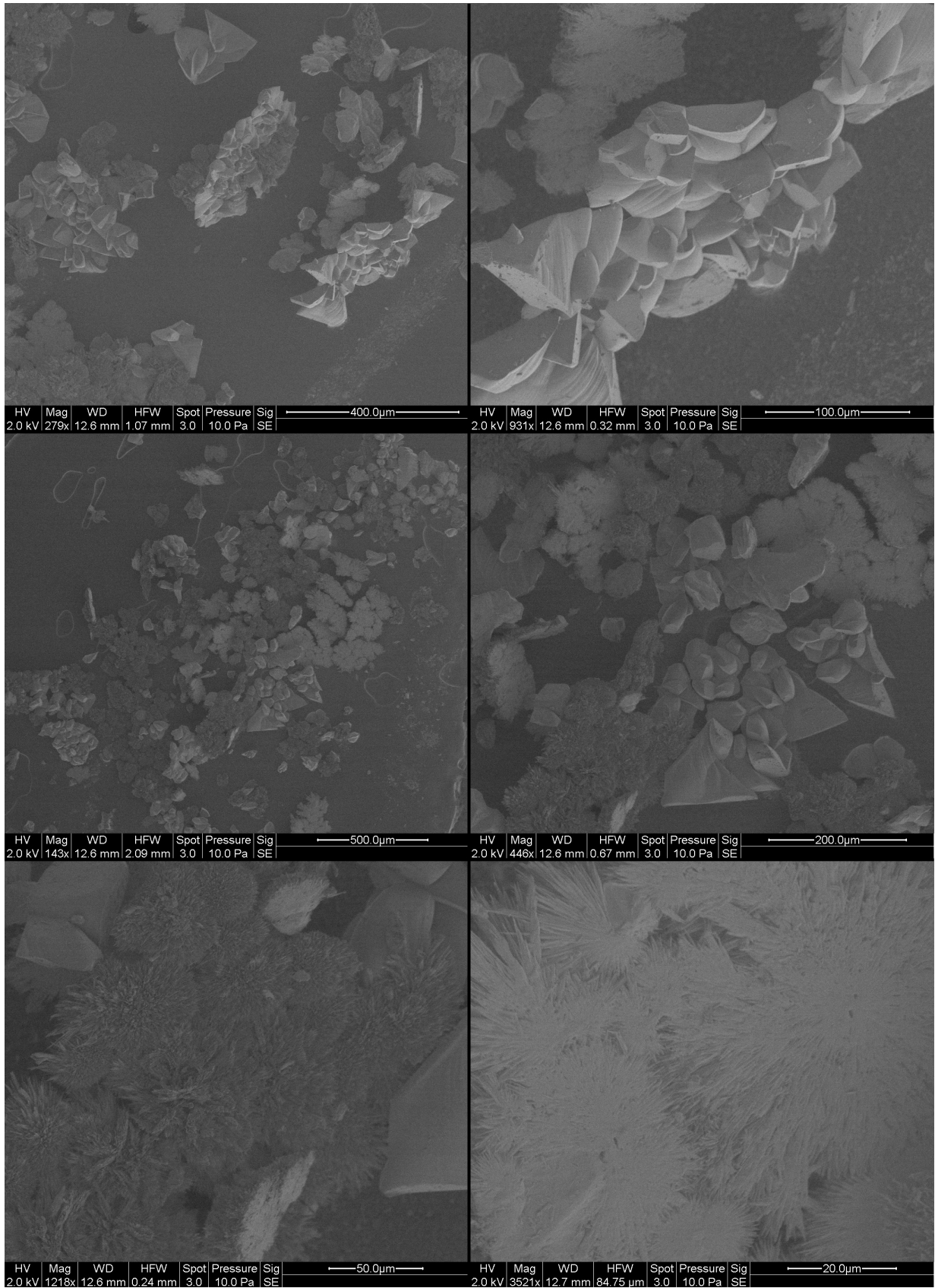


Figure 35: CH9. 200ppm CO₂, 25°C, 10mM Ca²⁺

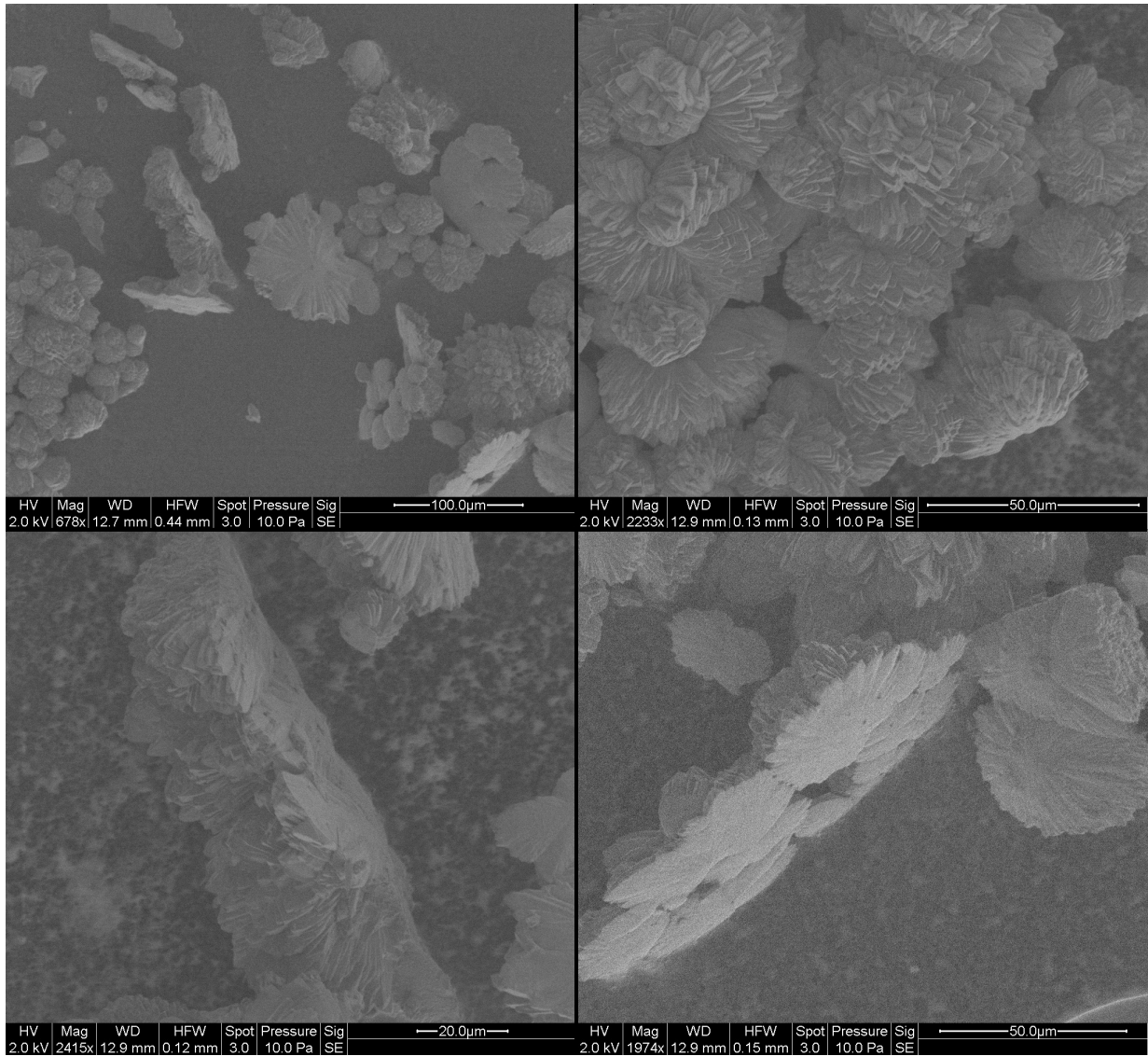


Figure 36: CH10. 200ppm CO₂, 10°C, 30mM Ca²⁺

3 Additional figures

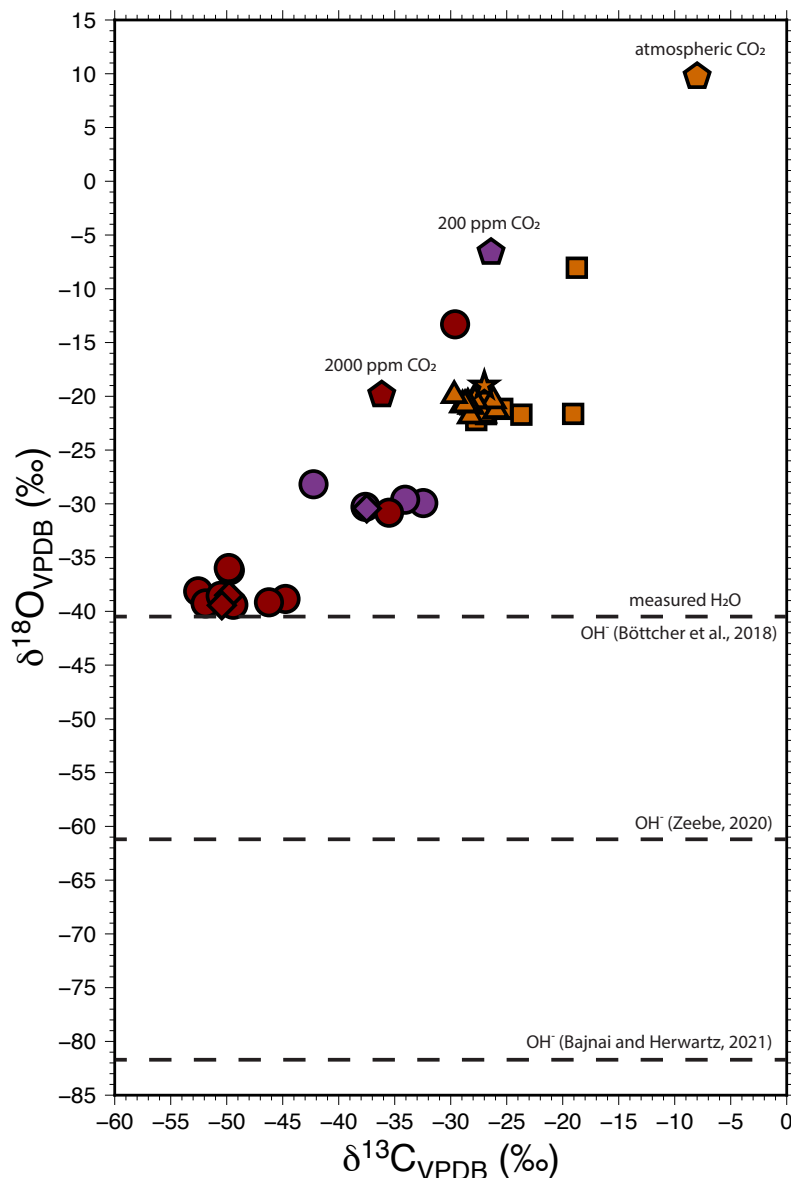


Figure 37: Isotopic compositions of precipitated carbonates and gas sources. The data are grouped by gas source, with the 200 ppm CO₂ experiments in purple, 2000 ppm CO₂ experiments in red, and open air experiments using the modern CO₂ atmosphere in orange. Pentagons are the gas sources, circles are 25°C gas tank experiments, diamonds are 10°C gas tank experiments, upright triangles are 25°C open air experiments, inverted triangles are 10°C experiments, and squares are open air experiment crystals from the bottom of the beaker. The isotopic outliers are CH21 and CH23 (red circles), and CH22 beaker crystals (orange square). The orange star represents the most highly fractionated travertine from The Cedars (Christensen et al., 2021). The average measured $\delta^{18}\text{O}$ of our experimental solutions is $\approx -40.4\text{‰}$ VPDB, which would subsequently result in OH⁻ that is $\approx -61.3\text{‰}$, -81.6‰ , or -40.4‰ VPDB using $1000\ln\alpha_{\text{OH}^- - \text{H}_2\text{O}}$ from Zeebe (2020), Bajnai and Herwartz (2021), or that proposed by Böttcher et al. (2018), respectively.

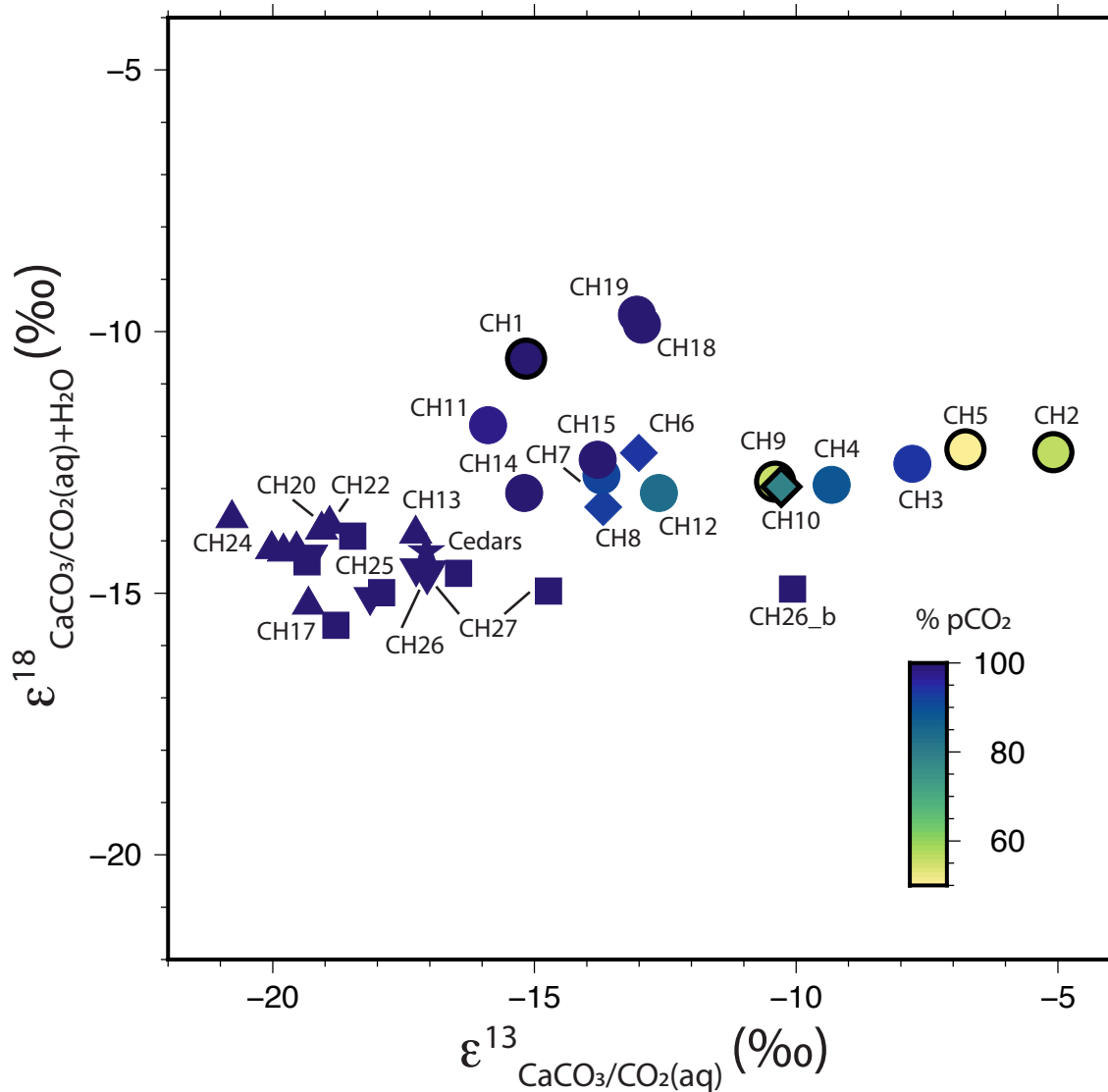


Figure 38: Carbon and bulk oxygen kinetic isotope fractionations (KIFs) for all experiments of this study, calculated as $\epsilon = (\alpha - 1) \cdot 1000$. Gas tank experiments (25°C - circles; 10°C - diamonds) on 200 ppm CO_2 (black outline) or 2000 ppm CO_2 (no outline). Open air experiments (25°C - upright triangles; 10°C - inverted triangles) with crystals from the bottom of those beakers (squares). The star represents the KIFs determined from The Cedars, California (Christensen et al., 2021). Experiments are color coded according to the average experiment pCO_2 as a percent of the pCO_2 of its gas source (i.e. 200 ppm or 2000 ppm CO_2 gas tanks). All open-air experiments are plotted as 100%.

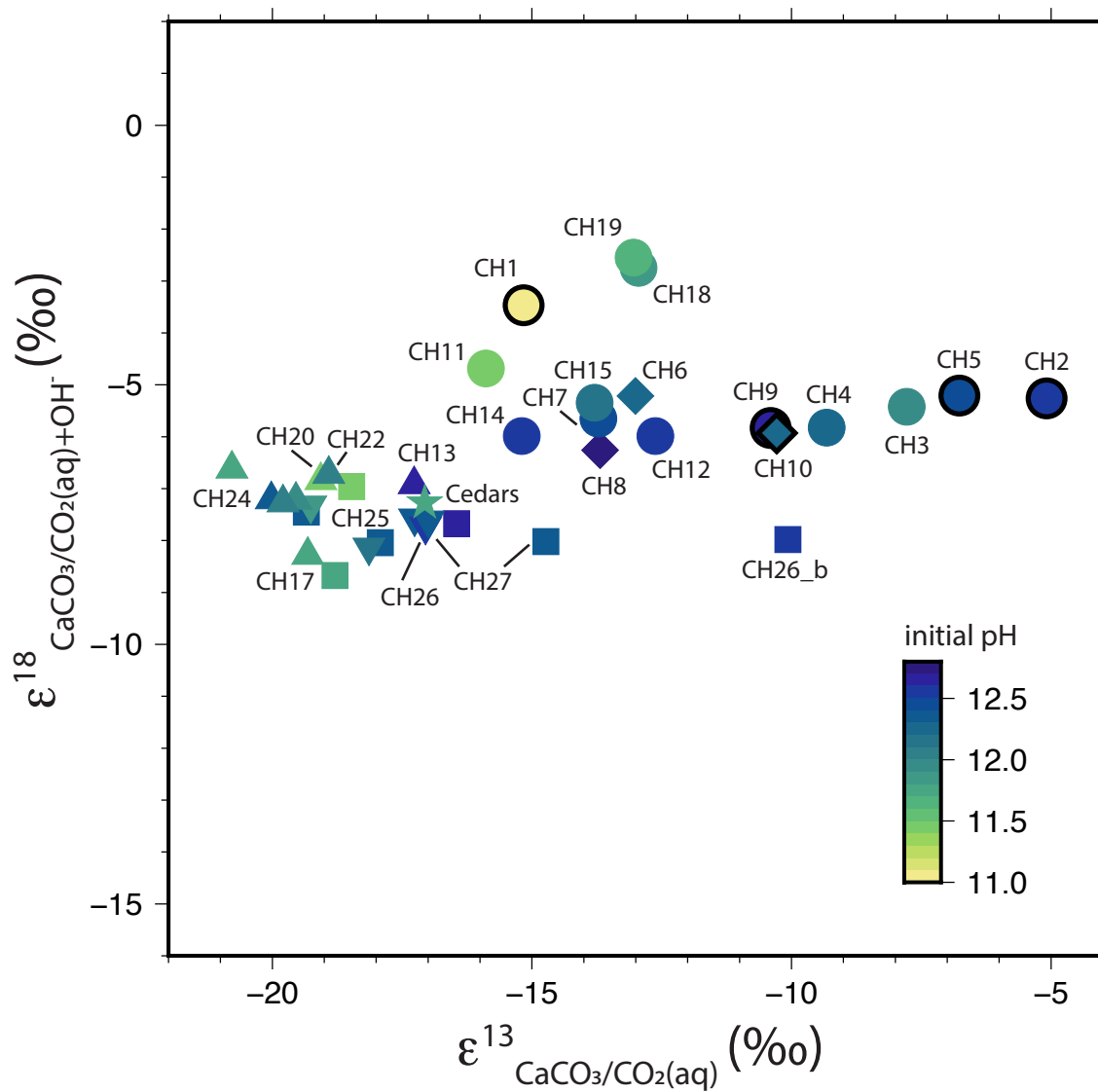


Figure 39: Carbon and bulk oxygen kinetic isotope fractionations (KIFs) for all experiments of this study, calculated as $\epsilon = (\alpha - 1) \cdot 1000$. Gas tank experiments (25°C - circles; 10°C - diamonds) on 200 ppm CO₂ (black outline) or 2000 ppm CO₂ (no outline). Open air experiments (25°C - upright triangles; 10°C - inverted triangles) with crystals from the bottom of those beakers (squares). The star represents the KIFs determined from The Cedars, California (Christensen et al., 2021). $1000\ln\alpha_{\text{OH}^- - \text{H}_2\text{O}} \approx -21.5\text{‰}$ from Zeebe (2020) is used when calculating the KIFs.

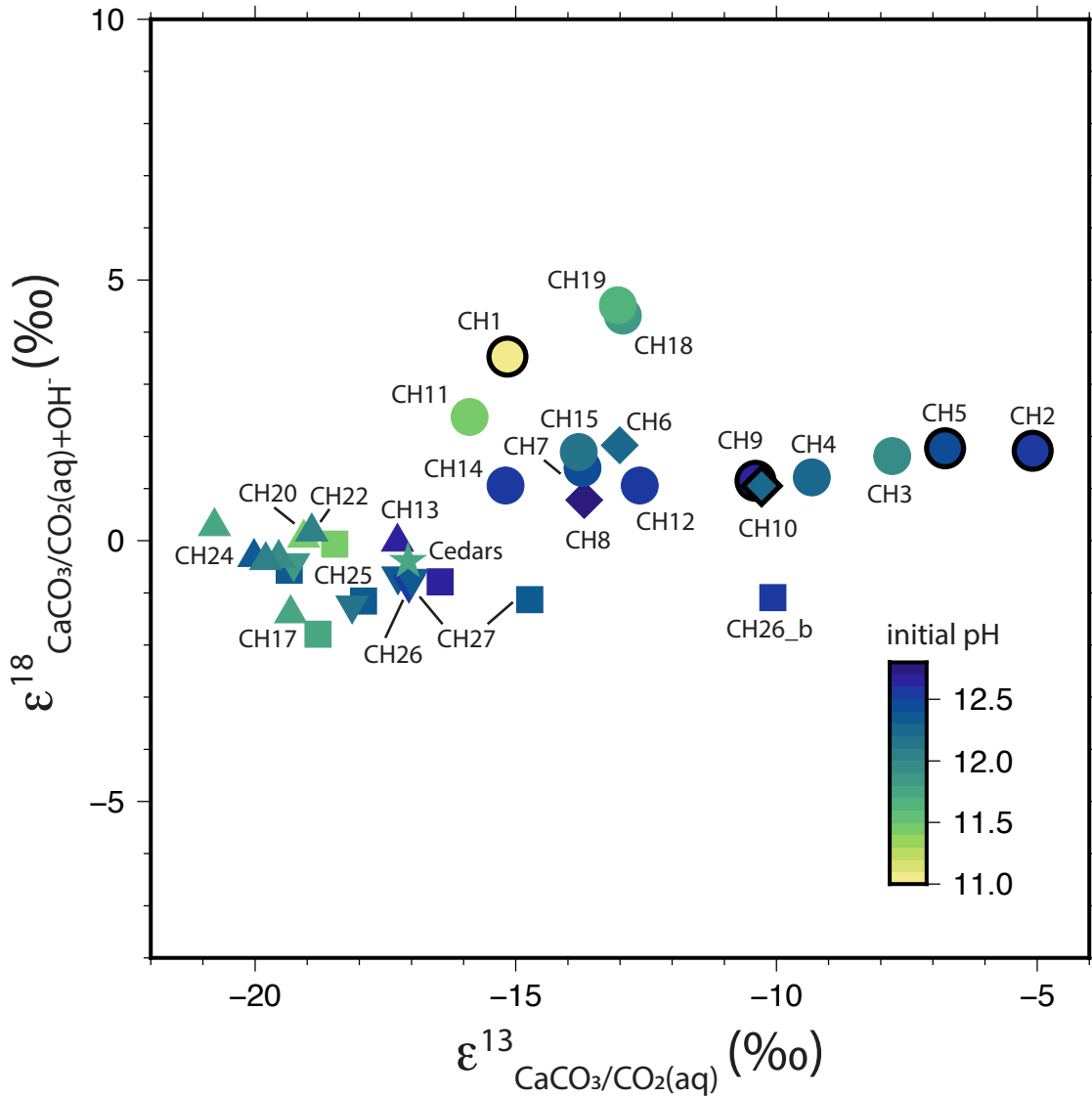


Figure 40: Carbon and bulk oxygen kinetic isotope fractionations (KIFs) for all experiments of this study, calculated as $\epsilon = (\alpha - 1) \cdot 1000$. Gas tank experiments (25°C - circles; 10°C - diamonds) on 200 ppm CO₂ (black outline) or 2000 ppm CO₂ (no outline). Open air experiments (25°C - upright triangles; 10°C - inverted triangles) with crystals from the bottom of those beakers (squares). The star represents the KIFs determined from The Cedars, California (Christensen et al., 2021). $1000\ln\alpha_{\text{OH}^- - \text{H}_2\text{O}} \approx -42.53\text{‰}$ from Bajnai and Herwartz (2021) is used when calculating the KIFs.

REFERENCES CITED

Chapter II

- Andersson M. P., Dobberschütz S., Sand K. K., Tobler D. J., De Yoreo J. J. and Stipp S. L. S. (2016) A Microkinetic Model of Calcite Step Growth. *Angew. Chemie* **128**, 11252–11256.
- Bajnai D. and Herwartz D. (2021) Kinetic Oxygen Isotope Fractionation between Water and Aqueous OH⁻ during Hydroxylation of CO₂. *ACS Earth Sp. Chem.* **5**, 3375–3384.
- Bar-Matthews M., Marean C. W., Jacobs Z., Karkanas P., Fisher E. C., Herries A. I. R., Brown K., Williams H. M., Bernatchez J., Ayalon A. and Nilssen P. J. (2010) A high resolution and continuous isotopic speleothem record of paleoclimate and paleoenvironment from 90 to 53 ka from Pinnacle Point on the south coast of South Africa. *Quat. Sci. Rev.* **29**, 2131–2145.
- Barkan E. and Luz B. (2012) High-precision measurements of ¹⁷O/¹⁶O and ¹⁸O/¹⁶O ratios in CO₂. *Rapid Commun. Mass Spectrom.* **26**, 2733–2738.
- Beck W. C., Grossman E. L. and Morse J. W. (2005) Experimental studies of oxygen isotope fractionation in the carbonic acid system at 15°, 25°, and 40°C. *Geochim. Cosmochim. Acta* **69**, 3493–3503.
- Böhm F., Eisenhauer A., Tang J., Dietzel M., Krabbenhöft A., Kisakürek B. and Horn C. (2012) Strontium isotope fractionation of planktic foraminifera and inorganic calcite. *Geochim. Cosmochim. Acta* **93**, 300–314.
- Böttcher M. E., Neubert N., Escher P., von Allmen K., Samankassou E. and Nägler T. F. (2018) Multi-isotope (Ba, C, O) partitioning during experimental carbonatization of a hyper-alkaline solution. *Chemie der Erde* **78**, 241–247.
- Bottinga Y. (1968) Calculation of Fractionation Factors for Carbon and Oxygen Isotopic Exchange in the System Calcite-Carbon Dioxide-Water. *J. Phys. Chem.* **72**, 800–807.
- Bowen G. J. and Wilkinson B. (2002) Spatial distribution of δ¹⁸O in meteoric precipitation. *Geology* **30**, 315–318.
- Brennan S. T., Lowenstein T. K. and Horita J. (2004) Seawater chemistry and the advent of biocalcification. *Geology* **32**, 473–476.

- Budd D. A., Hammes U. and Ward W. B. (2000) Cathodoluminescence in Calcite Cements: New Insights on Pb and Zn Sensitizing, Mn Activation, and Fe Quenching at Low Trace-Element Concentrations. *SEPM J. Sediment. Res.* **70**, 217–226.
- Carpenter S. J. and Lohmann K. C. (1992) Sr/Mg ratios of modern marine calcite: Empirical indicators of ocean chemistry and precipitation rate. *Geochim. Cosmochim. Acta* **56**, 1837–1849.
- Charlton S. R. and Parkhurst D. L. (2011) Modules based on the geochemical model PHREEQC for use in scripting and programming languages. *Comput. Geosci.* **37**, 1653–1663.
- Chen S., Gagnon A. C. and Adkins J. F. (2018) Carbonic anhydrase, coral calcification and a new model of stable isotope vital effects. *Geochim. Cosmochim. Acta* **236**, 179–197.
- Christensen J. N., Watkins J. M., Devriendt L. S., DePaolo D. J., Conrad M. E., Voltolini M., Yang W. and Dong W. (2021) Isotopic fractionation accompanying CO₂ hydroxylation and carbonate precipitation from high pH waters at The Cedars, California, USA. *Geochim. Cosmochim. Acta* **301**, 91–115.
- Christensen J. N., Watkins J. M., Devriendt L. S., DePaolo D. J., Conrad M. E., Voltolini M., Yang W. and Dong W. (2023) Corrigendum to “Isotopic fractionation accompanying CO₂ hydroxylation and carbonate precipitation from high pH waters at The Cedars, California, USA” [*Geochim. Cosmochim. Acta* 301 (2021) 91–115]. *Geochim. Cosmochim. Acta* **343**, 416–419.
- Clark I. D., Fontes J. C. and Fritz P. (1992) Stable isotope disequilibria in travertine from high pH waters: Laboratory investigations and field observations from Oman. *Geochim. Cosmochim. Acta* **56**, 2041–2050.
- Clark I. D. and Lauriol B. (1992) Kinetic enrichment of stable isotopes in cryogenic calcites. *Chem. Geol.* **102**, 217–228.
- Cléroux C., Cortijo E., Anand P., Labeyrie L., Bassinot F., Caillon N. and Duplessy J. C. (2008) Mg/Ca and Sr/Ca ratios in planktonic foraminifera: Proxies for upper water column temperature reconstruction. *Paleoceanography* **23**, 1–16.
- Coggon R. M., Teagle D. A. H., Smith-Duque C. E., Alt J. C. and Cooper M. J. (2010) Reconstructing Past Seawater Mg/Ca and Sr/Ca from Mid-Ocean Ridge Flank Calcium Carbonate Veins. *Science* **327**, 1114–1117.
- Coplen T. B. (2007) Calibration of the calcite-water oxygen-isotope geothermometer at Devils Hole, Nevada, a natural laboratory. *Geochim. Cosmochim. Acta* **71**, 3948–3957.
- Coplen T. B., Kendall C. and Hopple J. (1983) Comparison of stable isotope reference samples. *Nature* **302**, 236–238.
- Daëron M., Drysdale R. N., Peral M., Huyghe D., Blamart D., Coplen T. B., Lartaud F. and Zanchetta G. (2019) Most Earth-surface calcites precipitate out of isotopic equilibrium. *Nat. Commun.* **10**, 1–7.

- Davis K. J., Dove P. M., Wasylenki L. E. and De Yoreo J. J. (2004) Morphological consequences of differential Mg^{2+} incorporation at structurally distinct steps on calcite. *Am. Mineral.* **89**, 714–720.
- De Lucia M. and Kühn M. (2013) Coupling R and PHREEQC: efficient programming of geochemical models. *Energy Procedia* **40**, 464–471.
- Dennis K. J. and Schrag D. P. (2010) Clumped isotope thermometry of carbonatites as an indicator of diagenetic alteration. *Geochim. Cosmochim. Acta* **74**, 4110–4122.
- DePaolo D. J. (2011) Surface kinetic model for isotopic and trace element fractionation during precipitation of calcite from aqueous solutions. *Geochim. Cosmochim. Acta* **75**, 1039–1056.
- Devriendt L. S., Watkins J. M. and McGregor H. V. (2017) Oxygen isotope fractionation in the CaCO_3 -DIC- H_2O system. *Geochim. Cosmochim. Acta* **214**, 115–142.
- Dietzel M., Tang J., Leis A. and Köhler S. J. (2009) Oxygen isotopic fractionation during inorganic calcite precipitation - Effects of temperature, precipitation rate and pH. *Chem. Geol.* **268**, 107–115.
- Dietzel M., Usdowski E. and Hoefs J. (1992) Chemical and $^{13}\text{C}/^{12}\text{C}$ - and $^{18}\text{O}/^{16}\text{O}$ -isotope evolution of alkaline drainage waters and the precipitation of calcite. *Appl. Geochemistry* **7**, 177–184.
- Edgar K. M., Anagnostou E., Pearson P. N. and Foster G. L. (2015) Assessing the impact of diagenesis on $\delta^{11}\text{B}$, $\delta^{13}\text{C}$, $\delta^{18}\text{O}$, Sr/Ca and B/Ca values in fossil planktic foraminiferal calcite. *Geochim. Cosmochim. Acta* **166**, 189–209.
- Eigen M. (1964) Proton Transfer, Acid-Base Catalysis, and Enzymatic Hydrolysis. Part I: ELEMENTARY PROCESSES. *Angew. Chemie Int. Ed. English* **3**, 1–19.
- Eiler J. M. (2007) “Clumped-isotope” geochemistry—The study of naturally-occurring, multiply-substituted isotopologues. *Earth Planet. Sci. Lett.* **262**, 309–327.
- Escobar J., Hodell D. A., Brenner M., Curtis J. H., Gilli A., Mueller A. D., Anselmetti F. S., Ariztegui D., Grzesik D. A., Pérez L., Schwab A. and Guilderson T. P. (2012) A \sim 43-ka record of paleoenvironmental change in the Central American lowlands inferred from stable isotopes of lacustrine ostracods. *Quat. Sci. Rev.* **37**, 92–104.
- Falk E. S., Guo W., Paukert A. N., Matter J. M., Mervine E. M. and Kelemen P. B. (2016) Controls on the stable isotope compositions of travertine from hyperalkaline springs in Oman: Insights from clumped isotope measurements. *Geochim. Cosmochim. Acta* **192**, 1–28.
- Fantle M. S. (2015) Calcium isotopic evidence for rapid recrystallization of bulk marine carbonates and implications for geochemical proxies. *Geochim. Cosmochim. Acta* **148**, 378–401.
- Folk R. L. (1994) Interaction between bacteria, nanobacteria, and mineral precipitation in hot springs of Central Italy. *Géographie Phys. Quat.* **48**, 233–246.

- Gabitov R. I., Watson E. B. and Sadekov A. (2012) Oxygen isotope fractionation between calcite and fluid as a function of growth rate and temperature: An in situ study. *Chem. Geol.* **306–307**, 92–102.
- Ghosh P., Adkins J., Affek H., Balta B., Guo W., Schauble E. A., Schrag D. and Eiler J. M. (2006) ^{13}C - ^{18}O bonds in carbonate minerals: A new kind of paleothermometer. *Geochim. Cosmochim. Acta* **70**, 1439–1456.
- Ghosh P., Eiler J., Campana S. E. and Feeney R. F. (2007) Calibration of the carbonate “clumped isotope” paleothermometer for otoliths. *Geochim. Cosmochim. Acta* **71**, 2736–2744.
- Green M. and Taube H. (1963) Isotopic fractionation in the OH^- - H_2O exchange reaction. *J. Phys. Chem.* **67**, 1565–1566.
- Grotzinger J. P. and Kasting J. F. (1993) New constraints on Precambrian ocean composition. *J. Geol.* **101**, 235–243.
- Guo W. (2009) *Carbonate Clumped Isotope Thermometry: Application to Carbonaceous Chondrites and Effects of Kinetic Isotope Fractionation*. PhD thesis. California Institute of Technology.
- Guo W. (2020) Kinetic clumped isotope fractionation in the DIC- H_2O - CO_2 system: Patterns, controls, and implications. *Geochim. Cosmochim. Acta* **268**, 230–257.
- Guo W. and Zhou C. (2019) Triple oxygen isotope fractionation in the DIC- H_2O - CO_2 system: A numerical framework and its implications. *Geochim. Cosmochim. Acta* **246**, 541–564.
- Habermann D. (2002) Quantitative cathodoluminescence (CL) spectroscopy of minerals: Possibilities and limitations. *Mineral. Petrol.* **76**, 247–259.
- Halevy I. and Bachan A. (2017) The geologic history of seawater pH. *Science* **355**, 1069–1071.
- Hardie L. A. (1996) Secular variation in seawater chemistry: An explanation for the coupled secular variation in the mineralogies of marine limestones and potash evaporites over the past 600 m.y. *Geology* **24**, 279.
- Helgeson H. C. and Kirkham D. H. (1976) Theoretical Prediction of the Thermodynamic Properties of Aqueous Electrolytes At High Pressures and Temperatures - 3. Equation of State for Aqueous Species At Infinite Dilution. *Am J Sci* **276**, 97–240.
- Hill P. S., Tripathi A. K. and Schauble E. A. (2014) Theoretical constraints on the effects of pH, salinity, and temperature on clumped isotope signatures of dissolved inorganic carbon species and precipitating carbonate minerals. *Geochim. Cosmochim. Acta* **125**, 610–652.
- Ichikuni M. (1973) Partition of strontium between calcite and solution: effect of substitution by manganese. *Chem. Geol.* **11**, 315–319.

- Jiang, L. Q., Carter, B. R., Feely, R. A., Lauvset, S. K. and Olsen, A. (2019) Surface ocean pH and buffer capacity: past, present and future. *Sci Rep* **9**, 18624.
- Kelson J. R., Huntington K. W., Schauer A. J., Saenger C. and Lechler A. R. (2017) Toward a universal carbonate clumped isotope calibration: Diverse synthesis and preparatory methods suggest a single temperature relationship. *Geochim. Cosmochim. Acta* **197**, 104–131.
- Kim S.-T., Hillaire-Marcel C. and Mucci A. (2006) Mechanisms of equilibrium and kinetic oxygen isotope effects in synthetic aragonite at 25 °C. *Geochim. Cosmochim. Acta* **70**, 5790–5801.
- Kim S.-T. and O’Neil J. R. (1997) Equilibrium and nonequilibrium oxygen isotope effects in synthetic carbonates. *Geochim. Cosmochim. Acta* **61**, 3461–3475.
- Kluge T., John C. M., Jourdan A. L., Davis S. and Crawshaw J. (2015) Laboratory calibration of the calcium carbonate clumped isotope thermometer in the 25-250°C temperature range. *Geochim. Cosmochim. Acta* **157**, 213–227.
- Kupriyanova E. V and Pronina N. A. (2011) Carbonic Anhydrase: Enzyme That Has Transformed the Biosphere. *Russ. J. Plant Physiol.* **58**, 197–209.
- Larsen K., Bechgaard K. and Stipp S. L. S. (2010) The effect of the Ca^{2+} to CO_3^{2-} activity ratio on spiral growth at the calcite 1014 surface. *Geochim. Cosmochim. Acta* **74**, 2099–2109.
- Lemarchand D., Wasserburg G. J. and Papanastassiou D. A. (2004) Rate-controlled calcium isotope fractionation in synthetic calcite. *Geochim. Cosmochim. Acta* **68**, 4665–4678.
- Levitt N. P., Eiler J. M., Romanek C. S., Beard B. L., Xu H. and Johnson C. M. (2018) Near Equilibrium ^{13}C - ^{18}O Bonding During Inorganic Calcite Precipitation Under Chemo-Stat Conditions. *Geochemistry, Geophys. Geosystems* **19**, 901–920.
- Lopez O., Zuddas P. and Faivre D. (2009) The influence of temperature and seawater composition on calcite crystal growth mechanisms and kinetics: Implications for Mg incorporation in calcite lattice. *Geochim. Cosmochim. Acta* **73**, 337–347.
- Lowenstein T. K., Timofeeff M. N., Brennan S. T., Hardie L. A. and Demicco R. V. (2001) Oscillations in Phanerozoic seawater chemistry: Evidence from fluid Inclusions. *Science* **294**, 1086–1088.
- Machel H.-G. (1985) Cathodoluminescence in Calcite and Dolomite and its Chemical Interpretation. *Geosci. Canada* **12**, 139–147.
- Mackensen A. and Schmiiedl G. (2019) Stable carbon isotopes in paleoceanography: atmosphere, oceans, and sediments. *Earth-Science Rev.* **197**, 102893.
- Major R. P. and Wilber R. J. (1991) Crystal habit, geochemistry, and cathodoluminescence of magnesian calcite marine cements from the lower slope of Little Bahama Bank. *Geol. Soc. Am. Bull.* **103**, 461–471.

- Mason R. A. (1987) Ion microprobe analysis of trace elements in calcite with an application to the cathodoluminescence zonation of limestone cements from the Lower Carboniferous of South Wales, U.K. *Chem. Geol.* **64**, 209–224.
- Mavromatis V., Gautier Q., Bosc O. and Schott J. (2013) Kinetics of Mg partition and Mg stable isotope fractionation during its incorporation in calcite. *Geochim. Cosmochim. Acta* **114**, 188–203.
- Mavromatis V., Montouillout V., Noireaux J., Gaillardet J. and Schott J. (2015) Characterization of boron incorporation and speciation in calcite and aragonite from co-precipitation experiments under controlled pH, temperature and precipitation rate. *Geochim. Cosmochim. Acta* **150**, 299–313.
- Mavromatis V., Schmidt M., Botz R., Comas-Bru L. and Oelkers E. H. (2012) Experimental quantification of the effect of Mg on calcite-aqueous fluid oxygen isotope fractionation. *Chem. Geol.* **310–311**, 97–105.
- McCaffrey M. A., Lazar B. and Holland H. D. (1987) The Evaporation Path of Seawater and the Coprecipitation of Br⁻ and K⁺ with Halite. *J. Sediment. Petrol.* **57**, 928–937.
- McConnaughey T. (1989) ¹³C and ¹⁸O isotopic disequilibrium in biological carbonates: I. Patterns. *Geochim. Cosmochim. Acta* **53**, 151–162.
- McCrea J. M. (1950) On the Isotopic Chemistry of Carbonates and a Paleotemperature Scale. *J. Chem. Phys.* **18**, 849–857.
- Millero F. J., Graham T. B., Huang F., Bustos-Serrano H. and Pierrot D. (2006) Dissociation constants of carbonic acid in seawater as a function of salinity and temperature. *Mar. Chem.* **100**, 80–94.
- Millero F., Huang F., Graham T. and Pierrot D. (2007) The dissociation of carbonic acid in NaCl solutions as a function of concentration and temperature. *Geochim. Cosmochim. Acta* **71**, 46–55.
- Mook W. G. (1986) ¹³C in atmospheric CO₂. *Netherlands J. Sea Res.* **20**, 211–223.
- Morse J. W., Wang Q. and Tsio M. Y. (1997) Influences of temperature and Mg:Ca ratio on CaCO₃ precipitates from seawater. *Geology* **25**, 85–87.
- Nielsen L. C., DePaolo D. J. and De Yoreo J. J. (2012) Self-consistent ion-by-ion growth model for kinetic isotopic fractionation during calcite precipitation. *Geochim. Cosmochim. Acta* **86**, 166–181.
- O’Leary M. H. (1988) Carbon Isotopes in Photosynthesis. *Bioscience* **38**, 328–336.
- Paquette J. and Reeder R. J. (1995) Relationship between surface structure, growth mechanism, and trace element incorporation in calcite. *Geochim. Cosmochim. Acta* **59**, 735–749.

- Passey B. H. and Henkes G. A. (2012) Carbonate clumped isotope bond reordering and geospeedometry. *Earth Planet. Sci. Lett.* **351–352**, 223–236.
- Peral M., Daëron M., Blamart D., Bassinot F., Dewilde F., Smialkowski N., Isguder G., Bonnin J., Jorissen F., Kissel C., Michel E., Vázquez Riveiros N. and Waelbroeck C. (2018) Updated calibration of the clumped isotope thermometer in planktonic and benthic foraminifera. *Geochim. Cosmochim. Acta* **239**, 1–16.
- Pingitore N. E., Eastman M. P., Sandidge M., Oden K. and Freiha B. (1988) The coprecipitation of manganese(II) with calcite: an experimental study. *Mar. Chem.* **25**, 107–120.
- Pinsent B. R. W., Pearson L. and Roughton F. J. W. (1956) The kinetics of combination of carbon dioxide with ammonia. *Trans. Faraday Soc.* **52**, 1594–1598.
- Richter D. K., Götze T., Götze J. and Neuser R. D. (2003) Progress in application of cathodoluminescence (CL) in sedimentary petrology. *Mineral. Petrol.* **79**, 127–166.
- Sade Z. and Halevy I. (2017) New constraints on kinetic isotope effects during CO₂(aq) hydration and hydroxylation: Revisiting theoretical and experimental data. *Geochim. Cosmochim. Acta* **214**, 246–265.
- Sade Z., Yam R., Shemesh A. and Halevy I. (2020) Kinetic fractionation of carbon and oxygen isotopes during BaCO₃ precipitation. *Geochim. Cosmochim. Acta* **280**, 395–422.
- Srivastava A. and Verkouteren R. M. (2018) Metrology for stable isotope reference materials: ¹³C/¹²C and ¹⁸O/¹⁶O isotope ratio value assignment of pure carbon dioxide gas samples on the Vienna PeeDee Belmnite-CO₂ scale using dual-inlet mass spectrometry. *Anal. Bioanal. Chem.* **410**, 4153–4163.
- Sun W., Jayaraman S., Chen W., Persson K. A. and Ceder G. (2015) Nucleation of metastable aragonite CaCO₃ in seawater. *Proc. Natl. Acad. Sci. U. S. A.* **112**, 3199–3204.
- Swart P. K., Burns S. J. and Leder J. J. (1991) Fractionation of the stable isotopes of oxygen and carbon in carbon dioxide during the reaction of calcite with phosphoric acid as a function of temperature and technique. *Chem. Geol. Isot. Geosci. Sect.* **86**, 89–96.
- Tang J., Dietzel M., Fernandez A., Tripathi A. K. and Rosenheim B. E. (2014) Evaluation of kinetic effects on clumped isotope fractionation (Δ_{47}) during inorganic calcite precipitation. *Geochim. Cosmochim. Acta* **134**, 120–136.
- Tang J., Köhler S. J. and Dietzel M. (2008) Sr²⁺/Ca²⁺ and ⁴⁴Ca/⁴⁰Ca fractionation during inorganic calcite formation: I. Sr incorporation. *Geochim. Cosmochim. Acta* **72**, 3718–3732.
- Tang J., Niedermayr A., Köhler S. J., Böhm F., Kisakürek B., Eisenhauer A. and Dietzel M. (2012) Sr²⁺/Ca²⁺ and ⁴⁴Ca/⁴⁰Ca fractionation during inorganic calcite formation: III. Impact of salinity/ionic strength. *Geochim. Cosmochim. Acta* **77**, 432–443.

- Teng H. H., Dove P. M. and De Yoreo J. J. (2000) Kinetics of calcite growth: Surface processes and relationships to macroscopic rate laws. *Geochim. Cosmochim. Acta* **64**, 2255–2266.
- Tripathi A. K., Hill P. S., Eagle R. A., Mosenfelder J. L., Tang J., Schauble E. A., Eiler J. M., Zeebe R. E., Uchikawa J., Coplen T. B., Ries J. B. and Henry D. (2015) Beyond temperature: Clumped isotope signatures in dissolved inorganic carbon species and the influence of solution chemistry on carbonate mineral composition. *Geochim. Cosmochim. Acta* **166**, 344–371.
- Trolier M., White J. W. C., Tans P. P., Masarie K. A. and Gemery P. A. (1996) Monitoring the isotopic composition of atmospheric CO₂: Measurements from the NOAA global air sampling network. *J. Geophys. Res. Atmos.* **101**, 25897–25916.
- Turchyn A. V. and DePaolo D. J. (2019) Seawater Chemistry Through Phanerozoic Time. *Annu. Rev. Earth Planet. Sci.* **47**, 197–224.
- Uchikawa J., Penman D. E., Zachos J. C. and Zeebe R. E. (2015) Experimental evidence for kinetic effects on B/Ca in synthetic calcite: Implications for potential B(OH)₄⁻ and B(OH)₃ incorporation. *Geochim. Cosmochim. Acta* **150**, 171–191.
- Uchikawa J. and Zeebe R. E. (2012) The effect of carbonic anhydrase on the kinetics and equilibrium of the oxygen isotope exchange in the CO₂-H₂O system: Implications for δ¹⁸O vital effects in biogenic carbonates. *Geochim. Cosmochim. Acta* **95**, 15–34.
- Urey H. C. (1947) The Thermodynamic Properties of Isotopic Substances. *J. Chem. Soc.*, 562–581.
- van Dijk J., Fernandez A., Storck J. C., White T. S., Lever M., Müller I. A., Bishop S., Seifert R. F., Driese S. G., Krylov A., Ludvigson G. A., Turchyn A. V., Lin C. Y., Wittkop C. and Bernasconi S. M. (2019) Experimental calibration of clumped isotopes in siderite between 8.5 and 62 °C and its application as paleo-thermometer in paleosols. *Geochim. Cosmochim. Acta* **254**, 1–20.
- Vogel J. C., Grootes P. M. and Mook W. G. (1970) Isotopic fractionation between gaseous and dissolved carbon dioxide. *Zeitschrift für Phys.* **230**, 225–238.
- Wacker U., Fiebig J., Tödter J., Schöne B. R., Bahr A., Friedrich O., Tütken T., Gischler E. and Joachimski M. M. (2014) Empirical calibration of the clumped isotope paleothermometer using calcites of various origins. *Geochim. Cosmochim. Acta* **141**, 127–144.
- Wang L., Ruiz-Agudo E., Putnis C. V. and Putnis A. (2011) Direct observations of the modification of calcite growth morphology by Li⁺ through selectively stabilizing an energetically unfavourable face. *CrystEngComm* **13**, 3962–3966.
- Wang Z., Gaetani G., Liu C. and Cohen A. (2013) Oxygen isotope fractionation between aragonite and seawater: Developing a novel kinetic oxygen isotope fractionation model. *Geochim. Cosmochim. Acta* **117**, 232–251.
- Watkins J. M. and Hunt J. D. (2015) A process-based model for non-equilibrium clumped isotope effects in carbonates. *Earth Planet. Sci. Lett.* **432**, 152–165.

- Watkins J. M., Hunt J. D., Ryerson F. J. and DePaolo D. J. (2014) The influence of temperature, pH, and growth rate on the $\delta^{18}\text{O}$ composition of inorganically precipitated calcite. *Earth Planet. Sci. Lett.* **404**, 332–343.
- Watkins J. M., Nielsen L. C., Ryerson F. J. and Depaolo D. J. (2013) The influence of kinetics on the oxygen isotope composition of calcium carbonate. *Earth Planet. Sci. Lett.* **375**, 349–360.
- Watson E. B. (2004) A conceptual model for near-surface kinetic controls on the trace- element and stable isotope composition of abiogenic calcite crystals. *Geochim. Cosmochim. Acta* **68**, 1473–1488.
- Wolthers M., Nehrke G., Gustafsson J. P. and Van Cappellen P. (2012) Calcite growth kinetics: Modeling the effect of solution stoichiometry. *Geochim. Cosmochim. Acta* **77**, 121–134.
- Yumol L. M., Uchikawa J. and Zeebe R. E. (2020) Kinetic isotope effects during CO_2 hydration: Experimental results for carbon and oxygen fractionation. *Geochim. Cosmochim. Acta* **279**, 189–203.
- Zaarur S., Affek H. P. and Brandon M. T. (2013) A revised calibration of the clumped isotope thermometer. *Earth Planet. Sci. Lett.* **382**, 47–57.
- Zachos J., Pagani H., Sloan L., Thomas E. and Billups K. (2001) Trends, rhythms, and aberrations in global climate 65 Ma to present. *Science* **292**, 686–693.
- Zeebe R. E. (1999) An explanation of the effect of seawater carbonate concentration on foraminiferal oxygen isotopes. *Geochim. Cosmochim. Acta* **63**, 2001–2007.
- Zeebe R. E. (2007) An expression for the overall oxygen isotope fractionation between the sum of dissolved inorganic carbon and water. *Geochemistry, Geophys. Geosystems* **8**, 1–7.
- Zeebe R. E. (2014) Kinetic fractionation of carbon and oxygen isotopes during hydration of carbon dioxide. *Geochim. Cosmochim. Acta* **139**, 540–552.
- Zeebe R. E. (2020) Oxygen isotope fractionation between water and the aqueous hydroxide ion. *Geochim. Cosmochim. Acta* **289**, 182–195.
- Zeebe R. E. and Wolf-Gladrow D. (2001) *CO₂ in seawater: equilibrium, kinetics, isotopes.*, Elsevier, Amsterdam.
- Zeebe R. E., Wolf-Gladrow D. A. and Jansen H. (1999) On the time required to establish chemical and isotopic equilibrium in the carbon dioxide system in seawater. *Mar. Chem.* **65**, 135–153.
- Zhang J., Quay P. D. and Wilbur D. O. (1995) Carbon isotope fractionation during gas-water exchange and dissolution of CO_2 . *Geochim. Cosmochim. Acta* **59**, 107–114.
- Zuddas P. and Mucci A. (1998) Kinetics of calcite precipitation from seawater: II. The influence of the ionic strength. *Geochim. Cosmochim. Acta* **62**, 757–766.

Chapter III

- Adkins J. F., Boyle E. A., Curry W. B. and Lutringer A. (2003) Stable isotopes in deep-sea corals and a new mechanism for “vital effects.” *Geochim. Cosmochim. Acta* **67**, 1129–1143.
- Baker E. B. (2015) Carbon and Oxygen Isotope Fractionation in Laboratory-Precipitated, Inorganic Calcite. University of Oregon.
- Beck W. C., Grossman E. L. and Morse J. W. (2005) Experimental studies of oxygen isotope fractionation in the carbonic acid system at 15°, 25°, and 40°C. *Geochim. Cosmochim. Acta* **69**, 3493–3503.
- Berner R. A. and Morse J. W. (1974) Dissolution Kinetics of Calcium Carbonate in Sea Water IV. Theory of Calcite Dissolution. *Am. J. Sci.* **274**, 108–134.
- Bertucci A., Innocenti A., Zoccola D., Scozzafava A., Allemand D., Tambutté S. and Supuran C. T. (2009) Carbonic anhydrase inhibitors: Inhibition studies of a coral secretory isoform with inorganic anions. *Bioorganic Med. Chem. Lett.* **19**, 650–653.
- Bertucci A., Innocenti A., Scozzafava A., Tambutté S., Zoccola D. and Supuran C. T. (2011a) Carbonic anhydrase inhibitors. Inhibition studies with anions and sulfonamides of a new cytosolic enzyme from the scleractinian coral *Stylophora pistillata*. *Bioorganic Med. Chem. Lett.* **21**, 710–714.
- Bertucci A., Tambutté S., Supuran C. T., Allemand D. and Zoccola D. (2011b) A New Coral Carbonic Anhydrase in *Stylophora pistillata*. *Mar. Biotechnol.* **13**, 992–1002.
- Bigeleisen J. and Mayer M. G. (1947) Calculation of Equilibrium Constants for Isotopic Exchange Reactions. *J. Chem. Phys.* **15**, 261–267.
- Brennkmeijer C. A. M., Kraft P. and Mook W. G. (1983) Oxygen isotope fractionation between CO₂ and H₂O. *Chem. Geol.* **41**, 181–190.
- Charlton S. R. and Parkhurst D. L. (2011) Modules based on the geochemical model PHREEQC for use in scripting and programming languages. *Comput. Geosci.* **37**, 1653–1663.
- Chen S., Gagnon A. C. and Adkins J. F. (2018) Carbonic anhydrase, coral calcification and a new model of stable isotope vital effects. *Geochim. Cosmochim. Acta* **236**, 179–197.
- Christensen J. N., Watkins J. M., Devriendt L. S., DePaolo D. J., Conrad M. E., Voltolini M., Yang W. and Dong W. (2021) Isotopic fractionation accompanying CO₂ hydroxylation and carbonate precipitation from high pH waters at The Cedars, California, USA. *Geochim. Cosmochim. Acta* **301**, 91–115.
- Clark I. D., Fontes J. C. and Fritz P. (1992) Stable isotope disequilibria in travertine from high pH waters: Laboratory investigations and field observations from Oman. *Geochim. Cosmochim. Acta* **56**, 2041–2050.

- Coplen T. B. (2007) Calibration of the calcite-water oxygen-isotope geothermometer at Devils Hole, Nevada, a natural laboratory. *Geochim. Cosmochim. Acta* **71**, 3948–3957.
- Coplen T. B., Kendall C. and Hopple J. (1983) Comparison of stable isotope reference samples. *Nature* **302**, 236–238. De Goeyse S., Webb A. E., Reichart G.-J. and De Nooijer L. J. (2021) Carbonic anhydrase is involved in calcification by the benthic foraminifer *Amphistegina lessonii*. *Biogeosciences* **18**, 393–401.
- De Lucia M. and Kühn M. (2013) Coupling R and PHREEQC: efficient programming of geochemical models. *Energy Procedia* **40**, 464–471.
- De Simone G. and Supuran C. T. (2012) (In)organic anions as carbonic anhydrase inhibitors. *J. Inorg. Biochem.* **111**, 117–129.
- Del Prete S., Vullo D., Scozzafava A., Capasso C. and Supuran C. T. (2014) Cloning, characterization and anion inhibition study of the δ -class carbonic anhydrase (TweCA) from the marine diatom *Thalassiosira weissflogii*. *Bioorganic Med. Chem.* **22**, 531–537.
- DePaolo D. J. (2011) Surface kinetic model for isotopic and trace element fractionation during precipitation of calcite from aqueous solutions. *Geochim. Cosmochim. Acta* **75**, 1039–1056.
- Devriendt L. S., McGregor H. V. and Chivas A. R. (2017a) Ostracod calcite records the $^{18}\text{O}/^{16}\text{O}$ ratio of the bicarbonate and carbonate ions in water. *Geochim. Cosmochim. Acta* **214**, 30–50.
- Devriendt L. S., Watkins J. M. and McGregor H. V. (2017b) Oxygen isotope fractionation in the CaCO_3 -DIC- H_2O system. *Geochim. Cosmochim. Acta* **214**, 115–142.
- Dionisio-Sese M. L. and Miyachi S. (1992) The Effect of Sodium Chloride on Carbonic Anhydrase Activity in Marine Microalgae. *J. Phycol.* **28**, 619–624.
- DOE (1994) Handbook of Methods for the Analysis of the Various Parameters of the Carbon Dioxide System in Sea water. Version 2, Dickson A. G. and Goyet C., Eds., ORNL/CDIAC-74, Oak Ridge, Tennessee.
- Furla P., Allemand D. and Orsenigo M. N. (2000) Involvement of H^+ -ATPase and carbonic anhydrase in inorganic carbon uptake for endosymbiont photosynthesis. *Am. J. Physiol. - Regul. Integr. Comp. Physiol.* **278**, R870–R881.
- Guo W. (2020) Kinetic clumped isotope fractionation in the DIC- H_2O - CO_2 system: Patterns, controls, and implications. *Geochim. Cosmochim. Acta* **268**, 230–257.
- Guo W. and Zhou C. (2019) Triple oxygen isotope fractionation in the DIC- H_2O - CO_2 system: A numerical framework and its implications. *Geochim. Cosmochim. Acta* **246**, 541–564.
- Henry R. P. (2001) Environmentally mediated carbonic anhydrase induction in the gills of euryhaline crustaceans. *J. Exp. Biol.* **204**, 991–1002.

- Hermoso M., Horner T. J., Minoletti F. and Rickaby R. E. M. (2014) Constraints on the vital effect in coccolithophore and dinoflagellate calcite by oxygen isotopic modification of seawater. *Geochim. Cosmochim. Acta* **141**, 612–627.
- Hong M. and Teng H. H. (2014) Implications of solution chemistry effects: Direction-specific restraints on the step kinetics of calcite growth. *Geochim. Cosmochim. Acta* **141**, 228–239.
- Jacobson R. L. and Langmuir D. (1974) Dissociation constants of calcite and CaHCO_3^+ from 0 to 50°C. *Geochim. Cosmochim. Acta* **38**, 301–318.
- Kim S.-T., Gebbinck C. K., Mucci A. and Coplen T. B. (2014) Oxygen isotope systematics in the aragonite–CO₂–H₂O–NaCl system up to 0.7 mol/kg ionic strength at 25 °C. *Geochim. Cosmochim. Acta* **137**, 147–158.
- Kim S.-T., Hillaire-Marcel C. and Mucci A. (2006) Mechanisms of equilibrium and kinetic oxygen isotope effects in synthetic aragonite at 25 °C. *Geochim. Cosmochim. Acta* **70**, 5790–5801.
- Kim S.-T. and O’Neil J. R. (1997) Equilibrium and nonequilibrium oxygen isotope effects in synthetic carbonates. *Geochim. Cosmochim. Acta* **61**, 3461–3475.
- Kimball J. B., Dunbar R. B. and Guilderson T. P. (2014) Oxygen and carbon isotope fractionation in calcitic deep-sea corals: Implications for paleotemperature reconstruction. *Chem. Geol.* **381**, 223–233.
- Mass T., Drake J. L., Peters E. C., Jiang W. and Falkowski P. G. (2014) Immunolocalization of skeletal matrix proteins in tissue and mineral of the coral *Stylophora pistillata*. *Proc. Natl. Acad. Sci. U. S. A.* **111**, 12728–12733.
- McConnaughey T. (1989) ¹³C and ¹⁸O isotopic disequilibrium in biological carbonates: I. Patterns. *Geochim. Cosmochim. Acta* **53**, 151–162.
- Millero F. J., Graham T. B., Huang F., Bustos-Serrano H. and Pierrot D. (2006) Dissociation constants of carbonic acid in seawater as a function of salinity and temperature. *Mar. Chem.* **100**, 80–94.
- Millero F., Huang F., Graham T. and Pierrot D. (2007) The dissociation of carbonic acid in NaCl solutions as a function of concentration and temperature. *Geochim. Cosmochim. Acta* **71**, 46–55.
- Mitsunaga K., Akasaka K., Shimada H., Fujino Y., Yasumasu I. and Numanoi H. (1986) Carbonic anhydrase activity in developing sea urchin embryos with special reference to calcification of spicules. *Cell Differ.* **18**, 257–262.
- Morse J. W. (1978) Dissolution kinetics of calcium carbonate in sea water: VI. The near-equilibrium dissolution kinetics of calcium carbonate-rich deep sea sediments. *Am. J. Sci.* **278**, 344–353.

- Moya A., Tambutté S., Bertucci A., Tambutté E., Lotto S., Vullo D., Supuran C. T., Allemand D. and Zoccola D. (2008) Carbonic anhydrase in the scleractinian coral *Stylophora pistillata*: Characterization, localization, and role in biomineralization. *J. Biol. Chem.* **283**, 25475–25484.
- Mucci A. (1983) The solubility of calcite and aragonite in seawater at various salinities, temperatures, and one atmosphere total pressure. *Am. J. Sci.* **283**, 780–799.
- Nancollas G. H. and Reddy M. M. (1971) The crystallization of calcium carbonate. II. Calcite growth mechanism. *J. Colloid Interface Sci.* **37**, 824–830.
- Nielsen L. C., DePaolo D. J. and De Yoreo J. J. (2012) Self-consistent ion-by-ion growth model for kinetic isotopic fractionation during calcite precipitation. *Geochim. Cosmochim. Acta* **86**, 166–181.
- Nielsen S. A. and Frieden E. (1972) Some chemical and kinetic properties of oyster carbonic anhydrase. *Comp. Biochem. Physiol. Part B Comp. Biochem.* **41**, 875–889.
- O’Leary M. H. (1984) Measurement of the isotope fractionation associated with diffusion of carbon dioxide in aqueous solution. *J. Phys. Chem.* **88**, 823–825.
- Pinsent B. R. W., Pearson L. and Roughton F. J. W. (1956) The kinetics of combination of carbon dioxide with ammonia. *Trans. Faraday Soc.* **52**, 1594–1598.
- Ruiz-Agudo E., Kowacz M., Putnis C. V. and Putnis A. (2010) The role of background electrolytes on the kinetics and mechanism of calcite dissolution. *Geochim. Cosmochim. Acta* **74**, 1256–1267.
- Ruiz-Agudo E., Putnis C. V., Wang L. and Putnis A. (2011) Specific effects of background electrolytes on the kinetics of step propagation during calcite growth. *Geochim. Cosmochim. Acta* **75**, 3803–3814.
- Sade Z. and Halevy I. (2017) New constraints on kinetic isotope effects during CO₂(aq) hydration and hydroxylation: Revisiting theoretical and experimental data. *Geochim. Cosmochim. Acta* **214**, 246–265.
- Sofer Z. and Gat J. R. (1972) Activities and Concentrations of Oxygen-18 in Concentrated Aqueous Salt Solutions: Analytical and Geophysical Implications. *Earth Planet. Sci. Lett.* **15**, 232–238.
- Spero H. J., Bijma J., Lea D. W. and Bernis B. E. (1997) Effect of seawater carbonate concentration on foraminiferal carbon and oxygen isotopes. *Nature* **390**, 497–500.
- Tambutté S., Holcomb M., Ferrier-Pagès C., Reynaud S., Tambutté É., Zoccola D. and Allemand D. (2011) Coral biomineralization: From the gene to the environment. *J. Exp. Mar. Bio. Ecol.* **408**, 58–78.

- Tang J., Köhler S. J. and Dietzel M. (2008) $\text{Sr}^{2+}/\text{Ca}^{2+}$ and $^{44}\text{Ca}/^{40}\text{Ca}$ fractionation during inorganic calcite formation: I. Sr incorporation. *Geochim. Cosmochim. Acta* **72**, 3718–3732.
- Taube H. (1954) Use of Oxygen Isotope Effects in the Study of Hydration of Ions. *J. Phys. Chem.* **58**, 523–528.
- Uchikawa J., Chen S., Eiler J. M., Adkins J. F. and Zeebe R. E. (2021) Trajectory and timescale of oxygen and clumped isotope equilibration in the dissolved carbonate system under normal and enzymatically-catalyzed conditions at 25 °C. *Geochim. Cosmochim. Acta* **314**, 313–333.
- Uchikawa J. and Zeebe R. E. (2012) The effect of carbonic anhydrase on the kinetics and equilibrium of the oxygen isotope exchange in the $\text{CO}_2\text{-H}_2\text{O}$ system: Implications for $\delta^{18}\text{O}$ vital effects in biogenic carbonates. *Geochim. Cosmochim. Acta* **95**, 15–34.
- Uchikawa J. and Zeebe R. E. (2013) No discernible effect of Mg^{2+} ions on the equilibrium oxygen isotope fractionation in the $\text{CO}_2\text{-H}_2\text{O}$ system. *Chem. Geol.* **343**, 1–11.
- Urey H. C. (1947) The Thermodynamic Properties of Isotopic Substances. *J. Chem. Soc.*, 562–581.
- Uzdowski E. and Hoefs J. (1993) Oxygen isotope exchange between carbonic acid, bicarbonate, carbonate, and water: A re-examination of the data of McCrea (1950) and an expression for the overall partitioning of oxygen isotopes between the carbonate species and water. *Geochim. Cosmochim. Acta* **57**, 3815–3818.
- Uzdowski E., Michaelis J., Bottcher M. E. and Hoefs J. (1991) Factors for the oxygen isotope equilibrium fractionation between aqueous and gaseous CO_2 , carbonic acid, bicarbonate, carbonate, and water (19 °C). *Z. Phys. Chem.* **170**, 237–249.
- Wang L., Ruiz-Agudo E., Putnis C. V. and Putnis A. (2011) Direct observations of the modification of calcite growth morphology by Li^+ through selectively stabilizing an energetically unfavourable face. *CrystEngComm* **13**, 3962–3966.
- Watkins J. M., DePaolo D. J. and Watson E. B. (2017) Kinetic Fractionation of Non-Traditional Stable Isotopes by Diffusion and Crystal Growth Reactions. *Rev. Mineral. Geochemistry* **82**, 85–125.
- Watkins J. M., Hunt J. D., Ryerson F. J. and DePaolo D. J. (2014) The influence of temperature, pH, and growth rate on the $\delta^{18}\text{O}$ composition of inorganically precipitated calcite. *Earth Planet. Sci. Lett.* **404**, 332–343.
- Watkins J. M., Nielsen L. C., Ryerson F. J. and DePaolo D. J. (2013) The influence of kinetics on the oxygen isotope composition of calcium carbonate. *Earth Planet. Sci. Lett.* **375**, 349–360.
- Wolthers M., Nehrke G., Gustafsson J. P. and Van Cappellen P. (2012) Calcite growth kinetics: Modeling the effect of solution stoichiometry. *Geochim. Cosmochim. Acta* **77**, 121–134.

- Yumol L. M., Uchikawa J. and Zeebe R. E. (2020) Kinetic isotope effects during CO₂ hydration: Experimental results for carbon and oxygen fractionation. *Geochim. Cosmochim. Acta* **279**, 189–203.
- Zeebe R. E. (2007) An expression for the overall oxygen isotope fractionation between the sum of dissolved inorganic carbon and water. *Geochemistry, Geophys. Geosystems* **8**, 1–7.
- Zeebe R. E. (2014) Kinetic fractionation of carbon and oxygen isotopes during hydration of carbon dioxide. *Geochim. Cosmochim. Acta* **139**, 540–552.
- Zeebe R. E. (2020) Oxygen isotope fractionation between water and the aqueous hydroxide ion. *Geochim. Cosmochim. Acta* **289**, 182–195.
- Zeebe R. E. and Wolf-Gladrow D. (2001) CO₂ in seawater: equilibrium, kinetics, isotopes. Elsevier Oceanography Series, Amsterdam.
- Zhang H., Blanco-Ameijeiras S., Hopkinson B. M., Bernasconi S. M., Mejia L. M., Liu C. and Stoll H. (2021) An isotope label method for empirical detection of carbonic anhydrase in the calcification pathway of the coccolithophore *Emiliana huxleyi*. *Geochim. Cosmochim. Acta* **292**, 78–93.
- Zuddas P. and Mucci A. (1998) Kinetics of calcite precipitation from seawater: II. The influence of the ionic strength. *Geochim. Cosmochim. Acta* **62**, 757–766.

Chapter IV

- Andersson, M. P., Dobberschütz, S., Sand, K. K., Tobler, D. J., De Yoreo, J. J., & Stipp, S. L. S. (2016a). A Microkinetic Model of Calcite Step Growth. *Angewandte Chemie*, *128*(37), 11252–11256. <https://doi.org/10.1002/ange.201604357>
- Andersson, M. P., Rodriguez-Blanco, J. D., & Stipp, S. L. S. (2016b). Is bicarbonate stable in and on the calcite surface? *Geochimica et Cosmochimica Acta*, *176*, 198–205. <https://doi.org/10.1016/j.gca.2015.12.016>
- Baker E. B. (2015). *Carbon and Oxygen Isotope Fractionation in Laboratory-Precipitated, Inorganic Calcite*. (Master's thesis). Eugene, OR: University of Oregon.
- Bar-Matthews, M., Ayalon, A., & Kaufman, A. (1997). Late Quaternary Paleoclimate in the Eastern Mediterranean Region from Stable Isotope Analysis of Speleothems at Soreq Cave, Israel. *Quaternary Research*, *47*(2), 155-168. <https://doi.org/10.1006/qres.1997.1883>
- Beck, W. C., Grossman, E. L., & Morse, J. W. (2005). Experimental studies of oxygen isotope fractionation in the carbonic acid system at 15°, 25°, and 40°C. *Geochimica et Cosmochimica Acta*, *69*(14), 3493–3503. <https://doi.org/10.1016/j.gca.2005.02.003>

- Bottinga, Y. (1968). Calculation of Fractionation Factors for Carbon and Oxygen Isotopic Exchange in the System Calcite-Carbon Dioxide-Water. *Journal of Physical Chemistry*, *72*(3), 800–807. <https://doi.org/10.1021/j100849a008>
- Charlton, S. R., & Parkhurst, D. L. (2011). Modules based on the geochemical model PHREEQC for use in scripting and programming languages. *Computers and Geosciences*, *37*(10), 1653–1663. <https://doi.org/10.1016/j.cageo.2011.02.005>
- Chen, S., Gagnon, A. C., & Adkins, J. F. (2018). Carbonic anhydrase, coral calcification and a new model of stable isotope vital effects. *Geochimica et Cosmochimica Acta*, *236*, 179–197. <https://doi.org/10.1016/j.gca.2018.02.032>
- Coplen, T. B. (2007). Calibration of the calcite-water oxygen-isotope geothermometer at Devils Hole, Nevada, a natural laboratory. *Geochimica et Cosmochimica Acta*, *71*(16), 3948–3957. <https://doi.org/10.1016/j.gca.2007.05.028>
- Daëron, M., Drysdale, R. N., Peral, M., Huyghe, D., Blamart, D., Coplen, T. B., Lartaud, F., & Zanchetta, G. (2019). Most Earth-surface calcites precipitate out of isotopic equilibrium. *Nature Communications*, *10*(1), 1–7. <https://doi.org/10.1038/s41467-019-08336-5>
- Darkins, R., Kim, Y. Y., Green, D. C., Broad, A., Duffy, D. M., Meldrum, F. C., & Ford, I. J. (2022). Calcite Kinetics for Spiral Growth and Two-Dimensional Nucleation. *Crystal Growth and Design*, *22*(7), 4431–4436. <https://doi.org/10.1021/acs.cgd.2c00378>
- De Lucia, M., & Kühn, M. (2013). Coupling R and PHREEQC: efficient programming of geochemical models. *Energy Procedia* *40*, 464–471. <https://doi.org/10.1016/j.egypro.2013.08.053>
- Devriendt, L. S., Watkins, J. M., & McGregor, H. V. (2017). Oxygen isotope fractionation in the CaCO₃-DIC-H₂O system. *Geochimica et Cosmochimica Acta*, *214*, 115–142. <https://doi.org/10.1016/j.gca.2017.06.022>
- Dietzel, M., Tang, J., Leis, A., & Köhler, S. J. (2009). Oxygen isotopic fractionation during inorganic calcite precipitation - Effects of temperature, precipitation rate and pH. *Chemical Geology*, *268*(1-2), 107–115. <https://doi.org/10.1016/j.chemgeo.2009.07.015>
- Elderfield, H., & Ganssen, G. (2000). Past temperature and $\delta^{18}\text{O}$ of surface ocean waters inferred from foraminiferal Mg/Ca ratios. *Nature*, *405*(6785), 442–445. <https://doi.org/10.1038/35013033>
- Feng, W., Casteel, R. C., Banner, J. L., & Heinze-Fry, A. (2014). Oxygen isotope variations in rainfall, drip-water and speleothem calcite from a well-ventilated cave in Texas, USA: Assessing a new speleothem temperature proxy. *Geochimica et Cosmochimica Acta*, *127*, 233–250. <https://doi.org/10.1016/j.gca.2013.11.039>
- Gabitov, R. I., Watson, E. B., & Sadekov, A. (2012). Oxygen isotope fractionation between calcite and fluid as a function of growth rate and temperature: An in situ study. *Chemical Geology*, *306–307*, 92–102. <https://doi.org/10.1016/j.chemgeo.2012.02.021>

- Gascoyne, M. (1992). Palaeoclimate determination from cave calcite deposits. *Quaternary Science Reviews*, 11(6), 609–632. [https://doi.org/10.1016/0277-3791\(92\)90074-I](https://doi.org/10.1016/0277-3791(92)90074-I)
- Gratz, A. J., Hillner, P. E., & Hansma, P. K. (1993). Step dynamics and spiral growth on calcite. *Geochimica et Cosmochimica Acta*, 57(2), 491–495. [https://doi.org/10.1016/0016-7037\(93\)90449-7](https://doi.org/10.1016/0016-7037(93)90449-7)
- Grotzinger, J. P., & Kasting, J. F. (1993). New constraints on Precambrian ocean composition. *Journal of Geology*, 101(2), 235–243. <https://doi.org/10.1086/648218>
- Halevy, I., & Bachan, A. (2017). The geologic history of seawater pH. *Science*, 355(6329), 1069–1071. <https://doi.org/10.1126/science.aal4151>
- Hong, M., & Teng, H. H. (2014). Implications of solution chemistry effects: Direction-specific restraints on the step kinetics of calcite growth. *Geochimica et Cosmochimica Acta*, 141, 228–239. <https://doi.org/10.1016/j.gca.2014.06.023>
- Jacobson, R. L., & Langmuir, D. (1974). Dissociation constants of calcite and CaHCO_3^+ from 0 to 50°C. *Geochimica et Cosmochimica Acta*, 38(2), 301–318. [https://doi.org/10.1016/0016-7037\(74\)90112-4](https://doi.org/10.1016/0016-7037(74)90112-4)
- Kempe, S., & Degens, E. T. (1985). An early soda ocean? *Chemical Geology*, 53(1–2), 95–108. [https://doi.org/10.1016/0009-2541\(85\)90023-3](https://doi.org/10.1016/0009-2541(85)90023-3)
- Kim, S.-T., & O’Neil, J. R. (1997). Equilibrium and nonequilibrium oxygen isotope effects in synthetic carbonates. *Geochimica et Cosmochimica Acta*, 61(16), 3461–3475. [https://doi.org/10.1016/S0016-7037\(97\)00169-5](https://doi.org/10.1016/S0016-7037(97)00169-5)
- Lacey, J. H., Leng, M. J., Peckover, E. N., Dean, J. R., Wilke, T., Francke, A., Zhang, X., Masi, A., & Wagner, B. (2018). Investigating the environmental interpretation of oxygen and carbon isotope data from whole and fragmented bivalve shells. *Quaternary Science Reviews*, 194, 55–61. <https://doi.org/10.1016/j.quascirev.2018.06.025>
- Larsen, K., Bechgaard, K., & Stipp, S. L. S. (2010). The effect of the Ca^{2+} to CO_3^{2-} activity ratio on spiral growth at the calcite 1014 surface. *Geochimica et Cosmochimica Acta*, 74, 2099–2109. <https://doi.org/10.1016/j.gca.2009.12.028>
- Leng, M. J., & Marshall, J. D. (2004). Palaeoclimate interpretation of stable isotope data from lake sediment archives. *Quaternary Science Reviews*, 23(7–8), 811–831. <https://doi.org/10.1016/j.quascirev.2003.06.012>
- Leng, M., Barnker, P., Greenwood, P., Roberts, N., & Reed, J. (2001). Oxygen isotope analysis of diatom silica and authigenic calcite from Lake Pinarbasi, Turkey. *Journal of Paleolimnology*, 25, 343–349. <https://doi.org/10.1023/A:1011169832093>

- Levitt, N. P., Eiler, J. M., Romanek, C. S., Beard, B. L., Xu, H., & Johnson, C. M. (2018). Near Equilibrium ^{13}C - ^{18}O Bonding During Inorganic Calcite Precipitation Under Chemo-Stat Conditions. *Geochemistry, Geophysics, Geosystems*, *19*(3), 901–920. <https://doi.org/10.1002/2017GC007089>
- McCrea, J. M. (1950). On the Isotopic Chemistry of Carbonates and a Paleotemperature Scale. *Journal of Chemical Physics* *18*(6), 849–857. <https://doi.org/10.1063/1.1747785>
- Millero, F., Huang, F., Graham, T., & Pierrot, D. (2007). The dissociation of carbonic acid in NaCl solutions as a function of concentration and temperature. *Geochimica et Cosmochimica Acta* *71*(1), 46–55. <https://doi.org/10.1016/j.gca.2006.08.041>
- Nielsen, L. C., De Yoreo, J. J., & DePaolo, D. J. (2013). General model for calcite growth kinetics in the presence of impurity ions. *Geochimica et Cosmochimica Acta*, *115*, 100–114. <https://doi.org/10.1016/j.gca.2013.04.001>
- Olsen, E. K., Watkins, J. M., & Devriendt, L. S. (2022). Oxygen isotopes of calcite precipitated at high ionic strength: CaCO_3 -DIC fractionation and carbonic anhydrase inhibition. *Geochimica et Cosmochimica Acta*, *325*, 170–186. <https://doi.org/10.1016/j.gca.2022.01.028>
- Paquette, J., & Reeder, R. J. (1995). Relationship between surface structure, growth mechanism, and trace element incorporation in calcite. *Geochimica et Cosmochimica Acta*, *59*(4), 735–749. [https://doi.org/10.1016/0016-7037\(95\)00004-J](https://doi.org/10.1016/0016-7037(95)00004-J)
- Perdikouri, C., Putnis, C. V., Kasiopas, A., & Putnis, A. (2009). An atomic force microscopy study of the growth of a calcite surface as a function of calcium/total carbonate concentration ratio in solution at constant supersaturation. *Crystal Growth and Design* *9*(10), 4344–4350. <https://doi.org/10.1021/cg900200s>
- Plummer, L. N., & Busenberg, E. (1982). The solubilities of calcite, aragonite and vaterite in CO_2 - H_2O solutions between 0 and 90°C , and an evaluation of the aqueous model for the system CaCO_3 - CO_2 - H_2O . *Geochimica et Cosmochimica Acta*, *46*(6), 1011-1040. [https://doi.org/10.1016/0016-7037\(82\)90056-4](https://doi.org/10.1016/0016-7037(82)90056-4)
- Romanek, C. S., Grossman, E. L., & Morse, J. W. (1992). Carbon isotopic fractionation in synthetic aragonite and calcite: Effects of temperature and precipitation rate. *Geochimica et Cosmochimica Acta*, *56*(1), 419–430. [https://doi.org/10.1016/0016-7037\(92\)90142-6](https://doi.org/10.1016/0016-7037(92)90142-6)
- Ruiz-Agudo, E., & Putnis, C. V. (2012). Direct observations of mineral fluid reactions using atomic force microscopy: the specific example of calcite. *Mineralogical Magazine*, *76*(1), 227–253. <https://doi.org/10.1180/minmag.2012.076.1.227>
- Ruiz-Agudo, E., Putnis, C. V., Rodriguez-Navarro, C., & Putnis, A. (2011). Effect of pH on calcite growth at constant $a_{\text{Ca}^{2+}}/a_{\text{CO}_3^{2-}}$ ratio and supersaturation. *Geochimica et Cosmochimica Acta* *75*(1), 284–296. <https://doi.org/10.1016/j.gca.2010.09.034>

- Sade, Z., Yam, R., Shemesh, A., & Halevy, I. (2020). Kinetic fractionation of carbon and oxygen isotopes during BaCO₃ precipitation. *Geochimica et Cosmochimica Acta*, *280*, 395–422. <https://doi.org/10.1016/j.gca.2020.04.025>
- Sand, K. K., Tobler, D. J., Dobberschütz, S., Larsen, K. K., Makovicky, E., Andersson, M. P., Wolthers, M., & Stipp, S. L. S. (2016). Calcite Growth Kinetics: Dependence on Saturation Index, Ca²⁺:CO₃²⁻ Activity Ratio, and Surface Atomic Structure. *Crystal Growth and Design*, *16*(7), 3602–3612. <https://doi.org/10.1021/acs.cgd.5b01792>
- Spero, H. J., Bijma, J., Lea, D. W., & Bernis, B. E. (1997). Effect of seawater carbonate concentration on foraminiferal carbon and oxygen isotopes. *Nature* *390*(6659), 497–500. <https://doi.org/10.1038/37333>
- Strassen, P., Dupuis, C., Morsi, A. M., Steurbaut, E., & Speijer, R. P. (2009). Reconstruction of a latest Paleocene shallow-marine eutrophic paleoenvironment at Sidi Nasseur (Central Tunisia) based on foraminifera, ostracoda, calcareous nannofossils and stable isotopes ($\delta^{13}\text{C}$, $\delta^{18}\text{O}$). *Geologica Acta*, *7*(1), 93–112. <https://doi.org/10.1344/105.000000273>
- Teng, H. H., Dove, P. M., & De Yoreo, J. J. (2000). Kinetics of calcite growth: Surface processes and relationships to macroscopic rate laws. *Geochimica et Cosmochimica Acta*, *64*(13), 2255–2266. [https://doi.org/10.1016/S0016-7037\(00\)00341-0](https://doi.org/10.1016/S0016-7037(00)00341-0)
- Uchikawa, J., Chen, S., Eiler, J. M., Adkins, J. F., & Zeebe, R. E. (2021). Trajectory and timescale of oxygen and clumped isotope equilibration in the dissolved carbonate system under normal and enzymatically-catalyzed conditions at 25 °C. *Geochimica et Cosmochimica Acta*, *314*, 313–333. <https://doi.org/10.1016/j.gca.2021.08.014>
- Uchikawa, J., & Zeebe, R. E. (2012). The effect of carbonic anhydrase on the kinetics and equilibrium of the oxygen isotope exchange in the CO₂-H₂O system: Implications for $\delta^{18}\text{O}$ vital effects in biogenic carbonates. *Geochimica et Cosmochimica Acta*, *95*, 15–34. <https://doi.org/10.1016/j.gca.2012.07.022>
- Urey, H. C. (1947). The Thermodynamic Properties of Isotopic Substances. *Journal of the Chemical Society*, 562–581. <https://doi.org/10.1039/JR9470000562>
- van Geldern, R., Joachimski, M. M., Day, J., Jansen, U., Alvarez, F., Yolkin, E. A., & Ma, X. P. (2006). Carbon, oxygen and strontium isotope records of Devonian brachiopod shell calcite. *Palaeogeography, Palaeoclimatology, Palaeoecology*, *240*(1-2), 47–67. <https://doi.org/10.1016/j.palaeo.2006.03.045>
- Watkins, J. M., & Devriendt, L. S. (2022). A combined model for kinetic clumped isotope effects in the CaCO₃-DIC-H₂O system. *Geochemistry, Geophysics, Geosystems*, *23*(8), e2021GC010200. <https://doi.org/10.1029/2021GC010200>
- Watkins, J. M., Hunt, J. D., Ryerson, F. J., & DePaolo, D. J. (2014). The influence of temperature, pH, and growth rate on the $\delta^{18}\text{O}$ composition of inorganically precipitated calcite. *Earth and Planetary Science Letters*, *404*, 332–343. <https://doi.org/10.1016/j.epsl.2014.07.036>

- Watkins, J. M., Nielsen, L. C., Ryerson, F. J., & DePaolo, D. J. (2013). The influence of kinetics on the oxygen isotope composition of calcium carbonate. *Earth and Planetary Science Letters*, *375*, 1–12. <https://doi.org/10.1016/j.epsl.2013.05.054>
- Wolthers, M., Charlet, L., & Van Cappellen, P. (2008). The surface chemistry of divalent metal carbonate minerals: A critical assessment of surface charge and potential data using the charge distribution multi-site ion complexation model. *American Journal of Science*, *308*(8), 905–941. <https://doi.org/10.2475/08.2008.02>
- Wolthers, M., Nehrke, G., Gustafsson, J. P., & Van Cappellen, P. (2012). Calcite growth kinetics: Modeling the effect of solution stoichiometry. *Geochimica et Cosmochimica Acta*, *77*, 121–134. <https://doi.org/10.1016/j.gca.2011.11.003>
- Zachos, J., Pagani, H., Sloan, L., Thomas, E., & Billups, K. (2001). Trends, rhythms, and aberrations in global climate 65 Ma to present. *Science*, *292*(5517), 686–693. <https://doi.org/10.1126/science.1059412>
- Zeebe, R. E. (1999). An explanation of the effect of seawater carbonate concentration on foraminiferal oxygen isotopes. *Geochimica et Cosmochimica Acta*, *63*(13-14), 2001–2007. [https://doi.org/10.1016/S0016-7037\(99\)00091-5](https://doi.org/10.1016/S0016-7037(99)00091-5)
- Zeebe, R. E. (2007). An expression for the overall oxygen isotope fractionation between the sum of dissolved inorganic carbon and water. *Geochemistry, Geophysics, Geosystems*, *8*(9), 1–7. <https://doi.org/10.1029/2007GC001663>
- Zhang, J., & Nancollas, G. H. (1998). Kink density and rate of step movement during growth and dissolution of an AB crystal in a nonstoichiometric solution. *Journal of Colloid and Interface Science*, *200*(1), 131–145. <https://doi.org/10.1006/jcis.1997.5357>
- Zhang, J., Quay, P. D., & Wilbur, D. O. (1995). Carbon isotope fractionation during gas-water exchange and dissolution of CO₂. *Geochimica et Cosmochimica Acta*, *59*(1), 107–114. [https://doi.org/10.1016/0016-7037\(95\)91550-D](https://doi.org/10.1016/0016-7037(95)91550-D)

Chapter V

- Bajnai, D., & Herwartz, D. (2021). Kinetic Oxygen Isotope Fractionation between Water and Aqueous OH⁻ during Hydroxylation of CO₂. *ACS Earth and Space Chemistry*, *5*(12), 3375–3384. <https://doi.org/10.1021/acsearthspacechem.1c00194>
- Barkan, E., & Luz, B. (2012). High-precision measurements of ¹⁷O/¹⁶O and ¹⁸O/¹⁶O ratios in CO₂. *Rapid Communications in Mass Spectrometry*, *26*(23), 2733–2738. <https://doi.org/10.1002/rcm.6400>
- Beck, W. C., Grossman, E. L., & Morse, J. W. (2005). Experimental studies of oxygen isotope fractionation in the carbonic acid system at 15°, 25°, and 40°C. *Geochimica et Cosmochimica Acta*, *69*(14), 3493–3503. <https://doi.org/10.1016/j.gca.2005.02.003>

- Böttcher, M. E., Neubert, N., Escher, P., von Allmen, K., Samankassou, E., & Nögler, T. F. (2018). Multi-isotope (Ba, C, O) partitioning during experimental carbonatization of a hyper-alkaline solution. *Chemie der Erde*, *78*(2), 241–247. <https://doi.org/10.1016/j.chemer.2018.01.001>
- Charlton, S. R., & Parkhurst, D. L. (2011). Modules based on the geochemical model PHREEQC for use in scripting and programming languages. *Computers and Geosciences*, *37*(10), 1653–1663. <https://doi.org/10.1016/j.cageo.2011.02.005>
- Chavagnac, V., Ceuleneer, G., Monnin, C., Lansac, B., Hoareau, G., & Boulart, C. (2013). Mineralogical assemblages forming at hyperalkaline warm springs hosted on ultramafic rocks: A case study of Oman and Ligurian ophiolites. *Geochemistry, Geophysics, Geosystems*, *14*(7), 2474–2495. <https://doi.org/10.1002/ggge.20146>
- Christensen, J. N., Watkins, J. M., Devriendt, L. S., DePaolo, D. J., Conrad, M. E., Voltolini, M., Yang, W., & Dong, W. (2021). Isotopic fractionation accompanying CO₂ hydroxylation and carbonate precipitation from high pH waters at The Cedars, California, USA. *Geochimica et Cosmochimica Acta*, *301*, 91–115. <https://doi.org/10.1016/j.gca.2021.01.003>
- Christensen, J. N., Watkins, J. M., Devriendt, L. S., DePaolo, D. J., Conrad, M. E., Voltolini, M., Yang, W., & Dong, W. (2023). Corrigendum to “Isotopic fractionation accompanying CO₂ hydroxylation and carbonate precipitation from high pH waters at the Cedars, California, USA” [Geochim. Cosmochim. Acta 301 (2021) 91–115], *Geochimica et Cosmochimica Acta*, *343*, 416–419. <https://doi.org/10.1016/j.gca.2022.09.022>
- Clark, I. D., Fontes, J. C., & Fritz, P. (1992). Stable isotope disequilibria in travertine from high pH waters: Laboratory investigations and field observations from Oman. *Geochimica et Cosmochimica Acta*, *56*(5), 2041–2050. [https://doi.org/10.1016/0016-7037\(92\)90328-G](https://doi.org/10.1016/0016-7037(92)90328-G)
- Coplen, T. B. (2007). Calibration of the calcite-water oxygen-isotope geothermometer at Devils Hole, Nevada, a natural laboratory. *Geochimica et Cosmochimica Acta*, *71*(16), 3948–3957. <https://doi.org/10.1016/j.gca.2007.05.028>
- De Lucia, M., & Kühn, M. (2013). Coupling R and PHREEQC: efficient programming of geochemical models. *Energy Procedia* *40*, 464–471. <https://doi.org/10.1016/j.egypro.2013.08.053>
- Devriendt, L. S., Watkins, J. M., & McGregor, H. V. (2017). Oxygen isotope fractionation in the CaCO₃-DIC-H₂O system. *Geochimica et Cosmochimica Acta*, *214*, 115–142. <https://doi.org/10.1016/j.gca.2017.06.022>
- Dietzel, M., Usdowski, E., & Hoefs, J. (1992). Chemical and ¹³C/¹²C-and ¹⁸O/¹⁶O-isotope evolution of alkaline drainage waters and the precipitation of calcite. *Applied Geochemistry*, *7*(2), 177–184. [https://doi.org/10.1016/0883-2927\(92\)90035-2](https://doi.org/10.1016/0883-2927(92)90035-2)
- Eigen, M. (1964). Proton Transfer, Acid-Base Catalysis, and Enzymatic Hydrolysis. Part I: ELEMENTARY PROCESSES. *Angewandte Chemie International Edition in English*, *3*(1), 1–19. <https://doi.org/10.1002/anie.196400011>

- Epstein, S., & Zeiri, L. (2023). Oxygen and Carbon Isotopic Compositions of Gases Respired by Humans. *Proceedings of the National Academy of Sciences of the United States of America*, 85(6), 1727–1731. <https://doi.org/https://doi.org/10.1073/pnas.85.6.1727>
- Falk, E. S., Guo, W., Paukert, A. N., Matter, J. M., Mervine, E. M., & Kelemen, P. B. (2016). Controls on the stable isotope compositions of travertine from hyperalkaline springs in Oman: Insights from clumped isotope measurements. *Geochimica et Cosmochimica Acta*, 192, 1–28. <https://doi.org/10.1016/j.gca.2016.06.026>
- Flude, S., Györe, D., Stuart, F. M., Zurakowska, M., Boyce, A. J., Haszeldine, R. S., Chalaturnyk, R., & Gilfillan, S. M. V. (2017). The inherent tracer fingerprint of captured CO₂. *International Journal of Greenhouse Gas Control*, 65(August), 40–54. <https://doi.org/10.1016/j.ijggc.2017.08.010>
- Folk, R. L. (1994). Interaction between bacteria, nannobacteria, and mineral precipitation in hot springs of Central Italy. *Géographie Physique et Quaternaire*, 48(3), 233–246.
- Giampouras, M., Garrido, C. J., Zwicker, J., Vadillo, I., Smrzka, D., Bach, W., Peckmann, J., Jiménez, P., Benavente, J., & García-Ruiz, J. M. (2019). Geochemistry and mineralogy of serpentinization-driven hyperalkaline springs in the Ronda peridotites. *Lithos*, 350–351, 105215. <https://doi.org/10.1016/j.lithos.2019.105215>
- Green, M., & Taube, H. (1963). Isotopic fractionation in the OH⁻-H₂O exchange reaction. *Journal of Physical Chemistry*, 67(7), 1565–1566. <https://doi.org/10.1021/j100801a507>
- Jacobson, R. L., & Langmuir, D. (1974). Dissociation constants of calcite and CaHCO₃⁺ from 0 to 50°C. *Geochimica et Cosmochimica Acta*, 38(2), 301–318. [https://doi.org/10.1016/0016-7037\(74\)90112-4](https://doi.org/10.1016/0016-7037(74)90112-4)
- Kelemen, P. B., & Matter, J. (2008). In situ carbonation of peridotite for CO₂ storage. *Proceedings of the National Academy of Sciences of the United States of America*, 105(45), 17295–17300. <https://doi.org/10.1073/pnas.0805794105>
- Kelly, K. E., Silcox, G. D., Sarofim, A. F., & Pershing, D. W. (2011). An evaluation of ex situ, industrial-scale, aqueous CO₂ mineralization. *International Journal of Greenhouse Gas Control*, 5(6), 1587–1595. <https://doi.org/10.1016/j.ijggc.2011.09.005>
- Kemache, N., Pasquier, L. C., Mouedhen, I., Cecchi, E., Blais, J. F., & Mercier, G. (2016). Aqueous mineral carbonation of serpentinite on a pilot scale: The effect of liquid recirculation on CO₂ sequestration and carbonate precipitation. *Applied Geochemistry*, 67, 21–29. <https://doi.org/10.1016/j.apgeochem.2016.02.003>
- Kim, S.-T., Hillaire-Marcel, C., & Mucci, A. (2006). Mechanisms of equilibrium and kinetic oxygen isotope effects in synthetic aragonite at 25 °C. *Geochimica et Cosmochimica Acta*, 70(23), 5790–5801. <https://doi.org/10.1016/j.gca.2006.08.003>

- Kitano, Y. (1962). The behavior of various inorganic ions in the separation of calcium carbonate from a bicarbonate solution, *Bulletin of the Chemical Society of Japan* 35(12), 1973–1980. <https://doi.org/10.1246/bcsj.35.1973>
- Mervine, E. M., Humphris, S. E., Sims, K. W. W., Kelemen, P. B., & Jenkins, W. J. (2014). Carbonation rates of peridotite in the Samail Ophiolite, Sultanate of Oman, constrained through ^{14}C dating and stable isotopes. *Geochimica et Cosmochimica Acta*, 126, 371–397. <https://doi.org/10.1016/j.gca.2013.11.007>
- Mook, W. (1986). ^{13}C in atmospheric CO_2 . *Netherlands Journal of Sea Research*, 20(2-3), 211–223. [https://doi.org/10.1016/0077-7579\(86\)90043-8](https://doi.org/10.1016/0077-7579(86)90043-8)
- Morrill, P. L., Kuenen, J. G., Johnson, O. J., Suzuki, S., Rietze, A., Sessions, A. L., Fogel, M. L., & Nealson, K. H. (2013). Geochemistry and geobiology of a present-day serpentinization site in California: The Cedars. *Geochimica et Cosmochimica Acta*, 109, 222–240. <https://doi.org/10.1016/j.gca.2013.01.043>
- Olsen, E. K., Watkins, J. M., & Devriendt, L. S. (2022). Oxygen isotopes of calcite precipitated at high ionic strength: CaCO_3 -DIC fractionation and carbonic anhydrase inhibition. *Geochimica et Cosmochimica Acta*, 325, 170–186. <https://doi.org/10.1016/j.gca.2022.01.028>
- Palandri, J. L., & Reed, M. H. (2004). Geochemical models of metasomatism in ultramafic systems: Serpentinization, rodingitization, and sea floor carbonate chimney precipitation. *Geochimica et Cosmochimica Acta*, 68(5), 1115–1133. <https://doi.org/10.1016/j.gca.2003.08.006>
- Pinsent, B. R. W., Pearson, L., & Roughton, F. J. W. (1956). The kinetics of combination of carbon dioxide with ammonia. *Transactions of the Faraday Society*, 52, 1594–1598. <https://doi.org/10.1039/tf9565201512>
- Sade, Z., & Halevy, I. (2017). New constraints on kinetic isotope effects during $\text{CO}_2(\text{aq})$ hydration and hydroxylation: Revisiting theoretical and experimental data. *Geochimica et Cosmochimica Acta*, 214, 246–265. <https://doi.org/10.1016/j.gca.2017.07.035>
- Sade, Z., Yam, R., Shemesh, A., & Halevy, I. (2020). Kinetic fractionation of carbon and oxygen isotopes during BaCO_3 precipitation. *Geochimica et Cosmochimica Acta*, 280, 395–422. <https://doi.org/10.1016/j.gca.2020.04.025>
- Srivastava, A., & Verkouteren, R. M. (2018). Metrology for stable isotope reference materials: $^{13}\text{C}/^{12}\text{C}$ and $^{18}\text{O}/^{16}\text{O}$ isotope ratio value assignment of pure carbon dioxide gas samples on the Vienna PeeDee Belmnite- CO_2 scale using dual-inlet mass spectrometry. *Analytical and Bioanalytical Chemistry*, 410, 4153–4163. <https://doi.org/10.1007/s00216-019-01740-2>
- Swart, P. K., Burns, S. J., & Leder, J. J. (1991). Fractionation of the stable isotopes of oxygen and carbon in carbon dioxide during the reaction of calcite with phosphoric acid as a function of temperature and technique. *Chemical Geology: Isotope Geoscience Section*, 86(2), 89–96. [https://doi.org/10.1016/0168-9622\(91\)90055-2](https://doi.org/10.1016/0168-9622(91)90055-2)

- Trolier, M., White, J. W. C., Tans, P. P., Masarie, K. A., & Gemery, P. A. (1996). Monitoring the isotopic composition of atmospheric CO₂: Measurements from the NOAA global air sampling network. *Journal of Geophysical Research Atmospheres* 101(20), 25897–25916. <https://doi.org/10.1029/96jd02363>
- Usdowski, E., & Hoefs, J. (1986). ¹³C/¹²C partitioning and kinetics of CO₂ absorption by hydroxide buffer solutions. *Earth and Planetary Science Letters*, 80(1-2), 130–134. [https://doi.org/10.1016/0012-821X\(86\)90025-7](https://doi.org/10.1016/0012-821X(86)90025-7)
- Vogel, J. C., Grootes, P. M., & Mook, W. G. (1970). Isotopic fractionation between gaseous and dissolved carbon dioxide. *Zeitschrift Für Physik*, 230(3), 225–238. <https://doi.org/10.1007/BF01394688>
- Yumol, L. M., Uchikawa, J., & Zeebe, R. E. (2020). Kinetic isotope effects during CO₂ hydration: Experimental results for carbon and oxygen fractionation. *Geochimica et Cosmochimica Acta*, 279, 189–203. <https://doi.org/10.1016/j.gca.2020.03.041>
- Zeebe, R. E. (2020). Oxygen isotope fractionation between water and the aqueous hydroxide ion. *Geochimica et Cosmochimica Acta*, 289, 182–195. <https://doi.org/10.1016/j.gca.2020.08.025>
- Zhang, J., Quay, P. D., & Wilbur, D. O. (1995). Carbon isotope fractionation during gas-water exchange and dissolution of CO₂. *Geochimica et Cosmochimica Acta*, 59(1), 107–114. [https://doi.org/10.1016/0016-7037\(95\)91550-D](https://doi.org/10.1016/0016-7037(95)91550-D)